SPELEOTHEM-BASED RECONSTRUCTION OF THE PALAEOHYDROLOGY IN THE TROPICAL WESTERN PACIFIC

accepted in fulfilment of the requirements for the degree of

DOCTOR OF NATURAL SCIENCES (Dr. rer. nat.)

from the KIT Department of
Civil Engineering, Geo- and Environmental Sciences
of the Karlsruhe Institute of Technology (KIT)
approved

DISSERTATION

of

Dipl. Geoökol. Arno Nothstein (geb. Hartmann)

born in Starnberg

Day of oral examination:	December 13, 2019
Reviewer:	Prof. Dr. Thomas Neumann
Second Reviewer:	Prof. Dr. Denis Scholz
Advisor:	Dr. Elisabeth Eiche

Karlsruhe, 2020

SPELÄOTHEM-BASIERTE REKONSTRUKTION DER PALÄOHYDROLOGIE IM TROPISCHEN WEST-PAZIFIK

Zur Erlangung des akademischen Grades eines

DOKTORS DER NATURWISSENSCHAFTEN (Dr. rer. nat.)

von der KIT Fakultät für
Bauingenieur-, Geo- und Umweltwissenschaften
des Karlsruher Instituts für Technologie (KIT)
genehmigte

DISSERTATION

von

Dipl. Geoökol. Arno Nothstein (geb. Hartmann)

geboren in Starnberg

Tag der mündlichen Prüfung:	13. Dezember 2019
Referent:	Prof. Dr. Thomas Neumann
Korreferent:	Prof. Dr. Denis Scholz
Beraterin:	Dr. Elisabeth Eiche

Karlsruhe, 2020

Acknowledgement and Funding

This work would not have been possible without the support of all the people who helped me in various ways. Therefore, I would like to express my gratitude towards them.

First and foremost, I would like to thank my supervisors and advisors: I direct my thanks to **Prof. Dr. Thomas Neumann** for entrusting me with such a challenging project, for his never-failing support and for his trust in my abilities and decisions. To **Prof. Dr. Denis Scholz** I am grateful for his willingness to act as external supervisor. I would like to thank **Dr. Elisabeth Eiche** for her long lasting support in scientific, practical and organisational matters.

I would also like to thank the members of my PhD Commission for their support: Prof. Dr. Thomas Neumann, Prof. Dr. Denis Scholz, Prof. Dr. Orphal, Prof. Dr.Ing. Dr.h.c.mult. Franz Nestmann, Prof. Dr. Nico Goldscheider and Prof. Dr. Stefan Norra.

Furthermore, I would like to express my gratitude to all my colleagues at the AGW for the motivating, productive and friendly working atmosphere. It has been a pleasure for me to work in this team. I would like to acknowledge in particular:

- **Ralf Wachter** for his infinite patience while helping me solve all sorts of technical problems. The development of the automated water sampling devices within the framework of my PhD would have been impossible without his technical expertise and his great ideas.
- **Gesine Preuss** for conducting a myriad of IR-MS measurements of speleothem powder samples and for practical advice on stable isotope analytics
- **Claudia Mößner** for the ICP-MS results I used in my PhD project
- **Beate Oetzel** for her help with XRD and CSA analyses
- **Kristian Nikoloski** for formatting the speleothems and for preparing them for microscopic analyses

I also received support from many colleagues outside the KIT. I am grateful to the caving association **SPEKUL** (Leuven, Belgium), especially to **Dr. David Lagrou** and **Lieven DeBontridder**, for training me in caving and for their help with extracting the speleothems from the karst caves in Northern Vietnam. I am also thankful to **Ho Tien Chung** and the staff members of the Vietnam Institute of Geosciences and Mineral Resources (**VIGMR**, Hanoi, Vietnam) for their appreciated support with organising and conducting the six field trips to the study area in Northern Vietnam.

To my colleagues at the Institute for Geosciences at the University of Mainz, **Dr. Dana Riechelmann, Dr. Regina Mertz-Kraus** and **M.Sc. Alexander Budsky** I am thankful for their help with formatting the speleothems and the LA-ICP-MS measurements.

I also thank **Dr. Andrea Schröder-Ritzrau, René Eichstädter** and their colleagues in radiometric dating at the Institute for Environmental Physics at the Heidelberg Acadamy of Sciences for dating the speleothems and for discussions about the plausibility of the age models constructed from the dating results.

My thanks also go to **Dr. Marc Luetscher** of the Swiss Institute for Speleology and Karst Studies (SISKA) for his valuable advice and discussions concerning the scientific and technical aspects of developing automated water sampling devices.

I also express my thanks to the cave associations "Höhlen- und Heimatverein Laichingen e.V." and "Forschungsgruppe Höhle und Karst Franken e.V.", especially to **Rolf Riek** and **Dieter Preu** and **Annette Preu**, for their support in testing the automated water sampling devices and for granting us access to the cave sites.

I would also like to thank my fellow PhD students and peers for valuable discussions on how to illustrate and present scientific results: **Dr. Alexandra Nothstein, Dr. Andreas Holbach, Dr. Nicolas Börsig, Dr. Yuan Chen, Dr. Helena Banning, Dr. Sebastian Potsch, Dr. Peter Illner, Dr. Anna Ender, M.Sc. Phlipp Holz, M.Sc. Thomas Andrew, M.Sc. Flavia Digiacomo and M.Sc. Magnus Schneider**.

For their contributions to my work and for forming productive teams with me, I would like to thank the following colleagues for whom I was happy to supervise their bachelor or master thesis: **M.Sc. Philipp Holz, M.Sc. Alexandra Roth, M.Sc. Karin Kiefer, B.Sc. Carolin Dreher, B.Sc. Fanny Heller, B.Sc. Sebastian Meyer, B.Sc. Nina Schwark, B.Sc. Peter Nickolaus, B.Sc. Yannis Geiger and B.Sc. Pia Labenski.**

I would also like to express my gratitude towards **Dr. Alexandra Nothstein** for proof-reading and valuable comments on how to write comprehensible English sentences.

Last, but certainly not least, I am thankful to my family and friends for their much appreciated support.

This work was funded by:

- a scholarship by the Graduate School for Climate and Environment (GRACE) at the KIT (Karlsruhe Institute of Technology)
- the joint research project “KaWaTech” in Vietnam (02WCL1291A), funded by the BMBF (Federal Ministry for Education and Research)
- the joint research project “KaWaTech Solutions” in Vietnam (02WCL1415), funded by the BMBF
- a grant by the Karlsruhe House of Young Scientists (KHYS) at the KIT for establishing and consolidating professional networks with scientists abroad
- coverage for the conference attendance of the Goldschmidt Conference in Paris, France in 2017 by GRACE, KIT
- coverage for the conference attendance of the GeoBremen Conference in Bremen, Germany in 2017 by GRACE, KIT

Abstract

The Monsoons form an immense and dynamic system that encompasses the entire globe that has profound impacts on almost half of the Earth's population with regard to water consumption, agriculture, energy and transportation as well as natural disasters such as floodings and land slides. They also represent integral components of the Global Climate System transporting moisture across great distances to drive the most powerful precipitating systems on Earth. In spite of their importance the Monsoons are not yet fully understood, in particular with respect to global warming and climate models need to be improved to solve this issue. To help improve climate models and to deepen the understanding of Monsoon dynamics in Southeast Asia, Part I of this thesis focuses on generating high-quality palaeo-data from two stalagmites from two caves in Northern Vietnam, within the transiton zone between the Indian Summer Monsoon (ISM) and the East Asian Summer Monsoon (EASM) from which palaeo-data are still sparse. For reconstructing past local and regional climatic conditions during the last 8,000 years of the Holocene and the transition from Heinrich Stadial 1 to the Bølling-Allerød warm period (16.2 – 13.4 ka BP), this thesis applies a multi-proxy approach combining speleothem stable oxygen and carbon isotopes, trace elements as well as fabric types in conjunction with a multi-parameter monitoring of the present-day cave environment. The results reflect the variability of the Asian Summer Monsoon (ASM) in the ISM/EASM transition zone on sub-orbital to centennial time-scales and are in line with published proxy records from stalagmites, other environmental archives and modelling results. The multi-proxy results are mainly interpreted in terms of local to supra-regional water availability and atmospheric circulation and highlight the importance of the ISM in driving the infamous and controversially discussed $\delta^{18}O$ signal in Chinese stalagmites. Considering the new multi-proxy palaeo-data, the upstream rainout mechanism appears to be the most important process in generating the supra-regional pattern of stalagmite $\delta^{18}O$ records that has emerged over the last decade. Furthermore, based on these new data, the hypothesis is formulated that precipitation feeding the Chinese stalagmites has a significant contribution of isotopically heavy rain, probably originating from a more local source such as the South China Sea. The new carbon isotope and trace element data reflect local variations in water availability as well as events of high infiltration and/or cave flooding that are reconstructed in this region for the first time.

The interpretation of speleothem proxy signals as conducted in Part I of this thesis can be both facilitated and improved by investigating the present-day environmental framework of speleothem formation at each specific study site in multi-year monitoring studies. Of particular interest is the isotopic and geochemical composition of the dripwater forming the speleothem utilised for generating geochemical time series from palaeo-data. In order to establish the fundamental linkage between changes in these proxy signals in the dripwater and the corresponding fluctuations in their natural drivers such as rainfall and cave ventilation, dripwaters need to be sampled repeatedly over the course of months to years. But, repeated manual collection of dripwater samples is not only time-consuming but also expensive and logistically challenging, particularly in remote areas with poor or no infrastructure - where most karst caves are located. As this problem can only be solved by automation, two dripwater autosamplers were developed within the framework of this thesis, both are presented and discussed in Part II. A first successful case study applying the second prototype autosampler demonstrates the technical value of the device itself as well as the scientific benefit of the data the autosampler makes accessible. For the first time, the relationship between high-frequency fluctuations in cave air CO_2 concentrations on a sub-daily time-scale and the resulting high-frequency variations in dripwater $\delta^{13}C_{DIC}$ (DIC = dissolved inorganic carbon) was established and quantified. This relationship has important implications for speleothem science in general and the interpretation of speleothem $\delta^{13}C$ records in particular.

Kurzfassung

Die Monsune bilden ein immenses und dynamisches System, das den gesamten Globus umgibt und welches fast die Hälfte der Weltbevölkerung fundamental beeinflusst, sowohl in Bezug auf Wasserverbrauch, Landwirtschaft, Energie und Verkehr, als auch in Bezug auf Naturkatastrophen wie Überschwemmungen und Erdrutsche. Sie stellen gleichzeitig integrale Komponenten des Globalen Klimasystems dar, indem sie feuchte Luftmassen über große Entfernungen hinweg transportieren und die mächtigsten Niederschlagssysteme der Erde speisen. Trotz ihrer Bedeutung sind die Monsune noch nicht vollständig verstanden, insbesondere hinsichtlich globaler Erwärmung, und Klimamodelle müssen verbessert werden, um dieses Problem zu lösen. Um die Verbesserung von Klimamodellen zu unterstützen und das Verständnis der Monsundynamik in Südostasien zu vertiefen, fokussiert Teil 1 dieser Thesis auf die Generierung hochqualitativer Paläodaten aus zwei Stalagmiten aus zwei Höhlen in Nordvietnam, innerhalb der Übergangszone zwischen dem Indischen Sommermonsun (ISM) und dem Ostasiatischen Sommermonsun (EASM), aus welcher Paläodaten immer noch kaum vorhanden sind. Für die Rekonstruktion der lokalen und regionalen Klimabedingungen während der letzten 8.000 Jahre des Holozäns und während des Übergangs von dem Heinrich Stadial 1 zu der Bølling-Allerød Warmphase (16.2 – 13.4 ka BP) wird in dieser Thesis ein Multiproxyansatz angewendet, welcher die stabilen Isotope von Sauerstoff und Kohlenstoff, Spurenelemente sowie Kristallmorphologie-Typen kombiniert, in Verbindung mit einem Multiparameter-Monitoring der heutigen Höhlenumgebung. Die Ergebnisse spiegeln die Variabilität des Asiatischen Sommermonsuns (ASM) innerhalb der Übergangszone zwischen ISM und EASM auf sub-orbitaler Zeitskala bis zur Zeitskala von Jahrhunderten wider, in Übereinstimmung mit veröffentlichten Proxyaufzeichnungen aus Stalagmiten, anderen Umweltarchiven sowie Ergebnissen von Modellsimulationen. Die Multiproxyergebnisse werden vorrangig im Sinne von lokaler bis supra-regionaler Wasserverfügbarkeit und atmosphärischer Zirkulation interpretiert und unterstreichen die Bedeutung des ISM als Initiator des berühmten und kontrovers diskutierten $\delta^{18}O$-Signals in chinesischen Stalagmiten. Unter Berücksichtigung der neuen Multiproxy-Paläodaten scheint der Mechanismus des luvseitigen Ausregnens (upstream rainout mechanism) der wichtigste Prozess zu sein, welcher das supra-regionale Muster von Stalagmit-basierten $\delta^{18}O$-Aufzeichnungen erschafft, welches in den letzten zehn Jahren zutage getreten ist. Zudem wird basierend auf diesen neuen Daten die Hypothese aufgestellt, dass der Niederschlag, der die chinesischen Stalagmiten gebildet hat, einen signifikanten Anteil an isotopisch schwerem Regen hat, welcher sich wahrscheinlich aus einer nähergelegenen Quelle speist, etwa aus dem Chinesischen Meer. Die neuen Daten zu Kohlenstoffisotopen und Spurenelementen spiegeln lokale Schwankungen in der Wasserverfügbarkeit wider, sowie Ereignisse besonders hoher Infiltration und/oder Höhlenüberflutungen, welche damit in dieser Region zum ersten Mal rekonstruiert werden.

Die Interpretation von Proxysignalen aus Speläothemen, wie in Teil 1 dieser Thesis durchgeführt, kann vereinfacht und verbessert werden, indem die heutigen Umwelt-Rahmenbedingungen in Bezug auf die Speläothembildung an dem jeweiligen Untersuchungsort in mehrjährigen Monitoring-Studien untersucht werden. Von besonderem Interesse ist hierbei die isotopische und geochemische Zusammensetzung des Tropfwassers, welches die Speläotheme bildet, die für die Generierung der geochemischen Zeitreihen aus Paläodaten verwendet werden. Um die fundamentale Verknüpfung zwischen Veränderungen dieser Proxysignale im Tropfwasser und den entsprechenden Schwankungen in deren natürlichen Auslösern wie etwa Niederschlag und Höhlenbelüftung herzustellen, müssen Tropfwässer über mehrere Monate bis Jahre wiederholt beprobt werden. Die wiederholte händische Tropfwasserbeprobung ist jedoch nicht nur zeitaufwänding, sondern auch teuer und logistisch anspruchsvoll, vor allem in weit entlegenen Gebieten mit schlechter oder ohne Infrastruktur – in denen sich die meisten Karsthöhlen befinden. Da dieses Problem nur durch Automatisierung gelöst werden kann, wurden im Rahmen dieser Thesis zwei automatische Tropfwasser-Probenehmer entwickelt, sie werden in Teil II dargestellt und diskutiert. Eine erste erfolgreiche Fallstudie unter Einsatz des zweiten Probenehmer-Prototypen zeigt den technischen Wert des Geräts selbst auf sowie den wissenschaftlichen Nutzen der Daten, die der automatische Probenehmer zugänglich macht. Zum ersten Mal wurde die Beziehung zwischen hoch-frequenten Schwankungen der CO_2-Konzentration in der Höhlenluft auf Zeitskalen von unter einem Tag und den daraus resultierenden hoch-frequenten Änderungen in den $\delta^{13}C_{DIC}$-Werten (DIC = gelöster anorganischer Kohlenstoff) im Tropfwasser hergestellt und quantifiziert. Diese Beziehung hat wichtige Implikationen für die Speläothemforschung im Allgemeinen und die Interpretation von $\delta^{13}C$-Aufzeichnungen in Speläothemen im Besonderen.

“Look deep into nature and you will understand everything better.”

- Albert Einstein -

Table of Contents

List of Figures

List of Tables

1 Introduction

To many, the Monsoon is merely an abstract and distant phenomenon sporadically reported on in the weather report. However, in reality, the American, the African, the Australian and the Asian Monsoons together form an immense and dynamic system that encompasses the entire globe (Figure 2.19; Schönwiese, 2013) that has profound impacts on almost half of the Earth's population, in a direct or an indirect sense. The regions directly influenced by the Monsoons are among the most populated ones on Earth so that "the occurrence of extreme events, such as heavy precipitation or droughts, can have significant impacts on millions of people who live in monsoon regions and rely on water for human consumption, agriculture, energy, and transportation" (Carvalho & Jones, 2016). Not only do billions of people depend on the fresh water supplied by the Monsoons, Monsoons can also have devastating effects on human lives through their capacity to cause natural disasters such as floodings and land slides that kill people every year.

However, Monsoons not only supply water and endanger human lives, they also represent integral components of the Global Climate System. In contrast to the much narrower historical definition of Monsoons, today they are defined as "planetary manifestations of pronounced thermal contrasts between large land masses and ocean basins enhanced by the existence of high elevations and plateaus, such as the Tibetan Plateau" (Carvalho & Jones, 2016). As Carvalho and Jones (2016) put it, within the Global Climate System the Monsoons constitute "efficient engines [that] pump moisture from large ocean basins across great distances in meandering flows that reach tropical lands during summer to drive the most powerful precipitating systems on Earth".

In spite of the importance of the Monsoons for the world's population as well as for global climate and despite the scientific progress of the last decades in understanding the Monsoons, in general, "there are many unresolved questions of how the continual warming of the planet will affect the monsoons" (Carvalho & Jones, 2016). To answer theses questions, the climate models simulating the Monsoons need to be improved. This is especially true for Southeast Asia where the Monsoon dynamics are currently not well understood. While current climate models are capable of capturing the large-scale features in atmospheric circulation, they fail to reproduce modern-day meteorlogical observations of the timing of maximum rainfall over Indochina and of interannual rainfall variability in Southeast Asia (Prof. Gideon Henderson; www.earth.ox.ac.uk/research-groups/isotopes-and-climate/asian-monsoon/; accessed: March 15th, 2019).

However, improving climate models requires information on past climatic conditions (palaeo-data) that act as a reference the model simulations can be tested against. Palaeo-data gained from natural archives such as ice cores or speleothems are also fundamental to improving the

understanding of Monsoon dynamics which, in turn, is crucial for both disaster and resource management with regard to the Monsoons.

To achieve this goal, the first part of this PhD thesis (Part I) focuses on generating high-quality palaeo-data from two speleothems (stalagmites) from two caves in Northern Vietnam, Southeast Asia. This region is particularly well-suited for helping close the gaps in the geographical coverage with palaeo-data as palaeo-data from speleothems are still sparse in the tropics (McDermott, 2004).

Speleothems can be defined as "dense and crystalline secondary precipitates in caves that are primarily made up of the mineral calcite" (Ford & Williams, 2007). As environmental archives, they have the capacity to effectively record information about climatic and environmental conditions that have prevailed during their formation, in the form of geochemical parameters that are "proxies" for the actual climatic and environmental parameters (Fairchild et al., 2006). Therefore, speleothems can be used to reconstruct past climates and environments and they are remarkably well suited for it for several reasons (Section 2.1.4), including their capacity to record a number of different geochemical proxy signals, such as stable isotope ratios and trace element concentrations. To achieve a more reliable and more comprehensive reconstruction of the past, the first part of this PhD thesis applies a multi-proxy approach, combining speleothem stable oxygen and carbon isotopes, trace elements as well as fabric types.

However, these speleothem proxy signals can be challenging to interpret. To enable the interpretation of these geochemical time series or to increase their interpretability investigating the present-day environmental framework of speleothem formation at each specific study site is also crucial. Such investigations offer the opportunity to understand the way each drip site feeding the studied speleothems reacts to changes in meterological and environmental conditions such as rainfall, temperature or atmospheric circulation. By establishing the linkage between changes in the proxy signals in the dripwater and the corresponding fluctuations in their driving factors, this knowledge can be extrapolated to the past in order to achieve a more comprehensive and reliable reconstruction of past climates and environments.

Because a specific drip site may be governed in its behaviour by a certain suite of forcing mechanisms that differs from that of other drip sites, even within the same cave, extensive present-day monitoring studies of each drip site are strongly recommended to identify the respective main controlling factors (Fairchild & Baker, 2012). For optimal results, such monitoring studies should be conducted over several seasons (years) and include measurements of meteorological parameters, the chemical and isotopic composition of dripwaters, drip rate and the fundamental properties of the cave atmosphere such as temperature, relative humidity and pCO_2 (Lachniet, 2009).

But, repeated manual collection of dripwater samples is not only time-consuming but also expensive and logistically challenging, particularly in remote areas with poor or no infrastructure - where most karst caves are located. As this problem can only be solved by

automation, two dripwater autosamplers were developed within the framework of this PhD thesis. Both are presented and discussed in the second part of this thesis (Part II).

Part I:
SPELEOTHEM-BASED RECONSTRUCTION OF THE PALAEOHYDROLOGY IN THE TROPICAL WESTERN PACIFIC

2 State of the Art

2.1 Karst and Speleothem Formation

As already mentioned in the Introduction speleothems grow in areas dominated by carbonate rock. The global distribution of these areas is shown in Figure 2.1.

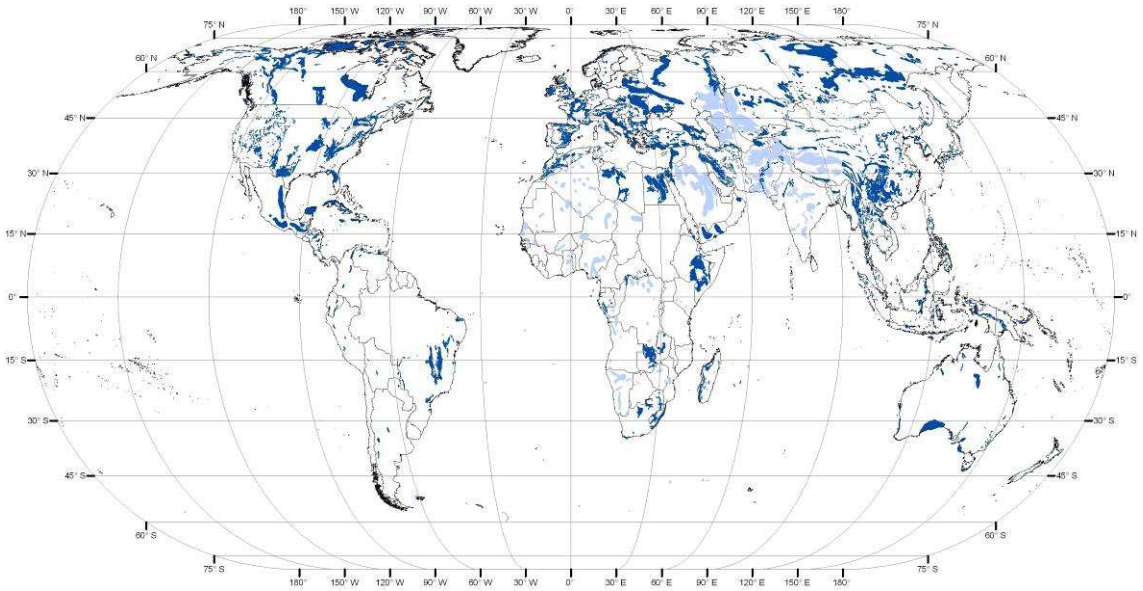

Figure 2.1: Major carbonate rock outcrops of the world. Dark-blue shading illustrates pure and continuous carbonate rock, light-blue shading indicates impure or discontinuous carbonate rock. Map from Ford & Williams (2007), produced using GIS on Eckert IV equal-area projection from regional maps; updated by Paul Williams & Yin Ting Fong, available on http://web.env.auckland.ac.nz/our_research/karst/, accessed: 26th July 2016.

Compared to other types of rock, carbonate bedrock is generally relatively soluble (Bahlburg & Breitkreuz, 2012) if brought into contact with meteoric water. In those cases where the carbonate bedrock is also dense, massive and pure, it features a low primary (matrix) porosity. Both factors – high solubility and low primary porosity – make carbonate bedrock highly susceptible to the process of karstification, the formation of karst (Ford & Williams, 2007).

2.1.1 Karst and Karstification

Karst can therefore be defined as a "terrain with distinctive hydrology and landforms that arise from a combination of high rock solubility and well developed secondary (fracture) porosity […] characterised by sinking streams, caves, enclosed depressions, fluted rock outcrops, and large springs" (Ford &Williams, 2007).

Karst landscapes develop over time under the influence of meteoric water in contact with carbon dioxide (CO_2) with which it forms carbonic acid (H_2CO_3) that dissolves the carbonate bedrock. This process leads to the high secondary porosity typical of karst landscapes and is illustrated in the following based on the concept of the Carbonate / Carbonic Acid System:

This system describes the interactions and transformations of the different inorganic species of carbon (C) in aqueous natural systems, which include CO_2, the bicarbonate ion HCO_3^- and the carbonate ion, CO_3^{2-} which are summarised by the term of dissolved inorganic carbon (DIC). Depending on pH value, DIC is distributed between these inorganic species as illustrated in Figure 2.2.

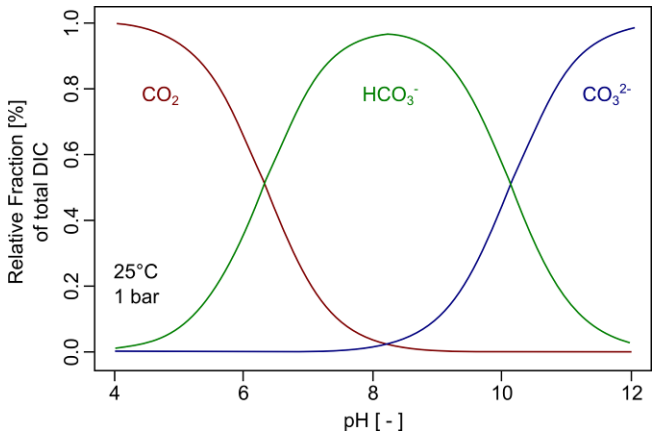

Figure 2.2: Distribution between the different inorganic carbon species in aqueous solution depending on pH value, computed for 25°C and 1 bar. Modified from Appelo & Postma (2005).

The first step of carbonate bedrock dissolution is the physical dissolution of gaseous CO_2 in water according to Henry's Law partitioning, i.e. $C_{solution} = K_H \times pCO_2$, where K_H is the Henry's Law constant and pCO_2 is the partial pressure of CO_2 above the solution (Darling et al., 2006):

$$CO_2\,(g) \leftrightarrow CO_2\,(aq) \qquad 2.1$$

Part of the dissolved CO_2 reacts with water to form H_2CO_3, that subsequently deprotonates:

$$CO_2\,(aq) + H_2O\,(aq) \leftrightarrow HCO_3^-\,(aq) + H^+\,(aq) \quad 2.2$$

$$HCO_3^-\,(aq) \leftrightarrow CO_3^{2-}\,(aq) + H^+\,(aq) \quad 2.3$$

While the chemical exchange between the different DIC species occurs relatively fast, the step of CO_2 dissolution in water is rate-determining (Darling et al., 2006). As will be illustrated in Section 2.4, this has implications on speleothem carbon isotopy.

The entire process of carbonic acid dissolving solid carbonate phases is fundamental to karstification and can be summarised as follows:

$$CaCO_3\,(s) + CO_2\,(g) + H_2O\,(aq) \leftrightarrow Ca^{2+}\,(aq) + 2\,HCO_3^-\,(aq) \quad 2.4$$

Given sufficient time, this process continues until a thermodynamic equilibrium is reached between carbonate (here: calcite) dissolution and precipitation (Darling et al., 2006) at which point the solution is saturated with calcite. The backward reaction of Equation 2.4 describes the precipitation of calcite from solution:

$$Ca^{2+}\,(aq) + 2\,HCO_3^-\,(aq) \leftrightarrow CaCO_3\,(s) + CO_2\,(g) + H_2O\,(aq) \quad 2.5$$

Combined, the above described reactions lead to the formation of the typical vertical structure of carbonate bedrock at an advanced stage of karstification (Figure 2.3) as the natural context of speleothems.

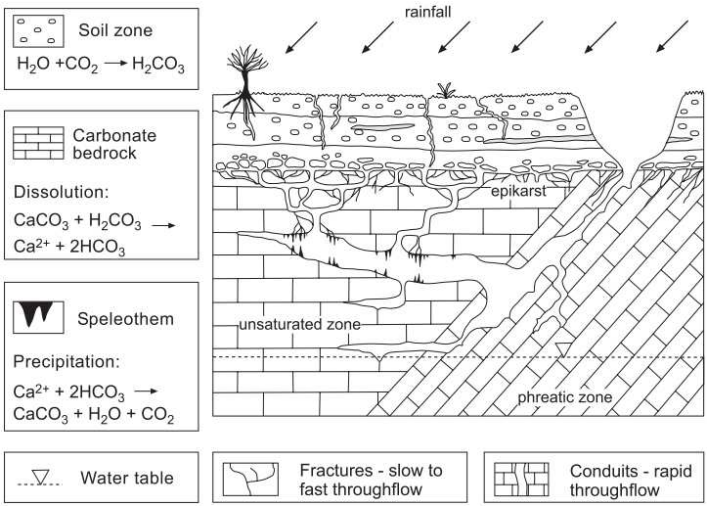

Figure 2.3: Environmental setting and vertical structure of carbonate karst landscapes. Insets show the primary chemical processes leading to speleothem formation, and different types of porosity and flow regime. From Fairchild et al. (2007).

Meteoric water infiltrates into the biologically active soil zone. As a result of both microbial decay of organic matter (OM) and plant (root) and animal respiration, the soil zone is strongly enriched in CO_2, with CO_2 concentrations of up to 1-3 weight-% (Blume et al., 2016) compared to the atmosphere, where present-day CO_2 partial pressures (pCO_2) are about 400 ppmV (Le Quéré et al., 2015). Infiltrating water and CO_2 react to carbonic acid which, together with biogenic acids, leads to chemical dissolution of the carbonate bedrock, leaving the carbonate rock underneath the soil zone strongly fissured. As water tends to be undersaturated with respect to carbonate within this fissured zone (the upper epikarst) and the overlying soil zone, they are referred to as dissolution zone where calcite dissolution predominates.

As carbonate dissolution proceeds during downward percolation of water (Equation 2.4), the Carbonate / Carbonic Acid System approaches thermodynamic equilibrium and eventually percolating waters become saturated with respect to carbonate. Below this point, within the lower epikarst and the karst caves underneath (precipitation zone), percolating waters become oversaturated with carbonate and the resulting carbonate precipitation (Equation 2.5) leads to the formation of speleothems inside caves, as described in the following section.

2.1.2 Speleothem Formation

Le Châtelier's principle states that a chemical system in thermodynamic equilibrium will react to any disturbance that disequilibrates the system by re-establishing equilibrium via an increased forward or backward reaction (Mortimer et al., 2015). For instance, the removal of reaction products will cause an increased forward reaction, the removal of reactants will enhance the backward reaction.

For net carbonate precipitation from carbonate-saturated percolating waters (Equation 2.5) to happen, CO_2 and/or water would have to be removed from the system, as both reactants (aqueous HCO_3^- and CO_3^{2-}) cannot be supplied by any other means than by dripwater flow itself. So, in theory, speleothems could be formed by removal of CO_2 or water.

As early as 1960, Bögli had already explained the enhanced carbonate dissolution and speleothem formation observed in tropical regions with the higher amounts of organically derived CO_2 available in the tropics compared to higher latitudes. The view that speleothem formation is indeed mainly caused by CO_2-degassing rather than evaporation was confirmed four years later, by a dripwater study of Holland et al. (1964) who observed that, during $CaCO_3$ precipitation, dripwater Mg concentrations remained virtually constant. This finding indicates that evaporation does not significantly drive speleothem formation, except for a special type of speleothem (helictites; Hill & Forti, 1997).

According to Henry's Law, CO_2-degassing from a solution occurs when the pCO_2 in the solution exceeds the pCO_2 in the gas phase in contact with the solution. Such a chemical gradient can typically be found at the cave ceiling (Figure 2.3) as the cave atmosphere features pCO_2 values that can be as low as surface atmospheric pCO_2 values as a consequence of air mass exchange between the cave and outside (Spötl et al., 2005). Consequently, CO_2 degasses from the dripwater at the cave ceiling where it forms stalactites. When drops at the active tip of stalactites fall to the cave floor, the impact causes further CO_2-degassing and $CaCO_3$ precipitation, leading to the formation of stalagmites (Figure 2.4; Fairchild et al., 2007).

2.1.3 The Karst Cave

The Karst Cave is the primary locus of speleothem formation (Figure 2.4). Here, the palaeoenvironmental proxy signals are recorded within the speleothem fabrics. Both the recording and the potential modifications of the orignal proxy signals depend on the conditions and the processes that prevail within (and above) the cave (Fairchild et al., 2006).

This section only covers the conditions/processes inside the cave themselves. The way by which these conditions/processes influence the proxy signals is described in detail in the following sections .

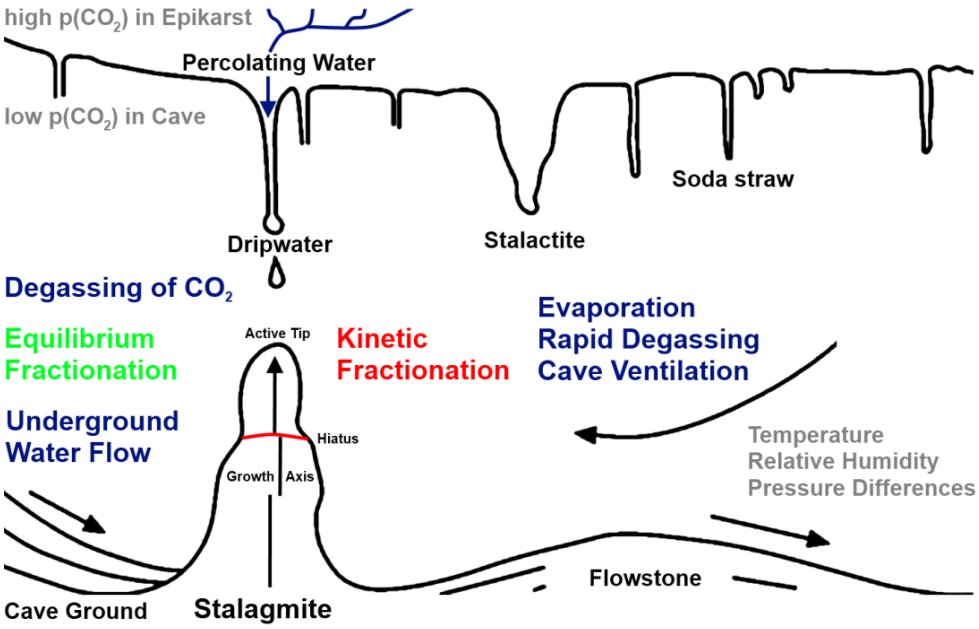

Figure 2.4: The karst cave – The formation of speleothem fabrics (black) depends on various processes (blue) and conditions (grey) that can vary over both time and space. Also illustrated are hydrological routing (top) and features of stalagmite growth (bottom) including both growth stops (hiatuses) and changes in main growth direction. Modified from Fairchild et al. (2006).

2.1.3.1 Cave Processes

Figure 2.4 illustrates the complexity of cave systems regarding the growth of speleothems, hence the process by which palaeo-proxy variables are recorded within speleothem fabrics. Several different processes impact on speleothem growth (proxy recording), such as degassing of CO_2 from dripwater, evaporation and cave ventilation, but also changes in the regional or local water table, among others (Fairchild & Baker, 2012). The cave-internal processes again relate to various cave-external processes acting within the different communicating spheres, i.e. lithosphere, hydrosphere, pedosphere, biosphere and atmosphere.

For example, changes in rainfall amount may significantly impact on infiltration, percolation and therefore dripwater flow, which would cause responses in speleothem growth rate, but on stable isotope ratios and incorporation of trace elements as well.

2.1.3.2 Cave Atmosphere

These processes again depend on a number of environmental conditions, in particular on cave air temperature as an important control on isotope fractionation (Section 2.2), on relative humidity governing evaporation processes, on partial pressure of cave air pCO_2 as a major control on speleothem growth rate as well as on air pressure differences between the inside of the cave and outside as the drivers for cave ventilation. Cave ventilation again has implications for evaporation and rapid CO_2-degassing from cave dripwaters and thus impacts on both speleothem growth rate and kinetic fractionation (Fairchild et al., 2006), as outlined in detail in the following sections.

2.1.4 Speleothems – Archives of the Past

There are a number of reasons why speleothems are remarkably well suited for reconstructing past climates and environments (Fairchild et al. 2006; Fairchild & Baker, 2012). These are summarised in the following:

1. **Absolute and highly accurate dating**: Last generation analytical instruments utilising the Uranium/Thorium (U/Th) decay chain yield very precise and accurate ages within its range of application that spans the last 600,000 years. Consequently, U/Th dating is considered to be the most robust geochronometer currently available for the late Quaternary (Hellstrom, 2006). This allows for the various geochemical time series extracted from speleothems to be compared to and matched with other records of palaeoenvironmental change. Precise chronologies are also crucial for identifying leads and lags between different components of the climate system which are necessary to determine which component is the driver and which is the responding component (McDermott, 2004).

2. **Good spatial and temporal coverage**: Speleothems can grow (quasi-)continuously and over very large time spans (10^3-10^5 years), while offering good temporal resolution (up to sub-annual). Thanks to that, even palaeoenvironmental conditions lying in the very far past can be reconstructed and processes that operate on large timescales can be identified and documented, for example glacial/interglacial cycles. Additionally, speleothems can be found in all major carbonate rock outcrop areas which are distributed over a wide spectrum of longitudes and latitudes (Figure 2.1, Section 2.1). The combination of spatial and temporal coverage of speleothems have contributed significantly to the investigation of global teleconnections between widely separated regions on Earth over the last years (Wong & Breecker, 2015). One of the most prominent examples for such a teleconnection is the linkage between Northern Hemisphere glaciation and Asian Monsoon dynamics (e.g. Cheng et al., 2016).

3. **Protection from alteration**: Speleothems are relatively well-protected from erosion and other secondary alteration processes due to the highly stable conditions in terms of speleothem growth in most caves (e.g. low likelihood of evaporative corrosion).

4. **Multiple proxies**: Speleothems record numerous physical and geochemical proxy signals, such as stable isotope ratios and trace element concentrations. If these different proxy indicators are combined in a multi-proxy approach, past events and conditions can be reconstructed a lot more reliably and in more detail.

2.2 Stable Isotope Fractionation

Isotope fractionation can be defined as a "process by which one isotope [of an isotope pair] is favoured over the other during a phase change" (Lachniet, 2009), for exampe, during evaporation from liquid to vapour or during CO_2 degassing from speleothem dripwaters. In his pioneering work dating from 1961, Craig established that the partitioning of "water isotopes", i.e. isotopes of oxygen and hydrogen in their respective combinations in the water molecule, by meteorological processes followed a systematic pattern (Lachniet, 2009). Isotope fractionation happens during any thermodynamic reaction as a consequence of differences in reaction rate of the various molecular species involved (Clark & Fritz, 1997).

Reactions resulting in isotope fractionation may be simple physical changes of state (e.g. evaporation of water to vapour) or chemical transformations (e.g. formation of H_2CO_3 from water-CO_2 interaction) that may occur in aqueous, mineral-solution and gas-solution phase systems. Fractionations caused by multi-step reactions can be expressed as the sum of all single-step fractionations (Clark & Fritz, 1997). Fractionation can take place under equilibrium conditions ("equilibrium fractionation"; Section 2.2.1), with forward and backward reactions proceeding at identical rates, or under non-equilibrium conditions ("kinetic fractionation"; Section 2.2.2). But the underlying principle remains the same, which is the difference in bond strength between the heavier and the lighter isotope of an isotope pair of a given element, for example ^{18}O vs. ^{16}O in case of oxygen.

Each molecular bond an atom forms within a molecule reaches maximum strength which corresponds to minimum potential energy, referred to as "zero-point energy" at a specific interatomic distance (Figure 2.5).

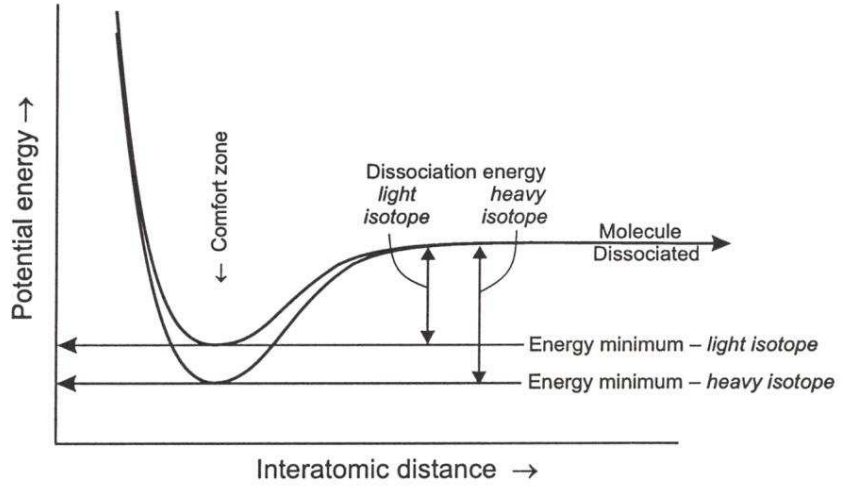

Figure 2.5: Isotope fractionation – Heavy isotopes exhibit lower potential energy minima within a molecule and therefore higher dissociation energies than do light isotopes. Light isotopes will thus react more readily during physicochemical reactions. From Clark & Fritz (1997).

The heavy isotope forms stronger bonds within the molecule (lower energy minimum), which can be mainly ascribed to its low rotational frequency (the decisive of the three molecular movements) compared to the light isotope (Clark & Fritz, 1997). For the atom to participate in any thermodynamic reaction, these molecular bonds must be broken. As the light isotope forms weaker bonds, these are more easily broken (at given thermodynamic conditions such as temperature and pressure), which causes the light isotopes to react more readily.

2.2.1 Equilibrium Fractionation

The just mentioned fundamental circumstance favours the preferential partitioning of heavy isotopes into the more condensed phase, i.e. the solid phase in mineral-solution reactions and the aqueous phase in vapour-liquid reactions. Thus in the case of oxygen, under equilibrium conditions, ^{18}O isotopes tend to become concentrated in the ocean, whereas the vapour phase in equilibrium gets enriched in ^{16}O isotopes.

In the case of stable carbon isotopes, ^{13}C as the heavy isotope is preferentially partitioned into the more condensed phase compared to ^{12}C as the light isotope. For example, in a system comprising aqueous bicarbonate and solid carbonate minerals, ^{13}C becomes enriched in the mineral phase by equilibrium fractionation (McDermott, 2004). However, the largest fractionation "step" that also dominates C-isotopy in speleothems within the Carbonate-Carbonic Acid System is the isotopic partitioning between bicarbonate ions and molecular CO_2, as outlined in detail in Section 2.4. This step is fundamental to the process of speleothem precipitation by CO_2-degassing from dripwater (McDermott, 2004).

Isotopic composition can be expressed using the δ notion, which is defined as follows (Darling et al., 2006):

$$\delta = (R_{sample}/R_{standard} - 1) \times 1000 \qquad 2.6$$

with R representing the ratio of the heavier isotope to the lighter isotope of the specific element. As differences in isotope ratios are intrinsically small, the value of 1 is subtracted and δ values are expressed in units of per mille (‰).

$R_{standard}$ is the isotope ratio of an internationally recognised standard material. In the case of O- and C-isotopes measured in carbonates such as speleothems, this standard material is Vienna Pee Dee Belemnite (V-PDB), where PDB refers to the Cretaceous belemnite formation at Peedee in South Carolina, USA.

Concordantly, $\delta^{18}O$ and $\delta^{13}C$ are both given by:

$$\delta^{18}O_{spel}[‰] = \left({}^{18}O/{}^{16}O_{sample} \Big/ {}^{18}O/{}^{16}O_{VPDB} - 1 \right) \times 1000 \qquad 2.7$$

$$\delta^{13}C_{spel}[‰] = \left({}^{13}C/{}^{12}C_{sample} \Big/ {}^{13}C/{}^{12}C_{VPDB} - 1 \right) \times 1000 \qquad 2.8$$

The δ value of the reference material (V-PDB) is 0 ‰ per definition. Therefore, material exhibiting positive δ values are referred to as "isotopically enriched", containing higher portions of the heavier isotope compared to the reference material, whereas negative δ values denote that the material is "isotopically depleted", containing higher portions of the lighter isotope compared to the reference material. The reference material for water is Vienna Standard Mean Ocean Water (V-SMOW), with its δ also being 0 ‰ per definition. While some processes relevant to speleothem-based palaeostudies are pure equilibrium fractionation processes, such as condensation, others may represent kinetic fractionation processes or a mixture of both.

2.2.2 Kinetic Fractionation

Kinetic fractionation happens under conditions far from isotopic equilibrium. Disequilibrium is caused by sudden disturbances of an existing equilibrium state, such as sudden changes in temperature, pressure or addition/removal of a reactant (Clark & Fritz, 1997). Kinetic fractionation can either enhance or diminish mass-discrimination during fractionation, depending on the reaction pathway (Clark & Fritz, 1997). For example, calcite precipitation under equilibrium conditions causes calcite to be isotopically enriched (in ^{18}O) over the aqueous bicarbonate. With increasing rate of calcite precipitation, the system moves away from isotopic equilibrium, and the isotopic difference decreases towards nil (Clark & Fritz, 1997).

A typical process potentially causing significant kinetic fractionation is evaporation. This process may occur in karst caves where it exerts a strong influence on the isotopic fraction of oxygen and carbon species. As kinetic fractionation can have strong effects and can be hard to quantify in its effect on speleothem time series, it is advantageous if speleothem deposition at or close to isotopic equilibrium can be demonstrated (Lachniet, 2009).

Furthermore, many biologically mediated reactions, such as redox reactions and photosynthesis, lead to isotopic fractionation, discriminating against the heavy isotope in the course of metabolic pathways. As biological processes often occur very rapidly and represent essentially irreversible reactions, they can often be regarded as kinetic fractionation. For instance, photosynthesis in the case of C_3-type vegetation, causes fractionation between the carbon in fixated atmospheric CO_2 and the carbon in the carbohydrates plants produce of about -17 ‰ (Clark & Fritz, 1997). Consequently, carbon of plant material is isotopically depleted relative to its source CO_2.

The third fractionation process is diffusive fractionation, which arises from differences in diffusive velocities between two isotopes of an isotope pair (Clark & Fritz, 1997). All fractionation processes (equilibrium, kinetic and diffusive) depend on temperature, with increasing temperature leading to decreasing fractionation (Figure 2.6).

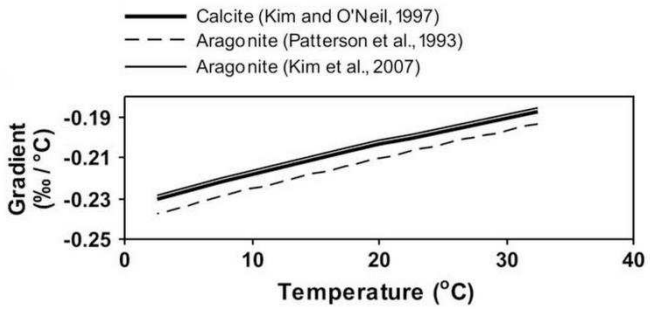

Figure 2.6: Temperature dependency of oxygen isotope fractionation between water and $CaCO_3$ (solid line = calcite; dashed line = aragonite). Isotopic fractionation expressed as $\delta^{18}O$/temperature gradient is stronger at lower temperatures. Aragonite exhibits an isotopic offset to calcite of ~0.7 to 0.8‰. From Lachniet (2009).

2.3 Oxygen Isotopes in Speleothems – Indicators of the Hydrological Cycle

The main reservoirs influencing the O-isotopy of speleothems are atmospheric moisture, precipitation and surface/groundwater (Lachniet, 2009). The two processes that predominantly control O-isotopy in these reservoirs are evaporation and condensation, and both are primarily related to temperature and relative humidity (Lachniet, 2009). As a consequence, the O-isotopic composition of speleothems can be mainly regarded as a climate signal which is generated within the hydrological cycle. Figure 2.7 schematically summarises the isotopic composition within the various reservoirs and the factors by which these are controlled.

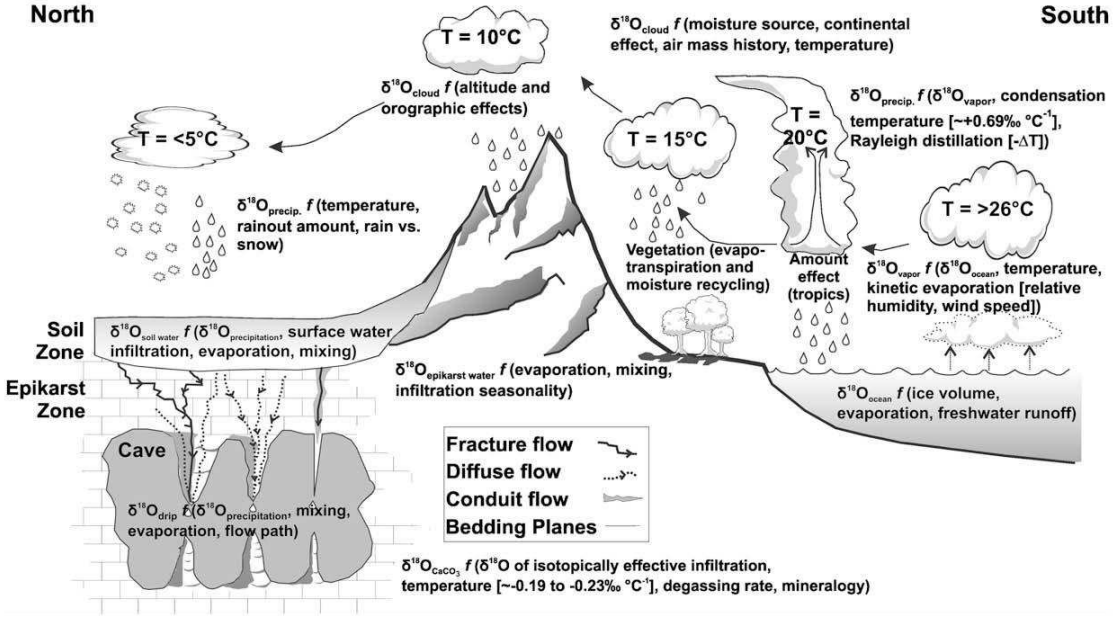

Figure 2.7: The $\delta^{18}O$ Climate Signal - The predominant controlling mechanisms are primarily related to temperature and relative humidity that determine $\delta^{18}O$ values through the various processes and phase changes in the different reservoirs, from ocean via atmosphere, hydrosphere, soil and epikarst zones to speleothem $CaCO_3$. From Lachniet (2009).

2.3.1 Generation and Transmission of the Oxygen Isotope Climate Proxy Signal

This $\delta^{18}O$ climate signal is generated within the atmosphere, starting with evaporation from the ocean as the main global moisture source. This moisture is then transported away from the source region and is subject to the fundamental process of Rayleigh distillation (Section 2.3.1.1) along the advection path. Eventually, condensation transfers atmospheric moisture to clouds that produce precipitation once sufficient droplet size is reached. Precipitation that falls on the catchment area of karst caves may then infiltrate into the ground surface, percolate downward through soil zone and epikarst to finally reach the cave, where the O-isotope signal is recorded by speleothem precipitation. On the way from the surface to the stalagmite tip, the $\delta^{18}O$ climate signal may be modified, by the process of evaporation and mixing. Signal generation and modification are discussed in the following.

2.3.1.1 Evaporation - From Ocean Water to Atmospheric Moisture

Initiation of the $\delta^{18}O$ climate signal occurs over the ocean. Its isotopic composition is mainly governed by processes that strongly relate to ocean salinity, at least in regional terms. A tendency towards heavy water isotope enrichment (high $\delta^{18}O$ values) is caused by evaporation which represents a crucial process (Lachniet, 2009).

Light isotope enrichment (low $\delta^{18}O$) is favoured by precipitation over the ocean, sea ice melt and freshwater runoff, as these inputs are commonly isotopically light with regard to oxygen. As a consequence, ocean $\delta^{18}O$ values are sensitive to the proximity to river discharge (e.g. the Mississippi River) and zones of high evaporation (e.g. the Mediterranean Ocean). Furthermore, ocean O-isotopy is impacted on by both ocean and atmospheric circulation. In combination, these factors lead to a consistent pattern of $\delta^{18}O$ values in the Earth's oceans (Figure 2.8).

Equilibrium fractionation

Equilibrium fractionation causes O-isotopic depletion of the resulting vapour, i.e. atmospheric moisture, so that it exhibits lower $\delta^{18}O$ values than its ocean counterpart. This fractionation step depends on temperature, which can be mathematically expressed as follows (Clark & Fritz, 1997), where T represents the temperature of the phase change [K]:

$$1000 \ln \alpha_{liquid-vapour} = 1.137 \left(10^6/T_k^2\right) - 0.4156 \left(\frac{10^3}{T_k}\right) - 2.0667 \qquad 2.9$$

For example, at 25°C (298.15K), the equilibrium fractionation from ocean water to vapour accounts for 9.34 ‰, which will consequently feature a $\delta^{18}O$ value of -9.34 ‰ (V-SMOW).

Kinetic fractionation

Additionally, kinetic fractionation takes place if evaporation happens under relative humidity of less than 100%, where evaporation and condensation are in disequilibrium. This may be estimated as follows (Clark & Fritz, 1997):

$$\Delta\varepsilon^{18}O_{liquid-vapour} = 14.2\ (1-h)‰ \qquad 2.10$$

$\Delta\varepsilon^{18}O_{liquid-vapour}$ represents the kinetic fractionation between liquid and vapour, whereas h denotes relative humidity. For example, kinetic fractionation associated with evaporation at a relative humidity of 85% is 2.13 ‰. Equilibrium and kinetic fractionation steps combined, the "first charge" of vapour formed from V-SMOW has a $\delta^{18}O$ value of -11.47 ‰.

Rayleigh Distillation

In contrast to evaporation, condensation of vapour to liquid, as it occurs in clouds, for instance, is a pure equilibrium process. Because ^{18}O is preferentially incorporated into the more condensed phase, $\delta^{18}O$ values of rain will be higher than that of the vapour remaining uncondensed. The latter will itself decrease slightly due to the preferential removal of ^{18}O (Lachniet, 2009).

For further condensation of atmospheric moisture to take place, the cloud temperature must decrease. Cooling of air masses may arise from several processes, such as advection into regions of lower temperature, orographic or frontal lifting, convection or convergence (Lachniet, 2009).

The four last mentioned processes lead to temperature decreases by the Joule Thompson effect, i.e. cooling due to expansion, while air parcel expansion results from lifting to greater heights where atmospheric pressure is lower. Thus, the quantity of moisture condensed (degree of condensation) – and consequently the remaining cloud vapour's $\delta^{18}O$ value - is therefore primarily controlled by the total drop in temperature and the initially available mass of moisture in the cloud (Dansgaard, 1954). This process of progressive condensation and lowering of precipitation $\delta^{18}O$ value is called Rayleigh distillation (Figure 2.9). The $\delta^{18}O$ value of the remaining vapour can be approximated by (Dansgaard, 1954):

$$\delta^{18}O_{vapour(f)} \approx \delta_0{}^{18}O_{vapour(f)} + \varepsilon^{18}O_{liquid-vapour} \times \ln f \qquad 2.11$$

$\delta_0{}^{18}O_{vapour(f)}$ denotes the initial vapour $\delta^{18}O$ value, f represents the fraction of moisture remaining in the cloud, and $\varepsilon^{18}O_{liquid-vapour}$ is the equilibrium fractionation between vapour and liquid (nearly identical to the notion of $1000\ln\alpha$). At a given temperature T, the $\delta^{18}O$ value of precipitation at fraction remaining (f) is given by:

$$\delta^{18}O_{rain(f)} \approx \delta_0{}^{18}O_{vapour(f)} + \varepsilon^{18}O_{liquid-vapour(T)}$$

Consequently, for instance, the first rain ("first distillation process") to fall (at f = 95% and RH = 85%) at 25 °C features a $\delta^{18}O$ value of -2.61 ‰ (V-SMOW).

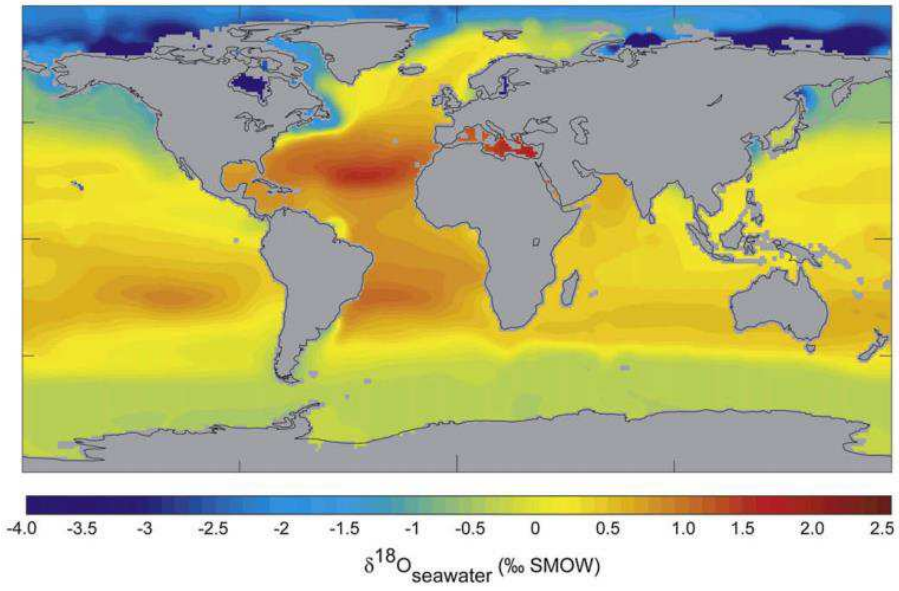

Figure 2.8: Global distribution of $\delta^{18}O$ in the ocean – Highest values are found in subtropical zones characterised by intense evaporation (also Mediterranean Sea); Lowest values are associated with input of isotopically light surface water. The $\delta^{18}O$ values of regional precipitation and cave drips therefore depend on moisture source and the environmental controls on ocean evaporation. Derived data by LeGrande & Schmidt (2006), from Lachniet (2009).

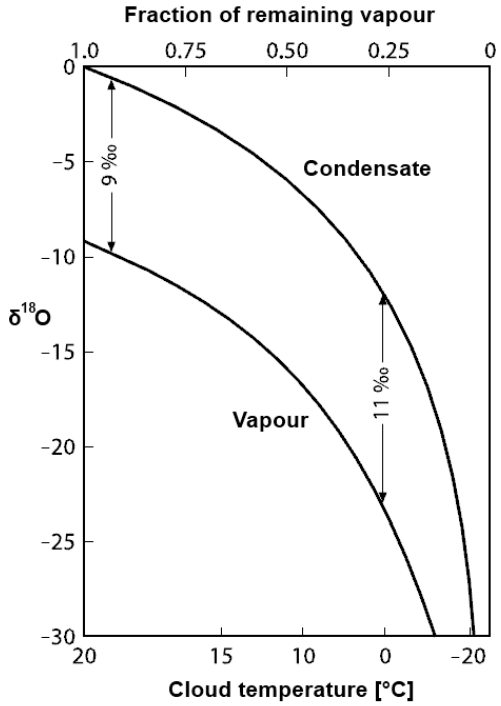

Figure 2.9: Rayleigh Distillation – With increasing degree of rainout, both condensate (rain) and vapour (atmospheric moisture) become increasingly isotopically lighter. This relationship is fundamental for most of the known "isotopic effects". From Hoefs (2015).

Progressive steps of cooling and rainout are a result of altitude, latitude and orographic effects, all of which cause rainfall $\delta^{18}O$ values to decrease with continuing rainout. In combination, all these effects (Section 2.3.2) result in a specific pattern in global rainfall $\delta^{18}O$ values (Figure 2.10). Data depicted in the figure are interpolations of annual mean values of $\delta^{18}O$ as they have been recorded by the Global Network for Isotopes in Precipitation (GNIP) of the IAEA (International Atomic Energy Agency) and the WMO (World Meteorological Organisation).

Rainfall $\delta^{18}O$ also depends on moisture source and atmospheric circulation that mediates between moisture source and moisture sink regions. Additionally, because of the multiplicity of controlling factors, two different air masses originating from the same source region may have unique rainout histories and different final precipitation $\delta^{18}O$ values (Bowen & Wilkinson, 2002). The above mentioned "isotopic effects" are summarised in the following section.

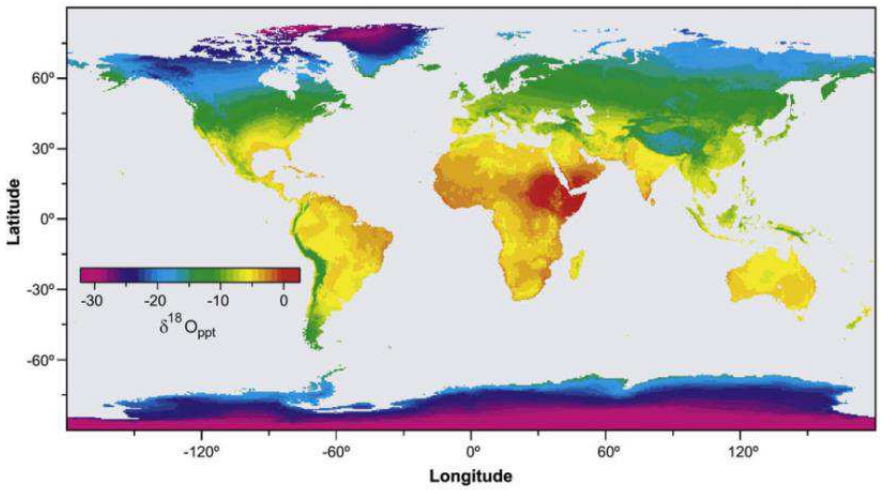

Figure 2.10: Global distribution of $\delta^{18}O$ in rainfall (as interpolated from annual means recorded by GNIP stations). Rainfall $\delta^{18}O$ values decrease from low to high latitudes and altitudes as a consequence of Rayleigh distillation due to decreasing temperatures along the advection path of air masses. Moisture source is also crucial. Data from Bowen & Wilkinson, 2002, from Lachniet (2009).

2.3.2 The Isotopic Effects

2.3.2.1 Temperature Effect

The temperature effect is the positive correlation between mean annual temperature (MAT) at-a-site, e.g. above a karst cave, and the mean $\delta^{18}O$ value of precipitation ($d\delta^{18}O_p/dT$; Dansgaard, 1964; Fricke & O'Neil, 1999). Both observations (Fricke & O'Neil, 1999) and modelling (e.g. Schmidt et al, 2007) indicate that the slope of the $d\delta^{18}O_p/dT$ relationship is non-linear and may vary substantially over time and space for many regions on Earth, ranging from +0.17 ‰/°C to +0.9 ‰/°C. Temporal variation of the $d\delta^{18}O_p/dT$ slope may result from changes in the seasonality of precipitation, as rainfall O-isotopy varies with season (Denton et al., 2005) and/or changes in moisture source.

It appears, however, that condensation temperature of individual rainfall events is a more important control on precipitation $\delta^{18}O$ values than some statistical surface temperature mean such as the MAT, which implies that proxy records such as speleothems are biased towards the climatic conditions associated with precipitation events. Another bias is exerted by the difference in isotopic effectiveness of single rainfall events: If rainfall is not intense enough to produce significant infiltration and subsequent percolation to the speleothem, its water input to the cave system will be lost due to evaporation and water retention within soil zone and epikarst. Therefore, only precipitation events sufficiently intense to produce percolation water have an influence on speleothem isotopy, and are then referred to as isotopically effective (Section 2.3.2.4).

The temperature effect is also manifested on a seasonal basis, with seasonal variations accounting for a few ‰ in the low latitudes and up to 15 ‰ in high-latitude regions, with lower $\delta^{18}O$ values typically related to winter (Rozanski et al., 1993) although variations in $\delta^{18}O_p$ may also relate to seasonal changes in moisture source.

2.3.2.2 Altitude Effect

The altitude effect denotes the decrease in $\delta^{18}O$ values with increasing altitude, relating to the decrease in MAT with elevation (Clark & Fritz, 1997) along the local atmospheric lapse rate of typically -5 to -6 °C/km altitude difference. It is associated with both decreasing condensation temperatures and progressive Rayleigh distillation extent as the air mass is lifted over an orographic barrier which causes progressive rainout of air moisture. Typical gradients range from -2 to -3 ‰ $\delta^{18}O$/km altitude difference (e.g. Fleitmann et al., 2004). The lee-side of mountain ranges may display pronounced "isotopic rain shadows".

2.3.2.3 Continental Effect

The continental effect describes the decrease in $\delta^{18}O$ with increasing distance from the ocean as the primary moisture source (Dansgaard, 1964; Rozanski et al., 1993; Clark & Fritz, 1997) and is due to progressive cooling and rainout of an air mass as it traverses a continent. It should be noted that the continental effect may be partly counteracted by contribution of continental moisture recycled back to the atmosphere by evaporation of soil water, lakes and rivers (Lachniet, 2009; after Koster et al., 1993). Surface water bodies typically exhibit higher $\delta^{18}O$ values than atmospheric moisture as their water is derived from isotopically heavier rain which represents condensed moisture. Thus, moisture recycling leads to a decrease in $\delta^{18}O$/distance-to-sea gradients along an advection path. Plant respiration also recycles moisture back to the atmosphere but is non-fractionating (Gat, 1996).

2.3.2.4 Amount Effect

The amount effect is the observed decrease in rainfall $\delta^{18}O$ values with increased rainfall amount ($d\delta^{18}O_p/dP$) (Dansgaard, 1964; Rozanski et al., 1993; Risi et al., 2008) and is dominant in tropical regions where deep convection is common, which is promoted where sea surface temperatures (SST) are >27.5 °C (Lachniet, 2009). Convection and subsequent lifting of an air parcel results from both atmospheric heating and in the equatorial zone additionally from trade wind convergence within the intertropical convergence zone (ITCZ; Section 0).

The at-a-site amount effect varies in magnitude, depending on numerous factors, comprising the initial mass of water vapour in the air parcel, SST, degree of cooling related to convection depth and even cloud microclimate dynamics (Risi et al., 2008), as well as evaporation of raindrops during periods of sparse rains (Dansgaard, 1964; Risi et al., 2008) when RH is low and thus the influence of evaporation becomes more prominent. For example, Lachniet & Patterson (2006) observed magnitudes ranging from -1.6 to -2.85 ‰ per 100mm monthly precipitation difference at a strong inverse correlation between rainfall amount and rainfall $\delta^{18}O$ ($r = 0.89$) in Panama, a humid tropical region within the heart of the ITCZ.

Weighted averages of annual $\delta^{18}O$ values exhibit a similar inverse relationship (r = -0.66). From Barbados, Jones et al. (2000) documented gradients of -2.2 to -2.75 ‰/100mm of monthly rain. Fleitmann et al. (2004) measured variations in rainfall $\delta^{18}O$ values by ~2‰ as a function of rainfall amount in southern Oman. In contrast to the well-established temporal relationship, the amount effect is difficult to establish in a spatial sense, between different sites or stations. This between site $\delta^{18}O$ variability is probably best explained by controls of regional atmospheric circulation which integrates rainout amount along the moisture trajectory (Sturm et al., 2007).

2.3.2.5 Source Effect

The source effect describes the circumstance that air masses derived from different moisture sources have distinct $\delta^{18}O$ values (Rozanski et al., 1993; Clark & Fritz, 1997), and arises from varying air mass histories and moisture source temperature, additional to regional differences in ocean $\delta^{18}O$ values (LeGrande & Schmidt, 2006). Far-travelled moisture may exhibit lower $\delta^{18}O$ values than moisture that has been transported only over short distances as has been documented, for instance, for southern Brazil by Cruz et al. (2005) and Sturm et al. (2007).

On the basis of stable isotopes, it may be possible to constrain mixing of separate moisture sources (source apportionment), as has been successfully performed for the region of northern India that receives its moisture from the Bay of Bengal or the Arabian Sea (Sengupta & Sarkar, 2006). Changes in moisture source may be related to variations in seasonality, where moisture contribution from multiple dominant source regions differs with season, typically wet vs. dry season in low latitudes and winter vs. summer in high latitudes. These changes in seasonality may result in abrupt variations in $\delta^{18}O$ values on palaeoclimate timescales (Wang et al., 2001; Denton et al., 2005).

2.3.3 Potential Proxy Signal Modification during Downward Transfer to the Speleothem

Contributions of O-atoms derived from dissolution of the carbonate bedrock are negligible in their influence on dripwater O-isotopy, as water contains about 10^4 as many O-atoms as $CaCO_3$ (Lachniet, 2009). Although the $\delta^{18}O$ signal is thus independent of the carbonate system in a direct sense, it may still become modified by various processes that are effective during downward signal transfer to the cave where it is finally recorded.These processes have the potential of modifying the original climate signal, and comprise mixing, evaporative enrichment and kinetic fractionation.

2.3.3.1 Mixing

After infiltration, water originated from different rainfall events is likely to become mixed within the soil and epikarst zone as a result of slow underground water flow (e.g. by seepage) and/or high underground water storage (Figure 2.11).

By the mechanism of mixing, single $\delta^{18}O$ signals relating to the conditions that prevailed during single rainfall events (synoptic weather conditions), get combined to a bulk $\delta^{18}O$ signal. The extent of integration over multiple rainfall events depends on the above mentioned hydro(geo)logical properties of the site-specific system. Deep caves at tens to hundreds of metres below the surface are particularly prone to this mixing integration. They are therefore poorly suited for reconstruction of high-frequency variations (e.g. sub-annual to annual) in past environmental conditions, but are well suited for the identification and tracking of lower-frequency variations (e.g. multidecadal to orbital), as high-frequency variations are effectively averaged out by mixing. Other important aspects influencing the temporal resolution of speleothem time series are speleothem growth rate and sampling spatial resolution (Section 4.4).

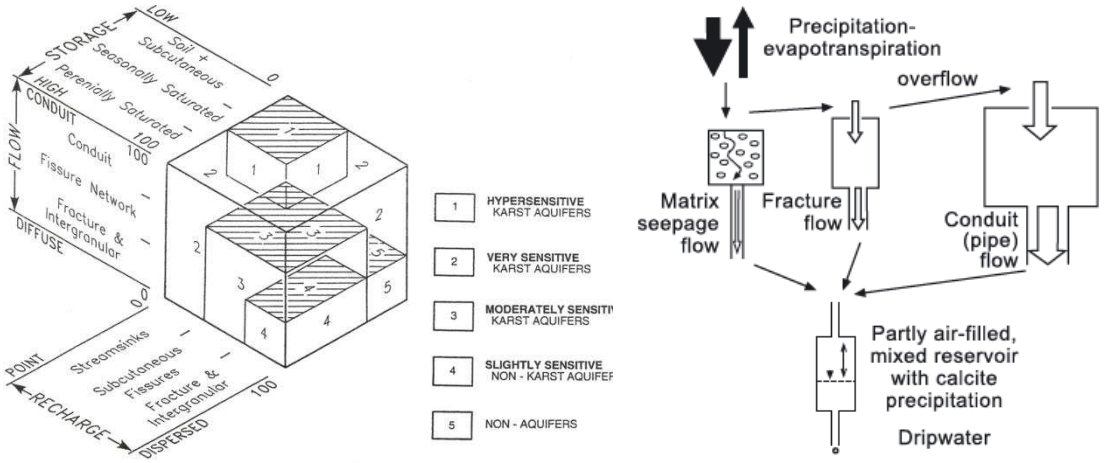

Figure 2.11: Left: Storage and flow of percolating waters in karstic settings yielding different degrees of karst aquifer sensitivity to geochemical influences from the surface. From Ford & Williams (2007); Right: Combination of relevant types of flow paths that leads to a site-specific suite of flow regimes that is reflected in speleothem dripwater. From Fairchild et al. (2007).

2.3.3.2 Evaporative Enrichment

Under conditions of low relative humidity that can be typically encountered in arid climates, for instance the regions of the subtropical lows, the $\delta^{18}O$ climate signal is potentially subject to evaporative enrichment of percolating waters and even of raindrops before they hit the ground. This may lead to more or less erratic shifts in speleothem $\delta^{18}O$ towards higher values. Although tropical climates are rather characterised by the predominance of high RH, evaporative enrichment may still influence speleothem $\delta^{18}O$ in tropical monsoon-type climates, most likely during the respective dry season (Lachniet, 2009). Evaporation is strongest at the surface compared to soil and epikarst. Thus, its extent will also depend on near-surface water storage and downward flow velocity.

2.3.3.3 Kinetic Fractionation

Along the pathway of downward percolating dripwaters and especially within cave systems, the $\delta^{18}O$ signal is potentially modified by kinetic fractionation via the process of evaporation. Conditions favouring evaporation are low RH, long dripwater residence time on a stalactite or stalagmite tip and intense cave ventilation which typically increases with decreasing distance to openings or cave entrances. Although kinetic fractionation caused by evaporation has often been described as confounding the $\delta^{18}O$ climate signal, it may itself be considered as a palaeoenvironmental indicator. In tropical regions where the amount effect dominates, dripwater evaporation during periods of reduced rainfall and lower infiltration rates would increase dripwater $\delta^{18}O$ in the same sense as the amount effect (Fleitmann et al., 2004). The effects of increased aridity may therefore get recorded in multiple ways (severalfold) which could amplify the climatic aridity signal. Kinetic fractionation within caves may also be triggered by rapid CO_2-degassing from dripwaters and the subsequent rapid calcite depositions, as time may not suffice for isotopic equilibrium to get established.

2.4 Carbon Isotopes in Speleothems – Indicators of the Local Carbon Cycle

Although speleothem C-isotopy has not yet been studied as thoroughly as speleothem O-isotopy (McDermott, 2004) it has rapidly evolved into a fundamental component of palaeoenvironmental reconstructions based on speleothem geochemistry. Unlike $\delta^{18}O$ that can mostly be considered as a climate signal characterising the hydrological cycle, $\delta^{13}C$ is rather regarded as an environmental signal in the stricter sense. This is because the $\delta^{13}C$ signal is initiated predominantly in the terrestrial environment, i.e. the ecosystem overlying the speleothem-forming caves (Fairchild, et al., 2006).

Obviously, the ecosystem as the locus of primary signal initiation also depends on climatic conditions, particularly on temperature and humidity, in multiple ways and on various timescales, but these factors may often be less important than other environmental conditions, which are often highly local in their nature. Strictly spoken, the speleothem $\delta^{13}C$ signal depends directly only on processes and conditions that prevail within the catchment area of a given karst cave, as cave waters including speleothem-feeding dripwaters are derived from this limited area.

Consequently, information on past environmental conditions that can be derived from speleothem C-isotopy primarily refer to the cave's catchment area, which is why C-isotopy (and trace element patterns, Section 2.5) can be expected to vary substantially from one cave to another. In extreme cases, even single drip sites within the same cave may differ in their "physiology", being governed by a different suite of processes (Fairchild, et al., 2006). This illustrates the significance of detailed monitoring in order to establish the physiological behaviour of each drip site.

However, if several speleothems from the same cave exhibit very similar geochemical archives, their time series consolidate each other and proxy data interpretation can be conducted with much higher fidelity. Such replication of speleothem time series using multiple speleothems from the same cave is also of benefit in the case of trace elements and O-isotopy, for example for demonstrating speleothem growth in isotopic equilibrium (Lachniet, 2009).

In contrast to dripwater O-isotopic composition, C-isotopy is determined by the isotopic compositions of the dominant terrestrial C-reservoirs. As atmospheric carbon input to percolating waters is often negligible, it can be stated that "C-isotope ratios in speleothems usually reflect the balance between isotopically light biogenic carbon derived from the soil CO_2 and heavier carbon dissolved from the limestone bedrock" (McDermott et al., 2006).

The speleothem $\delta^{13}C$ signal is initiated at the surface above the cave where soil CO_2 dissolves in rainwater percolating through the soil and the epikarst to form carbonic acid and to chemically dissolve the carbonate host rock on its way downward to the cave where $CaCO_3$ again precipitates in the form of stalactites and stalagmites (Section 2.1). In the course of these chemical transformations, C-isotopes become partitioned between the different C-species and phases due to isotopic fractionation that causes ^{13}C to concentrate in the more condensed phase.

Figure 2.12 depicts the various fractionation steps that relate $\delta^{13}C$ values of the main C-reservoirs, i.e. host rock DIC and soil CO_2, to $\delta^{13}C$ values of speleothem calcite. Additionally, the figure shows that soil CO_2 that is derived from predominant C_3-type vegetation (Section 2.4.2.2) with typical $\delta^{13}C$ values of around -23 ‰ converts into speleothem $CaCO_3$ displaying $\delta^{13}C$ values of around -14 ‰.

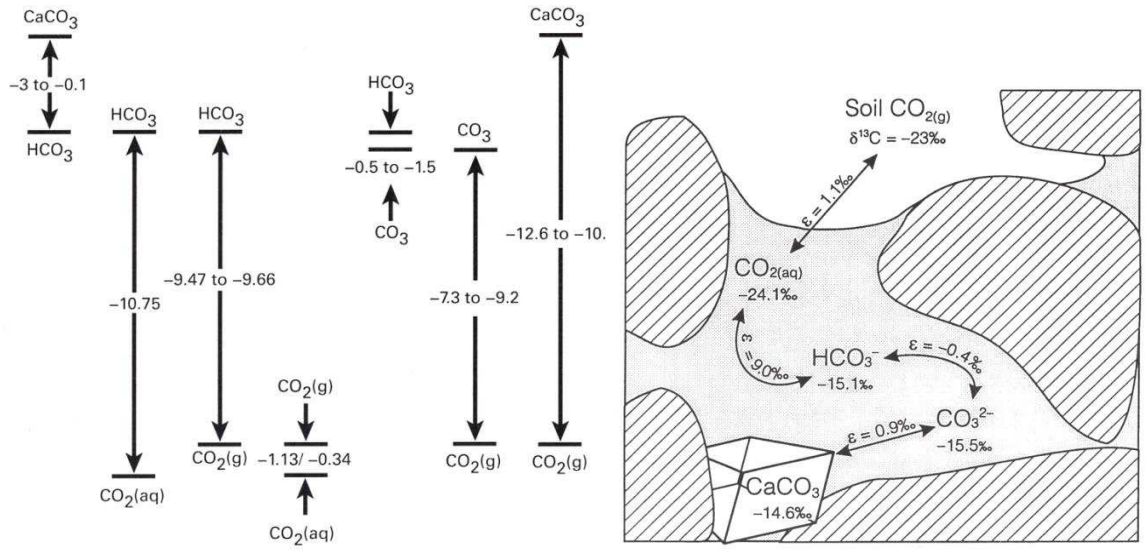

Figure 2.12: Left: C-isotopy of the Carbonate/Carbonic Acid System – Isotopic partitioning between CO_2 and HCO_3^- clearly dominates speleothem-related fractionation steps. Modified from Darling et al. (2006); Right: Fractionation steps from gaseous soil CO_2 to solid $CaCO_3$. From Clark & Fritz (1997).

This implies a predominant control on $\delta^{13}C$ values by soil CO_2, which is not given under all conditions. The actual conditions within soil zone and epikarst under which calcite saturation is reached can be described with a concept of two end-member systems (Hendy, 1971), referred to as "open system" and "closed system".

2.4.1 Open System Dissolution vs. Closed System Dissolution

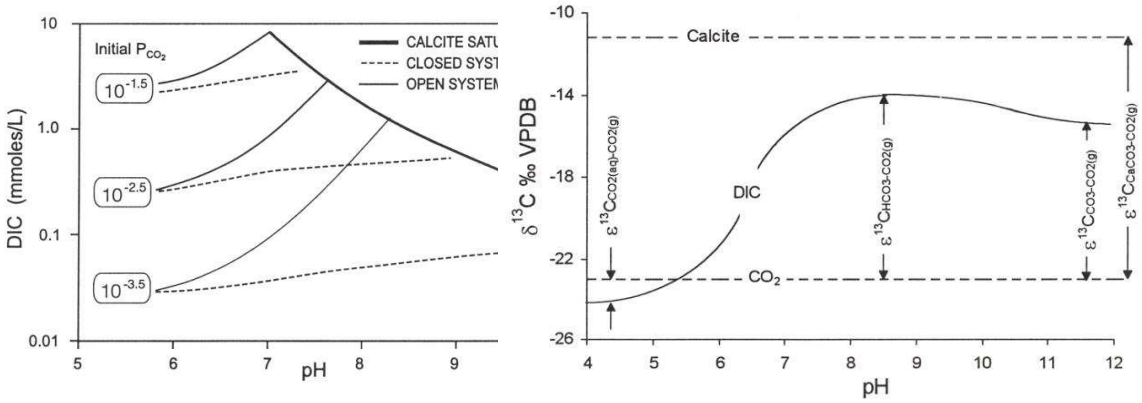

Figure 2.13: Left: The evolution of pH and DIC as percolating waters dissolve calcite under open and closed system conditions for different initial values of pCO_2 - Open system dissolution yields higher DIC concentrations at saturation, as calcite aggressivity is higher due to CO_2 replenishment from the soil zone. From Clark & Fritz (1997); Right: Under open system conditions, enrichment of DIC (solid line) in ^{13}C reflects continual exchange with soil CO_2 of the respectively dominating C-species at increasing pH (CO_2 at low pH, HCO_3^- at intermediate pH, CO_3^{2-} at high pH). From Clark & Fritz (1997).

Under open system conditions, chemical equilibration between the downward percolating water and a hypothetical infinite reservoir of soil CO_2 is maintained at all times (McDermott et al., 2006). Consequently, carbon derived from isotopically light organic matter predominates over carbon from inorganic sources (Fairchild, et al., 2006). These conditions represent the common case, as demonstrated by the finding that 80-95 % of the ^{14}C activity of modern carbon in waters and speleothems is caused by organic material (Genty, et al., 2001). In general terms, open system dissolution leads to a progressive increase in HCO_3^- content of percolating water as it dissolves more limestone in the unsaturated zone, and to isotopically lighter cave waters, hence calcite precipitates (Fairchild, et al., 2006).

Under closed system conditions, downward percolating water loses contact with the (finite) soil CO_2 reservoir as soon as carbonate dissolution commences (Hendy, 1971). As a result, C-isotopy of the host rock exerts a strong influence on that of the DIC, and, in turn, on speleothem $\delta^{13}C$. Closed system dissolution is important in soils that are (quasi-)free of carbonates and if no CO_2 sources exist within the epikarst. Generally, contents of Ca^{2+} and DIC are much lower compared to open system dissolution and speleothem $\delta^{13}C$ values tend to be much higher (Fairchild, et al., 2006). Figure 2.13 is an illustration of both closed and open system dissolution until $CaCO_3$ saturation is reached.

In reality, most natural systems are likely to be partially open with both dripwater DIC concentration and $\delta^{13}C$ values lying between those expected from pure open and closed end-member system conditions. The balance between open and closed system dissolution can be constrained by calculating the mass fraction of ^{14}C-dead using radiocarbon data on independently dated stalagmites, although other effects such as ageing of organic matter in the overlying soil reservoir have to be considered at some sites (e.g. Genty et al., 2001).

Not only the contribution from the two main C-reservoirs to speleothem $\delta^{13}C$ values may vary, but also their specific C-isotopy can change depending on various factors: The carbonate bedrock in which karst caves form displays both fairly homogeneous and high $\delta^{13}C$ values. Marine carbonates that are globally the most abundant exhibit $\delta^{13}C$ values of ~0 ‰, with a range from -2 to +3 ‰ depending on age, depositional environment and mineral phase (Darling et al., 2006). In contrast to the host rock, $\delta^{13}C$ values of soil CO_2 can vary substantially both spatially and temporally, responding to a number of different conditions and processes, as described in the following section.

2.4.2 Controls on Soil CO_2 Carbon Isotopic Composition

2.4.2.1 Soil Microbial Activity

Enhanced soil CO_2 contents are a result of both plant/animal respiration and particularly of the microbially mediated decomposition of organic matter. Therefore, soil pCO_2 can be considered as an indicator of the activity of the soil microbial community. Under environmental conditions that are unfavourable for microbial activity, such as severe dryness, reduced microbial turn-over could lead to a reduced contribution of soil CO_2 to dripwater C-isotopy, which would be reflected by increased $\delta^{13}C$ in speleothems (Fairchild, et al., 2006).

Variations in microbial organic matter decay may also be associated with changes in the composition of microbial communities. For instance, prolonged periods of soil flooding would favour anaerobic microbial strains that show lower metabolic rates than aerobic microorganisms. However, as karst landscapes normally lack significant surface runoff, anaerobic conditions within the soil zone above carbonate karst caves are rather unlikely to form.

2.4.2.2 Vegetation Type

Photosynthesis is conducted by plants using different metabolic pathways, which impacts on the C-isotopic composition of the plant material they produce, as is illustrated in Figure 2.14. In terrestrial ecosystems, the C_3 pathway ("Calvin cycle") dominates, especially in temperate and high-latitude regions and typically produces plant material with $\delta^{13}C$ values around -27 ‰ (Darling et al., 2006). The two other photosynthetic pathways represent evolutionarily younger adaptations of higher plants to dry conditions:

The C_4 pathway ("Hatch-Slack cycle") is dominant in tropical and savannah grasses, and typically produced plant material exhibits $\delta^{13}C$ values of -13 ‰ (Figure 2.14). C_4-type vegetation is therefore isotopically heavier than C_3-type vegetation. This relative isotopic enrichment during photosynthesis is due to physiological mechanisms that increase intercellular pCO_2 values. This leads to reduced relative differences in kinetic energy between isotopically light and heavy CO_2 and thus to decreased isotopic discrimination (Hoefs, 2015).

The much less abundant CAM (Crassulacean acid metabolism) cycle occurs mostly in succulents in arid ecosystems and can essentially be described as diurnal switching between C_3 and C_4 pathways, which leads to intermediate $\delta^{13}C$ values (Figure 2.14).

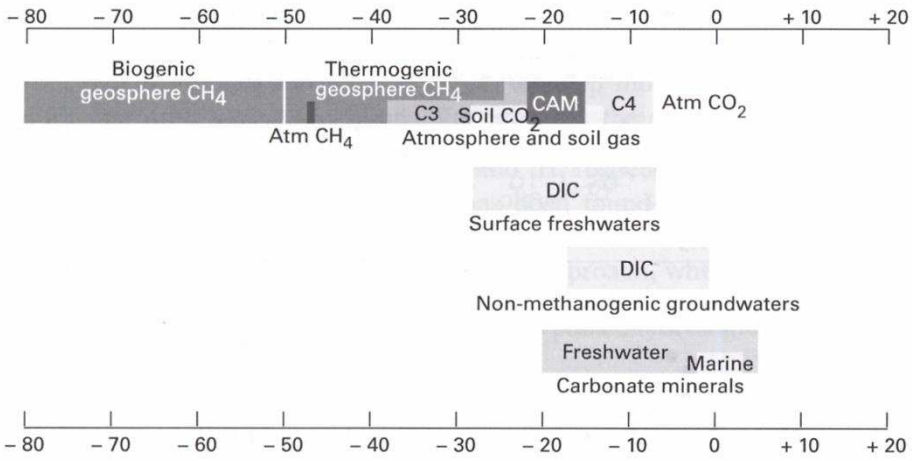

Figure 2.14: C-isotopy of the different types of C-reservoirs (solid, liquid, gas) relevant to speleothem palaeostudies. Modified from Darling et al. (2006).

Under conditions of a C_3-dominated plant assemblage, dripwaters in equilibrium with soil respired CO_2 display $\delta^{13}C$ values in the range -26 to -20 ‰, and corresponding speleothem $\delta^{13}C$ values are within the range -14 to -6 ‰ (McDermott et al., 2006). If the plant assemblage is C_4-dominated, dripwater $\delta^{13}C$ values cluster around -16 to -10 ‰, whereas corresponding speleothem $\delta^{13}C$ values may vary from -6 to +2 ‰ (McDermott et al., 2006). This general trend may be superimposed by changes in the proportion of open vs. closed system conditions (Figure 2.15).

If the ecosystem above a given cave site is limited in its activity and/or density by climatic conditions such as dryness or low temperatures, periods of climatic amelioration would increase ecosystem productivity and thus promote the production of isotopically light soil biogenic CO_2, which results in lowered $\delta^{13}C$ values (Genty, et al., 2001).

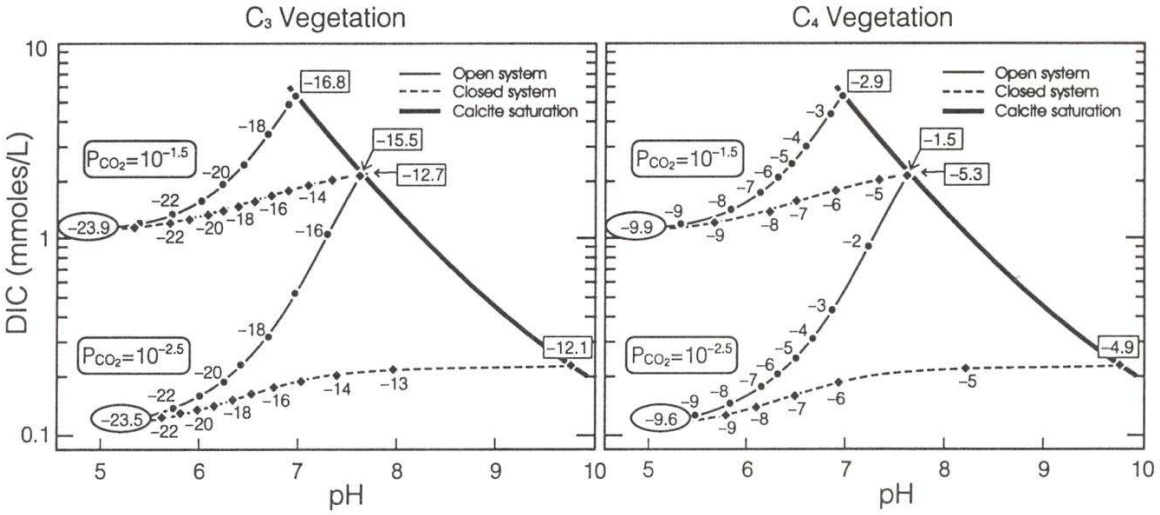

Figure 2.15: Combined effect of dominating photosynthetic pathway and proportion of open vs. closed system conditions – Predominant C_3-type vegetation yields far lower final $\delta^{13}C$ values in DIC at saturation (calcite precipitate) relative to C_4-type vegetation. The greater enrichments observed under closed system conditions (dashed lines) are due to mixing of the initial DIC with DIC derived from isotopically heavy marine carbonate. From Clark & Fritz (1997).

2.4.2.3 Vegetation Density/Amount

Vegetation amount is another crucial factor of the speleothem $\delta^{13}C$ signal as reductions in vegetational cover, or more precisely, vegetational biomass, are a possible cause for shifts towards heavier C-isotopes, as the input of light C-isotopes diminishes. Variations in vegetation amount may relate to natural causes, either local, such as lahars that destroy vegetation within the limited area of their course, or regional to over-regional, as is the case with climatic controls. For instance, reductions in $\delta^{13}C$ values have been well documented for periods of major global glaciation (Fairchild, et al., 2006). A widely documented anthropogenic cause for speleothem $\delta^{13}C$ increases is deforestation (Fairchild, et al., 2006), and changes in vegetation cover influencing speleothem $\delta^{13}C$ may also relate to past agricultural practices.

2.4.2.4 Prior Calcite Precipitation (PCP)

Another process influencing speleothem $\delta^{13}C$ values is the precipitation of $CaCO_3$ along the dripwater flowpath, prior to the cave. This process is referred to as prior calcite precipitation (PCP).

As $CaCO_3$ precipitation is mainly caused by CO_2-degassing from dripwaters, for PCP to occur, a gas phase with relatively low pCO_2 must be present within the pore volume (Fairchild, et al., 2006). This is thought to be likely under relatively dry conditions when pore spaces are not entirely filled with percolating water. Thus, PCP may be considered as an indicator of dryness, or at least drying of the active flow path (hydrological routing). As PCP is associated with degassing of isotopically light CO_2, the remaining dripwater becomes isotopically enriched during the process. Thus, subsequent speleothem $\delta^{13}C$ values will be higher.

The process of PCP also impacts on dripwater trace element contents (Fairchild, et al., 2006). As most trace elements present in dripwater exhibit partition coefficients (that represent their relative abundance in solution and mineral phase) with respect to calcite significantly smaller than unity, trace elements become enriched in the remaining dripwater. PCP consequently causes the speleothem contents of these trace elements to rise. This circumstance illustrates the potential in combining different proxy signals, such as stable isotope ratios and trace element patterns for a more precise and confident interpretation of proxy data.

If CO_2-degassing occurs too quickly for isotopic equilibration to be reached, for example, due to intense cave ventilation with low pCO_2 ambient air, $\delta^{13}C$ values in the dripwater and consequently in the speleothem are increased even further due to kinetic carbon isotope fractionation.

2.4.2.5 Lack of equilibration

As described in Section 2.1.1, the dissolution of CO_2 in water (Equation 2.1) is the rate-determining step of bedrock carbonate dissolution. Therefore, dripwater percolation may be so rapid that isotopic equilibration with the otherwise often dominant soil CO_2 reservoir is not achieved. In this case, speleothem $\delta^{13}C$ would fail to reflect the $\delta^{13}C$ prevalent within the soil zone and instead entrain isotopically heavier atmospheric CO_2 (McDermott, 2004). Thus, this lack of equilibration constitutes a possible mechanism for shifts towards higher speleothem $\delta^{13}C$ values that relates to low percolation water transit times which is indicative of high and therefore fast flow.

2.5 Trace Elements in Speleothems – Indicators of Climate and Environment

As speleothem-based palaeostudies have until recently focused mainly on stable isotope ratios, especially of oxygen, the understanding of processes controlling trace element incorporation into speleothem fabrics is still very limited. This applies particularly to elements that tend to be transported in colloidal form, where lacking understanding is partly due to the difficulties related with colloid sampling from dripwaters (Fairchild & Treble, 2009).

Trace elements therefore represent a still very active research front, and identification of new potential proxy indicators (e.g. Mg as an aridity index) happens on a year-to-year base. Therefore, discussion of trace elements in the present work will focus on the most principle processes relevant on the timescale observed.

Trace elements incorporated in speleothem fabrics might originate from different sources, including the atmosphere, the pedosphere, the biosphere and the lithosphere (Fairchild & Treble, 2009). As is the general case with geochemical cycles, the importance of each source for the speleothem trace element signal depends on the size of each of the reservoirs, i.e. the abundance of each trace element within the respective source. For instance, a very thin soil layer overlying epikarst and cave will have only little or no influence on speleothem trace element geochemistry, even more so, if trace element contents within this soil layer are low.

However, not only reservoir size, but also the flux from those source reservoirs to the sink reservoir is important. In the case of speleothems, this flux depends on the mobility of the trace elements from the surface to the stalagmite tip. Consequently, a trace element that is strongly fixated within one or more source reservoirs, will not significantly impact on the speleothem trace element signal, even if present at high concentrations.

While the issue of element mobility and transport will be treated in Section 2.5.1.2, the different sources for trace elements in speleothems are discussed in the following section.

2.5.1 Trace Element Sources, Transport and Incorporation

2.5.1.1 Trace Element Sources

The Carbonate Host Rock

The mainpart of trace element cations originates from chemical $CaCO_3$ dissolution in the soil zone and epikarst (Fairchild et al., 2007). This seems to apply particularly to those trace elements that would be expected to occur as trace constituents of the carbonate bedrock. In particular, Mg represents such a typical trace "contaminant" in calcitic carbonate.

Furthermore, mineral phases other than calcite may be present within the carbonate host rock and function as sources for trace elements in speleothems. An example is the P-bearing mineral apatite that represents the most likely inorganic P source within the aquifer.

In addition, both soil zone and surficial deposits (such as ash layers) overlying the epikarst are potential sources of trace elements in speleothems. In particular, P is often described as an indicator of biomass turnover and can therefore be regarded as reflecting the status of the overlying ecosystem (Fairchild & Treble, 2009). A schematic overview of the various sources for trace elements in speleothems including major processes of transport and element cycling is given in Figure 2.16.

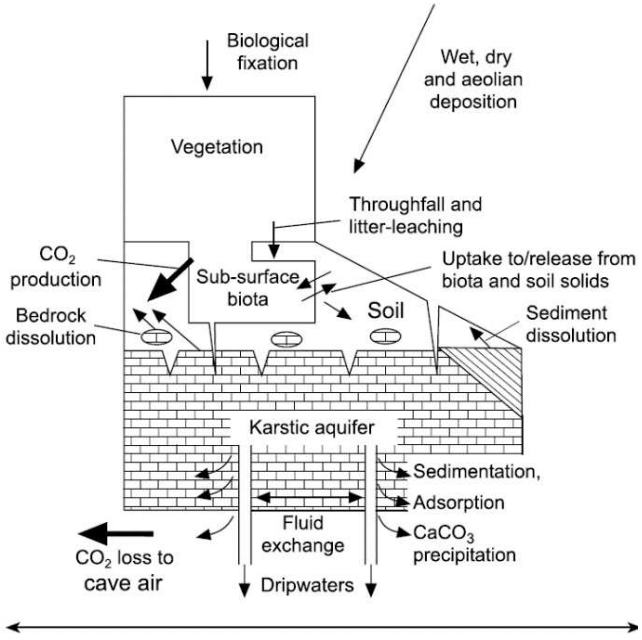

Figure 2.16: Schematic overview of trace element sources and of processes involved in their transport and cycling within the karstic system. From Fairchild & Treble (2009).

The Soil Zone and Surface Deposits

Soil layer constituents and other surface deposits represent another potential source for speleothem trace elements. For example, Verheyden et al. (2000) found a clear discrepancy in Sr isotopic signature between a stalagmite from the Père Noël Cave in Belgium and the overlying partly dolomitised Givetian limestone. Even the lowest $^{87}Sr/^{86}Sr$ value from the 16 analysed speleothem sub-samples (0.70881) still obviously exceeds the Sr isotope values measured in the bedrock (0.70808 for calcite; 0.70818 for dolomite). As marine Sr inputs have been estimated to be only 2% at this site, the authors have posited a significant contribution of Sr from a detrital silicate end member featuring high proportions of radiogenic Sr such as clay particles from the soil zone or recent terrigenous sediment like loess, dust or tephra (Banner et al., 1996). Assuming a $^{87}Sr/^{86}Sr$ ratio of 0.72 for this detrital phase, the authors calculated a maximum contribution to the speleothem Sr signal of about 10%, which is a considerable contribution bearing in mind that the soil cover at the site is only about 40 cm thick (Verheyden et al., 2000).

The Atmosphere

Under favourable conditions, atmospheric particles such as aeolian dust can noticeably influence the trace element inventory of a speleothem (e.g. Goede et al. 1998; Ayalon et al. 1999; Bar-Matthews et al. 1999; Verheyden et al. 2000; Frumkin & Stein 2004; Zhou et al., 2009). For instance, Goede et al. (1998) found a bimodal distribution of Sr in a 84–57 ka stalagmite from Frankcombe Cave, Tasmania, hinting at Sr contributions from two sources. By analysing both Sr concentrations and Sr isotope ratios ($^{87}Sr/^{86}Sr$), the authors were able to detect Sr input from a non-limestone source, namely the high $^{87}Sr/^{86}Sr$ marine carbonates from the exposed continental shelf between Tasmania and Australia. This finding enabled the authors to reconstruct the regional atmospheric circulation with more northwesterly winds during interstadials and more westerly winds during stadials. This study is all the more astounding as it consistently relates a stadial with a reduced input of aeolian material, whereas, in more general terms, it is widely accepted that stadials have been cold and dry and are therefore rather related to generally increased aeolian transport due to reduced wash-out of atmospheric particles by rain (e.g. Rasmussen et al., 2008).

In accordance with this general observation, Bar-Matthews et al. (1999) reconstructed enhanced inputs of sea spray and dust during the last glacial to the their study site above Soreq Cave, Israel, based on high Sr concentrations and $^{87}Sr/^{86}Sr$ ratios in a multi-speleothem stack covering the last 60 ka. Abruptly decreasing $^{87}Sr/^{86}Sr$ ratios in the early Holocene are interpreted as both a reduced aeolian input and an increased supply of Sr to the cave from the low $^{87}Sr/^{86}Sr$ dolomitic host rock as a consequence of intensified weathering in a warmer and wetter eastern Mediterranean climate (Ayalon et al., 1999).

In their study of stalagmite SJ3 from Sichuan province in Central China spanning the last deglaciation (10-20 ka), Zhou et al. (2009) followed the same reasoning to identify changes in the strength of the East Asian Winter Monsoon (EAWM). The authors determined a stronger winter monsoon, characterised by increased Sr concentrations and isotope ratios, during the cold-dry Heinrich Event 1 (H1) and LGM, and a weaker winter monsoon during the warm-wet mid-Holocene including the Bølling/Allerød (B/A) warm period.

Not only aeolian dust particles, but also marine aerosol particles (marine spray) have been reported to contribute to speleothem geochemistry in some cases, especially at sites in proximity to the sea (e.g. Bar-Matthews et al., 1999; Baker et al., 2000; Fairchild et al. 2000; Tremaine et al., 2016). For example, Baker et al. (2000) calculated from ocean water composition that 23 - 50% of dripwater Mg at five drip sites in the Villars Cave in SW France (some 180 km east of the Atlantic) was sourced from marine spray, assuming that 100% of dripwater Cl originates from the sea. For Sr, this proportion was only 2 - 5%. Applying the same approach, Fairchild et al. (2000) determined that 20% of dripwater Sr, but only 3% of Mg in Clamouse Cave in S France were of marine origin. For Ernesto Cave in NE Italy, they found only a negligible marine aerosol contribution to dripwater geochemistry. After a two-year automated dripwater sampling in Niue Cave in the tropical South Pacific, Tremaine et al. (2016) calculated seasalt contributions of 84% of Mg, 17% of Sr and even 19% of Ca.

Although both atmospheric particles, such as aeolian dust (e.g. Ayalon et al., 1999; Zhou et al., 2009; Goede et al., 1998) or particularly marine aerosol particles (e.g. Baker et al., 2000; Fairchild et al., 2000), and soil layer constituents (e.g. Verheyden et al., 2000) have been suggested as potential sources of speleothem Mg and Sr, both elements are mainly derived from dissolution of carbonate bedrock and secondary minerals along the flow path (Fairchild et al., 2006; Fairchild & Treble, 2009). Consequently, the main processes driving dripwater concentrations of Mg and Sr, at constant external source strength and hydrological routing, are (1) differential dissolution of bedrock calcite and dolomite, (2) selective leaching of Mg and Sr with respect to Ca, (3) incongruent dolomite dissolution (IDD), and (4) PCP along dripwater flow paths, as summarised by Fairchild et al. (2000).

2.5.1.2 Trace Element Transport

Trace element response to environmental conditions within the karst system depends fundamentally on their preferential mode of transport (Figure 2.17). For example, high dripwater flow as is typical for large conduits would increase supply of particles (e.g. Fe, Mn) to the cave, but reduce supply of elements that depend on long contact times between percolating water and the carbonate host rock (e.g. Mg, Sr).

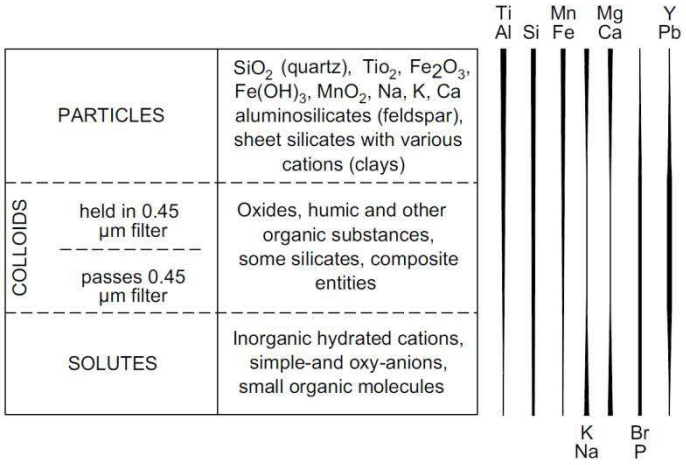

Figure 2.17: Transport modes of trace elements as particles, colloids and solutes – Tendency towards specific transport modes of some trace elements is illustrated by vertical lines (right). From Fairchild & Treble (2009).

2.5.1.3 Trace Element Incorporation

Trace elements can be distinguished according to their behaviour towards incorporation into speleothem fabrics (Fairchild et al., 2007): Trace elements may substitute for Ca^{2+} and CO_3^{2-} in the regular $CaCO_3$ crystal lattice (as Sr and Mg), occupy crystal lattice defect sites (such as P in the form of phosphate species), or may be predominantly incorporated in the form of solid and/or fluid inclusions. Some species, however, may exhibit multiple types of behaviour, such as Sr that may also occupy crystal lattice defect sites if Sr dripwater concentrations are sufficiently high (Fairchild et al. 2001).

The tendendy of trace elements substitute for Ca^{2+} and CO_3^{2-} in the regular $CaCO_3$ crystal lattice can be described with element-specific partition coefficients (D) that represent the relative abundance in solution and mineral phase, with partition coefficient close to unity indicating a high affinity of the respective element to be incorporated in the mineral phase. The partition coefficient of Mg (D_{Mg}) depends on temperature (Oomori et al., 1987; Huang and Fairchild, 2001; Day and Henderson, 2013), while D_{Sr} is affected by stalagmite growth rates or kinetics (Lorens, 1981; Baker et al., 1998; Banner et al., 2007).

As the temperature sensitivity of Mg incorporation into carbonate is relatively low and as the growth kinetics sensitivity of Sr incorporation has proven difficult to constrain under natural cave conditions (Borsato et al., 2007; Gabitov & Watson, 2006; Huang & Fairchild, 2001), the most commonly suggested control on speleothem Mg/Ca and Sr/Ca ratios is dripwater composition. This composition varies as a function of changing source strength, hydrological re-routing, water-rock interaction and PCP, with the latter two relating to seepage water residence time (Fairchild & Treble, 2009).

However, both D_{Mg} and D_{Sr} can be additionally affected by changes in mineralogy and crystal structure (Holland et al., 1964; Riechelmann et al., 2016). As defect site density in speleothems generally increases with growth rate, high contents in trace elements preferentially occupying these defect sites (such as P) might function as proxy indicators of growth rate. However, it is not yet settled, what growth rate thresholds need to be exceeded for such effects to manifest themselves (Fairchild & Treble, 2009).

2.5.2 Important Processes and their Implications for Palaeoreconstructions

2.5.2.1 PCP

PCP leads to rising Mg/Ca and Sr/Ca values in dripwater and finally in speleothem fabrics, as both Mg and Sr are distributed between solution and carbonate mineral corresponding to partition coefficients of much less than unity (Morse & Bender, 1990; Rimstidt et al., 1998), which leaves the remaining dripwater enriched in Mg and Sr. PCP also causes dripwater and speleothem $\delta^{13}C$ values to rise (Section 2.4.2.4). The resulting effect of increasing and covarying values of Mg/Ca, Sr/Ca and $\delta^{13}C$ has very often been demonstrated from dripwater (Fairchild et al., 2006; Karmann et al., 2007; McDonald et al., 2004; Tooth & Fairchild, 2003) and speleothem analysis (McDermott et al., 2004; Treble et al., 2005), successfully modelled (Fairchild & McMillan, 2007; Johnson et al., 2006) and interpreted as evidence for a dominating PCP control (e.g. Griffiths et al., 2010; Johnson et al., 2006).

Therefore, increased Mg/Ca and Sr/Ca ratios (Sr/Ca decreased by IDD) have very often been interpreted as indicators of palaeoaridity on subannual to decadal scale (Baldini et al., 2002; Fairchild et al., 2001; Huang et al., 2001; Johnson et al., 2006; Treble et al., 2003) and on greater time scales (Li et al., 2005; Verheyden et al., 2000), an interpretation corroborated by evidence from instrumental rainfall data (e.g. Karmann et al., 2007; Tooth & Fairchild, 2003). This circumstance illustrates the potential in combining different proxy signals, such as stable isotope ratios and trace element patterns for a more precise and confident interpretation of proxy data.

2.5.2.2 Dilution

High dripwater flow rates are suggested to have a diluting effect on some trace elements. This line of thought is consistent with PCP, as PCP leads to increases in trace element content and is supposed to be associated with dry conditions along the flowpath of dripwaters. For instance, Mg/Ca and Sr/Ca ratios in dripwater have been documented to increase with persisting drought conditions (McDonald et al., 2004).

However, other elements may exhibit higher concentrations under conditions of high flow. This is likely to be the case if downward transport of these elements to the cave is limited under low-flow conditions, as can be expected to be true for elements that are predominantly transported in corpuscular form.

2.5.2.3 Dissolution of Bedrock Carbonates

Dissolution within the overlying aquifer represents a key process for trace element supply to the cave (Fairchild & Baker, 2012). Concordantly, increased trace element concentrations in dripwaters, and thus in speleothem fabrics, are suggested to relate to high dwell times of percolating waters within the aquifer, which is thought to enhance dissolution-derived trace element input due to longer contact times between percolating water and carbonate bedrock that potentially contains "foreign" mineral phases (Fairchild & Treble, 2009).

This relationship seems particularly likely in the case of Mg, and increases in Mg concentrations have often been attributed to enhanced dolomite dissolution (Fairchild & Treble, 2009). A supporting argument of this line of thought is the fact that dolomite dissolution is slower than calcite dissolution. Thus, increased contact times would favour dolomite dissolution. In addition, low Mg contents have been found to coincide with high amounts of inclusions and P-rich laminae in some cases (Fairchild et al. 2001), which might in turn mirror high-flow conditions and short contact times.

Due to kinetic discrimination of dolomite versus calcite during dissolution, increased seepage water residence times (related to low flow) lead to increases in Mg/Ca ratios (e.g. Fairchild et al., 2000). Enhanced ratios of both Mg/Ca and Sr/Ca have been explained by drainage of low-permeability soil and aquifer compartments dominated by seepage-flow (selective leaching) under conditions of dryness-related low flow (e.g. Baker et al., 2000; Musgrove & Banner, 2004).

Contrarily, during incongruent dolomite dissolution (IDD), dolomite dissolves as calcite precipitates, which causes dripwater Mg/Ca ratios to rise, but Sr/Ca ratios to decline (Roberts et al., 1998), as dolomite usually contains less Sr than calcite (Tucker & Wright, 1990). As IDD is enhanced at higher residence times, it also relates to low flow rates and drier conditions.

2.5.2.4 Hydrological Routing

Changes in hydrological routing are another possible mechanism that could explain trace element variations, and have often been suggested to relate to variations in Mg and Sr variations (Fairchild et al., 2000). As different flow paths exhibit different dominating flow regimes, alternative hydrological routing can be expected to change the characteristic behaviour of a specific drip site regarding the trace element concentrations of its dripwaters.

For instance, a shift from seepage to conduit flow predominance (by overflow as illustrated in Figure 2.11, right) would reduce the concentrations of elements mainly derived from seepage flow, such as Sr and Mg, and enhance concentrations of elements that predominantly originate from conduit flow, such as particles bearing Fe and Mn.

2.6 Further Indicators of Past Climatic and Environmental Conditions in Speleothems

2.6.1 Speleothem Growth

2.6.1.1 Lamination and Growth Cessation - Hiatuses

One marked component of speleothem growth is the potential display of lamination, which may be defined as "repeated stacking of the fabrics in an ordered succession" (Fairchild et al., 2007), and can be found in many speleothems, at least in parts. Lamination is caused by faint parallel growth layers ("laminae"), the smallest features of speleothem growth to be distinguished with the naked eye. Laminae are often a result of variations in the abundance and scale of fluid inclusions (Ford & Williams, 2007) and therefore can be considered as reflecting changes in deposition rates, with high lamina thickness representing fast growth (Fairchild, et al., 2006).

Banding of larger scale is due to variations in crystal texture or incorporation of impurities, which reflect the history of the growth surface. Such optical properties may help the construction of geochemical time series (Fairchild, et al., 2006). For example, specific optical features may in cases be correlated with corresponding geochemical patterns, such as dark layers with high trace metal content.

Hiatuses

Even more marked layering may result from periods of growth intermittence, as speleothem growth may not only change in rate, but also cease completely, thereby forming hiatuses. Haituses can be associated with drying, re-solution under dominance of dissolution at the growth front or with other forms of erosion, e.g. condensation corrosion, or with deposition of foreign particles. In the proximity of hiatuses, structural integrity of the speleothem fabrics can be greatly reduced, so that stalagmites may well break at these fragile locations (Fairchild, et al., 2006).

2.6.1.2 Speleothem Growth Rate

Growth rate is another important feature of speleothems that can help in reconstructing past conditions, particularly in those cases in which speleothem growth rate is limited by a low number of specific environmental parameters, such as supersaturation state or dripwater flow.

Determination of growth rate can be conducted either by layer counting if lamination is sufficiently distinct or by interpolation between U-series dating points, whereas the latter does obviously not attain high temporal resolution, with the exception of very fast growing speleothems and very high-resolution dating protocols.

Growth Rate Spectrum

Speleothem growth rate displays important high-frequency, seasonal variations, even at continuous deposition, depending on seasons of intense rainfall and the lag between precipitation at the surface and soil water emergence in the cave (Ford & Williams, 2007). Measurements from show caves have yielded growth rates between <0.005 and 7 mm/a, whereas the upper limit is likely to be overestimated. Growth rates calculated as means based on radiometric dating also show wide differences, by four orders of magnitude, are highly site-specific, and can even vary within one cave. Estimated mean growth rates amount to about 100 µm/a, and do usually not exceed 1,000 µm/a. Theoretically possible growth rates are often not reached in reality due to high cave pCO_2 and/or low driprate(Fairchild et al., 2007).

Factors of Speleothem Growth Rate

Growth rate usually increases with rising temperatures and moisture (Fairchild, et al., 2001): Typical growth rates range from 10-100 µm/a in regions of cool temperate climate to 300-500 µm/a in subtropical and tropical climates (Fairchild, et al., 2006). However this general rule of thumb does not apply to stalagmites growing under peat soils, as these grow fastest under warm and dry conditions (Fairchild, et al., 2001).

This circumstance suggests that the growth rate of a given speleothem depends on a cave site-specific or even drip site- specific suite of environmental factors. The identification of this speleothem-specific suite of growth-rate controlling factors is likely to yield additional constraints on the (potentially large) spectrum of possible conditions that prevailed in the past. Comprehensive present-day monitoring studies examining these parameters are required to establish the existing linkages.

As dripwater supersaturation with respect to $CaCO_3$ is mainly triggered by CO_2-degassing, the pCO_2 gradient between dripwater and cave air is a crucial factor of speleothem growth rate. Changes of this gradient may either originate from changed dripwater pCO_2, which primarily depends on the proportion of open vs. closed system conditions, and/or from variations in cave pCO_2.The latter is largely determined by the rate of CO_2-degassing from dripwater (related to dripwater input rates) and by cave ventilation (Fairchild et al., 2007). High cave ventilation enhances speleothem growth rates by lowering cave air pCO_2.

The process of cave ventilation may exhibit strong links to high-frequency variations in the atmospheric pressure difference between the cave interior and the external atmosphere, which result from both synoptic weather systems and the constancy of cave temperatures. In more general terms, cave ventilation depends on both climate and geometry of the cave passages under investigation.

However, cave ventilation can also be predominantly controlled by a cave stream. In this case, RH will be ~100 % at all times and cave air pCO_2 will depend on that of the stream, which may show seasonality (Fairchild, et al., 2006).

Unfortunately, not much is known about how cave pCO_2 in such a case varies on greater timescales (decades to centuries), and what mechanisms drive pCO_2 in underground cave streams. On the seasonal timescale, cave ventilation has been demonstrated to strongly influence pCO_2 of both dripwater and cave air, as well as carbon isotope ratios recorded in speleothems (Spötl et al., 2005).

2.6.1.3 Speleothem Macroscopic Properties and Crystal Morphology

Additionally to geochemical proxy signals that are only accessible by complex and expensive analytical instruments, many other characteristics of speleothems that are in parts visible to the naked eye potentially contain information valuable for palaeoenvironmental reconstruction. These include speleothem overall shape (with uniform shapes reflecting stable conditions in cave and dripwater), colour (which is a consequence of ionic and/or detrital contaminations of foreign material such as metals, organic molecules or of porosity variations) and diameter (which depends on flow rates, saturation state with respect to $CaCO_3$ and fall height of the feeding dripwater; Ford & Williams, 2007). Another very important feature of speleothems are their respective fabrics (= texture: geometry and spatial arrangement of single crystals that compose a synchronous growth layer/lamina) and their variations within one single speleothem (Fairchild et al., 2007). Detailed analysis of fabrics however requires (e.g. electron) microscopic techniques.

Crystal morphology

Crystal morphology of speleothems is related to both flow and chemical composition of the feeding dripwater. Main factors are therefore drip rate and chemical composition, capillary or gravitational supply of ions to crystal growth sites, rate of CO_2-degassing, and the variability in all the above factors (Fairchild et al., 2007). Single crystals in stalagmites actually represent composites of individual crystallites, between which small spaces are left during the crystallisation process. These are either removed by subsequent lateral crystallite coalescence (overgrowth) or preserved as fluid inclusions (Fairchild et al., 2007).

The latter are thought to conserve dripwaters of past times, which provides the opportunity to "directly" measure chemical and isotopic composition of past precipitation – a crucial unknown in equations used for calculation of palaeotemperatures (Lachniet, 2009). Crystal morphology of speleothems reacts to environmental conditions during their formation, and can thus be utilised for their reconstruction. For example, flooding of speleothems during periods of cave submergence leads to the formation of distinctive competitive growth fabrics (Dickson, 1993).

Crystal defects typically indicate either fast speleothem growth or (high) availability of foreign ions or particles (detritus) that may function as growth inhibitors, but may also be caused by fluctuations in flow rate, periodic exposure of the growing crystal faces to the cave air, rapid outgassing or chemical dissolution due to undersaturated dripwaters (Fairchild et al., 2007). Crystal defects are most abundant under conditions of intense evaporation (Ford & Williams, 2007).

2.6.2 Speleothem Mineralogy and Fabric Types

Although secondary precipitates in caves are mainly composed of calcite which is more abundant than all others combined, they may also be partly composed of aragonite ($CaCO_3$, a modification of calcite) and gypsum ($CaSO_4$ x 2 H_2O). Other carbonates and hydrated carbonates are of much smaller significance (Ford & Williams, 2007). As different mineral phases behave differently to the same forcing mechanisms, mineralogical investigations should accompany palaeoenvironmental studies of speleothems. The second-most abundant mineral phase found in speleothems is aragonite.

Aragonite

In speleothems, aragonite principally forms radiating clusters of needles (so-called "whiskers"), but may also form massive or acicular specimen that can be laminated with calcite or display a patchy appearance after inversion to calcite (Ford & Williams, 2007). Several processes can lead to the substituting formation of aragonite instead of calcite: The principal factor is the depletion of Ca ions in solutions rich in Mg, which is normally caused by PCP (Section 2.4.2.4). Other possible factors are ion substitution, for instance by Sr, and unspecified effects of organics or other seed nuclei at growth initiation. In the domain of calcite and dolomite, aragonite is metastable, i.e. thermodynamically instable, but kinetically stable, and is therefore naturally prone to inversion to calcite, although not much is known about the typical rates of this process (Ford & Williams, 2007). If conversion between calcite and aragonite occurs, geochemical signals are likely to be modified, in practice however, this seems to be only a minor concern (Fairchild & Treble, 2009). Figure 2.18 illustrates the evolutionary path of a hypothetical karst groundwater and the respectively dominant mineral phases.

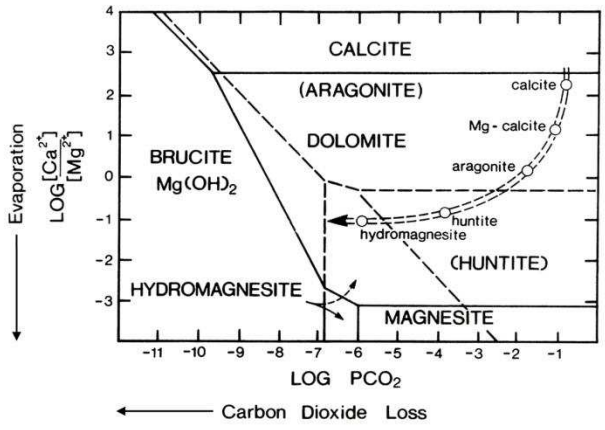

Figure 2.18: Stable and metastable (dashed lines) phase relationships in a calculated system of Ca-Mg-CO_2-H_2O. Dashed-lined arrow depicts a model evolutionary path for a hypothetical water. From Ford & Williams (2007).

Fabric types

Frisia et al. (2000) have developed a classification of different fabric types that can be used for palaeoenvironmental reconstruction through microscopic analysis (Section 4.7):

The "columnar fabric" characteristically contains only few crystal defects, and stalagmites composed of this fabric type are typically translucent and potentially feature lamination that might be even annual. It commonly forms under conditions of comparably low dripwater supersaturation, low foreign ion content and relatively constant flow.

The "microcrystalline fabric" is characterised by irregularly stacked crystallites and high crystal defect density, and has been documented in alpine stalagmites with annual lamination, in which it forms milky, opaque and porous layers. Crystallites of this type also typically feature dislocations and repetitive twinning, all signs of strong disturbances within the system related to flow variability and periodic input of growth inhibitors such as humic acids (Fairchild et al., 2007).

The "dendritic fabric" consists of crystallites arranged in branches similar to a dendrite crystal, and features a high density of crystal defects. This fabric type is highly porous, which again indicates highly variable growth conditions, i.e. varying discharge, strong outgassing events and periodic capillary flow – as opposed to gravitational flow.

The "fan fabric" is typical for aragonite and is generated by acicular, needle-shaped or ray crystals that radiate from a central nucleus. Single aragonite crystals may be identified by their common display of microtwinning (Frisia et al., 2002).

2.7 Ideal Choice of Stalagmites

In order to extract and use stalagmites actually suited for the reconstruction of palaeoclimatic and palaeoenvironmental conditions, an ideal choice of stalagmites would meet the following requirements:

A stalagmite with an actively dripping stalactite is commonly better suited than an inactive stalagmite as the active drip site enables for drip water analyses that help understand the drip site-specific suite of factors controlling dripwater geochemistry. Furthermore, if the stalagmite is still growing at the time of extraction, the modern-day carbonate precipitates can be analysed to, for example, for demonstrating calcite precipitation in isotopic equilibrium or for identifying kinectic fractionation.

Stalagmites with a sufficiently simple growth symmetry are favourable as it enables for precise and reliable sub-sampling due to the physical continuitiy of the growth laminae. If possible, stalagmite should not be extracted too close to the cave entrance or other connections to the outside as relative humidity at such sites may be significantly below 100% which can cause stable isotope time series, especially $\delta^{18}O$, to be influenced by kinetic effects due to evaporation. Additionally, caves or sites inside a specific cave should be chosen where cave ventilation is not too strong in order to avoid kinetic effects on speleothem $\delta^{13}C$ signals due to rapid CO_2-degassing.

Speleothem uranium contents should be sufficient to enable precise and accurate dating, while high detrital Th contents should be avoided. In general, stalagmites with undisturbed growth are favourable for palaeostudies, including the absence of detrital layers that prevent precise dating and that can complicate interpretation of speleothem geochemical time series. For instance, stalagmites regularly covered by fine cave sediments inside water-bearing caves due to periods of cave submergence should be avoided.

Finally, as the geochemical behaviour of different drip sites and their corresponding stalagmites might vary between caves in a region and even between drip sites within the same cave, replication of palaeoenvironmental proxy signals by analysing multiple stalagmites from the same cave and stalagmites from multiple caves in a region that cover the same growth period is advantageous.

2.8 The Asian Monsoon

The Asian Monsoon is part of the global system of monsoons that zonally encompasses the entire globe (Figure 2.19) and that comprises the American, the African, the Australian and the Asian Monsoon (Schönwiese, 2013). This PhD thesis focuses on the Asian Monsoon and its evolution over time. In order to provide a framework for the investigation of past changes in the Asian Monsoon, its present-day dynamics are shortly reviewed here. For this, the Asian Monsoon is divided into its three subsystems, the Indian Summer Monsoon (ISM), the East Asian Summer Monsoon (EASM) and the Winter Monsoon (WM). All three subsytems are relevant to this investigation as the study area is located right in the transition zone of these subsystems (An, 2014).

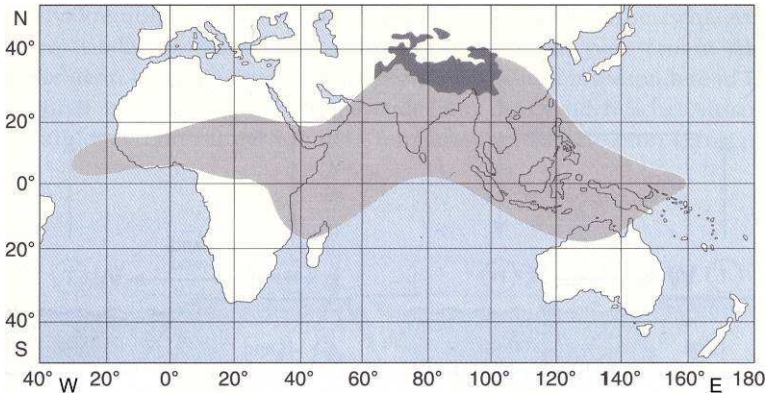

Figure 2.19: Area influenced by the different monsoon systems (light grey shading). The dark grey shading represents areas where ground level is above 3,000 m altitude that enhance monsoon dynamics and impact on atmospheric circulation. (Schönwiese, 2003, adapted from Hendl et al., 1988 and Heyer & Chmielewski, 1998).

This transition zone (TZ) is illustrated in Figure 2.21. On its northern border, the TZ is limited by the northern limit of the Summer Monsoon, its western boundary has been defined by Wang (2006), its eastern boundary by Ke (1999).

2.8.1 The Indian Summer Monsoon

In contrast to the subtropical monsoons, the ISM is a tropical monsoon and, by that, a monsoon in the narrower sense as it is mainly caused by the seasonal migrations of the Innertropical Convergence Zone (ITCZ; Schönwiese, 2013). The ITCZ is an equatorial band of low pressure systems with intense convection of warm and moist air that results from the strong insolation at and near the equator that causes evaporation and intense rainfall. At the top of troposphere these now colder and drier air masses are forced towards the respective pole on each hemisphere by the stratospheric temperature inversion. During their dynamically induced descent at the latitude of the persistent subtropical highs, the air masses become warmer and drier.

At the surface these warm and dry air masses then move back towards the ITCZ at the equator as trades, completing the Hadley cell on each hemisphere. As a result of the Coriolis force, the trade winds are deflected to the right relative to their direction of movement on the Northern Hemisphere (NH) and to the left on the Southern Hemisphere (SH). In conjunction with friction at the Earth's surface that prevents a purely geostrophic wind (from eastery directions), the distinct circulation patterns of the northeast and southeast trade winds on the NH and SH, respectively, are created (Schönwiese, 2013; Häckel, 2016). Trade wind convergence in the ITCZ closes the circulation loop of the Hadley cell. If moving over the ocean, the air masses absorb high amounts of moisture on their path to rain out at the ITCZ which adds to precipitation amounts there.

Therefore, the ITCZ is a zone of both ample and intense precipitation. The ITCZ is not stationary but rather moves along with the solar zenith that changes with season, to the north during NH summer, to the south during NH winter. This pattern would be symmetrical with respect to the equator if land and ocean surfaces were evenly distributed between the NH and SH. Due to the overbalance of land surfaces of India and Asia adjacent to the Indian Ocean, the ITCZ migrates further north during NH summer and reaches its northernmost position over the Tibetan Plateau in July (Figure 2.20, bottom), at the peak of summer (Vorlaufer, 2011). Consequently, on their way to the ITCZ, the southeast trades originating over the Indian Ocean between Australia and Africa become southwest trades after crossing the equator due to the Coriolis force and predominantly hit the Indian subcontinent and the Asian continent in a northeasterly direction as southwesterly winds (Figure 2.20, bottom). On landfall these now very moist and warm air masses lead to significant precipitation that is even intensified due to orographic lifting at the southern flanks of the Himalayan Mountains. Parts of these air masses have a more southerly trajectory and cross Southeast Asia in northeasterly directions that become northerly directions at the latitude of South China. These airmasses supply monsoon rainfall over the study area in Northern Vietnam after crossing the north-south oriented mountain ranges of Myanmar (e.g. the Arakan Mountains), Thailand and Laos where they already lose part of their moisture (Weischet & Endlicher, 2000). Summing up, it can be stated that the ISM carries moisture originating from the Indian Ocean and leads to ample rainfall over southern Asia, southeastern Asia and southwestern China (An et al., 2014).

The intensity of the ISM is increased by the differential heating of the Southasian continent compared to the Indian Ocean, especially of the west-east oriented Tibetan Plateau (TP) due to its enormous size and mean altitude of 4,500 masl (Klose, 2016). Over the TP a latent heat anomaly forms within the mid-troposphere (Yanai et al., 1992) which results is a thermal ground level low with pressures typically below 1,000 mbar (Häckel, 2016) that stabilises the primarily ITCZ-driven monsoon regime. The TP also effectively shields large parts of South Asia from cold polar air masses (Klose, 2016), but not the study area in Northern Vietnam (Figure 2.21 left). With respect to the interior of Asia, the TP represents a geographic barrier that prevents high rainfall amounts east of it, both directly and due to divergence of the westerlies (dividing them into a southerly and a northerly branch) which causes enhanced

subsidence east of the TP and thus decreased rainfall probability (Manabe & Broccoli, 1990). Therefore, the westerlies play an important role in generating/maintaining Asian deserts, but they also supply a climatic teleconnection between Asia and the North Atlantic (Porter & Zhisheng, 1995).

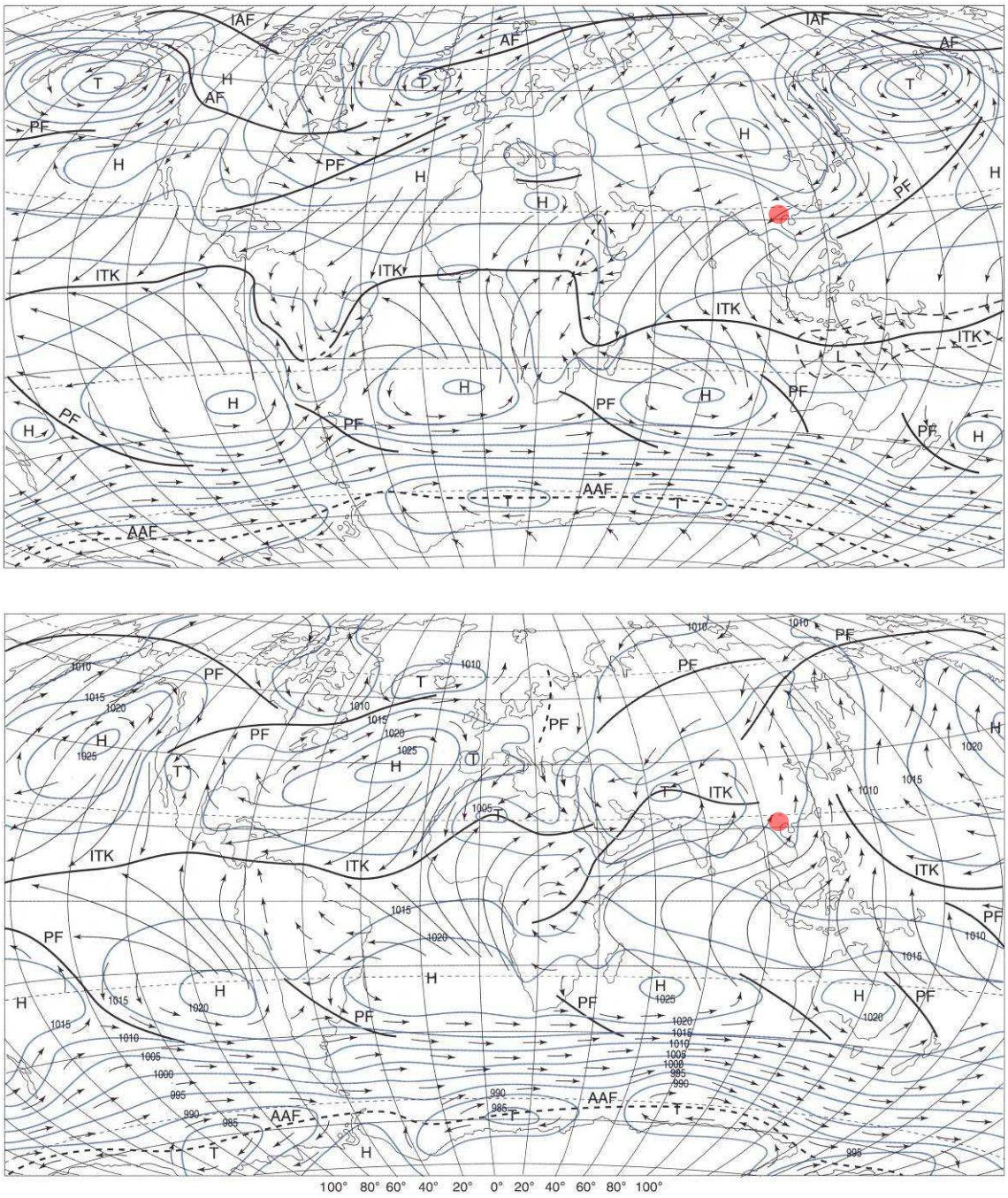

Figure 2.20: Top: Sea level pressure (blue contours; H = high; T = low) and prevalent wind directions (black arrows) in relation to the main frontal zones (PF = polar front; AF = arctic front; IAF = interarctic front; AAF = antarctic front) and the intertropical convergence zone (ITK) in January averaged over the period 1931-1960 (Schönwiese, 2003 adapted from Liljequist & Cehak, 1994); Bottom: Same as above, but for July; The red dot indicates the location of the study area for this PhD thesis.

2.8.2 The East Asian Summer Monsoon

The EASM is a subtropical monsoon and is mainly caused by differential heating between land and ocean surfaces in the mid-latitude West Pacific in NH summer, rather than by the ITCZ (Schönwiese, 2013). Air masses originating from the South China Sea and from the West Pacific north of it are drawn to the thermal lows over Southeast and East Asia resulting in southeasterly winds over Eastern China (Figure 2.21, right; Weischet & Endlicher (2000) from Flohn (1950)) where they induce precipitation on landfall and due to orographic lifting. Further north, these air masses converge with westerly winds of the westwind zone at the polar front (Figure 2.20) and thereby become deflected to the east to yield southerly and even southwesterly wind directions. This convergence forces the air masses to ascend and leads to rainfall in Eastern and Northern China. While it has been reported that most of the moisture fueling precipitation in northern China within the EASM region originates from the tropical Pacific (An et al., 2014), recent meteorological (Ding et al., 2004) and modelling studies (Clemens et al., 2010; Pausata et al., 2011) suggest that most of the moisture precipitating over China during the EASM primarily originates from the Indian Ocean (Johnson, 2011).

Being a subtropical monsoon, the EASM is generally weaker than the ISM which is also evident from its relatively small vertical dimension. While ISM convection usually reaches altitudes of around 6,000 m, EASM convection normally does not exceed several hundred meters (Heyer & Chmielewski, 1998) and precipitation amounts are therefore generally smaller. Furthermore, the EASM can be distinguished from the ISM based on the differing orographic boundaries on the northern limit of the two sub-systems and on zonal differences in land-ocean configuration (An et al., 2014).

2.8.3 The Winter Monsoon

The WM is caused by the thermal anticyclone referred to as Siberian High that forms over the snow-coverd part of Asia (roughly between 40°N and 60°N) during NH winter as a result of strong continental cooling of the land surface (Figure 2.21, left; Klose, 2016). This high pressure system with pressures typically exceeding 1,035 mbar (Häckel, 2016), which is one of the most stable on the globe, generates cold and dry air masses that move away from its center. The air masses on its eastern and northeastern flanks initially migrate southeast towards the polar front over the West Pacific (Figure 2.20). Due to the combination of the Coriolis force and friction at and near the land surface, these northerly winds are transformed into northeasterly winds (Klose, 2016) that cross the study area in Northern Vietnam and bring cold and dry air to it. Figure 2.21 (left) also shows that the study area in Northern Vietnam lies within the zone influenced by cold surges from Inner Asia in NH winter.

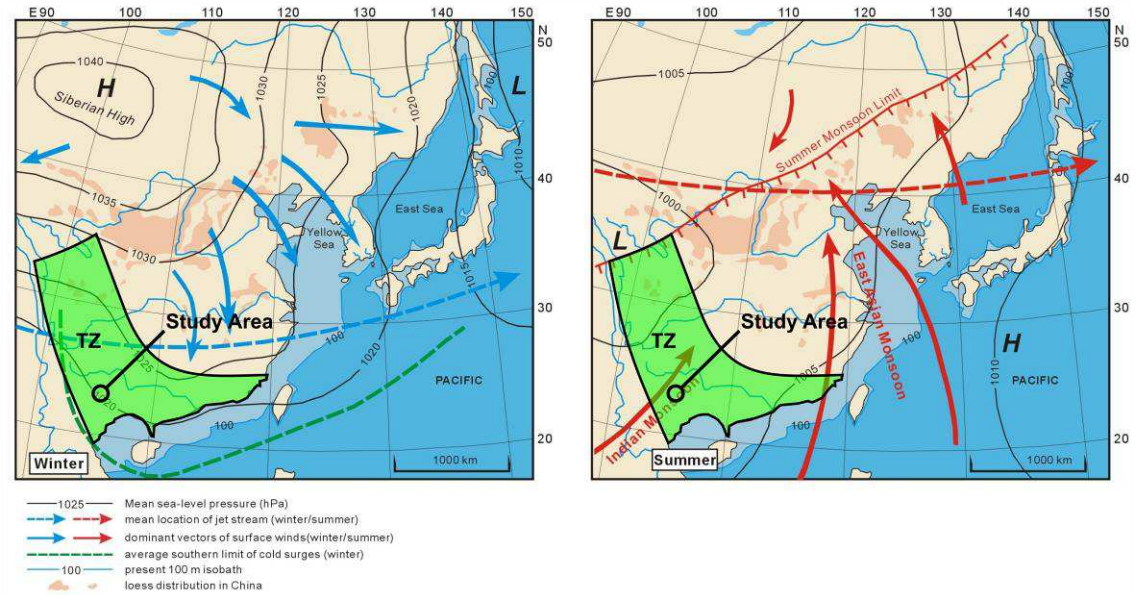

Figure 2.21: Left: Depiction of the Siberian High that causes the dry and cold Winter Monsoon with northerly and northeasterly wind direction in the study area in Northern Vietnam (black circle) in NH winter; Right: Schematic illustration of the main wind directions and air mass trajectories related to the EASM and the ISM together with the approximate northern limit of EASM influence in NH summer. Figure modified from Yi (2011), modified from Yancheva et al. (2007). The green shaded area represents the transition zone (TZ) between ISM and EASM.

2.8.4 The Stalagmite $\delta^{18}O$ Proxy in Monsoon Asia

Since the publication of the first stalagmite $\delta^{18}O$ record from the Asian Monsoon region in 2001 (Wang et al., 2001), their interpretation has been controversial. By today, a large number of studies based on stalagmite $\delta^{18}O$ values have been performed in the Asian Monsoon region, with most studies focussing on the EASM sub-region (Wang et al., 2001; Yuan et al., 2004; Dykoski et al., 2005; Wang et al., 2005; Hu et al., 2008; Wang et al., 2008; Zhang et al., 2008; Cai et al., 2010; Dong et al., 2010; Tan et al., 2010; Cheng et al., 2012; Jiang et al., 2012; Zhang et al. 2013; Cheng et al. 2016b; Cheng et al. 2016a). From the ISM sub-region, a growing number of publications are emerging (Neff et al., 2001; Fleitmann, 2003; Fleitmann et al., 2004; Sinha et al., 2005; Cai et al., 2006; Fleitmann et al., 2007; Sinha et al., 2007; Shakun et al., 2007; Berkelhammer et al., 2010; Sinha et al. 2011; Cai et al., 2012; Cai et al., 2015). The locations of the proxy records discussed in the following are shown in Figure 2.22, together with the northern limit of the modern-day Asian Summer Monsoon and averaged moisture fluxes based on reanalysis data.

With increasing number of publications the interpretation of stalagmite $\delta^{18}O$ values in the EASM region evolved: In the absence of an obvious relationship between precipitation $\delta^{18}O$ and temperature (temperature effect) or precipitation amount (amount effect) in modern-day rainfall data from the nearby Guilin area (Li et al.; 2000), Wang et al. (2001) related changes in $\delta^{18}O$ values in stalagmites from Hulu cave (32°30’ N,119°10’ E) in eastern China to variations in the relative contribution of isotopically light summer precipitation (–9‰ to –13‰) and isotopically heavier winter precipitation (–3 to +2‰) to annual totals.

Investigating a stalagmite from Dongge cave (25°17’ N, 108°5’ E) in southern China, about 1,200 km westsouthwest (upwind / “upstream”) of Hulu cave, Yuan et al. (2004) found $\delta^{18}O$ variations very similar to those previously observed in the Hulu stalagmites by Wang et al. (2001). They argued that the amplitude of the observed $\delta^{18}O$ fluctuations in both records (4.7 ‰) is far too high to be explained by the change in the calcite/water fractionation of oxygen isotopes with temperature alone (only –0.23 ‰ / °C; Friedman & O'Neil, 1977) and therefore concluded that the stalagmite $\delta^{18}O$ signals from Dongge/Hulu mainly reflected the $\delta^{18}O$ of meteoric precipitation.

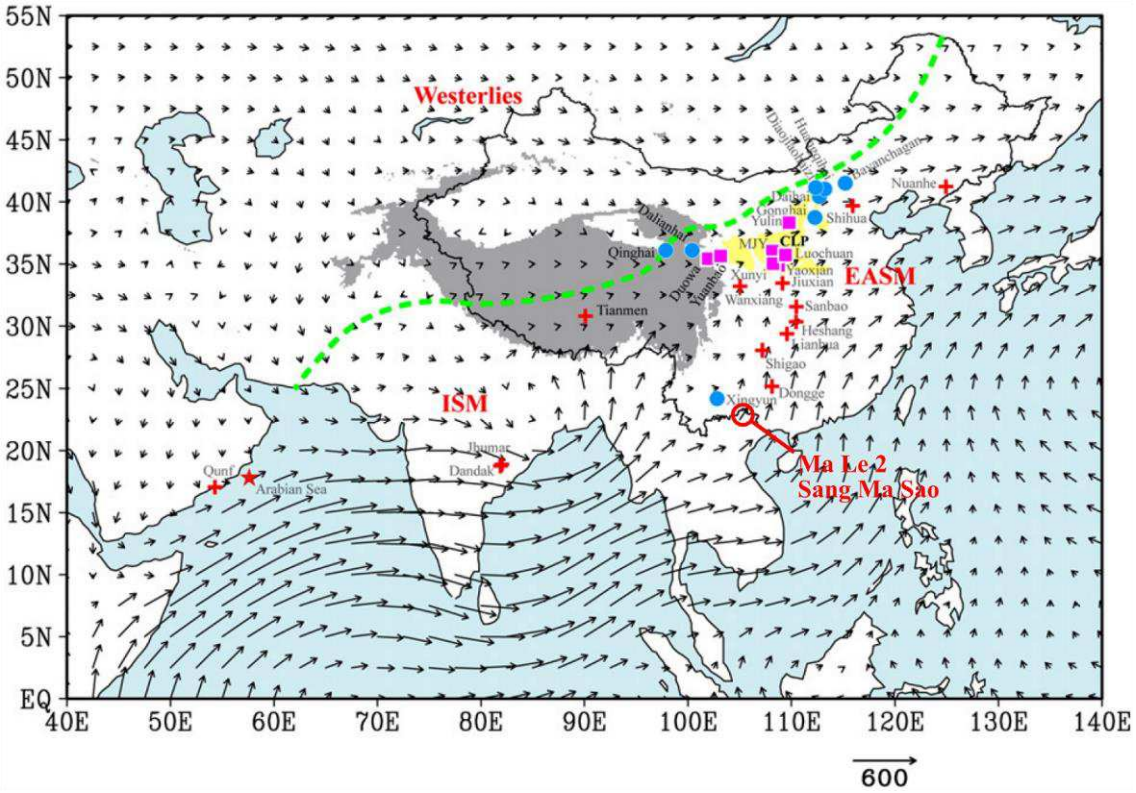

Figure 2.22: Locations of the precipitation and moisture proxy records discussed in the text (red crosses = stalagmite records; blue circles = lake sediment records; purple rectangles = Loess magnetic susceptibility records). The black arrows indicate water vapor flux vectors ($kg \cdot m^{-1} \cdot s^{-1}$) averaged over the summer months June, July and August as a vertical integration from the surface to the 300 hPa level for the period 1971–2000 based on NCEP/NCAR reanalysis data (Kalnay et al., 1996; scale in the right bottom corner). The green dashed line illustrates the northern limit of the modern-day Asian Summer Monsoon (Chen et al., 2010). The areas shaded in yellow and grey are the Chinese Loess Plateau and areas above 3000 masl, respectively. Reprinted with permission from Liu et al. (2015).

Yuan et al. (2004) further argued that the predominant characteristic in the observed and modelled spatial distribution of precipitation $\delta^{18}O$ is the trend towards lower $\delta^{18}O$ values with increasing latitude (Rozanski et al., 1993; Araguás-Araguás et al., 1998; LeGrande & Schmidt, 2006; LeGrande & Schmidt, 2009) and that this trend can be modelled on the basis of Rayleigh fractionation (Dansgaard, 1964). Rayleigh fractionation causes decreasing water vapour and precipitation $\delta^{18}O$ values along the trajectory of moist air masses due to preferential removal of ^{18}O via condensation and rainout on the way from the respective moisture source to moisture sinks where precipitation occurs. Based on this process, often referred to as "upstream depletion mechanism", Yuan et al. (2004) came to the conclusion that precipitation $\delta^{18}O$ at the Hulu and Dongge sites primarily depends on the amount of water vapour removed from the moist air masses originating from the tropical Indo-Pacific. Importantly, this moisture loss reflects precipitation integrated over the entire trajectory of the moist air masses.

Using a slightly modified version of the Rayleigh equation (Criss, 1999) and estimations of absolute humidity in tropical moisture source regions, they calculated that "the amount of precipitation integrated between tropical sources and southeast China is today 87% of mid-Holocene/Last Interglacial values and was 65% of mid-Holocene/Last Interglacial values at glacial times [here represented by the Heinrich event 1 (H1) at about 16 ka BP]" (Yuan et al., 2004).

Following the reasoning of Yuan et al. (2004) adopting the upstream depletion mechanism, Hu et al. (2008) investigated a stalagmite $\delta^{18}O$ record from Heshang cave (30°27′ N, 110°25′ E) located about 600 km downwind of Dongge cave, between Dongge and Hulu caves. As Heshang cave lies in the same moisture transport pathway as Dongge cave (Figure 2.22; Kalnay et al., 1996), Hu et al. (2008) were able to eliminate any potential additional controls on precipitation (hence stalagmite) $\delta^{18}O$ such as moisture source $\delta^{18}O$ and location, upstream rainfall and temperature by subtracting the stalagmite $\delta^{18}O$ values from Heshang cave from the corresponding ones from a new high-resolution stalagmite record from Dongge cave (Wang et al., 2005).

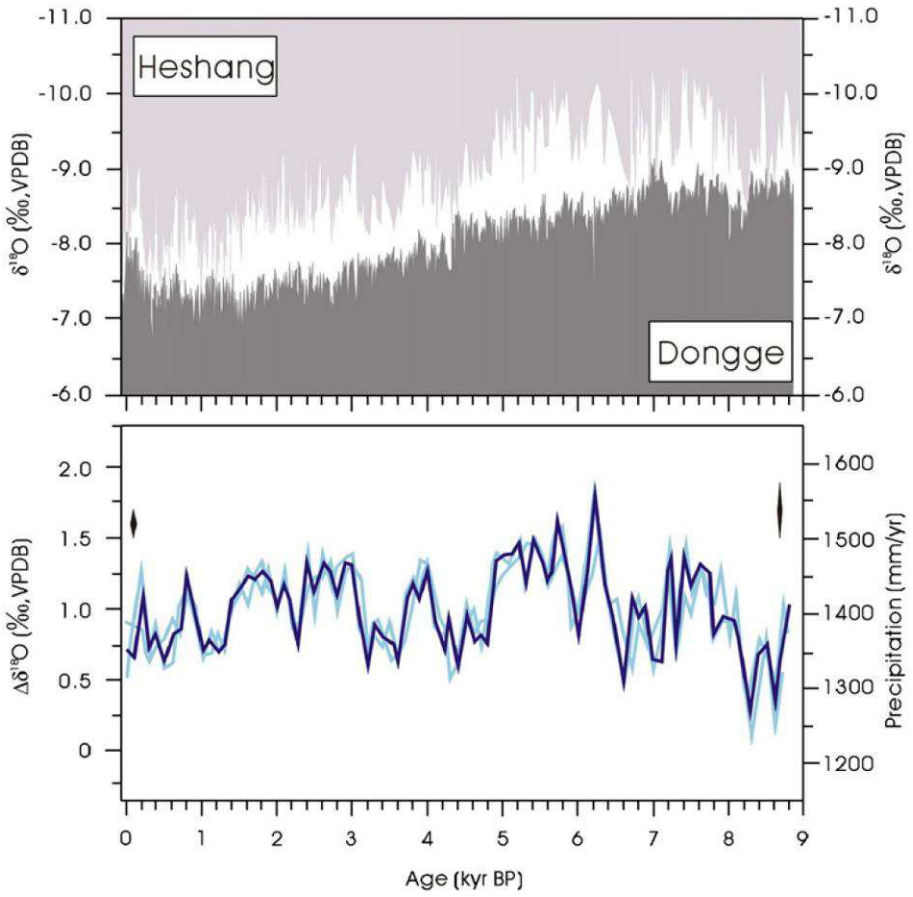

Figure 2.23: Top: The stalagmite $\delta^{18}O$ records from Heshang (light-grey) and Dongge caves (dark-grey; axes reversed). Bottom: The $\Delta\delta^{18}O$ signal (dark-blue line) calculated by differencing both records. The bright-blue line represents the $\Delta\delta^{18}O$ signal when the Dongge record is shifted by 50 years in both directions relative to the Heshang record to test the robustness of the $\Delta\delta^{18}O$ signal to age uncertainty. The diamond on the left indicates analytical uncertainty (0.15 ‰), the one on the right also includes the uncertainty resulting from the scatter about the linear relationship between $\Delta\delta^{18}O$ and instrumental rainfall data between the two sites. Figure from Hu et al. (2008).

They noted that, for this approach to be valid, it is required that both cave sites are sufficiently close to one another to exhibit a comparable temperature history, that differences in the altitude of cave recharge (precipitation formation) are corrected for and that moisture transport pathways have remained relatively constant over the reconstructed period. Hu et al. (2008) argued that the resulting $\Delta\delta^{18}O$ signal is solely influenced by the precipitation amount between the two cave sites. Comparison of five decadal $\Delta\delta^{18}O$ values with the corresponding precipitation amounts (spanning the last 54 years) averaged from six meteorological stations in the region corroborated this relationship and enabled Hu et al. (2008) to calibrate the $\Delta\delta^{18}O$ signal to average annual rainfall (Figure 2.23, bottom).

Based on this quantitative relationship, Hu et al. (2008) concluded that rainfall in southwest China was 8% higher than today during the Holocene climatic optimum (about 6 ka BP) so that today's rainfall amounts to about 92% of mid Holocene rainfall. Compared to the 87% of mid Holocene rainfall estimated for the range between tropical sources and southeast China (Yuan et al., 2004), this indicates a slightly lower rainfall change in southwest China.

Numerous additional studies in the EASM-dominated region of the last decade (Wang et al., 2008; Zhang et al., 2008; Cai et al.; 2010; Dong et al.; 2010; Tan et al., 2010; Cheng et al., 2012; Jiang et al., 2012; Zhang et al. 2013; Cheng et al. 2016a; Cheng et al. 2016b) have shown that the consistent temporal pattern of relative stalagmite $\delta^{18}O$ variations initially observed at the sites of Hulu, Heshang and Dongge caves can indeed by found over a much larger area as previously thought, resulting in a coherent stalagmite $\delta^{18}O$ signal spanning the latitudinal range from 17 °N to 42 °N (Liu et al., 2015).

Even more strikingly, studies from the ISM-dominated region (Neff et al., 2001, Fleitmann, 2003; Fleitmann et al., 2004; Sinha et al.; 2005; Cai et al., 2006; Fleitmann et al., 2007; Sinha et al., 2007; Shakun et al., 2007; Berkelhammer et al., 2010; Sinha et al. 2011; Cai et al., 2012; Cai et al., 2015) have also found this consistent stalagmite $\delta^{18}O$ signal (on orbital to millennial time-scales) confirming that it reflects large-scale (supra-regional) variations in atmospheric circulation (Cheng et al., 2016b) primarily related to the Indian Summer Monsoon. It is the ISM that generates the initial $\delta^{18}O$ signal via the amount effect in dependence of the mean latitudinal summer position of the ITCZ over the Arabian Peninsula (Burns et al., 2001; Neff et al., 2001; Fleitmann, 2003). This upstream depletion mechanism leads to decreasing $\delta^{18}O$ values in stalagmites and modern rainfall along the water vapor transport route (Yang et al., 2014; Liu et al., 2015) from the western Indian Ocean over southern Oman and India to Southeast Asia (Figure 2.22). The similar pattern in modern rainfall and stalagmite $\delta^{18}O$ values suggests that this modern-day moisture transport route was similar during the entire Holocene (Yang et al., 2014) and that the Indian Ocean represents the main moisture source in the ISM region as well as reaching into the EASM region to where it was modelled to contribute around 60% of total moisture input (Liu et al., 2014).

Summing up all the discussed findings, the stalagmite $\delta^{18}O$ signal in the Asian Monsoon region is most likely initiated in the Indian Ocean where it reflects local precipiation amount via the amount effect. The signal is then transferred to both ISM and EASM regions where the consistent decrease in $\delta^{18}O$ values along the main moisture transport pathway reflects progressive rainout due to Rayleigh fractionation, described as the upstream depletion mechanism. Therefore, the difference in stalagmite $\delta^{18}O$ values from cave sites located in the same moisture transport pathway can be expected to represent the amount of precipitation integrated between the two sites. In order to evaluate the conistency of this large-scale explanatory pattern with the new stalagmite $\delta^{18}O$ records from Ma Le 2 and Sang Ma Sao caves generated for this thesis, they are illustrated in its context in Section 6.1.

3 Study Area in Northern Vietnam

The study area of this PhD thesis is located just west of Dong Van City, the capital of Dong Van District, Ha Giang Province, Northern Vietnam, a few kilometres south of the Chinese border (Figure 3.1). Large portions of the geology of this area (Section 3.2) and its surroundings are dominated by carbonate rocks (Figure 3.1). In conjunction with the subtropical monsoon-type climate (Section 3.1.1), the conditions are favourable for intense karstification which has led to the formation of a strongly karstified landscape, called turmkarst (Ford & Williams, 2007).

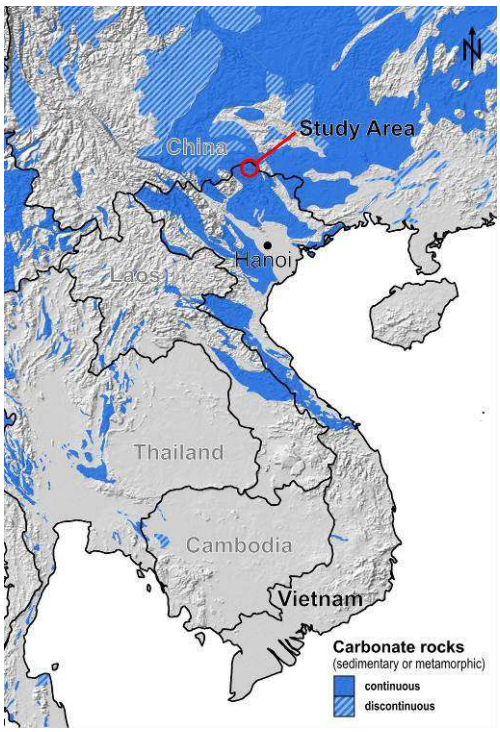

Figure 3.1: Overview map indicating the location of the study area in Northern Vietnam. The blue shading represents occurrences of carbonate rock from the world karst aquifer map (Chen et al., 2017).

Important hallmarks of turmkarst are an extreme topography with great differences in altitude between the karst hills and the valleys surrounding them, the lack of survace runoff and the formation of karst caves that often channel subsurface water flow in underground rivers (Ford & Williams, 2007). Surface runoff only happens where rock occurs at the topographic surface with low or no permeability to water (aquitards/aquicludes), where it is concentrated into rivers. In the study area, there are three main surface rivers: The Ma Le, the Seo Ho and the Nho Quế (Figure 3.2). The river Ma Le is of particular relevance to this study as it flows through the cave Ma Le 2 after entering the subsurface about 200 m upstream.

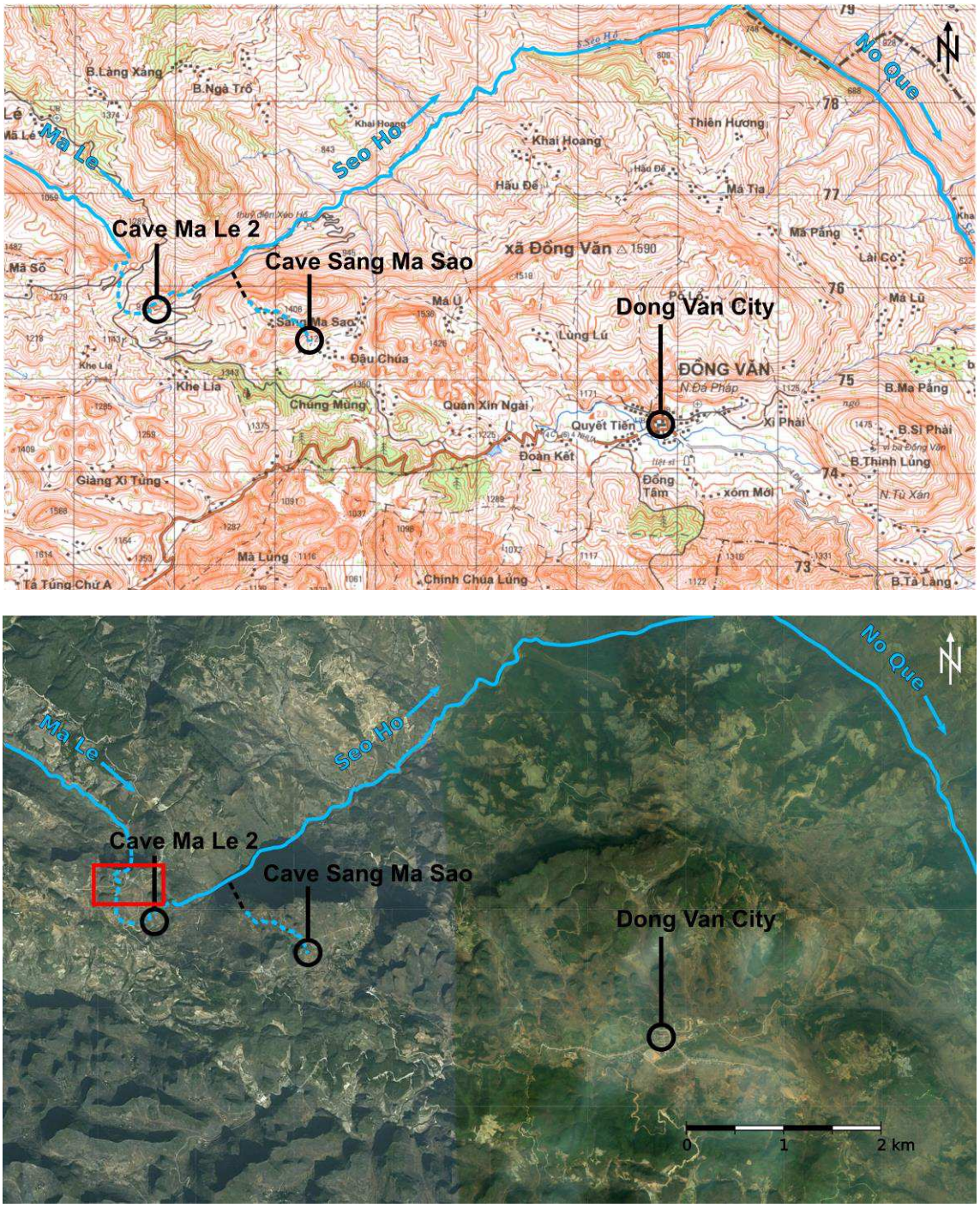

Figure 3.2: Top: Study area including location of the two studied caves Ma Le 2 (23°17'23.17"N, 105°18'45.67"E; altitude entrance 1,015 meters above sea level; masl) and Sang Ma Sao (23°17'11.54"N, 105°19'40.15"E; altitude entrance 1,138 masl) on a topographic map (1:50,000; NARENCA, 2002). The vertical distance between contours is 20 m, the black squares represent 1 x 1 km^2. The three most important rivers in the study area are highlighted in bright blue, underground sections (inside caves Ma Le 2 and Sang Ma Sao) are indicated by a dashed line. The black dashed line represents a hydraulic connection confirmed by artificial tracer tests (Ender, Goeppert & Goldscheider, 2018) with yet unknown course; Bottom: Same section as above, but from satellite imagery (CNES/Airbus, map data from Google; accessed on September 14th, 2014). The red rectangle designates the area where the vegetation was mapped.

3.1 Geographical Setting

3.1.1 Climate

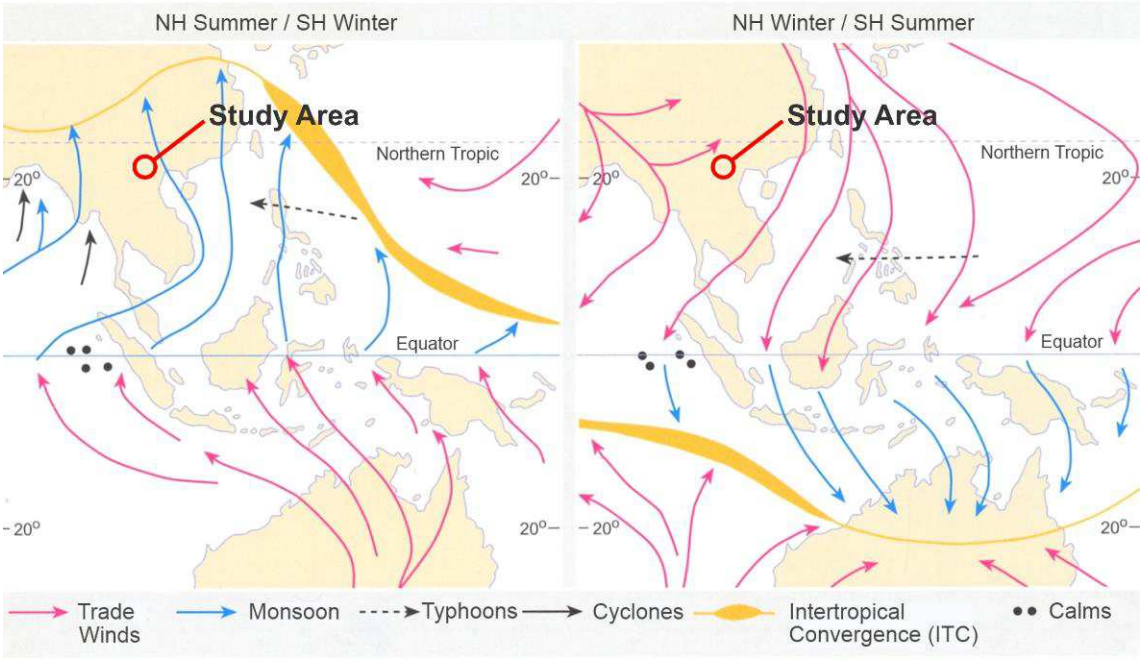

Figure 3.3: The Asian Monsoon System that generates ample precipitation in the study area in Northern Vietnam in NH Summer via both the Indian and East Asian Summer Monsoon subsystems, while only little rainfall occurs during NH winter as a consequence of cold and dry Winter Monsoon winds from the Siberian High in Inner Asia (adapted from Vorlaufer, 2011). The yellow lines are an approximate illustration of the ITCZ's northernmost and southernmost position, respectively. Typhoons supplying additional moisture to the study area are represented by dashed black lines.

The climate in the study area is dominated by the Asian Monsoon System with its three subystems, the ISM, the EASM and the WM (Section 2.8). Consequently, the largest portion (almost 80%) of annual rainfall occurs in the rainy season during the Northern Hemisphere (NH) summer from May to September (Figure 3.4) due to monsoon-driven rainfall events related to the ISM and EASM. During NH winter, the cold and dry winds from the Siberian High in the North caused by the WM lead to dry conditions in the study are and suppress rainfall.

However, Northern Vietnam is not entirely without rain during winter as maritime air masses advecting from the South China Sea in the east still supply moisture. This advection has been related to low-pressure areas generated where WM airmasses from the North converge with northeast trades (Pedelarborde 1958, from Weischet & Endlicher, 2000) which leads to lifting and cooling of the air masses, condensation and consequently precipitation.

Another mechanism that supplies moisture to and therefore causes rainfall in the study area, but that is unrelated to the large-scale monsoon circulation patterns, are typhoons. Typhoons typically move in westerly directions and make landfall in a band between 15° N and 20° N, but can also occur further south and north and transport moisture to the study area from the South China Sea (Weischet & Endlicher, 2000; Figure 3.5 left). They can happen between late NH summer and early NH winter, but their frequency clearly peaks in September closely followed by October (Figure 3.5 right).

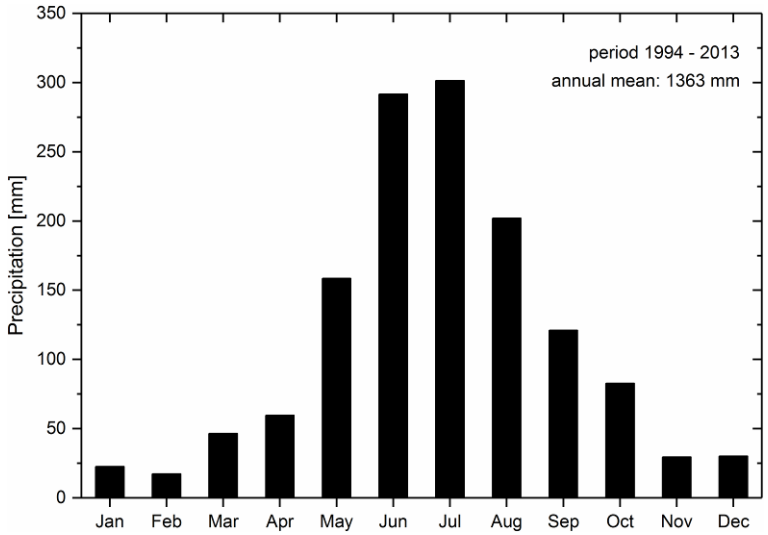

Figure 3.4: Monthly means of precipitation from a weather station in Dong Van District, averaged over the period 1994 – 2013 (NCHMF, 2017).

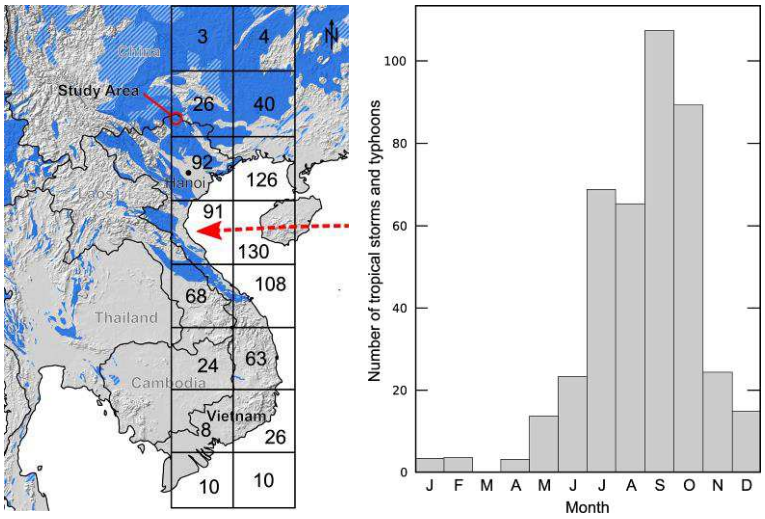

Figure 3.5: Left: Number of typhoon occurrences over the period 1884-1967 (adapted from Weischet & Endlicher, 2000; from U.S. Dept. of Commerce, 1970) and main typhoon trajectory (dashed red line); underlying map is the same as Figure 3.1; Right: Typhoon frequency by month for the same period.

Over the instrumental record of roughly 20 years, rainfall amount in the study area does not seem to be clearly correlated to the ENSO phenomenon (Figure 3.6). In this case, El Niño and La Niña years are defined by the Oceanic Niño Index (ONI) in °C calculated for the Niño 3.4 region (5°N – 5°S, 120°W - 170°W) as three-month running means of the ERSST.v5 sea surface temperature (SST) anomalies relative to 30-year reference periods that are updated every five years (NOAA, 2017). El Niño events are defined as positive SST anomalies exceeding 0.5 °C and La Niña events are negative SST anomalies exceeding 0.5 °C. In the instrumental record there is also no apparent positive or negative long-term trend in rainfall amount (Figure 3.6).

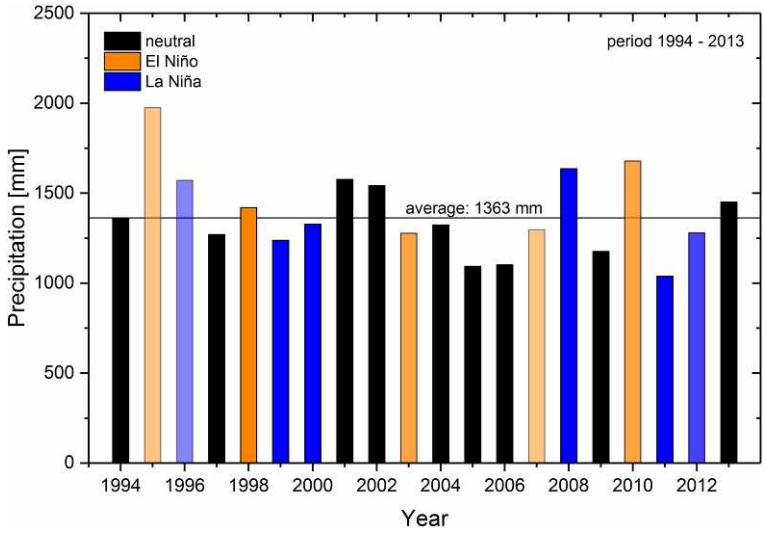

Figure 3.6: Annual precipitation amounts from a weather station in Dong Van District for the period 1994 – 2013 (NCHMF, 2017). El Niño and La Niña years (according to the ONI, region Niño 3.4; NOAA, 2017) are indicated by orange and blue bars, respectively with colour intensity illustrating the strength of the respective event.

Temperature data are not available for the weather station in Dong Van District, but for a station in Ha Giang City (22°49' N, 104°58' E), about 65 km southwest of the study area (Figure 3.7). The warmest three months are June to August with average temperatures above 25 °C. In Ha Giang City, even during the winter months, average temperatures do not fall below 15 °C, but absolute minima as low as 3.2 °C (December 1999) have been recorded. Due to the difference in altitude between Ha Giang (180 masl) and Dong Van (more than 1,000 masl), even lower temperatures can be expected for the study area.

In contrast to other regions such as Northern Laos, Northern Vietnam is not shielded by mountain ranges from advection of cold air from Inner Asia during the Winter Monsoon months (Weischet & Endlicher, 2000). As a consequence, even at ground level, temperatures as low as 2.2°C have been recorded in Lao-Kai City in the valley of the Red River in the province of the same name, just west of Ha Giang Province in Northern Vietnam. In Hanoi, the capital of Vietnam, although situated more than 400 km more southerly and almost 1,000 m lower than the study area, temperatures as low as 5.6°C have been measured (Weischet & Endlicher, 2000).

Temperatures at higher altitudes are commonly lower than at ground level (Schönwiese, 2013), which explains why winter precipitation in the study area can even fall as snow. With an average surface air temperature in Lao-Kai, Ha Giang and Hanoi of about 15°C (Weischet & Endlicher, 2000), Northern Vietnam features an abnormally cold winter for a subtropical region.

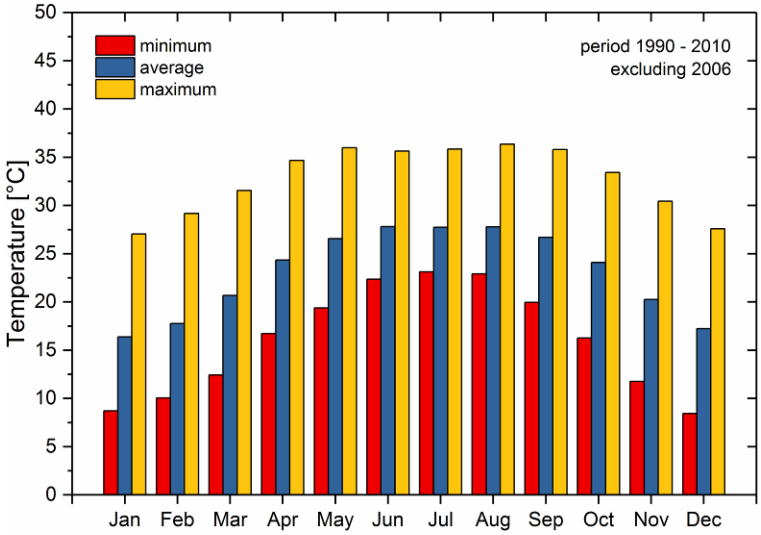

Figure 3.7: Monthly means of temperature from a weather station in Ha Giang City, averaged over the period 1990 – 2010 excluding 2006 (NCHMF, 2017).

3.1.2 Surface Overlying the Studied Caves

At the surface above cave Ma Le 2 a rough mapping of the vegetation was conducted during the dry season on March 3rd, 2014, with the focus on investigating the imprint of the local vegetation on the carbon isotope signal recorded in the stalagmites growing inside cave Ma Le 2, in particular in stalagmite VML22. Therefore, the main goal of the vegetation mapping was to describe vegetation density and collect plant samples for later carbon isotope analysis (Section 4.5) rather than describing the plant species composition as in common vegetation mapping. Within the mapped area (red rectangle in Figure 3.2 bottom) a total of 31 sub-areas were defined (Figure 4.7) that enclosed a relatively homogeneous vegetation cover. The descriptions of these areas are listed in the Appendix (Table A.1).

Summarising the results of this vegetation mapping, it can be stated that almost no trees or shrubs are present at the surface over cave Ma Le 2 and that most of the occurring plant species are herbaceous plants. The overall vegetation density is intermediate with typically high densities in agriculturally used areas and low densities in areas that are not used as fields as these areas are often host rock outcrops with no or little soil cover.

On the whole, despite the hilly terrain with its many steep slopes, large portions of the surface are used for agriculture, and the cultivated crops grow particularly densely in more horizontal parts of the area. A high portion of the available plant biomass is made up of only a few different plant species which were therefore sampled for later carbon isotope analysis. A photographic documentation of these plants is given in the Appendix (Figure A.4 and Figure A.5). In addition to the occurrence of these crops, a typical feature of the agricultural land are piles of corn remains which are stored on the fields after the corn harvest and burned by the farmers at the beginning of the rainy season to fertilise the soils (Appendix, Figure A.4 and Figure A.5), according to local farmers interviewed in the area. Furthermore, the marked discrepancy between the rainfall amounts during the rainy and the dry season (Figure 3.4) lead to noticeable differences in vegetation cover between the seasons (Figure 3.8 and Figure 3.9) with decreased vegetation cover during the dry season.

Figure 3.8: Overview (facing west) of the terrain and the vegetation at the surface above cave Ma Le 2 at the end of the rainy season (August 4th, 2014) and a similar section at the end of the dry season (March 3rd, 2014). The pictures show the western half of the area mapped for its vegetational cover.

The soils in the area above cave Ma Le 2 are developed to great depths, at least to several meters (Figure 3.11) in accordance with very deep soils found in and around Dong Van City (Figure 3.10) that mirror the intense and long weathering typical for subtropical regions (Scheffer et al., 2010). The soil colour is mostly dominated by brown to strongly red tones indicating the presence of Fe-oxides such as goethite and hematite (Scheffer et al., 2010).

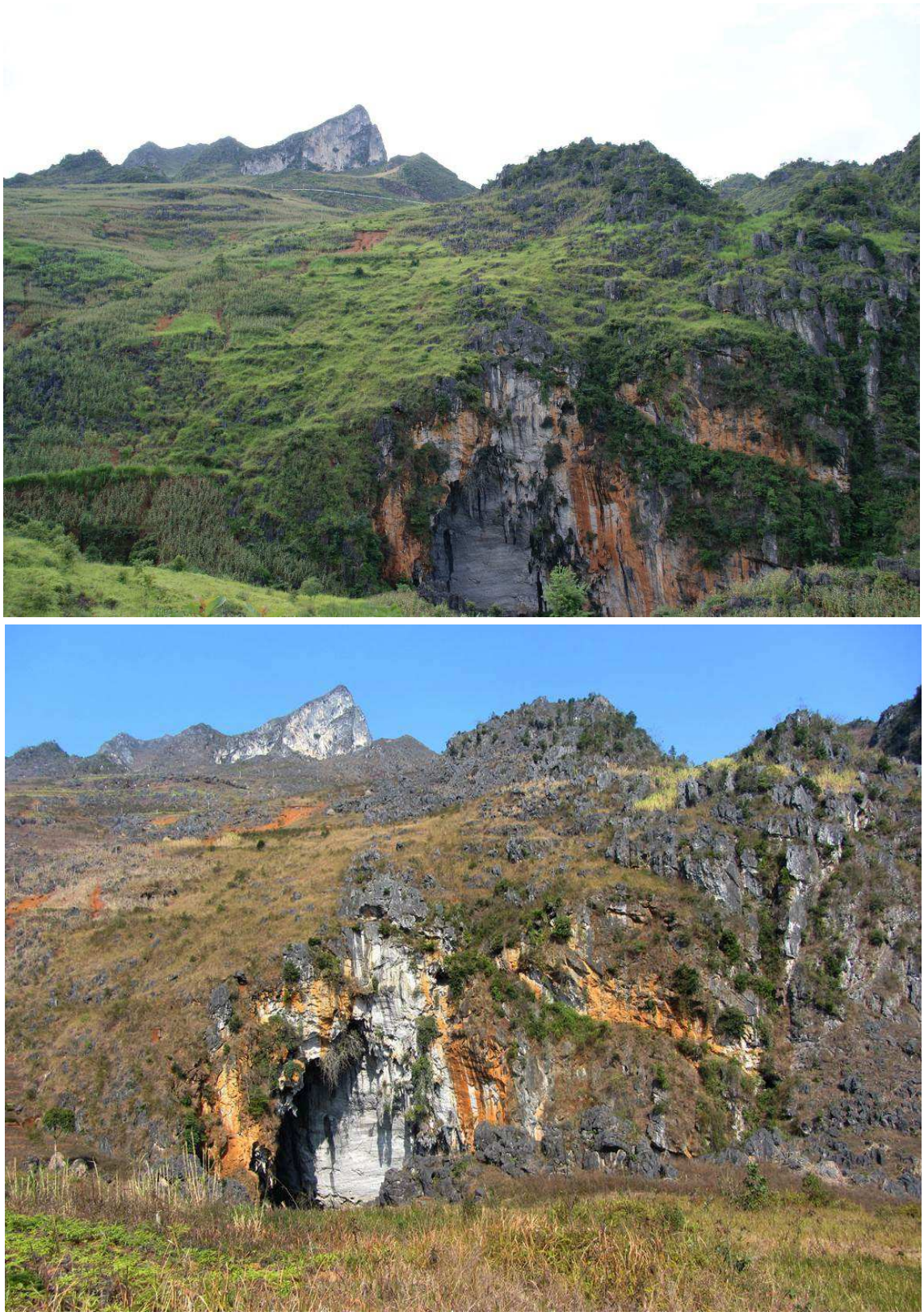

Figure 3.9: Entrance of cave Ma Le 2 (bottom center) and the steep terrain above the cave with its vegetation cover at the end of the rainy season (top; August 4th, 2014) and at the end of the dry season (bottom; April, 6th, 2016; David Lagrou, SPEKUL). Both pictures face northwest.

Figure 3.10: Picture illustrating the great depth to which the soils in the study area are developed and their intense red-brown colour. Picture taken at the southwest end of Dong Van City (April 4th, 2016).

Figure 3.11: Soil profile (SP01) at the surface above cave Ma Le 2; left: Overview illustrating the great depth of the soils in the study area (Vietnamese colleague, Doan The Anh, VIGMR, as scale); right: Close-ups on the soil layers 1 and 2 (top), layer 3 (middle) and layer 4 (bottom). Pictures taken at 23°17'32.1'' N, 105°18'16.7'' E, 1,299 masl, on April 11th, 2016.

The vegetation at the surface above cave Sang Ma Sao was not mapped as there is little or not vegetation in that area. The few plants that do grow there were sampled for later carbon isotope analysis. The lack of vegetation seems to be caused by the very steep slopes and the resulting very thin soils (< 50 cm depth; Figure 3.12) and regular mass movements downhill. Only the highest hills of the area are covered by trees, interestingly where soils are virtually absent (e.g. Figure 3.14). In an interview on March 28th, 2016, a local farmer stated that the vegetation cover in the area had stayed basically the same with the trees being restricted to the hill tops since his childhood some 70 years ago. This statement is consistent with information from representatives of the Water Resource University (Hanoi) that confirm that large areas in Northern Vietnam have been deforested decades or even centuries ago (oral comm.; project workshop with the Ha Giang People's Committee; December 2nd, 2013) which prompted the Vietnamese government to initiate reforestation programs the effects of which can be seen in the study area today. Agriculture is restricted to flatter terrain inside the closed depression of Sang Ma Sao village (Figure 3.13).

Without anthropogenic activity like deforestation and agriculture, Northern Vietnam comprising the study area would likely be covered with dense natural vegetation. A rough map of the natural vegetation type to be expected in that region as a consequence of the environmental conditions suggests that Northern Vietnam is located in a transition zone from evergreen rainforest in the south to warm-temperate humid forest in the north (e.g. southern parts of China; Walter & Breckle, 1999). This suggests a natural predominance of C3-vegetation in this area. The soils in the area above cave Sang Ma Sao are very thin (< 50 cm; Figure 3.12) and support only a very scarce vegetation cover. The soils are typically red-brown and contain high amounts of host rock fragments. Soil development seems to be disturbed regularly in this area due to mass movements downhill that result from the steep slopes. Therefore, the soils are of a Rendzina-like type, however with signs of Fe-oxide coatings that indicate the development of Cambisols.

Figure 3.12: Soil at the surface above cave Sang Ma Sao where the soil sample SMS Soil01 was taken representing the depth range 0 - 20 cm (March 28th, 2016). The scale reaches a depth of about 40 cm.

Figure 3.13: Overview (top) and detailed view (bottom; both facing northwest) of the terrain and the vegetation at the surface above cave Sang Ma Sao during the dry season (March 28th, 2016). The cave entrace is located at the northwestern edge of the closed depression (behind the central hill in the top image).

Figure 3.14: Entrance of cave Sang Ma Sao (bottom center) and the steep terrain above the cave with its vegetation cover during the dry season (March, 28th, 2016; facing northwest).

3.1.3 Erosion

Figure 3.15: Evidence of intense erosion in the study area; Top: Gully erosion on the east slope of the Seo Ho valley (left: uphill; right: downhill; December 5th, 2013); Bottom left: High load of suspended particles in the Seo Ho river after a rainfall event during the rainy season (July 28th, 2015; direction upstream); Bottom right: Detritus deposited on the walls inside cave Ma Le 2 reaching a height of up to ten meters (March 31st, 2016).

Within the study area, topographic surfaces vary widely in altitude which leads to a very hilly terrain with steep slopes. For instance, the Ma Le river system just upstream of cave Ma Le 2 (Figure 3.2 top) features hills with altitudes around 1,500 masl, while the river itself runs at an altitude around 1,000 masl. In combination with the subtropical monsoon-type climate (Section 3.1.1), this entails a great potential for erosion (Scheffer et al., 2010), especially at the onset of the rainy season each year (Section 3.1.1). At this time of the year the soils are very dry and their capacity to absorb rainwater is low. Therefore, the rainwater cannot infiltrate into the soils and generates strong surface runoff leading to erosion (Blume et al., 2016). Another factor that increases the potential for erosion is intense precipitation with high amounts of rainwater falling in short periods of time. Such events of extreme rainfall can also occur in connection with typhoons passing the study area coming from the South China Sea east of Vietnam (Section 3.1.1). The eroded material is then transported from the surface to the underground and into caves via rivers and streams (Figure 3.15). Detrital material is not only deposited on the walls of caves, but also on stalagmites and is subsequently incorporated into the stalagmites as soon as stalagmite growth resumes.

3.2 Geological Setting

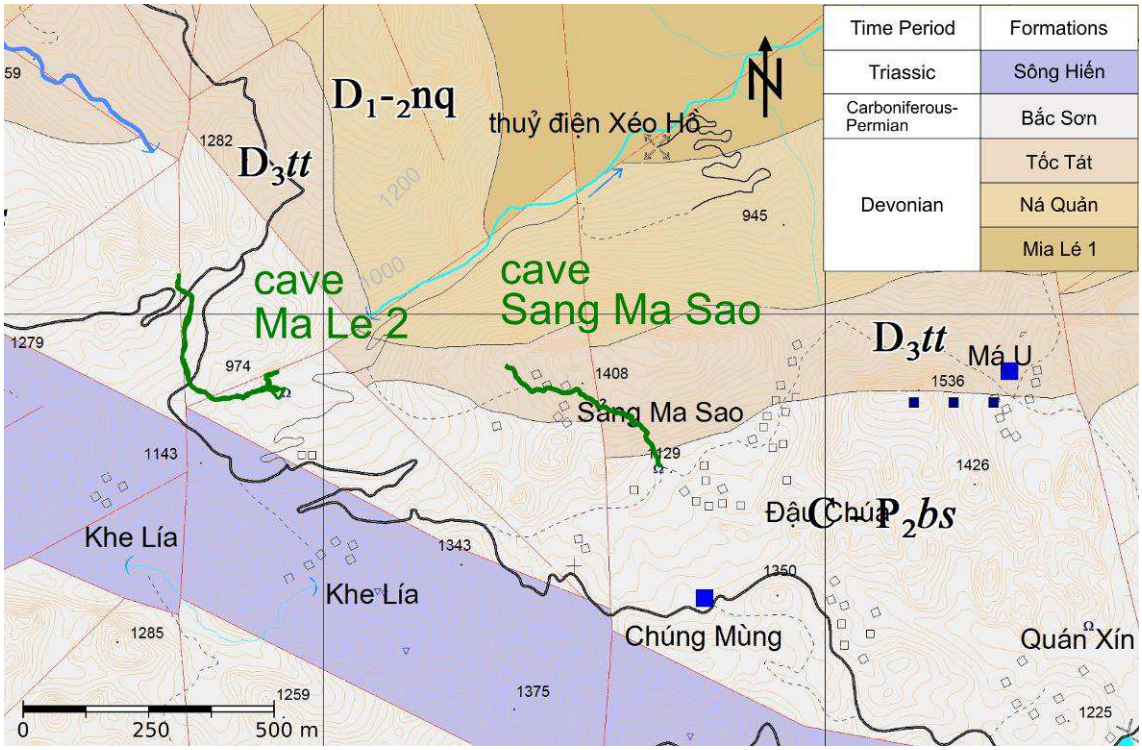

Figure 3.16: Geological Formations in the study area (scale 1:50,000; mapping performed by staff of the VIGMR in 2015; unpublished). Caves Ma Le 2 and Sang Ma Sao are indicated as green lines; the red lines indicate faults.

The geology of Northern Vietnam is dominated by strongly karstified carbonate formations that form the southern edge of the South China Carbonate platform, the largest karst region of the world (Masschelein et al., 2007). The study area's geology (Figure 3.16) comprises five geological formations from three different time periods: The Mía Lé, Ná Quản and Tốc Tát Formations have been deposited during the Devonian, the Bắc Sơn Formation during the Carboniferous and the Permian, while the Sông Hiến Formation is of Triassic age. The Mía Lé Formation (D_1 ml) consists of clayish siltstone and marlaceous siltstone and can be subdivided into two Subformations. The Lower Subformation (D_1 ml_2) is made up of black-grey, greenish-grey clay shale with a thickness of 230 m, the Upper Subformation (D_1 ml_1) contains sandstone, siltstone, clay shale and marlaceous shale with an overal thickness of 500 m. The Ná Quản Formation (D_{1-2} nq) comprises marble, cherty shale, cherty limestone as well as dolomite limestone and is 500 – 520 m thick. According to the latest geological mapping (map scale 1:50,000; mapping performed by staff of the VIGMR in 2015; unpublished) the Ná Quản Formation is the only formation in the study area that contains dolomite. The Tốc Tát Formation (D_3 tt) consists of red-veined limestone and manganese-bearing cherty limestone with a thickness of 200 m. The Bắc Sơn Formation (C-P_2 bs) comprises massive limestone, oolitic limestone as well as clayish limestone and is the thickest formation in the study area at 1,000 – 1,200 m.

The topmost geological layer is the Sông Hiến Formation ($T_1 sh_1$) which consists of marlaceous shale, siltstone and calcareous sandstone with a thickness of 600 – 620 m. While the Bắc Sơn Formation is highly karstifyable and acts as an aquifer, the Tốc Tát, Ná Quản and Mía Lé Formation are less karstifyable due to contaminations with clays and silicates and can act as aquicludes.

With respect to the geochemical properties of the studied stalagmites, the two most important geological formations are the Bắc Sơn Formation and the Tốc Tát Formation as cave Ma Le 2 has developed within the Bắc Sơn Formation while cave Sang Ma Sao has developed with both formations. With regard to detrital material from the surface flushed into the caves by their respective cave stream and deposited on the stalagmite, however, the other formations are important as well, as they constitute potential source regions for this detrital material. As the stream in cave Ma Le 2 is fed by the Ma Le river (upper left corner in Figure 3.16) the Tốc Tát and Ná Quản Formations represent potential source regions for detritus incorporated in stalagmite VML22. In case of stalagmite VSMS2, the Sông Hiến Formation is a possible source region because the stream in Sang Ma Sao cave is fed from the closed depression around Sang Ma Sao village (topographic map in Figure 3.2).

From a tectonic standpoint, the study area is located at the far eastern edge of the region influenced by the formation of the Himalaya. The tectonic impact on the regional formations has caused them to deform and to break up into smaller units, especially during the middle Palaeocene (Tran et al., 2013). The study area contains two main fault systems, an earlier system in NW-SE directions that exhibits a major structural control and a later system in NE-SW directions that caused relatively weak shifts along its faults (Van et al., 2004).

3.3 Studied Caves

In order to find stalagmites actually suited for the reconstruction of palaeoclimatic and palaeoenvironmental conditions (Section 2.7) a total of twelve karst caves in the study region in Northern Vietnam were scanned for suitable stalagmites (in chronological order): Dong Van Cave, Sang Tung, Ma Le 1, Ma Le 2, Ma Le 3, Pai Lung, Dong Nguyet, Tia Sang, Sang Ma Sao, New Cave 01, New Cave 02 and New Cave 03. The last four were discovered and entered for the first time in the course of this PhD project. Only four out of the twelve scanned caves contained potentially suitable stalagmites (Sang Tung, Ma Le 2, Tia Sang and Sang Ma Sao). As the one promising stalagmite in cave Sang Tung could not be collected for lack of permission by the responsible Vietnamese official, this cave is not further discussed.

From the three remaining caves a total of twelve stalagmites were collected: Two from cave Ma Le 2 (VML21, VML22), five from cave Tia Sang (VTS1 to VTS5) and five from cave Sang Ma Sao (VSMS1 to VSMS5). Unfortunately, all five stalagmites from cave Tia Sang turned out to be unsuited for palaeostudies for two main reasons.

First, they contain too many detrital components as evident from their overall dark interiour, which effectively impedes reliable U/Th dating (Section 4.3). Second, their internal structure with often high porosity (Figure 3.17) and strongly and frequently shifting growth directions is too complex for sampling at high spatial resolution (Section 4.4). These issues also apply to stalagmites VSMS1 and VSMS3 from cave Sang Ma Sao. Stalagmite VML21 from cave Ma Le 2 has a too complex internal structure and is too thin for high-resolution sampling.

Figure 3.17: The top part of stalagmite VTS1 as an example for a stalagmite unsuited for palaeoreconstruction (about 40 cm long and 10 cm across): Top view (left) and cross section (right) at the base.

As a consequence, out of the twelve stalagmites that looked promising from the outside, only four proved indeed suitable for reconstructing palaeoclimatic and palaeoenvironmental conditions. As palaeostudies based on high-resolution multi-proxy data sets from speleothems are both expensive and time-consuming, this PhD project focuses on stalagmites VML22 and VSMS2 because these cover both the Last Deglaciation and the Holocene which had been defined as the time period of interest. Therefore, only caves Ma Le 2 and Sang Ma Sao are discussed in the following. The location of both caves is indicated in Figure 3.2.

3.3.1 Cave Ma Le 2

The map of cave Ma Le 2 is shown in Figure 3.18. The original mapping of the cave was conducted in a collaboration of staff from VIGMR, SPEKUL and BVKCA in 2004 (Masschelein et al., 2007), in 2015 slight corrections were made based on new and highly precise distance data generated with a DistoX 310 laser measurement device (Leica) together with Doan The Anh (VIGMR).

The entrance to cave Ma Le 2 is located at 23°17'23.17"N, 105°18'45.67"E at an altitude of 1,015 masl. The cave is almost 900 m long and is inclined upstream by +52 m and connects two sumps at its upstream and downstream end, respectively (Figure 3.18, left). The thickness of the overlying carbonate rock is about 30 m at the entrance and about 165 m directly above the dripsite at which stalagmite VML22 has been growing. This site is located at some 600 m distance upstream of the entrance at an altitude of around 10 m above the level of the cave entrance.

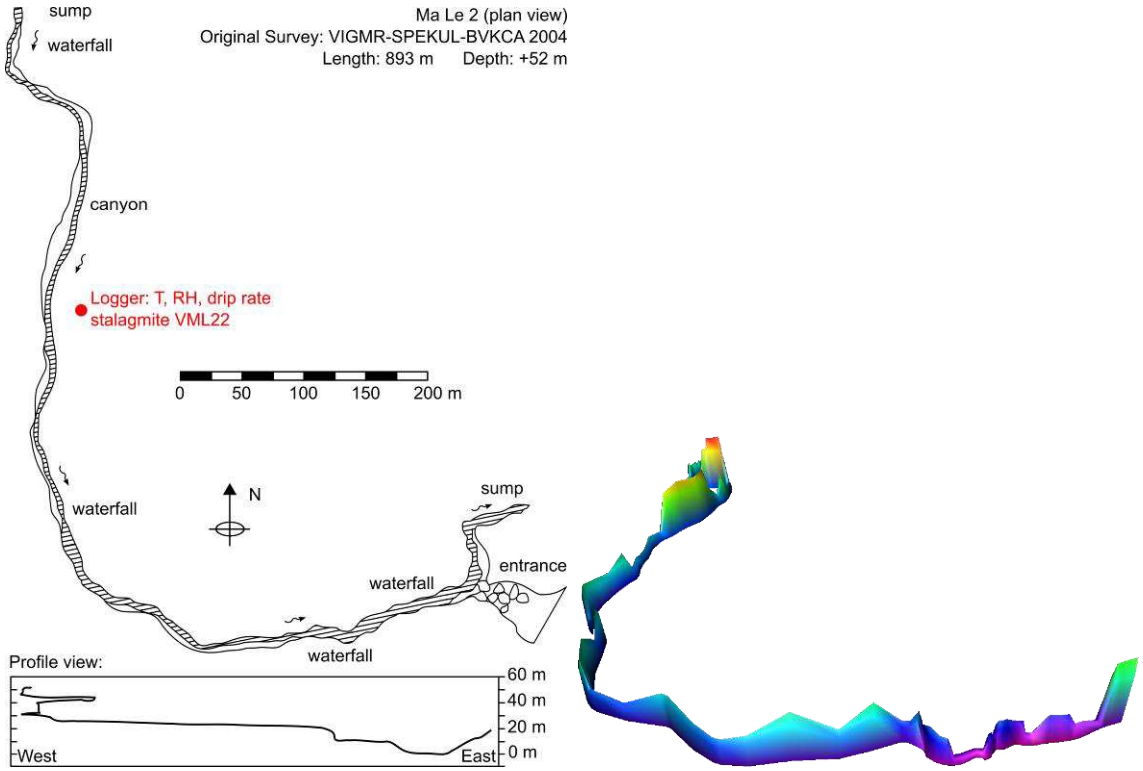

Figure 3.18: Maps of cave Ma Le 2: Left: Top view and plan view. The locations of stalagmite VML22 and the logger for measurements of temperature (T), relative humidity (RH) and drip rate are indicated in red. The hatched area represents the cave stream. Right: 3D-view of the cave passages (facing north, at an angle of 30°) constructed with the Cave XO and the Compass software (Fountain Computer; versions 5.15.2.24.5 and 5.16.4.13.189, respectively).

Cave Ma Le 2 features almost no branching, exclusively linear passages so that it can be classified as an "ideal pipe" (Ford & Williams, 2007), although the cave river has cut down deeply into the carbonate host rock during the vadose phase of the cave's evolution, following the direction of two local faults in NE-SW and in N-S directions, respectively (Figure 3.16). This intense vadose entrenchment has produced an elliptical to canyon-like cross-section and a very high cave ceiling is, exceeding 50 m in some passages (Figure 3.18 right) although it is often masked from view by extensive sinter bodies that effectively form a secondary ceiling.

Especially the N-S fault dips slightly to the east so that the actual height of the ceiling cannot be measured in all of the cave's passages. Investigating the actual ceiling height in these passages would require very difficult and time-consuming cave climbing. With regard to further classifications cave Ma Le 2 can be described as a vadose limestone speleothem cave that is fault-guided and forms a fluvial system. By connecting the two rivers Ma Le and Seo Ho it is also an active subtropical short-cut cave (Ford & Williams, 2007) featuring a perennial cave stream with flows of some 1 - 1.5 m^3/s during the rainy season and some 0.1 m^3/s during the dry season (Ender, Goeppert & Goldscheider, 2018). Such perennial cave streams usually keep relative humidity at 100% so that kinetic oxygen isotope fractionation caused by evaporation (Section 2.2.2) can be excluded.

Figure 3.19: Aeroliths on the ceiling of cave Ma Le 2 indicating a prevalent downstream wind direction. These aeroliths are particularly frequent close to the upstream end of the cave (March 31st, 2016).

Cave Ma Le 2 is richly ornate with speleothems although stalagmite formation is prohibited in most parts of the cave by the cave stream. Among the different types of speleothems present in the cave such as columns, draperies, stalagmites and stalactites are many aeroliths that are all directed downstream (Figure 3.19) indicating prevalent downstream winds. Such winds might be caused by the cave stream as flowing water tends to entrain the overlying air masses through friction. This process would generate a more or less steady air flow out of the cave just above the water. That such an air flow indeed exists in the cave system today was confirmed by air flow velocity measurements using a hot bead anemometer (Testo 445) the results of which are shown in Table 3.1. Measured air flow velocities almost reach 0.5 m/s just above the water surface and consistently decrease with increasing height, as does temperature. An air flow into the cave close to the ceiling to compensate for the river-induced outflow is presumed but could not be unambiguously confirmed due to the great height of the actual cave ceiling. Overall, cave Ma Le 2 is susceptible to intense ventilation as a result of its fast-flowing stream and its great entrance (Figure 3.9) that is 40 m high and 40 m across.

Table 3.1: Air flow velocities in cave Ma Le 2 measured with a Testo 445 hot bead anemometer on March 26th, 2016. The locations of the measurements are indicated in Figure 3.18 left.

Location	Height [cm]	Velocity [m/s]	Temperature [°C]
Stalagmite VML22	50	0.02	19.9
Sinter plateau downstream of stalagmite VML22	5	0.05	18.8
Stream next to sinter plateau	10	0.31	17.0
	50	0.20	17.6
	120	0.14	17.8
	200	0.04	18.0
1st waterfall downstream	10	0.45	16.7
2nd waterfall downstream	10	0.32	16.6
3rd waterfall downstream	10	0.31	16.6
	50	0.24	16.8
	100	0.19	17.0
	150	0.17	17.1
	200	0.07	17.5

Intriguingly, the cave walls are covered in detrital material along the entire length of the cave at a height of up to 10 m (Figure 3.15 bottom right; Figure 3.20), easily visible against the white colour of the cave ceiling (that might be caused by moonmilk; Hill & Forti, 1997). This detritus cover is most likely evidence of at least one event with correspondingly high water levels during which the detrital material transported by the cave stream from the surface into the cave has been deposited on the walls. Detritus deposition is most likely under low velocity conditions that favor sedimentation whereas high flow velocities tend to wash the cave walls clean again (Figure 3.20 bottom right). For water flow to slow down the hydraulic head along the cave's length needs to be diminished, which most probably happened as a result of backwater events. Such events can either be caused by a blocking of the cave stream by falling debris, or by the flow into the cave system exceeding the flow the cave system can effectively pipe through. As the passages of cave Ma Le 2 feature a large cross-section along the entire length of the cave, the first mechanism would be most effective at the cave's outlet where the cave's cross-section is smallest. Therefore, it is less likely that this mechanism causes regular backwater events as it requires debris to always fall into the stream at the cave's outlet.

The main phase of speleothem formation in cave Ma Le 2 seems to be terminated as most stalactites are dry year-round. The drip water of the few stalactites that are still active appears not to be oversatured with calcite as demonstrated by glass plates placed on multiple dripsites that show no precipitates after an exposure of more than two years. This also applies to the dripsite of stalagmite VML22 (Figure 3.22). In general, speleothem formation in cave Ma Le 2 seems to be disturbed as all stalagmites present in the cave display a "cloddy" appearance with fabrics consisting of separate "nodules" that have grown on top of each other in a relatively disorderly fashion.

This is also true for the lower parts of stalagmite VML22 (total length about 50 cm; Figure 3.21). Interestingly, at some 15 cm from its top, fabrics become more regular so that conditions inside the cave must have changed to favour a more orderly growth of stalagmite VML22.

Figure 3.20: Top and bottom left: Detrital material deposited on the walls of cave Ma Le 2 at heights of up to ten metres indicating at least one event of high water levels within the cave (white parts are at the cave's ceiling). Bottom right: Detritus-free area on the cave wall where the cave stream flows against the wall at high speeds ("cut bank") eroding away the detritus cover (April 4th, 2016).

Figure 3.21: Stalagmite VML22 over its entire length (about 50 cm) with disturbed growth in its lower section and more orderly growth in its upper section.

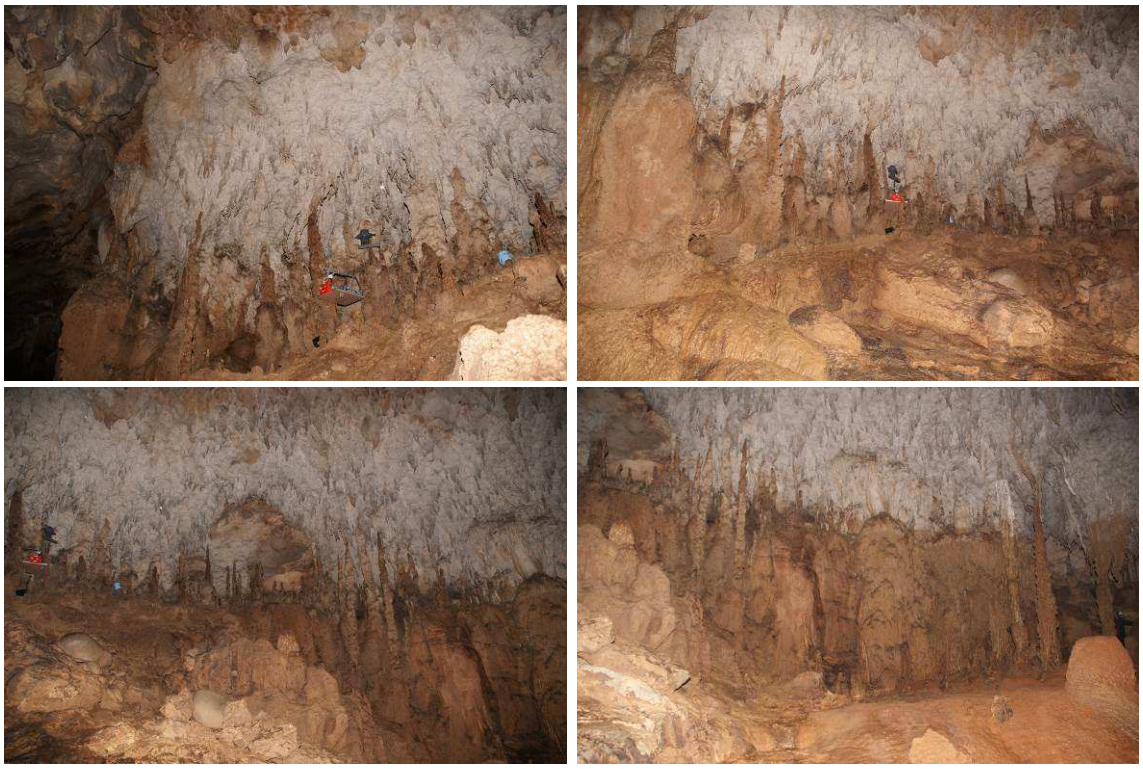

Figure 3.22: Location of stalagmite VML22 in cave Ma Le 2. The stalagmite grew at the position of the grey drip water collection container which also holds the drip rate logger, well below the water level of the backwater event indicated by the detritus covering the cave walls. Pictures continuous from left to right (March 31th, 2016). One stalactite was feeding stalagmite VML22 (drip fall height about 1,2 m).

Monitoring of the cave environment was performed at the location of stalagmite VML22 (Figure 3.18 left): Drip rate at the dripsite of stalagmite VML22 was logged at 30-minute-intervals with a Stalagmate Mark 3 drip rate logger (TGC-0011, Driptych) over a period of almost 2.5 years (Figure 3.23). Temperature (T) and relative humidity (RH) were logged five times per day (at intervals of 4 hours and 48 minutes) with a Tinytag TGP-4500 (Gemini Loggers; accuracy: ± 0.5°C at 8°C and ± 3.0% RH at 25°C) over a period of about one year. The data sets for T and RH are shorter than that for drip rate because T and RH (together with CO_2 concentrations) were initially measured with another logger that failed however after only eleven days (Figure 3.25) due to condensation inside the logger's casing that damaged the sensors although this should have been prevented by hydrophobic filters. Furthermore, the T and RH data since the last read-out on March 25th, 2016 have been lost due to a technical problem with the logger's batteries and memory.

Drip rate mostly varies between 6 and 10 drips in 30 minutes, with an average of 7.9 drips and a median of 8 drips (n = 11.562 single measurements). Although the variation is quite small, drip rate still clearly changes with season, being increased during the rainy season and decreased during the dry season in a pattern that closely resembles the distribution of rainfall amount over the year (Figure 3.4) without any significant lags compared to the rainfall signal.

In addition to this seasonal pattern, drip rate fluctuated on smaller sub-seasonal time scales. This variation is mostly on a weekly scale with an amplitude of 1 to 2 drips per 30 minutes, but even variations on a daily scale occur occasionally, for instance from May 3rd to May 4th, 2015. Overall, drip rate in 2016 was lower than in 2015 by about 1 drip / 30 min.

These results indicate that the dripsite of stalagmite VML22 is supplied with drip water from a flow path network that comprises both slow and fast flow components. Parts of the overlying epikarst seem to have a certain water storage capacity in which the water from multiple rainfall events is mixed and released more gradually, while other parts of the flow path network appear to transmit rainwater more quickly to the dripsite so that even single rainfall events are discernible from drip rate monitoring. This suggests that mixing of rainwater from multiple rainfall events does take place, while particularly strong rainfall events can still stand out among the seasonal drip rate variation.

Over the entire monitoring period of more than one year, relative humidity has constantly remained at 100 % (Figure 3.24), consistent with the existence of a perennial cave stream. At times when the logger did not record 100 % RH, it measured 0 % RH. Because this is most likely due to condensation on the humidity sensor according to the manufacturer's manual, this reading indicates an oversaturation of the cave air with respect to water rather than a drop in RH. The logger's recording of 100 % RH was confirmed by independent RH measurements using an Assmann aspiration psychrometer (November 5th, 2015) that yielded the same temperature for both the wet and the dry thermometer. Under these conditions kinetic oxygen isotope fractionation due to evaporation (Section 2.3.3.2) is highly unlikely.

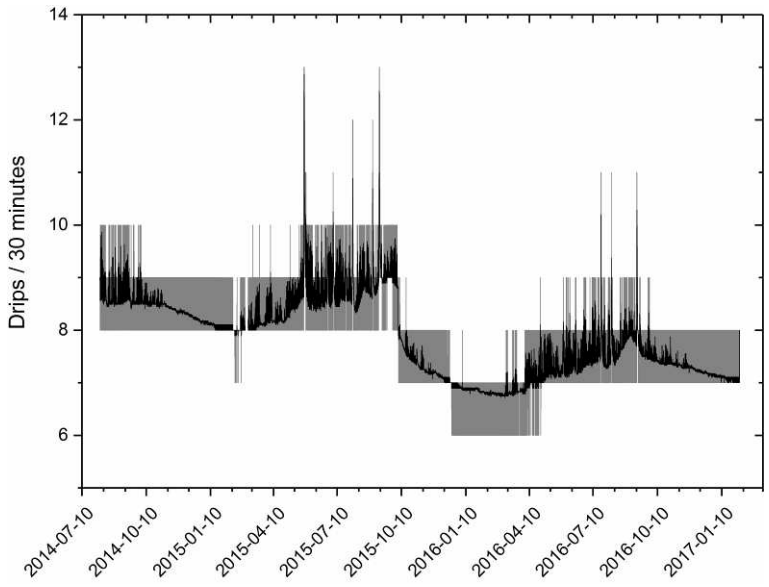

Figure 3.23: Drip rate at the drip site of stalagmite VML22 in cave Ma Le 2, logged in intervals of 30 minutes (grey line). The black line is a 12-point running mean (weighted adjacent-averaging) representing 6-hour-intervals.

Measured temperature (Figure 3.24) ranges from 17.2 °C to 21.3 °C, with an average of 19.3 °C and a median of 19.6 °C (n = 1,951). As in the case of drip rate, temperature clearly varies with season, being increased during the rainy season in NH summer and decreased during the dry season in NH winter. Over the monitored period this leads to an inter-seasonal change of more than 4 °C. On smaller (weekly) time scales, temperature fluctuates by less than 1 °C, while daily variations are so weak that they are indiscernible from measurement noise.

The temperature amplitude of more than 4 °C over about one year indicates that cave Ma Le 2 reacts relatively quickly to changes in ambient air temperature outside the cave. Due to the high thermal inertia of the overlying carbonate host rock, these temperature fluctuations are unlikely to be the sole result of thermal conduction, but require the process of convection. They therefore indicate a certain air exchange between the cave and ambient air. Intriguingly, this air exchange seems insufficient to reduce RH to values below 100%.

As already mentioned, T, RH and CO_2 concentrations were initially measured with a CM-0018 logger (CO2Meter). Although the device failed after only eleven days due to condensation inside the logger's casing that should have been prevent by the equipped hydrophobic filters, the recorded data (Figure 3.25) still prove that ventilation events take place in cave Ma Le 2 as was previously hypothesised based on the large cave entrance, on the fast-flowing cave stream entraining the overlying air and on high-amplitude cave air temperature fluctuations. The data indicate an event from March 1st to March 3rd, 2014, during which outside air replaced parts of the cave air which resulted in the cave air being slightly warmer (up to 2°C higher than 17.4 °C before), drier (97 % RH rather than ≥ 100 % RH before) and depleted in CO_2 (600 ppmV) compared to before and after the ventilation event (800 to 1200 ppmV).

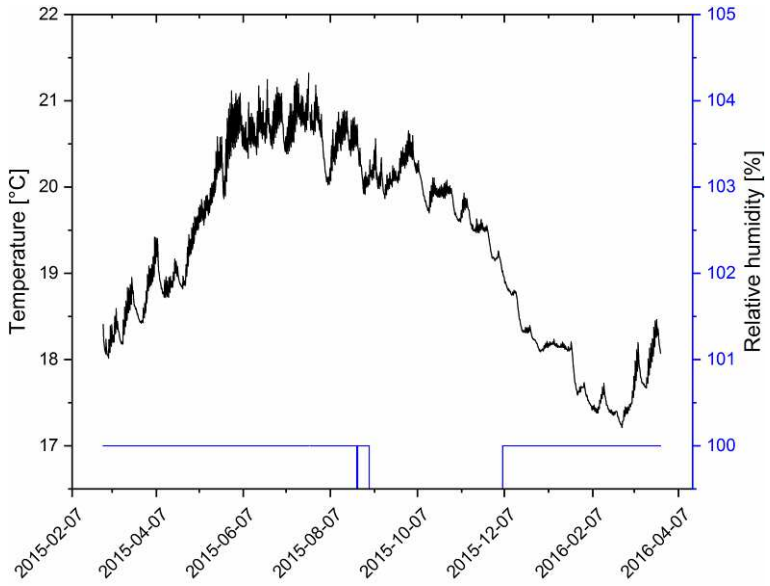

Figure 3.24: Temperature and relative humidity in cave Ma Le 2 at the position of stalagmite VML22, logged five times per day (interval: 4h48min). Where RH is not 100%, the logger recorded 0% RH, likely due to condensation on the humidity sensor thus indicating an oversaturation of the cave air with respect to water.

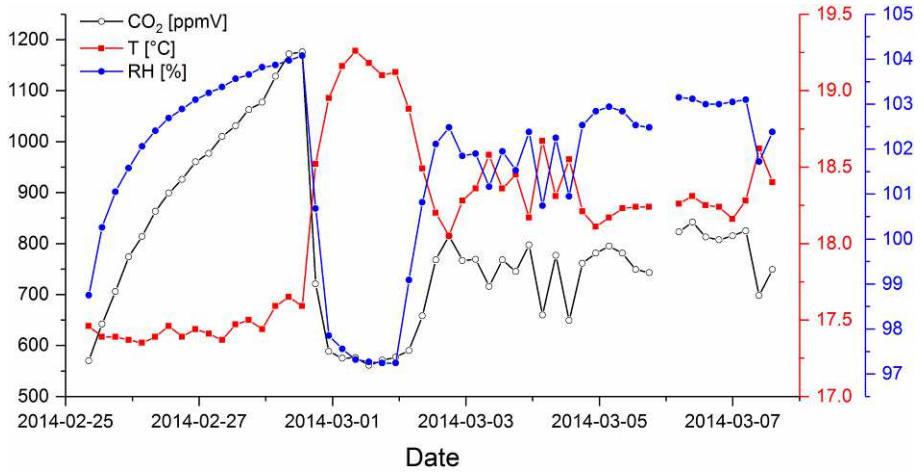

Figure 3.25: Temperature, relative humidity and CO_2 concentrations in cave Ma Le 2 at the location of stalagmite VMl22 logged five times per day (interval: 4h48min) with a CM-0018 (CO2Meter). The data gap is due to a data read-out before re-installing the logger. Axis designations and units are given in the legend.

3.3.2 Cave Sang Ma Sao

The map of cave Sang Ma Sao is shown in Figure 3.26. The mapping of the cave was conducted in 2015 within the framework of the joint project "KaWaTech Vietnam" (funded by the BMBF; 02WCL1291A) in 2015 under the lead of Yves Dubois (the names of all collaborators are given in Figure 3.26).

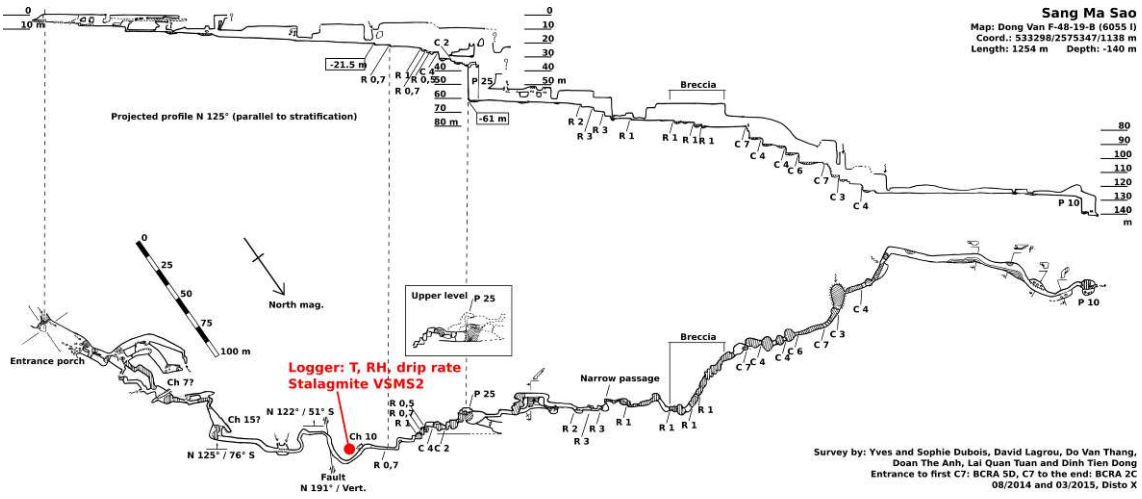

Figure 3.26: Maps of cave Sang Ma Sao in profile view (top) and plan view (bottom). The locations of stalagmite VSMS2 and the loggers for measurements of temperature (T), relative humidity (RH) and drip rate are indicated in red. The hatched area represents the cave stream.

The entrance to cave Sang Ma Sao is located at 23°17'11.54"N, 105°19'40.15"E at an altitude of 1,138 masl. The cave is almost 1,300 m long is inclined downstream by -140 m and ends downstream in a sump. The thickness of the overlying carbonate rock is about 10 m at the entrance and about 165 m directly above the dripsite at which stalagmite VSMS2 has been growing. This site is located at some 250 m distance downstream of the entrance at an altitude of around 15 m below the level of the cave entrance.

Similar to cave Ma Le 2, cave Sang Ma Sao features almost no branching and can also be classified as an "ideal pipe" (Ford & Williams, 2007), while the cave river has not cut down as deeply into the carbonate host rock during the vadose phase as in cave Ma Le 2. The vadose entrenchment seems to follow the direction of the local fault in N-S direction only in a small passage (Figure 3.16), while the cave is rather developed in a NW-SE direction parallel to a fault that is known south of Sang Ma Sao cave, between the Sông Hiến and the Bắc Sơn Formations. The cross-section is also elliptical to canyon-like as in cave Ma Le 2, but the cave ceiling is not as high (not exceeding 30 m), except for the location of a great waterfall (P 25 in Figure 3.26). Most of the passages of cave Sang Ma Sao are very narrow and many tend to dip slightly to the southwest (Figure 3.28 top). Overall the cave features many passages that are both narrow and low (Figure 3.28 bottom) which makes cave Sang Ma Sao highly susceptible to backwater events (and dangerous to enter) as even small increases in cave stream flow can lead to exceedances of the cave's "carrying capacity".

With regard to other classifications cave Sang Ma Sao can be described as highly similar to cave Ma Le 2 (Section 3.3.1), but the cave stream, albeit perennial, features significantly lower flows with flow rates ranging from some 7 L/s during the dry season to some 20 - 30 L/s during the rainy season (Ender, Goeppert & Goldscheider, 2018). However, its effect on relative humidity and consequently kinetic oxygen isotope fractionation caused by evaporation appear to be similar.

Cave Sang Ma Sao contains speleothems mainly in the form of impressive flowstones rather than stalagmites, but speleothem formation is prevented in the bed of the cave stream. In contrast to cave Me Le 2, aeroliths are very rare and often not obvious in cave Sang Ma Sao suggesting that downstream winds induced by the cave stream are much weaker. Air movement was confirmed by measurements (November 5th, 2015) that yielded an air flow velocity of 0.12 m/s at the first low passage close to the cave entrance and of 0.07 m/s at the logger's position at a height of 3 m. Overall, it can be stated the cave Sang Ma Sao is most likely far less susceptible to ventilation than cave Ma Le 2 due to the low flow of the cave stream, the much smaller cave entrance (about 10 m high and 10 m across) as well as to the many low and narrow cave passages.

Figure 3.27: Boulders in cave Sang Ma Sao indicating former high-flow conditions of the cave stream (picture facing downstream; March 27th, 2016).

Figure 3.28: Passages in cave Sang Ma Sao: Narrow but high passages (top) dipping soutwest and low passages (bottom) at the beginning of the cave (left) and just downstream of the location of stalagmite VSMS2 (right). All pictures face downstream (March 27th, 2016).

Another remarkable difference to cave Ma Le 2 is the absence of detrital material on most of the walls of cave Sang Ma Sao. However, sediments are frequent inside the cave, including relatively large boulders with diameters of up to 30 cm (Figure 3.27) that indicate that cave stream flow must have been significantly higher during past periods. The high flow velocities during these high-flow events have probably enabled the river water to wash the cave walls clean of any detrital material deposited on them during past backwater events. An interesting feature of many parts of the cave walls is a black crust (Figure 3.30) the formation of which is still under investigation. The dripsite of stalagmite VSMS2 together with its extraction is shown in Figure 3.29.

Figure 3.29: Location of stalagmite VSMS2 in cave Sang Ma Sao. The stalagmite grew at the position of the grey drip water collection container (left; facing downstream; March 27th, 2016) which also holds the drip rate logger and was extracted using a metal saw (right; picture taken by Tran Diep Anh (VIGMR) on March 13th, 2015). Stalagmite VSMS2 was fed by drip water from a single stalactite with a drip fall height of 15 cm.

Figure 3.30: Black crust on the walls of cave Sang Ma Sao (left picture taken by Lai Quan Tuan (VIGMR) on March 12th, 2014; right: March 27th, 2016).

Monitoring of the cave environment was performed at the location of stalagmite VSMS2 (Figure 3.26, bottom) using the same equipment as for stalagmite VML22. Drip rate at the dripsite of stalagmite VSMS2 (Figure 3.31) was recorded over a period of about nine months, while the logger failed to record drip rate in the subsequent logging period indicating a drip rate of zero drips per 30 minute invertal (not shown) due to a yet unknown technical problem.

Drip rate in cave Sang Ma Sao varies more strongly than in cave Ma Le 2, ranging from 16 to 44 drips in 30 minutes, with an average of 24.6 drips and a median of 23 drips (n = 11,562) with a total amplitude of 28 drips / 30 min. Drip rate clearly changes with season, generally being increased during the rainy season and decreased during the dry season, but peak drip rate (September 7th, 2015) seems to lag behind the long-term peak rainfall amount (July; Figure 3.4) by about two months. In addition to this seasonal pattern, drip rate fluctuated on smaller sub-seasonal time scales. As in cave Ma Le 2, this variation is mostly on a weekly scale with an amplitude of up to 5 drips per 30 minutes, but variations on a daily scale also occur occasionally, for instance on December 10th, 2015. Potential fluctuations in drip rate on longer time scales cannot be assessed on the basis of this data set.

These results indicate that the dripsite of stalagmite VSMS2, similar to the on of stalagmite VML22, is supplied with drip water from a flow path network that comprises both slow and fast flow components. Analogously, this suggests that mixing of rainwater from multiple rainfall events does take place, while particularly strong rainfall events can still stand out among the seasonal drip rate variation. The overall larger amplitude of drip rate variation compared to the dripsite of stalagmite VML22 implies that the dripsite of stalagmite VSMS2 reacts more strongly to short- and medium-term (daily to weekly) changes of meteoric water supply due to a higher portion of fast-flow components in the overlying flow path network.

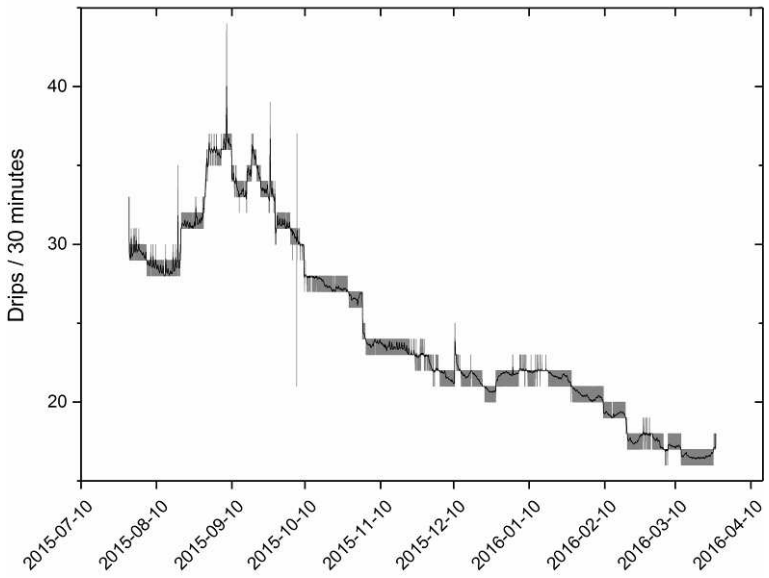

Figure 3.31: Drip rate at the drip site of stalagmite VSMS2 in cave Sang Ma Sao, logged in intervals of 30 minutes (grey line). The black line is a 12-point running mean (weighted adjacent-averaging) representing 6-hour-intervals.

As in cave Ma Le 2, relative humidity has constantly remained at 100 % (Figure 3.32) over the entire monitoring period of about two years, again consistent with the existence of a perennial cave stream. Condensation on the humidity sensor has again led to an erroneous reading of 0 % RH in spite of the related oversaturation of the cave air with respect to water. The logger's recording of 100 % RH was confirmed by independent RH measurements using an Assmann aspiration psychrometer (November 6th, 2015) which renders kinetic oxygen isotope fractionation due to evaporation unlikely.

Measured temperature (Figure 3.32) ranges from 19.1 °C to 21.4 °C, with an average of 20.1 °C and a median of 20.4 °C (n = 3,647). Consequently, this site in cave Sang Ma Sao seems about 0.8 °C warmer than the site in cave Ma Le 2, mainly because temperatures do not decrease as much during winter. As the logging periods are not identical, but only partly overlap, they are not entirely comparable. Temperature in Sang Ma Sao cave also clearly varies with season, being increased in NH summer and decreased in NH winter, with no apparent lag behind the long-term ambient air temperature peak (August; Figure 3.7). Summer in the year 2016 was about 1.5 °C and 0.5 °C warmer than in 2015 and 2017, respectively.

The inter-seasonal change of 2.3 °C between winter and summer 2016 is noticeably lower than the > 4 °C change measured in cave Ma Le 2. The shorter-term temperature fluctuations are also much lower than in cave Ma Le 2, with only one exception (September 7th, 2015). Both observations indicate that cave Sang Ma Sao reacts less strongly to changes in ambient air temperature outside the cave which is consistent with a relatively weak ventilation of cave Sang Ma Sao compared to cave Ma Le 2.

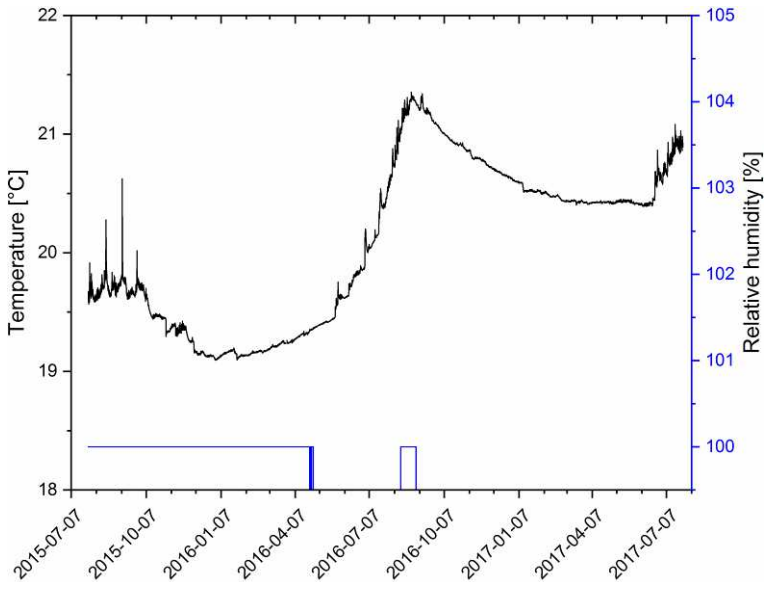

Figure 3.32: Temperature and relative humidity in cave Sang Ma Sao at the position of stalagmite VSMS2, logged at 30-minutes-intervals. Where RH is not 100%, the logger recorded 0% RH, likely due to condensation on the humidity sensor thus indicating an oversaturation of the cave air with respect to water.

4 Materials and Methods

4.1 Stalagmite Extraction and Preparation

Stalagmites VML22 and VSMS2 were extracted from cave Ma Le 2 and cave Sang Ma Sao, respectively, using a metal saw instead of hammer and chisel in order to prevent any damage to the stalagmites during extraction. Stalagmite VML22 was collected on February 22nd, 2014 and stalagmite VSMS2 on March 13th, 2015.

To meet the requirements of all subsequent analyses with regard to the form of the stalagmite samples the stalagmites needed to be prepared and formatted: After collection from the caves the stalagmites were cut in half along their central growth axis using a stationary saw (Conrad) with a 2 mm wide diamond-coated blade. To provide an exact reference for a second cut, the stalagmite halves were tightly wrapped in cling film and embedded in blocks of fine-grained modelling plaster with the original cut face facing down. Both halves were then cut again lengthwise parallel to the first cut to obtain stalagmite slabs of about 1.5 cm thickness for easier handling of the stalagmite samples.

As both the subsequent sample extraction (using a Micromill; Section 4.4) and all of the analyses were conducted at high-resolution and at precise depths (here: Z-position) within the sample the two sides of the stalagmite slabs needed to be exactly parallel to each other. This was achieved by abrading the slabs using a MPS 2120 surface grinder (G&N; SiC with a P400 grit size) until the surface was plain and smooth. For high-quality microscope images and an exact positioning of the drill bit during micromilling and of the laser during LA-ICP-MS analyses the stalagmites' growth laminae were made visible by manually pre-polishing the slabs' top sides with a SiC sandpaper with a P800 grit size. The final lapping of the slabs was conducted with a PM2A lapping machine (Logitech) using a diamond polish with a 1 µm grit size (Struers).

Because the measurement chamber of the LA-ICP-MS can only hold samples with the maximum dimensions of 10 cm x 5 cm, the stalagmite slabs needed to be halved. As cutting the slabs is impossible without the loss of stalagmite material to be analysed, the slabs were broken into two after pre-cutting them from the bottom side down to a thickness of 1-2 mm with a band-saw (1 mm diamond blade; Proxxon MICRO Bandsaw MBS/E). For UV-microscopic analysis (Section 4.7.2) slides with a thickness of 200 µm were produced using the Petro Thin thin sectioning system (Buehler), while their thickness were subsequently reduced to 50 µm for VIS-microscopic analysis (Section 4.7.1) to achieve the desired optical effects such as the differing transmission of light depending on the three-dimensional orientation of the crystals within the samples.

Micromilling and all of the analyses were conducted on one of the two slabs of each stalagmite, except for the sample extraction for U/Th dating which was done on the opposite slab. To obtain sufficient sample material for U/Th dating these slabs were first cut along their central growth axis perpendicular to the slab surface and then chunks were cut out along the cutting edge with the band-saw accounting for the inclination of the growth laminae (Figure 4.1).

Figure 4.1: Slab of stalagmite VML22 after extraction of samples for U/Th dating using a band-saw. To minimize the error due to subsample mixing the cuts follow the inclination of the growth laminae (left: top view; right: perpendicular view on the cutting edge).

4.2 Macroscopic Characteristics of the Studied Stalagmites

This section characterises the two studied stalagmites on a macroscopic level, for instance, with regard to their colour and porosity. All depth-related information in the following are given relative to the top of the respective stalagmite as "depth from top" (DFT).

4.2.1 Stalagmite VML22

The part of stalagmite VML22 suited for palaeoreconstruction, where growth geometry is not too complex and porosity not too high (from hereon referred to as "stalagmite VML22"), is about 10.4 cm long and 6 - 7 cm wide at its lower half, whereas the upper half gradually tapers off towards the stalagmite's tip (Figure 4.2). While the lowest quarter or so also features brownish tones, the overall colour impression is greyish with brighter growth laminae alternating with greyish laminae. For instance, an area dominated by white tones ranges from 2 to 6 mm DFT, while an area dominated by grey tones spans 6 - 20 mm DFT. A very distinct feature of stalagmite VML22 is a well-defined black layer around 88 mm DFT along the growth axis (which corresponds to 90 mm DFT along the track along which the analyses were conducted represented by the black line in Figure 4.2).

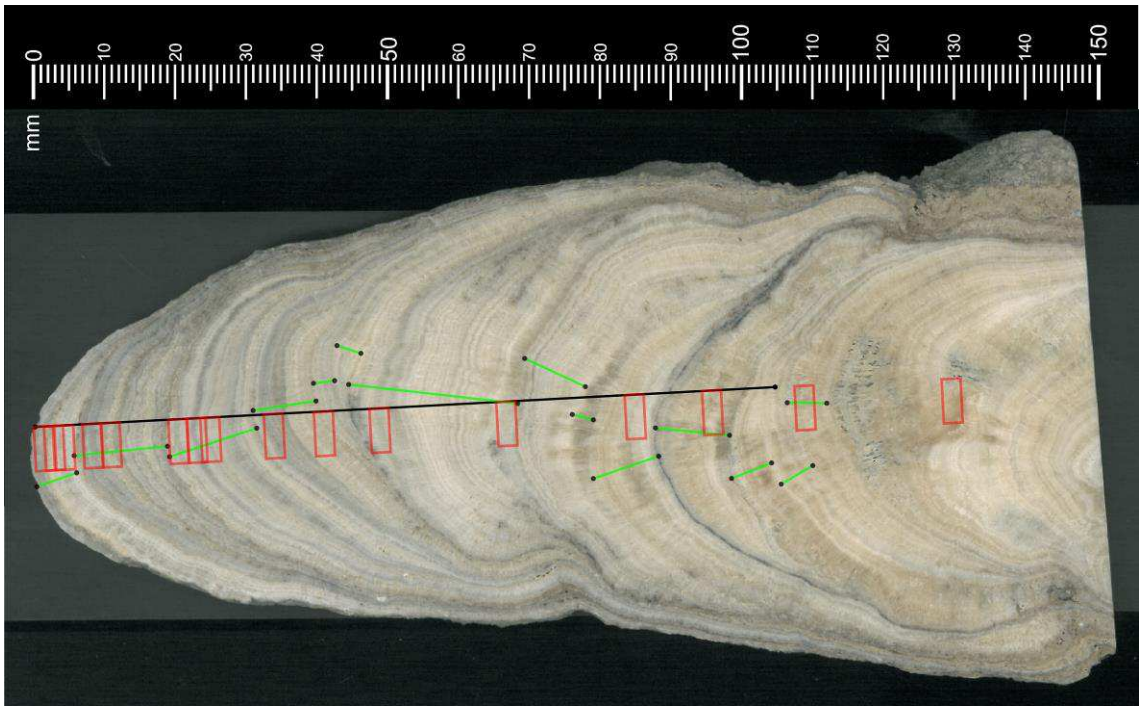

Figure 4.2: Slab of stalagmite VML22 (flatbed scan) including shifts of the central growth axis and changes in growth growth direction (bright green) and locations of the samples extracted for U/Th dating (red rectangles). The black line represents the axis along which micromilling and LA-ICP-MS analyses were performed.

The growth laminae also differ in translucence. For example, the range 52 to 65 mm DFT features alternations of white opaque laminae and more translucent laminae that are rather grey in their colour impression. The most prominent translucent sections along the central growth axis are located at 23, 32 - 36, 76 - 79 and 96 - 99 mm DFT, respectively.

While the porosity in stalagmite VML22 is relatively low overall, growth direction appears to have changed quite frequently with noteable shifts in the position of the central growth axis. These shifts are so numerous and strong that a practical sampling and analysis protocol (with analyses along straight lines) likely cannot account for all of them. In the case of stalagmite VML22, the largest discrepancy between the actual locus of the central growth axis and the locus of the geochemical analyses (Figure 4.2) exists at 45 mm DFT.

4.2.2 Stalagmite VSMS2

Stalagmite VSMS2 is 15 cm long and 4.5-5 cm wide over most of its length giving it a general cylindrical shape, only over the topmost 25 mm it tapers off towards the stalagmite's tip (Figure 4.3). In contrast to stalagmite VML22, VSMS2 features an overall brownish colour impression while grey, black and whitish tones are almost completely absent. The brightest colours are present within the topmost 4 mm.

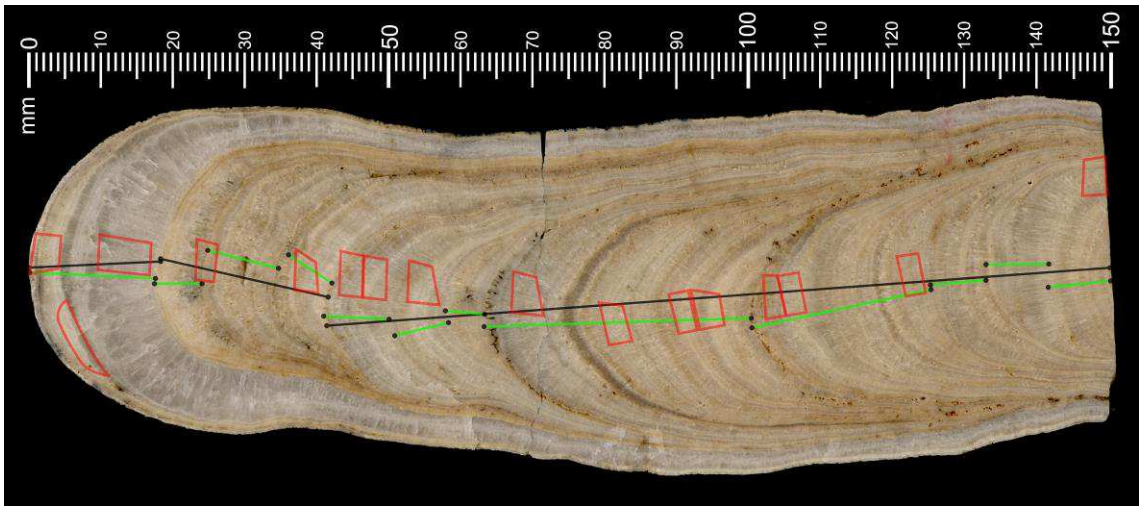

Figure 4.3: Slab of stalagmite VSMS2 (flatbed scan) including shifts of the central growth axis (bright green) and locations of the samples extracted for U/Th dating (red rectangles). The black lines represent the axes along which micromilling and LA-ICP-MS analyses were performed.

The most prominent macroscopic feature of stalagmite VSMS2 is a section between 4 and 18 mm DFT that is highly translucent and seems to exclusively consist of pure carbonate minerals/crystallites, strongly contrasting with the rest of the stalagmite. This might indicate that this section is virtually free of any detrital components that cause brownish to blackish tones in stalagmites. Another translucent section is situated at 74 – 76 mm DFT but appears darker and more brownish than the translucent whitish section at 4- 18 mm DFT, probably as an effect of the darker laminae directly on top of it. The laminae between 65 and 74 mm DFT are also relatively translucent.

Another important difference to stalagmite VML22 is the generally higher porosity of stalagmite VSMS2. This porosity is particularly noticeable in conjunction with darker brown layers, such as at 41, 63 – 65 and 100 – 104 mm DFT, but is not restricted to these depths, as shows, for instance, the section from 18 to 36 mm DFT. Furthermore, changes in growth direction and shifts in the position of the central growth axis are generally less pronounced than in stalagmite VML22 so that the lines along which sampling and analyses were conducted (Figure 4.3) are a good approximation of the central growth axis.

4.3 Dating using the Uranium/Thorium decay chain and Age Model construction

The suitability of speleothems for palaeoreconstruction greatly stems from the fact that they can be both accurately and absolutely dated using the U/Th decay chain, up to 650.000 years back in time (Richards & Dorale, 2003). U/Th dating is considered the "most robust geochronometer available over much of the Quaternary" (Hellstrom, 2006) which makes it a go-to dating method in speleothem research.

Fundamentally, U/Th dating is based on the separation of U from its daughter isotopes as a consequence of differences in solubility and/or chemical behaviour of the involved chemical species (Schwarcz, 1989): Initially, U occurs together with its daughter isotopes bound in rather insoluble silicates and/or oxides. Through weathering, mother and daughters are set free, but U forms soluble and therefore mobile complexes (mainly as the uranyle ion UO_2^{2+}), while its daugthers such as ^{230}Th are insolube and thus less mobile (Mortimer et al., 2015). Consequently, only the mother isotope U is present in karst cave dripwaters and gets incorporated in stalagmites growing from them. With this incorporation the atomic clock is set to zero and starts ticking due to the radioactive decay of U within the stalagmite. The (diminishing) discrepancy in abundance between mother and daugther isotopes is a function of time and can thus be used as a chronometer. Eventually a secular radioactive equilibrium is reached where the activity of the U-daugthers is equal to the activity of the U-mother isotope and the atomic clock stops ticking after about 600,000 years (Schwarcz, 1989; Bourdon, 2003).

Therefore, the applicability of U/Th dating relies on two basic assumptions: Firstly, at the time of stalagmite formation, Th as the daugther isotope is not present in the stalagmite or in known concentrations ($^{230}Th/^{234}U$ either zero or determinable). Secondly, the sample has always behaved as a closed system without any gains or losses of any of the isotopes other than by radioactive decay (Ivanovich & Harmon, 1992). Using equations 4.1 and 4.2, the age (t) of a stalagmite sample can be calculated (Ivanovich & Harmon, 1992):

$$\frac{^{234}U}{^{238}U}(t) = \left(\left(\frac{^{234}U}{^{238}U}\right)_0 - 1\right) \times e^{-\lambda_{234} t} + 1 \qquad 4.1$$

$$\frac{^{230}Th}{^{238}U}(t) = \left(1 - e^{-\lambda_{230} t}\right) + \left(\left(\frac{^{234}U}{^{238}U}\right)(t) - 1\right) \times \frac{\lambda_{230}}{\lambda_{230} - \lambda_{234}} \times \left(1 - e^{-(\lambda_{230} - \lambda_{234})}\right) \qquad 4.2$$

where t is time, $^{234}U/^{238}U$ and $^{230}Th/^{238}U$ are the activity ratios (the index 0 indicates the initial activity ratio) and where λ is the decay constant of the respective nuclide. Figure 4.4 illustrates the evolution of the $^{230}Th/^{234}U$ activity ratio until it reaches secular equilibrium for two different initial $^{234}U/^{238}U$ ratios (1.0 and 4.0).

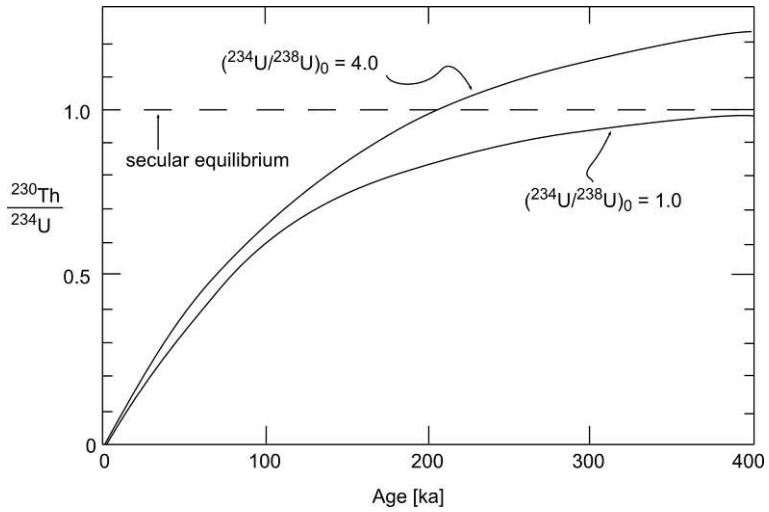

Figure 4.4: Evolution of the $^{230}Th/^{234}U$ activity ratio until it reaches secular equilibrium for two different initial $^{234}U/^{238}U$ ratios (1.0 and 4.0); adapted from Schwarcz (1989).

The main source for uncertainty in U/Th dating are low initial U contents and the contamination of a sample with detrital ^{230}Th incorporated in the stalagmite together with organic matter, colloids or fine sediments. If this initial ^{230}Th is not corrected for, the resulting ages can be significantly overestimated. It can be calculated from its ratio with the stable isotope ^{232}Th assuming that this ratio is constant ($^{230}Th/^{232}Th = 0.8 \pm 0.8$). Further assumptions for such a correction are a bulk earth $^{232}Th/^{238}U$ weight ratio in the continental crust of 3.8 and that ^{230}Th, ^{234}U and ^{238}U are in secular equilibrium (Goldstein, 2003; Hellstrom & Pickering, 2015).

For this PhD thesis, U/Th dating was performed using a Thermo Fisher Scientific iCap Q-ICP-MS (inductively coupled plasma – mass spectrometer) and a Thermo Fisher Scientific Neptune Plus MC-ICP-MS (MC = multi-collector) at the Institute for Environmental Physics, at the Heidelberg Academy of Sciences. Sample preparation and mass spectrometric analysis with the iCap Q were performed following the procedure of Douville et al. (2010). For the Neptune Plus measurements, the applied measurement protocols, data treatment including corrections and chemical sample preparation are described in detail in Arps (2017). The ages were calculated using the half-lives of Cheng et al. (2000) and corrected for detrital Th assuming a bulk earth $^{232}Th/^{238}U$ weight ratio of 3.8 ± 1.9 for the detritus and a secular equilibrium between ^{230}Th, ^{234}U and ^{238}U. Analytical errors are given in Table 5.1 and Table 5.2 at the 2σ-level and do not include half-life uncertainties.

The age model is the relationship between the depth within the stalagmite given as DFT and the age. For stalagmites VML22 and VSMS2 it was modelled with the algorithm StalAge based on the measured U/Th dates and their respective uncertainties (Scholz & Hoffmann, 2011). This algorithm applies Monte-Carlo simulations that fit ensembles of straight lines between three or more adjacent dating points (ages) to calculate the age model together with its 95%-confidence limits.

It also enables the iterative identifcation of major and minor outliers in the data prior to constructing the age model. After its construction the age model is screened for age inversions (Scholz & Hoffmann, 2011). Although several other algorithms for age model calculation are available, a comparison between these algorithms showed that they yield comparable results in relatively easy cases, but that StalAge together with the algorithm OxCal are more successful at calculating reliable age models from stratigraphically complex samples with a limited number of U-series ages (Scholz et al., 2012).

Refining the calculated age models by counting annual laminae (e.g. Tan et al., 2006; Baker et al., 2008; Tan et al., 2014) discernible from differences in their transmissivity of visible or ultraviolet light or in their trace element concentrations was not possible in the case of stalagmites VML22 and VSMS2 due to their low growth rate and the lack of lamination over larger sections along their growth axes.

4.4 Sample Extraction by Micromilling

Sample extraction from stalagmites VML22 and VSMS was performed using a Micromill (New Wave Research) with a hardened-steel drill bit with a spherical tip (ø = 300 µm). The samples were extracted continuously in linear trenches along an approximation of the stalagmites' central growth axis (black lines in Figure 4.2 and Figure 4.3). In order to achieve sample masses of at least 1 mg (sufficient for 2-3 repeated isotope measurements), these trenches were set to be 4 mm across, 600 µm deep and 200 µm wide (= dimension in growth direction) using the Micromill software (New Wave Research) resulting in a nominal spatial resolution of the resulting isotope data (Section 5.2) of 200 µm. Due to minor deviations in the spatial calibration of the Micromill system, the actual spatial resolution is 189 µm for stalagmite VML22 and 199 µm for stalagmite VSMS2.

To take account of the varying curvature of the growth laminae, the trenches were not always exactly perpendicular to the growth axis but more or less inclined relative to the growth axis depending on curvature. The total depth of 600µm of each sample trench was achieved in three separate milling steps of 200 µm each to prevent damage to the sample and/or the drill bit due to excessive force. Vertical and horiztonal feed were set to 75 µm/s, drill bit rotation was set to 50% to reduce the loss of sample material during milling. Between consecutive trenches, both the stalagmite surface and the drill bit were thoroughly cleaned with a brush. From stalagmite VML22 a total of 555 samples were micromilled, from stalagmite VSMS2 a total of 750 samples.

4.5 Stable Isotope Analysis by IR-MS

The samples micromilled from the stalagmites were analysed for the stable isotope composition of oxygen ($\delta^{18}O$) and carbon ($\delta^{13}C$) by isotope-ratio mass spectrometry (IR-MS) using a Delta V Advantage mass spectrometer (Thermo Fisher Scientific) coupled to an on-line, automated carbonate preparation system (GasBench II; Thermo Fisher Scientific). In this system, the sample vials sealed by rubber septa are flushed with He so that the atmosphere inside the vials is free of CO_2 and O_2, and 103% orthophosphoric acid is added to release CO_2 from the complete dissolution of the ~ 1 mg carbonate samples over 90 minutes at 72°C. Using He as carrier gas, the sample CO_2 then passes a gas-phase chromatograph to separate it from other gases and is injected into the mass spectrometer for analysis (e.g. Clark & Fritz, 1997), in this case in ten pulses of 100 µL each. The results obtained from these ten injections are then averaged to yield the final results.

Calibration was conducted using the NBS19 standard material. Precision is determined by the absolute standard deviation (ASD) of repeated measurements of the Carrara Marble standard material, with an average accuracy of 0.03 ‰ for $\delta^{13}C$ and of 0.09 ‰ for $\delta^{18}O$, respectively (n = 150) . For stalagmite VML22, precision was ≤ 0.08 ‰ for $\delta^{18}O$ and ≤ 0.03 ‰ for $\delta^{13}C$ (n = 301). The average precision of the individual measurements (n = 605) was 0.06 ‰ and 0.04 ‰ for $\delta^{18}O$ and $\delta^{13}C$, respectively. In case of stalagmite VSMS2, precision was ≤ 0.09 ‰ for $\delta^{18}O$ and ≤ 0.04 ‰ for $\delta^{13}C$ (n = 358). The average precision of the individual measurements (n = 835) was 0.05 ‰ and 0.04 ‰ for $\delta^{18}O$ and $\delta^{13}C$, respectively. All results are reported in the δ notation [‰] relative to the V-PDB standard.

4.6 Trace Element Analysis by LA-ICP-MS

Trace element concentrations were determined along the approximated growth axis of stalagmites VML22 and VSMS2 (black lines in Figure 4.2 and Figure 4.3) by LA-ICP-MS (LA = laser ablation) using an Agilent 7500ce mass spectrometer coupled to an ESI NWR 193 laser ablation system with an ArF excimer laser at the Institute of Geosciences at the University of Mainz. The measurements were conducted with a laser spot size of 110 µm, at a laser wavelength of 193 nm, a scan speed (lateral feed) of 15 µm/s, a pulse repetition rate of 10 Hz and an energy density of ~3 J/cm^2. Prior to scanning a washout of 20 s was performed after a laser warmup of 15 s. The resulting data have a spatial resolution of 6.4 µm.

Calibration was conducted using the NIST SRM 612 reference material, accuracy was verified with the USGS MACS-3 carbonate standard as this standard material is the most similar to the sample material. Precision was determined with the NIST SRM 610, the USGS GSD-1G and the USGS BHVO-2G reference materials. To prevent any potential contamination, the stalagmite surface was pre-ablated prior to the actual measurements as well as the surface of all standard materials except for the USGS MACS-3 standard due to its fragility.

Pre-ablation was conducted at a lateral feed of 50 µm/s after a 2-second laser warmup without a washout. As an additional quality control, some sections along the stalagmites' growth axis were analysed twice with a lateral offset of about 2 mm in between.

Blank quantification was performed by recording the measurement signal (produced by internal processes within the analytical instrument, e.g. by the carrier gas) without ablation of any sample material for about 15 seconds before and in between measurement runs. For reasons of practicality this is done by activating the laser with the shutter just in front of it closed, as the laser triggers the recording of the measurement signal automatically to circumvent the need for manual blank quantification.

To transform the raw data (in counts/second) into the final concentration values in µg/g, they were processed according to standard procedure as follows: The raw data (count rates) of all measured elements are corrected for blanks by subtraction and then divided by the corresponding blank-corrected count rates of Ca in order to account for internal signal instabilities during analysis. As a first outlier control the results of standard materials (not of the samples) are then filtered to remove all measurement values that either exceed their respective median by more than 30% or that are below their respective median by more than 30%. In the case of the standard materials all data values generated during each ablation run before and between analyses of the stalagmite samples are averaged for later calibration and precision evaluation.

The transformation of the now blank-corrected count rates into uncorrected concentration values (µg/g) is conducted using the following equation:

$$c_{uncorr} = CR_{bc} * \frac{IA_{Ca}}{IA_E} * \frac{AW_E}{AW_{Ca}} * c(Ca) \qquad 4.3$$

c_{uncorr}: uncorrected element concentration [µg/g]
CR_{bc}: blank corrected count rate [-]
IA_{Ca}: isotope abundance of ^{43}Ca (= 0.00135) [-]
IA_E: abundance of a specific isotope of the respective element, e.g. ^{25}Mg (= 0.1003) [-]
AW: atomic weight of Ca and the respective element (E) [g/mol]
c(Ca): concentration of Ca [µg/g] in the calibration or reference standard from the literature (e.g.: NIST SRM 612 with c(Ca) = 85050 µg/g) or in the stalagmite sample

For this transformation of the stalagmite sample values a Ca concentration of 38 wt-% instead is assumed to account for potential impurities within the stalagmite. The calibration factor is calculated by dividing the uncorrected element concentrations of the NIST SRM 612 reference matieral by the published concentration value for each respective element. The element concentrations in the other standard materials and in the stalagmite samples are corrected by dividing the uncorrected concentrations by the calibration factor for each element.

All published values and reference values used for the calibration and verification of the measurement quality were taken from Jochum et al. (2005) and/or Jochum et al. (2012).

Precision and accuracy of the trace element analyses with LA-ICP-MS are shown in Table 4.1 for stalagmite VML22 and in Table 4.2 Table 4.1for stalagmite VSMS2. Precision is usually below 5 % except for the Cd measurements in the USGS BHVO-2G standard where the relative standard deviation (RSD) is 62 %. Accuracy is high for elements like Mg, Sr, Mn and Cu with deviations from the published reference concentration below or close to 5 %. The results for the remaining elements are less accurate, in particular for Si and P (Table 4.1 andTable 4.2) which can therefore only be interpreted qualitatively. These inaccuracies can partly be explained with mass interferences during analysis, for instance of single Si ions with two oxygen ions. The generally low precision of the measurements of the MACS-3 standard material is due to the inhomogeneity of the standard material (being a pressed powder pellet) rather than a low measurement quality. The elements Fe, Zn and Sr were quantified based on the analysis of multiple isotopes. In this thesis the isotope was chosen for which the results deviated less from the published reference concentration, in case of stalagmite VML22, ^{57}Fe, ^{67}Zn and ^{88}Sr. For better comparability, the same isotopes for chosen for stalagmite VSMS2.

Table 4.1: Quality of the trace element analyses with LA-ICP-MS for stalagmite VML22. Precision is determined by the relative standard deviation (RSD) of repeated measurements (n = 12) of the NIST SRM 610 and USGS GSD-1G standard materials. Accuracy is represented by the deviation (Dev.) from the reference concentration in the USGS MACS-3 standard material as published in the literature (n = 12).

Isotope	**Na**	**Mg**	**Al**	**Si**	**P**	**Mn**	**Fe**	**Cu**	**Zn**	**Rb**	**Sr**	**Cd**	**Ba**	**U**
NIST SRM 610														
Dev. [%]	5	24	1	5	12	3	-32	3	5	<0.5	-2	-2	-3	-1
RSD [%]	**3**	**1**	**1**	**1**	**3**	**1**	**1**	**1**	**2**	**2**	**1**	**3**	**2**	**3**
USGS GSD-1G														
Dev. [%]	1	13	14	2	24	<0.5	-40	-2	13	3	-1	47	4	3
RSD [%]	**3**	**1**	**1**	**2**	**3**	**1**	**1**	**3**	**6**	**2**	**<0.5**	**7**	**1**	**2**
USGS MACS-3														
Dev. [%]	**-11**	**<0.5**	**14**	**49**	**100**	**-3**	**-5**	**-6**	**-7**	**-21**	**5**	**-10**	**20**	**11**
RSD [%]	2	2	8	14	11	4	11	6	7	30	2	5	6	9

Table 4.2: Quality of the trace element analyses with LA-ICP-MS for stalagmite VSMS2. Precision is determined by the relative standard deviation (RSD) of repeated measurements (n = 24) of the NIST SRM 610 and USGS BHVO-2G standard materials. Accuracy is represented by the deviation (Dev.) from the reference concentration in the USGS MACS-3 standard material as published in the literature (n = 24).

Isotope	**Na**	**Mg**	**Al**	**Si**	**P**	**Mn**	**Fe**	**Cu**	**Zn**	**Rb**	**Sr**	**Cd**	**Ba**	**U**
NIST SRM 610														
Dev. [%]	3	24	-1	4	7	5	-37	5	4	<0.5	1	<0.5	-3	-2
RSD [%]	**3**	**2**	**2**	**4**	**4**	**3**	**4**	**4**	**4**	**4**	**1**	**4**	**2**	**4**
USGS BHVO-2G														
Dev. [%]	-21	5	10	-12	-15	-7	-52	-14	6	-11	-1	17	-4	-6
RSD [%]	**1**	**1**	**1**	**1**	**1**	**1**	**1**	**2**	**2**	**1**	**1**	**62**	**1**	**3**
USGS MACS-3														
Dev. [%]	**-7**	**1**	**14**	**96**	**88**	**-1**	**-19**	**3**	**13**	**35**	**8**	**<0.5**	**19**	**15**
RSD [%]	3	2	12	34	21	6	19	8	19	55	5	6	12	17

For post-analysis processing of the data, all negative values were removed and outliers were detected using the Grubbs test (Grubbs, 1969) and deleted. Furthermore, to adapt the spatial resolution of the element data to the spatial resolution of the stable isotope data, the element data were averaged accordingly using an algorithm written in the programming language R (R Core Team, 2013; source code in Appendix C.5). This algorithm groups the element data into the depth (DFT) increments the isotope data integrate over (multiples of 189 µm for stalagmite VML22 and of 199 µm for stalagmite VSMS2). Over each of these increments the algorithm averages the measured element concentrations to produce element concentration values that correspond to their respective stable isotope data point.

4.7 Microscopic Analysis

4.7.1 Optical Microscopy

Optical microscopic analysis of stalagmites VML22 and VSMS2 was performed with a Leica DM750M microscope (Leica Microsystems Limited) at five times magnification. The microscope images shown in this work were taken with a Leica ICC50 HD camera using the LAS EZ 3.0.0 (Build: 629) software (both from Leica Microsystems Limited).

Microscopic analysis using reflected light was conducted on the stalagmite slabs (thickness of 1.5 cm; Section 4.1). For image acquisition the following settings were used for optimal image quality: The illumination level of the primary light source (four light-emitting diodes) was set to 14 out of the 14 available levels, the aperture was 100% open and a white balance was conducted on a white area of the respective stalagmite sample.

Exposure time was set manually to 77.0 ms, enhancement to 12x, gamma to 0.7 and saturation to 100. The images were taken with a format of 2,048 x 1,536 pixels, with a medium sharpening effect and with both polarisers inserted with the left polariser being set to 90°. For easier orientation the microscope image was tilted horizontally and vertically. The pictures were taken along a raster of 2 mm (in X-direction; left / right from the operator's perspective) times 1.5 mm (in Y-direction) in order to achieve sufficient (but not excessive) overlap between consecutive images for later image stitching.

To display the microscopic information contained in single images in their context of the stalagmite's internal structure, the single images were then stitched using the Photostitch software (version 3.1.22.46; Canon Utilities). For stalagmite VML22 a total of 1,083 images were taken of which 224 were stitched, for stalagmite VSMS2 926 images were stitched out of the 2,450 images taken.

Microscopic analysis using transmitted light was conducted on thin slides (thickness of 50 µm; Section 4.1) of the sample stalagmites. For optimal image acquisition, the following settings were chosen: The primary light source was set to maximum, the lower aperture was 100% open, the upper aperture (condenser) was opened to a minimum and positioned at an intermediate level (Z-position), and a white balance was conducted on a white area of the respective stalagmite sample. Exposure time was set automatically, the remaining settings were identical to the ones chosen for reflected light analysis. For stalagmite VML22 a total of 120 images were taken and stitched, for stalagmite VSMS2 a total of 300 images were taken and.

4.7.2 UV-Microscopy

UV-microscopic analysis of stalagmites VML22 and VSMS2 was performed with an Axio Imager Z1 epifluorescence microscope using the ZEN blue software (lite edition 2.3; both from Carl Zeiss Microscopy) at ten times magnification. Images were acquired with an AxioCAM HRm camera (Carl Zeiss Microscopy).

Microscopic analysis was conducted on thick slides (thickness of 200 µm; Section 4.1) of the sample stalagmites using the Brightfield, DAPI, FITC, DsRed and Alexa Fluor 660 filters. Images were taken with exposure times manually set to 48.0, 333.4, 726.8, 648.8 and 1227.4 ms, respectively, at a resolution of 2,776 x 2,080 pixels using the live speed acquisition mode without autofocus. Focus was achieved manually with the Brightfield filter active, the primary light source was set to four tick marks. The pictures were taken along a raster of about 0.7 mm (in X-direction; left / right from the operator's perspective) times 0.5 mm (in Y-direction) in order to achieve sufficient (but not excessive) overlap between consecutive images for later image stitching. After acquisition the images were optimised using the automatic best fit correction of the histogram of all five channels offered by the Zen blue software. The images were then exported from the .czi file format to the .jpeg format for stitching.

Stitching was again performed with the Photostitch software. However, as the stitching algorithm of this software caused erroneous modifications of the pictures' original colour when stitching images in Y-direction (Figure 4.5), only the stitching in X-direction was possible without losing the original fluorescence signal contained within the images. For stalagmite VML22 a total of 564 images were taken of which 141 were stitched, for stalagmite VSMS2 91 images were stitched out of the 1,254 images taken covering the depth range from 40 mm DFT to its base.

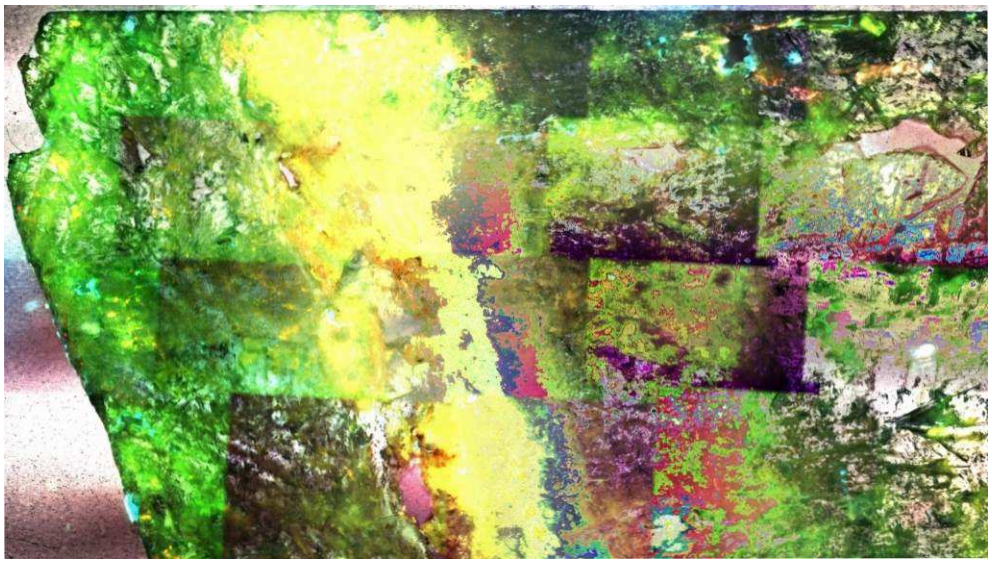

Figure 4.5: Erroneous results (colour distortions; bright purple and red colours) when stitching UV-microscope images with the Photostich software. The contours of the separate images in this 4 x 5 mosaic (about 3.5 x 2.5 mm) are still visible.

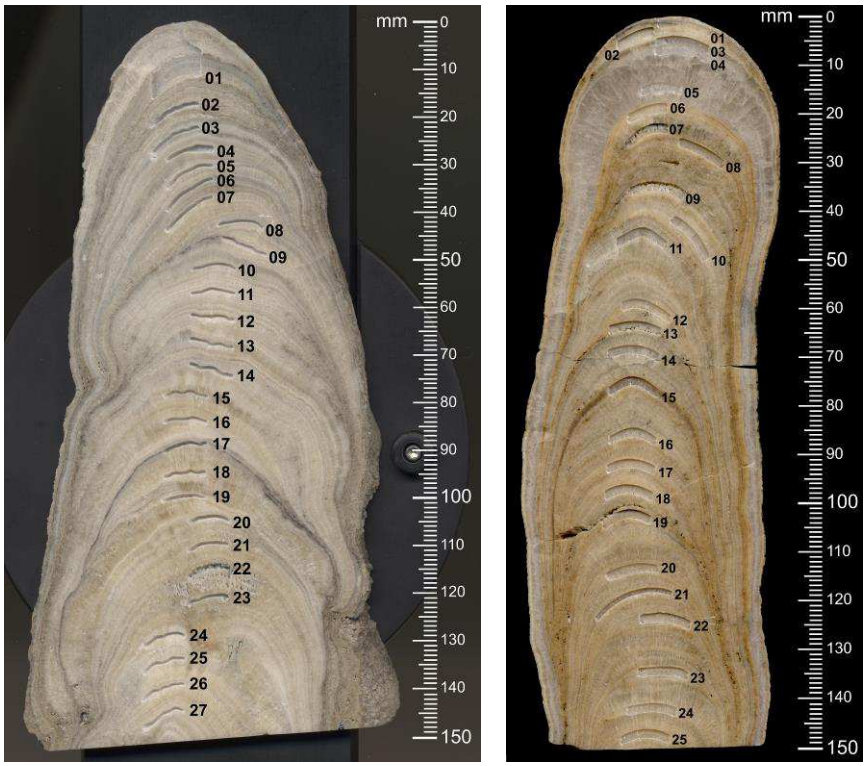

Figure 4.6: Locations of the samples extracted from stalagmite VML22 (left) and VSMS2 (right) for XRD analysis, numbered in black.

4.8 Mineralogical Analysis by XRD

Mineralogical analysis was executed on ~ 10 mg samples micromilled from each stalagmite using X-ray diffractometry (XRD). From stalagmite VML22 a total of 27 samples were micromilled using a spherical hardened steel drill bit (ø 300 µm) in curved trenches 600 µm deep, 300 µm wide and 10 mm across (Figure 4.6, left). From stalagmite VSMS2 a total of 25 samples were micromilled using a cylindrical hardened steel drill bit (ø 1 mm) in curved trenches 200 µm deep, 2 mm wide and 10 mm across, VSMS2, except for sample 21 with the trench being 1 mm wide and 20 mm across (Figure 4.6, right). All other settings were as described in Section 4.4

For complete homogenisation the micromilled samples were pestled with a corundum mortar and subsequently applied to monocrystalline Si-wafers using isopropanole as the sample size was too low for using the standard sample carrier. XRD analysis of the samples from stalagmite VML22 was performed with a D500 diffractometer (Siemens) over an angle range of 3° to 63°, with a step size of 0.01° and a step speed of 0.5°/min, at 25 mA and 45 kV. The samples from stalagmite VSMS2 were analysed using a D8 Discover diffracometer (Bruker). To determine suitable measurement settings a quick test scan was conducted first. The measurement duration (step speed) was then adapted so that the lowest peak in the diffractogram reaches an intensity of 1,000 counts.

The step size was adjusted so the the upper half of the highest peak is detected by at least seven data points. Both requirements were met at a step size of 0.02° and a measurement time of 38.4 s per step, at 40 mA and 40 kV. Measurements were conducted over an angle range of 2° to 82°, with the air scatter screen active and the sample rotating at a speed of 30,000°/min. The background of all diffractograms was subtracted using the DIFFRAC.EVA software (Bruker AXS 2010-2015; release 2015; version 4.1.1) and the diffractograms were evaluated based on the X-ray diffractometry peaks from the PDF-2 2002 database (sets 1-52 plus 65 plus 70-89).

4.9 Analyses of Host Rock, Soils and Plants

In order to characterise the environment of the studied caves, a number of analyses were conducted on samples of host rock (Section 4.9.1), soils (Section 4.9.2) and plants (Section 4.9.3) from the study area. These analyses comprise the mineralogical and geochemical composition of host rock and soils as well as the stable carbon isotope ratios of host rock, soils and plants. Figure 4.7 shows the sampling locations at the surface above cave Ma Le 2. All host rock, soil and plant samples are listed in Table 4.3.

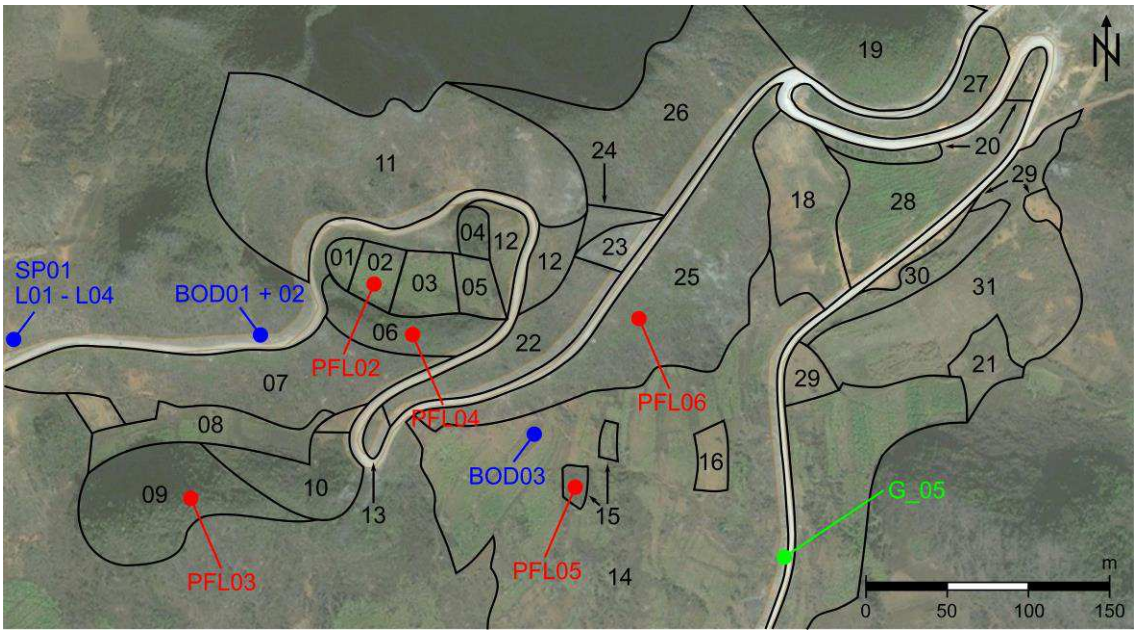

Figure 4.7: Aerial view (Bing, © Digital Globe; accessed: March 7th, 2014) of the surface above cave Ma Le 2 including the positions of the rock sample (green), soil samples (blue) and plant samples (red). The black numbers designate the areas (black contours) defined during the mapping of the vegetation (carried out on March 7th, 2014). The location of this area relative to the entrance of cave Ma Le 2 is shown in Figure 3.2. All samples are listed in Table 4.3.

Table 4.3: List of all host rock, soil and plant samples taken from inside or at the surface above caves Ma Le 2 and Sang Ma Sao.

Category	Sample label	Description
Host Rock:		
cave Ma Le 2:	G_02-1	from just upstream of the position of stalagmite VML22
	G_02-2	from just downstream of the position of stalagmite VML22
	G_05	from the surface above the cave; 23°17'24.0'' N; 105°18'34.9'' E; 1,115 masl
cave Sang Ma Sao:	G2-01 to -09	rocks from inside the cave
	SMS BC	black crust from the cave wall
Soils:		
above Ma Le 2:	BOD01	23°17'33.5'' N; 105°18'25.6'' E; 1,275 masl; depth range 30 - 60cm; bright-brown23°17'30.4'' N; 105°18'32.1'' E;
	BOD02	as BOD01, but representative for layer from 60 cm downwards; red-brown; very hard
	BOD03	23°17'31.7'' N; 105°18'31.3'' E; 1,200 masl; depth range 15 - 20 cm
	SP01 L01	23°17'32.1'' N; 105°18'16.7'' E; 1,299 masl; representative of
	SP01 L02	as SP01 L01, but representative of layer 2 (45 – 70 cm depth)
	SP01 L03	as SP01 L01, but representative of layer 3 (70 – 100 cm depth)
	SP01 L04	as SP01 L01, but representative of layer 4 (from 100 cm downwards)
above Sang Ma Sao:	SMS Soil01 0-10 cm	23°17'12.9'' N; 105°19'37.8'' E; 1,172 masl; depth range 0 - 10
	SMS Soil01 20-15 cm	as SMS Soil 01 0-10 cm, but depth range 20 - 15 cm
	SMS Soil01 ~35 cm	as SMS Soil 01 0-10 cm, but depth ~ 35 cm
	SMS Soil02	23°17'12.1'' N; 105°19'37.8'' E; 1,172 masl; 0 – 20 cm
	SMS Soil02 coarse	coarse fraction of SMS Soil02 (> 2 mm)
Plants:		
above Ma Le 2:	PFL02	23°17'34.4'' N; 105°18'27.9'' E; area ML2-02
	PFL03	23°17'29.7'' N; 105°18'24.1'' E; area ML2-09
	PFL04	23°17'33.4'' N; 105°18'28.6'' E; area ML2-06
	PFL05	23°17'30.4'' N; 105°18'32.1'' E; area ML2-15
	PFL06	23°17'33.3'' N; 105°18'32.8'' E; area ML2-25
above Sang Ma Sao:	SMS PL01	23°17'13.6'' N; 105°19'37.8'' E
	SMS PL02 to PL04	close to SMS PL01; SMS PL02 is the same species as PFL04

4.9.1 Host Rock Analyses

As a preparation for subsequent geochemical and mineralogical analyses, representative pieces of the host rock samples were transformed into fine powder with the use of a rock crimper, a type BB1 jaw crusher (Retsch) and a TS vibratory disc mill (Siebtechnik) with corundum discs with a milling duration of two minutes. In between samples the discs were cleaned by milling laboratory quartz sand for two minutes, brushing the discs, dusting them off with pressurised air and cleaning them with isopropanole.

Stable isotope analysis of the carbonate host rock samples was performed by IR-MS as described for the stalagmite samples in Section 4.5. Calibration was conducted using the NBS19 standard material. Precision is determined by the absolute standard deviation (ASD) of repeated measurements of the Carrara Marble standard material, with an average accuracy of 0.03 ‰ for $\delta^{13}C$ and of 0.09 ‰ for $\delta^{18}O$, respectively (n = 150). Precision was ≤ 0.10 ‰ for $\delta^{18}O$ and ≤ 0.07 ‰ for $\delta^{13}C$ (n = 13). The average precision of the individual measurements (n = 7) was 0.04 ‰ and 0.03 ‰ for $\delta^{18}O$ and $\delta^{13}C$, respectively. Mineralogical analysis was executed by XRD as described for the stalagmite samples in Section 4.8, using the D8 Discover diffracometer (Bruker), but applying standard XRD sample holders instead of Si-wafers.

The geochemical composition of the host rock samples was analysed using an X-Series II ICP-MS (Thermo-Fisher Scientific) subsequent to a full chemical digestion of about 100 mg of the sample powder using 40% hydrofluoric acid (suprapure) and 70% perchloric acid (normapure) in closed Teflon sample tubes at 120°C over 16 hours, after sample pre-oxidation with 65% nitric acid (subboiled). Temperature was controlled with a DigiPREP MS system (SCP Science). After evaporating the acids, nitric acid was added to re-dissolve the samples and evaporated three times to remove residues of the acids. For subsequent analysis the samples were dissolved in 50 mL ultrapure water. To test the quality of the chemical digestion and of the analytical measurement, the JDo-1 standard material was also analysed as well as two blanks for later blank correction.

Calibration solutions were prepared with the CertiPUR® ICP Multi Element Standard VI (Merck) used as stock solution and with additional 1000 ppm CertiPUR® ICP standards (Merck) containing P, Mg, Mn and Ca. based on these stock solutions, multi element standard solutions of the following concentrations were prepared: 0.5, 1.0, 2.5, 5.0, 10, 25, 100, 250, 500 and 1,000 ppb. For Na, Mg and K a 5 ppm standard solution was prepared. For calibration in higher concentration ranges of Al, Fe and Ca, two additional solutions were prepared, one containing 10 ppm of Al and Fe, and 50 ppm of Ca, one containing 25 ppm of Al and Fe, and 100 ppm of Ca. For Th calibration, Th solutions were prepared containing 2.5, 5 and 10 ppb of Th.

In order to correct for potential fluctuations in the analytical signal, 50 µL of an internal standard containing scandium (^{45}Sc), rhodium (^{103}Rh), indium (^{115}In) and thulium (^{169}Tm) at a concentration of 1 mg/L were pipetted into all samples, including the blanks (1% HNO_3). All samples were analysed after diluting them with 1% HNO_3 by a factor of five, blanks and standards were analysed without dilution.

For element quantification, the following isotopes were chosen: ^{23}Na, ^{25}Mg, ^{27}Al, ^{31}P, ^{39}K, ^{43}Ca, ^{47}Ti, ^{55}Mn, ^{56}Fe, ^{65}Cu, ^{66}Zn, ^{85}Rb, ^{88}Sr, ^{137}Ba, ^{232}Th and ^{238}U. While P, Mn, Fe, and Zn were measured in CCT-ED measuring mode to avoid isotopic interferences (KED energy barrier of 2 V), the remaining elements were analysed in standard measuring mode. For determining element concentrations, each sample was scanned three times in peak-jump mode, with each scan consisting of 40 sweeps with a dwell time of 25 ms each and an acquisition time of 15 seconds per run. For all measurements the following Ar gas flows were chosen: Nebulizer gas flow of 0.87 L/min, auxiliary gas flow of 0.68 L/min, and cooling gas flow of 13 L/min.

High blank values for Rb yielded a negative concentration in the JDo-1 standard after blank correction and a chemical yield of -33 %. Due to this erroneous result, the concentration of Rb was below 0.5 mg/kg in all host rock samples and is not illustrated or discussed further. Compared to the JDo-1 standard material, chemical yields (excluding Rb) were good with an average of 103.7 % (n = 15) and a median of 100.3 %. Concentrations of Cu (yield: 64.8 %) were too low, while concentrations for Ca (yield: 177.8 %) were too high. The precision (σ) of all sample measurements was 1.5 % on average, ranging from 0.5 % (Sr) to 3.2 % (Cu). The limits of detection based on seven measurements of ultrapure water was 0.001 mg/L for Na, Mg, Al, K and Fe and 0.005 mg/L for Ca. For all other elements, the limit of detection was below 0.1 µg/L, except for P (1.5 µg/L).

4.9.2 Soil Analyses

Stable Isotope Analysis by IR-MS

The soil samples were prepared for analysis by drying in an oven at 40 °C for at least 48 hours, removing the coarse fraction (> 2 mm) by sieving and by transforming the samples into sample powder with a vibratory disc mill as described for the host rock samples (Section 4.9.1). Samples were stored in an exsiccator until they were analysed.

Stable carbon isotope analysis of the organic matter contained within the soil samples was performed with a NA-1500 element analyser (Carlo-Erba) coupled to an Optima gas-ion mass spectrometer (Micromass UK Ltd.) using the continuous-flow mode. Prior to the measurement, the inorganic carbon in the samples was removed with hydrochloric acid by pressing the acid through the samples and through a filter. During analysis, the helium carrier gas flow was set to 90 to 100 mL/min and temperatures in the oxidation reactor (Cr_2O_3) and the reduction reactor (Cu) were adjusted to 1,020 °C and 650 °C, respectively. Calibration was performed using the NBS-21 standard material.

Analytical quality was tested with repeated measurements of the NBS-21 (n = 11) and the USGS-24 (n = 29) standard materials. The $\delta^{13}C$ results are accurate to less than 0.1 ‰ and 0.01 ‰, respectively and precision is 0.05 ‰ (absolute standard deviation) and 0.04 ‰, respectively.

Mineralogical and Geochemical Analysis by XRD, ICP-MS and CSA

Mineralogical analysis of the soil samples was executed by XRD as described for the stalagmite samples in Section 4.8, using the D8 Discover diffracometer (Bruker), but applying standard XRD sample holders instead of Si-wafers.

The geochemical composition of the soil samples was performed as described for the host rock samples in Section 4.9.1, but using the GXR-2 standard material for reference. Compared to the GXR-2 standard material, overall chemical yields were slightly too low with an average of 88.2 % (n = 15) and a median of 92.2 %. Especially the concentrations of Al (yield: 41.3 %) and of Sr (yield: 62.2 %) were too low, while concentrations for Cu (yield: 106.7 %) were slightly too high. The precision (σ) of all sample measurements was 0.8 % on average, ranging from 0.5 % (Sr) to 1.5 % (Na). The limits of detection are the same as for the host rock analyses (Section 4.9.1).

Carbon analysis of the soil samples (about 200 mg) was performed with a CS-2000 element analyser (Eltra) using the induction furnace at an O_2-pressure of 1.5 bar , an infrared measurement cell flow of 10 L/h and temperatures of about 1,350 °C. Measurement time was typically 50 seconds. For calibration, the 92811-3020 and 92400-3050 standard materials (Eltra) were used for the low carbon concentrations channel, the 92400-3100 standard material (Eltra) for the high carbon concentrations channel. Analytical quality was monitored by repeated measurements of these standards. For the low concentration channel, accuracy defined as the relative deviation from the target value was 2.9 % on average (n = 11), for the high concentration channel, accuracy was 1.0 % on average (n = 7). Precision (σ) with regard to the absolute carbon content was 0.02 % and 0.06 %, respectively.

Total carbon content was measured in the original soil powder samples. For the analysis of the organic carbon content, the inorganic carbon contained in the samples in the form of calcite was removed from a separate batch of samples with 19% hydrochloric acid added to the CSA cups at about 70 °C until the chemical reaction has completely ceased. After evaporating the acids, ultrapure water was added and evaporated at 100 °C three times to remove residues of the acid. The samples were stored in an exsiccator for at least 72 hours for equilibration and drying. The carbon analysis of this batch of samples yielded the organic carbon content. The inorganic carbon content was calculated by subtracting the organic from the total carbon content.

4.9.3 Plants - Carbon Isotope Analysis by IR-MS

Stable isotope analysis of the carbon contained in the plant samples was performed as described for the soil samples (Section 4.9.2), however after a different pre-treatment. Prior to the measurement, the plant samples were cut and broken into small pieces and freeze-dried for at least 24 hours using an Alpha 1-4 freeze drier (Christ) and a 12 Two Stage vacuum pump (Edwards). The plant samples were also transformed into sample powder using a vibratory disc mill (Section 4.9.1), but with mill run times of 10 minutes. Measurement quality is the same as for the soil sample analyses (Section 4.9.2).

4.10 Statistical Analyses

To investigate the nature of the different stalagmite proxy signals and especially the relationships between them not only in a qualitative but also in a quantitative way, different statistical methods were applied.

4.10.1 Spearman Rank Coefficients (ρ)

To analyse the association of the proxy signals contained within the stalagmites, Spearman rank coefficient (ρ) were calculated using the software Origin to construct correlation matrices. Spearman's ρ was favoured over Pearson's correlation coefficient because it is independent of outliers. In case of stalagmite VML22, correlation coefficients were calculated for the overall dataset, in case of stalagmite VSMS2 both for the overall dataset, as well as for its three growth periods separately. Values of one indicate maximum positive correlation between two data sets, values of minus one indicate maximum negative correlation, while values close to zero indicate that the two data sets are not correlated to one another (Schönwiese, 2013).

4.10.2 Autocorrelation Coefficients (ACC)

A critical aspect of time series is their inherent signal to noise ratio, as many natural signals show both regular cyclic components and stochastic noise (Fairchild et al., 2006). For reconstructing past climatic and environmental conditions, the time series used should exhibit a high signal to noise ratio for them to represent interpretable signals of past conditions.

Whether a palaeosignal is noisy or clear can be assessed with the help of autocorrelation coefficients (ACC) that indicate how consistent the variations within a give data set are. For this work, the lag-1 autocorrelation coefficients (Lag-1 ACC; Spearman's ρ) were calculated for each geochemical record from the stalagmites by duplicating each record, shifting it by one data point relative to the original record and by calculating Spearman's ρ for each pair of data sets consisting of the original and the shifted data set.

An inherently noisy signal yields ACC values close to zero, whereas a highly persistent signal yields ACC values near one (Lachniet, 2009). However, low ACC values can also indicate that a time series was sampled at an insufficient resolution (undersampling).

4.10.3 Frequency Analysis with REDFIT

The mechanisms that drive the variations observed in a given climatic or environmental signal may be determined by identifying cyclic behaviour within that signal. For instance, the diurnal cycle of near-surface air temperature can be attributed to the diurnal cycle of solar insolation at a specific site (especially in regions with a high temperature amplitude between day and night). Palaeoclimatic and palaeoenvironmental time series can be scanned for potential cyclic behaviour using frequency analysis which investigates at which frequency the variations observed in a given data set occur. Frequencies at which these variations occur often are visible as peaks in the resulting frequency spectrum. Based on those frequencies (or their inverse, the cycle curation, or periodicity), the underlying processes may be identified.

For this thesis, the frequency analysis of the geochemical records from the two stalagmites was performed with the program REDFIT (Schulz & Mudelsee, 2002) that is executed via a Windows command window. For the frequency analysis of the stable isotope data, the following program settings were used: nsim = 1000, mctest = F, rhopre = -99.0, ofac = 4.0, hifac = 1.0, n50 = 1 and iwin = 0. For the frequency analysis of the trace element data, the program settings were changed to ofac = 2.0 (stalagmite VML22) and 5.0 (stalagmite VSMS2) and to n50 = 5 as computer memory would have been insufficient using the same settings used for the analysis of the stable isotope data sets.

4.11 Site-specific Monitoring

4.11.1 Oxygen Isotopes in Rainwater

Rainwater samples for later analysis of oxgen isotopes were collected manually by members of the local communities of Ma Le and of Sang Ma Sao at the start of rainfall events occuring over approximately one entire year. Sample collection in Ma Le Commune was performed using a plastic funnel screwed to a plastic rainwater container (Figure 4.8). In this set-up, evaporation is reduced by the conical shape of the funnel and its small outlet (not shown). Sample collection in Sang Ma Sao Commune was conducted by a member of the local community using 5 mL brown glass bottle attached to a HOBO metal rainwater container (Figure 4.9) via a 3D-print-out.

4.11.2 Cave Climate and Stalactite Drip Rate

Inside of both Ma Le 2 and Sang Ma Sao Caves, cave climate parameters as well as drip rate at the stalactite corresponding to stalagmite VML22 and VSMS2, respectively, were analysed using the following instruments and loggers. Air flow velocities were measured using a hot bead anemometer (Testo 445). Temperature and relative humidity were logged five times per day, at intervals of 4 hours and 48 minutes, with Tinytag TGP-4500 (Gemini Loggers) loggers with an accuracy of ± 0.5°C at 8°C and ± 3.0% RH at 25°C. Additionally, relative humidity was measured with an Assmann aspiration psychrometer. Furthermore, over an eleven-day period, T, RH and cave air CO_2 concentrations were measured with a CM-0018 logger (CO2Meter) inside Ma Le 2 Cave. Drip rate at the dripsites of stalagmites VML22 and VSMS2 was logged at 30-minute-intervals with a Stalagmate Mark 3 drip rate logger (TGC-0011, Driptych; Mattey & Collister, 2008).

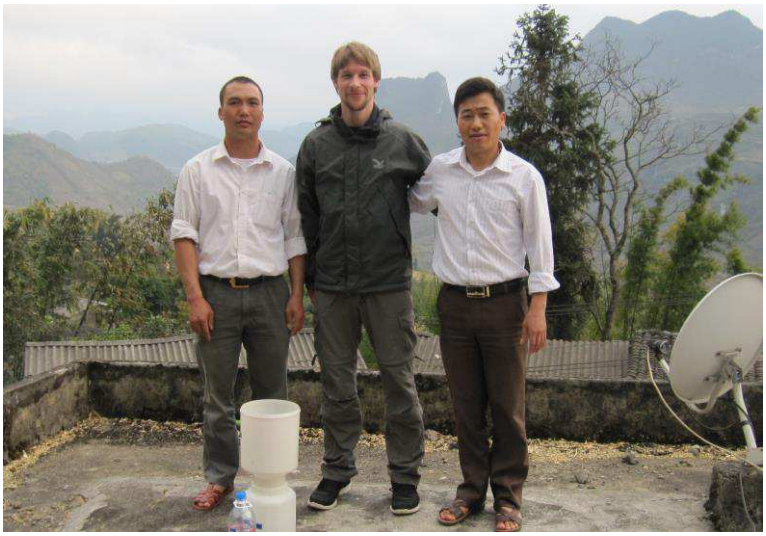

Figure 4.8: Rainwater container (white) used for rainwater sampling in the community of Ma Le. Rainwater collection was performed in cooperation with the local community (mayor of Ma Le Commune on the right; co-worker of Ma Le Commune on the left).

Figure 4.9: HOBO rainwater container used for rainwater sampling in the community of Sang Ma Sao. Rainwater collection was performed by a member of the local community.

5 Results

5.1 Radiometric Dating and Age Models

5.1.1 Stalagmite VML22

The age model for stalagmite VML22 as constructed with the algorithm *StalAge* based on the available U/Th dating points is shown in Figure 5.1. All U/Th dating results are summarised in Table 5.1.

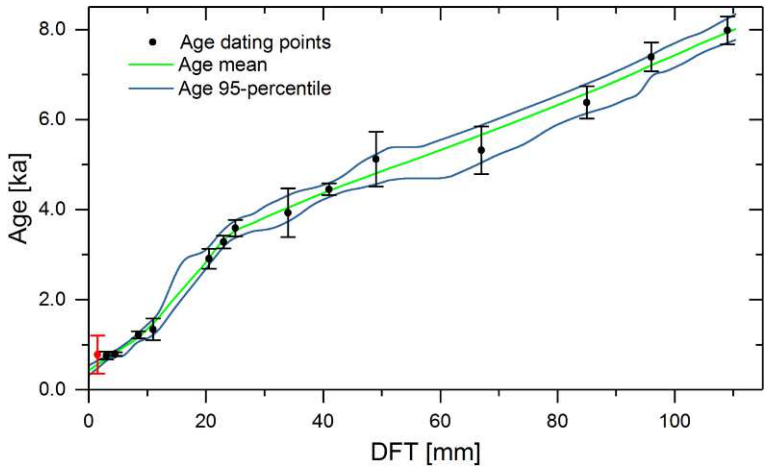

Figure 5.1: The age model for stalagmite VML22. The uppermost dating point (red) was omitted from the age model construction due to its large error resulting from high concentrations of detrital ^{232}Th.

According to this age model, stalagmite VML22 has ceased growing about 430 years BP (before present; present = 2015 A.D.) with the 95% confidence interval of the model output ranging from 540 to 320 years BP. Although not used for the age model construction itself, the uppermost obtainable dating point at DFT 1.5 mm confirms that stalagmite growth has indeed not continued up to the present. For two samples (DFT 1 mm and 18 mm), age determination was not possible due to insufficient chemical yields (Table 5.1). For the base of stalagmite VML22 (DFT 107 mm), the age model yields an age of 7,830 years (95% confidence interval: 8,100 to 7,610 years BP). Stalagmite VML22 does not feature any unambiguous indications of hiatuses, be it in the age model or in the fabrics (Section 5.4.1) and seem to were growing continuously.

Overall, the age model of stalagmite VML22 is quite precise with errors ranging from 40 years to 610 years, with an average of 270 years and a median of 230 years (n = 14). With an average of 140 years (n = 8), especially the Neptune Plus ages are precise.

Table 5.1: Analytical results from U/Th dating of stalagmite VML22. All errors are given as absolute values. Results with grey shading were obtained from the iCAP-Q ICP-MS measurements, all other samples were analysed with the Neptune Plus MC-ICP-MS. The date at DFT 1.5 mm (red) was omitted from the age model construction due to its high error resulting from high concentrations of detrital ^{232}Th.

DFT [mm]	Age_{corr} [ka]	Error [ka]	Age_{uncorr} [ka]	Error [ka]	$\delta^{234}U_{init}$ [‰]	Error [‰]	^{238}U [ng/g]	Error [ng/g]	^{232}Th [ng/g]	Error [ng/g]	$^{230}Th/^{238}U$ [-]	Error [-]	$^{230}Th/^{232}Th$ [-]	Error [-]	$\delta^{234}U_{corr}$ [‰]	Error 2σ [‰]
1	no age determination, low crop						90.94	0.17	1.184	0.021	0.023	0.011	5.4	2.5	651.3	8.7
1.5	0.78	0.42	1.62	0.05	636.2	8.4	114.91	0.02	5.492	0.026	0.024	0.0063	1.5	0	634.8	8.4
3	**0.76**	**0.09**	0.93	0.02	614.2	3.5	128.05	0.01	1.224	0.004	0.0137	0.0013	4.4	0.1	612.9	3.5
4.5	**0.79**	**0.04**	0.85	0.02	623.5	3.5	125.42	0.01	0.391	0.001	0.0125	0.0005	12.3	0.3	622.1	3.5
8.5	**1.22**	**0.08**	1.37	0.03	634	6.1	84.88	0.01	0.863	0.004	0.0203	0.0012	7.7	0.2	631.8	6.1
11	**1.34**	**0.24**	1.81	0.06	638.8	4.4	104.37	0.02	2.758	0.033	0.0268	0.0036	3.1	0.1	636.4	4.4
18	no age determination, low crop						112.18	0.31	2.672	0.053	0.059	0.011	7.7	1.3	608.5	9.4
20.5	**2.91**	**0.22**	3.32	0.09	658.6	5	106.16	0.03	2.548	0.034	0.0495	0.0033	6.3	0.2	653.3	4.9
23	**3.28**	**0.14**	3.54	0.07	643.5	3.4	101.26	0.02	1.484	0.016	0.0522	0.0021	11	0.2	637.6	3.3
25	**3.59**	**0.18**	3.94	0.07	639.3	8.6	98.16	0.03	1.931	0.011	0.0579	0.0026	9	0.1	632.8	8.5
34	**3.93**	**0.54**	4.05	0.55	659.8	24.8	88.68	0.16	0.6109	0.0075	0.0602	0.0081	26.9	3.6	652.5	7.9
41	**4.45**	**0.13**	4.71	0.04	625.6	4	97.26	0.01	1.459	0.004	0.0684	0.0019	14	0.1	617.8	4
49	**5.12**	**0.61**	5.49	0.59	641.1	10.6	90.29	0.18	1.89	0.019	0.0801	0.0088	11.8	1.2	631.9	10.4
67	**5.32**	**0.53**	5.4	0.51	542.5	9.8	100.13	0.2	0.4183	0.0047	0.0742	0.0071	55	5.2	534.4	9.6
85	**6.38**	**0.36**	6.46	0.36	560.4	21.8	90.71	0.16	0.4335	0.0037	0.0894	0.0048	57.9	3.1	550.4	8.6
96	**7.39**	**0.32**	7.45	0.31	662.8	7.5	103.06	0.19	0.3387	0.0027	0.1092	0.0044	102.8	4.2	649	7.3
109	**7.98**	**0.31**	8.05	0.31	644.2	7.6	103.45	0.14	0.4315	0.0025	0.1163	0.0043	86.3	3.1	629.8	7.5

From the age model output, the growth rate of stalagmite VML22 has been determined by linear interpolation between adjacent values (Figure 5.2), calculating the quotient of the respective depth and time increments. Computed values range from 5.7 µm/a (µm/year) to 23 µm/a, with an average of 17 µm/a and a median of 18 µm/a. With the span of calculated growth rates amounting to only 17.3 µm/a, the growth rate of stalagmite VML22 can be described as relatively constant as a whole.

Figure 5.2 shows the VML22 growth rate plotted in the time domain. During the first 4,000 years, VML22 has been growing at a fairly constant rate of 19 µm/a on average (median also 19 µm/a), ranging from 16 µm/a to 23 µm/a. At about 3.7 ka BP, however, the growth rate decreased noticeably for some 650 years to reach a new baseline state at growth rates averaging approximately 6.7 µm/a which lasted from 3.0 ka to 1.4 ka BP. Between 1.4 ka and 0.8 ka BP, VML22 growth rate features a local maximum centered at 1.0 ka BP with values of 13 µm/a. Until the end of the growth period at 0.43 ka BP, growth rates gradually declined to values of 11 µm/a.

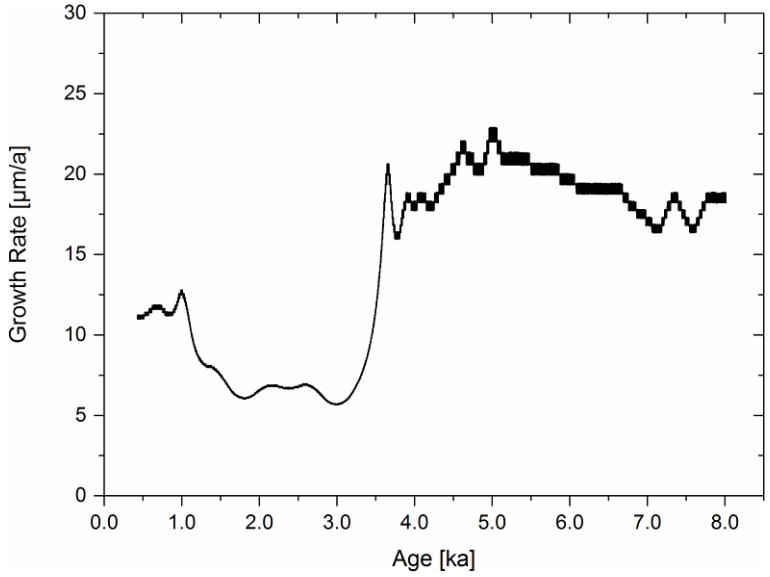

Figure 5.2: Growth rate of stalagmite VML22 plotted in the time domain.

5.1.2 Stalagmite VSMS2

The age model for stalagmite VSMS2 was constructed with the algorithm *StalAge* based on the available U/Th dating points is shown in Figure 5.3. All U/Th dating results are summarised in Table 5.2.

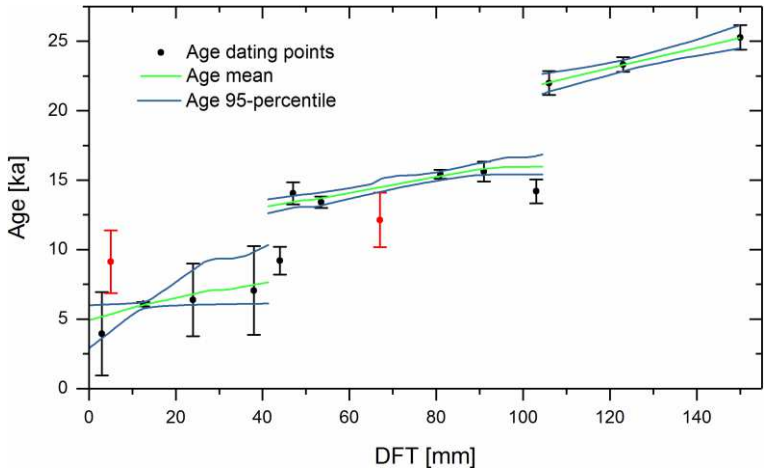

Figure 5.3: The age model for stalagmite VSMS2. The dating points at DFT 5 mm and 67 mm (red) were omitted from the age model construction as they are not in stratigraphic order and exhibit large errors.

According to this age model, stalagmite VSMS2 has ceased growing about 4,9 ka BP with the 95% confidence interval of the model output ranging from 6.0 ka to 2.9 ka BP. Two dating points (DFT 5 mm and 67 mm) were omitted from the age model construction as they are not in stratigraphic order and feature great errors resulting from high concentrations of detrital ^{232}Th. For the base of stalagmite VSMS2 (DFT 150 mm), the age model yields an age of 25.2 ka BP (95% confidence interval: 26.1 ka to 24.5 ka BP).

However, stalagmite VSMS2 has not been growing continuously. The age model suggests two hiatuses, with the first hiatus being centered around DFT 104.4 mm ranging from 21.9 ka to 16.0 ka BP (spanning about 5.9 ka) and the second hiatus being centered around DFT 41.3 mm ranging from 13.1 ka to 7.7 ka BP (spanning about 5.4 ka). The locations of both hiatuses are confirmed by the microscopic analysis of the stalagmite fabrics that yielded increased porosity and darker colour tones at these two depths (Figure 4.3 and Figure 5.31).

Contrarily to stalagmite VML22, the age model of stalagmite VSMS2 is quite imprecise overall, as expected from the high contents of detrital material already evident from the macroscopic brownish colour impression. Dating errors range from 0.16 ka to 3.2 ka, with an average of 1.2 ka and a median of 0.85 ka (n = 13). The date with the lowest error by far (160 years) corresponds to the sample from DFT 12.5 mm located within the section spanning DFT 4 mm to 18 mm (Figure 4.3) that is virtually free of detrital contamination.

Table 5.2: Analytical results from U/Th dating of stalagmite VSMS2. All errors are given as absolute values. All samples were analysed with the Neptune Plus MC-ICP-MS. The dates at DFT 5 mm and 67 mm (red) were omitted from the age model construction as they are not in stratigraphic order.

DFT [mm]	Age_{corr} [ka]	Error [ka]	Age_{uncorr} [ka]	Error [ka]	$\delta^{234}U_{init}$ [‰]	Error [‰]	^{238}U [ng/g]	Error [ng/g]	^{232}Th [ng/g]	Error [ng/g]	$^{230}Th/^{238}U$ [-]	Error [-]	$^{230}Th/^{232}Th$ [-]	Error [-]	$\delta^{234}U_{corr}$ [‰]	Error [‰]
3	**3.95**	**3.00**	10.26	0.11	1860.3	160.1	131.85	0.03	73.192	0.635	0.2326	0.0770	1.3	0.0	1839.6	157.5
5	**9.12**	**2.26**	14.08	0.13	1648.2	107.1	93.67	0.01	39.630	0.075	0.3010	0.0493	2.2	0.0	1641.4	103.8
12.5	**6.08**	**0.16**	6.27	0.14	1533.7	7.7	18.58	0.01	0.311	0.02	0.1404	0.0036	25.7	0.6	1507.5	7.5
24	**6.39**	**2.62**	12.23	0.17	2075.8	178.3	201.09	0.05	110.86	1.056	0.2937	0.0702	1.6	0.0	2038.7	174.5
38	**7.06**	**3.19**	14.07	0.19	2091.3	217.6	137.44	0.04	89.257	0.852	0.3303	0.0834	1.6	0.0	2050.5	212.5
44	**9.20**	**1.00**	11.12	0.09	1558.9	5.9	92.65	0.02	16.943	0.080	0.2463	0.0020	4.1	0.0	1518.9	3.8
47	**14.05**	**0.80**	15.59	0.13	1646.2	5.6	90.06	0.02	13.629	0.062	0.3482	0.0027	7.0	0.1	1582.1	4.0
53.3	**13.40**	**0.41**	14.23	0.23	1687.1	18.3	129.89	0.02	9.929	0.122	0.3205	0.0087	13.0	0.3	1624.4	17.5
67	**12.14**	**1.96**	16.83	0.29	1895.6	123.4	140.45	0.03	60.384	0.807	0.3802	0.0450	2.7	0.1	1831.7	118.8
81	**15.42**	**0.32**	15.99	0.22	1737.5	13.4	140.42	0.02	7.550	0.095	0.3646	0.0068	21.0	0.4	1663.4	12.8
91	**15.62**	**0.71**	17.30	0.27	1885.9	43.2	127.99	0.02	20.837	0.287	0.4057	0.0152	7.7	0.2	1804.4	41.1
103	**14.20**	**0.86**	15.87	0.24	1831.5	5.5	89.06	0.03	15.617	0.0.4	0.3785	0.0052	6.5	0.1	1759.5	3.2
106	**21.99**	**0.85**	24.06	0.41	1943.2	55.4	95.60	0.02	19.389	0.270	0.5510	0.0161	8.2	0.2	1826.1	51.8
123	**23.32**	**0.53**	24.32	0.39	1908.6	26.4	122.04	0.02	12.131	0.1758	0.5589	0.0104	17.1	0.4	1786.9	24.6
150	**25.27**	**0.88**	27.20	0.53	1964.3	54.5	79.66	0.15	15.271	0.088	0.618	0.015	9.92	0.18	1828.9	50.5

Based on the age model output, the growth rate of stalagmite VSMS2 (Figure 5.4) ranges from 8.9 µm/a to 160 µm/a. Growth rates exceeding this maximum value represent artefacts of the StalAge algorithm where the age model output is a horizontal line with the calculated ages remaining constant despite of changing depth within the stalagmite. These values were therefore omitted from Figure 5.4. The overall average growth rate is 15.9 µm/a.

During the first period of growth from 25.3 ka to 21.9 ka BP, VSMS2 has been growing at a fairly constant rate of 13.3 µm/a on average. During the second period of growth from 16.0 ka to 13.1 ka BP, growth rate was higher with an average of 20.6 µm/a and growth rate peaks at 53.3 µm/a at 13.6 ka BP. During the the third period of growth from 7.7 ka to 4.9 ka BP, growth rate was lower again with an average of 14.2 µm/a. At 7.2 ka BP calculated growth rate peaks at 160 µm/a. Growth rate features a weak negative trend during the third growth period of VSMS2. In general, as sudden and relatively short-term peaks in growth rate are likely to represent artefacts of the StalAge algorithm due to 1) an insufficient number of dating points and/or 2) insufficient dating precision, these peaks are to be interpreted with caution. More gradual variations in medium- to long-term averages of growth rate can be considered more reliable.

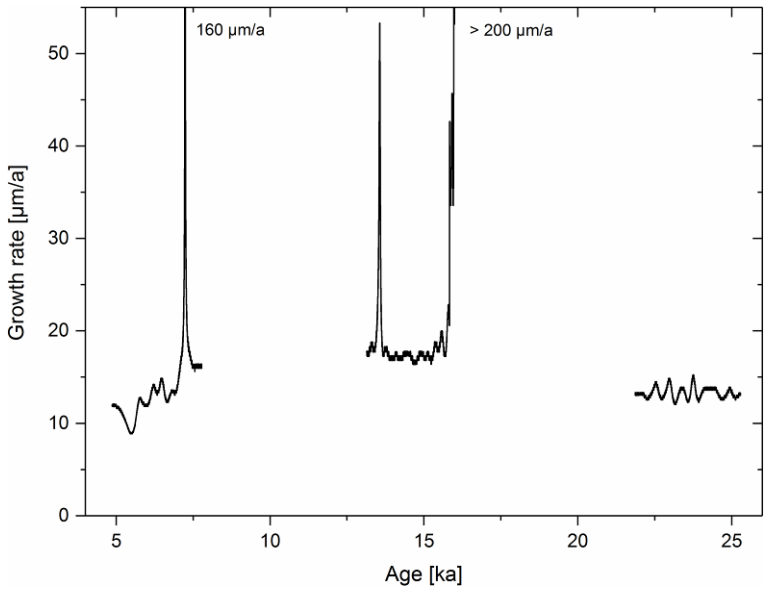

Figure 5.4: Growth rate of stalagmite VSMS2 plotted in the time domain.

5.2 Stable Isotopes in Stalagmites

5.2.1 Stalagmite VML22

The results of the stable isotope analysis of stalagmite VML22 are shown in Figure 5.5, both in the depth and the time domain. According to the age model (Section 5.1), the spatial resolution of the isotope data of 194 µm (Section 4.4) translates into a nominal temporal resolution ranging from 8.5 a to 34.3 a, depending on growth rate, with an average of 13.3 a and a median of 10.6 a. As multiple data points are needed to resolve any palaeoenvironmental signal of a given periodicity to avoid aliasing and smoothing (Fairchild et al., 2006), the actual temporal resolution of the VML22 stable isotope data can be classified as multi-decadal. Therefore any palaeoenvironmental signal with a less than multi-decadal periodicity will not be resolved by the stable isotope data of stalagmite VML22.

Values of VML22 $\delta^{18}O$ (n = 555) range from -10.91 ‰ to -8.20 ‰ (amplitude: 2.71 ‰), with the average being -9.31 ‰ and the median being -9.30 ‰, whereas $\delta^{13}C$ values (n = 555) range from -8.48 ‰ to -1.29 ‰ (amplitude: 7.19 ‰), with an average of -3.72 ‰ and a median of -3.62 ‰. Both data curves are highly similar to each another as a whole, as evident from high positive correlation coefficients (Section 5.6.2.1) and both feature a clear overall trend towards increased values with decreasing age. This overall trend is superimposed by higher frequency variations on multi-decadal to centennial timescales and seems to be reversed from about 1.0 ka BP onwards in the case of $\delta^{18}O$ (Figure 5.5 bottom). The behaviour of both isotope signals is also highly similar on centennial timescales, as illustrated by the 20-point smoothed curves shown in Figure 5.6.

Most of the positive and negative anomalies relative to the long-term increasing trend in both proxy signals are synchronous or quasi-synchronous: For $\delta^{18}O$, the most marked negative excursions occur at 7.5, 4.5, 3.1 and 2.7 ka BP, as well as from 1.0 ka BP onwards with local minima at 0.9, 0.8, 0.6 ka BP and at the point of growth stop at 0.43 ka BP. The two most important positive excursions are centered at 7.6 and 5.1 ka BP. Several other peaks can be found at 4.0, 3.8, 3.7, 3.4 and 2.5 ka BP. The three most pronounced negative excursions in $\delta^{13}C$ values occur at 7.5, 3.3 and 0.8 ka BP, with the last trough being the broadest, spanning the period from 1.0 to 0.7 ka BP. The trough at 3.3 ka BP is quasi-synchronous with the trough in $\delta^{18}O$ values at 3.1 ka BP. Further troughs are present at 7.5, 7.3, 6.4, 5.8, 5.5 and 3.7 ka BP. Positive excursions in $\delta^{13}C$ values can be found at 7.7 and 5.2 ka BP as for $\delta^{18}O$. Further peaks occur at 6.8, 6.7, 4.0, and 2.5 ka BP, with lower peaks at 3.4, 2.1 and 1.3 ka BP.

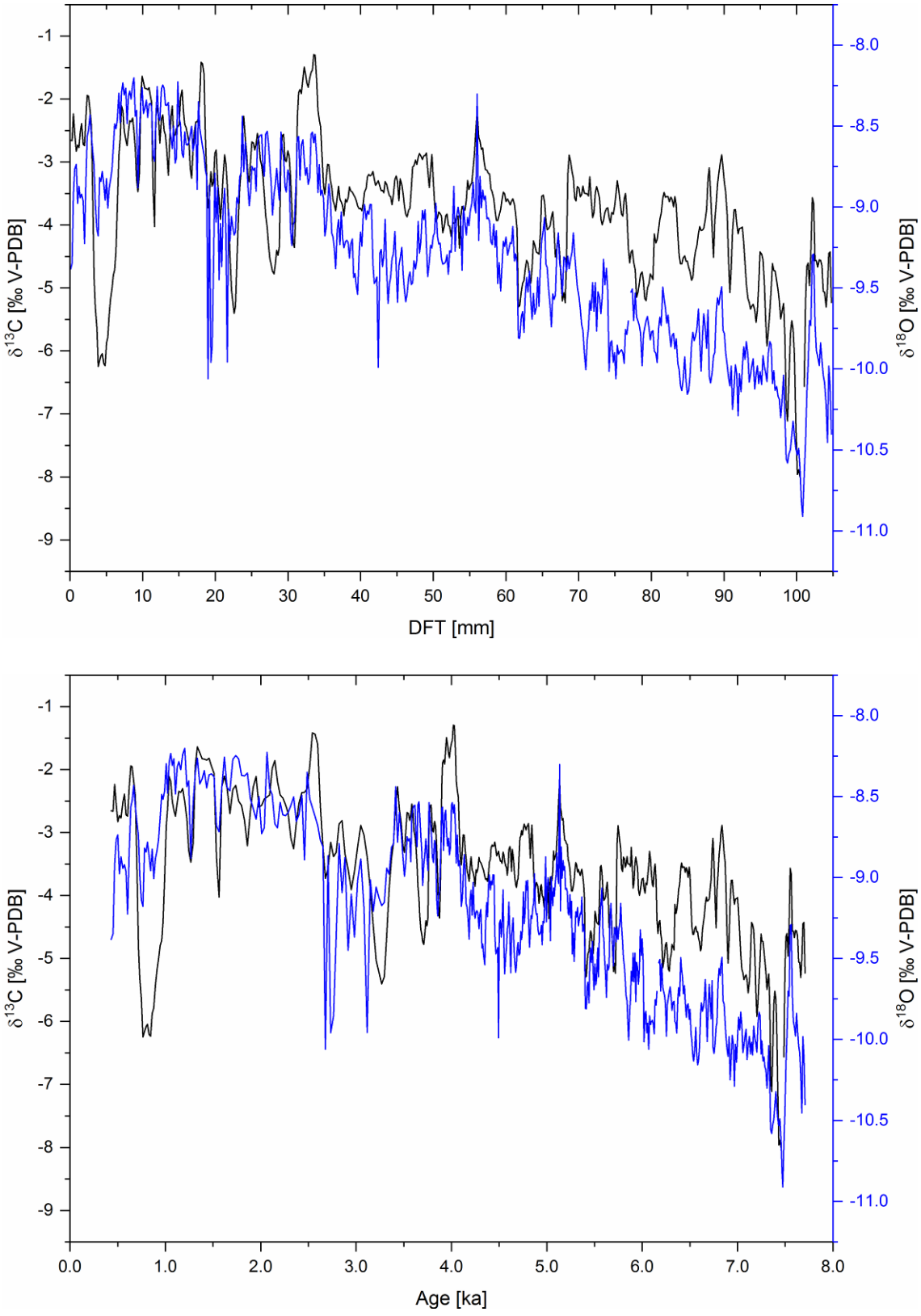

Figure 5.5: Stable isotopes of oxygen ($\delta^{18}O$) and carbon ($\delta^{13}C$) of stalagmite VML22 plotted in the depth domain (top) and the time domain (bottom) in ‰ relative to the V-PDB standard.

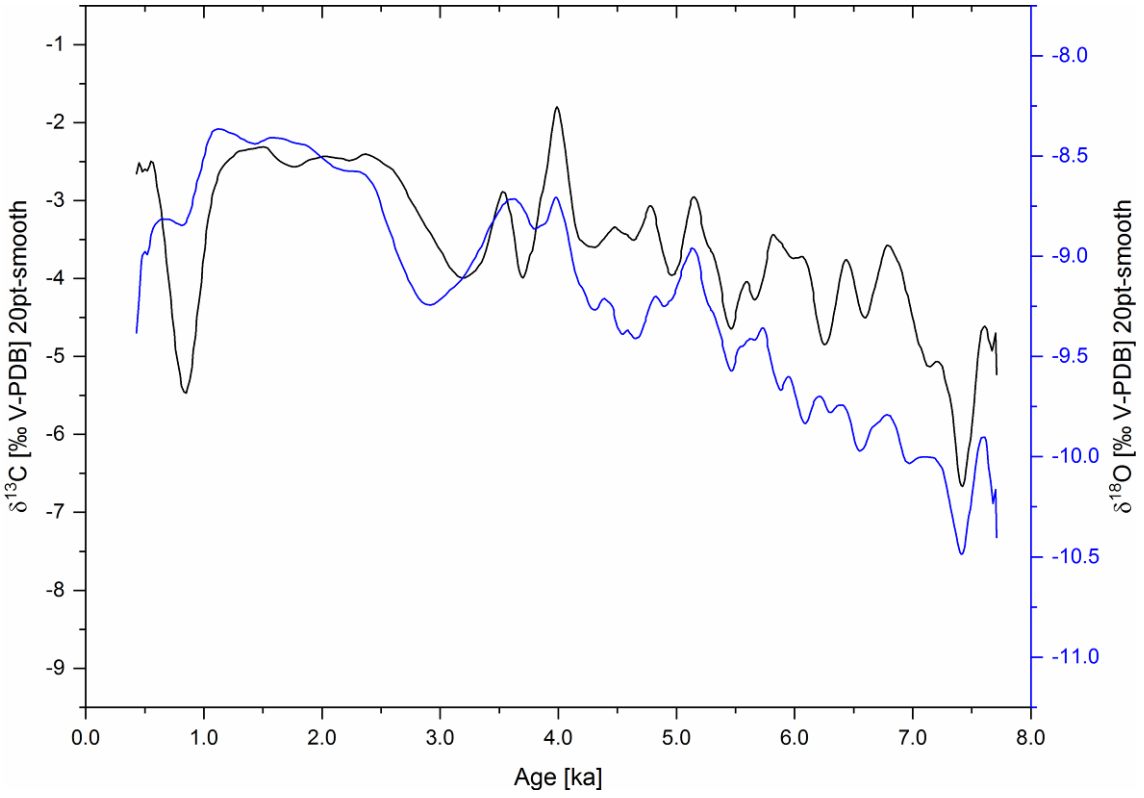

Figure 5.6: Values of $\delta^{18}O$ and $\delta^{13}C$ of stalagmite VML22 plotted as 20-point smoothed curves (weighted Adjacent Averaging) illustrating the similar behaviour of both stable isotope signals on centennial timescales.

On timescales of multiple decades and centuries, the plots of $\delta^{18}O$ and $\delta^{13}C$ slightly differ from one another. All in all, $\delta^{13}C$ values vary more widely with amplitudes between local minima and maxima of up to 4 ‰ compared to $\delta^{18}O$ values varying at maximum amplitudes closer to 1.5 ‰. Relative to their respective maximum amplitude of variation, however, the $\delta^{18}O$ record of stalagmite VML22 appears to be somewhat more erratic and less conservative than the $\delta^{13}C$ record, for example around 3.0 ka BP. This suggests either that the $\delta^{18}O$ signal is more sensitive to short-term changes in its driving forces than the $\delta^{13}C$ signal, or that the $\delta^{13}C$ signal is slower to respond to such changes.

One prominent example for these differences in behaviour is the steeper increase of $\delta^{13}C$ values compared to $\delta^{18}O$ from about 7.6 ka to 5.8 ka BP. After a period during which both signals match closely in behaviour from approximately 5.8 ka to 4.2 ka BP, both increases and decreases in $\delta^{13}C$ values from 4.2 ka to 3.3 ka BP are more pronounced than those of $\delta^{18}O$ values, albeit in good temporal agreement. From 3.3 ka to 1.0 ka BP, the two proxy signals again evolve very similarly, except for the period of high-frequency high-amplitude variability in the $\delta^{18}O$ values around 3.0 ka BP already mentioned above.

The very pronounced trough in $\delta^{13}C$ values (4 ‰ amplitude) spanning the period from 1.0 ka to 0.7 ka BP, centered at 0.8 ka BP, corresponds to a synchronous trough in $\delta^{18}O$ values, although the latter is much less prominent. This trough in $\delta^{18}O$ values, however, is superimposed by a decreasing trend from 1.0 ka BP until stalagmite VML22 stopped growing, which is not evident from the $\delta^{13}C$ data set.

5.2.2 Stalagmite VSMS2

The results of the stable isotope analysis of stalagmite VSMS2 are shown in Figure 5.7, both in the depth and the time domain. According to the age model (Section 5.1), the spatial resolution of the isotope data of 199 µm (Section 4.4) translates into a nominal temporal resolution ranging from 1.2 a during the peak growth rate of 160 µm/a to 22.5 a, depending on growth rate, with an average and a median of 12.5 a. Therefore, the actual temporal resolution of the VSMS2 stable isotope data can also be classified as multi-decadal,thus impeding the resolution of any palaeoenvironmental signal with a less than multi-decadal periodicity.

Values of VSMS2 $\delta^{18}O$ (n = 750) range from -12.28 ‰ to -8.46 ‰ (amplitude: 3.82 ‰), with the average being -8.89 ‰ and the median being -8.46 ‰, whereas $\delta^{13}C$ values (n = 750) range from -12.08 ‰ to -9.80 ‰ (amplitude: 2.28 ‰), with an average of -10.09 ‰ and a median of -9.80 ‰. As the behaviour of both stable isotope signals differs between the three growth periods separated by the two hiatuses, the isotope data corresponding to the three growth periods are illustrated in detail in Figure 5.8 and Figure 5.9 and described separately in the following.

During the first growth period (Figure 5.8 top) of stalagmite VSMS2 from 25.2 ka to 21.7 ka BP, $\delta^{18}O$ values (n = 225) range from -8.71 ‰ to -7.50 ‰ (amplitude: 1.21 ‰) with an average of -8.23 ‰ and a median of -8.28 ‰, while $\delta^{13}C$ values range from -10.00 ‰ to -8.60 ‰ (amplitude: 1.40 ‰), with an average of -9.48 ‰ and a median of -9.54 ‰. Neither of the two stable isotope signals features a robust long-term trend. While the $\delta^{13}C$ regression line has a slightly steeper slope (0.18 ‰), the low values of adjusted R^2 show that the behaviour of the isotope signals cannot be well described by linear trends.

Oxygen isotope values are relatively low (about -8.6 ‰) during the first 200 years of the record, but increase rapidly from -8.7 ‰ to the maximum value of the entire growth period (-7.5 ‰) within only 100 years. With an amplitude of 1.2 ‰, this is the largest change in this growth period. From this maximum value, $\delta^{18}O$ values decline to -8.7 ‰ between 24.9 ka and 23.5 ka BP, but erratically with high-frequency variation with amplitudes between 0.1 and 0.5 ‰. Values then rise to a local maximum of -7.8 ‰ at 23.1 ka BP and fall to a local minimum of -8.6 ‰ at 22.8 ka BP with further local maxima at 22.7, 22.3 and 21.9 ka BP separated by local minima at 22.6 and 22.0 ka BP.

Carbon isotope values behave inversely to the $\delta^{18}O$ values during parts of the first growth period with correlation coefficients (Section 5.6.1.2) indicating a weak negative correlation overall.

During the first 200 years of the record, $\delta^{13}C$ values are relatively high (about -8.8 ‰) and then decrease rapidly to a first local minimum of -9.7 ‰ at 24.8 ka. Until a local minimum of -10 ‰ is reached at 23.7 ka BP (preceding the local minimum in $\delta^{18}O$ by about 200 years), $\delta^{13}C$ values feature several local maxima that are synchronous with $\delta^{18}O$ maxima, e.g. at 24.7 and 24.3 ka BP, but also a local maximum at 24.0 ka BP that slightly lags behind the corresponding $\delta^{18}O$ maximum by about 50 years. While the subsequent local maximum at 22.9 ka BP is synchronous with the corresponding $\delta^{18}O$ minimum, the maximum at 23.3 ka BP precedes the $\delta^{18}O$ maximum by about 200 years. Between 22.9 ka and 22.6 ka BP, $\delta^{13}C$ values reach another maximum with -9.0 ‰ at 22.6 ka BP, contrasting the $\delta^{18}O$ minimum at that time. Until the end of the record, $\delta^{13}C$ values then decrease to -10 ‰ with local maxima/minima in synchronicity with $\delta^{18}O$ maxima/minima.

During the second growth period (Figure 5.8 bottom) of stalagmite VSMS2 from 16.0 ka to 13.2 ka BP, $\delta^{18}O$ values (n = 314) range from -10.37 ‰ to -6.13 ‰ (amplitude: 4.24 ‰) with an average of -7.81 ‰ and a median of -7.23 ‰, while $\delta^{13}C$ values range from -10.25 ‰ to -8.81 ‰ (amplitude: 1.44 ‰), with an average of -9.71 ‰ and a median of -9.78 ‰. While $\delta^{13}C$ values do exhibit only a weak long-term trend (regression slope: 0.12 ‰) towards lower values which does not well describe the signal's behaviour (adjusted R^2: 0.14), $\delta^{18}O$ values strongly (slope: 1.13 ‰) and clearly (adjusted R^2: 0.76) trend towards lower values. Despite this discrepancy in behaviour, both isotope signals are positively correlated to each other with an overalm Spearman's ρ of 0.60.

Oxygen isotope values start at an intermediate level at -8.4 ‰ and rapidly increase to values between -7.4 ‰ and -6.1 ‰ during the period from 16.0 to 14.4 ka BP. Until the end of this growth period at 13.2 ka BP, $\delta^{18}O$ values decrease from -7.0 ‰ to a minimum value of -10.4 ‰ (by 3.4 ‰) after a local maximum at 13.6 ka BP. In addition to these long-term patterns of change, $\delta^{18}O$ values exhibit high-frequency variability on multi-decadal and centennial timescales with amplitudes ranging from 0.1 ‰ to 1.0 ‰.

Carbon isotope values behave very similarly to oxygen isotope values on multi-decadal and centennial timescales which causes the overall positive correlation (Spearman's ρ of 0.60). However, on longer timescales, $\delta^{13}C$ values behave differently, most prominently by remaining quasi-constant at about -10 ‰ over the entire growth period while $\delta^{18}O$ values exhibit the marked long-term changes described above. The most noteable feature is a marked positive anomaly relative to its long-term baseline spanning a 600 year-period from 14.9 to 14.3 ka BP with a peak $\delta^{13}C$ value of -8.8 ‰, centered at 14.7 ka BP. If this rise in $\delta^{13}C$ values at the beginning of this period corresponds to the distinct increase in $\delta^{18}O$ values at 16.0 ka BP, it lags the $\delta^{18}O$ increase by 1,100 years. It should be noted, however, that $\delta^{13}C$ values do exhibit a peak reaching -9.2 ‰ at 16.0 ka BP that is masked by the $\delta^{18}O$ graph in Figure 5.8 (bottom). Both peaks are represented by a vertical line as the age model erroneously yields an infinite growth rate for this section of the stalagmite, as previously described (Section 5.1.2; Figure 5.3).

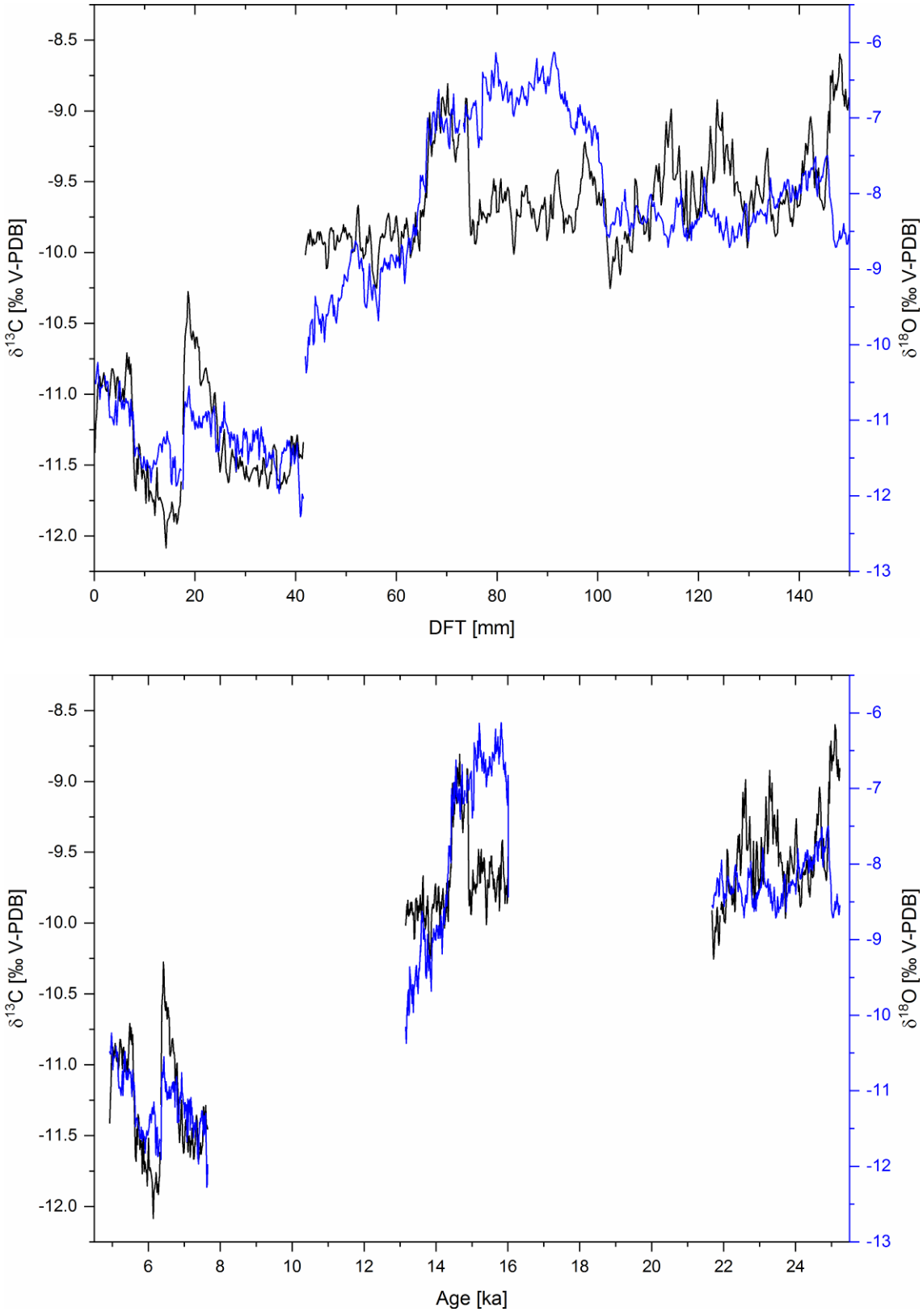

Figure 5.7: Stable isotopes of oxygen ($\delta^{18}O$) and carbon ($\delta^{13}C$) of stalagmite VSMS2 plotted in the depth domain (top) and the time domain (bottom) in ‰ relative to the V-PDB standard.

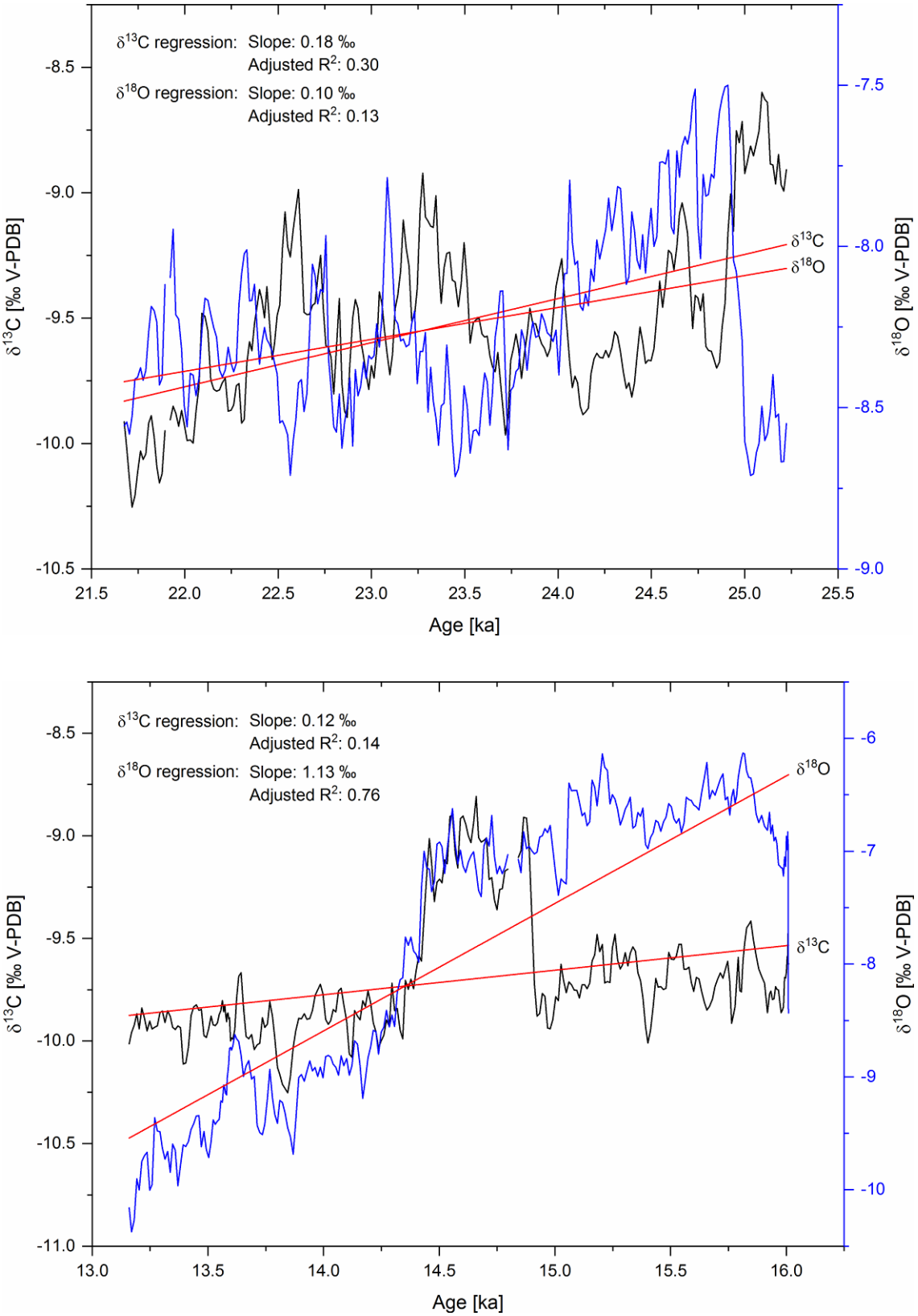

Figure 5.8: Values of $\delta^{18}O$ and $\delta^{13}C$ of stalagmite VSMS2 for the first (top) and second (bottom) growth period including linear regression (red lines).

During the last growth period (Figure 5.9) of stalagmite VSMS2 from 7.7 ka to 4.9 ka BP, $\delta^{18}O$ values (n = 207) range from -12.3 ‰ to -10.2 ‰ (amplitude: 2.0 ‰) with an average of -11.2 ‰ and a median of -11.3 ‰, while $\delta^{13}C$ values range from -12.1 ‰ to -10.3 ‰ (amplitude: 2.0 ‰), with an average of -11.3 ‰ and a median of -11.5 ‰. Although both $\delta^{18}O$ and $\delta^{13}C$ values exhibit a weak long-term trend towards increased values, with regression slopes of -0.25 ‰ and -0.16 ‰, respectively, their behaviour cannot be well described with linear trend lines (adjusted R^2: 0.27 and 0.1). As indicated by a Spearman's rank coefficient ρ of 0.70 (Table 5.12 in Section 5.6.2.2), both stable isotope signals are strongly positively correlated.

Oxygen isotope values are at their overall minimum of -12.3 ‰ at 7.6 ka BP and increase over the subsequent 1,200 years by almost 2 ‰ to a local maximum of -10.6 ‰ at 6.4 ka BP with additional high-frequency variability with amplitudes between 0.1 ‰ and 0.5 ‰ . From that maximum, $\delta^{18}O$ values drop rapidly to a local minimum of -11.9 ‰ at 6.3 ka BP over only 100 years. After reaching a local maximum at 6.1 ka BP, $\delta^{18}O$ values increase from a local minimum of -11.8 ‰ at 5.9 ka BP to their overall maximum value of -10.2 ‰ at the end of this growth period at 4.9 ka BP after another local maximum of -10.5 ‰ at 5.4 ka BP.

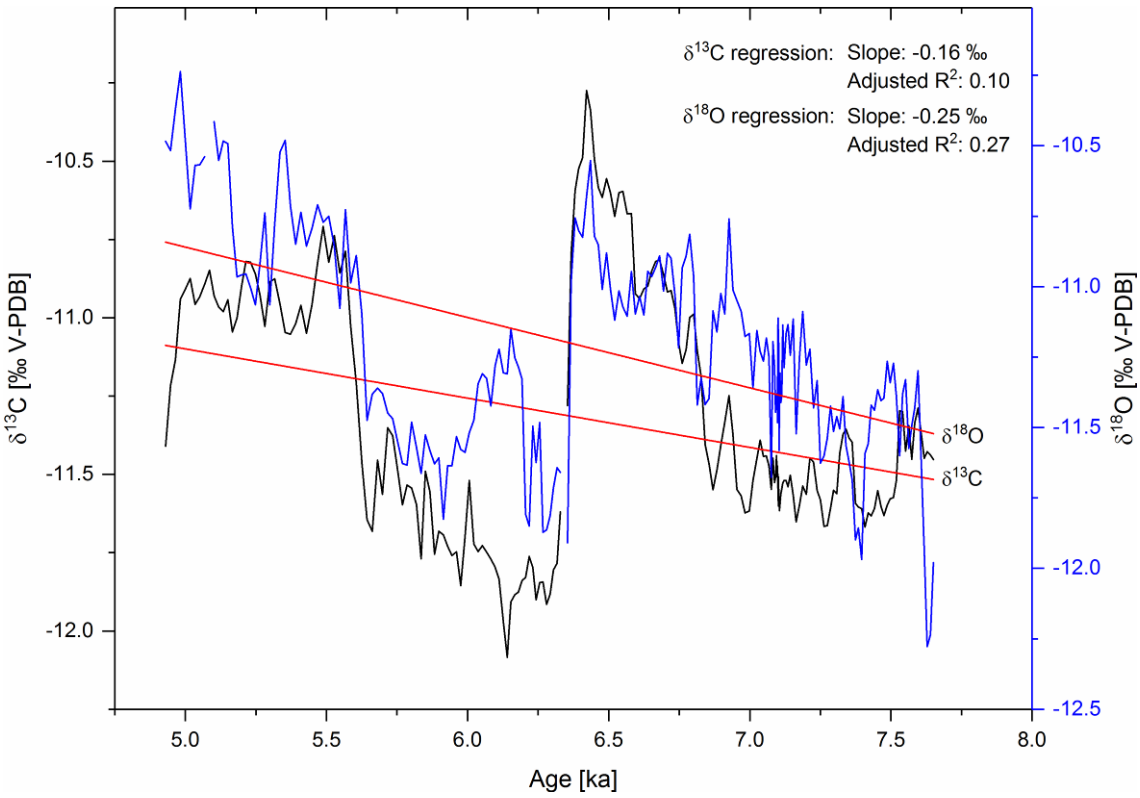

Figure 5.9: Values of $\delta^{18}O$ and $\delta^{13}C$ of stalagmite VSMS2 for the last of its three growth periods including linear regression (red line).

Carbon isotope values generally behave very similarly to oxygen isotope values on all timescales. While $\delta^{13}C$ values vary between -11.7 ‰ and -11.2 ‰ during the first 800 years of the last growth period instead of exhibiting a marked minimum as in the $\delta^{18}O$ values, they increase to their overall maximum of -10.3 ‰ at 6.4 ka BP. From that maximum, $\delta^{13}C$ values also drop rapidly by almost 2 ‰ to their overall minimum of -12.1 ‰, but some 250 years later than the $\delta^{18}O$ values, at 6.1 ka BP, which leads to the coincidence of a $\delta^{13}C$ minimum with a local $\delta^{18}O$ maximum at that time. From this overall minimum, $\delta^{13}C$ values increase again to reach a secondary local maximum of -10,7 ‰ at 5.5 ka BP with an especially steep increase from 5.7 ka BP on. Until 5.0 ka BP, $\delta^{13}C$ values vary between -11.1 ‰ and -10.7 ‰ to decrease to -11.4 ‰ at the end of the record at 4.9 ka BP.

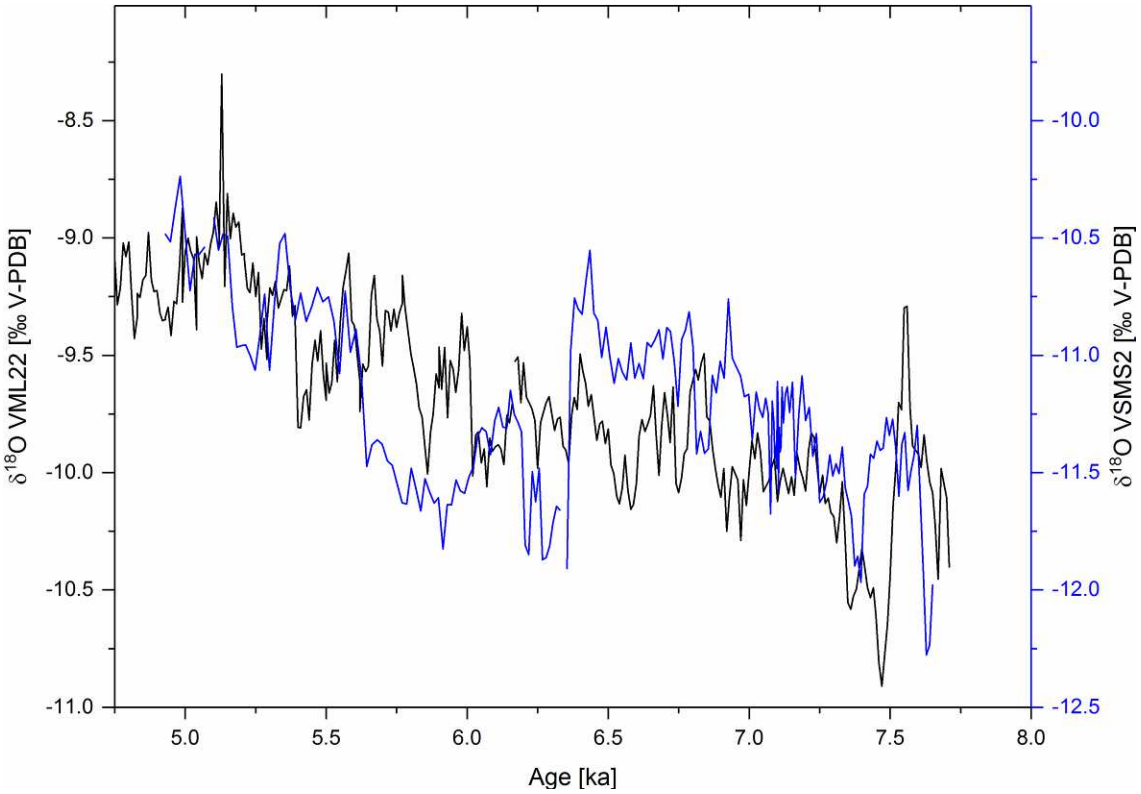

Figure 5.10: Oxygen isotope values from stalagmites VML22 and VSMS2 during the last growth period of VSMS2.

A comparison of the $\delta^{18}O$ values from stalagmite VSMS2 with those of stalagmite VML22 (Figure 5.10) for the period of overlap between the time series of the two stalagmites shows that both $\delta^{18}O$ data sets are in broad agreement. However, not all patterns are found in both data sets. For instance, the two peaks in VML22 $\delta^{18}O$ values centered around 5.9 and 5.7 ka BP do not have any equivalent in VSMS2 $\delta^{18}O$ values. Furthermore, local minima and maxima of the two records are not always synchronous, for instance, in the case of the local VML22 $\delta^{18}O$ minimum at 7.5 ka BP and the local VSMS2 $\delta^{18}O$ minimum at 7.4 ka BP.

As the age model of stalagmite VML22 is more accurate than that of stalagmite VSMS2, these mismatches are likely to result from errors in the VSMS2 age model. Although the $\delta^{18}O$ values from both stalagmites vary at similar frequencies and amplitudes, the $\delta^{18}O$ values in VML22 are about 1.5 ‰ higher than the $\delta^{18}O$ values in VSMS2.

Comparing the $\delta^{13}C$ values from stalagmite VSMS2 with those of stalagmite VML22 (Figure 5.11) yields similar results as the comparison of $\delta^{18}O$ values. It shows that also both $\delta^{13}C$ data sets are in broad agreement, but also that not all patterns are present in both data sets. For instance, the period of increased $\delta^{13}C$ values in stalagmite VML22 from 6.2 ka to 5.7 ka BP does not have an equivalent in VSMS2 $\delta^{13}C$ values. Furthermore, the amplitude of change in $\delta^{13}C$ values in VML22 (6 ‰) is about the 3-fold of that oberserved in VSMS2 (2 ‰) during the period of co-eval growth. In addition, VML22 $\delta^{13}C$ values are about -4.2 ‰ on average and thus about 7.1 ‰ higher than VSMS2 $\delta^{13}C$ values.

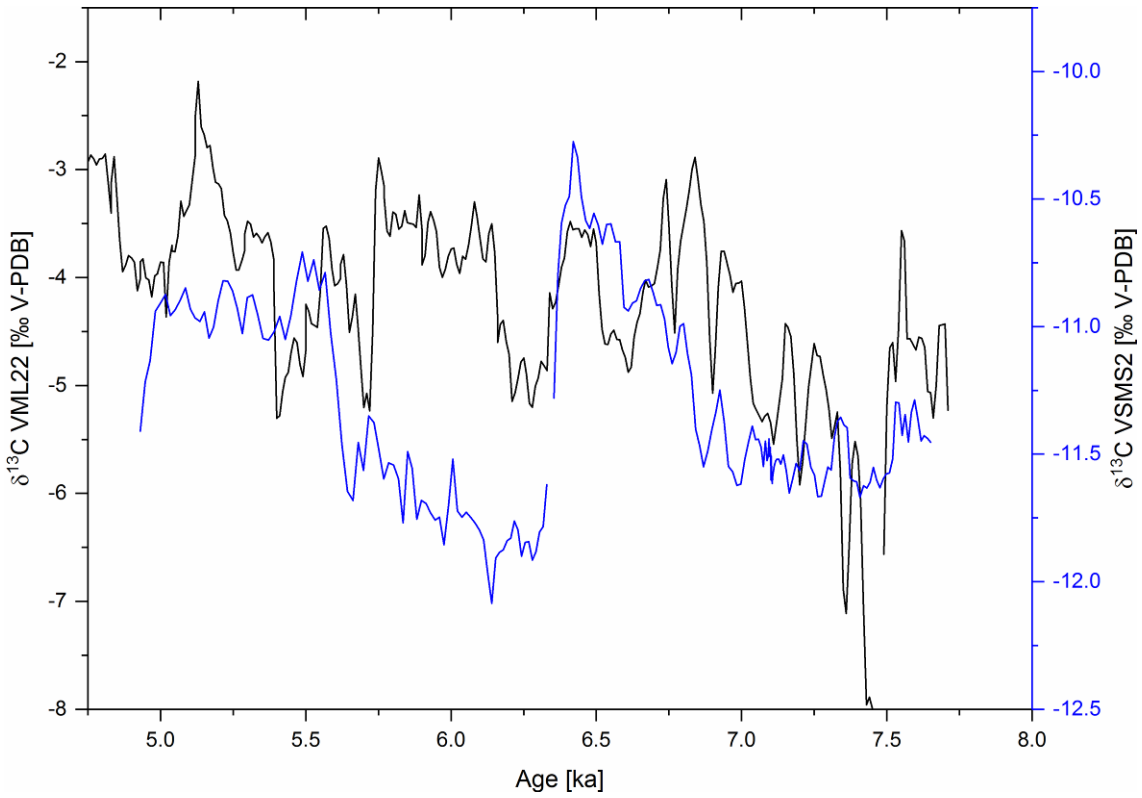

Figure 5.11: Carbon isotope values from stalagmites VML22 and VSMS2 during the last growth period of VSMS2

5.3 Trace Elements in Stalagmites

5.3.1 Stalagmite VML22

On the basis of the statistical analysis including the calculation of Spearman rank coefficients grouped in a correlation matrix (Table 5.8 in Section 5.6.2), three major groups of stable isotopes and chemical elements were identified, with the elements of each of these "geochemical groups" correlating positively with one another, henceforth referred to as Group I, II and III. Group I contains both stable isotope signals ($\delta^{18}O$ and $\delta^{13}C$) as well as Mg, Sr and Ba. Group II comprises Si, Al, Fe, Mn, Na, Cu, Zn and Rb, while Group III is made up of P and U.

As an overview of the elements analysed in stalagmite VML22 most relevant to this study, Figure 5.12 shows the concentrations of Mg, Sr, Ba, Fe, Mn and P plotted in the time domain. Because these elements represent all major "geochemical groups" that are made up of elements correlating positively with one another as evident from the statistical analysis (correlation matrix in Table 5.8 in Section 5.6.2) including Fe and P, they are illustrated here first, while the different geochemical groups will be discussed subsequently. According to the age model (Section 5.1), the spatial resolution of 6.4 µm translates into a nominal temporal resolution ot the trace element data ranging from 0.9 a to 3.6 a, depending on growth rate, with an average of 2.6 a and a median of 2.9 a. The actual resolution of the VML22 trace element data can therefore be classified as decadal and processes with an annual periodicity will consequently not be resolved by the trace element data of stalagmite VML22.

Descriptive statistics for all VML22 trace element data, including minimum, mean, median, maximum as well as the number of data points (n) remaining after removal of negative values and outliers, are summarised in Table 4.1. With an average concentration of almost 2,600 µg/g, Mg is by far the most abundant element in VML22 apart from Ca. The second most abundant element is P (335 µg/g), and both Si and Fe are present at concentrations around 100 µg/g. With an average of about 50 µg/g, Sr is the fifth most abundant element in VML22.

Similarly to $\delta^{18}O$ and $\delta^{13}C$, Mg, Sr and Ba exhibit a clear increasing trend (with decreasing age), considering the data sets in their entirety. While this is also true for Fe to a lesser extent, Mn concentrations do not follow any long-term trend, rather being dominated by distinct peaks of varying duration superimposed on a quasi-constant baseline. This peak-dominated behaviour can also be found in the case of Fe. In contrast to all elements mentioned above, P concentrations clearly trend towards decreased values on the long term. Superimposed on the described long-term increasing and decreasing trends are variations with frequencies ranging from decades to multiple centuries, as described in the following.

Table 5.3: Descriptive statistics for all trace element data of stalagmite VML22. Concentrations are given in µg/g.

	n	Minimum	Mean	Median	Maximum
Mg	17240	608	2598	2567	4682
Sr	17192	16.4	56.8	56.7	97.4
Ba	16963	0.23	4.55	4.43	9.43
Fe	16840	37.5	111	109	202
Mn	15991	0.02	1.25	0.71	8.56
P	17251	54.5	335	324	779
Si	16589	9.19	127	119	360
Al	16421	0.04	7.08	3.08	55.9
Na	16599	0.01	12.7	8.77	70.0
U	16994	0.002	0.07	0.06	0.24
Cu	12909	0.03	0.68	0.47	3.92
Zn	11957	0.21	3.71	2.77	20.7
Rb	7538	0.02	0.07	0.04	0.34
Cd	7809	0.09	0.27	0.15	1.33

In the case of Mg, these shorter-term variations can be described as multi-decadal troughs that appear at 7.6, 7.3, 5.8, 5.5, 2.8, 1.6 and 1.3 ka BP, while the most prominent negative deviation from the long-term increasing trend is a multi-centennial trough spanning the period from 1.1 to 0.48 ka BP, centered at 0.76 ka BP, during which Mg concentrations are about 800 µg/g lower compared to the positive long-term trend (indicated as a red line in Figure 5.13). All these troughs correspond to similar troughs in the $\delta^{13}C$ record of stalagmite VML22, emphasising the similarity of both proxy signals. The most marked positive anomalies with respect to the positive long-term trend occur at around 4.0 ka BP and at 1.4 and 0.5 ka BP, with Mg concentrations 650 to 800 µg/g higher compared to the long-term trend. None of the Mg peaks coincides with any peak of any element from Group II.

As the concentrations of Sr and Ba evolve in a quasi-identical fashion, both proxy records can be described as one. While most of the troughs in the Mg curve do not seem to have corresponding counterparts in the curves of Sr and Ba, the most prominent trough from 1.1 to 0.48 ka BP corresponds to several multi-decadal troughs in Sr and Ba concentrations with minima at 0.96, 0.81 and 0.60 ka BP. The negative anomaly at 7.6 ka BP also appears in the Sr and Ba data sets. Other negative deviations from the positive long-term trend occur at 7.8, 7.1, 4.9, 4.3 and 3.3 ka BP. The most important positive excursions occur at around 4.0 ka BP and at 2.2 ka BP, in close resemblance to local maxima of the Mg curve, and at 6.9, 6.8 ka BP. Several Sr and Ba peaks coincide with peaks of the elements of Group II, here represented by Mn. These occur at 7.9, 6.9, 6.8 and 1.6 ka BP.

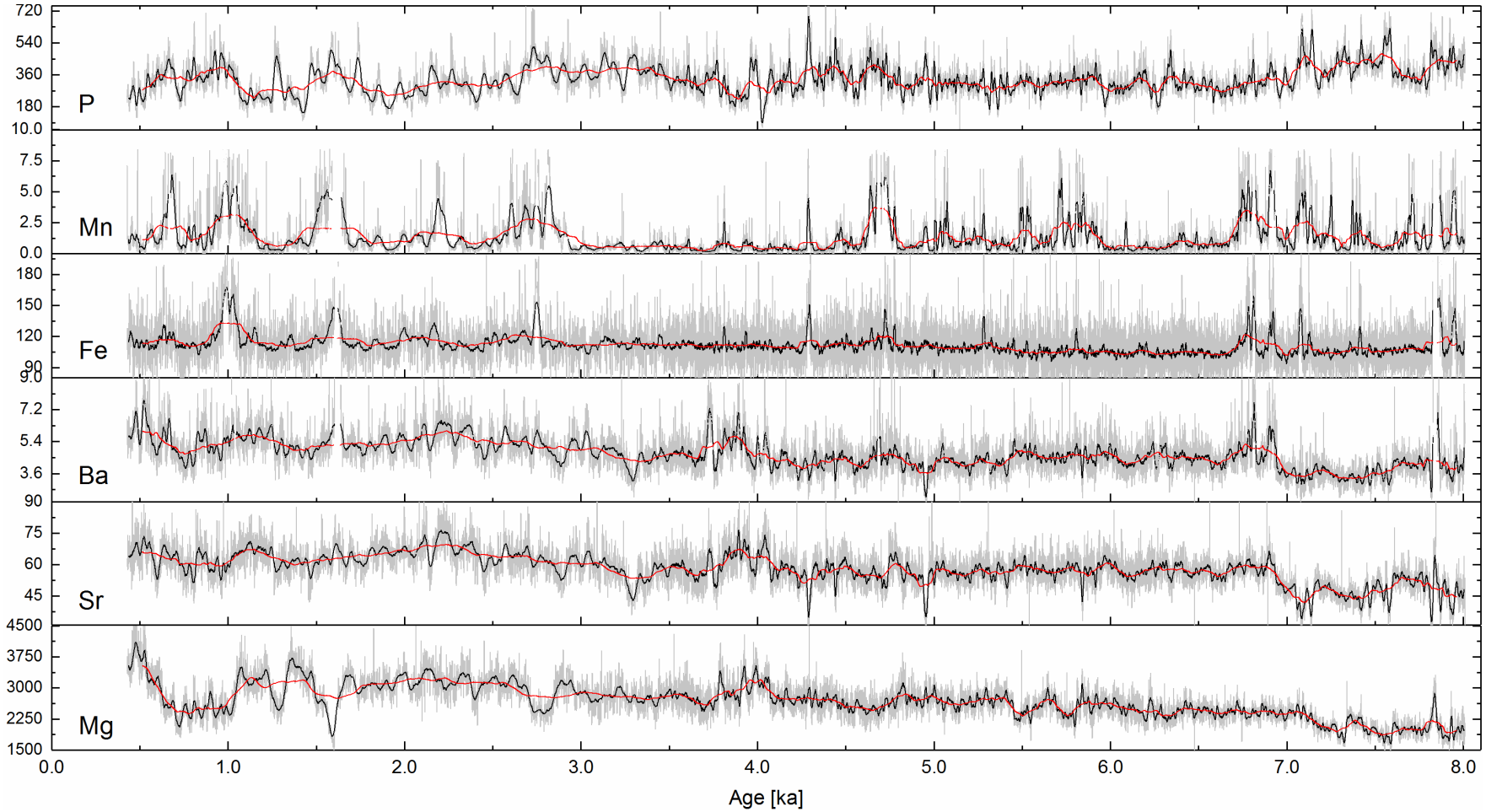

Figure 5.12: Overview of the most important trace elements for this study from stalagmite VML22, plotted in the time domain. All concentrations are given in µg/g. Grey lines indicate the original concentrations after all corrections, black lines are 30-pt smoothed data (weighted Adjacent-Averaging), red lines are 300-pt smoothed data. Based on statistical analyses (Section 5.6.2.1), Mg, Sr and Ba are attributed to geochemical Group I, Fe and Mn are attributed to Group II and P is attributed to Group III.

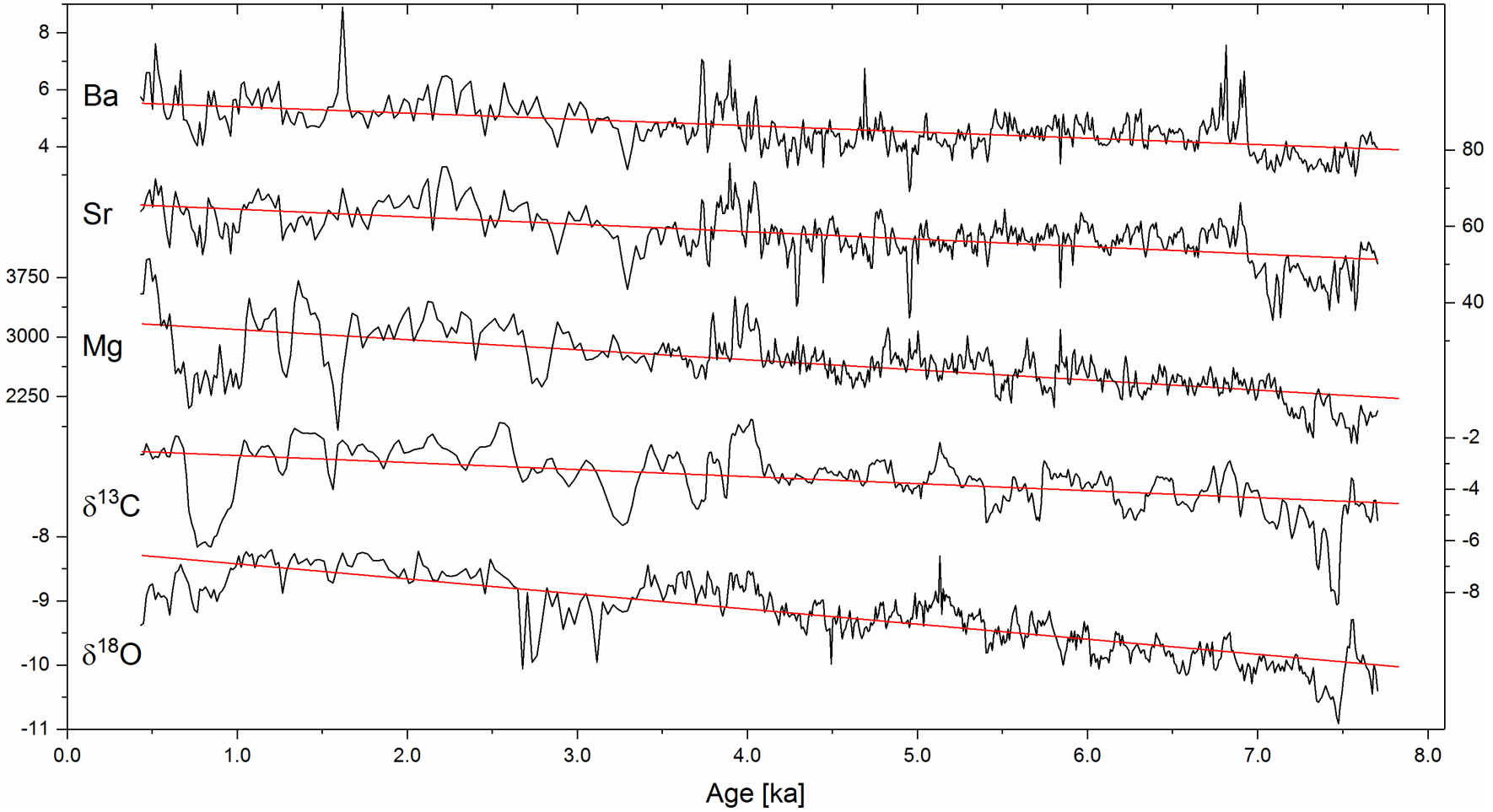

Figure 5.13: Geochemical proxy records of stalagmite VML22 attributed to Group I: $\delta^{18}O$, $\delta^{13}C$, Mg, Sr and Ba. Both stable isotope ratios are expressed in ‰ as δ values relative to the V-PDB standard, all trace element concentrations are given in µg/g and are averaged to match the resolution of the isotope data sets (Section 4.6). Linear regression lines are indicated in red.

While Fe concentrations feature a positive long-term trend, the overall behaviour of the element in stalagmite VML22 is still dominated by separate and distinct peaks, in close resemblance to the behaviour of all Group II elements. The most important peaks are centered at 8.0, 7.9, 7.1, 6.9, 6.8, 5.3, 4.7, 4.3, 2.7, 1.6 and 1.0 ka BP. Manganese concentrations also peak at all these times, but also at additional times, for example at 7.7, 7.3, 5.7 and 5.5 ka BP, among others. In general, Mn peaks appear to be somewhat broader than those of Fe.

Consistent with intermediate values of Spearman's ρ between P and the elements of Group II (Section 5.6.2.1) indicating some degree of positive correlation, some of the peaks in P concentration appear to be synchronous to peaks of the Group II elements, represented by Mn in Figure 5.12. Examples are peaks at 7.1, 4.9, 4.7, 4.3, 3.8 ka BP and, most noticeably, multiple peaks during the period from about 2.9 ka BP to the end of stalagmite growth at 0.43 ka BP. In general, peaks in P concentration mirror, albeit in a more muted way, the multi-peak clusters of the Group II elements described below. Again consistent with the respective negative correlation coefficients, Fe peaks tend to correspond to troughs in the concentration of Mg and especially of Sr, for instance at 7.6, 7.1, 4.9, 4.3 and 3.3 ka BP, and vice versa. However, the opposing behaviour of these elements is most evident regarding the longer-term (lower frequency) variations of these proxy signals, as indicated by the 300-point smoothed data sets in Figure 5.12.

For better comparability between the elements of Group I, the trace elements Mg, Sr and Ba are illustrated together with the stable isotope signals in Figure 5.13. While not all peaks and troughs in the curves are synchronous, the general evolution of all these signals is strikingly similar. This suggests that these proxy signals from stalagmite VML22 are either governed by a similar suite of processes or by processes that in some way relate to one another. Similarities and differences in behaviour are investigated in further detail below, by means of frequency analysis (Section 5.6.5).

The records of all remaining trace elements attributed to Group II are shown in Figure 5.14, except for Mn as it has already been presented above (Figure 5.12) and for better readability. The diagram illustrates the quasi-identical behaviour of all elements of Group II and the near-perfect match of their respective peaks. As already discussed above, using the example of Mn, the concentrations of these elements do not follow any long-term trend and are rather dominated by numerous peaks that clearly exceed a quasi-constant baseline. Not only do the peaks of all these elements coincide, even the relative height of the peaks for each element appears to be quasi-identical. Silicon and Fe are by far the most abundant trace elements of Group II in stalagmite VML22 (Table 4.1), with concentrations that average 127 µg/g and 111 µg/g, respectively, an entire order of magnitude higher than those of the third-most abundant element Na (12.7 µg/g on average), and more than three orders of magnitude higher than those of the least abundant element Rb (0.07 µg/g on average).

Despite these wide differences in concentration, all trace element records of Group II feature peaks in concentration at the same times. The only exception to this is Zn that does not show all the peaks of the remaining elements, for example at 3.8 and at 2.0 ka BP. The Zn peaks around 6.4 ka BP, however, seem slightly more pronounced compared to the remaining Group II elements.

The peaks in element concentration are not distributed equally over time. While most of the variability happens on a multi-decadal timescale and one single peak rarely spans more than a hundred years, the periods of extraordinarily high element concentrations seem to cluster at different points in time. These clusters are centered approximately at 7.8, 6.9, 4.7, 2.7, 2.1, 1.7, 1.0 and 0.7 ka BP, each spanning a period of about 100 to 300 years. A more isolated peak at 4.3 ka BP coincides with one of the most pronounced troughs in Sr concentrations. From about 3.5 ka BP on until the end of growth at 0.4 ka BP, the peaks appear to be broader than the peaks anteceding that period. However, this is likely to be an artefact of reduced temporal resolution resulting from decreased growth rates (Figure 5.15).

The records of both elements comprised in Group III, P and U, are shown in Figure 5.15 as well as Sr in order to illustrate the opposing behaviour of P and Sr mentioned above.

Cadmium concentrations are also included in the diagram as they also peak at 1.0 ka BP like all elements of Group II, but Cd will not be discussed in further detail due to the low number of data points remaining after removal of negative values and outliers (Table 4.1) and its low lag-1 autocorrelation coefficient (Table 5.13), shown below.

Despite a difference of three to four orders of magnitude between the average concentrations of P and U, both proxy signals evolve in a quasi-identical fashion, including the relative amplitude of the variations in concentration. This again indicates a close relation between the processes governing these two signals. However, U does not feature any long-term trend in concentration whereas P concentrations clearly follow a negative trend towards the present, as illustrated by the blue regression line in Figure 5.15. The positive covariation of P and therefore of U with the elements of Group II and the negative covariation with the elements of Group I, particularly with Sr, have already been described above.

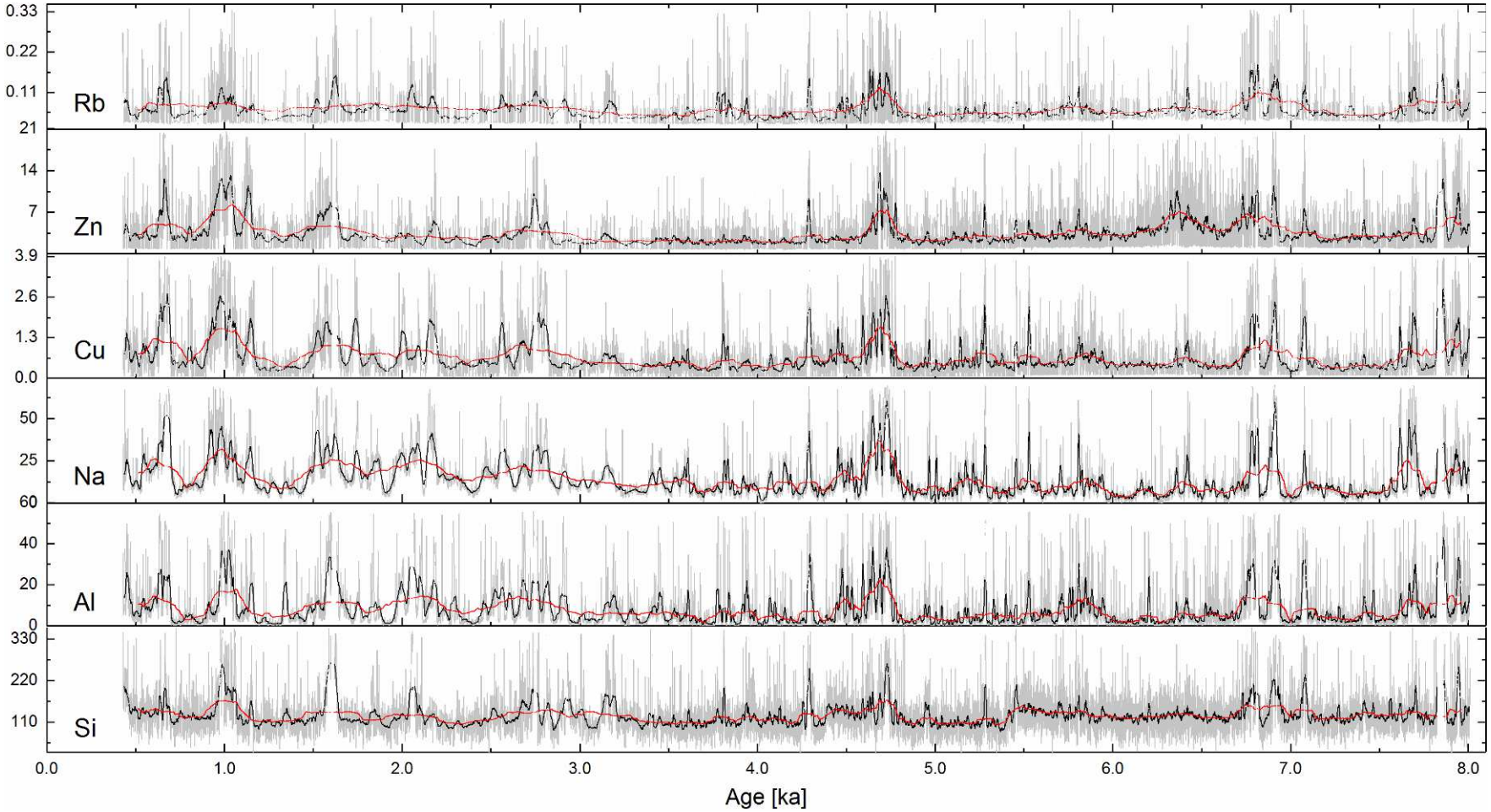

Figure 5.14: Geochemical proxy records of stalagmite VML22 attributed to Group II: Si, Al, Na, Cu, Zn and Rb. All concentrations are given in µg/g. Grey lines indicate the original concentrations after all corrections, black lines are 30-pt smoothed data (weighted Adjacent-Averaging), red lines are 300-pt smoothed data.

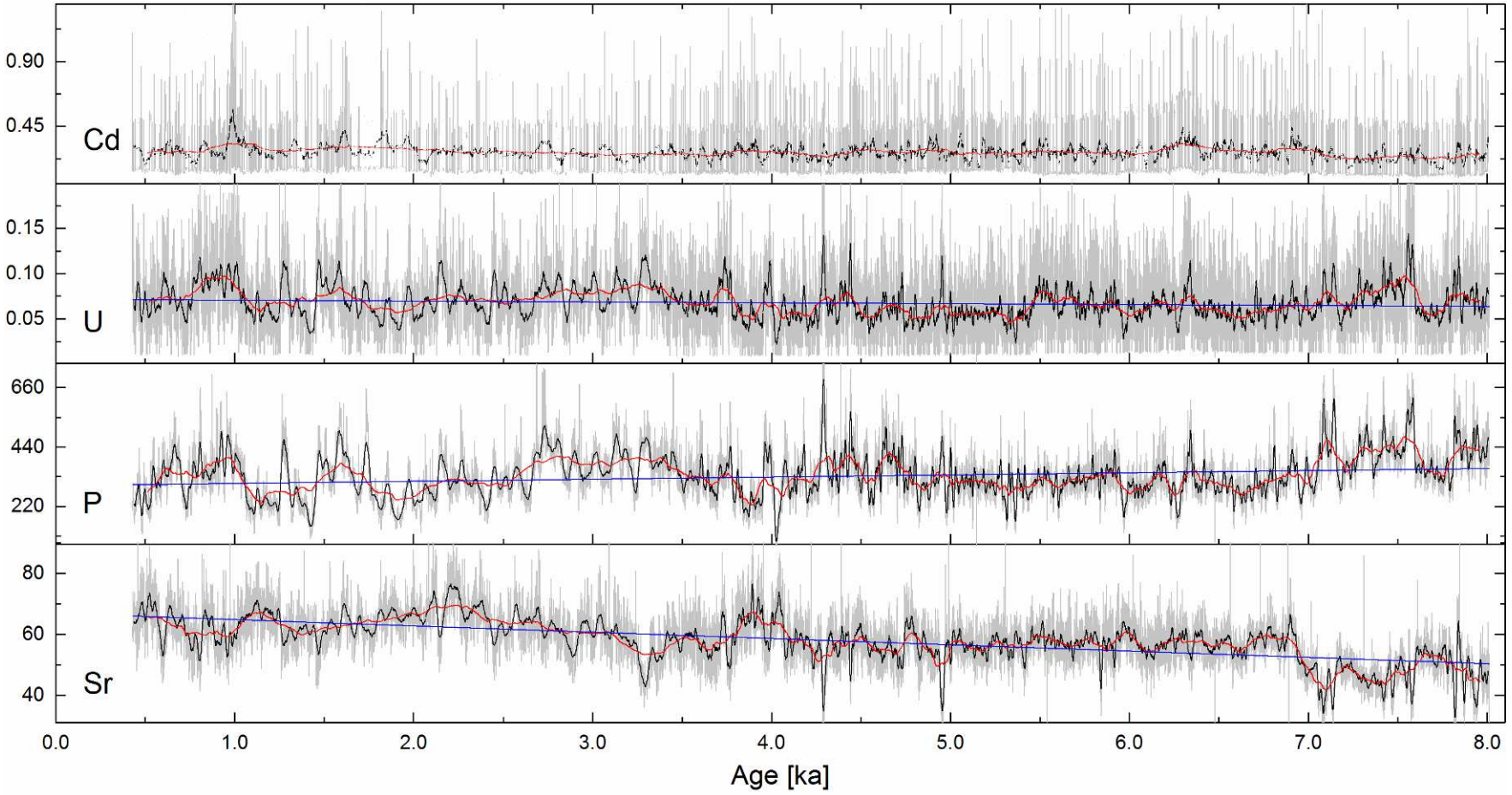

Figure 5.15: Geochemical proxy records of stalagmite VML22 attributed to Group III (P and U) including Sr for comparison and Cd for the sake of completeness. All concentrations are given in µg/g. Grey lines indicate the original concentrations after all corrections, black lines are 30-pt smoothed data (weighted Adjacent-Averaging), red lines are 300-pt smoothed data; regression lines are indicated in blue.

5.3.2 Stalagmite VSMS2

Analogously to stalagmite VML22, the geochemical signals generated from stalagmite VSMS2 were attributed to three different "geochemical groups" on the basis of positive Spearman rank coefficients within each group (Table 5.9 in Section 5.6.2). As in stalagmite VML22, Group I contains both stable isotope signals ($\delta^{18}O$ and $\delta^{13}C$) as well as Mg, Sr and Ba. Group II comprises Si, Al, Fe, Mn, Na, Ti, Th and Cd, while Group III is made up of P and U.

As an overview of the elements analysed in stalagmite VSMS2 most relevant to this study, Figure 5.16 shows the concentrations of Mg, Sr, Ba, Fe, Mn and P plotted in the time domain. Because these elements represent all major geochemical groups as distinguished based on the correlation matrix (Section 5.6.2.2) including Fe and P, they are illustrated here first, while the different geochemical groups will be discussed subsequently.

According to the age model (Section 5.1.2), the spatial resolution of 6.4 µm translates into a nominal temporal resolution of the trace element data ranging from 0.04 a to 0.7 a, depending on growth rate, with an average and a median of 0.4 a. The actual resolution of the VSMS2 trace element data can therefore be classified as multi-annual to decadal and processes with an annual periodicity will consequently not be resolved by the trace element data of stalagmite VSMS2.

Descriptive statistics for all VSMS2 trace element data, including minimum, mean, median, maximum as well as the number of data points (n) remaining after removal of negative values and outliers, are summarised in Table 5.4. With an average concentration of more than 1,315 µg/g, Mg is by far the most abundant element in VSMS2 apart from Ca. The second most abundant element is P (average: 785 µg/g), followed by Si (average: 524 µg/g). Contrarily to stlagmite VML22, the fourth most abundant element ist not Fe (average: 174 µg/g), but Al with an average concentration of around 290 µg/g, while it was almost absent from VML22. Average Sr concentrations in VSMS2 are around 11 µg/g, noticeably less than in VML22. In the case of Si and Al, the discrepancy between the mean and the median of the concentrations (about 280 µg/g and 130 µg/g, respectively) indicates that both elements feature a relatively high number of peak concentrations compared to a normal distribution, consistent with the corresponding histograms that are strongly skewed to the right (Section 5.6.1.2).

Table 5.4: Descriptive statistics for all trace element data of stalagmite VSMS2. Concentrations are given in µg/g.

	n	Minimum	Mean	Median	Maximum
Mg	23446	371	1315	1352	2912
Sr	23199	2.64	11.0	11.0	24.2
Ba	22819	0.22	3.87	3.63	10.4
Fe	22512	90.1	174	160	437
Mn	22070	0.01	2.09	1.36	19.8
P	23453	32.5	785	739	2613
Si	22727	20.7	524	240	3668
Al	22591	0.12	229	103	1694
Ti	20727	0.04	9.41	3.57	75.4
Na	21570	0.01	26.1	12.3	190
U	16884	0.01	0.11	0.10	0.38
Cu	22563	0.01	2.07	1.43	11.0
Zn	22316	0.08	21.1	10.2	436
Rb	20004	0.002	0.41	0.18	3.03
Cd	13036	0.06	0.39	0.29	2.07

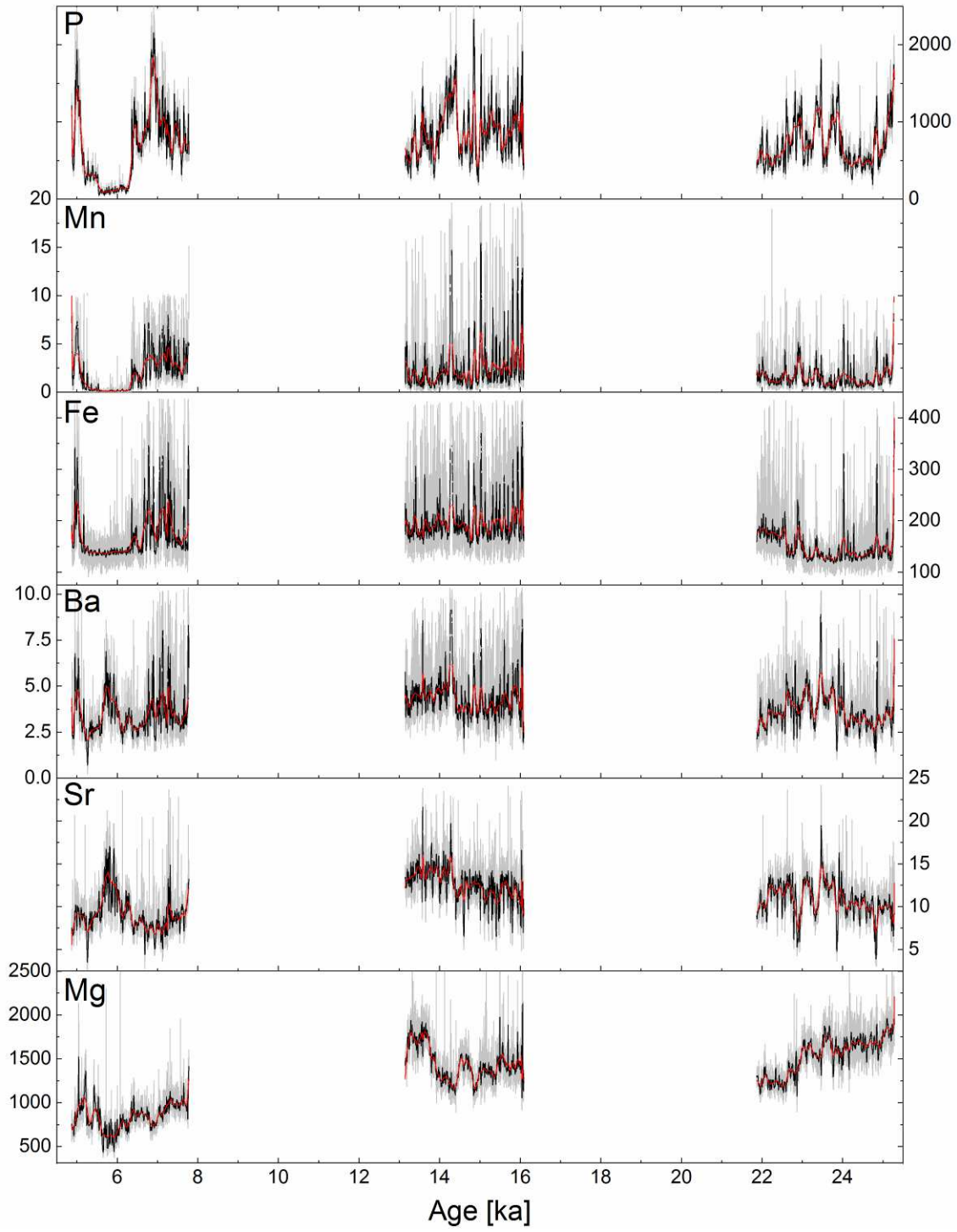

Figure 5.16: Overview of the most important trace elements for this study from stalagmite VSMS2, plotted in the time domain. All concentrations are given in µg/g. Grey lines indicate the original concentrations after all corrections, black lines are 30-pt smoothed data (weighted Adjacent-Averaging), red lines are 300-pt smoothed data.

For better readability, the three growth periods of stalagmite VSMS2 are discussed separately in the following. All trace element data are plotted in the depth domain in the Appendix.

5.3.2.1 First growth period

The first growth period of stalagmite VSMS2 ranges from 25.3 ka to 21.9 ka BP. The descriptive statistics for this period are summarised in Table 5.5.

Table 5.5: Descriptive statistics for all trace element data of stalagmite VSMS2 corresponding to its first growth period. Concentrations are given in µg/g.

	n	Minimum	Mean	Median	Maximum
Mg	7110	895	1537	1561	2824
Sr	7056	3.04	10.8	10.7	24.2
Ba	7047	0.75	3.65	3.46	10.3
Fe	7037	90.1	149	138	436
Mn	6983	0.02	1.50	1.08	19.0
P	7112	129	722	634	2124
Si	7051	39.5	369	165	3657
Al	7037	1.88	159	65.3	1684
Ti	6394	0.04	6.56	2.07	75.3
Na	6764	0.01	14.2	5.41	190
U	7078	0.01	0.10	0.09	0.38
Cu	7020	0.01	1.30	1.03	10.9
Zn	6986	0.27	6.42	5.12	291
Rb	5439	0.02	0.28	0.12	3.01
Cd	2866	0.08	0.25	0.12	1.87

Of all trace elements analysed in stalagmite VSMS2 for this study, Mg is the only one that also exhibits a negative long-term trend of its concentrations during the first growth period (Figure 5.17 and Figure 5.18). In contrast to the stable isotope signals, the negative trend of Mg concentrations can be well described with a linear regression as indicated by the high adjusted R^2 of 0.69. In accordance with the only significant positive Spearman's ρ with any other of the proxy signals from stalagmite VSMS2 ($\rho = 0.32$), the behaviour of Mg concentrations is most similar to the one of $\delta^{13}C$ values. In particular, the main local minima in $\delta^{13}C$ values at 24.8, 24.1, 23.7, 22.9 and 22.3 ka BP are well reproduced by corresponding minima in Mg concentrations. The main $\delta^{13}C$ local maxima do not have as obvious counterparts in Mg concentrations, except for corresponding maxima at 24.6, 24.0, 23.5 and 23.2 ka BP. For instance, the local maxima in $\delta^{13}C$ values at 23.3 ka and around 22.5 ka BP are not mirrored in Mg concentrations. The local maximum in Mg concentrations at 22.6 ka BP does not have a counterpart in any other of the proxy signals from VSMS2.

Strontium and Ba show very similar behaviour (Figure 5.17 and Figure 5.18), consistent with the high Spearman's ρ of 0.75. Their most distinctive common local maxima occur at 23.9 ka and especially at 23.4 ka BP, with secondary local maxima at 23.7, 23.0 and around 22.7 ka BP. Another peak in Ba concentrations at 24.8 ka BP is not apparent in Sr concentrations, but in all Group II elements (Figure 5.19). The most distinctive common local minima of Sr and Ba occur at 24.7, 23.8, 23.3 and 22.8 ka BP. The marked local maxima in Sr and Ba concentrations at 23.4 ka BP correspond to a marked local minimum in $\delta^{18}O$ values and the most prominent local maximum in P concentrations, while Sr and Ba behave inversely to P during the most of the first growth period.

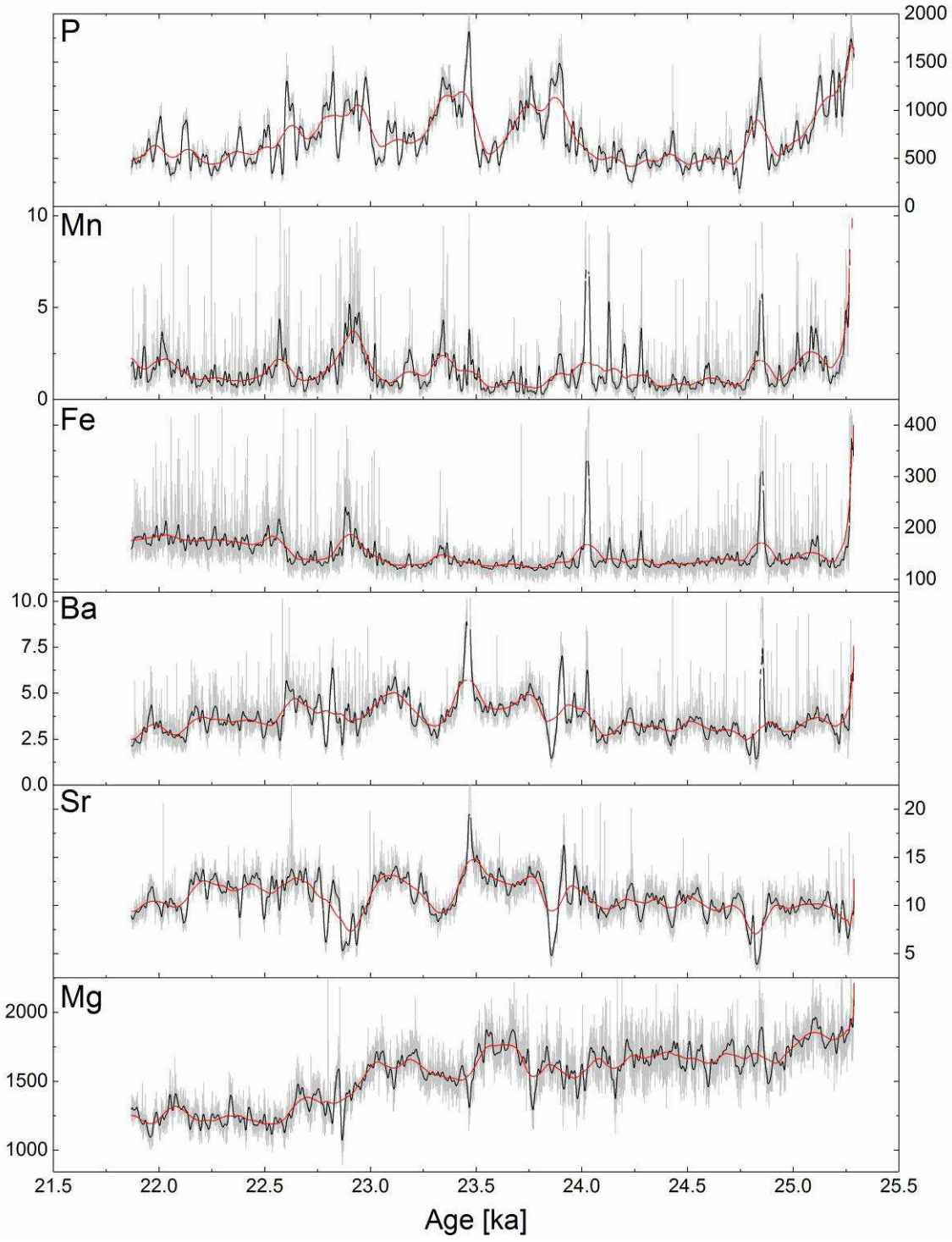

Figure 5.17: Trace element concentrations (in µg/g) of Mg, Sr, Ba, Fe, Mn and P from stalagmite VSMS2 during its first growth period. Grey lines indicate the original concentrations after all corrections, black lines are 30-pt smoothed data (weighted Adjacent-Averaging), red lines are 300-pt smoothed data.

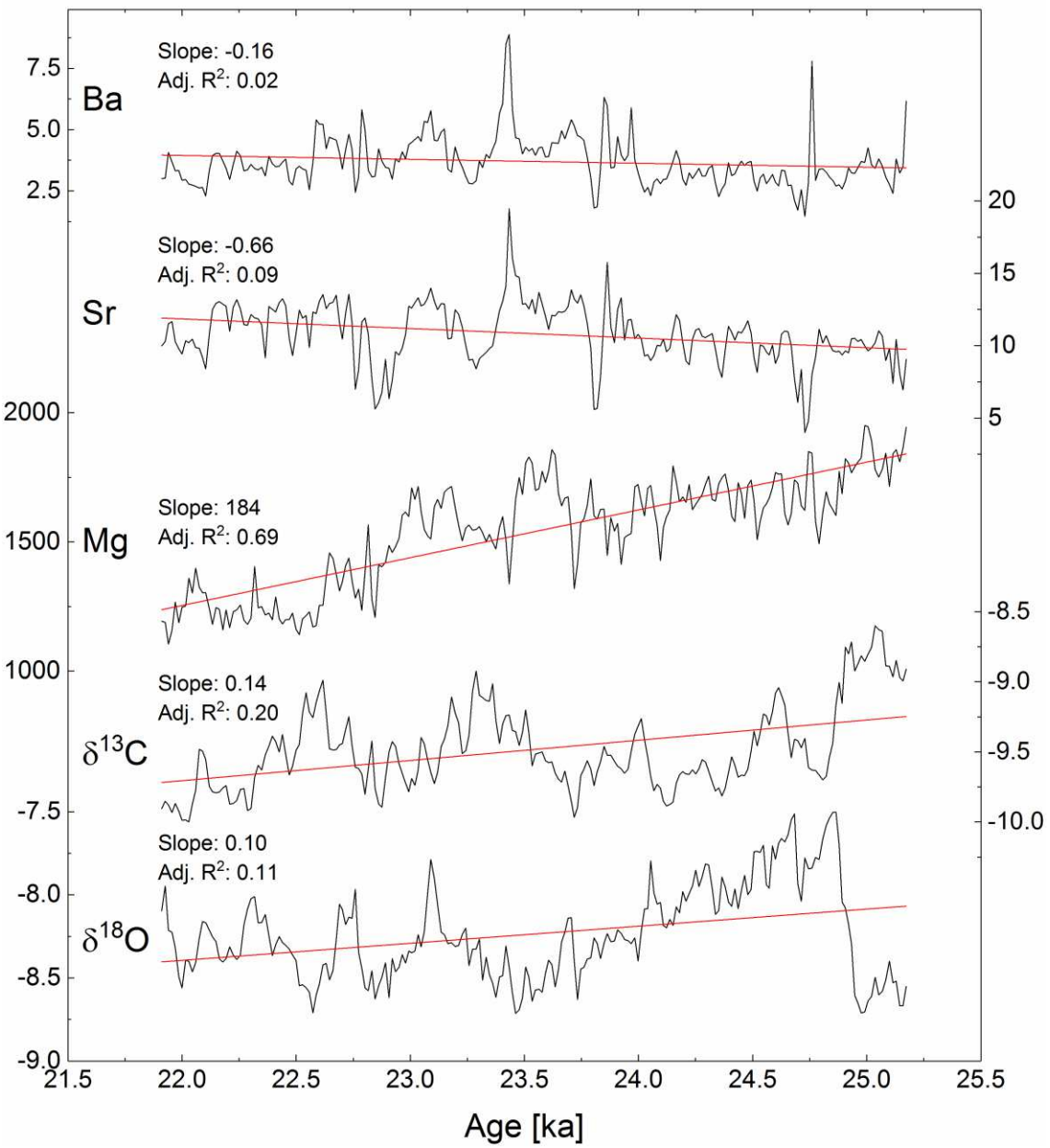

Figure 5.18: Geochemical proxy records during the first growth period of stalagmite VSMS2 attributed to Group I: $\delta^{18}O$, $\delta^{13}C$, Mg, Sr and Ba. Both stable isotope ratios are expressed in ‰ as δ values relative to the V-PDB standard, all trace element concentrations are given in µg/g and are averaged to match the resolution of the isotope data sets (Section 4.6). Linear regression lines are indicated in red.

In contrast to the elements attributed to Group I, Group II elements (Figure 5.19 and Figure D.21 in the Appendix) feature a quasi-constant baseline, on which distinct peaks in element concentration of varying duration are superimposed. In accordance with the generally high values of Spearman's ρ (Section 5.6.2.2) calculated for the elements of Group II their behaviour is quasi-identical and the match of their respective peaks is near-perfect. The most important peaks are centered at 25.3, 24.8, 24.0 and 22.9 ka BP, with secondary peaks at 25.1, 24.3, 24.2, 23.3 and 22.6 ka BP. Except for the concentration peaks at 23.3 ka BP, the period from 23.9 ka to 23.1 ka BP stands out by its unusually low trace element concentrations. While Mn concentrations do not exhibit this unusual low to the same extent as do the concentrations of the remaining Group II elements, this concentration low is not visible in Group I and Group III elements at all. After this concentration low from 23.9 to 23.1 ka BP, trace element concentrations are generally higher than before this period, especially the concentrations of Si.

The records of both elements comprised in Group III, P and U, are shown in Figure 5.20 including Mn for comparison. As in stalagmite VML22, P and U evolve in a quasi-identical fashion, even considering the relative amplitude of the variations in concentration, despite a difference of three to four orders of magnitude between the average concentrations of both proxy signals. This is consistent with the high Spearman's ρ (0.88) and again indicates a close relation between the processes governing these two signals. Main peaks in P and U concentrations are centered at 25.3, 24.8, 23.9, 23.8, 23.5, 23.0, 22.8 and 22.6 ka BP, with multiple secondary peaks, for instance 25.2 ka BP and at 22.5, 22.4, 22.1 and 22.0 ka BP. The overall concentration minima occur at 24.7 ka BP. As indicated by intermediate values of Spearman's ρ with Mn, several of the peaks in Mn concentration are mirrored by P and U concentration peaks, most notably at 25.3, 24.9, 23.3 and around 22.9 ka BP. However, other prominent Mn peaks are not reproduced by P and U, such as the most important Mn peak at 24.0 ka BP.

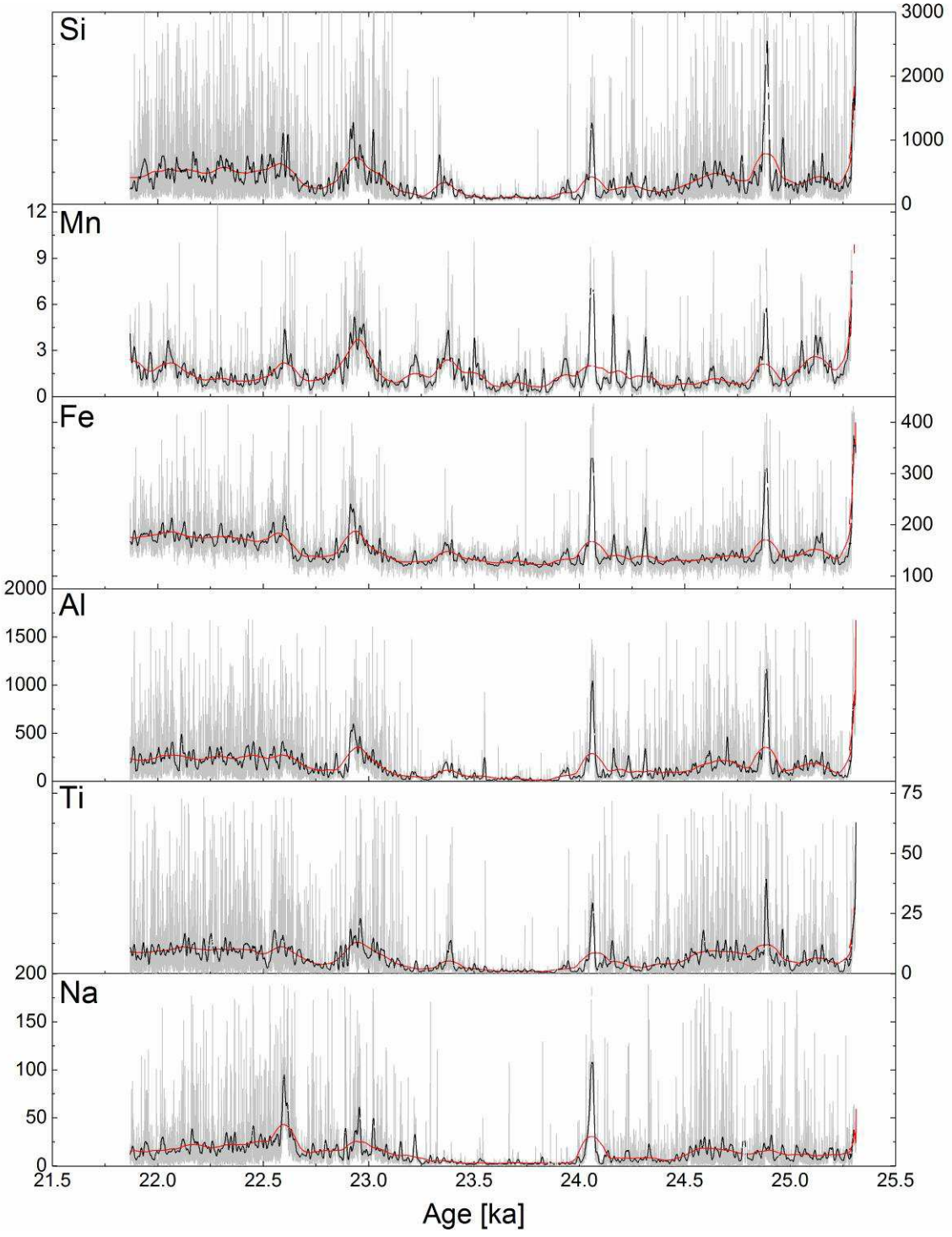

Figure 5.19: Concentrations of trace elements during the first growth period of stalagmite VSMS2 attributed to Group II (Si, Mn, Fe, Ti and Na) in µg/g. Grey lines indicate the original concentrations after all corrections, black lines are 30-pt smoothed data (weighted Adjacent-Averaging), red lines are 300-pt smoothed data.

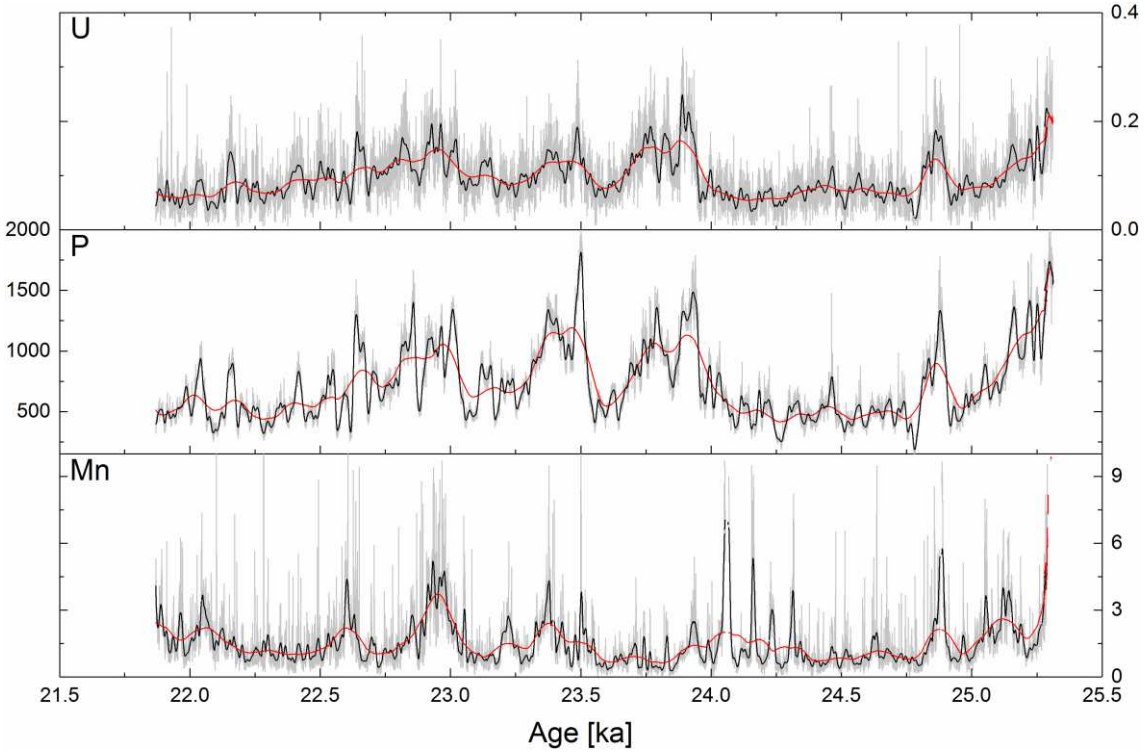

Figure 5.20: Concentrations of trace elements during the first growth period of stalagmite VSMS2 attributed to Group III (P and U) in µg/g including Mn for comparison. Grey lines indicate the original concentrations after all corrections, black lines are 30-pt smoothed data (weighted Adjacent-Averaging), red lines are 300-pt smoothed data.

5.3.2.2 Second growth period

The second growth period of stalagmite VSMS2 ranges from 16.0 ka to 13.1 ka BP. The descriptive statistics for this period are summarised in Table 5.6.

Table 5.6: Descriptive statistics for all trace element data of stalagmite VSMS2 corresponding to its second growth period. Concentrations are given in µg/g.

	n	Minimum	Mean	Median	Maximum
Mg	9872	885	1450	1419	2912
Sr	9737	4.86	12.48	12.5	24.1
Ba	9443	0.99	4.31	4.06	10.4
Fe	9275	115	197	178	436
Mn	9454	0.03	2.50	1.55	19.8
P	9877	179	894	844	2613
Si	9444	35.4	670	373	3660
Al	9304	1.37	303	160	1694
Ti	8940	0.04	11.8	5.42	75.4
Na	9439	0.01	33.5	20.3	190
U	9772	0.01	0.12	0.11	0.38
Cu	9569	0.05	2.35	1.73	11.0
Zn	9685	0.20	32.5	17.7	436
Rb	9013	0.002	0.49	0.26	3.01
Cd	5588	0.07	0.39	0.30	2.06

During the first half of the second growth period of stalagmite VSMS2, from 16.0 ka to 14.4 ka BP, Mg concentrations behave similarly to $\delta^{13}C$ values (Figure 5.21 and Figure 5.22) as suggested by a positive Spearman's ρ (0.20) calculated for this time period. Whereas three narrow peaks in Mg concentration at 15.9, 15.7 and 15.5 ka BP are not mirrored by corresponding peaks in $\delta^{13}C$ values, especially the broad positive excursion in $\delta^{13}C$ values ranging from 14.9 ka to 14.3 ka BP clearly has a counterpart in Mg concentrations, even if Mg concentrations increase about 100 years later than $\delta^{13}C$ values. Contrarily, during the second half of the second growth period of stalagmite VSMS2, Mg concentrations increase to reach their overall maximum values of 1,900 µg/g around 13.6 ka BP to remain at a high level around 1,750 µg/g on average until the end of the second growth period. In contrast during this entire period, $\delta^{13}C$ values remain relatively constant while $\delta^{18}O$ values even strongly decrease, consistent with Spearman's ρ values with Mg of -0.11 and -0.51, respectively. Considering the entire second growth period, Mg concentrations feature a relatively strong positive long-term trend.

Strontium and Ba do not share the marked behaviour of Mg, but behave similarly to one another as suggested by a high Spearman's ρ (0.59), with both signals exhibiting a slight positive long-term trend. Prominent common maxima occur at 16.0, 14.3 and 13.6 ka BP, whereas local maxima an Ba concentrations lack corresponding Sr peaks, for instance at 15.7, 15.6, 15.5, 15.0 and 14.8 ka BP. Some of these Ba peaks coincide with Mg peaks, especially in the first half of the second growth period of VSMS2, for example at 15.9, 15.7 and 15.5 ka BP. Strontium concentrations exhibit two marked local minima at 15.4 and 14.6 ka BP that are shared by Ba, albeit to a lesser extent.

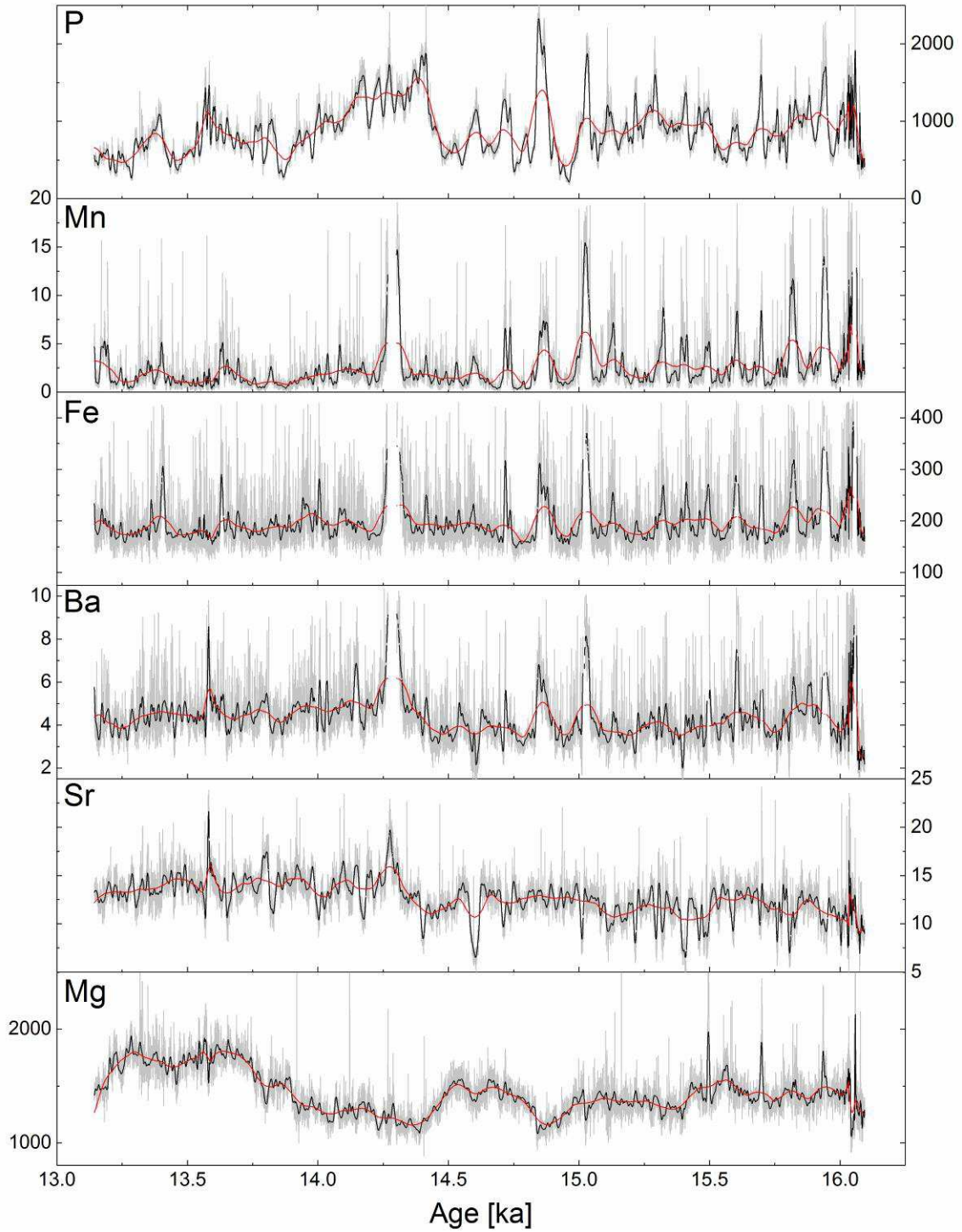

Figure 5.21: Trace element concentrations (in µg/g) of Mg, Sr, Ba, Fe, Mn and P from stalagmite VSMS2 during its second growth period. Grey lines indicate the original concentrations after all corrections, black lines are 30-pt smoothed data (weighted Adjacent-Averaging), red lines are 300-pt smoothed data.

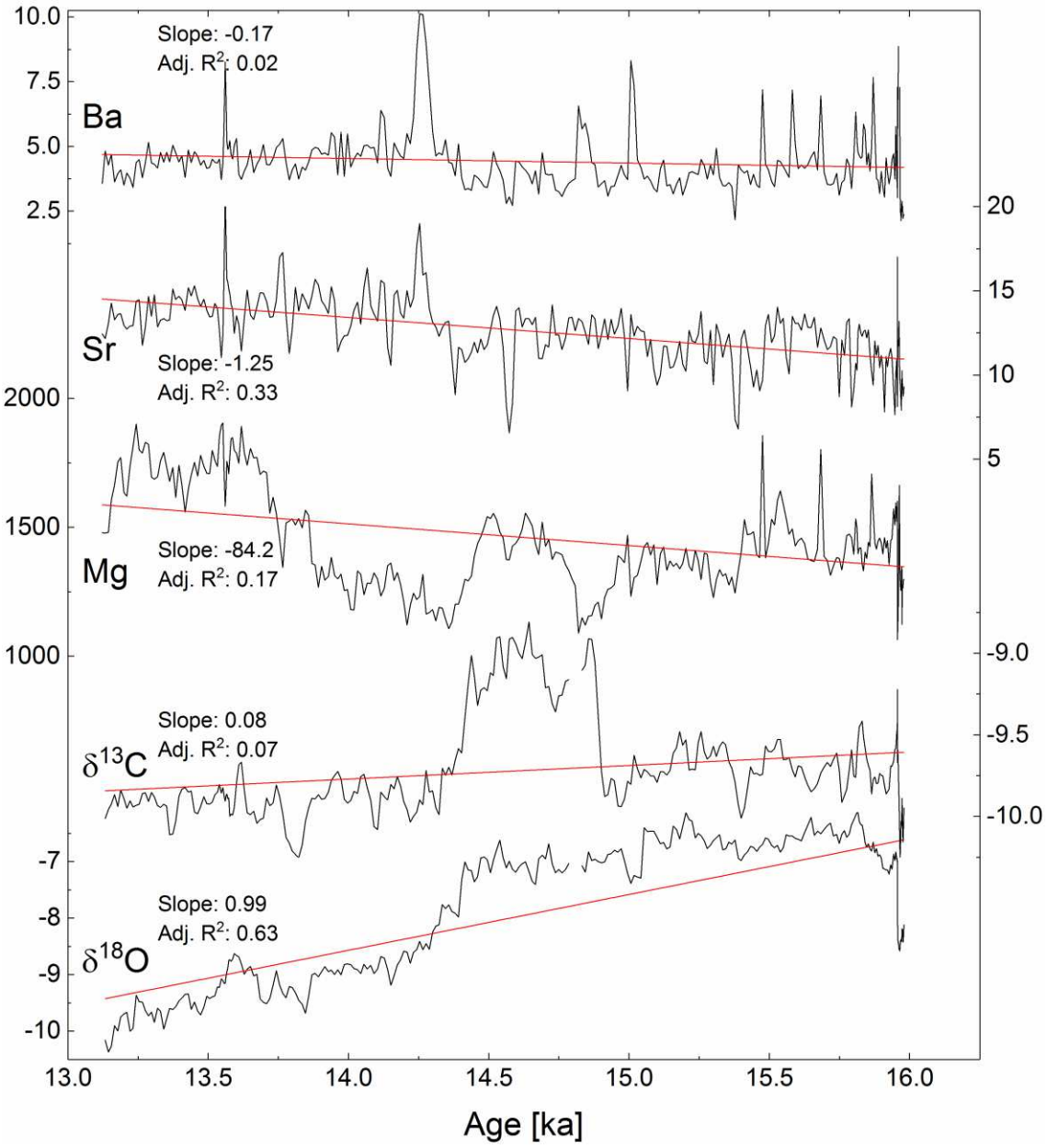

Figure 5.22: Geochemical proxy records during the second growth period of stalagmite VSMS2 attributed to Group I: $\delta^{18}O$, $\delta^{13}C$, Mg, Sr and Ba. Both stable isotope ratios are expressed in ‰ as δ values relative to the V-PDB standard, all trace element concentrations are given in µg/g and are averaged to match the resolution of the isotope data sets (Section 4.6). Linear regression lines are indicated in red.

As in stalagmite VML22 and during the first growth period, all Group II elements (Figure 5.23 and Figure D.22 in the Appendix) feature a quasi-constant baseline, on which distinct peaks in element concentration of varying duration are superimposed, again in contrast to the elements attributed to Group I. In accordance with the generally high values of Spearman's ρ (Section 5.6.2.2) calculated for the elements of Group II their behaviour is quasi-identical and their respective peaks match very well. The most prominent peak is centered at 14.3 ka BP and features trace element concentrations that are so high that they were classified as outliers by the Grubb's test and were removed. As the removal of these values as outliers does not alter the position of the element peaks it has no influence on the interpretation of the data. Further prominent element peaks occur at 16.1, 15.9, 15.8 and especially at 15.0 ka BP, with secondary peaks at 15.7, 15.6, 15.5, 15.4, 15.3, 15.1, 14.9 and 14.7 ka BP which suggests a fairly regular occurrence of these peaks at an interval of about 100 years. In particular Si exhibits further peaks at 14.6, 14.5 and 14.4 ka BP that are more muted in the other elements of Group II. After the most prominent peak at 14.3 ka BP, the peaks are less pronounced and lower than before the prominent peak, with the exception of Cu and Zn (Figure D.22) that feature several more peaks, for instance at 14.1, 13.4 and 13.3 ka BP. Zinc stands out among the Group II elements by its apparent high signal-to-noise ratio.

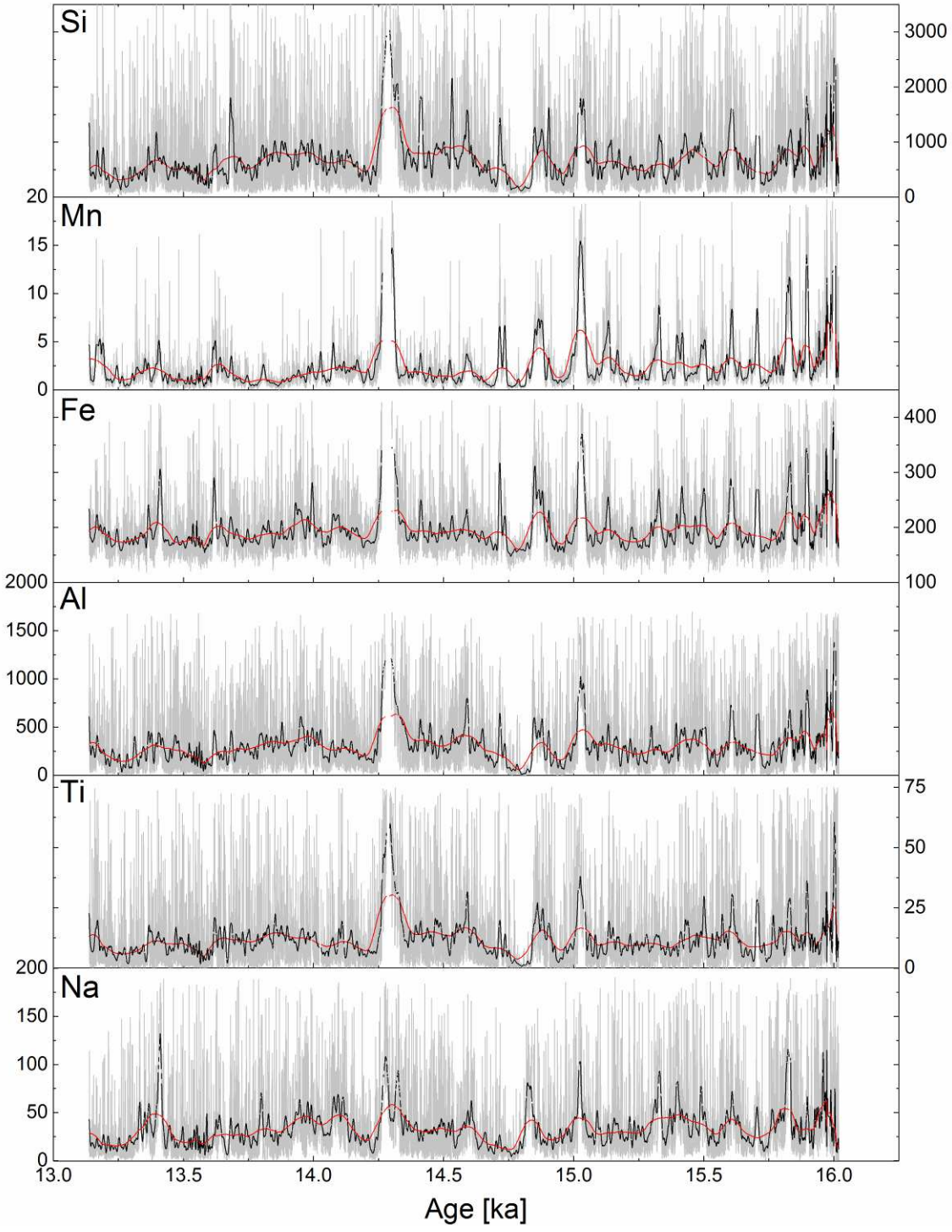

Figure 5.23: Concentrations of trace elements during the second growth period of stalagmite VSMS2 attributed to Group II (Si, Mn, Fe, Ti and Na) in µg/g. Grey lines indicate the original concentrations after all corrections, black lines are 30-pt smoothed data (weighted Adjacent-Averaging), red lines are 300-pt smoothed data.

The records of both elements comprised in Group III, P and U, are shown in Figure 5.24 including Mn for comparison. As in stalagmite VML22 and during the first growth period of VSMS2, P and U evolve in a quasi-identical fashion. This is again consistent with the high Spearman's ρ (0.90) and again indicates a close relation between the processes governing these two signals. Although P and U do not feature a constant baseline concentration as do the Group II elements, the elements of both Groups still share a number of peaks, for instance at 16.1, 15.9, 15.7, 15.3 and especially at 15.0 ka BP, among others. The most prominent peak in P concentrations is centered at 14.9 ka BP. At about 14.5 ka BP, P and U concentrations increase rapidly to reach local maxima at 14.4 ka BP. In contrast to the prior peak-dominated behaviour, from that point on P and U concentrations vary more gradually and exhibit a medium-term decreasing trend, superimposed by high-frequency (multi-decadal) variability, to reach a local minimum at 13.9 ka BP. Until 13.6 ka BP, P and U concentrations gradually increase again and then reach another local minimum at 13.5 ka BP. The last local maximum of the second growth phase occurs at 13.4 ka BP, the last local minimum at 13.3 ka BP.

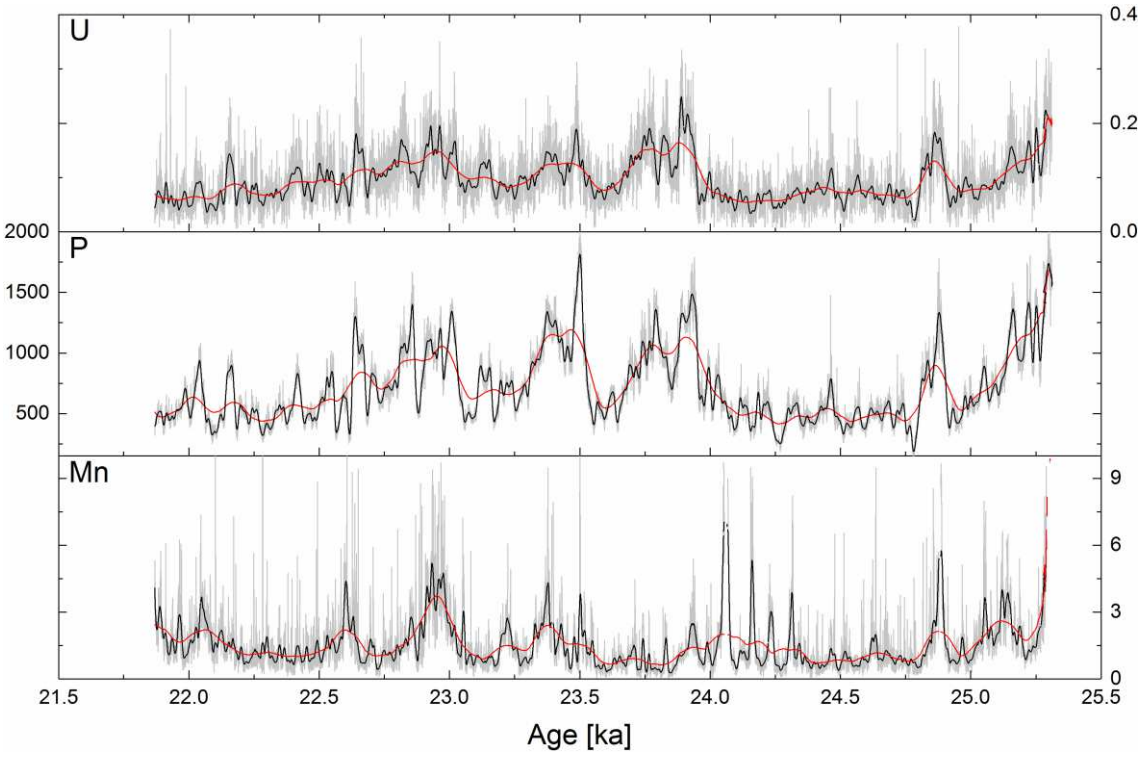

Figure 5.24: Concentrations of trace elements during the second growth period of stalagmite VSMS2 attributed to Group III (P and U) in µg/g including Mn for comparison. Grey lines indicate the original concentrations after all corrections, black lines are 30-pt smoothed data (weighted Adjacent-Averaging), red lines are 300-pt smoothed data.

5.3.2.3 Third growth period

The third growth period of stalagmite VSMS2 ranges from 7.8 ka to 4.9 ka BP. The descriptive statistics for this period are summarised in Table 5.7.

Table 5.7: Descriptive statistics for all trace element data of stalagmite VSMS2 corresponding to its third growth period. Concentrations are given in µg/g.

	n	Minimum	Mean	Median	Maximum
Mg	6462	370.6	862.4	861.4	2861
Sr	6404	2.642	9.005	8.528	23.64
Ba	6327	0.224	3.452	3.071	10.38
Fe	6198	90.57	169.6	150.8	436.9
Mn	5631	0.010	2.125	1.604	15.15
P	6462	32.49	688.1	673.7	2586
Si	6230	20.69	480.5	174.4	3668
Al	6248	0.118	198.1	71.90	1688
Ti	5391	0.111	8.766	3.088	75.35
Na	5365	0.008	28.14	11.88	190.0
U	32	0.016	0.137	0.126	0.290
Cu	5972	0.033	2.512	1.828	11.02
Zn	5643	0.080	19.86	14.00	84.60
Rb	5550	0.002	0.387	0.145	3.031
Cd	4581	0.056	0.479	0.374	2.065

During the first half of the third growth period of stalagmite VSMS2, from 7.8 ka to 6.3 ka BP, Mg concentrations exhibit a slight negative trend (Figure 5.25 and Figure 5.26), varying between about 1,500 and 2,000 µg/g, with the high-frequency variability being of only very low amplitude. From 6.3 ka to 5.7 ka BP, the behaviour of Mg changes and the high-frequency variability features an increased amplitude, while the average Mg concentrations decrease to reach the overall minimum of about 450 µg/g at 5.7 ka BP. Magnesium concentrations then increase to a local maximum at 5.4 ka BP and another local maximum at 5.2 ka BP after a broad trough centered at 5.3 ka BP. From 5.2 ka BP on, Mg concentrations exhibit a negative trend until the end of the third growth period, with the exception of a distinct Mg peak at 5.0 ka BP. During the second half of the third growth period of VSMS2 (6.3 ka to 4.9 ka BP), Mg concentrations behave similarly to $\delta^{13}C$ values (Figure 5.26), but not during the first half. Despite intermediate Spearman's ρ with the elements attributed to Group II, Mg does not share any of their peaks.

Strontium concentrations (Figure 5.25 and Figure 5.26) are relatively constant during the first half of the third growth period (7.8 ka to 6.3 ka BP), except for peaks at 7.8 and between 7.3 and 7.2 ka BP and for low-amplitude minima at 7.7, 7.6, 6.9 and especially at 6.7 ka BP.

During this period, Ba concentrations feature most of the peaks in the concentrations of the Group II elements, for instance at 7.8, 7.3, 7.1, 6.9 ka BP. However, from 6.3 ka to 5.7 ka BP, Sr and Ba concentrations are both noteably increased, in contrast to the reduced Mg concentrations during that period. Until the end of the third growth period at 4.9 ka BP, Sr concentrations remain fairly constant except for a distinct local minimum at 5.3 ka BP. While Ba concentrations also feature this minimum, they increase afterwards to several peaks also evident from the Group II elements, at 5.2, 5.0 and 4.9 ka BP. Overall, the behaviour of Ba during the third growth period can be described as a mixture between the behaviour of Sr and the one of the elements attributed to Group II.

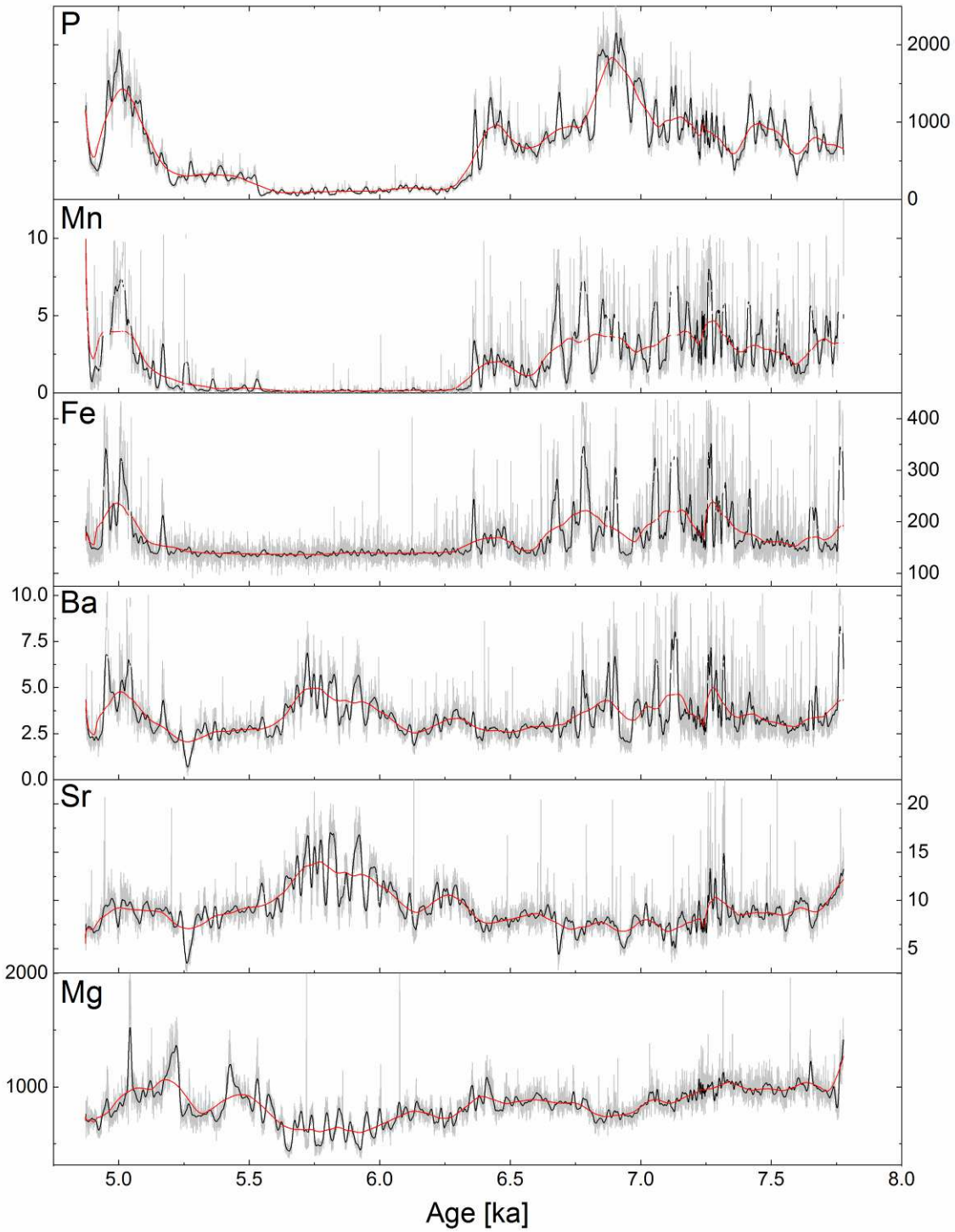

Figure 5.25: Trace element concentrations (in µg/g) of Mg, Sr, Ba, Fe, Mn and P from stalagmite VSMS2 during its third growth period. Grey lines indicate the original concentrations after all corrections, black lines are 30-pt smoothed data (weighted Adjacent-Averaging), red lines are 300-pt smoothed data.

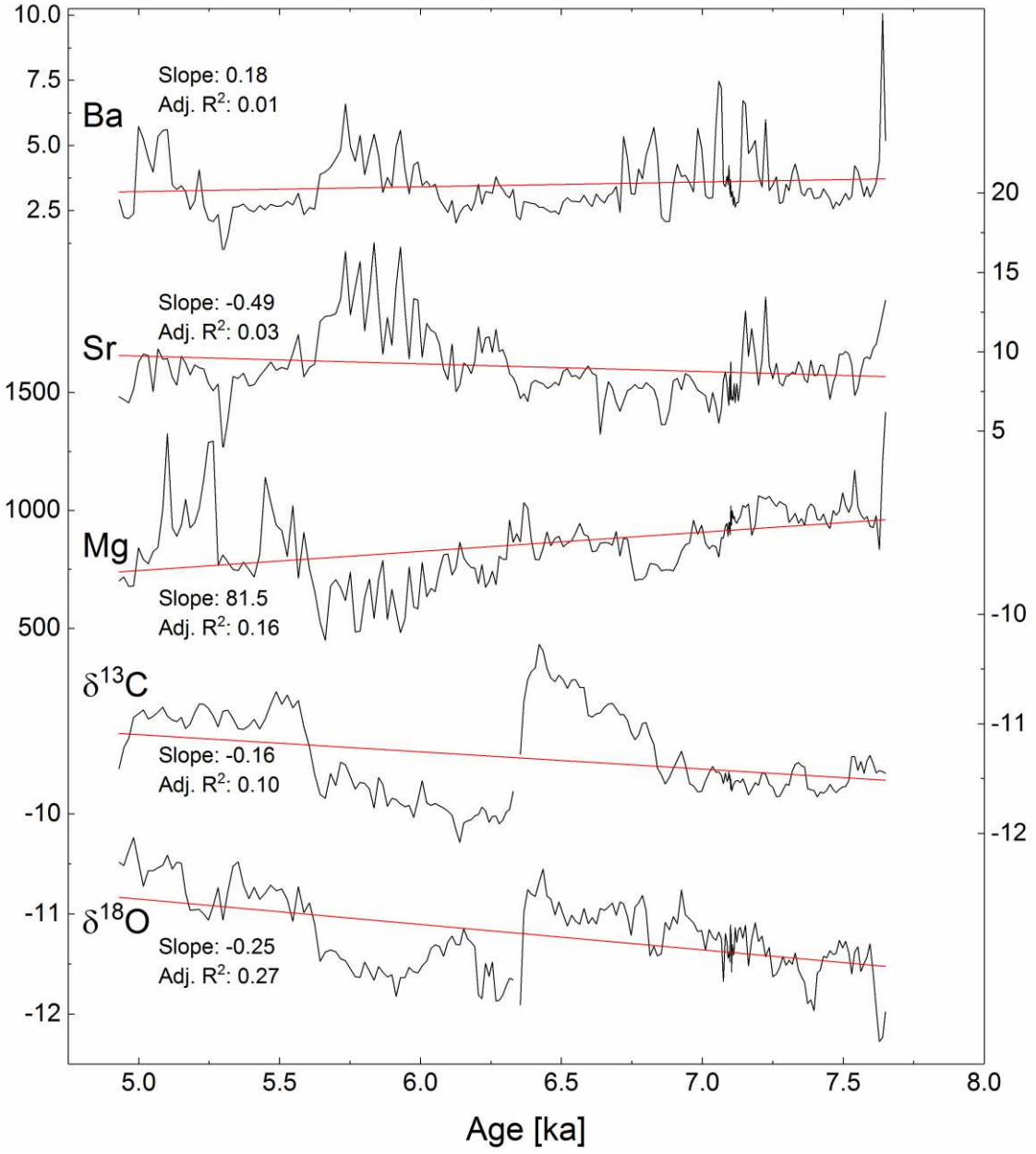

Figure 5.26: Geochemical proxy records during the third growth period of stalagmite VSMS2 attributed to Group I: $\delta^{18}O$, $\delta^{13}C$, Mg, Sr and Ba. Both stable isotope ratios are expressed in ‰ as δ values relative to the V-PDB standard, all trace element concentrations are given in µg/g and are averaged to match the resolution of the isotope data sets (Section 4.6). Linear regression lines are indicated in red.

The elements attributed to Group II (Figure 5.27 and Figure E.7) exhibit high-frequency high-amplitude variability in their concentrations during the first half of the third growth period, with the most prominent peak at 7.1 ka BP and numerous further important peaks, for instance at 7.8, 7.7, 7.3, 7.1, 6.9, 6.8 and 6.7 ka BP, among other smaller peaks. Their virtually identical behaviour is consistent with generally high values of Spearman's ρ (Section 5.6.2.2) calculated for these elements that are even higher than during the first and second growth periods, with Cd as the only exception (Figure E.7) that rather shows similar behaviour to Ba. Intriguingly, during most of the second half of the third growth period, from 6.3 ka to 5.3 ka BP, all elements attributed to Group II feature strongly reduced concentrations, in many cases close to zero. Only Na exhibits a peak at 5.3 ka, among several smaller peaks. From 5.3 ka BP until the end of the third growth period at 4.9 ka BP, Group II elements feature several distinct peaks at 5.2, 5.1, 5.0 and 4.9 ka BP.

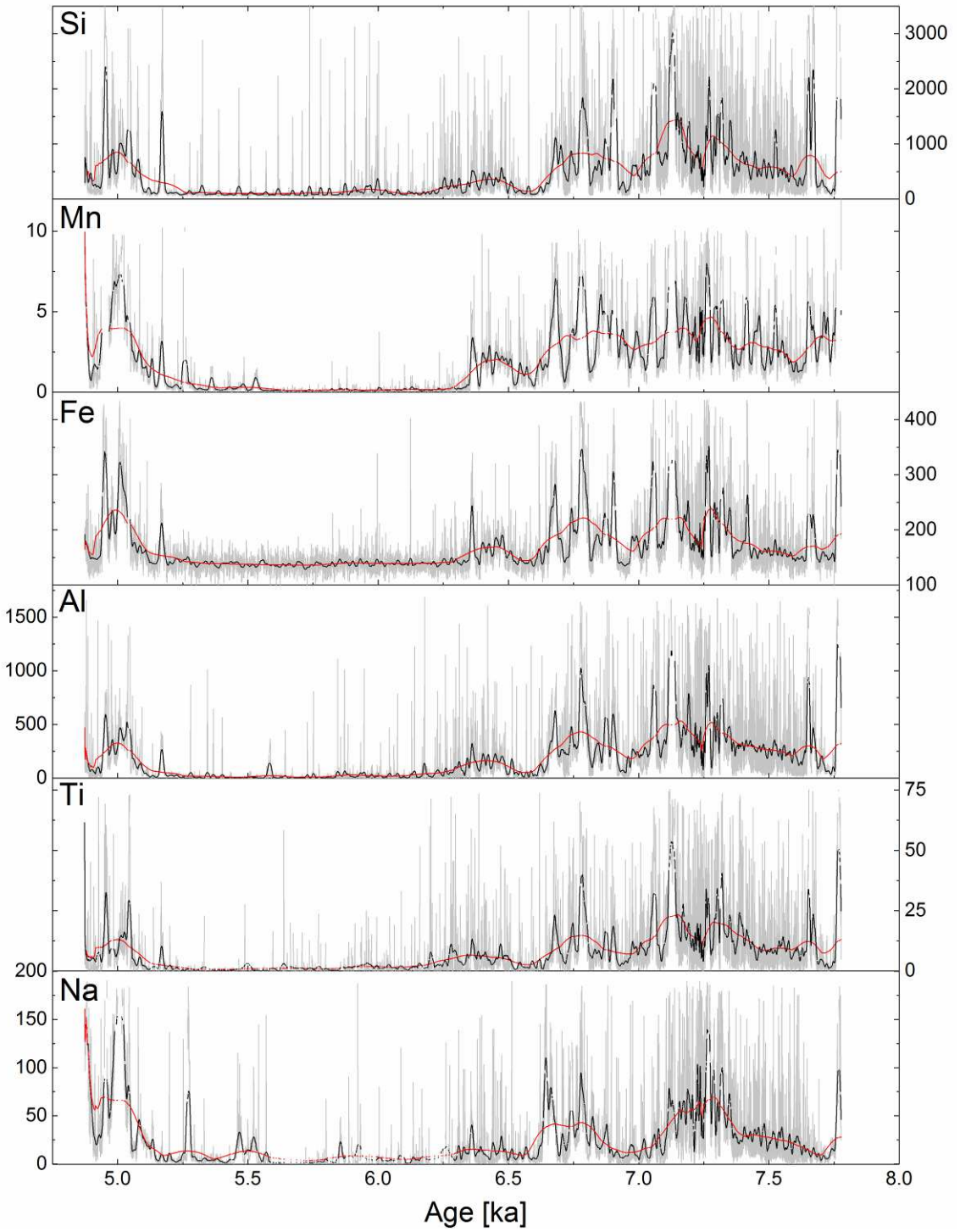

Figure 5.27: Concentrations of trace elements during the third growth period of stalagmite VSMS2 attributed to Group II (Si, Mn, Fe, Ti and Na) in µg/g. Grey lines indicate the original concentrations after all corrections, black lines are 30-pt smoothed data (weighted Adjacent-Averaging), red lines are 300-pt smoothed data.

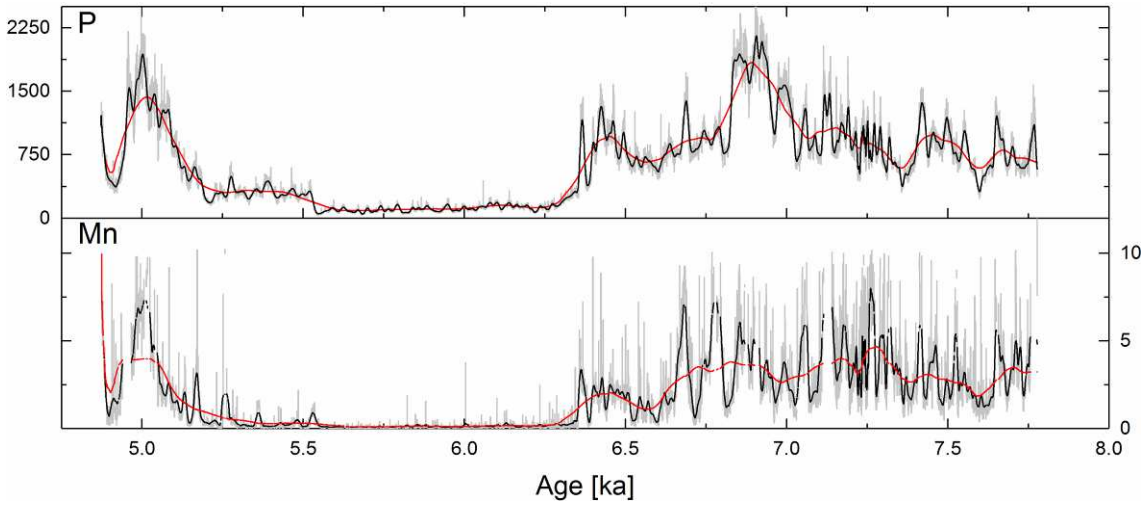

Figure 5.28: Concentrations of P in µg/g representing Group III during the third growth period of stalagmite VSMS2 including Mn for comparison. Grey lines indicate the original concentrations after all corrections, black lines are 30-pt smoothed data (weighted Adjacent-Averaging), red lines are 300-pt smoothed data.

From the two records initially comprised in Group III, only P is shown in Figure 5.28 (including Mn for comparison), as U concentrations are not available for this time period due to high blanks values and low initial U concentrations that produced negative concentrations after blank subtraction. In accordance with high Spearman's ρ values with Group II elements, P shares most of the peaks in concentrations of the Group II elements, for instance at 7.7, 7.4, 7.1, 6.7 and 6.4 ka BP as well as the multiple peaks at the end of the third growth period between 5.3 and 4.9 ka BP. Phosphorus also features strongly reduced concentrations from 6.3 ka to 5.3 ka BP, just as the Group II elements. However, P concentrations also peak at times when Group II elements do not or not as strongly, expecially at 7.0, 6.9 and 6.8 ka BP. In addition to the positive correlation with Group II elements, P is negatively correlated with Sr (Spearman's $\rho = -0.59$).

5.4 Microscopic Analysis

5.4.1 Stalagmite VML22

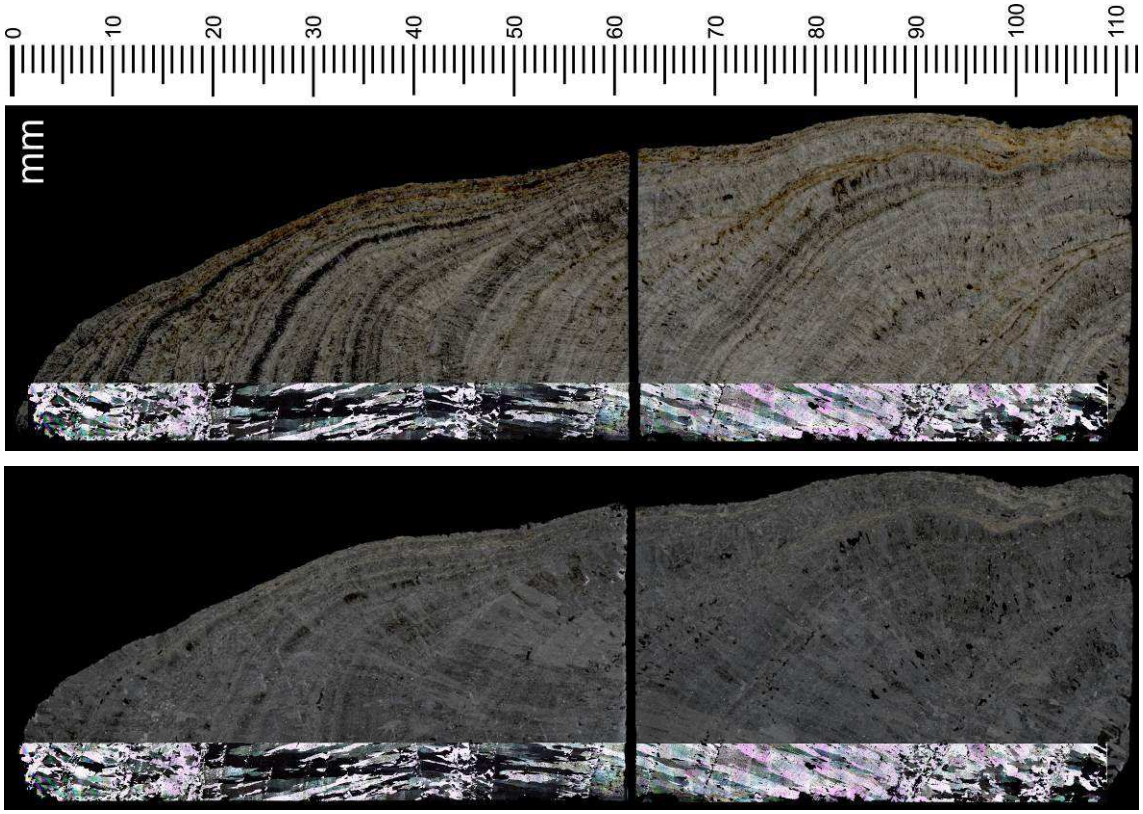

Figure 5.29: Reassembled microscope images (crossed polars) of stalagmite VML22 superimposed on flatbed scans (-15 brightness, +15 contrast) of the corresponding thin slides with a thickness of 200 µm (top) and 50 µm (bottom). The gap between the left and right stalagmite pieces is an inevitable result of thin slide production.

The reassembled microscopic images (crossed polars) of stalagmite VML22 are illustrated in Figure 5.29, superimposed on flatbed scans of the corresponding thin slides with a thickness of 200 µm (top) and 50 µm (bottom). Microstratigraphic logging according to Frisia (2015) was conducted on the line along which stable isotope and trace element analyses were performed, at the bottom edge of the images in Figure 5.29 (corresponding to the left edge of the images in Figure 5.30).

In stalagmite VML22, five different fabric types were identified: Columnar elongated (Ce), Columnar elongated with lateral overgrowth (Celo), Columnar microcrystalline (Cm), Mosaic calcite (Mc) and Micrite (M). The microstratigraphic log for the two pieces of stalagmite VML22 is shown in Figure 5.30 (left two images).

The microstratigraphic log of the bottom stalagmite piece spans the depth range from 109 mm to 62.5 mm DFT. From the stalagmite base to DFT 78.4 mm, the fabric type Cm is clearly dominating, with only two limited depth intervals featuring the fabric type Mc, from DFT 102.9 mm to 101.1 mm and from DFT 90.1 mm to 87.2 mm. Above DFT 75.4 mm, the fabric types are mainly Cm, from DFT 70.6 mm to 66.9 mm, and Ce in the depth range 78.3 mm to 70.7 mm DFT and 66.8 mm to 62.5 mm DFT. The two only exceptions are a potential minor hiatus (H) at 69 mm DFT and the fabric Celo at 63 mm DFT.

The microstratigraphic log of the top stalagmite piece spans the depth range from 61.3 mm to 0 mm DFT and is noteably more varied than that of the bottom stalagmite piece. Up to DFT 19.7, the dominant fabric type is Ce that is often alternating with the fabric type Celo. Columnar microcrystalline fabrics are restricted to DFT 57.5 – 55.1 mm and DFT 45.9 – 43.3 mm, including fabrics of the Mc type at DFT 45.3 – 44.2 mm. There are also multiple small Micrite layers, at 36, 34.7, 29.6 20.3 and 19.6 mm DFT. The depth range DFT 20 mm to 0 mm mostly comprises more complicated fabric types such as Cm and Mc, while the types Ce and Celo are restricted to the depth ranges DFT 9.5 – 6.6 mm and DFT 6.5 – 5.3 mm, respectively.

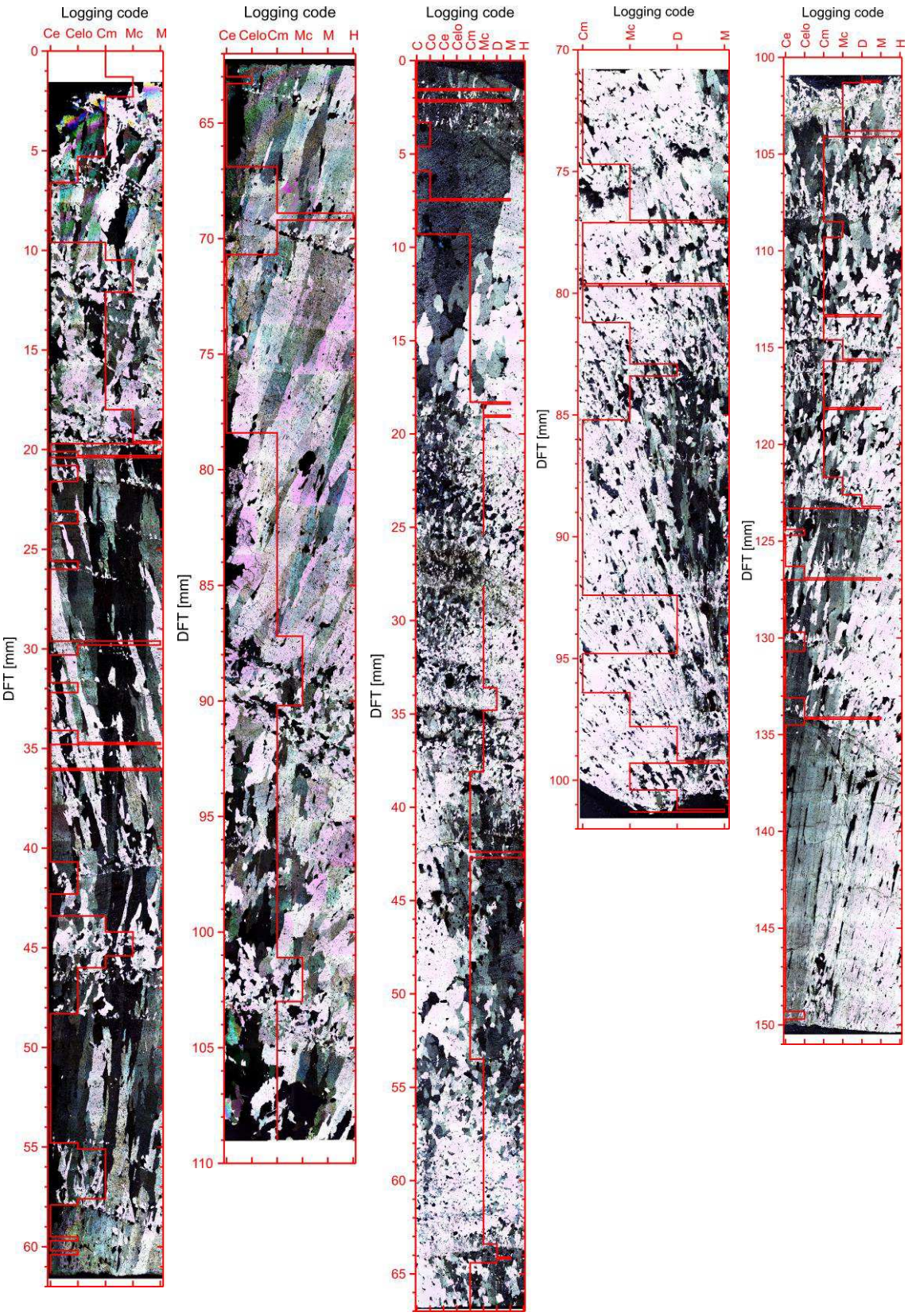

Figure 5.30: Microstratigraphic logs for stalagmites VML22 (left two) and VSMS2 (right three) superimposed on the corresponding thin slides (reassembled microscopic images aquired with crossed polars). Fabric types according to Frisia (2015): C = Columnar; Co = Columnar open; Ce = Columnar elongated; Celo = Ce with lateral overgrowth; Cm = Columnar microcrystalline; D = Dendritic; M = Micrite; Mc = Mosaic calcite; H = Hiatus. The log refers to the left edge of each image.

5.4.2 Stalagmite VSMS2

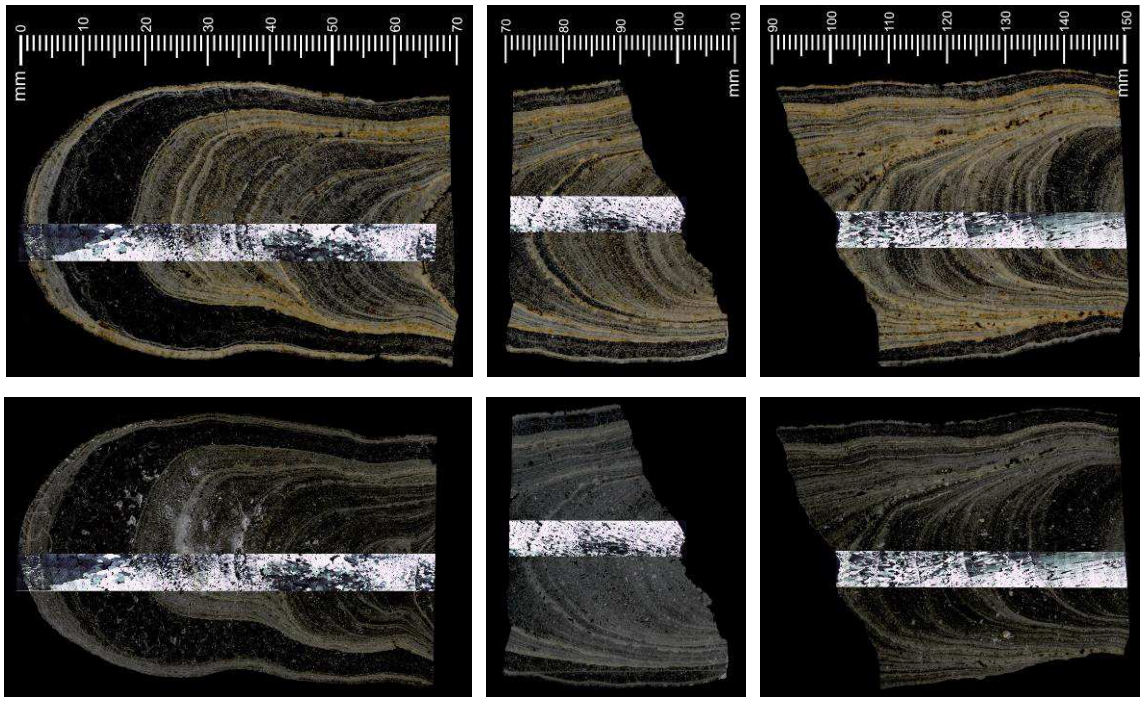

Figure 5.31: Reassembled microscope images (crossed polars) of stalagmite VSMS2 superimposed on flatbed scans (-15 brightness, +15 contrast) of the corresponding thin slides with a thickness of 200 µm (top) and 50 µm (bottom). The gap between the stalagmite pieces in a row is an inevitable result of thin slide production.

The reassembled microscopic images (crossed polars) of stalagmite VSMS2 are illustrated in Figure 5.31, superimposed on flatbed scans of the corresponding thin slides with a thickness of 200 µm (top) and 50 µm (bottom). For comparison with stable isotope and trace element data, microstratigraphic logging according to Frisia (2015) was conducted along the top edge of the microscope images in Figure 5.31 (corresponding to the left edge of the images in Figure 5.30).

In stalagmite VSMS2, eight different fabric types were identified: Columnar (C), Columnar open (Co), Columnar elongated (Ce), Columnar elongated with lateral overgrowth (Celo), Columnar microcrystalline (Cm), Mosaic calcite (Mc), Dendtritic (D) and Micrite (M). The microstratigraphic log for the three pieces of stalagmite VSMS2 is shown in Figure 5.30 (right three images).

The microstratigraphic log of the bottom stalagmite piece spans the depth range from 149.9 mm to 101.2 mm DFT. From the stalagmite base to DFT 123.3 mm, the fabric type Ce is clearly dominating, alternating multiple times with the Celo type at 149.5, 133.8, 130.2, 126.6 and 124.5 mm DFT.

Micrite layers are present at 134.1 mm DFT and 126.9 9 mm DFT. From 123.3 mm and 104.1 mm DFT, the dominating fabric type is Cm instead of Ce, with some sections featuring the Mc type, at 122.2, 115.1 and 108.9 mm DFT. At 122.9 mm DFT, the fabric is even dentritic, while further Micrite layers are present at 123.2, 118.1, 115.6, 113.3 and 101.2 mm DFT. This section is clearly separated from the next section by a distinct hiatus at 103.9 mm DFT. Above that hiatus, the fabric type Mc dominates with another dendritic section at DFT 101.1 -100.4 mm above a micrite layer at 101.2 mm DFT.

The microstratigraphic log of the top stalagmite piece spans the depth range from 66.7 mm to 0 mm DFT. Up to 9.3 mm DFT, the fabrics are mostly of the Cm and the Mc type. Dendritic layers are present at DFT 64.3 – 63.4 mm and DFT 34.7 – 33.6 mm, with thin layers of micrite type fabrics at 64.1, 19 and 18.3 mm DFT. At 42.5 mm DFT there is a distinct hiatus. In the depth range 28.1 - 25.5 mm DFT, the fabric could not be attributed ot any of the fabric types defined by Frisia (2015). I t can be described as erratic and disorderly with small crystal sizes around 100 µm diameter and diffuse crystal boundaries and likely increased contamination with foreign material. The depth range from 9.2 mm up to the stalagmite top is dominated by less complex fabrics comprising the C and the Co type, but still includes micrite layers at 7.4, 2.1 and 1.5 mm DFT.

5.5 XRD Results

All XRD analyses confirm that calcite is the predominant mineral phase in both stalagmite VML22 and stalagmite VSMS2, while aragonite was not identified, as illustrated in Figure 5.32 to Figure 5.38.

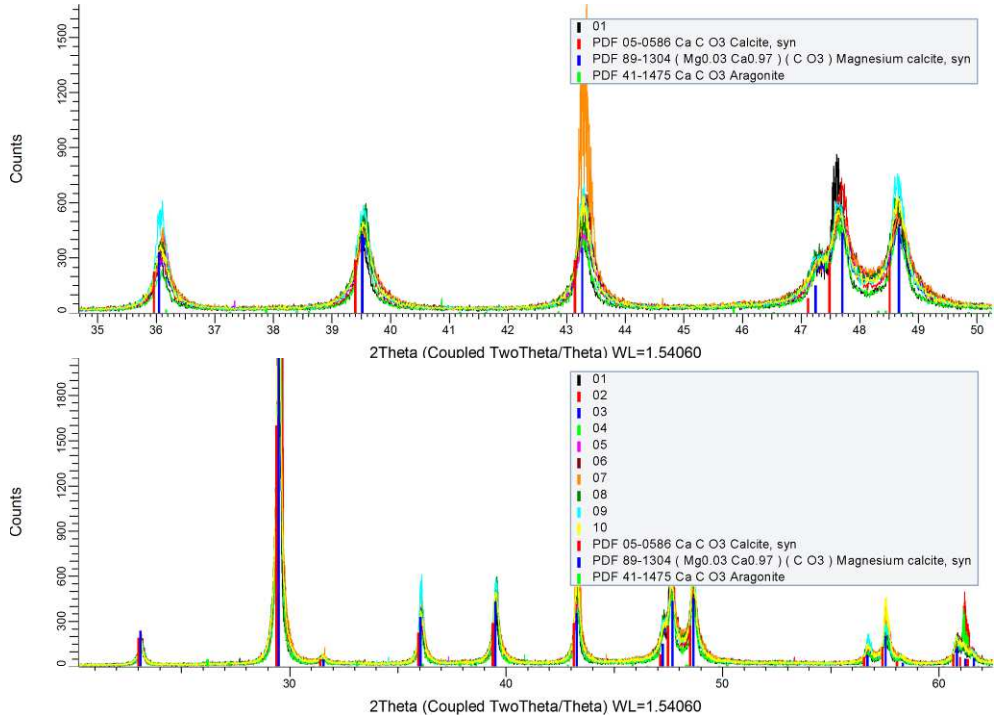

Figure 5.32: X-ray diffractograms for samples 01 to 10 from stalagmite VML22 including the peak positions of synthetic calcite, synthetic Mg-calcite and aragonite for reference (vertical bars); top: detail; bottom: overview. For better readability samples 02 to 10 are not included in the legend of the top sub-plot.

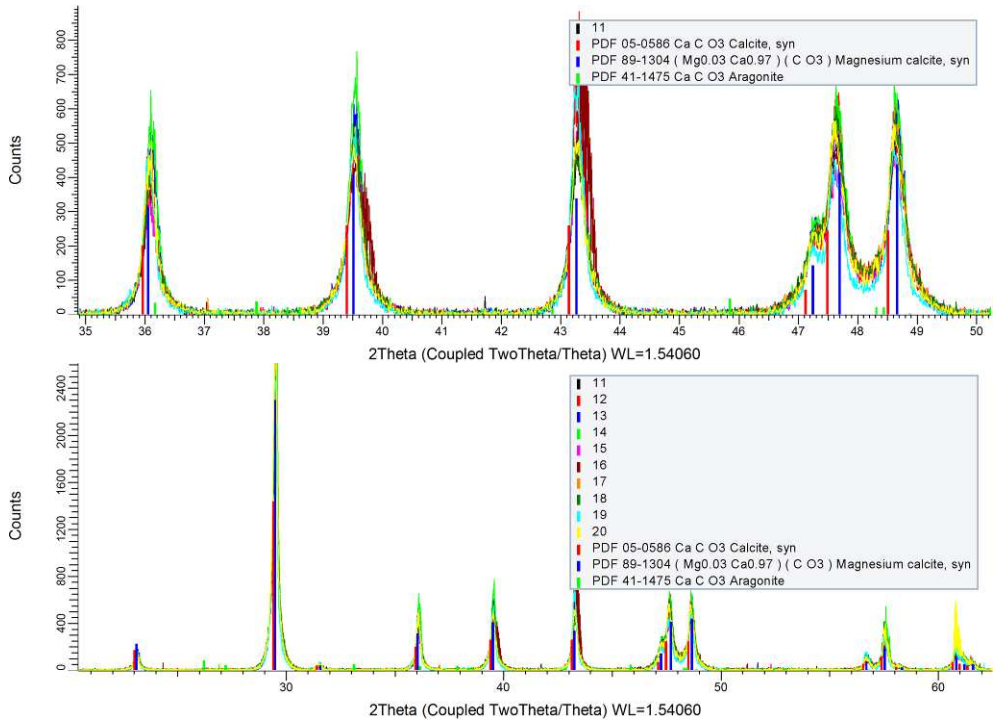

Figure 5.33: As Figure 5.32, but for samples 11 to 20.

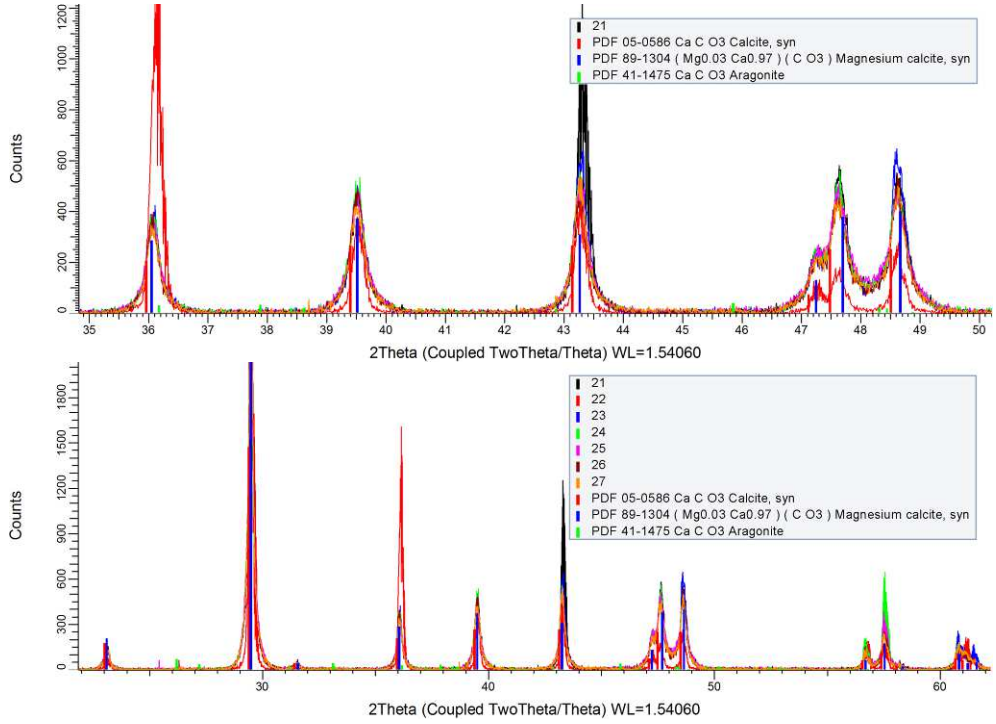

Figure 5.34: As Figure 5.32, but for samples 21 to 27.

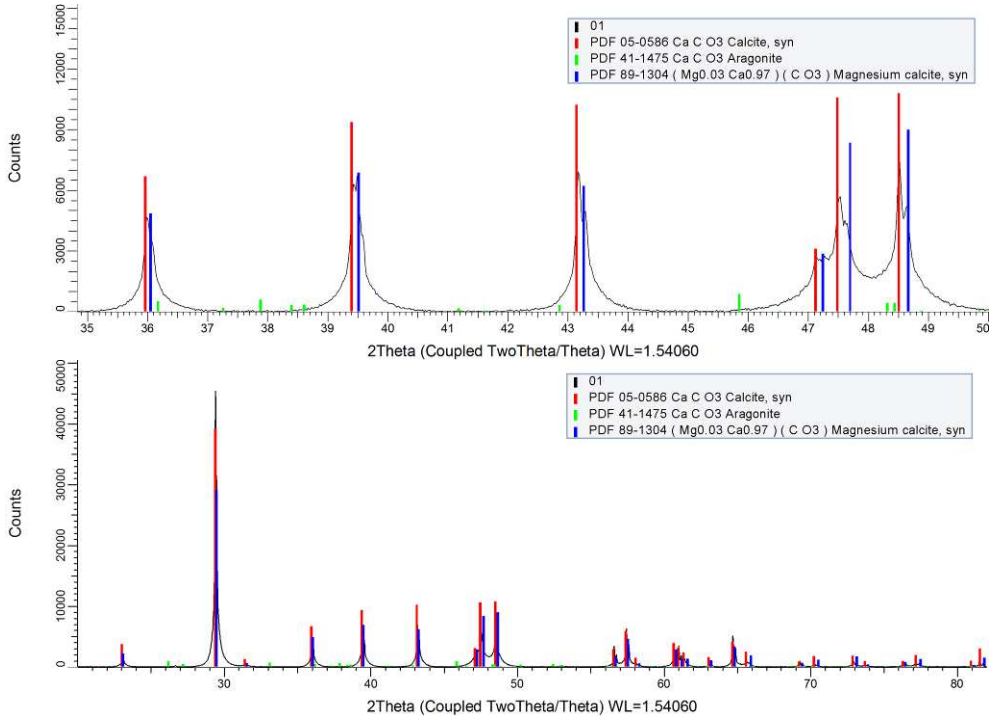

Figure 5.35: X-ray diffractograms for sample 01 from stalagmite VSMS2 (black line) including the peak positions of synthetic calcite, synthetic Mg-calcite and aragonite for reference (vertical bars); top: detail; bottom: overview.

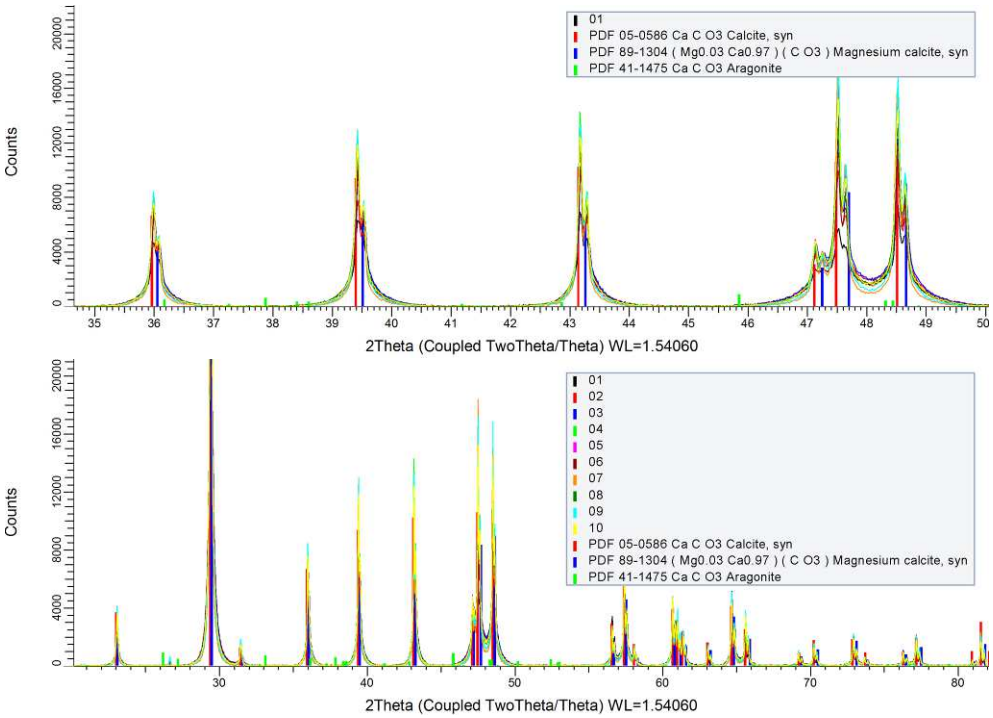

Figure 5.36: As All XRD analyses confirm that calcite is the predominant mineral phase in both stalagmite VML22 and stalagmite VSMS2, while aragonite was not identified, as illustrated in Figure 5.32 to , but for samples 01 to 10. For better readability samples 02 to 10 are not included in the legend of the top sub-plot.

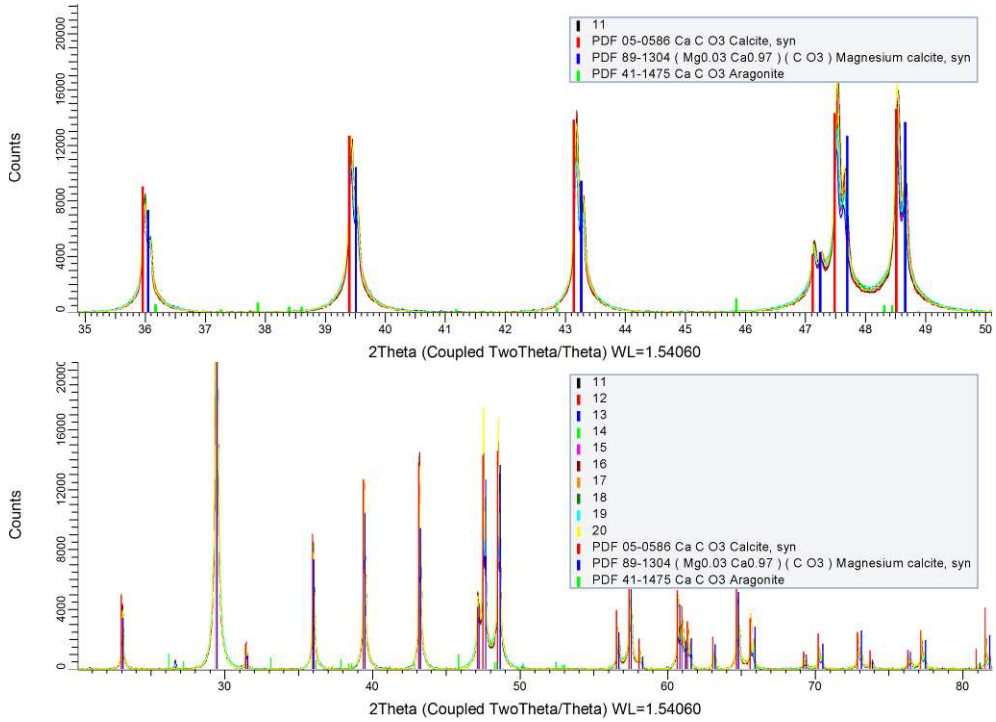

Figure 5.37: As All XRD analyses confirm that calcite is the predominant mineral phase in both stalagmite VML22 and stalagmite VSMS2, while aragonite was not identified, as illustrated in Figure 5.32 to , but for samples 11 to 20.

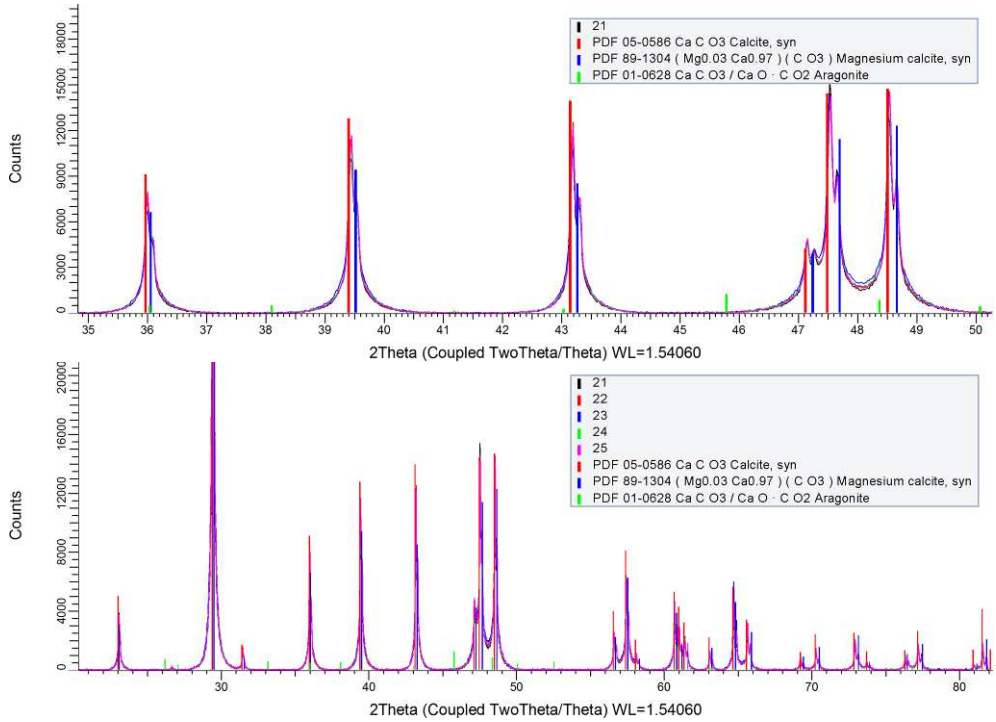

Figure 5.38: As All XRD analyses confirm that calcite is the predominant mineral phase in both stalagmite VML22 and stalagmite VSMS2, while aragonite was not identified, as illustrated in Figure 5.32 to , but for samples 21 to 25.

5.6 Statistical Analyses

5.6.1 Histograms

5.6.1.1 Stalagmite VML22

Figure 5.39 depicts the histograms of the geochemical records of stalagmite VML22 for $\delta^{18}O$, $\delta^{13}C$, Mg, Sr, Ba Fe, Mn and P. The histograms for Si, Al, Na, U, Cu, Zn, Rb and Cd are illustrated in Figure 5.40. Each plot also contains the absolute frequency density for a hypothetical normal distribution (indicated by a solid black line). Based on their histograms the geochemical signals of stalagmite VML22 can be divided into three groups:

One group of elements clearly features a right-skewed distribution. This group includes Mn, Al, Na, Cu, Zn and Rb. These are the elements present in the stalagmite at only low concentrations or at concentrations close to the detection limit of the LA-ICP-MS. The second group only contains Cd that shows a bimodal distribution and also low concentrations in the stalagmite. The third and largest group comprises the remaining geochemical records analysed in VML22, namely $\delta^{18}O$, $\delta^{13}C$, Mg, Sr, Ba, Fe, P, Si as well as U. All these proxy signals seem to show a normal distribution and their absolute frequency density appears to be a close match to the respective hypothetical normal distribution curve.

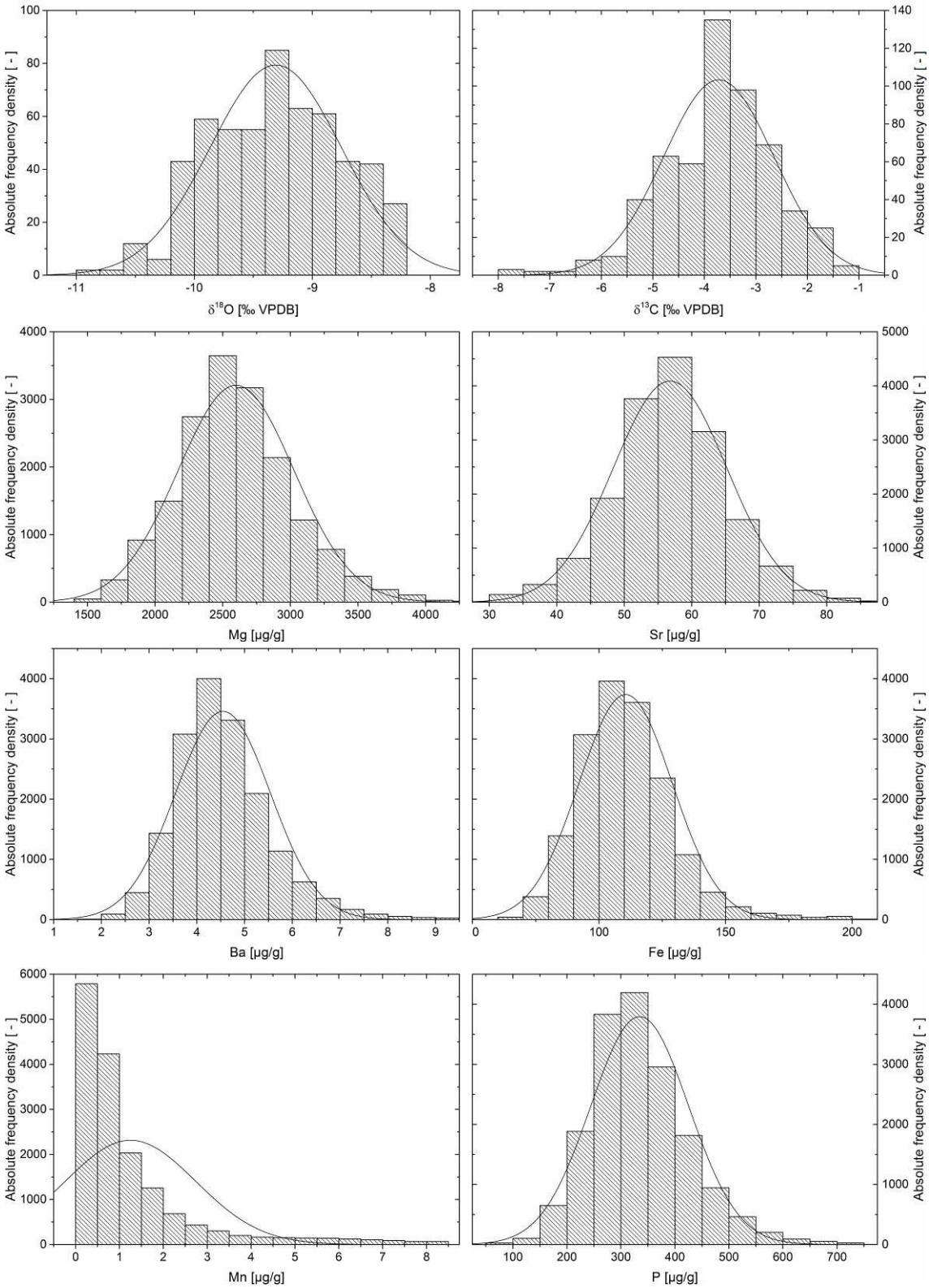

Figure 5.39: Histograms of the geochemical records of stalagmite VML22 for $\delta^{18}O$, $\delta^{13}C$, Mg, Sr, Ba Fe, Mn and P. The solid black line illustrates the absolute frequency density for a hypothetical normal distribution of the data in each graph.

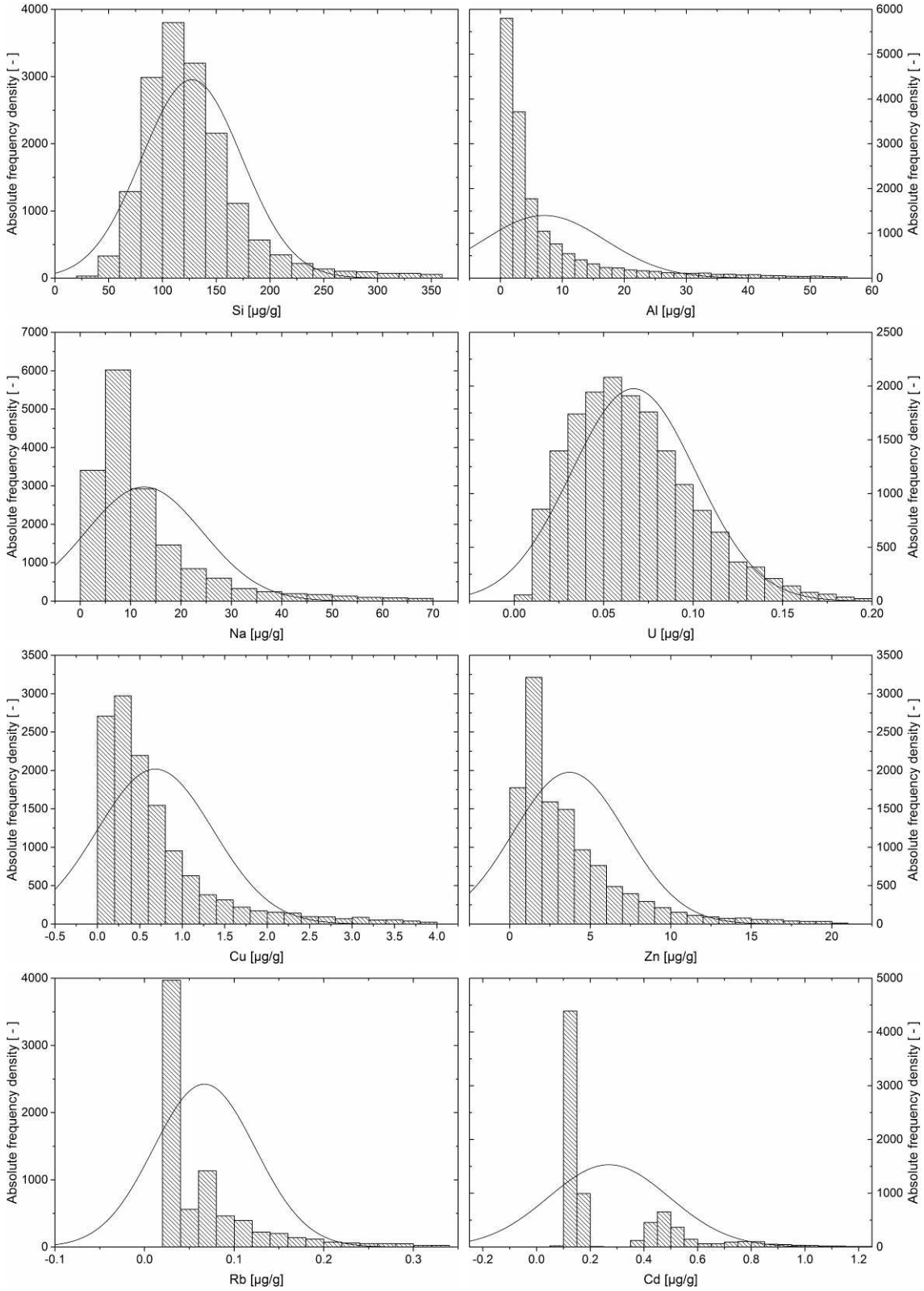

Figure 5.40: Histograms of the geochemical records of stalagmite VML22 for Si, Al, Na, U, Cu, Zn, Rb and Cd. The solid black line illustrates the absolute frequency density for a hypothetical normal distribution of the data in each graph.

5.6.1.2 Stalagmite VSMS2

Figure 5.41 depicts the histograms of the geochemical records of stalagmite VSMS2 for $\delta^{18}O$, $\delta^{13}C$, Mg, Sr, Ba Fe, Mn and P. The histograms for Si, Al, Na, U, Cu, Zn, Rb and Cd are illustrated in Figure 5.42. Each plot also contains the absolute frequency density for a hypothetical normal distribution (indicated by a solid black line). Similarly to stalagmite VML22, based on their histograms the geochemical signals of stalagmite VSMS2 can be divided into three groups:

One group of elements clearly features a right-skewed distribution. This group includes Fe, Mn, Si, Al, Na, Cu, Zn, Rb, Cd and Ti. Contrarily to stalagmite VML22, these elements are only partly present in the stalagmite at low concentrations or at concentrations close to the detection limit of the LA-ICP-MS (e.g. Rb), whereas some of the elements belonging to that group are present at high concentrations, such as Fe, Al and especially Si. The second group contains $\delta^{18}O$ and $\delta^{13}C$ that rather show a bimodal than a normal distribution, in consistence with the difference in values between the three growth periods of stalagmite VSMS2. The third group comprises the remaining geochemical records analysed in VSMS2, namely, Mg, Sr, Ba, P and U. All these signals seem to show a normal distribution and their absolute frequency density appears to be a close match to the respective hypothetical normal distribution curve.

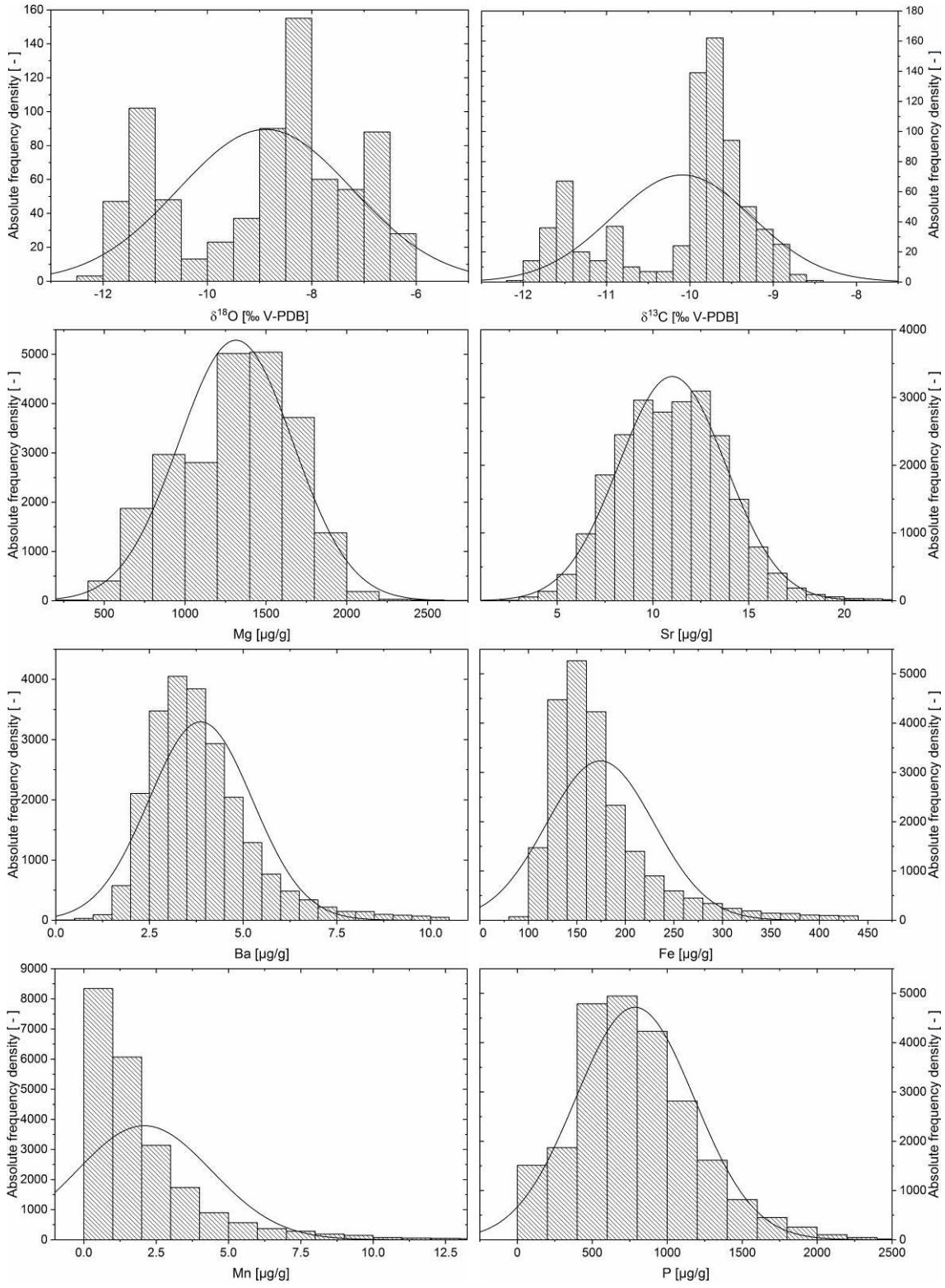

Figure 5.41: Histograms of the geochemical records of stalagmite VSMS2 for $\delta^{18}O$, $\delta^{13}C$, Mg, Sr, Ba Fe, Mn and P. The solid black line illustrates the absolute frequency density for a hypothetical normal distribution of the data in each graph.

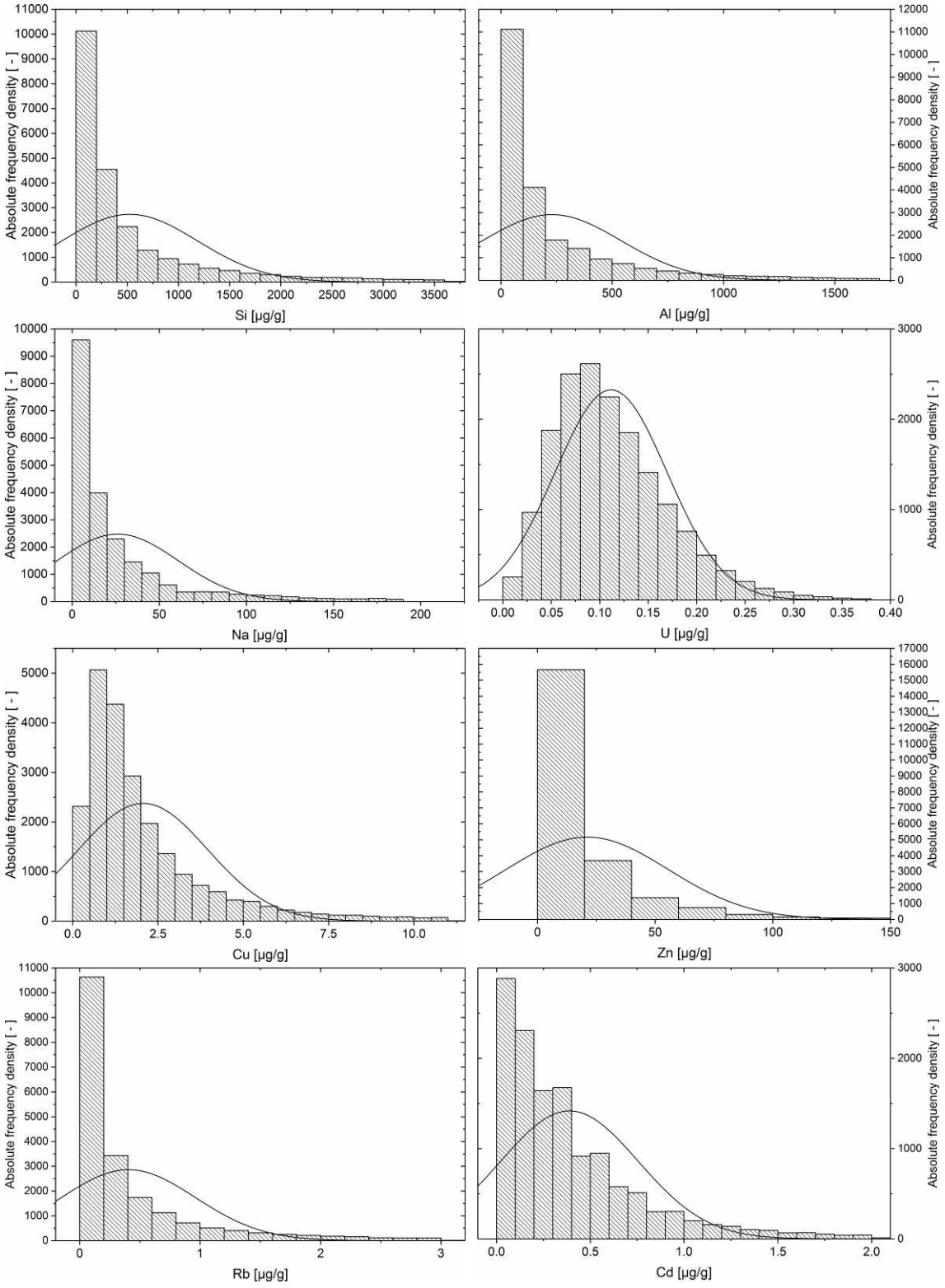

Figure 5.42: Histograms of the geochemical records of stalagmite VSMS2 for Si, Al, Na, U, Cu, Zn, Rb and Cd. The solid black line illustrates the absolute frequency density for a hypothetical normal distribution of the data in each graph.

5.6.2 Correlation Matrices

5.6.2.1 Stalagmite VML22

The Spearman's rank coefficients (ρ) were calculated for all geochemical records of stalagmite VML22 analysed in this study and are summarised as a matrix in Table 5.8. For the calculation of the coefficients, all trace element data were averaged to correspond to the isotope data sets as described in Section 4.6. Out of the 120 correlation coefficients, 43 indicate a positive correlation with $\rho \geq 0.3$ whereas only three indicate a negative correlation with $\rho \leq -0.3$. Twenty values in total are not significant at the 0.05 level, using the 2-tailed test of significance in the Origin software. All other values have passed the significance test.

Based on this correlation matrix, two main groups of geochemical records can be distinguished in the case of stalagmite VML22, as illustrated by two separate clusters of values with green shading indicating positive correlation in Table 5.8:

Group I comprises $\delta^{18}O$, $\delta^{13}C$, Mg, Sr and Ba that are all positively correlated to one another, with values of ρ ranging from 0.35 ($\delta^{13}C$ vs. Ba) to 0.88 (Sr vs. Ba), the latter representing the highest ρ value in the entire matrix. Apart from that maximum value, particularly high ρ values are achieved in the case of $\delta^{18}O$ vs. $\delta^{13}C$ (0.67), of $\delta^{18}O$ vs. Mg (0.71) and of $\delta^{13}C$ vs. Mg (0.70).

Group II contains Mn, Si, Al, Na, Cu, Zn and Rb, although Zn is less strongly correlated with the other elements of the group, with ρ values not exceeding 0.54 (Zn vs. Rb). In this group, ρ values range from 0.40 (Na vs. Zn) to 0.74 (Na vs. Cu). Particularly high ρ values are also achieved in the case of Na vs. Al (0.72) as well as of Mn vs. Al (0.68), Al vs. Rb (0.63), Si vs. Al (0.63) and Mn vs. Cu (0.62).

Iron appears to be positively correlated to elements of both groups mentioned above, although correlation coefficients are generally lower than within these two distinct groups. The strongest correlation of Fe and any other analysed element is with Na, with a ρ value of 0.58.

Phosphorus stands out amongst all studied geochemical signals, being the only element that is positively correlated with elements of Group II, with ρ values ranging from 0.24 to 0.34, but negatively correlated with elements of Group I. The strongest negative correlation of P and any other analysed element is with Sr, with a ρ value of -0.43. Correlation between P and Mg is also negative ($\rho = -0.36$). Although the correlation coefficients between P and the remaining elements of Group I are above -0.3, the correlation matrix suggests that these are also negatively correlated with P (e.g. $\rho(\delta^{13}C$ vs. P) = -0.24). Phosphorus is extraordinary in yet another way: It is the only element that shows any noteworthy correlation with U, the corresponding ρ value (0.72) being one of the highest in the entire matrix. Therefore P and U are attributed to Group III.

Apart from P, only Zn is negatively correlated with another element of the VML22 data set, namely with Mg ($\rho = -0.31$).

Table 5.8: Matrix of Spearman's rank correlation coefficients (ρ) for all geochemical records of stalagmite VML22 analysed in this study. Positive correlations are highlighted in green, negative correlations in red, with the strength of the correlation increasing with respective colour depth. All trace element data are averaged to correspond to the isotope data sets as described in Section 4.6. All values that are not significant at the 0.05 level (using the two-tailed test of significance) are shaded in grey.

	$\delta^{13}C$	$\delta^{18}O$	Mg	Sr	Ba	Fe	Mn	Si	Al	Na	Cu	Zn	Rb	P	U	Cd
$\delta^{13}C$	1	0.67	0.70	0.46	0.35	0.35	-0.01	-0.15	0.14	0.28	0.13	-0.17	-0.01	-0.27	-0.21	0.14
$\delta^{18}O$	0.67	1	0.71	0.54	0.47	0.48	-0.05	-0.22	0.04	0.29	0.11	-0.26	-0.08	-0.23	-0.01	0.12
Mg	0.70	0.71	1	0.51	0.40	0.36	-0.15	-0.22	0.00	0.13	0.00	-0.31	-0.14	-0.36	-0.14	0.09
Sr	0.46	0.54	0.51	1	0.87	0.27	-0.01	-0.02	0.06	0.25	0.14	-0.01	0.02	-0.43	-0.15	0.16
Ba	0.35	0.47	0.40	0.87	1	0.33	0.11	0.12	0.21	0.39	0.27	0.15	0.18	-0.26	0.02	0.16
Fe	0.35	0.48	0.36	0.27	0.33	1	0.30	0.25	0.49	0.58	0.48	0.14	0.29	0.19	0.13	0.06
Mn	-0.01	-0.05	-0.15	-0.01	0.11	0.30	1	0.49	0.68	0.55	0.62	0.53	0.52	0.31	0.15	0.07
Si	-0.15	-0.22	-0.22	-0.02	0.12	0.25	0.49	1	0.63	0.43	0.52	0.52	0.54	0.30	0.27	0.08
Al	0.14	0.04	0.00	0.06	0.21	0.49	0.68	0.63	1	0.72	0.67	0.47	0.63	0.34	0.17	0.06
Na	0.28	0.29	0.13	0.25	0.39	0.58	0.55	0.43	0.72	1	0.74	0.40	0.55	0.39	0.24	0.08
Cu	0.13	0.11	0.00	0.14	0.27	0.48	0.62	0.52	0.67	0.74	1	0.53	0.57	0.32	0.17	0.10
Zn	-0.17	-0.26	-0.31	-0.01	0.15	0.14	0.53	0.52	0.47	0.40	0.53	1	0.54	0.24	0.17	0.10
Rb	-0.01	-0.08	-0.14	0.02	0.18	0.29	0.52	0.54	0.63	0.55	0.57	0.54	1	0.25	0.13	0.14
P	-0.27	-0.23	-0.36	-0.43	-0.26	0.19	0.31	0.30	0.34	0.39	0.32	0.24	0.25	1	0.72	-0.06
U	-0.21	-0.01	-0.14	-0.15	0.02	0.13	0.15	0.27	0.17	0.24	0.17	0.17	0.13	0.72	1	0.03
Cd	0.14	0.12	0.09	0.16	0.16	0.06	0.07	0.08	0.06	0.08	0.10	0.10	0.14	-0.06	0.03	1

5.6.2.2 Stalagmite VSMS2

Spearman's rank coefficients (ρ) were calculated for all geochemical records of stalagmite VSMS2 analysed in this study and are summarised as a matrix in Table 5.9. For the calculation of the coefficients, all trace element data were averaged to correspond to the isotope data sets as described in Section 4.6. Out of the 153 correlation coefficients, 89 indicate a positive correlation with $\rho \geq 0.3$ whereas only one indicates a negative correlation with $\rho \leq -0.3$. Twenty-three values in total are not significant at the 0.05 level, using the 2-tailed test of significance in the Origin software. All other values have passed the significance test.

Based on this correlation matrix, two main groups of geochemical records can be distinguished in the case of stalagmite VSMS2, as illustrated by two separate clusters of values with green shading indicating positive correlation in Table 5.9:

Group I comprises $\delta^{18}O$, $\delta^{13}C$, Mg, Sr and Ba that are all positively correlated to one another, with values of ρ ranging from 0.12 ($\delta^{13}C$ vs. Ba and $\delta^{18}O$ vs Ba) to 0.75 ($\delta^{13}C$ vs. $\delta^{18}O$). Apart from that maximum value, particularly high ρ values are achieved in the case of $\delta^{13}C$ vs. Mg (0.64) and of $\delta^{18}O$ vs. Mg (0.50). Barium is also positively correlated with elements of Group II, with values of ρ of up to 0.30 (Ba vs. Fe).

Group II contains most of the remaining elements: Fe, Mn, Si, Al, Ti, Na, Cu, Zn, Rb, Th and Cd, with Cd being the least strongly correlated with the other elements of the group, with ρ values not exceeding 0.55 (Cd vs. Zn). In this group, ρ values range from 0.30 (Th vs. Cd) to 0.89 (Al vs. Si and Al vs. Rb). Particularly high ρ values are also achieved in the case of Rb and Fe in general, for instance vs. Al (0.89 and 0.85) and Si (0.89 and 0.83). Cadmium is also negatively correlated with elements of Group I, with ρ values of -0.33 vs. Mg and -0.27 vs. $\delta^{13}C$. Apart from these element pairs, only Mn and Sr are also negatively correlated with a ρ value close to -0.3 (-0.28).

The strongest positive correlation in the entire matrix is the one between P and U ($\rho = 0.90$), on the basis of which both elements can be attributed to Group III. Contrarily to stalagmite VML22, P and U in VSMS2 also correlate positively with elements of Group II with maximum ρ values of 0.54 (P vs. Cu) and 0.70 (U vs. Cu). Overall, the positive correlation of U with the Group II elements is slightly stronger than that of P.

Table 5.9: Matrix of Spearman's rank correlation coefficients (ρ) for all geochemical records of stalagmite VSMS2 analysed in this study. Positive correlations are highlighted in green, negative correlations in red, with the strength of the correlation increasing with respective colour depth. All trace element data are averaged to correspond to the isotope data sets as described in Section 4.6. All values that are not significant at the 0.05 level (using the two-tailed test of significance) are shaded in grey.

	$\delta^{13}C$	$\delta^{18}O$	Mg	Sr	Ba	Fe	Mn	Si	Al	Ti	Na	Cu	Zn	Rb	Th	Cd	P	U
$\delta^{13}C$	1	0.75	0.64	0.25	0.12	-0.07	0.01	0.01	0.01	0.02	-0.05	-0.13	-0.14	-0.01	0.00	-0.27	0.17	0.09
$\delta^{18}O$	0.75	1	0.50	0.24	0.12	0.15	0.10	0.19	0.19	0.19	0.16	-0.02	0.10	0.17	0.05	-0.10	0.17	0.23
Mg	0.64	0.50	1	0.36	0.21	-0.09	-0.05	-0.02	-0.01	0.01	-0.08	-0.13	-0.15	-0.04	-0.05	-0.33	0.07	-0.15
Sr	0.25	0.24	0.36	1	0.69	0.06	-0.28	0.01	-0.01	0.04	0.05	-0.13	-0.07	0.00	-0.12	-0.12	-0.11	-0.09
Ba	0.12	0.12	0.21	0.69	1	0.39	0.19	0.37	0.35	0.34	0.28	0.31	0.28	0.38	0.28	0.18	0.36	0.34
Fe	-0.07	0.15	-0.09	0.06	0.39	1	0.70	0.83	0.85	0.79	0.74	0.66	0.68	0.85	0.64	0.42	0.46	0.36
Mn	0.01	0.10	-0.05	-0.28	0.19	0.70	1	0.67	0.70	0.61	0.59	0.78	0.69	0.70	0.62	0.36	0.64	0.45
Si	0.01	0.19	-0.02	0.01	0.37	0.83	0.67	1	0.89	0.86	0.74	0.64	0.63	0.89	0.62	0.32	0.46	0.31
Al	0.01	0.19	-0.01	-0.01	0.35	0.85	0.70	0.89	1	0.87	0.75	0.67	0.64	0.89	0.62	0.33	0.46	0.30
Ti	0.02	0.19	0.01	0.04	0.34	0.79	0.61	0.86	0.87	1	0.71	0.59	0.57	0.84	0.58	0.31	0.38	0.24
Na	-0.05	0.16	-0.08	0.05	0.28	0.74	0.59	0.74	0.75	0.71	1	0.68	0.69	0.76	0.50	0.37	0.40	0.35
Cu	-0.13	-0.02	-0.13	-0.13	0.31	0.66	0.78	0.64	0.67	0.59	0.68	1	0.86	0.69	0.56	0.48	0.70	0.54
Zn	-0.14	0.10	-0.15	-0.07	0.28	0.68	0.69	0.63	0.64	0.57	0.69	0.86	1	0.67	0.49	0.55	0.63	0.50
Rb	-0.01	0.17	-0.04	0.00	0.38	0.85	0.70	0.89	0.89	0.84	0.76	0.69	0.67	1	0.64	0.35	0.48	0.32
Th	0.00	0.05	-0.05	-0.12	0.28	0.64	0.62	0.62	0.62	0.58	0.50	0.56	0.49	0.64	1	0.30	0.42	0.27
Cd	-0.27	-0.10	-0.33	-0.12	0.18	0.42	0.36	0.32	0.33	0.31	0.37	0.48	0.55	0.35	0.30	1	0.36	0.41
P	0.17	0.17	0.07	-0.11	0.36	0.46	0.64	0.46	0.46	0.38	0.40	0.70	0.63	0.48	0.42	0.36	1	0.90
U	0.09	0.23	-0.15	-0.09	0.34	0.36	0.45	0.31	0.30	0.24	0.35	0.54	0.50	0.32	0.27	0.41	0.90	1

As the three growth periods of stalagmite VSMS2 are separated by two hiatuses by about 5.9 ka and 5.4 ka, and because scatter plots of the geochemical records from VSMS2 suggest the existence of multiple statistical populations (Section 5.6.3.2), correlation matrices for each of the three growth periods were constructed separately as well and are given in Table 5.10 toTable 5.12.

First growth period: 25.3 ka to 21.9 ka BP

Out of the 153 calculated correlation coefficients, 38 indicate a positive correlation with $\rho \geq 0.3$ whereas 12 indicate a negative correlation with $\rho \leq -0.3$, and 57 values in total are not significant at the 0.05 level (Table 5.10). Compared to the correlation matrix integrating over all three growth periods, there are noticeably less positive and more negative and statistically insignificant correlations.

The geochemical records of the previously defined Group I are much less associated with one another compared to the correlation matrix integrating over all three growth periods. Only Sr and Ba are strongly positively correlated ($\rho = 0.75$), and $\delta^{13}C$ and Mg show a weak positive correlation ($\rho = 0.34$). Both stable isotope records correlate negatively with one another (-0.20) and $\delta^{18}O$ and Ba feature the strongest negative correlation among the Group I records (-0.40). The Group I records tend to be negatively correlated with all other geochemical records, except for $\delta^{13}C$ that features only statistically insignificant negative ρ values. Carbon isotopes are also positively correlated with Mn (0.34) and the Group III elements P (0.28) and U (0.24).

Of the previously defined Group II elements, especially Cu, Zn and Cd are less obviously associated with the remaining Group II elements. While the Group III elements P and U are still strongly positively correlated to one another (0.88), they only feature a positive correlation with Cu and Mn among the Group II elements. Phosphorus and U are negatively correlated with $\delta^{18}O$ (-0.42 and -0.37), but show a weak positive correlation with $\delta^{13}C$ (0.28 and 0.24).

Table 5.10: Matrix of Spearman's rank correlation coefficients (ρ) for all geochemical records of stalagmite VSMS2 analysed in this study during its first growth period (n = 225). Positive correlations are highlighted in green, negative correlations in red, with the strength of the correlation increasing with respective colour depth. All trace element data are averaged to correspond to the isotope data sets as described in Section 4.6. All values that are not significant at the 0.05 level (using the two-tailed test of significance) are shaded in grey.

	$\delta^{13}C$	$\delta^{18}O$	Mg	Sr	Ba	Fe	Mn	Si	Al	Ti	Na	Cu	Zn	Rb	Th	Cd	P	U
$\delta^{13}C$	1	-0.20	0.34	-0.10	0.01	-0.09	0.26	-0.08	-0.05	-0.07	-0.05	0.03	-0.10	-0.09	0.11	0.03	0.28	0.24
$\delta^{18}O$	-0.20	1	0.10	-0.21	-0.40	-0.17	-0.31	-0.01	0.00	0.08	0.06	-0.20	0.02	0.04	-0.06	-0.06	-0.42	-0.37
Mg	0.34	0.10	1	-0.21	-0.05	-0.43	-0.07	-0.32	-0.38	-0.37	-0.40	-0.15	-0.10	-0.37	-0.12	-0.12	0.04	0.05
Sr	-0.10	-0.21	-0.21	1	0.75	-0.25	-0.43	-0.31	-0.30	-0.24	-0.12	-0.18	-0.29	-0.29	-0.29	-0.13	-0.21	-0.10
Ba	0.01	-0.40	-0.05	0.75	1	-0.12	0.00	-0.21	-0.20	-0.19	-0.15	0.10	-0.11	-0.17	-0.05	-0.04	0.25	0.30
Fe	-0.09	-0.17	-0.43	-0.25	-0.12	1	0.76	0.80	0.85	0.75	0.65	0.20	0.32	0.79	0.52	0.23	0.00	-0.03
Mn	0.26	-0.31	-0.07	-0.43	0.00	0.76	1	0.57	0.59	0.45	0.39	0.47	0.25	0.55	0.52	0.20	0.47	0.34
Si	-0.08	-0.01	-0.32	-0.31	-0.21	0.80	0.57	1	0.84	0.82	0.74	0.05	0.17	0.80	0.51	0.17	-0.09	-0.07
Al	-0.05	0.00	-0.38	-0.30	-0.20	0.85	0.59	0.84	1	0.84	0.75	0.11	0.23	0.83	0.51	0.21	-0.11	-0.11
Ti	-0.07	0.08	-0.37	-0.24	-0.19	0.75	0.45	0.82	0.84	1	0.75	0.03	0.23	0.80	0.50	0.17	-0.18	-0.13
Na	-0.05	0.06	-0.40	-0.12	-0.15	0.65	0.39	0.74	0.75	0.75	1	0.03	0.10	0.76	0.44	0.19	-0.18	-0.12
Cu	0.03	-0.20	-0.15	-0.18	0.10	0.20	0.47	0.05	0.11	0.03	0.03	1	0.54	0.13	0.25	0.23	0.40	0.25
Zn	-0.10	0.02	-0.10	-0.29	-0.11	0.32	0.25	0.17	0.23	0.23	0.10	0.54	1	0.26	0.20	0.26	0.15	0.06
Rb	-0.09	0.04	-0.37	-0.29	-0.17	0.79	0.55	0.80	0.83	0.80	0.76	0.13	0.26	1	0.48	0.22	-0.07	-0.05
Th	0.11	-0.06	-0.12	-0.29	-0.05	0.52	0.52	0.51	0.51	0.50	0.44	0.25	0.20	0.48	1	0.16	0.11	0.08
Cd	0.03	-0.06	-0.12	-0.13	-0.04	0.23	0.20	0.17	0.21	0.17	0.19	0.23	0.26	0.22	0.16	1	0.13	0.10
P	0.28	-0.42	0.04	-0.21	0.25	0.00	0.47	-0.09	-0.11	-0.18	-0.18	0.40	0.15	-0.07	0.11	0.13	1	0.88
U	0.24	-0.37	0.05	-0.10	0.30	-0.03	0.34	-0.07	-0.11	-0.13	-0.12	0.25	0.06	-0.05	0.08	0.10	0.88	1

Second growth period: 16.0 ka to 13.1 ka BP

Out of the 153 calculated correlation coefficients, 84 indicate a positive correlation with $\rho \geq 0.3$ whereas only five indicate a negative correlation with $\rho \leq -0.3$, and 23 values in total are not significant at the 0.05 level (Table 5.11). Compared to the correlation matrix integrating over all three growth periods, there are still less positive and more negative and especially statistically insignificant correlations, but this discrepancy is not as obvious than with the correlation matrix integrating over the first growth period.

The geochemical records of the previously defined Group I are much less associated with one another compared to the correlation matrix integrating over all three growth periods, but $\delta^{13}C$ is strongly positively correlated with $\delta^{18}O$ ($\rho = 0.60$), while still being weakly negatively correlated with Mg (-0.14). Strontium is strongly positively correlated with Ba ($\rho = 0.59$) and shows a weak positive correlation with Mg ($\rho = 0.20$). The strongest negative correlation among the Group I records is again between $\delta^{18}O$ and Ba (-0.50) which is also the strongest negative correlation in the entire correlation matrix. Barium features weak positive correlations with the Group II elements, with ρ values up to 0.43 (vs. Si and Cu). The stable isotopes are weakly positively correlated with the Group III elements, especially $\delta^{18}O$ with U ($\rho = 0.37$).

The positive correlations between the Group II elements are noticeably stronger compared to the first growth period of stalagmite VSMS2, as are the positive correlations between Group II and Group III elements. The strongest positive correlation is between the Group III elements P and U (0.90), while both elements show a weak negative correlation with Mg and Sr.

Table 5.11: Matrix of Spearman's rank correlation coefficients (ρ) for all geochemical records of stalagmite VSMS2 analysed in this study during its second growth period (n = 318). Positive correlations are highlighted in green, negative correlations in red, with the strength of the correlation increasing with respective colour depth. All trace element data are averaged to correspond to the isotope data sets as described in Section 4.6. All values that are not significant at the 0.05 level (using the two-tailed test of significance) are shaded in grey.

	$\delta^{13}C$	$\delta^{18}O$	Mg	Sr	Ba	Fe	Mn	Si	Al	Ti	Na	Cu	Zn	Rb	Th	Cd	P	U
$\delta^{13}C$	1	0.60	-0.14	-0.31	-0.18	0.08	0.12	0.10	0.06	0.07	0.10	0.02	0.07	0.06	0.08	0.10	0.16	0.26
$\delta^{18}O$	0.60	1	-0.29	-0.50	-0.26	0.06	0.26	0.11	0.10	0.06	0.17	0.04	0.26	0.07	0.06	0.14	0.17	0.37
Mg	-0.14	-0.29	1	0.20	0.06	-0.11	-0.20	-0.15	-0.13	-0.08	-0.11	-0.26	-0.34	-0.17	-0.07	-0.24	-0.27	-0.21
Sr	-0.31	-0.50	0.20	1	0.59	-0.24	-0.43	-0.11	-0.17	-0.09	-0.12	-0.13	-0.14	-0.15	-0.18	-0.12	-0.24	-0.35
Ba	-0.18	-0.26	0.06	0.59	1	0.36	0.20	0.43	0.40	0.36	0.23	0.43	0.33	0.41	0.31	0.28	0.35	0.19
Fe	0.08	0.06	-0.11	-0.24	0.36	1	0.75	0.72	0.75	0.63	0.58	0.68	0.53	0.80	0.71	0.42	0.47	0.39
Mn	0.12	0.26	-0.20	-0.43	0.20	0.75	1	0.54	0.56	0.45	0.50	0.68	0.60	0.60	0.60	0.50	0.52	0.49
Si	0.10	0.11	-0.15	-0.11	0.43	0.72	0.54	1	0.80	0.76	0.55	0.53	0.42	0.82	0.58	0.29	0.37	0.33
Al	0.06	0.10	-0.13	-0.17	0.40	0.75	0.56	0.80	1	0.73	0.55	0.54	0.42	0.79	0.59	0.29	0.38	0.34
Ti	0.07	0.06	-0.08	-0.09	0.36	0.63	0.45	0.76	0.73	1	0.47	0.44	0.33	0.71	0.51	0.28	0.29	0.27
Na	0.10	0.17	-0.11	-0.12	0.23	0.58	0.50	0.55	0.55	0.47	1	0.65	0.61	0.60	0.45	0.41	0.44	0.42
Cu	0.02	0.04	-0.26	-0.13	0.43	0.68	0.68	0.53	0.54	0.44	0.65	1	0.83	0.61	0.52	0.62	0.74	0.62
Zn	0.07	0.26	-0.34	-0.14	0.33	0.53	0.60	0.42	0.42	0.33	0.61	0.83	1	0.51	0.45	0.69	0.61	0.56
Rb	0.06	0.07	-0.17	-0.15	0.41	0.80	0.60	0.82	0.79	0.71	0.60	0.61	0.51	1	0.62	0.35	0.41	0.35
Th	0.08	0.06	-0.07	-0.18	0.31	0.71	0.60	0.58	0.59	0.51	0.45	0.52	0.45	0.62	1	0.39	0.34	0.28
Cd	0.10	0.14	-0.24	-0.12	0.28	0.42	0.50	0.29	0.29	0.28	0.41	0.62	0.69	0.35	0.39	1	0.54	0.46
P	0.16	0.17	-0.27	-0.24	0.35	0.47	0.52	0.37	0.38	0.29	0.44	0.74	0.61	0.41	0.34	0.54	1	0.90
U	0.26	0.37	-0.21	-0.35	0.19	0.39	0.49	0.33	0.34	0.27	0.42	0.62	0.56	0.35	0.28	0.46	0.90	1

Third growth period: 7.7 ka to 4.9 ka BP

Out of the 153 calculated correlation coefficients, 77 indicate a positive correlation with $\rho \geq 0.3$ whereas 13 indicate a negative correlation with $\rho \leq -0.3$, and 18 values in total are not significant at the 0.05 level (Table 5.12). Compared to the correlation matrix integrating over all three growth periods, there are still less positive and more negative and especially statistically insignificant correlations, but this discrepancy is not as obvious than with the correlation matrix integrating over the first growth period.

The geochemical records of the previously defined Group I are less associated with one another compared to the correlation matrix integrating over all three growth periods, but $\delta^{13}C$ is strongly positively correlated with $\delta^{18}O$ ($\rho = 0.71$) and is weakly positively correlated with Mg (0.15), while still being negatively correlated with Sr (-0.34) and Ba (-0.20). Strontium is positively correlated with Ba ($\rho = 0.40$), but most noticeably shows negative correlations with all other geochemical records of stalagmite VSMS2 with ρ values down to -0.59 (vs. P). The strongest negative correlation among the Group I records is between $\delta^{18}O$ and Sr (-0.40).

Both Mg and Ba feature positive correlations with the Group II elements, with ρ values up to 0.51 (vs. Mn and Al) and 0.46 (vs. Rb), respectively. The stable isotopes are still weakly positively correlated with P, while U concentration data are not available for the third growth period of stalagmite VSMS2 as a result of high blank values that lead to negative concentration values when subtracted because U concentrations were below the limit of detection during the third growth period. Phosphorus is strongly positively correlated with all Group II elements, but strongly negatively correlated with Sr (-0.59).

Table 5.12: Matrix of Spearman's rank correlation coefficients (ρ) for all geochemical records of stalagmite VSMS2 analysed in this study during its third growth period (n = 208). Positive correlations are highlighted in green, negative correlations in red, with the strength of the correlation increasing with respective colour depth. All trace element data are averaged to correspond to the isotope data sets as described in Section 4.6. All values that are not significant at the 0.05 level (using the two-tailed test of significance) are shaded in grey.

	$\delta^{13}C$	$\delta^{18}O$	Mg	Sr	Ba	Fe	Mn	Si	Al	Ti	Na	Cu	Zn	Rb	Th	Cd	P
$\delta^{13}C$	1	0.71	0.15	-0.34	-0.20	0.19	0.22	0.04	0.02	-0.06	0.10	0.14	0.19	0.08	0.18	-0.19	0.35
$\delta^{18}O$	0.71	1	-0.01	-0.40	-0.33	0.10	0.12	-0.03	-0.06	-0.10	0.08	0.10	0.17	-0.01	0.09	-0.05	0.27
Mg	0.15	-0.01	1	-0.19	-0.05	0.47	0.51	0.46	0.51	0.48	0.45	0.46	0.45	0.45	0.26	-0.17	0.37
Sr	-0.34	-0.40	-0.19	1	0.40	-0.39	-0.50	-0.34	-0.39	-0.31	-0.31	-0.44	-0.52	-0.35	-0.25	-0.12	-0.59
Ba	-0.20	-0.33	-0.05	0.40	1	0.42	0.26	0.46	0.40	0.44	0.25	0.31	0.24	0.47	0.46	0.26	0.19
Fe	0.19	0.10	0.47	-0.39	0.42	1	0.87	0.89	0.90	0.87	0.75	0.87	0.81	0.91	0.77	0.21	0.76
Mn	0.22	0.12	0.51	-0.50	0.26	0.87	1	0.83	0.86	0.79	0.74	0.91	0.86	0.84	0.68	0.19	0.84
Si	0.04	-0.03	0.46	-0.34	0.46	0.89	0.83	1	0.92	0.91	0.75	0.85	0.79	0.91	0.71	0.24	0.72
Al	0.02	-0.06	0.51	-0.39	0.40	0.90	0.86	0.92	1	0.93	0.78	0.88	0.81	0.92	0.71	0.25	0.75
Ti	-0.06	-0.10	0.48	-0.31	0.44	0.87	0.79	0.91	0.93	1	0.75	0.84	0.77	0.89	0.67	0.25	0.68
Na	0.10	0.08	0.45	-0.31	0.25	0.75	0.74	0.75	0.78	0.75	1	0.83	0.72	0.77	0.55	0.13	0.62
Cu	0.14	0.10	0.46	-0.44	0.31	0.87	0.91	0.85	0.88	0.84	0.83	1	0.92	0.86	0.70	0.29	0.83
Zn	0.19	0.17	0.45	-0.52	0.24	0.81	0.86	0.79	0.81	0.77	0.72	0.92	1	0.81	0.61	0.39	0.88
Rb	0.08	-0.01	0.45	-0.35	0.47	0.91	0.84	0.91	0.92	0.89	0.77	0.86	0.81	1	0.74	0.24	0.74
Th	0.18	0.09	0.26	-0.25	0.46	0.77	0.68	0.71	0.71	0.67	0.55	0.70	0.61	0.74	1	0.16	0.58
Cd	-0.19	-0.05	-0.17	-0.12	0.26	0.21	0.19	0.24	0.25	0.25	0.13	0.29	0.39	0.24	0.16	1	0.34
P	0.35	0.27	0.37	-0.59	0.19	0.76	0.84	0.72	0.75	0.68	0.62	0.83	0.88	0.74	0.58	0.34	1

5.6.3 Scatter Plots

5.6.3.1 Stalagmite VML22

Figure 5.43 shows the scatter plot of $\delta^{18}O$ from stalagmite VML22 plotted against $\delta^{13}C$. Additionally to the respective scatter plot, the plot contains the Spearman's ρ value for the two elements plotted against each other, as well as the line that results from a linear regression calculated for the cross plot using the software Origin, together with the formula mathematically describing the regression line. As a measure for the goodness of the fit, the coefficient of determination (R^2) has been implemented in the plot, also calculated with the software Origin. In order to avoid the effect of artificially increased R^2 by increased numbers of variables used for the fitting, the adjusted R^2 is used as a quality measure, rather than merely R^2.

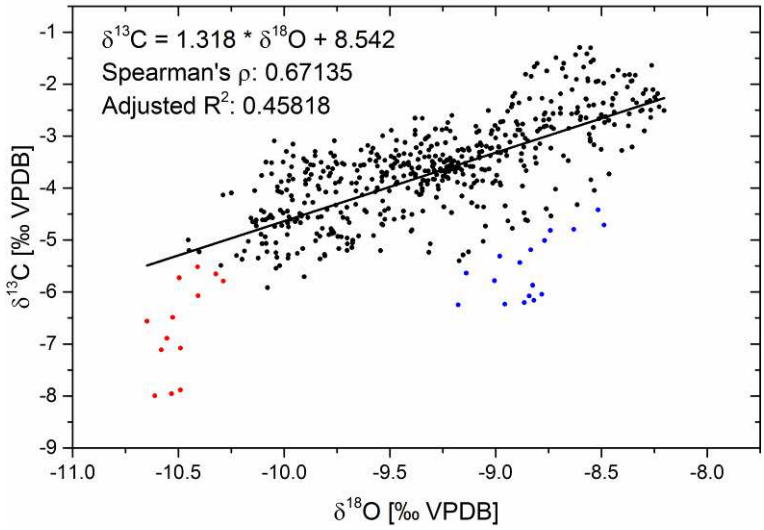

Figure 5.43: Scatter plot of VML22 $\delta^{18}O$ vs. $\delta^{13}C$ including a linear regression fit (solid line), the corresponding formula, the adjusted R^2 as a measure for the goodness of the fit and the value of the Spearmans's ρ. Data points in red and blue are adjacent data points clearly plotting below the regression line, respectively (see text for details).

On the one hand, the close match between data points and regression line mirrors the high value of Spearman's ρ for $\delta^{18}O$ vs. $\delta^{13}C$ (0.67). This linear correlation apparent over the entire data set of stalagmite VML22 suggests that both proxy signals are controlled by processes that influence the two signals in a similar fashion. On the other hand, the goodness of the fit is only moderate, with the value of adjusted R^2 being 0.46, and in two separate areas of the scatter plot a number of data points tend to lower $\delta^{13}C$ values relative to their corresponding $\delta^{18}O$ values, thus plotting noticeably below the regression line: Data points in blue in Figure 5.43 are isotope samples number 18 to 34, counted from the top of the stalagmite, and represent the time period 0.73 – 0.99 ka BP (3.4 – 6.5 mm DFT). Data points in red are isotope samples number 512 to 535 and represent the time period 7.39 – 7.64 ka BP (99.2 – 103.7 mm DFT).

This deviation towards decreased $\delta^{13}C$ values relative to their corresponding $\delta^{18}O$ values suggests the acting of a process leading either to decreased $\delta^{13}C$ values without influencing the corresponding $\delta^{18}O$ values, or causing increased $\delta^{18}O$ values without influencing the corresponding $\delta^{13}C$ values.

Figure 5.48 shows the scatter plots of the geochemical records of stalagmite VML22 for $\delta^{18}O$ and $\delta^{13}C$ plotted against Mg, Sr, Ba and Fe, respectively. As for the calculation of the correlation matrices (Section 5.6.2), trace element data were averaged to correspond to the isotope data sets. Detailed plots like the ones combined in Figure 5.48 were created for all elements plotted against $\delta^{18}O$ and $\delta^{13}C$, as well as against Mg and Al, to cover examples from both main groups of proxy signals identified in Section 5.6.2 (Group I and Group II). Additional detailed plots were created for element pairs with particularly strong (positive or negative) correlation as indicated by Spearman's ρ values, for example Sr vs. Ba ($\rho = 0.88$). As there are 240 scatter plots to be illustrated in total, all remaining scatter plots not displayed in detail were implemented in the form of scatter plot matrices and are shown in the Appendix.

As suggested by the high values of Spearman's ρ in the correlation matrix (Section 5.6.2), all elements of Group I show a linear relation with both $\delta^{18}O$ and $\delta^{13}C$, while this is slightly more evident in the case of $\delta^{18}O$ than of $\delta^{13}C$. The linear fit is most suited for Mg with values of R^2 of 0.5 for both $\delta^{18}O$ and $\delta^{13}C$, while the goodness of the fit is reduced for Sr with values of R^2 of 0.32 and 0.22 for $\delta^{18}O$ and $\delta^{13}C$, respectively. The linear regression for Ba versus $\delta^{18}O$ still yields an R^2 of 0.20, but for Ba vs. $\delta^{13}C$ the value of R^2 is only 0.11 so that the relationship between Ba and $\delta^{13}C$ cannot be well described with a linear regression. The linear regression appears to describe the relation between Mg, Sr and Ba fairly well (Figure C.4), as indicated by high to medium values of R^2: 0.69 (Sr vs. Ba), 0.32 (Mg vs. Sr) and 0.20 (Mg vs. Ba).

Both values of Spearman's ρ and adjusted R^2 indicate that the relationship between the elements of Group II and the elements of Group I cannot be well described with a linear correlation (Figure C.2 toFigure C.1). Furthermore, the scatter plots show that any alternative type of curve fitting (e.g. exponential or polynomial) will be just as ill-suited for describing the relation between the elements of both groups. This implies that the geochemical proxy signals from both groups are controlled by different suites of processes. Computed for the elements of Group II, the values of R^2 are generally high (e.g. Figure C.7) and the relation between these elements can therefore be well described linearly, with the only exception being Cd. For instance, values of R^2 for Al versus Fe, Mn, Si, Na, Zn and Rb are 0.55, 0.50, 0.66, 0.60, 0.42 and 0.57, respectively.

Although Spearman's ρ values computed for Fe vs. $\delta^{18}O$ (0.48) and $\delta^{13}C$ (0.35) are moderate and the majority of data points plot close to the regression line, a number of data points deviate strongly towards increased concentrations of Fe so that the corresponding values of R^2 are close to zero (0.08 for $\delta^{18}O$ and 0.03 for $\delta^{13}C$). This suggests that the highest Fe concentrations in stalagmite VML22 cannot be explained by the same processes that lead to the overall positive correlation between Fe and the other elements of Group I.

As the values of both Spearman's ρ and R^2 computed for Fe and the elements of Group II are much higher compared to those for Group I (e.g. R^2 of Fe vs. Al: 0.54), Fe is rather attributed to Group II than to Group I.

Phosphorus, on the other hand, can be attributed to the elements of Group I with which it is negatively correlated (Section 5.6.2). Values of R^2 for P versus $\delta^{18}O$, $\delta^{13}C$, Mg, Sr and Ba are 0.08, 0.10, 0.16, 0.31 and 0.08, respectively, so that a linear relation of P with these elements is the most evident for Mg and especially for Sr. The negative linear correlation of P with Mg and Sr is unique in the geochemistry of stalagmite VML22. The best linear fit of P with any other element, however, is achieved for U (R^2: 0.58) with which it is strongly positively correlated (ρ: 0.72). The relation of P with the elements of Group II cannot be adequately described with a linear regression, all values of R^2 are < 0.12. The corresponding scatter plots suggest that the positive correlation of P with the elements of Group II indicated by Spearman's ρ is superimposed by a more erratic relation between these elements as P concentrations in stalagmite VML22 vary widely in the respective low concentrations range of the Group II elements.

In a statistical sense, none of the 240 scatter plots of the geochemical proxy signals of stalagmite VML22 features multiple populations. Therefore, the data points of each proxy signal can be considered as a statistical unit and there are no subpopulations to be separated out for further analyses.

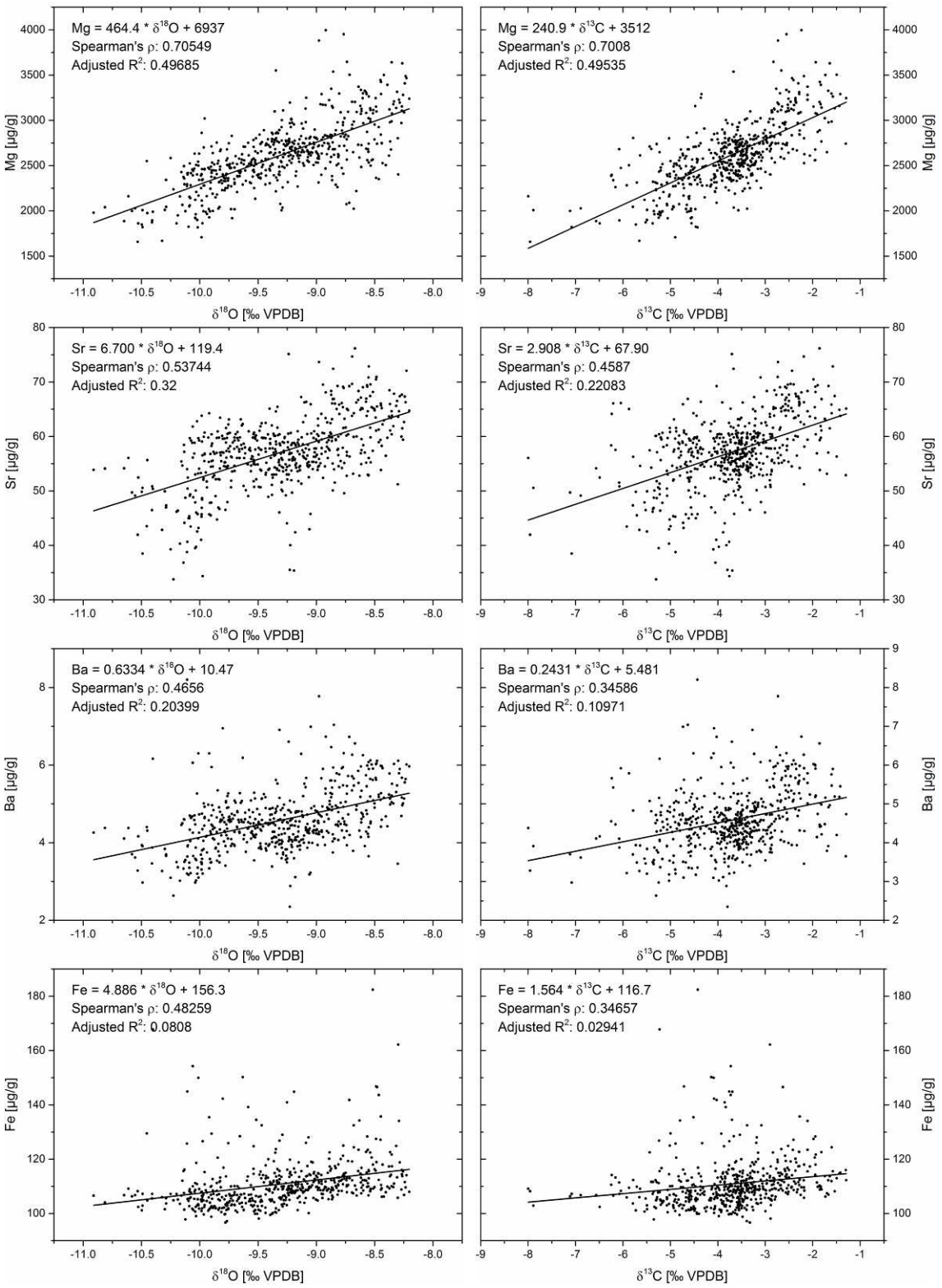

Figure 5.44: Scatter plots of the geochemical records of stalagmite VML22 for $\delta^{18}O$ and $\delta^{13}C$ plotted against Mg, Sr, Ba and Fe, respectively. Trace element data were averaged to correspond to the isotope data sets as described in the text.

5.6.3.2 Stalagmite VSMS2

Figure 5.45 shows the scatter plot of $\delta^{18}O$ from stalagmite VSMS2 plotted against $\delta^{13}C$ for all three growth periods, including linear regression fits (solid lines) and the corresponding adjusted R^2 as a measure for the goodness of the fit.

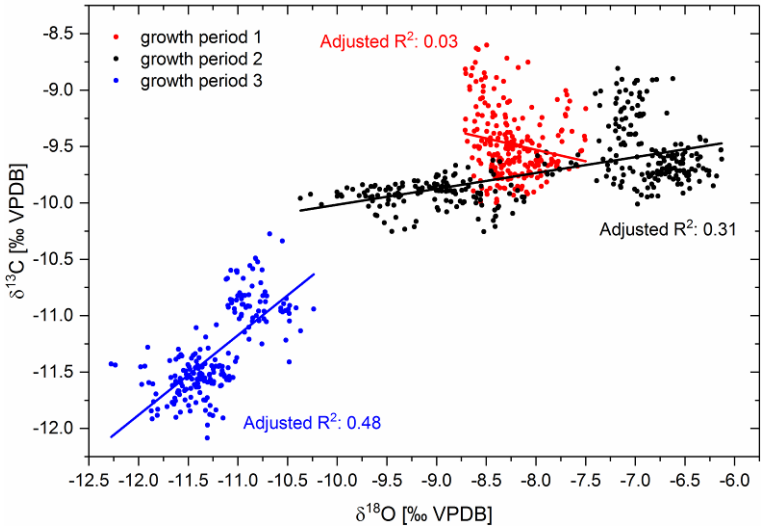

Figure 5.45: Scatter plot of $\delta^{18}O$ vs. $\delta^{13}C$ for all three growth periods of stalagmite VSMS2, including linear regression fits (colour-coded solid lines) and the corresponding adjusted R^2 as a measure for the goodness of the fit.

From a statistical standpoint, the stable isotope proxy signals of stalagmite VSMS2 feature multiple populations that can be attributed to the three different growth periods of VSMS2. Therefore, these subpopulations are separated out for further analyses. The goodness of the linear fit for each growth period corresponds well with the respective value of Spearman's ρ. During the first growth period, $\delta^{18}O$ and $\delta^{13}C$ are only weakly negatively correlated with one another ($\rho = -0.20$) and the relation between the isotope proxies cannot be well described with a linear regression as indicated by an adjusted R^2 close to zero. However, during the second growth period, $\delta^{18}O$ and $\delta^{13}C$ are strongly positively correlated with one another ($\rho = 0.60$) and their relation can be fairly well described linearly (adjusted $R^2 = 0.31$). This association is even stronger in the third growth period ($\rho = 0.71$; adjusted $R^2 = 0.48$), suggesting that both stable isotope proxies are influenced by a certain suite of processes in a similar fashion during the second and third growth period, but not during the first. All remaining scatter plots are implemented in the form of scatter plot matrices in Appendix C.1and C.2.

During the first growth period, the Group I elements are not strongly associated with one another (Figure C.12), with generally low values of ρ and adjusted R^2, except for Sr and Ba ($\rho = 0.75$; adjusted $R^2 = 0.46$) and, to a lesser extent, for $\delta^{13}C$ and Mg ($\rho = 0.34$; adjusted $R^2 = 0.15$).

During the second growth period (Figure C.13 top), the association between and $\delta^{18}O$ and $\delta^{13}C$ is the strongest ($\rho = 0.60$; adjusted $R^2 = 0.31$), while the association between $\delta^{13}C$ and Mg has vanished ($\rho = -0.14$; adjusted $R^2 = 0.03$).

Interestingly, the scatter plots of $\delta^{18}O$ versus the remaining Group I elements again suggest two statistical populations, especially in the case of $\delta^{13}C$ and Mg (Figure 5.46) which indicates a distinct shift in the relation between $\delta^{18}O$ and the remaining Group I elements around 14.4 ka BP (DFT 64.8 mm) which allows a differentiation between a first and a second part within the second growth period of stalagmite VSMS2. During the third growth period (Figure C.13 bottom), the association between and $\delta^{18}O$ and $\delta^{13}C$ is even stronger than during the second growth period ($\rho = 0.71$; adjusted $R^2 = 0.48$). All other Group I elements are not significantly associated with one another and their relation cannot be well described with linear regression as indicated by the overall low values of adjusted R^2.

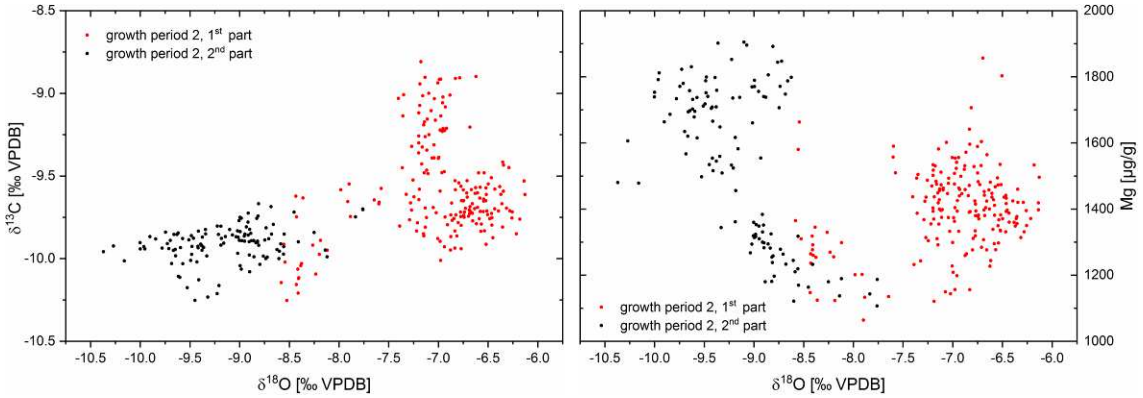

Figure 5.46: Scatter plot of $\delta^{18}O$ vs. $\delta^{13}C$ (left) and $\delta^{18}O$ vs. Mg (right) during the second growth period of stalagmite VSMS2, differentiating between the first part (red) until 14.4 ka BP and the second part (black) of the growth period.

The main elements attributed to Group II (Fe, Mn, Si, Al and Ti) are generally strongly associated with one another in a linear fashion as indicated by high values of ρ and of adjusted R^2, with the strength of this assocation generally increasing from the first growth period (Appendix, Figure C.14) over the second (Appendix, Figure C.15 top) to the third growth period (Appendix, Figure C.15 bottom). The remaining elements attributed to Group II (Na, Cu, Zn, Rb and Th) behave similarly, but their association to one another is weaker overall Appendix, (Figure C.16 and Figure C.17). Phosphorus and U (Appendix, Figure C.18) are strongly associated with one other during the first and second growth phases. For the third growth period U concentration data are not available as U concentrations were below the detection limit during that growth period.

5.6.4 Autocorrelation Coefficients

5.6.4.1 Stalagmite VML22

Table 5.13 summarises the lag-1 autocorrelation coefficients (Lag-1 ACC; Spearman's ρ) calculated for the geochemical records of stalagmite VML22. Again trace element data were averaged to correspond to the isotope data sets as described in Section 4.6 for the computation of the Lag-1 ACC. Values of the Lag-1 ACC for Rb and Cd are 0.38 and 0.14, respectively (grey shading), and are considered to be too low for these geochemical datasets to constitute valid geochemical signals of the palaeoenvironment. Rubidium and Cd are therefore omitted from all further analyses conducted within the framework of this thesis, another reason being that only less than half of the original data points remain after removal of negative values (below the limit of detection) and outliers (Table 4.1).

The remaining geochemical signals of stalagmite VML22 feature Lag-1 ACC that range from 0.55 (U) to 0.95 ($\delta^{13}C$). The highest Lag-1 ACC are achieved for those elements attributed to Group I based on their respective Spearman's rank coefficients in Section 5.6.2. Within this group, Lag-1 ACC range from a still high minimum of 0.78 (Ba) to a maximum of 0.95 ($\delta^{13}C$), closely followed by the second highest values of 0.93 ($\delta^{18}O$).

Table 5.13: Lag-1 autocorrelation coefficients for the geochemical records of stalagmite VML22. Values with grey shading are deemed too low for the proxy signals to be applicable for palaeoenvironmental reconstruction.

Data set	$\delta^{13}C$	$\delta^{18}O$	Mg	Sr	Ba	Fe	Mn	P
Lag-1 ACC	0.95	0.93	0.88	0.80	0.78	0.62	0.70	0.65
Data set	**Si**	**Al**	**Na**	**U**	**Cu**	**Zn**	**Rb**	**Cd**
Lag-1 ACC	0.56	0.60	0.69	0.55	0.59	0.66	0.38	0.14

5.6.4.2 Stalagmite VSMS2

Table 5.14 summarises the lag-1 autocorrelation coefficients (Lag-1 ACC; Spearman's ρ) calculated for the geochemical records of stalagmite VSMS2. Again trace element data were averaged to correspond to the isotope data sets for the computation of the Lag-1 ACC. Values of the Lag-1 ACC for Cd and Th are 0.51 and 0.44, respectively (grey shading), and are considered to be too low for these geochemical datasets to constitute valid geochemical signals of the palaeoenvironment. Cadmium and Th are therefore omitted from all further analyses conducted within the framework of this thesis, another reason being that only less than half of the original data points remain after removal of negative values (below the limit of detection) and outliers (Table 5.4).

The remaining geochemical signals of stalagmite VSMS2 feature Lag-1 ACC that range from 0.72 (Ti) to 0.99 ($\delta^{18}O$). The highest Lag-1 ACC are achieved for $\delta^{18}O$, $\delta^{13}C$ and Mg attributed to Group I based on their respective Spearman's rank coefficients in Section 5.6.2.2.

Within Group I, Lag-1 ACC range from a still high minimum of 0.74 (Ba) to a maximum of 0.99 ($\delta^{18}O$), closely followed by the second highest values of 0.98 ($\delta^{13}C$).

Lag-1 ACC were also computed separately for each of the three growth periods of stalagmite VSMS2. These values are comparable to the values computed for the entirety of each respective data set and are given in Table 5.15 to Table 5.17.

Table 5.14: Lag-1 autocorrelation coefficients for the geochemical records of stalagmite VSMS2. Values with grey shading are deemed too low for the proxy signals to be applicable for palaeoenvironmental reconstruction.

Data set	**$\delta^{13}C$**	**$\delta^{18}O$**	**Mg**	**Sr**	**Ba**	**Fe**	**Mn**	**P**	**Ti**
Lag-1 ACC	0.98	0.99	0.96	0.83	0.74	0.82	0.83	0.83	0.72
Data set	**Si**	**Al**	**Na**	**U**	**Cu**	**Zn**	**Rb**	**Cd**	**Th**
Lag-1 ACC	0.75	0.77	0.80	0.78	0.86	0.88	0.74	0.51	0.45

Table 5.15: Lag-1 autocorrelation coefficients for the geochemical records of stalagmite VSMS2 during its first growth period. Values with grey shading are deemed too low for the proxy signals to be applicable for palaeoenvironmental reconstruction.

Data set	**$\delta^{13}C$**	**$\delta^{18}O$**	**Mg**	**Sr**	**Ba**	**Fe**	**Mn**	**P**	**Ti**
Lag-1 ACC	0.91	0.91	0.89	0.78	0.72	0.75	0.62	0.78	0.72
Data set	**Si**	**Al**	**Na**	**U**	**Cu**	**Zn**	**Rb**	**Cd**	**Th**
Lag-1 ACC	0.74	0.77	0.73	0.76	0.63	0.67	0.68	0.03	0.30

Table 5.16: Lag-1 autocorrelation coefficients for the geochemical records of stalagmite VSMS2 during its second growth period. Values with grey shading are deemed too low for the proxy signals to be applicable for palaeoenvironmental reconstruction.

Data set	**$\delta^{13}C$**	**$\delta^{18}O$**	**Mg**	**Sr**	**Ba**	**Fe**	**Mn**	**P**	**Ti**
Lag-1 ACC	0.92	0.98	0.88	0.71	0.59	0.57	0.66	0.75	0.50
Data set	**Si**	**Al**	**Na**	**U**	**Cu**	**Zn**	**Rb**	**Cd**	**Th**
Lag-1 ACC	0.56	0.51	0.67	0.73	0.74	0.84	0.54	0.51	0.44

Table 5.17: Lag-1 autocorrelation coefficients for the geochemical records of stalagmite VSMS2 during its third growth period. The value for U is missing due to an insufficient number of data points.

Data set	**$\delta^{13}C$**	**$\delta^{18}O$**	**Mg**	**Sr**	**Ba**	**Fe**	**Mn**	**P**	**Ti**
Lag-1 ACC	0.94	0.88	0.82	0.76	0.70	0.80	0.85	0.88	0.81
Data set	**Si**	**Al**	**Na**	**U**	**Cu**	**Zn**	**Rb**	**Cd**	**Th**
Lag-1 ACC	0.79	0.86	0.80	-	0.90	0.92	0.80	0.51	0.51

5.6.5 Frequency Analysis

5.6.5.1 Stalagmite VML22

The results of the frequency analysis, the red-noise spectra, are illustrated in Figure 5.47 for $\delta^{18}O$, $\delta^{13}C$ (top), Mn and P (bottom), the remaining spectra are included in the Appendix. The bias-corrected estimated red-noise spectrum of the respective data set is plotted against the frequency of the variations inherent in each data set (black line). The higher the spectrum at a certain frequency, the more often the values of the data set vary at that specific frequency. This allows to identify potential cyclic patterns in the proxy signal variations with their respective cycle duration. The cycle duration is the inverse of its corresponding frequency and is referred to as "periodicity" in the following. In each graph, the pink, blue and red solid lines represent the 99%, the 95% and the 90% confidence level, respectively. Peaks in the red-noise spectra exceeding the 95% and/or 99% confidence level are labelled with a number that represents the respective periodicity (in years) of the cyclic behaviour represented by each peak. For example, the number 200 would indicate that a statistically significant number of variations in the respective proxy signal occur at intervals of 200 years, at a frequency of 1/200 = 0.005 $years^{-1}$.

The errors of each statistically significant periodicity detected in the data sets are not shown in the spectrum diagrams, but separately in Figure 5.48. The maximal absolute error of each peak in terms of frequency depends on the interval for which the spectrum is calculated: In case of the trace elements, for instance, the spectrum is calculated for frequencies at constant intervals of 0.00020 $years^{-1}$ (stable isotopes: 0.00007 $years^{-1}$). This yields a maximal absolute error of ±0.00020 $years^{-1}$. As the periodicity is the inverse of its corresponding frequency, the difference in periodicity between two adjacent frequencies, which represents the maximum error in terms of periodicity, is maximal for the lowest frequency and decreases with increasing frequency. For example, the difference between the first (0.00020 $years^{-1}$) and the second frequency (0.00040 $years^{-1}$) for which the spectrum is calculated equals to a cycle duration of about 2,528 years, while the difference between the second and the third frequency (0.00059 $years^{-1}$) equals to a cycle duration of about 843 years. Thus, the periodicity corresponding to the second frequency (2,528 years) has a positive error of 2,528 years and a negative error of 843 years.

As the maximum errors related with each peak in the frequency spectra are dramatically increased at low frequencies, i.e. long periodicities (as explained above), all periodicities exceeding 1,000 years are omitted and the discussion of the spectra focuses on periodicities of ≤ 150 years duration.

The number of periodicities exceeding the confidence levels of 95% and/or 99%, range from 14 ($\delta^{18}O$) to 47 (Ba) and are generally more numerous for the trace elements than the stable isotopes, although the Na data set also only yields 15 statistically significant periodicities. Most of the detected periodicities are multi-decadal (Figure 5.48), while the time series of Fe and Si also seem to contain several multi-year periodicities as short as three years.

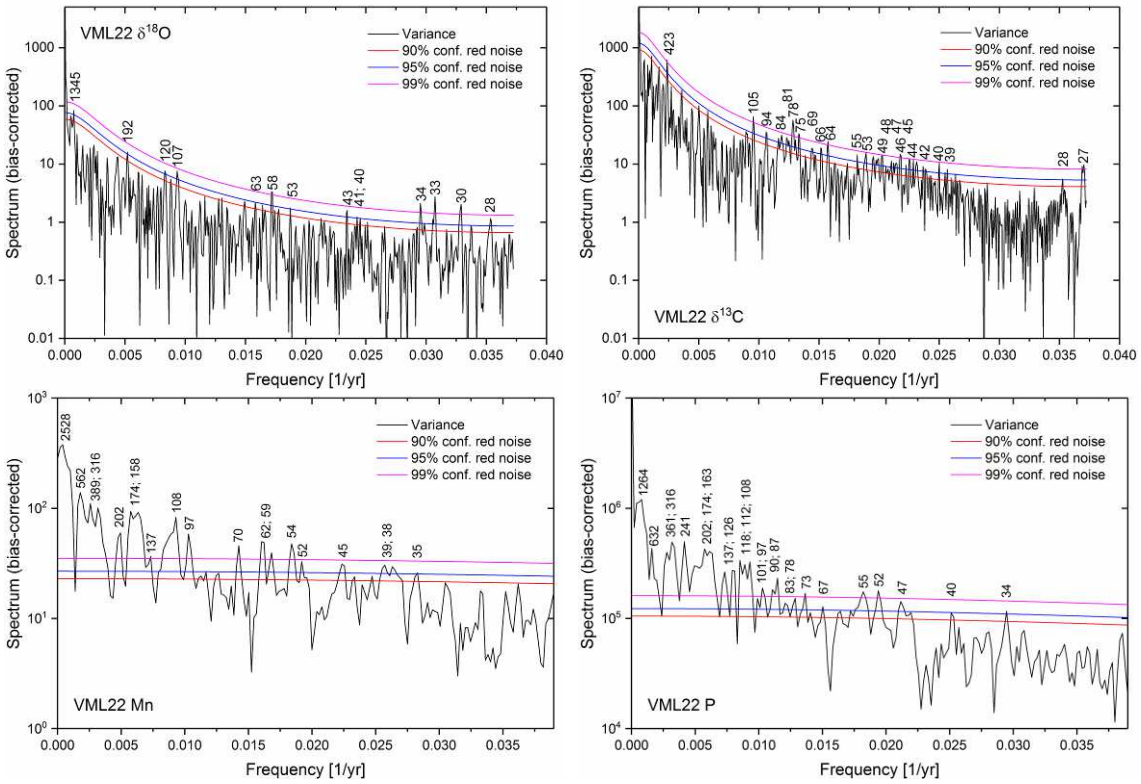

Figure 5.47: Estimated red-noise spectra of the proxy signals from stalagmite VML22 for $\delta^{18}O$, $\delta^{13}C$ (top), Mn and P (bottom). The numbers above peaks significant at the 95% and/or 99% confidence level indicate the respective periodicity (in years) of the potential cyclic behaviour represented by each peak.

Figure 5.48 might give the impression that the statistically significant periodicities (of up to 150 years) detected by frequency analysis are distributed fairly uniformly, especially if the error ranges are considered as well. However, Figure 5.49 demonstrates that the distribution of periodicities is not uniform, but that the periodicities rather seem to cluster in a range from about 30 to 70 years cycle duration. Periodicities shared by most (at least six) proxy signals are 28 ($\delta^{18}O$, $\delta^{13}C$, Sr, Ba, Si, Zn, U), 30 (Sr, Ba, Si, Fe, Zn), 34 ($\delta^{18}O$, Mg, Ba, P, U, Fe), 35 (Sr, Ba, Fe, Mn, Si, Al, Cu, Zn), 39 ($\delta^{13}C$, Mg, Sr, Ba, Fe, Mn, P, U, Al), 40 ($\delta^{18}O$, $\delta^{13}C$, P, U, Mg, Zn), 47 ($\delta^{13}C$, Mg, Fe, Cu) and 52 years (Ba, Si, Na, Mn, Fe, Cu, Zn, Mg, U). It is important to note that, considering dating uncertainty, it is impossible to tell these periodicities apart, but it is evident that multi-decadal periodicities are numerous in the geochemical time-series of stalagmite VML22. Two separate peaks in absolute frequency are identified at at 108 years (Mg, Mn, Fe, U, Zn, P) and 174 years (Si, U, P, Al, Na, Cu). These periodicities do not seem to be shared specifically by proxy signals attributed to the same geochemial group as defined in Section 5.6.2, but also by proxy signals attributed to different groups. However, the element pairs with the strongest correlation (Sr/Ba and P/U) share about half of their respective periodicities.

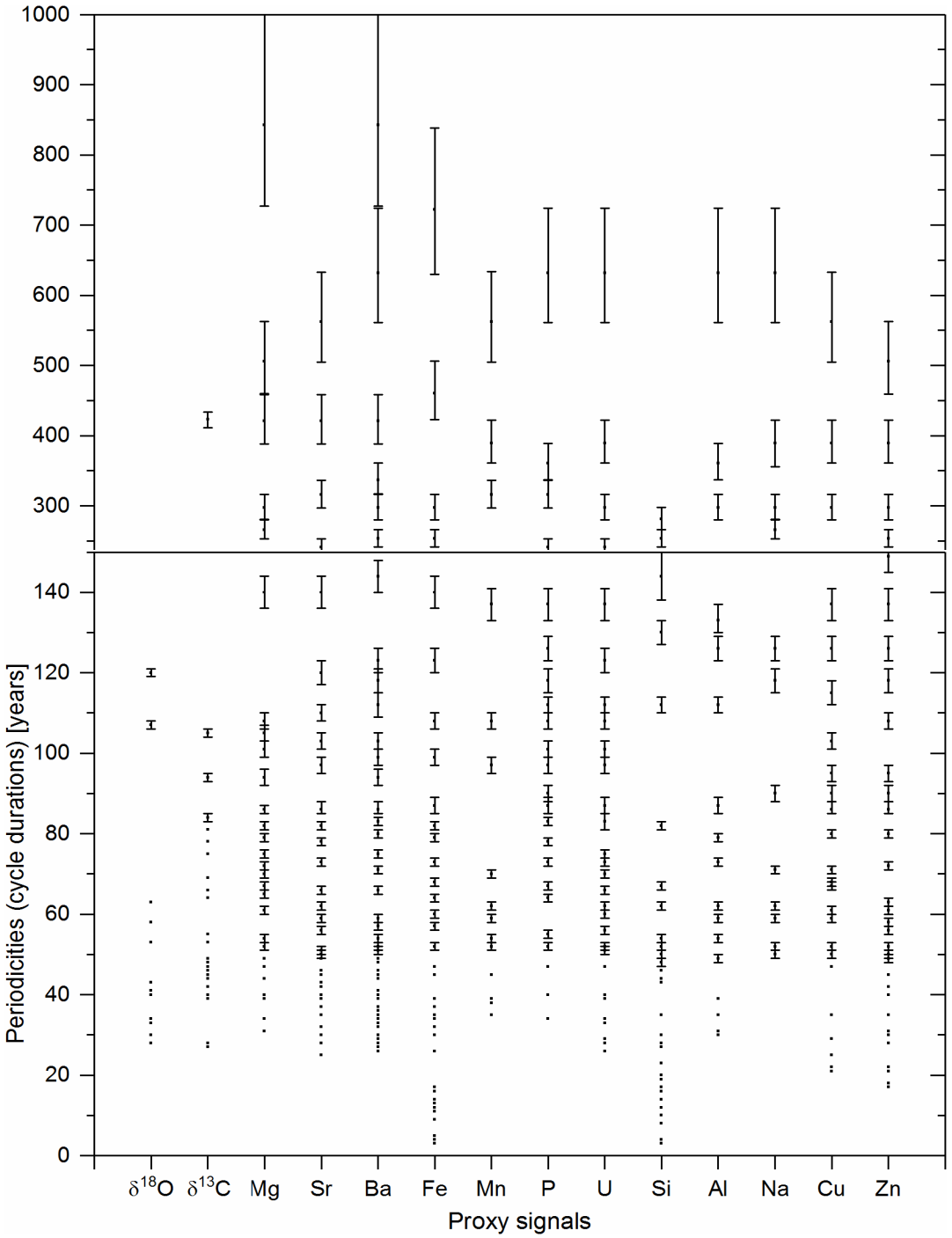

Figure 5.48: Statistically significant periodicities (cycle durations) identified by frequency analysis of the proxy records of stalagmite VML22 (rectangles), including their respective maximum error range down to ±1 years. All values are rounded to whole numbers. Note the change in scale at 150 years cycle duration (horizontal line). Higher periodicities are omitted due to their increased error.

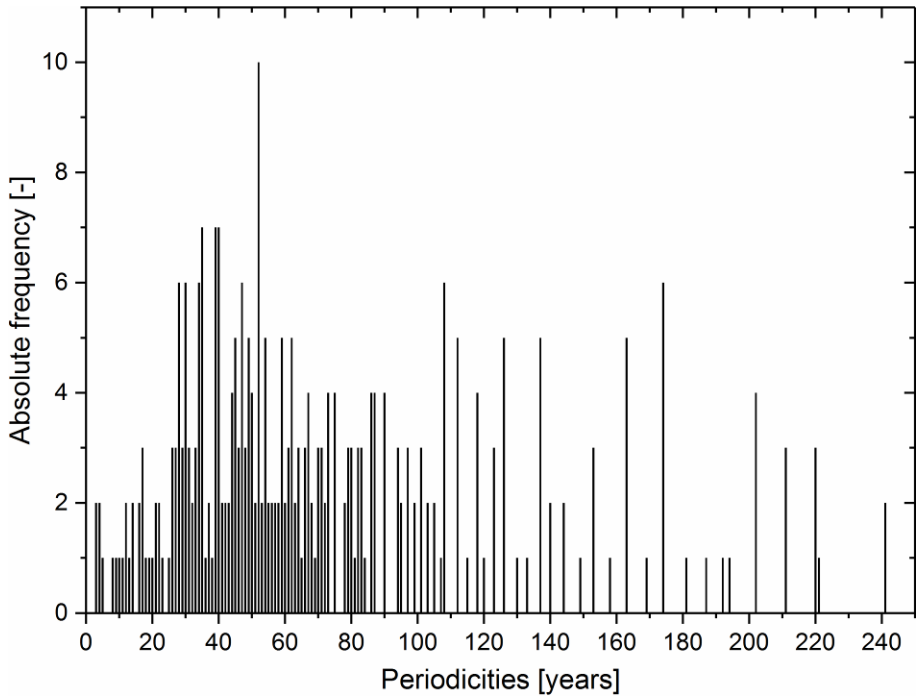

Figure 5.49: Absolute frequency distribution of all the periodicities (up to 250 years) in the geochemical records of stalagmite VML22 identified by frequency analysis.

5.6.5.2 Stalagmite VSMS2

As only the age model during the second growth period of stalagmite VSMS2 was deemed accurate enough for a successful frequency analysis, the first and third growth periods were not analysed for potential periodicities.

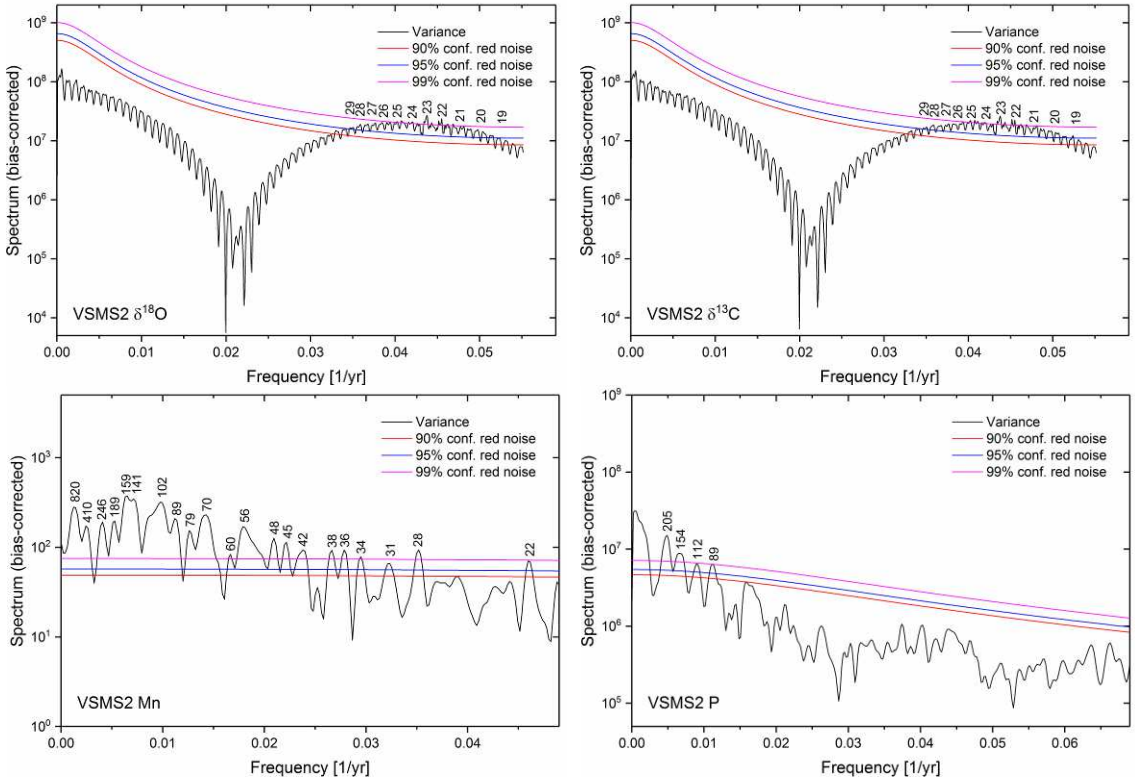

Figure 5.50: Estimated red-noise spectra of the proxy signals from stalagmite VSMS2 for $\delta^{18}O$, $\delta^{13}C$ (top), Mn and P (bottom). The numbers above peaks significant at the 95% and/or 99% confidence level indicate the respective periodicity (in years) of the potential cyclic behaviour represented by each peak.

Figure 5.50 shows the frequency spectra for $\delta^{18}O$, $\delta^{13}C$ (top), Mn and P (Figure 5.47bottom) only, the remaining spectra are included in the Appendix, while the errors of each statistically significant periodicity detected in the data sets are shown separately in Figure 5.51. Overall, the spectra are similar to those calculated for stalagmite VML22. However, the frequency spectra for $\delta^{18}O$ and $\delta^{13}C$ clearly stand out among the remaining spectra due to their distinctive shape with a local minimum at a frequency of 0.02 years $^{-1}$. Furthermore, both spectra are virtually (but not numerically) identical and only yield statistically significant values at the high-frequency end of the spectrum with periodicities ranging from 19 to 29 years. The first order variation in the spectra is superimposed by low-amplitude peaks that seem equally spaced. All these features suggest that the frequency analysis of both stable isotope data sets was unsuccessful and that the resulting spectra actually represent artefacts rather than interpretable results. It is also noteworthy that the spectrum of P only contains four periodicities that exceed the 95% and/or the 99% confidence level.

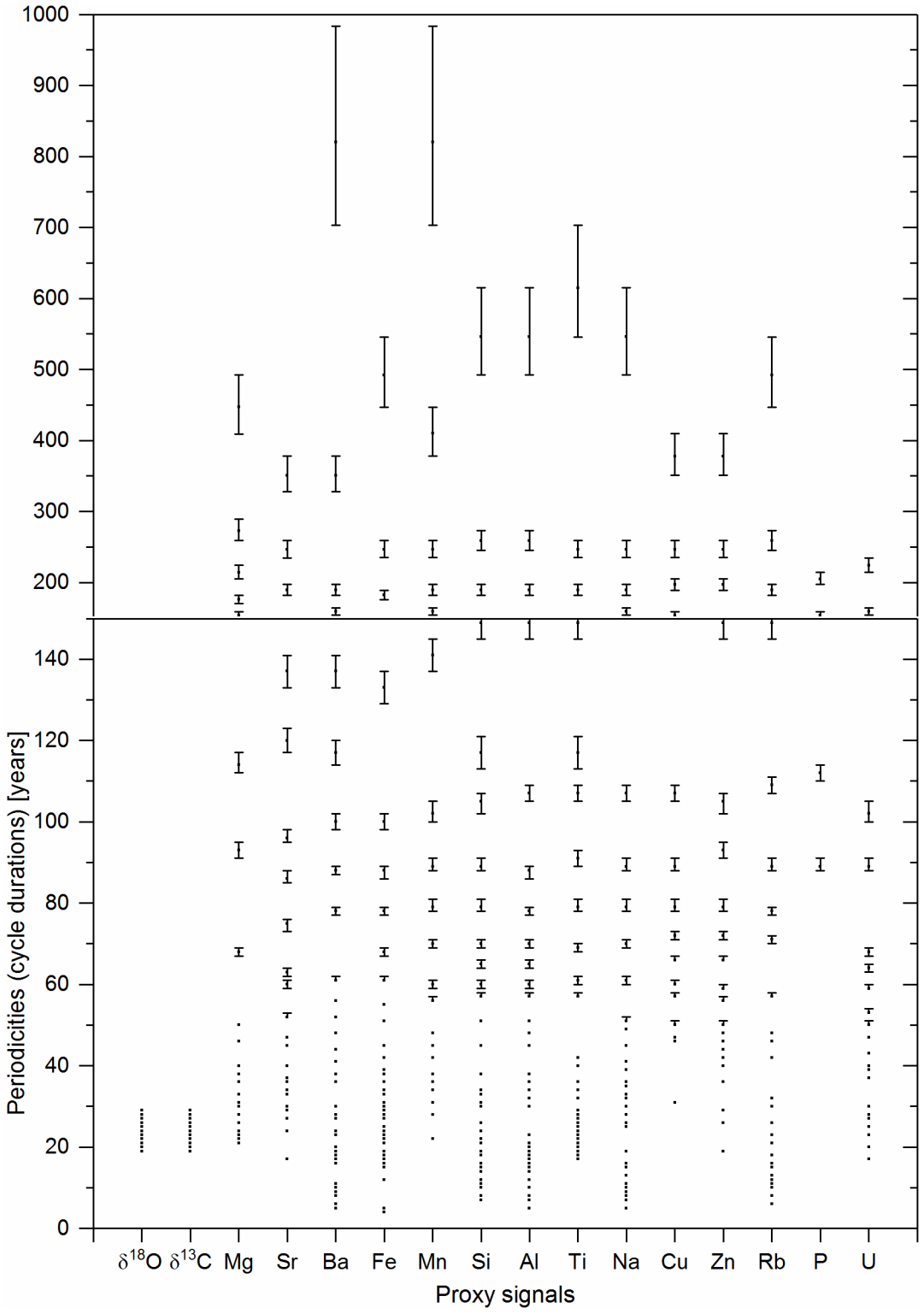

Figure 5.51: Statistically significant periodicities (cycle durations) identified by frequency analysis of the proxy records of stalagmite VSMS2 (rectangles), including their respective maximum error range down to ±1 years. All values are rounded to whole numbers. Note the change in scale at 150 years cycle duration (horizontal line). Higher periodicities are omitted due to their increased error.

Apart from the stable isotope data sets, frequency analysis was succesful. The number of periodicities exceeding the confidence levels of 95% and/or 99%, range from 15 (Cu) to 36 (Fe). As for stalagmite VML22, most of the detected periodicities are multi-decadal (Figure 5.51), while the time series of Ba, Fe, Si, Al, Na and Rb also contain several multi-year periodicities as short as four years.

Similarly to stalagmite VML22, Figure 5.52 demonstrates that the distribution of the statistically significant periodicities is not uniform, but that the periodicities rather cluster in a range from about 30 to 70 years cycle duration. Periodicities shared by most (at least eight) proxy signals are 19 ($\delta^{18}O$, $\delta^{13}C$, Al, Ba, Na, Cu, Si, Ti, Fe), 21 ($\delta^{18}O$, $\delta^{13}C$, Al, Si, Ti, Fe, Rb, Mn), 23 ($\delta^{18}O$, $\delta^{13}C$, Mg, Ba, Fe, Al, Ti, Rb, U), 24 ($\delta^{18}O$, $\delta^{13}C$, Mg, Sr, Ba, Fe, Si, Ti), 26 ($\delta^{18}O$, $\delta^{13}C$, Mg, Si, Ti, Na, Zn, Rb), 28 ($\delta^{18}O$, $\delta^{13}C$, Mg, Ba, Fe, Mn, Ti, Na, U), 30 (Mg, Sr, Ba, Fe, Si, Al, Na, Rb, U) and 36 years (Mg, Sr, Ba, Fe, Mn, Al, Na, Zn), with two separate peaks in absolute frequency at 89 years (Mn, Si, Na, Cu, Rb, P, U) and 189 years (Sr, Ba, Mn, Si, Al, Ti, Na, Rb). If the stable isotopes periodicities are not included, these are still the most frequently detected periodicities. As for stalagmite VML22, there is no obvious dependence between shared periodicities and attribution of the geochemical records to a specific geochemical group as defined in Section 5.6.2.

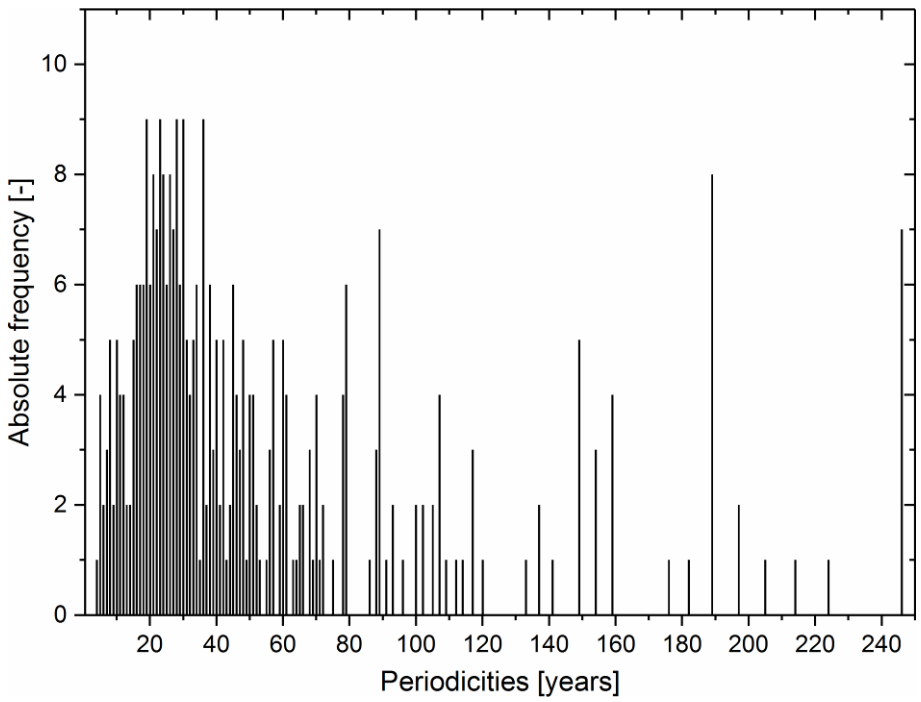

Figure 5.52: Absolute frequency distribution of all the periodicities (up to 250 years) in the geochemical records of stalagmite VSMS2 identified by frequency analysis.

5.7 Cave Environment

5.7.1 Characterisation of Host Rock, Soils and Plants

5.7.1.1 Host Rock Mineralogy

The host rock surrounding and overlying cave Ma Le 2 (samples G_05, G_02-1 and G_02-2) mainly consists of calcite and Mg-calcite (Figure 5.53). In some cases the reference peaks for a synthetic Mg-calcite containing 3 wt-% Mg plot at slightly higher 2θ values than the sample peaks in the diffractogram indicating that the actual sample contains less than 3 wt-% Mg. Only sample G2_05 clearly also features dolomite.

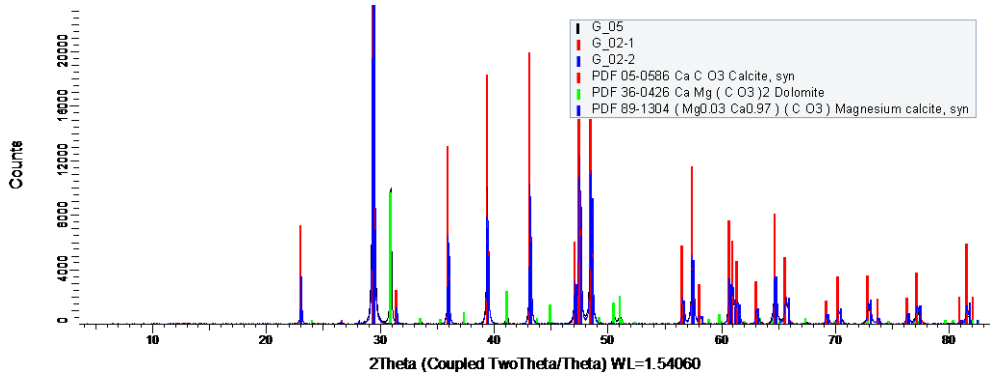

Figure 5.53: X-ray diffractograms for samples G_05, G_02-1 and G_02-2 including the peak positions of synthetic calcite, synthetic Mg-calcite and dolomite for reference (vertical bars).

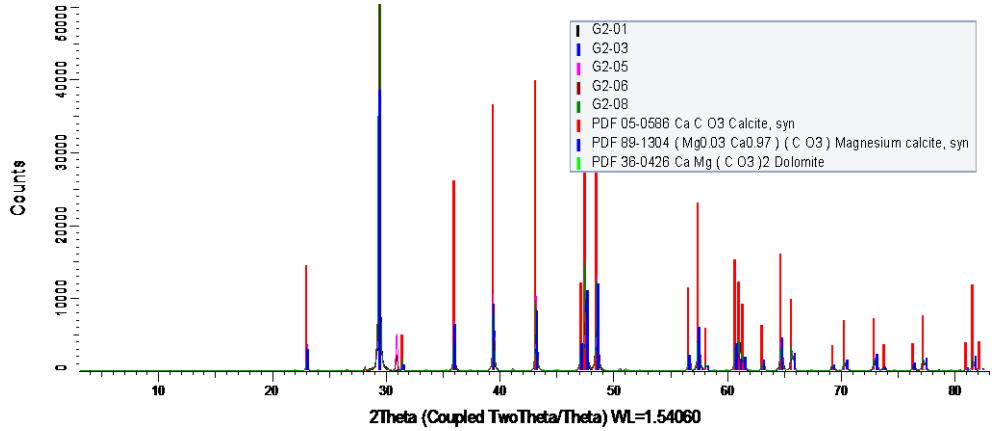

Figure 5.54: X-ray diffractograms for samples G2-01, -03, -05, -06 and -08 including the peak positions of synthetic calcite, synthetic Mg-calcite and dolomite for reference (vertical bars).

Of the host rock samples from inside cave Sang Ma Sao, the samples G2-01, -03, -05, -06 and -08 predominantly consist of calcite and Mg-calcite with a Mg content of less than 3 wt-% (Figure 5.54). The portion of dolomite is so low that it can barely be distinguished from background noise, even in sample G2-05 where the dolomite signal is strongest. Samples G2-02 and -04 mainly consist of quartz but also contain calcite (Figure 5.55). Additionally, dolomite is barely detectable in sample G2-04. While dolomite is only a minor constituent in all other rock samples from inside cave Sang Ma Sao, it is a major component in samples G2-07 and -09 (Figure 5.56) besides the dominant mineral calcite.

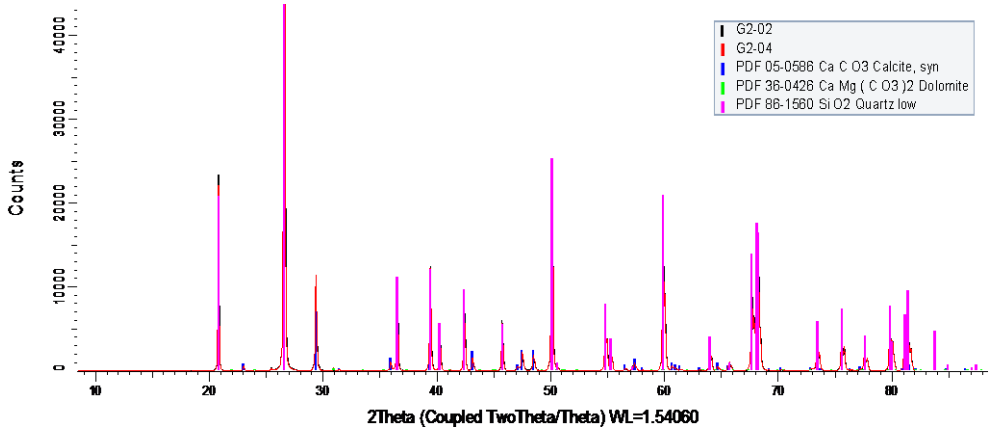

Figure 5.55: X-ray diffractograms for samples G2-02 and -04 including the peak positions of synthetic calcite, dolomite and quartz for reference (vertical bars).

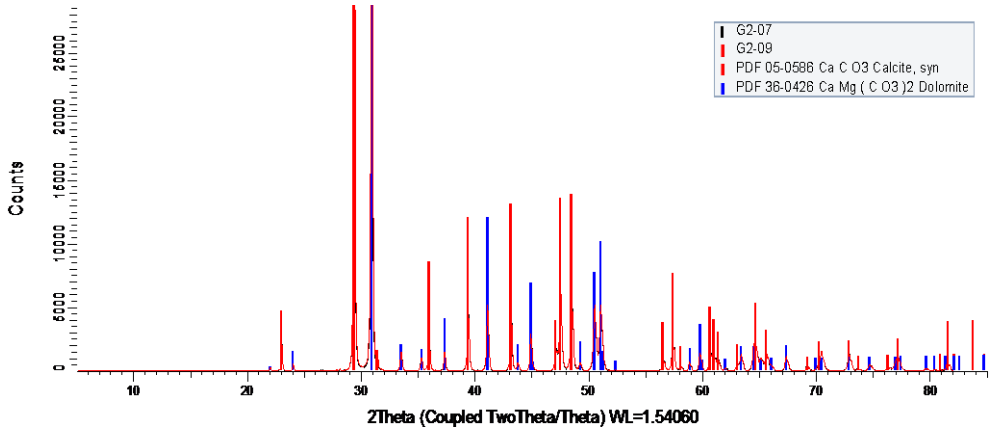

Figure 5.56: X-ray diffractograms for samples G2-07 and -09 including the peak positions of synthetic calcite and dolomite for reference (vertical bars).

The black crust found on the walls of cave Sang Ma Sao predominantly consists of hydroxylflouroxyapatite and hydroxylapatite (Figure 5.57), but also contains small amounts of calcite, dolomite and quartz.

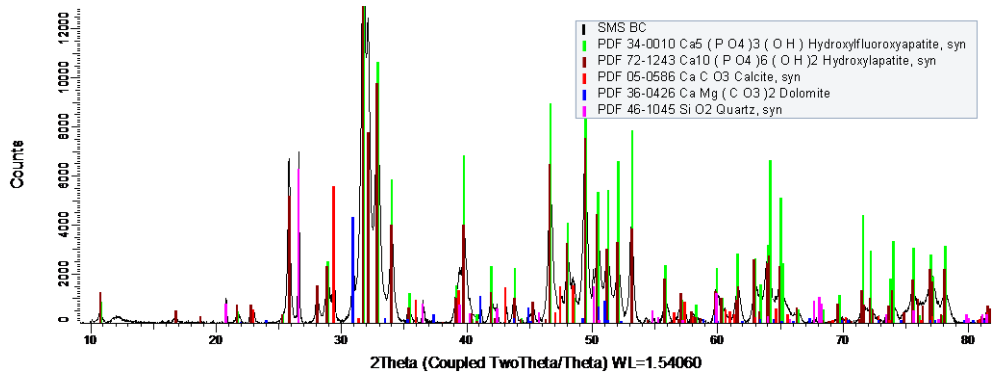

Figure 5.57: X-ray diffractogram for the black crust on the walls of cave Sang Ma Sao (sample SMS BC) including the peak positions of calcite, dolomite, quartz, hydroxylflouroxyapatite and hydroxylapatite for reference (vertical bars).

5.7.1.2 Host Rock Geochemistry

The geochemical composition of the host rock samples confirms the host rock mineralogy (Section 5.7.1.1). The predominance of calcite in most of the host rock samples is evident from the predominance of Ca with portions of almost 45 wt-% indicating that these samples almost exclusively consist of $CaCO_3$ (Figure 5.58 and Figure 5.59). In these samples, Mg is the second most abundant element, consistent with the identification of Mg-calcite and even small amounts of dolomite in the X-ray diffractograms.

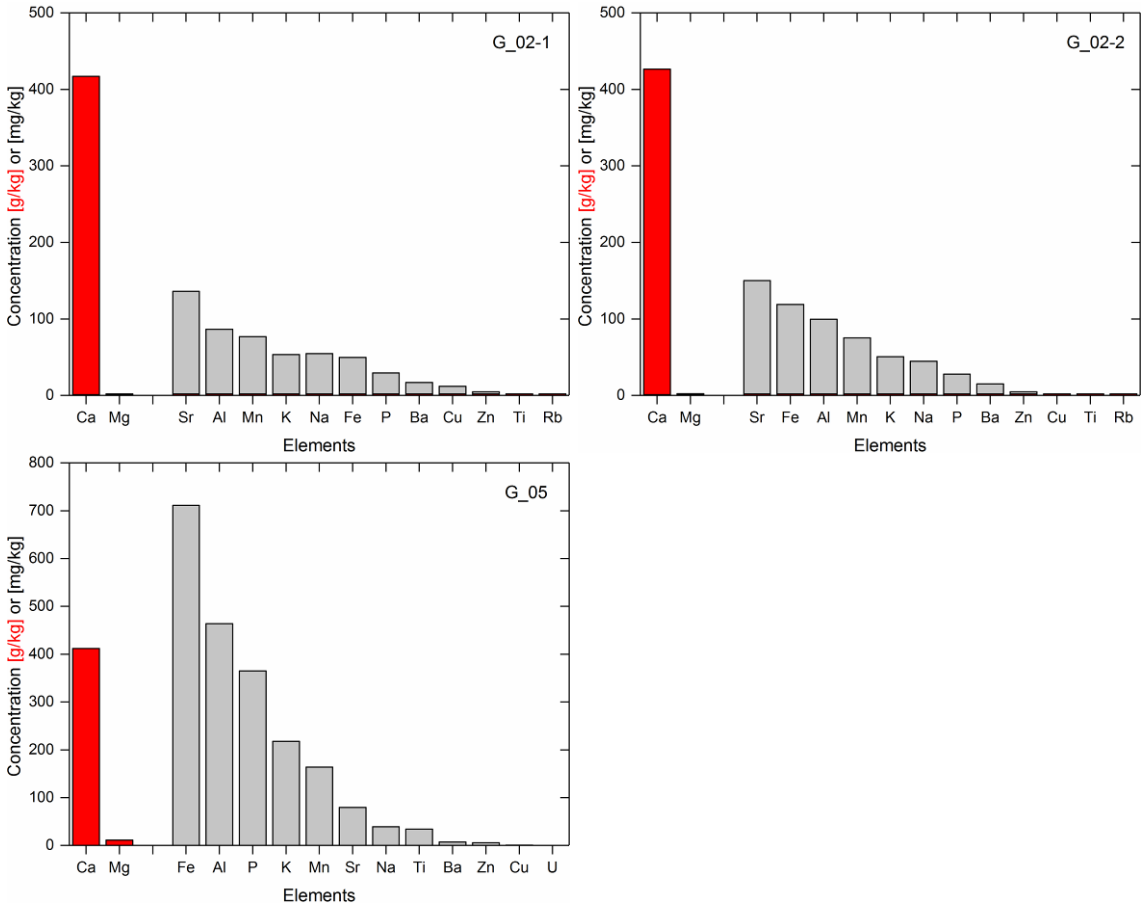

Figure 5.58: Geochemical composition from ICP-MS analyses of host rock samples G_02-1 and G_02-2 from inside Ma Le 2 cave and of sample G_05 from above cave Ma Le 2. Element concentrations are given in g/kg (red bars) and mg/kg (grey bars).

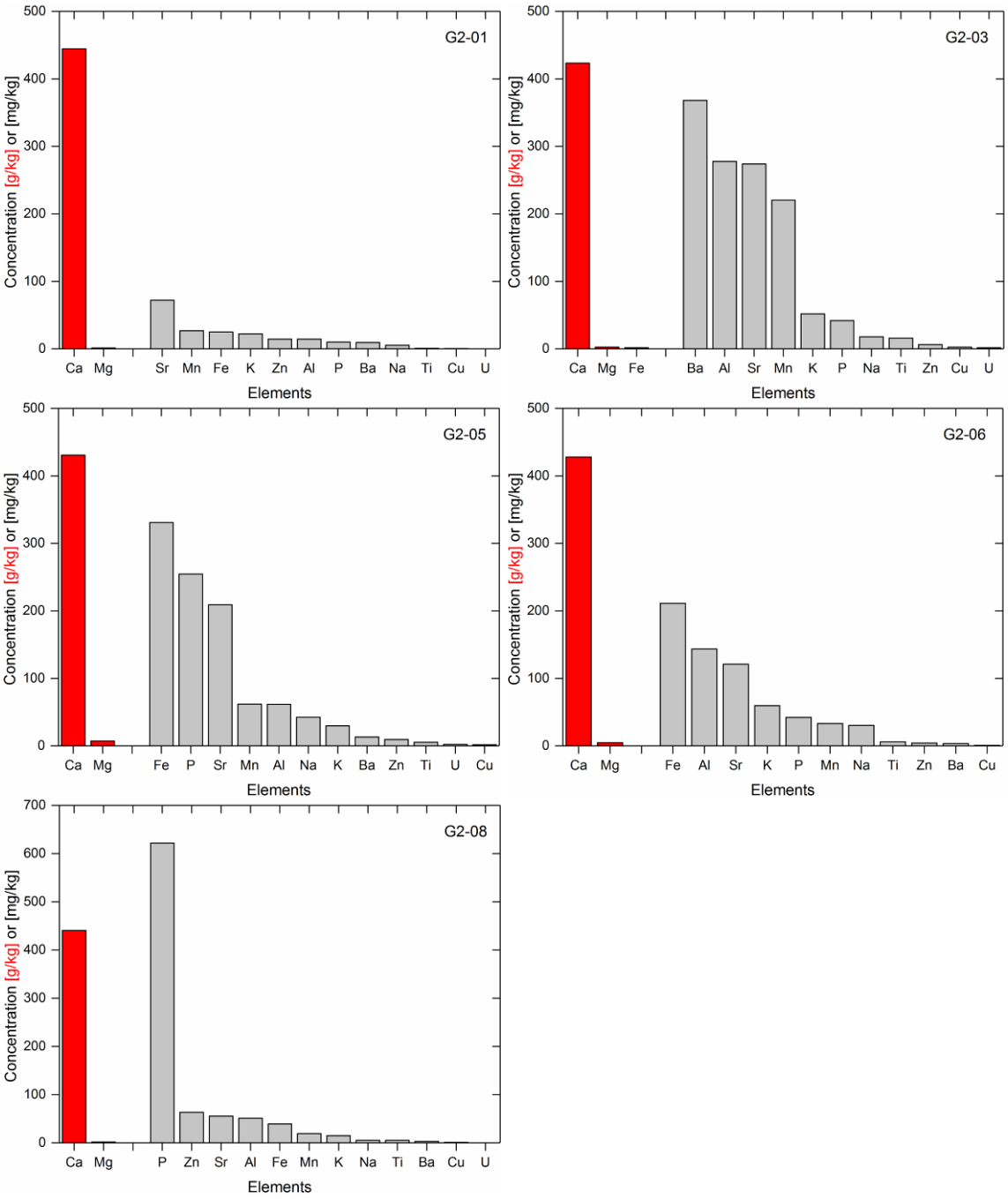

Figure 5.59: Geochemical composition from ICP-MS analyses of host rock samples G2-01, -03, -05, -06 and -08. Element concentrations are given in g/kg (red bars) and mg/kg (grey bars).

The only two host rock samples with Mg contents significantly exceeding several weight-‰ are samples G2-07 and -09 (Figure 5.60) with Mg portions of 6.1 and 6.3 wt-%, respectively. Together with the Ca contents reduced to 34.7 and 34.1 wt-% compared to 45 wt-%, respectively, this clearly indicates the presence of dolomite as a major component in these samples.

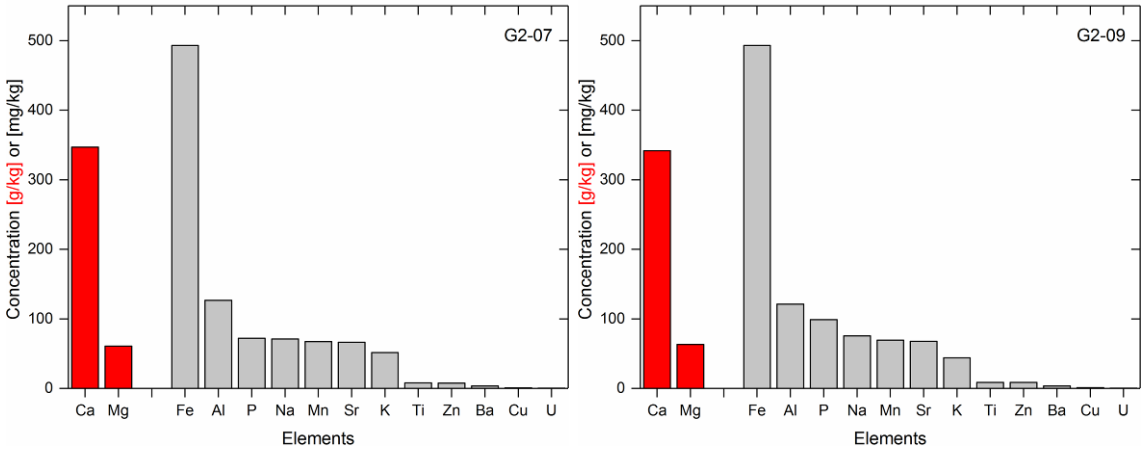

Figure 5.60: Geochemical composition from ICP-MS analyses of host rock samples G2-07 and -09. Element concentrations are given in g/kg (red bars) and mg/kg (grey bars).

Two of the host rock samples (G2-02 and -04) from inside cave Sang Ma Sao do not mainly consist of calcite, but are dominated by quartz (Figure 5.55). The geochemical composition of these two samples (Figure 5.61) confirms that calcite only constitutes a secondary component, with Ca contents of only 3.8 and 4.0 wt-%, respectively.

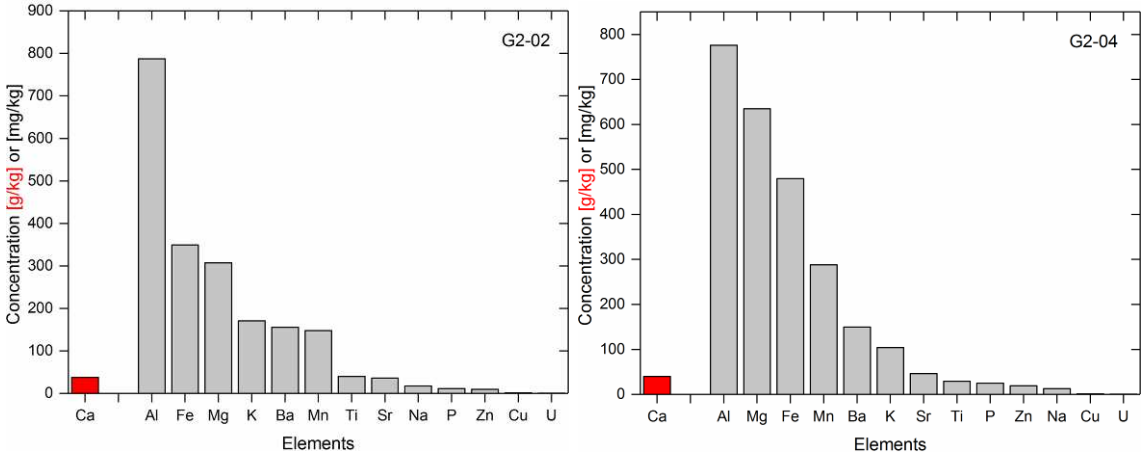

Figure 5.61: Geochemical composition from ICP-MS analyses of host rock samples G2-02 and -04. Element concentrations are given in g/kg (red bars) and mg/kg (grey bars).

Besides the predominant elements Ca, Mg and Si (in case of samples G2-02 and -04), all host rock samples contain other elements at various concentrations that do not reach one wt-‰ and therefore potentially contribute to the geochemical composition of the studied stalagmites. The most abundant of these elements are, depending on the individual samples, Fe and Al (G2-02 and -04), Ba (G2-03), Sr (G2-02) or P (G2-08). Sample G2-02 stands out by its low concentrations of elements other than Ca, sample G2-08 by its high P concentrations (620 mg/kg; Figure 5.59, bottom left) compared to the other host rock samples.

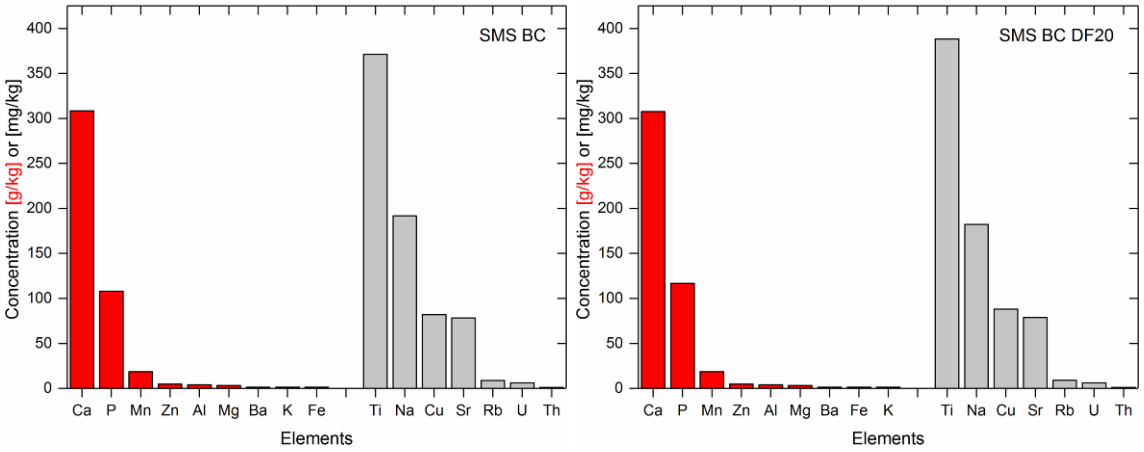

Figure 5.62: Geochemical composition from ICP-MS analysis of a sample of the black crust on the walls of cave Sang Ma Sao (sample SMS BC), after sample dilution by a factor of five (left) and 20 (right). Element concentrations are given in g/kg (red bars) and mg/kg (grey bars).

The geochemical composition of the black crust on the walls of cave Sang Ma Sao (sample SMS BC) is significantly different from the host rock composition. Although most abundant element in this sample is still Ca at 30.8 wt-%, the second most abund element is not Mg, but P at 10.8 wt-%, followed by Mn (1.9 wt-%). Furthermore, a large number of elements are present at concentrations exceeding one wt-%, including Zn, Al, Mg, Ba, K and Fe indicating an even more complex geochemistry than is evident from the corresponding mineralogy (Figure 5.57).

5.7.1.3 Soil Mineralogy

The soil samples from above cave Ma Le 2 are higly similar to each other in their mineralogical composition (Figure 5.63 andFigure 5.64). The topmost layers are clearly dominated by silicon dioxide or quartz but relatively small and broad peaks in the X-ray diffractograms indicate the presence of hematite, goethite and gibbsite.

The soils also contain a number of clay minerals, in particular kaolinite. The X-ray diffractograms are also consistent with the presence of other clay minerals of the kaolin group such as dickite and nacrite and clay minerals of the smectite group such as montmorillonite and nontronite. However, as X-ray diffractometry was performed on standard samples with randomly oriented mineral grains, these peaks in the diffractograms cannot be confidently attributed to specific clay mineral species. The lower layers of the soils (layer L04 in sample SP01 and layers 02 and 03 in sample BOD) also exhibit these peaks, but at higher signal intensities, while the peaks representing quartz are almost absent. The low height and the wide base of the diffractogram peaks suggest that the soil samples contain a large number of different mineral phases including clay minerals exhibiting similar but not identical d-values.

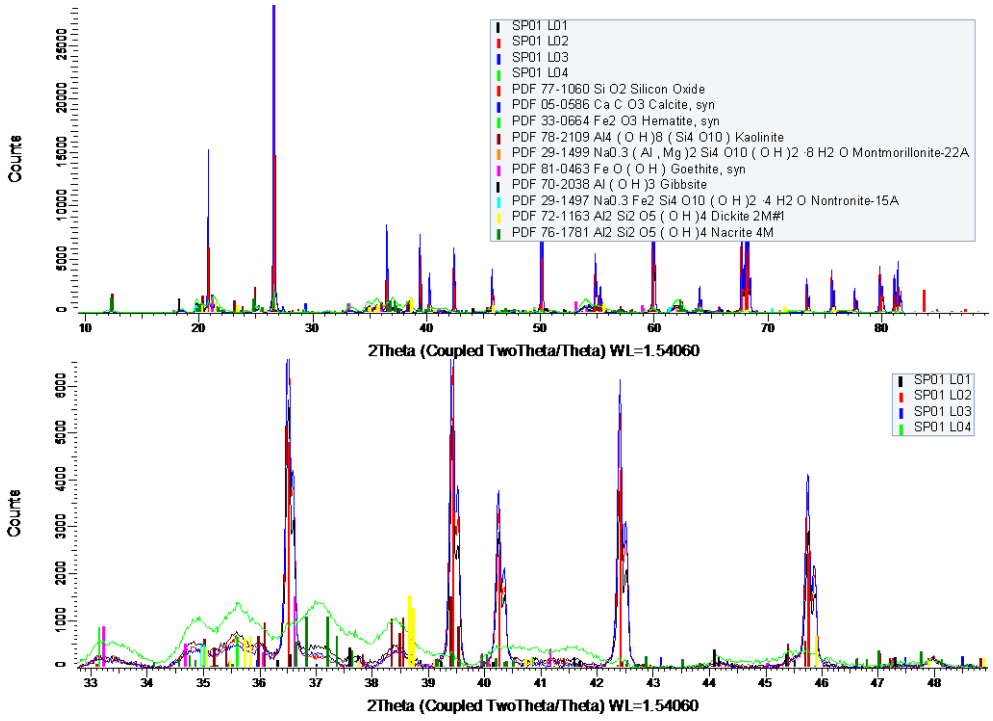

Figure 5.63: X-ray diffractograms for soil samples at site SP01 above cave Ma Le 2 from soil layers L01 to L04 including the peak positions of silicon dioxide, synthetic calcite, hematite, goethite, gibbsite, and of the clay minerals kaolinite, montmorillonite, nontronite, dickite and nacrite for reference (vertical bars); top: overview; bottom: detail. For better readability reference materials are not included in the legend of the bottom sub-plot.

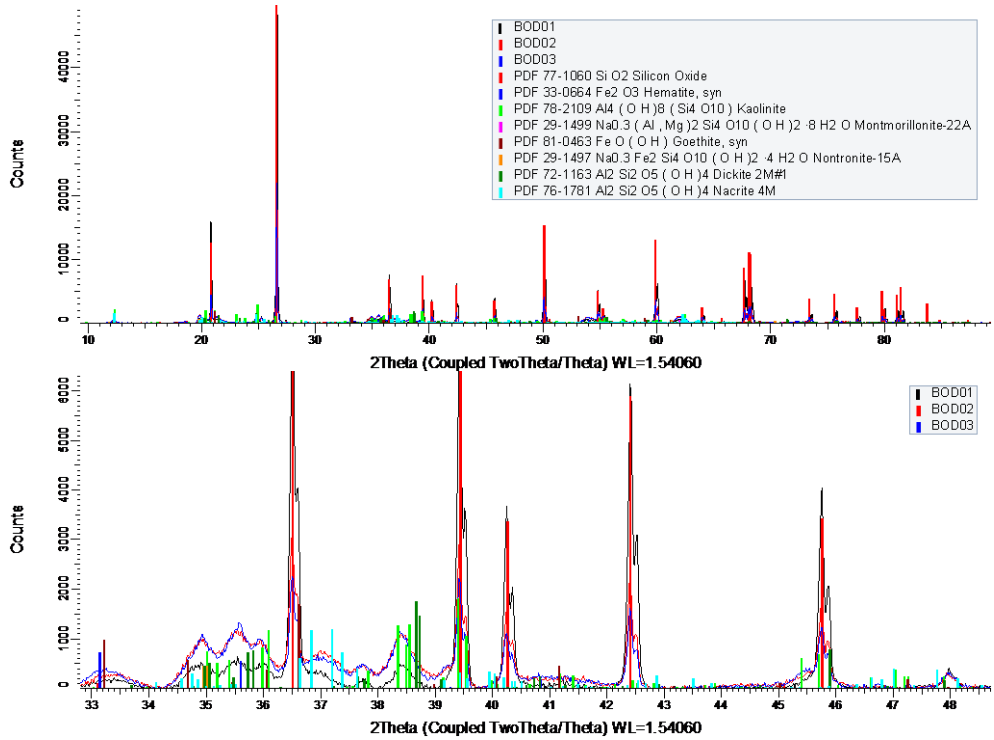

Figure 5.64: X-ray diffractograms for soil samples at site BOD01 above cave Ma Le 2 from soil layers 01 to 02 (BOD02) and at site BOD03 above cave Ma Le 2 including the peak positions of silicon dioxide, hematite, goethite and of the clay minerals kaolinite, montmorillonite, nontronite, dickite and nacrite for reference (vertical bars); top: overview; bottom: detail.

The soil samples from above cave Sang Ma Sao (Figure 5.65) contain much less silicon dioxide (quartz) than the ones from above cave Ma Le 2. At site SMS Soil01, the three depth increments from which soil samples were taken do not significantly differ in their mineralogical composition. Relatively small and broad peaks dominate the X-ray diffractograms of the Sang Ma Sao soils, again indicating the presence of a large number of different mineral phases with similar but not identical d-values.

The most prominent peaks are consistent with the presence of hematite, goethite and gibbsite as well as a number of clay minerals including kaolinite, dickite (in sample SMS Soil02) and nacrite from the kaolin group and montmorillonite from the smectite group. As outlined above, these different clay mineral species cannot be identified specifically as X-ray diffractometry was not performed on samples with oriented mineral grains, but the data still indicate the presence of numerous different clay mineral species.

While the presence of calcite can be inferred from the diffractogram of SMS Soil02, this is not the case for SMS Soil01. The coarse fraction (> 2 mm) of SMS Soil02 (Figure 5.67) mainly consists of calcite, but also contains small amounts of dolomite and quartz.

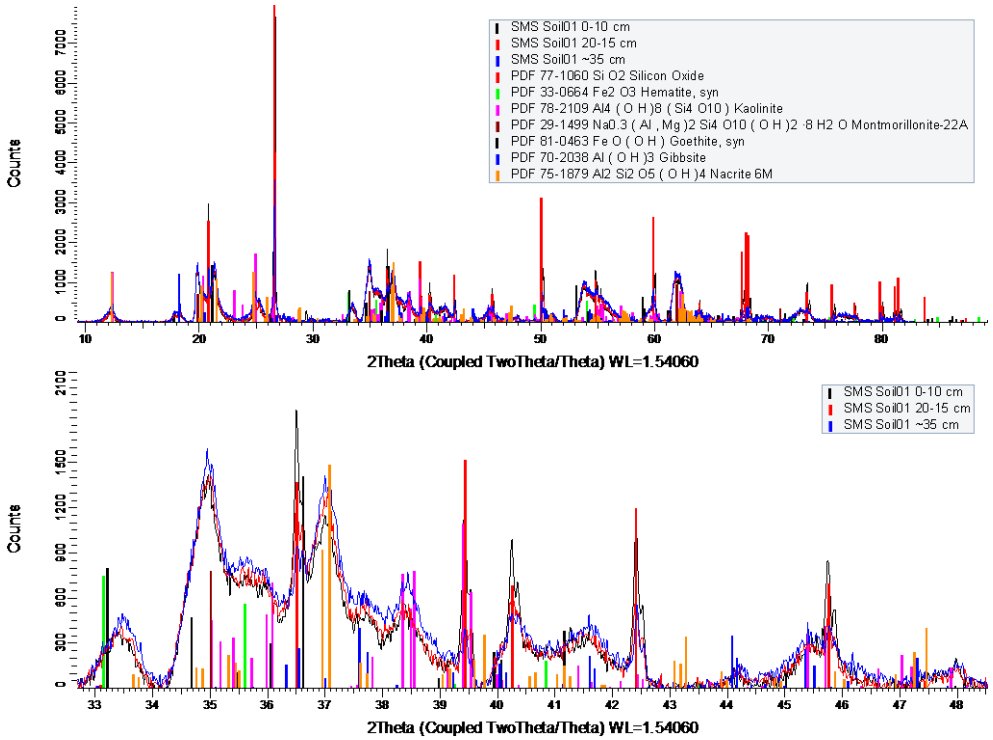

Figure 5.65: X-ray diffractograms for soil samples at site SMS Soil01 above cave Sang Ma Sao from soil layers 01 to 03 including the peak positions of silicon dioxide, hematite, goethite, gibbsite and of the clay minerals kaolinite, montmorillonite and nacrite for reference (vertical bars); top: overview; bottom: detail.

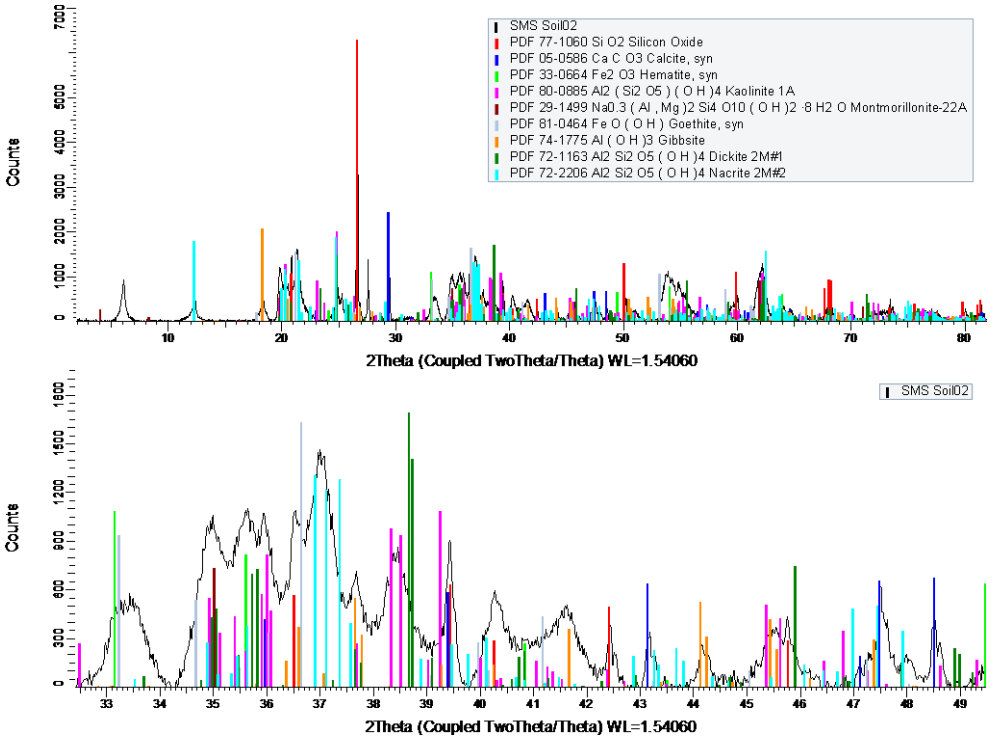

Figure 5.66: X-ray diffractogram for soil sample SMS Soil02 above cave Sang Ma Sao including the peak positions of silicon dioxide, hematite, goethite, gibbsite, calcite and of the clay minerals kaolinite, montmorillonite, dickite and nacrite for reference (vertical bars); top: overview; bottom: detail.

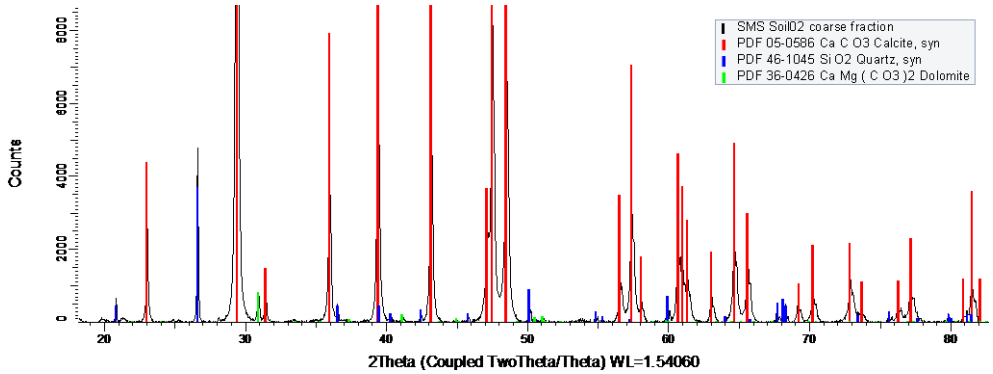

Figure 5.67: X-ray diffractogram for the coarse fraction (> 2 mm) of soil sample SMS Soil02 above cave Sang Ma Sao including the peak positions of calcite, quartz and dolomite for reference.

5.7.1.4 Soil Geochemistry

The geochemical composition is consistent with the mineral phases identified in the corresponding X-ray diffractograms (Section 5.7.1.3). In all soil samples the two most abundant elements are Al and Fe (Si not measured).

The two soil layers at site BOD01 are almost identical in geochemical composition (Figure 5.68 top) in a relative sense, while the absolute concentrations of Al and Fe in layer BOD01 (5.7 and 4.4 wt-%, respectively) are significantly lower than in layer BOD02 underneath (11.3 and 6.8 wt-%, respectively). These concentrations are similar to those measured at site BOD03 (Figure 5.68 bottom) where they amount to 11.8 and 8.4 wt-%, respectively. Titanium is the third most abundant element in all three samples, with Ca and K concentrations exceeding 1 wt-%. At site BOD03, also Mn and P exceed 1 wt-%.

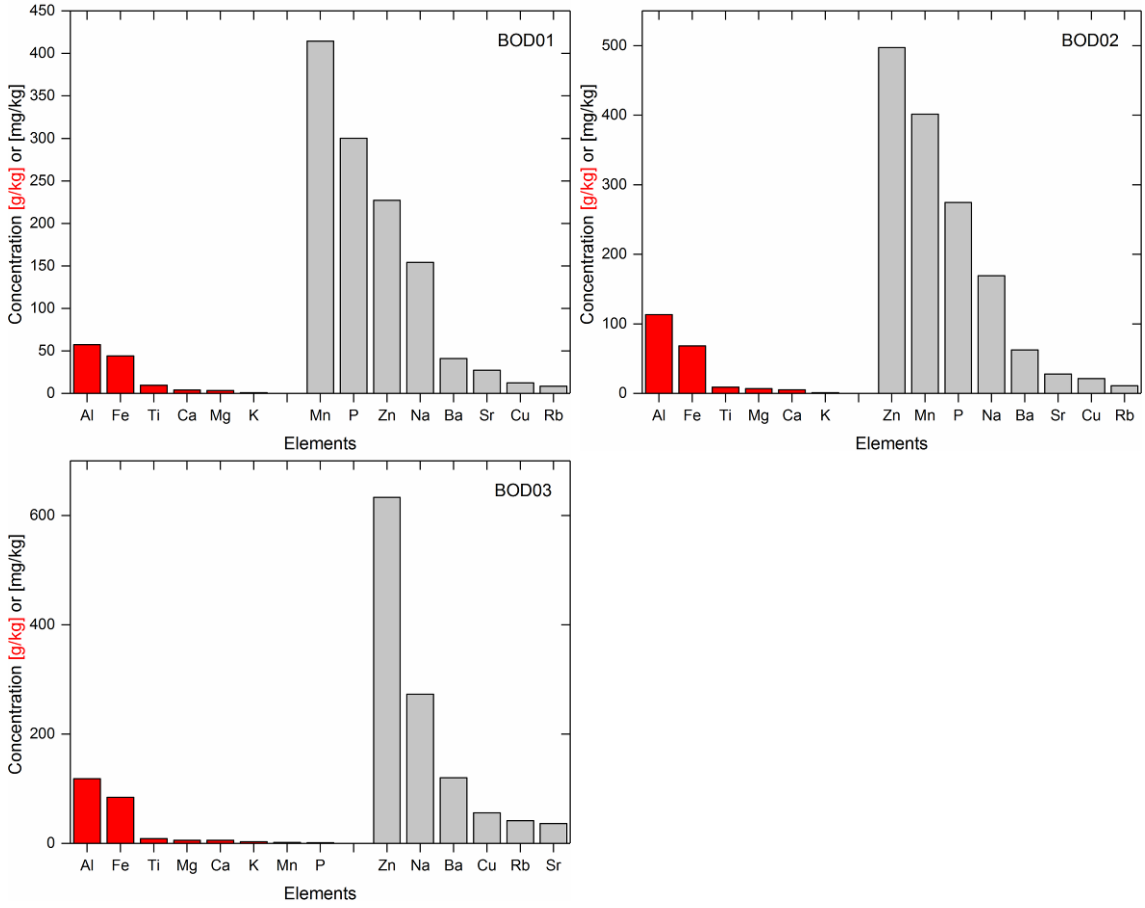

Figure 5.68: Geochemical composition from ICP-MS analyses of soil samples at site BOD01 from above cave Ma Le 2 cave from soil layers BOD01 and BOD02 and at site BOD03 from above cave Ma Le 2 cave. Element concentrations are given in g/kg (red bars) and mg/kg (grey bars).

At site SP01 above cave Ma Le 2, the three topmost soil layers contain noticeably lower amounts of Al and Fe compared to the bottom layer (Figure 5.69). While the topmost layer (L01) features Al and Fe concentrations of 6.4 and 5.6 wt-%, respectively, the two layers below (L02 and L03) exhibit concentrations of 4.2 and 3.9 wt-% and of 4.4 and 4.0 wt-%, respectively. Soil layer L04, however, contains 13.3 and 12.2 wt-% Al and Fe, respectively. The high abundance of Al and Fe in the soil samples corroborates the interpretation of the X-ray diffractograms indicating Al-bearing minerals such as gibbsite, Fe-bearing minerals like hematite, goethite and clay minerals such as kaolinite that contribute to the Al pool in the soils.

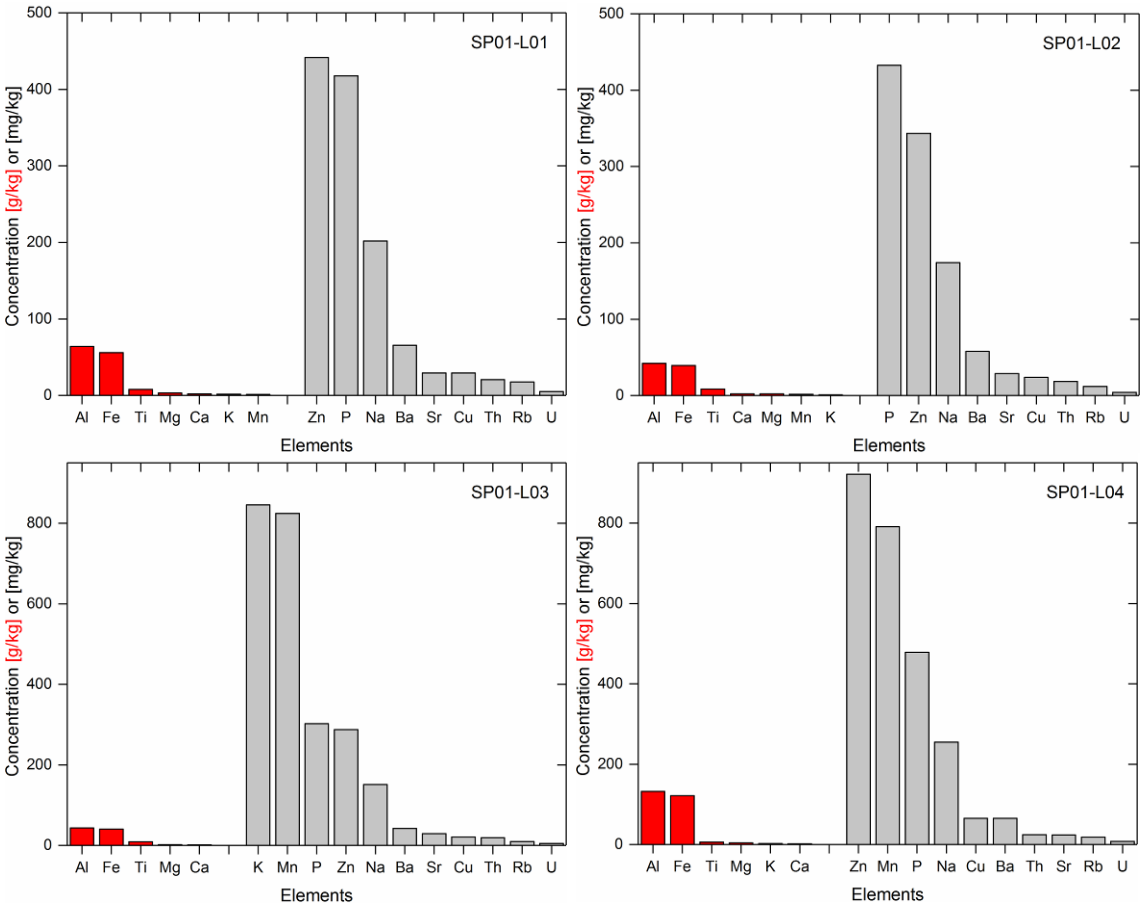

Figure 5.69: Geochemical composition from ICP-MS analyses of soil samples at site SP01 from above cave Ma Le 2 from soil layers L01 to L04. Element concentrations are given in g/kg (red bars) and mg/kg (grey bars).

In all four soil layers, Ti, Mg and Ca also occur in concentrations exceeding one wt-‰. Titanium is the most abundant element of this group, with concentrations around 8 wt-‰ or 0.8 wt-%. Potassium and Mn are present in similar, only slightly lower concentrations.

While Ca is partly associated with small amounts of calcite in the samples (except for L04), no mineral phases containing Mg and K per se, such as dolomite or feldspars, could be identified from the X-ray diffractograms. These elements are therefore likely associated with the clay mineral fractio, for instance, Mg could be associated with montmorillonite.

If actual Ti- and Mn-phases are present in the soil samples, their concentration is either too low for their detection by XRD or their peaks get lost in the wide and broad peaks in the diffractograms caused by amorphous mineral phases.

The soils above cave Sang Ma Sao are similar to those above cave Ma Le 2 with regard to their geochemical composition (Figure 5.70 and Figure 5.71). At site SMS Soil01, Al and Fe concentrations in the three analysed soil layers are 8.4 and 7.5 wt-%, 9.4 and 7.8 wt-% and 8.9 and 8.1 wt-%, respectively (Figure 5.70), at intermediate levels compared to the concentrations measured in the three topmost soil layers at site SP01 and the bottom layer at that site.

The third most abundant element is not Ti, but K with concentrations around 1.1 wt-%, but the elements present at concentrations exceeding one wt-‰ are the same (K, Mg, Ca, Ti and Mn). Phosphorus is slightly more abundant (up to almost 1 wt-%) than in the soils above cave Ma Le 2 (up to about 0.4 wt-%), especially in the top soil layers.

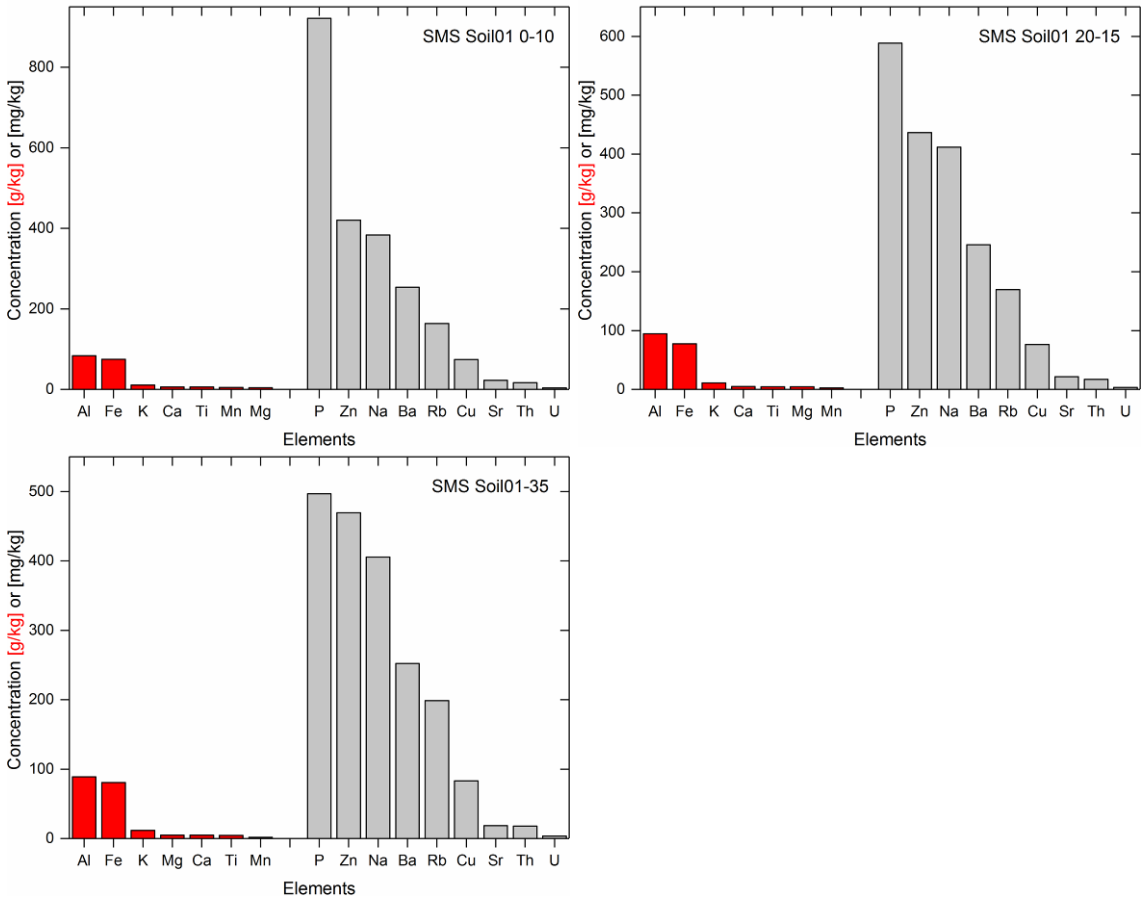

Figure 5.70: Geochemical composition from ICP-MS analyses of soil samples at site SMS Soil01 above cave Sang Ma Sao from 0-10 cm, 15-20 cm and 35 cm, respectively. Element concentrations are given in g/kg (red bars) and mg/kg (grey bars).

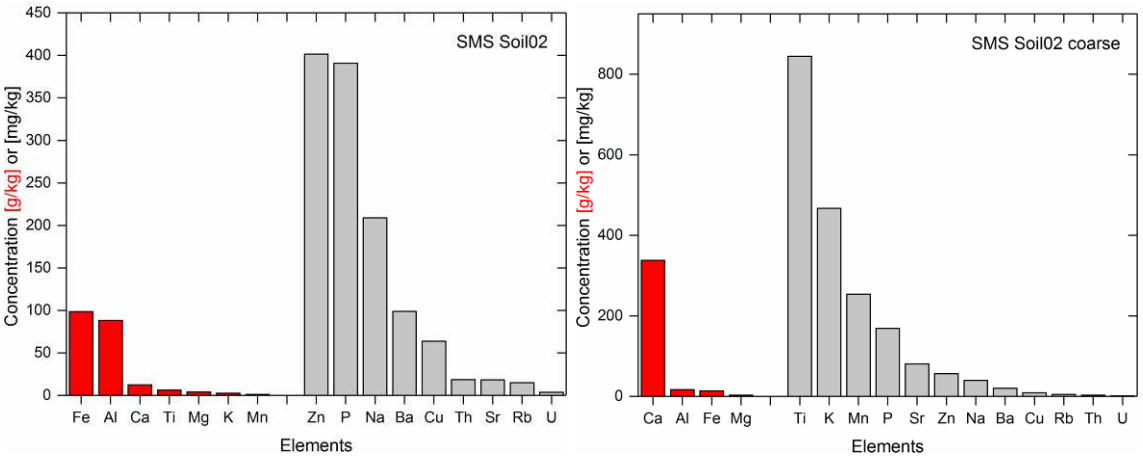

Figure 5.71: Geochemical composition from ICP-MS analyses of soil samples at site SMS Soil02 above cave Sang Ma Sao representing the fine fraction (left; ≤ 2 mm) and the coarse fraction (right; > 2 mm). Element concentrations are given in g/kg (red bars) and mg/kg (grey bars).

Soil sample SMS Soil02 features a similar geochemical composition as the other soil samples, although in this case Fe is the most abundant element with a concentration of 9.9 wt-%, closely followed by Al with a concentration of 8.8 wt-% (Figure 5.71 left). It also contains calcite as confirmed by the third most abundant element being Ca at 1.3 wt-%. Again Ti, Mg, K and Mn are the other elements with concentrations exceeding one wt-‰. The coarse fraction of this sample (Figure 5.71 right) mainly consists of calcite with 33.8wt-% Ca. The Mg (0.3 wt-%) seems to be associated mainly with dolomite (Figure 5.67). Although the diffractogram does not allow to deduce the presence of Al- and Fe-bearing mineral phases, the results of the geochemical analysis indicate that these also occur in the coarse fraction, most likely due to an agglomeration of clay particles.

5.7.1.5 Carbon Isotope ratios in Host Rock, Soils and Plants

Figure 5.72 illustrates the organic carbon isotope values ($\delta^{13}C$) of the plant samples (left) and the soil samples (right) collected at the surface of caves Ma Le 2 and Sang Ma Sao and additional soil samples taken in the study area (locations given in Table A.1 in the Appendix).

The $\delta^{13}C$ values of the plant samples from above cave Ma Le 2 range from -28.7 ‰ to -23.8 ‰, with an average of -27.0 ‰ and a median of -27.3 ‰. As these values are well within the range of $\delta^{13}C$ values of known C3-plants (Section 2.4.2.2), all these plants can be confidently categorised as C3-plants. Three of the four plant samples from above cave Sang Ma Sao (PL01, 02 and 04) exhibit similar $\delta^{13}C$ values ranging from -29.8 ‰ to – 25.6 ‰, with an average of -27.8 ‰ and a median of -28.0 ‰. This indicates that these three plants are also C3-plants. However, one plant sample (PF03) has a noticeably higher $\delta^{13}C$ value of -13.5 ‰ which is therefore identified as a C4-plant.

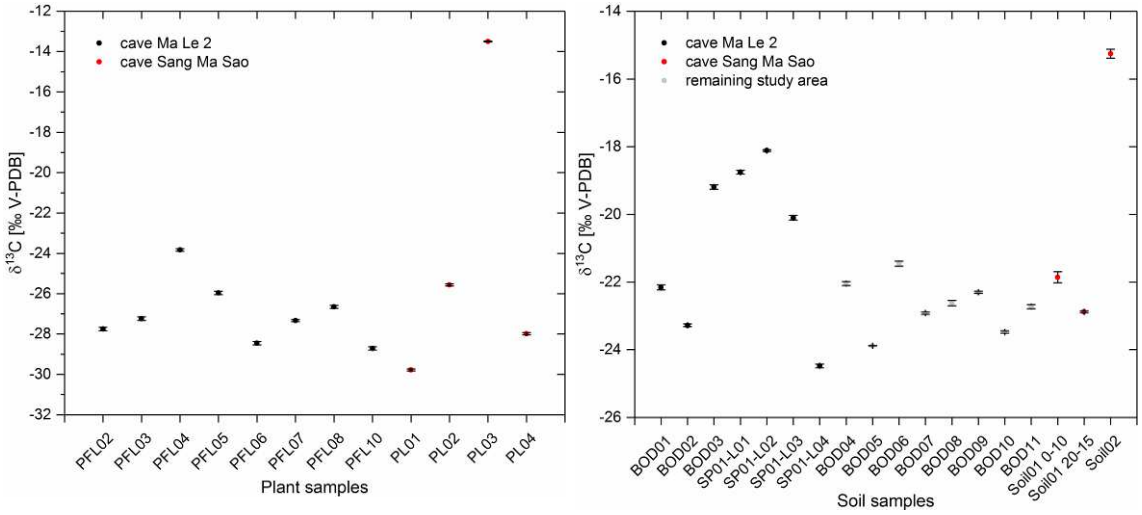

Figure 5.72: Carbon isotopes values ($\delta^{13}C$) of plant samples (left) and soil samples (right) including error bars.

The $\delta^{13}C$ values of the organic matter in the soil samples from above cave Ma Le 2 (Figure 5.72 right) range from -24.5 ‰ to -18.1 ‰, with an average of -20.8 ‰ and a median of -20.1 ‰. While the samples with the three lowest $\delta^{13}C$ values can still be attributed to a vegetation cover clearly dominated by C3-plants, the samples with the four highest $\delta^{13}C$ values indicate a vegetation composition including both C3- and C4 plants. Based on the simplifying assumption that C3-plants are represented by a discrete $\delta^{13}C$ value of -26 ‰ and that C4-plants are represented by a discrete $\delta^{13}C$ value of -13 ‰, the portion of C4-plants contributing to the mixed signal in the case the samples with the four highest $\delta^{13}C$ values can be calculated to about 61 %, 56 %, 52 % and 45 %, respectively. Interestingly, increased $\delta^{13}C$ values in organic matter seems to be related to soil samples collected at or near the surface, while deeper soil layers tend to lower $\delta^{13}C$ values. For instance, at site SP01 $\delta^{13}C$ values drop from -18.1 ‰ in the depth increment 45 - 70 cm (layer L02) to -20.1 ‰ in the depth increment 70 - 100 cm (L03) and finally to -24.5 ‰ in the depth increment below 100 cm. If deeper soil layers can be regarded as representing time periods further in the past, this trend could indicate that the contribution of C4-plants to the carbon pool of the soil has increased with time.

The $\delta^{13}C$ values of the organic matter in the soil samples additionally collected in the study area are generally lower than in the samples from above cave Ma Le 2, ranging from -23.9 ‰ to -21.5 ‰ with an average and a median of -22.7 ‰. This finding suggests that the contribution of C3-plants to the soils carbon pool exceeds the one of C4-plants if a larger area is considered.

Two of the three soil samples collected from above cave Sang Ma Sao feature organic matter $\delta^{13}C$ values that are comparable to the values in the soil samples from the larger area. With $\delta^{13}C$ values of -22.9 ‰ and -21.9 ‰, the organic matter is isotopically lighter than the one in the soil samples collected above cave Ma Le 2 suggesting a predominance of C3-plants contributing isotopically light carbon to the soil carbon pool.

However, one soil sample (Soil02) features a much higher organic matter $\delta^{13}C$ value of -15.3 ‰. A simplified calculation as described above yields C4-plant portion of about 88 %.

The carbon content of the soil samples is shown in Figure 5.73. Total carbon contents range from 0.5 to 4.2 wt-%, with an average of 2.0 wt-% and a median of 1.9 wt-%. In all samples organic carbon represents the larger fraction of total carbon, ranging from 59 to 95 %, with an average and a median of 80 %. The contents of total and organic carbon tend to decrease with increasing depth within the same soil profile. The soil sample with the highest organic matter $\delta^{13}C$ value (Soil02) is also the sample with the lowest organic carbon fraction of the total carbon content.

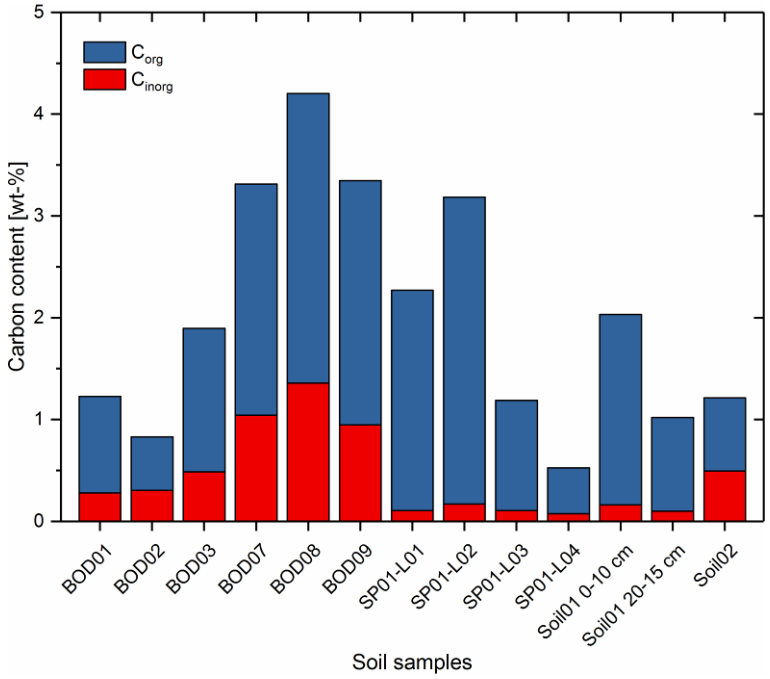

Figure 5.73: Organic and inorganic carbon content of the soil samples for the fine fraction (< 2 mm).

The $\delta^{13}C$ values of the carbonate host rock samples from cave Ma Le 2 (Figure 5.74, black) are 3.3 ‰ and 3.4 ‰. While three of the five host rock samples from cave Sang Ma Sao (Figure 5.74, red) feature similar values between 2.2 ‰ and 3.3 ‰, the two samples G2-01 and G2-08 feature much lower $\delta^{13}C$ values of -3.5 ‰ and -2.7 ‰, respectively. This indicates that the host rock in cave Sang Ma Sao is not homogenous with respect to carbon isotope values, despite their similar mineralogical and geochemical composition (Sections 5.7.1.1and 5.7.1.2) and despite the rock samples all originating from the vicinity of the drip site of stalagmite VSMS2.

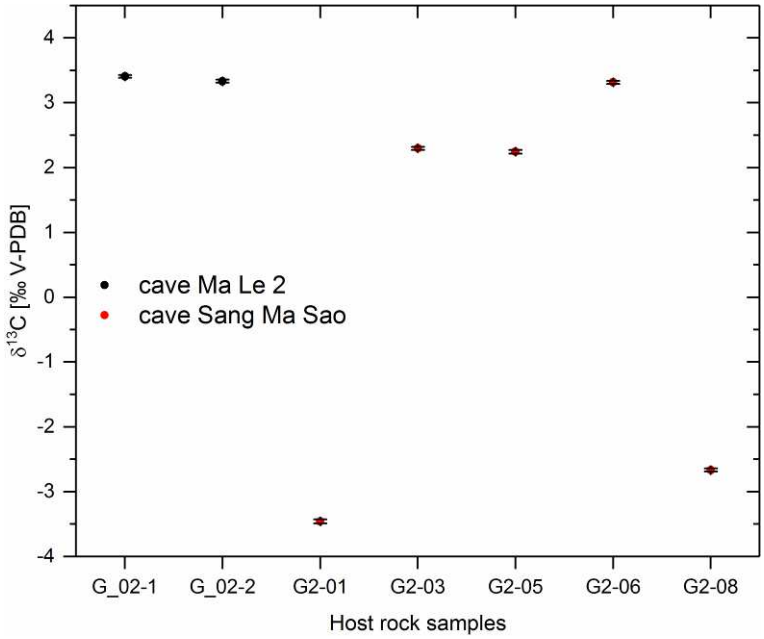

Figure 5.74: Carbon isotopes values ($\delta^{13}C$) of rock samples including error bars.

5.7.2 Oxygen Isotope ratios in Rainwater

The rainwater $\delta^{18}O$ and δD values determined in the manually collected rainwater samples in the study area were used to establish a preliminary Local Meteoric Water Line (LMWL) which is illustraed in Figure 5.75), in comparison with the Global Meteoric Water Line (GMWL) of Craig (1961). Both LMWLs established from rainater data from the communities of Ma Le (Figure 5.75, left) and of Sang Ma Sao (Figure 5.75, right) are highly similar to each other as well as to the GMWL. Only at very high $\delta^{18}O$ values, both LMWLs exhibit a weak positive anomaly relative to the $\delta^{18}O$- δD relationship of the GMWL.

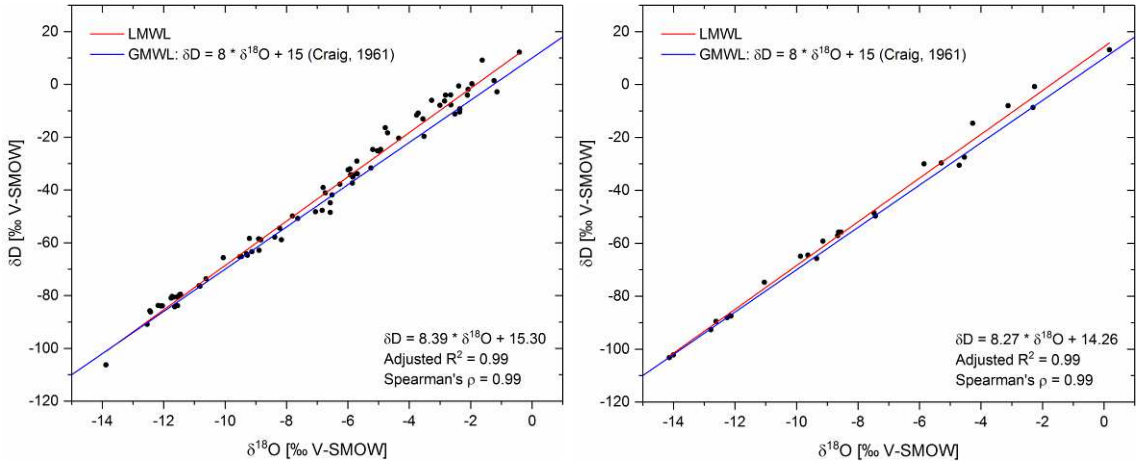

Figure 5.75: Local meteoric water lines (LMWL) based on 78 rainwater samples from Ma Le Commune (left) and 25 rainwater samples from Sang Ma Sao Commune (right) in comparison with the global meteoric water line (GMWL; Craig, 1961).

When plotted against the time of collection (Figure 5.76), the rainwater $\delta^{18}O$ values also show a similar pattern over the course of the year with higher values during the dry season and lower values during the rainy season. During the rainy season in 2015, average $\delta^{18}O$ value in rainwater collected at Ma Le Commune was -7.5 ‰, during the rainy season in 2016, it was -9.0 ‰, while it was -10.7 ‰ in in rainwater collected at Sang Ma Sao Commune. During the dry season between 2015 and 2016, average $\delta^{18}O$ value in rainwater was -4.5 ‰ at Ma Le Commune and -5.0 ‰ at Sang Ma Sao Commune. Therefore, the difference in average rainater δ18O between rainy and dry season was 5.7 ‰ at Sang Ma Sao Commune and ranged from 3.0 ‰ to 4.5 ‰, comparing the 2015/2016 dry season with the previous and the subsequent rainy season, respectively. In general, rainwater $\delta^{18}O$ values were highest at the end of the recorded dry seasons, with values of up to 0.2 ‰ in the case of Sang Ma Sao Commune and of -0.4 ‰ in the case of Ma Le Commune. Lowest rainwater $\delta^{18}O$ values were reached during the rainy season, with minima of -14.1 ‰ and -12.4 ‰, respectively.

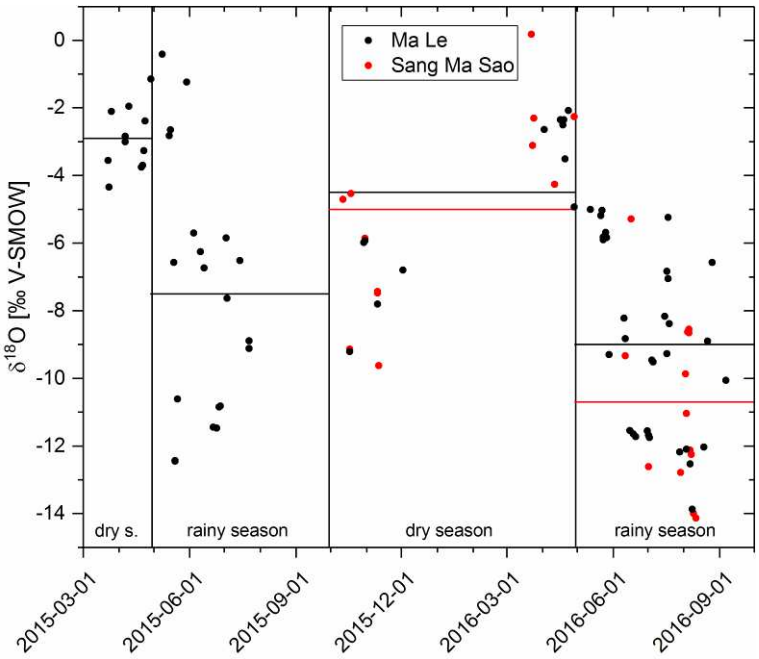

Figure 5.76: Oxygen isotope values in rainwater samples from Ma Le Commune (black) and Sang Ma Sao Commune (red). Horizontal lines represent the average rainwater $\delta^{18}O$ value of the respective season.

6 Discussion

6.1 The Evolution of the Asian Monsoon as Recorded in Northern Vietnam

The two new stalagmite $\delta^{18}O$ records from Northern Vietnam (VML22 from Ma Le 2 cave and VSMS2 from Sang Ma Sao cave) generated for this thesis are illustrated in Figure 6.1. For comparison, Figure 6.1 also includes stalagmite $\delta^{18}O$ records from the EASM-influenced region from cave sites roughly located along a SW-NE transect in China (from south to central China: Dongge, Heshang, and Sanbao cave; Figure 2.22) representing the consistent stalagmite $\delta^{18}O$ signal in Monsoon Asia discussed in Section 2.8.4. Multiple stalagmites from Sanbao cave (110°26' E, 31°40' N; Wang et al., 2008; Dong et al., 2010) precisely replicate this signal and illustrate impressively how robust this signal is, not only with regard to the gradual $\delta^{18}O$ change during the Holocene in parallel with summer insolation (Berger & Loutre, 1991), but also with regard to distinct millennial-scale climate fluctuations such as the cold Heinrich Stadial 1 (HS1), the Bølling/Allerød (BA) warm phase and the Younger Dryas (YD) cold phase. Both long-term (orbital) and medium-term (millennial) $\delta^{18}O$ variations are accurately reflected in the VML22 and the VSMS2 $\delta^{18}O$ record, respectively. This strongly suggests a common driver for these signals and confirms that the processes controlling the first-order fluctuations in stalagmite $\delta^{18}O$ values in both VML22 and VSMS2 on orbital and millennial time-scales are the same as in the entire EASM-influenced region.

Comparing the stalagmite $\delta^{18}O$ records with summer insolation (Figure 6.1; red curves) averaged over the months June, July and August for the latitude of the respective cave site, calculated from Earth orbit parameters using the equation of Berger & Loutre (1991), confirms that the Asian Monsoon is controlled by summer insolation on orbital timescales, in agreement with the orbital monsoon theory of John Kutzbach (Kutzbach, 1981). This theory has been confirmed by numerous climate proxy studies, including studies of multiple stalagmites from a specific site that have been combined to yield stalagmite composites spanning up to several glacial/interglacial cycles (Wang et al., 2001; Wang et al., 2008; Cheng et al., 2009; Cheng et al., 2012). Recently, one such stalagmite composite record was published from Sanbao cave in NE-China that spans the last 640,000 years (Cheng et al., 2016a), thereby covering the complete time span accessible by U/Th dating.

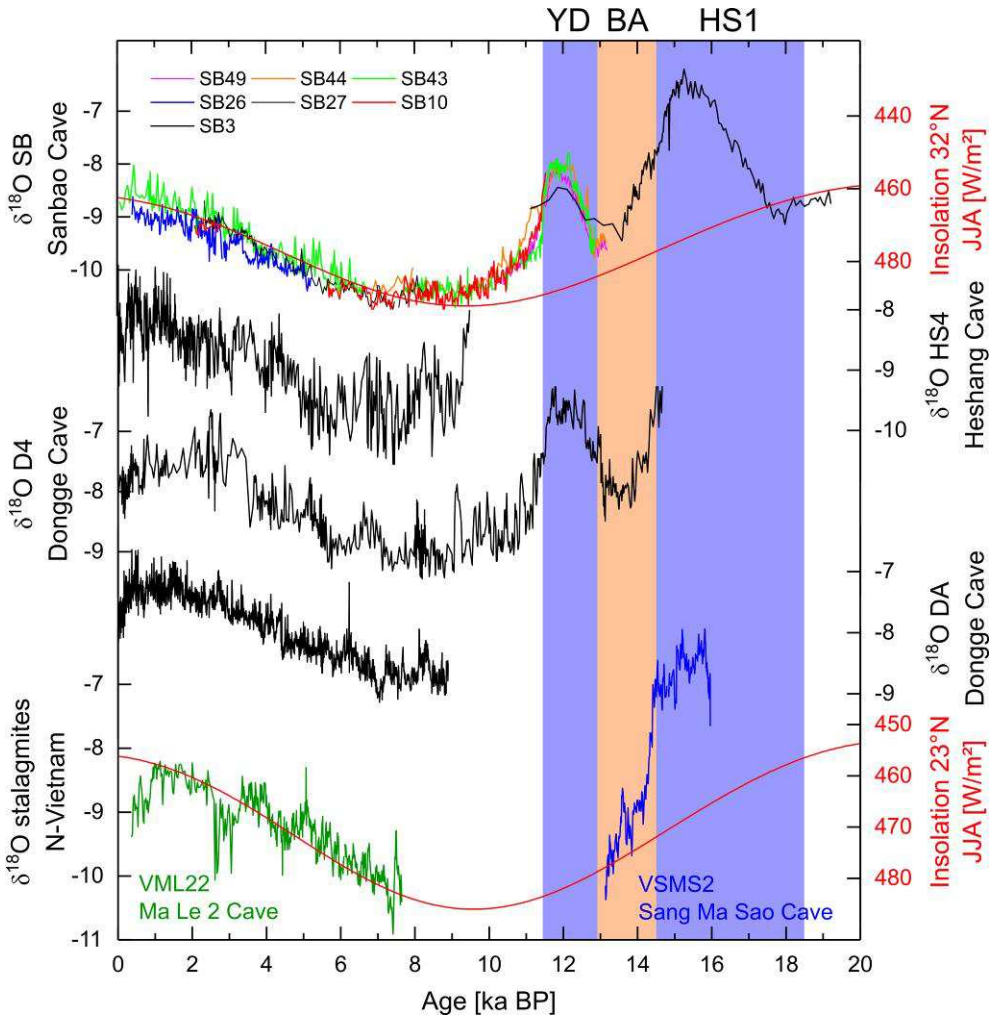

Figure 6.1: The two new stalagmite $\delta^{18}O$ records from Northern Vietnam (bottom; green and blue; V-PDB) generated for this thesis in comparison with stalagmite $\delta^{18}O$ records from the EASM-influenced region in China (Dongge: Dykoski et al., 2005 (D4) and Wang et al., 2005 (DA); Heshang: Hu et al., 2008; Sanbao: Wang et al., 2008 (SB3) and Dong et al., 2010 (all others)). All $\delta^{18}O$ values are given in ‰ relative to the V-PDB standard. The two red curves represent summer insolation averaged over the months June, July and August for 32°N and 23°N, respectively, calculated from Earth orbit parameters using the equation of Berger & Loutre (1991). Vertical bars designate distinct millenial-scale climate fluctuations discussed in the text (YD = Younger Dryas; BA = Bølling/Allerød; HS1 = Heinrich stadial 1).

Comparing the $\delta^{18}O$ values of stalagmite VML22 with stalagmite $\delta^{18}O$ records from the ISM region confirms the similarity between the records on millennial times-cales (Figure 6.2). The initial signal of ISM intensity can be represented by the $\delta^{18}O$ record of stalagmite Q5 from Qunf cave, southern Oman (Fleitmann, 2003) and can be tracked into the southern Tibetan Plateau, as shows the study of stalagmite TM18 from Tianmen Cave by Cai et al. (2012).

The ISM intensity signal is also documented in other kinds of proxy archives, such as upwelling records from the Arabian Sea (Gupta et al., 2003; Gupta et al., 2005), peat bog records from the southeastern Tibetan Plateau (Hong et al., 2003), and the titanium concentration profile from the Cariaco Basin in the tropical Atlantic, off the Venezuelan coast (Figure 6.2 top; Haug et al., 2001). Increased Ti concentrations are interpreted to reflect enhanced terrigenous input to the ocean sediment from riverine runoff due to enhanced precipitation related to a more northerly mean latitudinal position of the ITCZ (Haug et al., 2001). The mean ITCZ position is controlled by Northern Hemisphere summer insolation (NHSI) via a direct feedback and an indirect feedback through the effect of NHSI on sea surface conditions in the tropical Pacific (Fedorov & Philander, 2000).

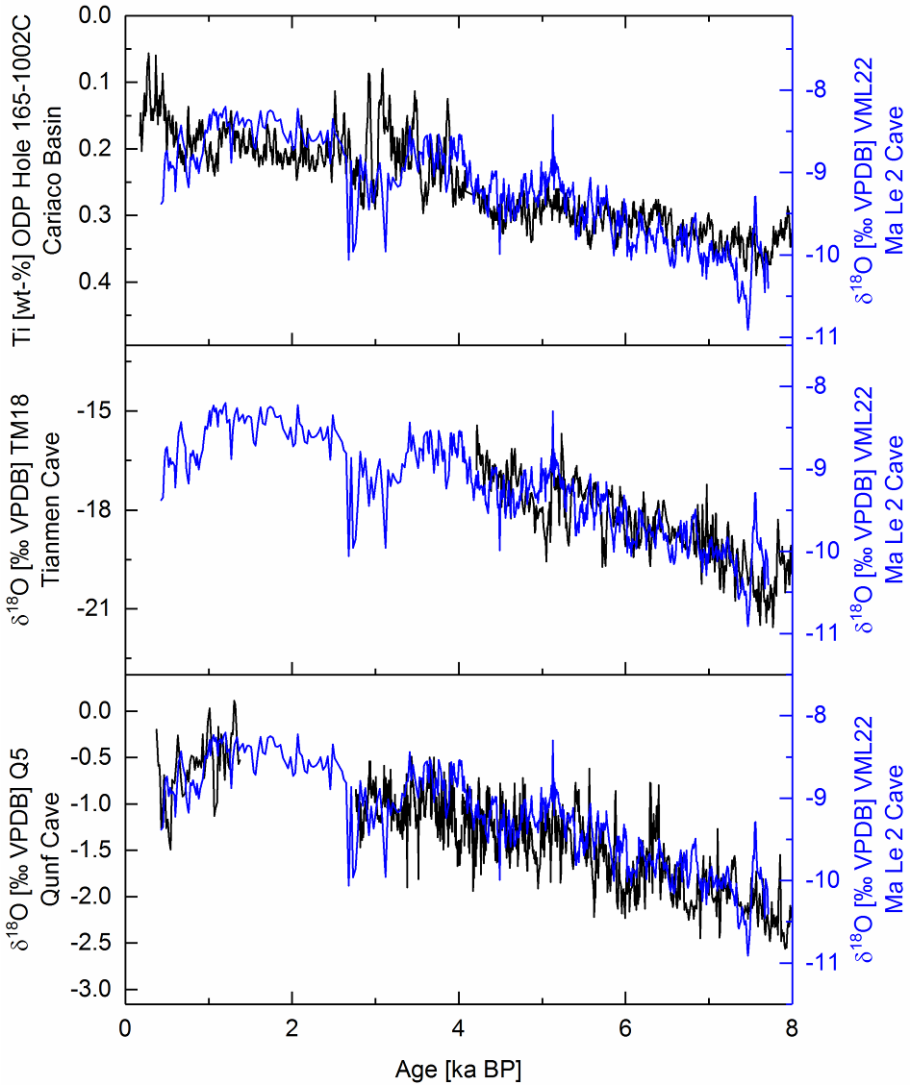

Figure 6.2: The $\delta^{18}O$ record from stalagmite VML22 from Northern Vietnam (right axes; blue) generated for this thesis in comparison with proxy records from the ISM-influenced region: Stalagmite $\delta^{18}O$ records Q5 from Qunf cave, southern Oman (Fleitmann, 2003) and TM18 from Tianmen Cave, southern Tibetan Plateau (Cai et al., 2012); sediment Ti contents in ODP hole 165-1002C from the Cariaco Basin, off the Venezuelan coast (Haug et al., 2001).

Intriguingly, while the relative $\delta^{18}O$ variations in stalagmite VML22 during the Holocene mirror the variations observed in the consistent stalagmite $\delta^{18}O$ signal in the Asian Monsoon region, the absolute $\delta^{18}O$ values in stalagmite VML22 are consistently too low by at least 2 ‰ to fit into the supra-regional pattern of stalagmite $\delta^{18}O$ values decreasing along the moisture transport pathway, as illustrated in Figure 6.3. VML22 $\delta^{18}O$ values rather plot between the stalagmite $\delta^{18}O$ values from southern and central China, while being closer to those from central China.

The absolute offset between stalagmite $\delta^{18}O$ values in stalagmites from Dongge and Ma Le 2 caves may be explained by the difference in cave temperature and in the elevation at which precipitation occurs that has been feeding the stalagmites. For a direct comparison of the two sites, both factors and their influence on isotope fractionation need to be accounted for (Hu et al., 2008). With a mean annual air temperature (MAT) of 19.5 °C at Ma Le 2 cave and of 15.6 °C at Dongge cave, the MAT difference is 3.9 °C. Assuming a similar temperature history of both sites due to their spatial proximity, the dependence of oxygen isotope fractionation on cave temperature would explain the stalagmite $\delta^{18}O$ values from Ma Le 2 cave being about 1 ‰ (V-PDB) lower than those from Dongge cave. The difference in elevation (Ma Le 2: 1,015 m; Dongge: 680 m) amounts to about 335 m.

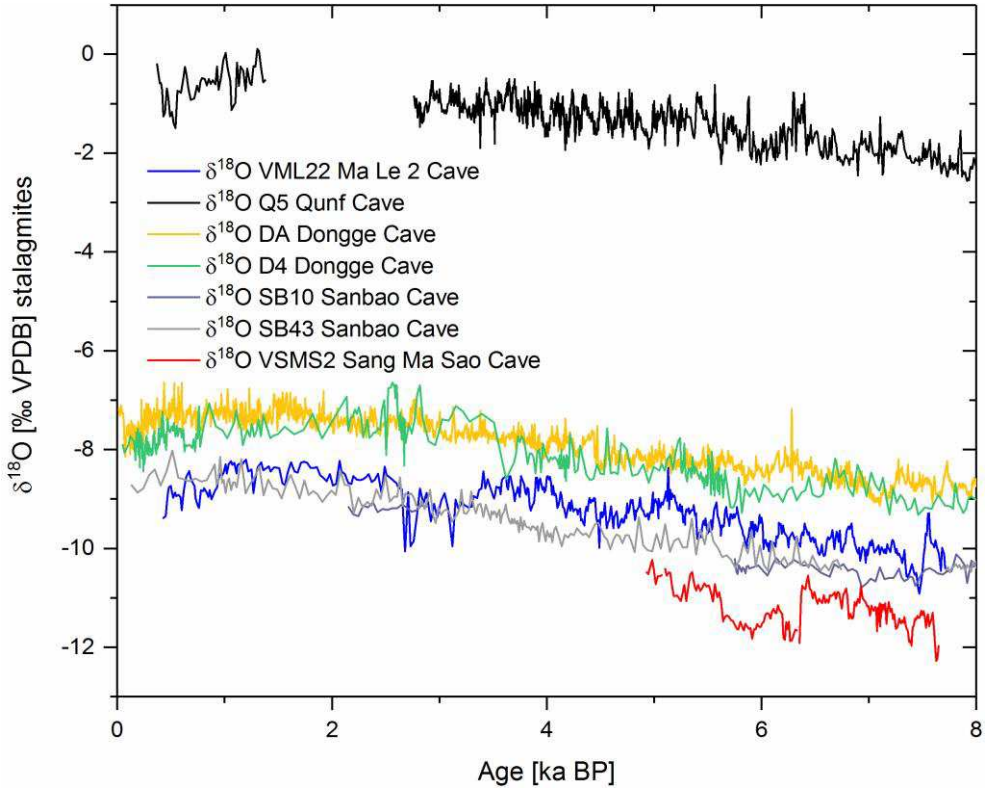

Figure 6.3: The $\delta^{18}O$ records from stalagmites VML22 and VSMS2 from Northern Vietnam in comparison with other stalagmite $\delta^{18}O$ records from the Asian Monsoon region plotted along the moisture transport pathway. The VML22 $\delta^{18}O$ values (blue) are too low by at least 2 ‰ to fit into the supra-regional pattern of stalagmite $\delta^{18}O$ values decreasing along the moisture transport pathway from the ISM region (Q5: Fleitmann, 2003) to the EASM region in southern (DA: Wang et al., 2005; D4: Dykoski et al., 2005) and central China (SB10 and SB43: Dong et al., 2010). The VSMS2 $\delta^{18}O$ values are even about 1.5 ‰ lower than the VML22 $\delta^{18}O$ values.

Based on the simplifying assumption that precipitation at both sites forms at a similar height relative to local ground levels and using an upper limit lapse rate of -3 ‰ $\delta^{18}O$ / km for the altitude effect (Gonfiantini et al., 2001; Poage & Chamberlain, 2001; Fleitmann et al., 2004; Lachniet & Patterson, 2006), this elevation difference accounts for another 1 ‰ by which the Ma Le 2 $\delta^{18}O$ values are expected to be lower than those from Dongge cave. Therefore, a value of 2 ‰ may be added to the Ma Le 2 $\delta^{18}O$ values to correct for differences in cave temperature and elevation.

As Dongge cave is located about 360 km southeast of Ma Le 2 cave and therefore downstream of it along the same moisture transport pathway, their stalagmite $\delta^{18}O$ records should be similar and their difference should reflect the amount of precipitation integrated between the two cave sites. After correcting for differences in cave temperature and elevation as described above, applying the two-site approach of Hu et al. (2008) by differencing 100a-averages of the stalagmite $\delta^{18}O$ records from Ma Le 2 and Dongge caves yields the corresponding $\Delta\delta^{18}O$ record illustrated in Figure 6.4. As the $\Delta\delta^{18}O$ record is supposed to represent the amount of precipitation integrated between the two cave sites it can be regarded as a measure for regional rainfall that can be expected to be related to local rainfall as recorded by proxies such as stalgmite $\delta^{13}C$ values. The $\delta^{13}C$ record in stalagmite VML22 can thus be used to test the plausibility of the $\Delta\delta^{18}O$ record as a proxy for regional rainfall and is therefore compared to it in Figure 6.4. There is a positive covariation between $\Delta\delta^{18}O$ and $\delta^{13}C$ values, especially with regard to the timing of the major fluctuations, even if not all of the observed variability is shared by both records, such as the local $\Delta\delta^{18}O$ minimum at 2.75 ka BP that is absent in the $\delta^{13}C$ record. Nevertheless, both records are strikingly similar to one another with increased $\Delta\delta^{18}O$ values generally corresponding to increased $\delta^{13}C$ values.

As increased $\delta^{13}C$ values in stalagmites are generally related to decreased water availability, regardless of the proposed underlying mechanism, the positive covariation between $\Delta\delta^{18}O$ and $\delta^{13}C$ values is the exact opposite of the behaviour expected if the $\Delta\delta^{18}O$ record reflected precipitation amount between the two cave sites via the upstream depletion mechanism outlined above. The upstream depletion mechanism would relate increased precipitation amount to increased $\Delta\delta^{18}O$ values. According to that premise, $\Delta\delta^{18}O$ values would be expected to covary negatively with stalagmite $\delta^{13}C$ values, not positively. As the positive correlation with other hydrologically sensitive proxies such as Mg and Sr concentrations (described below) further corroborates the interpretation of VML22 $\delta^{13}C$ values in terms of water availability, the upstream depletion mechanism alone cannot explain the difference in stalagmite $\delta^{18}O$ values between the two sites of Ma Le 2 and Dongge caves. However, an amount effect acting at the Ma Le 2 cave site, but not at the Dongge cave site could explain this seeming contradiction: During times of increased precipitation at Ma Le 2, the amount effect would cause decreased $\delta^{18}O$ values on-site, resulting in corresponding decreased values in the $\Delta\delta^{18}O$ record and, thus, a positive correlation with $\delta^{13}C$ values. Therefore, in contrast to the upstream depletion mechanism, a local amount effect would cause decreased $\Delta\delta^{18}O$ values to reflect increasing local rainfall amount, in accordance with the other hydrologically sensitive proxies ($\delta^{13}C$ values, Mg and Sr concentrations).

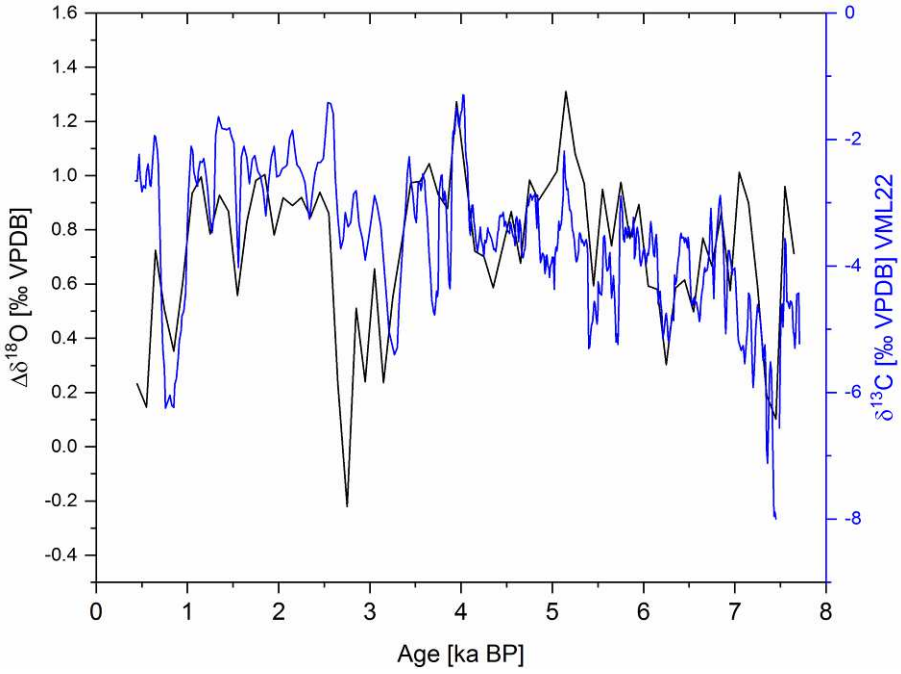

Figure 6.4: The $\Delta\delta^{18}O$ record calculated by subtracting 100a-averages of the $\delta^{18}O$ values in stalagmite DA from Dongge cave from those in stalagmite VML22 from Ma Le 2 cave (black) in comparison with the $\delta^{13}C$ record from stalagmite VML22 (blue) as a potential proxy for local water availability with decreased values indicating increased water availability.

However, there are several factors that cast doubt on the applicability of the two-site approach of Hu et al. (2008) in this case: Firstly, the corrections for differences in cave temperature and elevation between sites may not be valid. This can be deduced from comparing the sites of Ma Le 2 cave and Sanbao cave with an elevation of 1,900 masl and a MAT of 8.5 °C. In this case, the corrections for temperature and elevation cancel each other out which suggests that adding 2 ‰ to the $\delta^{18}O$ values in stalagmite VML22 as done for applying the two-site approach is not valid. Secondly, and more importantly, the $\delta^{18}O$ values in stalagmite VSMS2 are even lower by about 1.5 ‰ than those in stalagmite VML22 (Figure 6.3). Therefore, if the $\delta^{18}O$ values in stalagmite VSMS2 were used for a two-site comparison with Dongge cave site, even a 2 ‰ correction would be insufficient for the VSMS2 $\delta^{18}O$ values to exceed those of stalagmite DA from Dongge cave. Concordantly, the stalagmite $\delta^{18}O$ values at Ma Le 2/Sang Ma Sao caves are too low for the two-site comparison with Dongge cave to be valid. The covariation between the VML22 $\delta^{13}C$ record and the calculated $\Delta\delta^{18}O$ record (Figure 6.4) is probably an artefact and results from the positive correlation between the VML22 $\delta^{13}C$ and $\delta^{18}O$ records.

The fact that the $\delta^{18}O$ values in stalagmite VSMS2 are about 1.5 ‰ lower than those of stalagmite VML22 implies that the VML22 $\delta^{18}O$ values have been increased relative to the VSMS2 $\delta^{18}O$ values, most likely through evaporative enrichment. As both Ma Le 2 and Sang Ma Sao caves are located only two kilometres apart, the waterbalance at both sites can be regarded as virtually identical.

It is therefore more likely that evaporative enrichment of VML22 $\delta^{18}O$ values has occurred inside Ma Le 2 cave rather than at the surface above the cave, most probably due to a generally enhanced ventilation compared to Sang Ma Sao cave (Section 3.3) causing cave air relative humidity to drop below 100%. Enhanced ventilation in Ma Le 2 cave can also be deduced from $\delta^{13}C$ values that are about 7.1 ‰ higher in VML22 than in VSMS2 consistent with preferential removal of isotopically light CO_2 from drip water during CO_2-degassing due to increased cave ventilation. The importance of cave ventilation in controlling $\delta^{13}C$ values in stalagmite VML22 is further underpinned if a potential effect of soil layer thickness on vegetation cover/density and soil microbial activity is considered: As the soils above Ma Le 2 cave are significantly deeper than those above Sang Ma Sao cave that are very shallow, both vegetation cover/density and soil microbial activity can be expected to be at least similar at both sites if not higher above Ma Le 2 cave. This would cause a higher input of biogenic isotopically light CO_2 to the VML22 drip site and therefore VML22 $\delta^{13}C$ values would rather be anticipated to be lower than those in stalagmite VSMS2. Furthermore, the amplitude of change in $\delta^{13}C$ values in VML22 (6 ‰) is about the 3-fold of that oberserved in VSMS2 during the period of co-eval growth indicating that Ma Le 2 cave is a much more dynamic system with regard to stalagmite $\delta^{13}C$ values than Sang Ma Sao cave. This is consistent with a more significant cave ventilation control in Ma Le 2 cave.

While the discrepancies in $\delta^{18}O$ and $\delta^{13}C$ values between stalagmites VML22 and VSMS2 can partly be attributed to uncertainties in the age model of stalagmite VSMS2 (Section 5.1.2), another potential factor contributing to these discrepancies is kinetic fractionation due to evaporation and ventilation inside Ma Le 2 cave. However, the similarity of the VML22 $\delta^{18}O$ values to those from numerous stalagmites from the ISM and EASM regions indicates that kinetic fractionation is not sufficiently strong or random to efface the original climate signal contained in the $\delta^{18}O$ values on millennial timescales.

The $\delta^{18}O$ values from stalagmites VML22 and VSMS2 are by at least 2 ‰ and 3.5 ‰ (respectively) too low to fit into the supra-regional pattern of stalagmite $\delta^{18}O$ values decreasing along the moisture transport pathway from the ISM region to the EASM region in southern and central China (Figure 6.3). This negative offset suggests that precipitation feeding the Chinese stalagmites had a significant contribution of isotopically heavy rain, probably originating from a more local source such as the South China Sea that has not undergone such intense Rayleigh fractionation. This notion is consistent with modelling results that show that central China, for instance, receives only about 60% of its modern-day rainfall from the Indian Ocean (Liu et al., 2014). In particular East China receives significant portions of total moisture from the South China Sea and the North Pacific in addition to the Indian Ocean path, according to model simulations (Cai et al., 2015). This causes isotopically heavier water vapour and thus rainfall in East China compared to South China and Northern Vietnam (Figure 6.5). The Xiabailong cave site in South China would be suited for a two-site comparison with Ma Le 2 cave, but to the present day no speleothem $\delta^{18}O$ record spanning the mid- and late Holocene is available from that site.

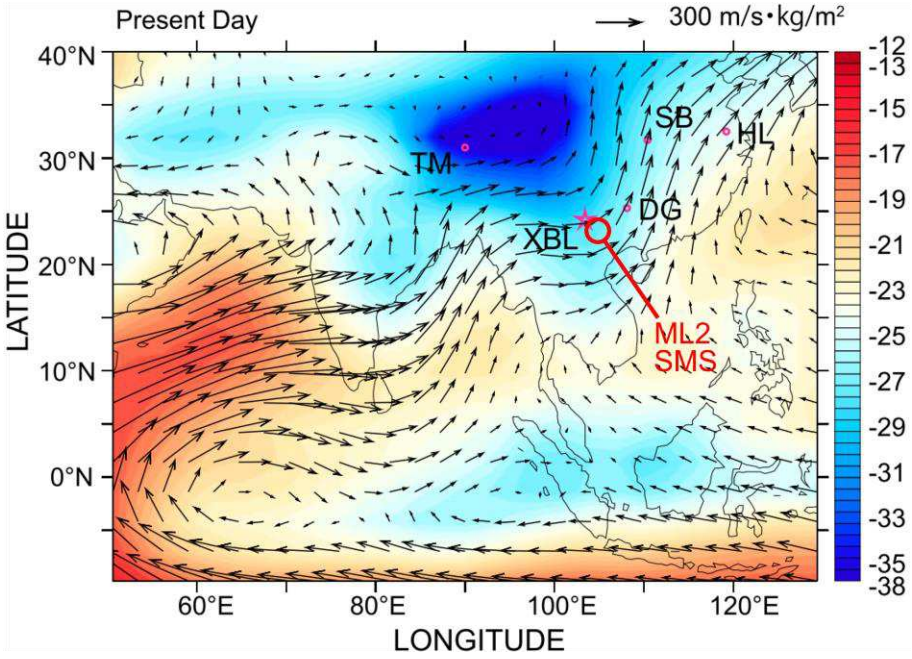

Figure 6.5: Modeled vapor transport (arrows, m s^{-1} x kg m^{-2}) averaged over the summer months June, July and August and $\delta^{18}O$ values (‰ V-SMOW) of the modern-day vapour integrated over the entire air column, indicated by the colour-shading (Cai et al., 2015). Symbols designate cave sites discussed in the text: Xiaobailong (XBL), Hulu (HL), Dongge (DG), Sanbao (SB), Tianmen (TM), Ma Le 2 (ML2) and Sang Ma Sao (SMS). Water vapour over East China is isotopically heavier than over the study area in Northern Vietnam. Figure modified from Cai et al. (2015).

6.2 Multi-proxy Evidence for Local Hydrological Change

The robust positive correlation between $\delta^{18}O$, $\delta^{13}C$ and the concentrations of Mg and Sr in stalagmite VML22 (Figure 5.8 and Figure 6.6) strongly suggests that these proxies have recorded local hydrological change linked to the large-scale variations in monsoon intensity outlined in Section 6.1. This is because a number of different processes cause increased values of all these proxies to potentially reflect reductions in water availability within the karst system feeding the stalagmite's drip site, as outlined in detail in Section 2.

While increased $\delta^{18}O$ values may mirror reduced rainfall via the amount effect or enhanced evaporative enrichment, increased $\delta^{13}C$ values can indicate an increase in the C4/C3 ratio of the vegetation growing at the surface above the cave, a decrease in vegetation cover/density or in soil microbial activity, the occurrence of prior calcite precipitation (PCP) or enhanced CO_2-degassing from dripwater as a result of decreased drip rates that cause longer dripwater residence times on the stalagmite tip. All these processes are usually related to drier conditions and therefore increased stalagmite $\delta^{13}C$ values often reflect locally decreased water availability. The same applies to a shift from a more open to a more closed system dissolution of the carbonate host rock if this shift is caused by diminished production of isotopically light CO_2, for instance, due to reductions in vegetation cover/density or soil microbial activity. Only if this shift to a more closed system dissolution is brought by the dripwater flowpath network being completely filled with water, a more closed system dissolution increasing stalagmite $\delta^{13}C$ values is not an indicator of decreased water availability.

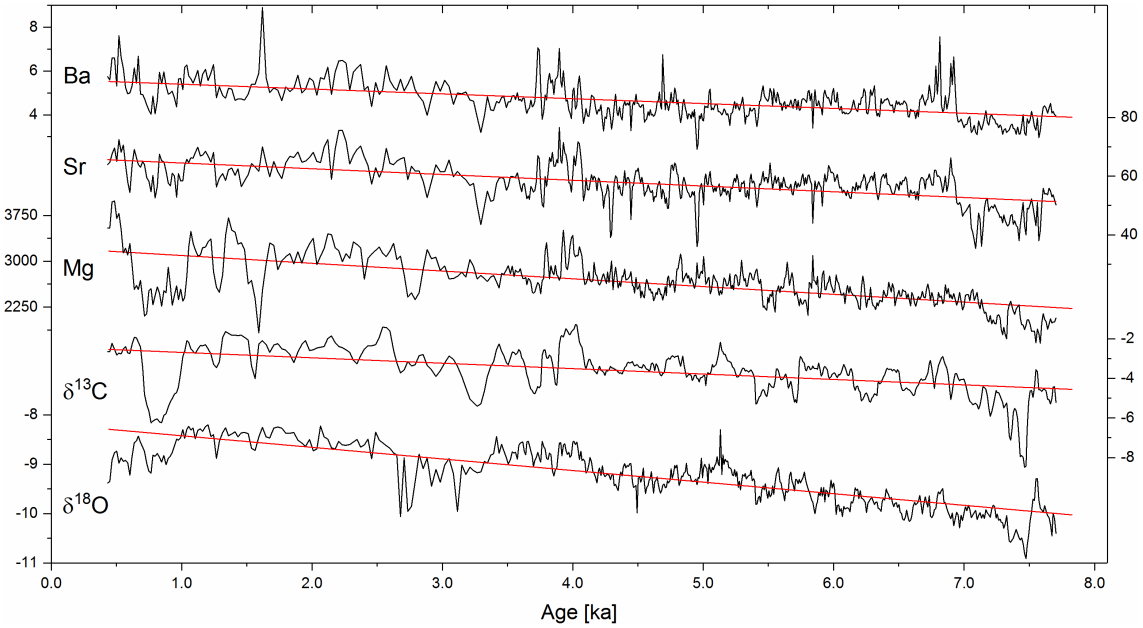

Figure 6.6: The robust positive correlation between $\delta^{18}O$, $\delta^{13}C$ (‰ V-PDB) and the concentrations of Mg, Sr and Ba (µg/g) in stalagmite VML22 strongly suggests that these proxies have recorded local hydrological change with increased values representing reduced water availability at the cave site.

If the flowpath network is water-saturated due to clogging, however, increased stalagmite $\delta^{13}C$ values still do not necessarily reflect an increase in local rainfall. Therefore, stalagmite $\delta^{13}C$ values represent a promising proxy for local precipitation, if anthropogenic influences, for instance through deforestation and cultivation of crops, can be confidently excluded. It should be noted that enhanced cave ventilation also increases stalagmite $\delta^{13}C$ values via preferential removal of isotopically light CO_2 during dripwater degassing. Cave ventilation is controlled by thermally or dynamically induced differences in air pressure between the cave and ambient air, rather than by variations in local precipitation amount.

Similarly, increased Mg/Ca and Sr/Ca ratios in karst cave dripwater and thus increased Mg and Sr concentrations in stalagmites are most commonly interpreted as indicators of palaeoaridity based on multiple processes (details in Section 2): As dolomite dissolution is kinetically discriminated versus calcite dissolution ("differential dissolution"), increased seepage water residence time within the karst system, related to low flow conditions, leads to increased Mg/Ca ratios. Enhanced ratios of both Mg/Ca and Sr/Ca in dripwater have been attributed to a relatively enhanced drainage of low-permeability soil and aquifer compartments that are dominated by seepage-flow ("selective leaching"), again corresponding to low flow conditions resulting from dryness. During incongruent dolomite dissolution (IDD), dolomite dissolves as calcite precipitates which leads to increased Mg/Ca ratios but decreased Sr/Ca. With IDD being enhanced at higher seepage water residence time, it also reflects low flow under relatively dry conditions. Most importantly, PCP as a process bound to drier conditions also enhances dripwater Mg/Ca and Sr/Ca ratios and therefore stalagmite Mg and Sr concentrations due to the small partition coefficients of Mg and Sr with respect to calcite. As PCP additionally leads to increased $\delta^{13}C$ values, increasing and covarying values of Mg/Ca, Sr/Ca and $\delta^{13}C$ are commonly interpreted as evidence for a dominating PCP control on these proxies and for reduced water availability within the karst system.

6.3 Evidence for Events of High Infiltration / Cave Flooding

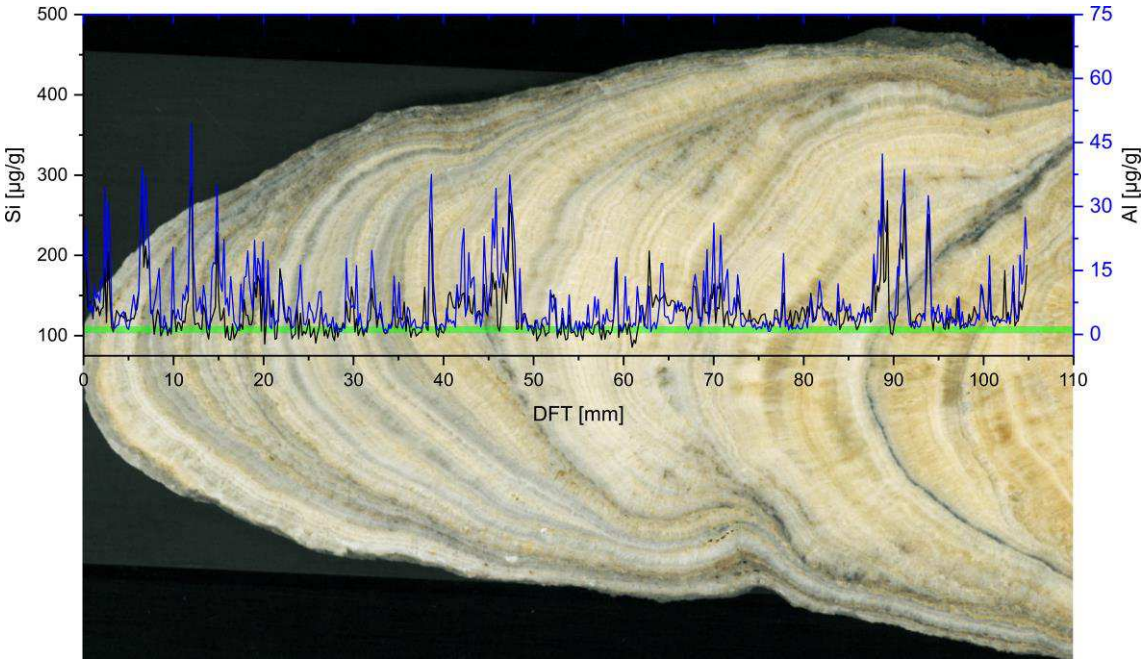

Figure 6.7: High concentrations of Group II elements in stalagmite VML22 correspond to darker laminae of brown to black colour (here represented by Si and Al) indicating events of high infiltration or even cave flooding during these times. The green line represents the locus of the LA-ICP-MS measurements. The contrast of the flatbed scan was enhanced to make the differences in colour and brightness easier to discern.

In addition to the proxies of the local hydrology discussed in the previous section, there is evidence in stalagmite VML22 of events during which infiltration of rainwater into the subsurface was extraordinarily high or even of events during which Ma Le 2 cave was completely flooded. This evidence consists of high concentrations of the Group II elements as defined in Section 5.3.1. These elements are commonly transported within the karst system in the form of particles and colloids (Section 2). Furthermore, a comparison of their concentration peaks with the colour of stalagmite VML22 shows that most of the peaks correspond to darker laminae of brownish to black colour Figure 6.7.

As the concentrations of Fe and Al in the soil zone (Section 5.7.1.4) are about three orders of magnitude higher than in the carbonate host rock (Section 5.7.1.2) and still significantly higher for the remaining Group II elements, the soil zone is probably the dominant source for these elements in stalagmite VML22. Furthermore, the relative height and width of the peaks of the different elements are highly similar which suggests that the particles incorporated in the stalagmite originate from the same source during each event.

The fact that redox-sensitive elements within Group II such as Mn are positively correlated with elements independent of redox reactions such as Al suggests that redox reactions have not played an important role during downward transport of soil particles with percolating waters.

High input of particles from the surface to the stalagmite tip is usually related to events of high infiltration of rainwater into the subsurface or even to events of cave flooding. As both of these events require strong precipitation, the concentration peaks of Group II elements in stalagmite VML22 may represent events of intense rainfall assuming that events of cave flooding have not been caused by a blocking of the cave stream outflow due to cave ceiling collapses. This assumption is reasonable in case of Ma Le 2 cave as its passages are too wide and high for debris from the cave ceiling to effectively block the cave stream, unless the ceiling collapses right at the outflow where the passage diameter is the lowest. For the same reason flooding events are also unlikely in Ma Le 2 cave so that high concentrations of detrital particles most likely reflect high infiltration events caused by intense rainfall.

As both Group I and Group II elements in stalagmite VML22 are likely to reflect the local hydrological conditions, albeit through different processes and on potentially differing timescales, both groups are compared in Figure 6.8, with Mg representing Group I and Si representing Group II as the most abundant element in each group.

Intriguingly, these two hydrology-sensitive proxies are not very similar to one another, in line with an only weak negative correlation between the two data sets ($\rho = -0.22$). While some peaks in Si concentration do coincide with troughs in Mg concentrations, such as at 2.8, 2.1, 1.0 and 0.7 ka BP, a similar number of the peaks occur at different times.

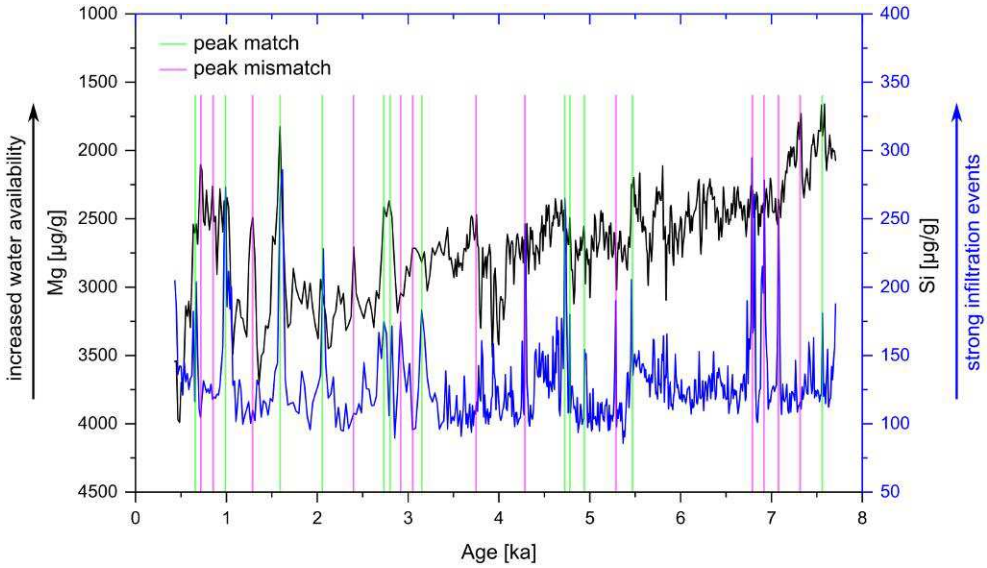

Figure 6.8: Comparison of Mg and Si concentrations in stalagmite VML22 as proxies of the local hydrological conditions. The axis for Mg is reversed for easier comparison. Vertical lines indicate peak matches and mismatches in green and purple, respectively.

For instance, the three prominent peaks in Si concentration at 7.1, 6.9 and 6.8 ka BP are not mirrored by troughs in Mg concentration as would be expected if there was a direct relation between increased water availability and the occurrence of strong infiltration events. Furthermore, the overall trend towards decreased water availability as indicated by the long-term increase in Mg concentrations (from past to present) is not reflected by a decreased frequency in infiltration events.

The overall different behaviour of the two proxies and the presence of high-frequency variability in both records complicate their comparison. As a result, even apparent peak matches might in fact be coincidental. Taking this into account, the similar number of peak mismatches and matches in Figure 6.8 suggests that increased water availability and strong infiltration events do not necessarily correlate in the case of Ma Le 2 cave, but rather behave independently from each other. One possible explanation for this independent behaviour might be that strong infiltration events are recorded in the stalagmite through enhanced Group II element concentrations, while being too short-lived to be recorded through decreased Group I element concentrations. In contrast, it seems that sufficiently strong increases in water availability can trigger strong infiltration events, for example at 1.6 ka BP.

It remains puzzling that the period from 1.0 to 0.6 ka BP which was relatively wet according to decreased Group I element concentrations corresponds to infiltration events only at the beginning and the end of the period, but not in between. This time of surprisingly low Group II element concentrations corresponds to the depth increment with the brightest colour (3 – 6 mm DFT; Figure 6.7) in stalagmite VML22, which confirms the low detrital contamination. This might imply another process at work during that time of enhanced water availabilty that impeded the input of detrital material from the soil zone into the subsurface flowpath network and thus the incorporation of detritus in the stalagmite. One potential mechanism having this effect is a hydrology-related increase in vegetation density/cover that counteracted soil erosion during precipitation events. This hypothesis is consistent with the stalagmite $\delta^{13}C$ values that decreased by 4 ‰ during the period 1.0 – 0.6 ka BP.

6.4 Hydrology of the Heinrich 1 / Bølling-Allerød Transition

Variability in the ASM system does not only occur on orbital timescales (Figure 6.1) on which it is controlled by Northern Hemisphere summer insolation (NHSI) as illustrated in Section 6.1, but the ASM also varies on the millennial time-scale which cannot be explained by the slow and gradual NHSI fluctuations caused by changes in the Earth's orbit around the sun. However, as millennial ASM variability is of similar amplitude as orbital ASM variability, it is important to identify it and to investigate its causes. Since the last glacial period that culminated in the Last Glacial Maximum (LGM), the most prominent example of ASM variability is the millennial-scale change during the Heinrich Stadial 1 (HS1; ~ 18.5 – 14.5 ka BP) and during the transition to the subsequent Bølling-Allerød warm period (BA; ~ 14.5 – 12.9 ka BP). Of minor amplitude, but still of NH-wide influence is the cooler Younger Dryas interval (YD; ~ 12.9 - 11.7 ka BP). While first identified in proxy records from marine sediments in the North Atlantic (Broecker, 1994) and from ice cores extracted from the Greenland ice sheet (Grootes & Stuiver, 1997), evidence of these climatically distinct periods has also been found in proxies recording the dynamics and intensity of the Asian Monsoon (e.g. Wang et al., 2001), revealing the existence of climatic relationships between distant regions on Earth, referred to as climatic teleconnections.

Comparing one of the first composite stalagmite $\delta^{18}O$ records from the EASM region spanning much of the last glacial (~ 75 – 11 ka BP) with the ice core $\delta^{18}O$ record from Greenland as a temperature proxy (Grootes & Stuiver, 1997), Wang et al. (2001) established that periods of reduced EASM intensity indicated by increased stalagmite $\delta^{18}O$ values corresponded with cold periods in Greenland and the North Atlantic, especially with Heinrich stadials (Broecker, 1994; Hemming, 2004). Since then, this observation made for the EASM region has been confirmed by numerous other climate proxy studies (e.g. Wang et al., 2005; Wang et al., 2008). The new $\delta^{18}O$ record from stalagmite VSMS2 from Sang Ma Sao cave in Northern Vietnam constructed for this thesis offers the opportunity to assess whether these millennial-scale monsoon fluctuations can also be identified in the transition zone between the EASM and the ISM.

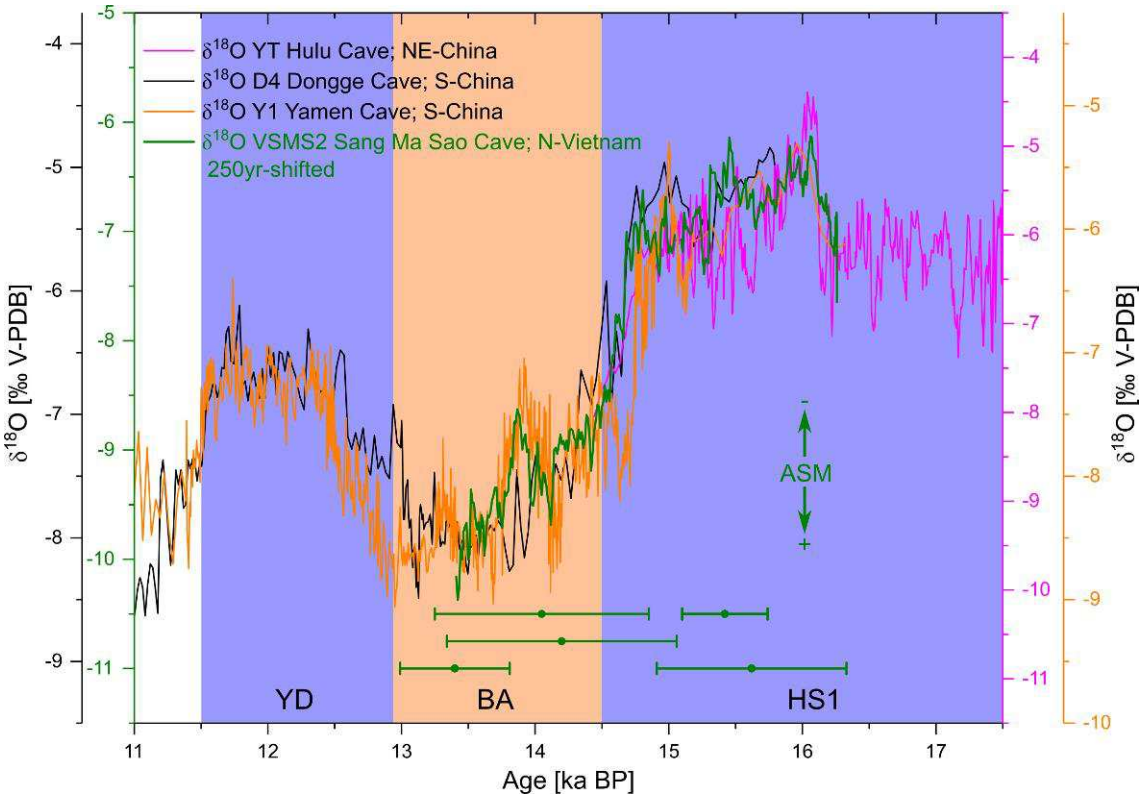

Figure 6.9: Millennial-scale monsoon fluctuations as recorded by the new stalagmite $\delta^{18}O$ record from Northern Vietnam within the EASM/ISM transition zone (green) and by stalagmite $\delta^{18}O$ records from China within the EASM region (Yamen: Yang et al., 2010 (Y1); Dongge: Dykoski et al., 2005 (D4); Hulu: Zhang et al., 2013 (YT). The VSMS2 chronology was shifted into the past by 250 years. The five green dots with error bars indicate the dating points available for VSMS2 for this period. YD = Younger Dryas; BA = Bølling/Allerød; HS1 = Heinrich stadial 1.

Figure 6.9 shows the millennial-scale monsoon fluctuations as recorded by the new stalagmite $\delta^{18}O$ record from Northern Vietnam within the EASM/ISM transition zone (green) during the period 16.3 – 13.4 ka BP in comparison to stalagmite $\delta^{18}O$ records from China within the EASM region. The distinct pattern of $\delta^{18}O$ variation in the Chinese stalagmites with increased values during the HS1 and decreased values during the BA are replicated very closely by $\delta^{18}O$ values in stalagmite VSMS2. Even fluctuations of minor amplitude are shared by the records from China and Northern Vietnam, for instance, the ~ 1.5 ‰ increase in $\delta^{18}O$ values between 16.3 and 16.0 ka BP. Another example is the positive excursion between 14.1 and 13.8 ka BP that is superimposed on the decreasing trend during the first half of the BA. While it is not discernible in the $\delta^{18}O$ record of stalagmite from Dongge cave due to insufficient resolution of the data, the record from Yamen cave (25°29′ N, 107°54′ E), about 30 km northwest of Dongge cave, clearly exhibits this positive excursion also identified in the VSMS2 record.

For this match to be achieved, the chronology of stalagmite VSMS2 had to be shifted into the past by 250 years. This approach is valid for multiple reasons: Firstly, the $\delta^{18}O$ record in stalagmite VSMS2 precisely reproduces the structure of $\delta^{18}O$ change in the Chinese stalagmites so that matching the Vietnamese record with the Chinese record is possible.

Secondly, the Chinese records are based on a robust chronology, while the dating errors (green dots and error bars in Figure 6.9) and therefore the uncertainties in the age model of stalagmite VSMS2 are considerable. Thirdly, a possible lag of the Vietnamese record behind the Chinese records does not make any systemic sense as the stalagmite $\delta^{18}O$ signal in the ASM region is generated in the Indian Ocean and is then transmitted to India and Southeast Asia, as outlined in Section 2.8.4. Therefore, if any temporal discrepancy between the Vietnamese and the Chinese stalagmite $\delta^{18}O$ records were to be expected, it would be a lead rather than a lag of the Vietnamese record.

Similar to the observations made for the Holocene (Section 6.1), the $\delta^{18}O$ values in stalagmite VSMS2 are lower than the ones in the South Chinese stalagmites by a constant offset of about 1.5 ‰. This confirms the hypothesis made in Section 6.1 that precipitation feeding the Chinese stalagmites had a significant contribution of isotopically heavy rain, probably originating from a more local source such as the South China Sea. With 1.5 ‰ the offset is slightly lower than the 2 – 3.5 ‰ offset observed during the Holocene. This implies either that local moisture sources also contributed more to precipitation feeding the Vietnamese stalagmites during the HS1 and the BA, or that monsoonal rainfall derived from the distant Indian Ocean played a diminished role in Northern Vietnam during that time, or both. Despite this offset, the similarity between the $\delta^{18}O$ records in Vietnamese and Chinese stalagmites strongly suggests a common process driving the observed variations and increases confidence in their interpretation in terms of climatic change, with decreased stalagmite $\delta^{18}O$ values indicating an increased intensity of the ASM (Figure 6.9; Dykoski et al., 2005; Yang et al., 2010; Zhang et al., 2013).

The current hypothesis linking periods of reduced ASM intensity to Greenland cold intervals is based on changes in the distribution of heat between the North Atlantic and the South Atlantic and its effect on the mean latitudinal position of the ITCZ. In the Atlantic Ocean, heat is transported from the Southern Hemisphere across the equator to the Northern Hemisphere by surface currents referred to as Atlantic Meridional Overturning Circulation (AMOC) as an important part of the global ocean circulation of surface and deep water called “Thermohaline Circulation” (THC) or “Great Ocean Conveyor” (Broecker, 2010). On its way from the tropics to the North Pole, these warm surface currents give off much of their heat, warming the North Atlantic in the region of the Gulf stream and the North Atlantic stream. Cooling and increases in salinity due to evaporation and salt rejection during freezing of sea water in the higher latitudes of the North Atlantic cause water density to increase until it is high enough to sink downward in the Labrador sea and the region between Greenland, Iceland and Norway, to flow back to the South Atlantic as North Atlantic Deep Water (NADW). Therefore, the stronger the AMOC, the more heat is transported from the South Atlantic to the North Atlantic and vice versa (Crowley, 1992).

This relationship gives rise to a distinct anti-phasing in the temperature evolution between Greenland and Antarctica as evidenced by temperature proxy records from Greenland and Antarctic ice cores (EPICA Community Members, 2006) and as confirmed by climate modelling (Vellinga & Wood, 2002), referred to as "bipolar seesaw" (Broecker, 1998). Modelling suggests that a reduced strength of the AMOC that has been related to the input of relatively low-density fresh (melt-)water to the North Atlantic causes an immediate reduction in northward heat transport and thus cooling in the North Atlantic (Vellinga & Wood, 2002). Within decades this temperature signal would be transmitted to the South Atlantic where it manifests itself in the form of increased surface temperatures (Rind et al., 2001; Vellinga & Wood, 2002; Schmittner et al., 2003). Modelling and climate proxy studies further suggest that cooling in the North Atlantic causing increased land/sea ice extent (Bitz et al., 2007; Jin et al., 2007) together with warming in the South Atlantic result in a southward shift of the mean latitudinal position of the ITCZ (Vellinga & Wood, 2002; Chiang & Bitz 2005; Denton et al., 2005; Broccoli et al., 2006; Denton et al., 2010). In turn, this causes weakening of Northern Hemisphere monsoon systems (e.g. Haug, et al., 2001; Cheng et al., 2006), strengthening of Southern Hemisphere monsoons systems and corresponding latitudinal shifts in the main precipitation belts (e.g. Ayliffe et al., 2013).

The new $\delta^{18}O$ record from stalagmite VSMS2 seems consistent with this hypothesis, as illustrated in Figure 6.10: During HS1, Greenland and North Atlantic SST and AMOC strength are reduced (Bard et al., 2000; Stuiver & Grootes, 2000; McManus et al., 2004). The reduction in AMOC strength manifests itself by an immediate decrease in the percentage of polar species in the foraminiferal assemblage in the South Atlantic in the region of the modern-day Subtropical Front (STF) of the Antarctic Circumpolar Current (ACC; Barker et al. 2009). Therefore, North Atlantic cooling corresponds to South Atlantic warming, in line with the bipolar seesaw hypothesis. Barker et al.(2009) attribute this fast response in foraminiferal species composition to the reduced AMOC strength to a southward shift of the northern fronts of the ACC. As polar foraminiferal species are practically absent north of the present-day STF but are dominant south of the Sub-Antarctic Front (SAF) south of the STF due to the steep SST gradient of > 7°C over only 5° latitude, even minor shifts in the latitudinal position of those fronts can induce marked variations in the percentage of polar foraminiferal species (Barker et al., 2009). North Atlantic cooling and South Atlantic warming seem to have resulted in a southward migration of the mean ITCZ position which, in turn, has caused reductions in ASM strength as evidenced by relatively high $\delta^{18}O$ values in stalagmite VSMS2 (green line in Figure 6.10). With the transition from HS1 to the BA warm period, all these processes are reversed: Greenland and North Atlantic SST and AMOC strength are increased, the ACC fronts as well as the ITCZ shift northward and ASM intensity is increased.

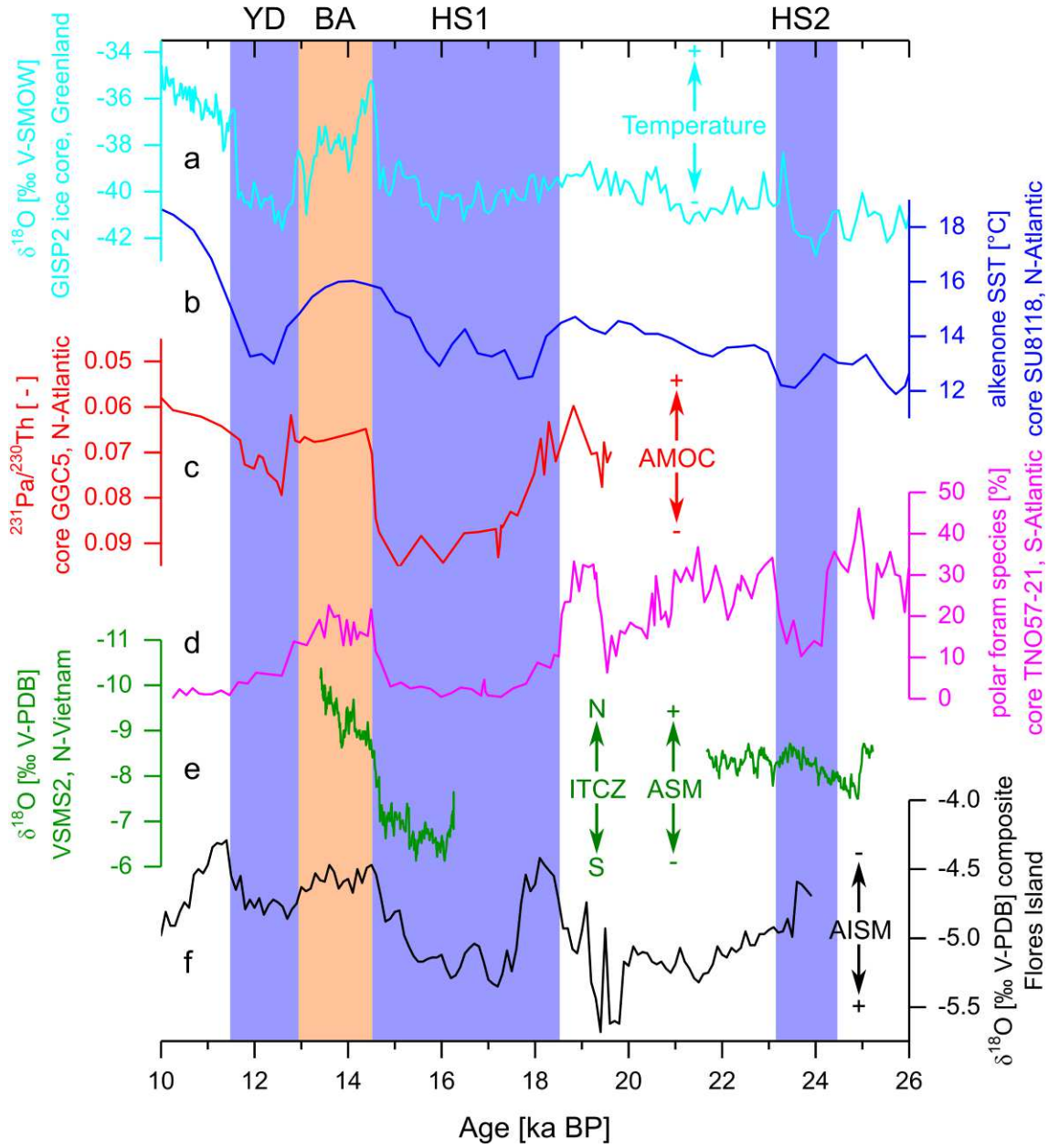

Figure 6.10: Comparison of palaeoclimate records over the last deglaciation. a) Greenland temperature from ice core GISP2 $\delta^{18}O$ values (Stuiver & Grootes, 2000); b) N-Atlantic SST from alkenone unsaturation ratios from marine sediment core SU8118 from the Iberian margin (Bard et al., 2000); c) AMOC strength from $^{231}Pa/^{230}Th$ ratios from marine sediment core GGC5 from the subtropical N-Atlantic (McManus et al., 2004); d) portion of polar foraminiferal species in marine sediment core TN057-21 from the S-Atlantic southwest of South Africa beneath the modern-day Subtropical Front (STF) of the Antarctic Circumpoloar Current (ACC; Barker et al., 2009); e) ASM intensity and meridional ITCZ position from $\delta^{18}O$ values of stalagmite VSMS2 from N-Vietnam (this study); f) intensity of the Australian-Indonesian Summer Monsoon (AISM) from a composite stalagmite $\delta^{18}O$ from Flores Island, Indonesia (Ayliffe et al., 2013). Axes for c) and e) are reversed. YD = Younger Dryas; BA = Bølling/Allerød; HS1 and HS2 = Heinrich stadials 1 and 2.

That these changes in ASM intensity are indeed related to latitudinal ITCZ migrations is suggested by one of the first (albeit low-resolution) stalagmite $\delta^{18}O$ records from the AISM domain on the Southern Hemisphere (Liang Luar cave, 8°32' S, 120°26' E; Flores Island, Indonesia) that covers these time intervals (Ayliffe et al., 2013). During HS1 and the BA, Ayliffe et al. (2013) interpret the $\delta^{18}O$ record in terms of Australian-Indonesian Summer Monsoon (AISM) intensity and precipitation amount as a result of latitudinal ITCZ migrations, with decreased $\delta^{18}O$ values indicating increased AISM intensity. As the ITCZ migrated south during HS1, AISM intensity increased while ASM intensity in the Northern Hemisphere decreased, indicating that AISM intensity is indeed synchronous and anti-phased with ASM intensity as previously suggested (Wang et al. 2006; Wang et al. 2007). Ayliffe et al. (2013) further back up their claim of a southward shift of the Australasian monsoon system during HS1 by referring to additional hydroclimate records from the Southern Hemisphere tropics including from southern Indonesia (Muller et al., 2012), southern Papua New Guinea (Shiau et al., 2011) and northern Australia (Mohtadi et al., 2011) that also indicate increased rainfall during HS1.

If ASM intensity is defined in terms of local rainfall amount, stalagmite $\delta^{18}O$ records should only be capable of tracking ASM intensity if they are significantly controlled by the amount effect. A hypothetical southward shift of the mean ITCZ position decreasing rainfall amounts in the Northern Hemisphere monsoon systems could then explain the observed increases in stalagmite $\delta^{18}O$ values in stalagmite VSMS2 and in Chinese stalagmites during HS1. However, several factors are in disagreement with the hypothesis of the mean ITCZ position determining local rainfall amount in subtropical Asia:

Firstly, the amount effect has proven difficult to constrain in analyses of modern data for rainfall amount and rainfall $\delta^{18}O$ values (Johnson & Ingram, 2004; Dayem et al., 2010), especially in the northern parts of China. This observation has led investigators to suggest non-local effects to control Chinese stalagmite $\delta^{18}O$ records (e.g. Liu et al., 2015), in particular the upstream depletion mechanism outlined in Section 2.8.4.

Secondly, climate model simulations suggest that the change in rainfall amount between full glacial conditions during the LGM and present-day conditions attributed to a southward shift of the ITCZ mainly manifests itself in the tropics and less in the subtropics in Asia (Chiang & Bitz, 2005), as illustrated in Figure 6.11. Therefore, a southward shift of the ITCZ due to increased land and sea ice cover during periods such as the LGM or HS1 can explain increased rainfall over the Indopacific just south of the equator as inferred by Ayliffe et al. (2013) from Liang Luar cave (8° S) as well as decreased rainfall over the Indopacific just north of the equator as inferred from stalagmites from northern Borneo (4° N; Partin et al., 2007; Carolin et al., 2013), but not necessarily further north at Sang Ma Sao cave (23° N) or at the Chinese cave sites.

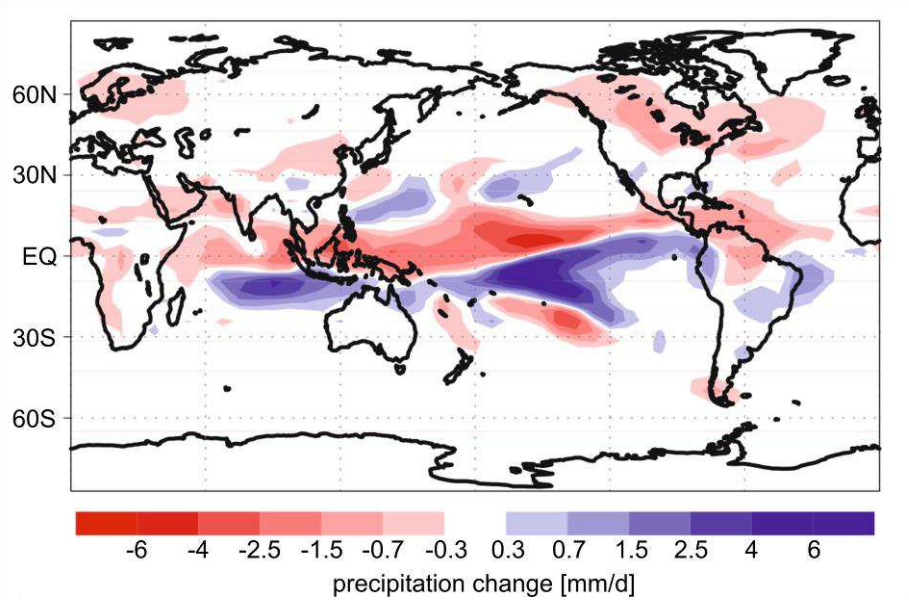

Figure 6.11: Precipitation change (mm/d) during the LGM compared to present-day conditions simulated with the CCM3 General Circulation Model (GCM) by Chiang and Bitz (2005), imposing LGM land ice extent from a reconstruction by Peltier (1994). Figure adapted from Chiang and Bitz (2005).

In view of this controversy, Pausata et al. (2011) simulated a Heinrich event using a fully coupled GCM (CCSM3) by imposing an abrupt freshwater input to the North Atlantic that causes sea ice in the northern North Atlantic to reach extents typical of Heinrich events (Hemming, 2004). They then compared the results for temperature, precipitation and precipitation $\delta^{18}O$ values with the ones from a model simulation of the LGM based on the insolation, atmospheric CO_2 concentrations, ice sheets and continental geometry at 21 ka BP (Otto-Bliesner et al., 2006).

Pausata et al. (2011) found a good agreement of the modelled increase in precipitation $\delta^{18}O$ values during Heinrich event 1 (H-1) compared to the LGM with the increase in stalagmite $\delta^{18}O$ values recorded in stalagmites from the ASM region (Figure 6.12). The modelled and observed $\delta^{18}O$ increases are largest in the northern parts of the Indian subcontinent and over the Tibetan Plateau. However, while the model comparison featured decreases in summer precipitation over the northern parts of the Indian Ocean, most parts of the Indian subcontinent and parts of the Tibetan Plateau (Figure 6.13), accounting for parts of the $\delta^{18}O$ increases via the amount effect, no decreases in total or summer precipitation were apparent in the EASM region.

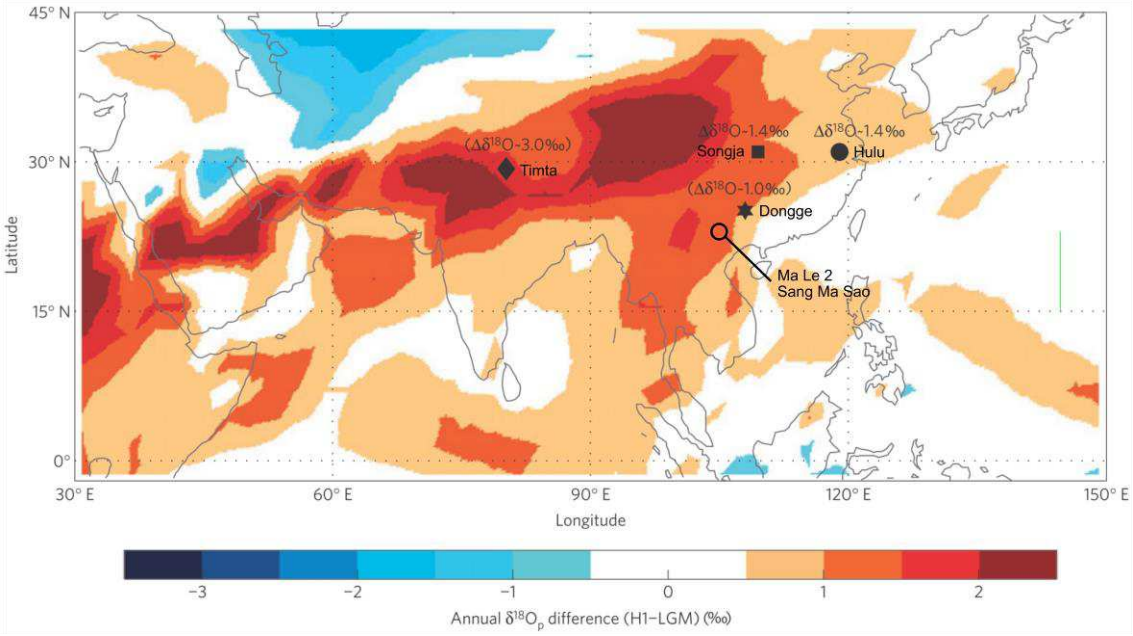

Figure 6.12: Precipitation $\delta^{18}O$ values (‰ V-SMOW) over the ASM region for a simulated Heinrich event (Pausata et al., 2011) compared to a simulated LGM. Symbols designate cave sites with numbers indicating the recorded increase in stalagmite $\delta^{18}O$ values during Heinrich event 1 (H-1): Timta (Sinha et al., 2005), Songja (Zhou et al., 2008), Hulu (Wang et al., 2008), Dongge (Yuan et al., 2004) Sang Ma Sao (this study). Figure adapted from Pausata et al. (2011).

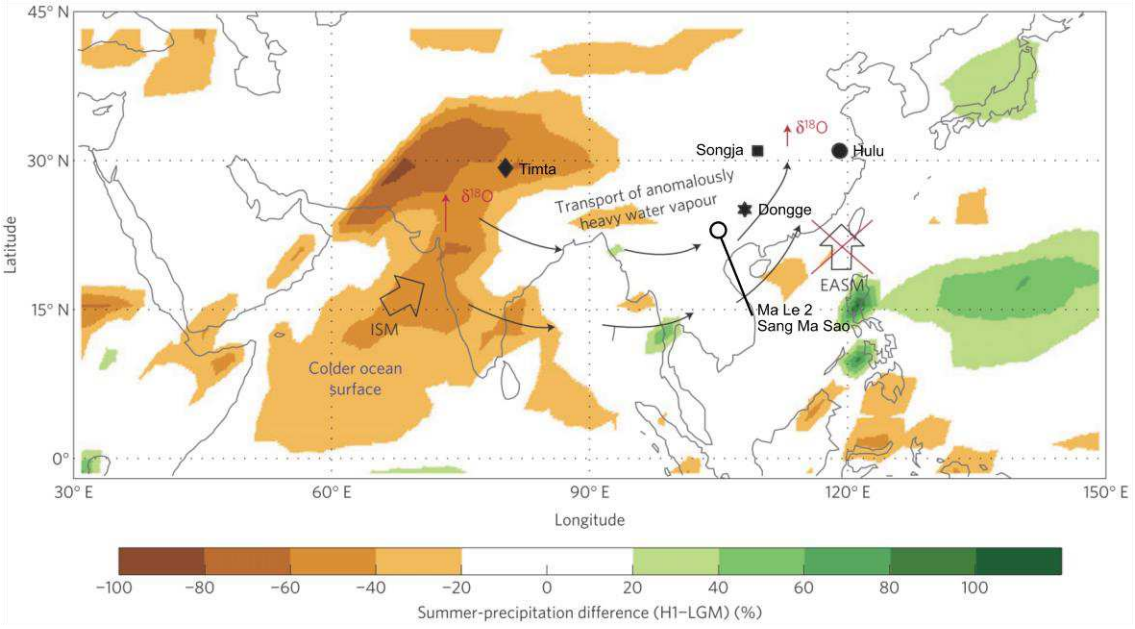

Figure 6.13: Summer precipitation amount (%) over the ASM region for a simulated Heinrich event (Pausata et al., 2011) compared to a simulated LGM. Symbols for cave sites as in Figure 6.12. Figure adapted from Pausata et al. (2011).

As winter precipitation within the ASM region is commonly isotopically heavier than summer precipitation (e.g. Wang et al., 2001; Johnson & Ingram, 2004) it has been suggested that changes in the relative contribution of winter/summer rainfall to annual totals is in part responsible for the $\delta^{18}O$ variations observed in stalagmites (e.g. Cheng et al., 2009), referred to as the seasonality effect. According to this hypothesis, a decreased ratio of summer to winter rainfall might contribute to the observed increase in stalagmite $\delta^{18}O$ values during H-1. Whereas Pausata et al. (2011) identified such a decrease of the summer/winter rainfall ratio at the site of Timta cave in northern India from a value of about 6.7 modelled for the LGM to about 2.8 during H-1 (Δ = 3.9), the ratio remained quasi-constant at the Chines cave sites. The ratio at Dongge cave (the closest to Sang Ma Sao cave among the studied sites) remained at a value of about 1.3.

Therefore, the increases in $\delta^{18}O$ values in stalagmites from the EASM region during the H-1 can neither be attributed to decreases in local rainfall amount via the amount effect, nor can they be attributed to decreases in the summer/winter rainfall ratio. In contrast, both the amount and the seasonality effect can explain the relatively large $\delta^{18}O$ increase in the stalagmite from Timta cave in northern India (Sinha et al., 2005). Based on these results, Pausata et al. (2011) suggested that the observed $\delta^{18}O$ increase in the Chinese stalagmites are predominantly caused by a non-local effect: Due to decreased SSTs in the northern Indian Ocean (Figure 6.13), convection and monsoon intensity in the ISM region diminished and caused increased precipitation $\delta^{18}O$ values via the amount effect. The thus isotopically heavier moisture was then transported to the EASM region including Northern Vietnam and China, both directly and indirectly after continental moisture recycling, where it caused isotopically heavier precipitation. This hypothesis also explains why the H-1 increase in $\delta^{18}O$ values in stalagmites from northern India in the ISM region is larger than that in the EASM region as the Indian subcontinent was additionally affected by a decrease in the summer/winter rainfall ratio. Consequently, the hypothesis of Pausata et al. (2011), being based on the upstream rainout mechanism (Section 2.8.4), does not imply a decrease in local rainfall amounts in the EASM region during the H-1 to explain the observed increase in stalagmite $\delta^{18}O$ values, in contrast to earlier work interpreting Chinese stalagmite $\delta^{18}O$ records as straight-forward proxies for EASM intensity in terms of local rainfall amount.

In order to examine which of the interpretations of stalagmite $\delta^{18}O$ records from the EASM region is more likely, further proxy records sensitive to local hydrological change are needed. The multi-proxy record from stalagmite VSMS2 from Northern Vietnam, shown in Figure 6.14, offers this possibility. As discussed in Sections 6.2 and 6.3, increased $\delta^{13}C$ values and Mg concentrations in stalagmites potentially indicate decreased local water availability, while a decrease in amplitude and/or frequency of elements related to detritus incorporated in stalagmites can reflect a decrease in amplitude and/or frequency of high infiltration events or events of cave flooding. In Figure 6.14, these elements in stalagmite VSMS2 are represented by Si.

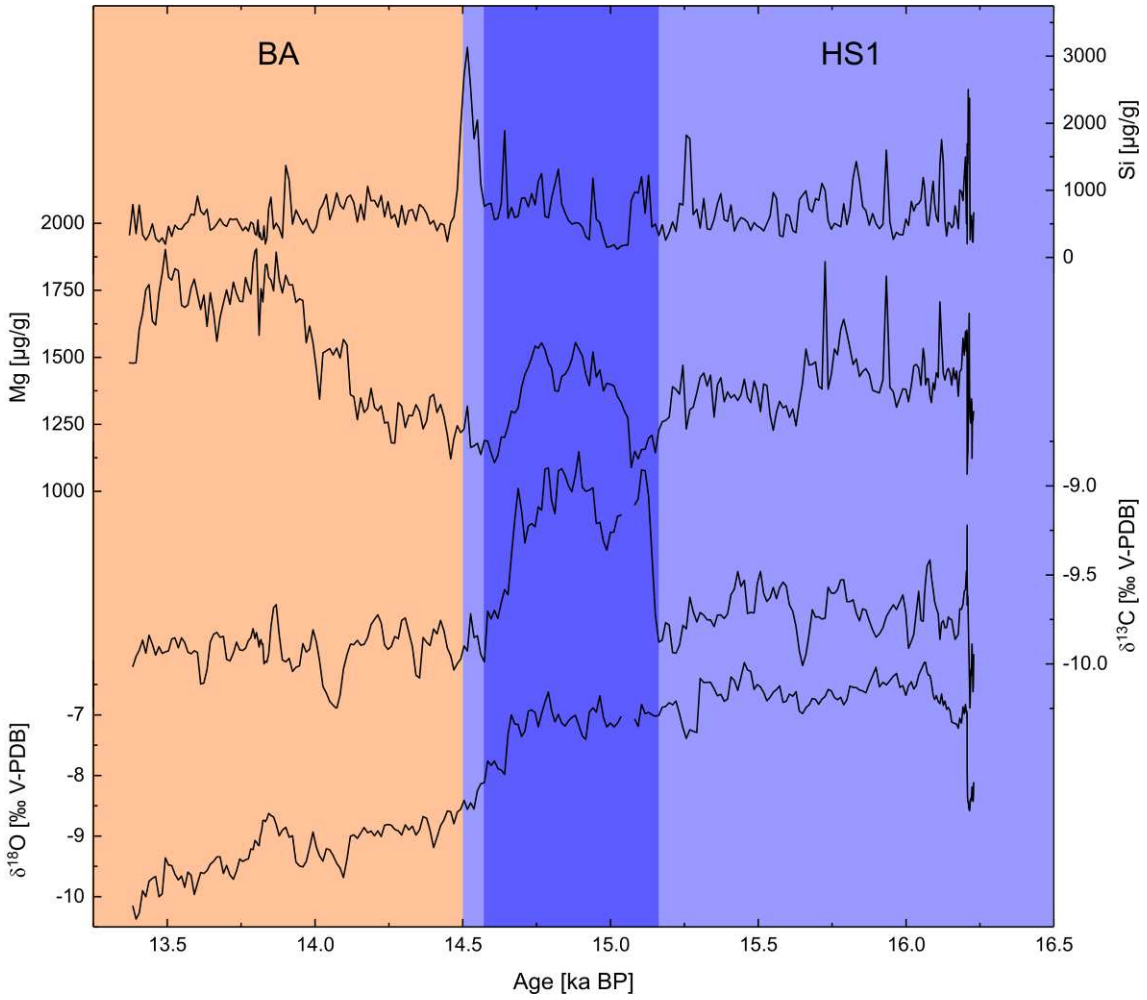

Figure 6.14: Comparison of potential proxies for hydrological conditions from stalagmite VSMS2 in Northern Vietnam. Note the difference in scale between the two stable isotope records. Original chronology shifted as in Figure 6.9. The dark-blue column indicates a period of increased $\delta^{13}C$ values and Mg concentrations between HS1 and the BA.

While VSMS2 $\delta^{18}O$ values markedly decreased by more than 4 ‰, from a maximum value of -6.2 ‰ during HS1 to a minimum value of -10.4 ‰ during the mid-BA at 13.5 ka BP, VSMS2 $\delta^{13}C$ values remained relatively constant throughout the almost 3,000 years of growth. During most of the time, $\delta^{13}C$ values varied around this quasi-constant baseline at -9.75 ‰ with amplitudes below 0.5 ‰. The most prominent feature in the VSMS2 $\delta^{13}C$ record from 16.2 to 13.4 ka BP is a 600 years-long period from 15.2 to 14.6 ka BP during which $\delta^{13}C$ values were increased by up to 1 ‰, reaching a maximum value of -8.75 ‰ at 14.9 ka BP. This positive excursion in $\delta^{13}C$ values coincided with increased Mg concentrations and therefore may reflect a reduction of local water avaiability during that period as a consequence of the hydrology-related processes outlined in Section 6.2. It is difficult to pinpoint which of the various processes causing increased $\delta^{13}C$ values and Mg concentrations during drier conditions is predominant during that time, but as the 1 ‰ increase in $\delta^{13}C$ values at 15.2 ka BP was very

abrupt, the responsible process(es) must be fast-acting, such as PCP. In contrast, the gradual increase in Mg concentrations from 14.6 to about 13.8 ka BP may, however, not be related to a local change in water availability which is indicated by the $\delta^{13}C$ record having remained relatively constant. A potential explanation for this discrepancy is a change in hydrological routing above the cave with increased occurrence of dolomite along the new flowpath which caused increased Mg concentrations but did not affect the $\delta^{13}C$ values.

Silicon concentrations during the 15.2 – 14.6 ka BP period do not exhibit pronounced decreases that could indicate a decrease in the amplitude/frequency of high infiltration/flooding events, except for a 50 years-long period around 15.0 ka BP. However, it is evident that the largest peak in Si concentrations occurs at 14.5 ka BP, directly after the presumably drier period possibly indicating a sudden increase in local rainfall amount and/or the occurrence of extraordinarily intense rainfall events.

The presumed dry spell during the 15.2 – 14.6 ka BP period could be caused by a maximum southward shift of the mean ITCZ position at the end of HS1. As the mean ITCZ position is thought to have migrated north again at the transition from HS1 to the BA, the reduction in local rainfall was counteracted after a relatively short time period and ended at 14.6 ka BP. Therefore, the $\delta^{13}C$ values and Mg concentrations during the 15.2 – 14.6 ka BP period are consistent with the ITCZ migration hypothesis. However, the $\delta^{18}O$ values do not exhibit any obvious increase during that period which suggests that they are indeed not related to local rainfall amount, as presumed according to the hypothesis suggested by Pausata et al. (2011) relating increased stalagmite $\delta^{18}O$ values from the EASM region during HS1 to decreased ISM intensity and the upstream rainout mechanism.

Interestingly, the decrease in Mg concentrations as well as in $\delta^{18}O$ and $\delta^{13}C$ values at 14.6 ka BP at the end of the presumed dry spell do coincide. This suggests that the shift of the mean ITCZ position back northwards during that time and the re-invigoration of the ISM due to increasing SSTs in the Indian Ocean during the BA happened at the same time. This might again indicate that these reorganisations at the HS1-BA transition are dynamically linked. It can thus be concluded that the new multi-proxy record from stalagmite VSMS2 is consistent with both changes in local hydrology at the HS1-BA transition and with non-local effects controlling the $\delta^{18}O$ signal in stalagmites from the EASM region including China and Northern Vietnam.

7 Conclusions

The new $\delta^{18}O$ records from stalagmites VML22 and VSMS2 accurately replicate the highly robust and consistent stalagmite $\delta^{18}O$ signal in Monsoon Asia, both in terms of long-term $\delta^{18}O$ variations on an orbital time-scale in parallel with summer insolation, as well as of medium-term $\delta^{18}O$ variations on a millennial time-scale related to the cold Heinrich Stadial 1, the Bølling/Allerød warm phase and the Younger Dryas cold phase. This strongly suggests a common driver for these signals and confirms that the processes controlling the first-order $\delta^{18}O$ fluctuations in stalagmites VML22 and VSMS2 are the same as in other stalagmites from the EASM-influenced region, at least on orbital and millennial time-scales.

The positive covariation of the $\delta^{18}O$ record of stalagmite VML22 with summer insolation calculated from Earth orbit parameters (Berger & Loutre 1991) confirms that the Asian Monsoon is controlled by summer insolation on orbital timescales, in agreement with the orbital monsoon theory of John Kutzbach (Kutzbach, 1981).

The new $\delta^{18}O$ record from stalagmite VML22 also exhibits highly similar behaviour to stalagmite $\delta^{18}O$ records from the ISM region on millennial time-scales as well as other proxy archives that document ISM intensity. Therefore, the new $\delta^{18}O$ records from stalagmites VML22 and VSMS2 generated within the framework of this PhD thesis are consistent with both the "EASM stalagmite $\delta^{18}O$ signal" as well as with proxy records reflecting ISM intensity, at least in relative terms. In absolute terms, however, the $\delta^{18}O$ values from stalagmites VML22 and VSMS2 are by at least 2 ‰ and 3.5 ‰ (respectively) too low to fit into the supra-regional pattern of stalagmite $\delta^{18}O$ values decreasing along the moisture transport pathway from the ISM region to the EASM region in southern and central China. While this anomaly inherently cannot be explained by the upstream depletion mechanism, this negative offset suggests that precipitation feeding the Chinese stalagmites had a significant contribution of isotopically heavy rain, probably originating from a more local source such as the South China Sea that has not undergone such intense Rayleigh distillation. This hypothesis is consistent with modelling results that show that central China receives only about 60% of its modern-day rainfall from the Indian Ocean (Liu et al., 2014) and that East China receives significant portions of total moisture from the South China Sea and the North Pacific in addition to the Indian Ocean (Cai et al., 2015).

This negative anomaly of the new $\delta^{18}O$ records from stalagmites VML22 and VSMS2 with respect to the established supra-regional pattern of stalagmite $\delta^{18}O$ values hampers the application of the „two-site approach" of Hu et al. (2008) to reconstruct the amount of precipitation integrated between the two sites of Ma Le 2 and Dongge cave as a measure for regional rainfall, even after correcting for differences in cave temperature and elevation.

The fact that the $\delta^{18}O$ values in stalagmite VSMS2 are about 1.5 ‰ lower than those of stalagmite VML22 during the period of coeval growth implies that the VML22 $\delta^{18}O$ values have been increased relative to the VSMS2 $\delta^{18}O$ values, most likely through evaporative enrichment due to a generally enhanced ventilation inside Ma Le 2 cave compared to Sang Ma Sao cave. This notion is consistent with the $\delta^{13}C$ values in stalagmite VML22 being about 7.1 ‰ higher than those in stalagmite VSMS2 as well as about three times as variable, as enhanced ventilation in Ma Le 2 cave would lead to preferential removal of isotopically light CO_2 from drip water during CO_2-degassing. This effect even seems to be strong enough to overcompensate the presumably higher input of biogenic isotopically light CO_2 to the VML22 drip site. Therefore, it is likely that both the $\delta^{18}O$ and $\delta^{13}C$ records in stalagmite VML22 have been influenced by kinetic fractionation due to evaporation and ventilation inside the cave. However, kinetic fractionation apparently has not been sufficiently strong or random to efface the original climate signal contained in the $\delta^{18}O$ values on millennial timescales, as suggested by the similarity of the VML22 $\delta^{18}O$ values to those from numerous stalagmites from the ISM and EASM regions.

The robust positive correlation between $\delta^{18}O$, $\delta^{13}C$ and the concentrations of Mg and Sr in stalagmite VML22 (Group I elements) strongly suggests that these proxies have recorded local hydrological change linked to the large-scale variations in monsoon intensity outlined in Section 6.1, with increased values of all four parameters indicating reduced water availability within the karst system. All four proxy signals exhibit a positive trend towards the present-day, in line with a gradual reduction in meteoric supply on orbital time-scales corresponding to reduced solar insolation, driven by long-term changes of the Earth's orbit.

Trace elements attributed to geochemical Group II in both stalagmites VML22 and VSMS2 are evidence of events during which infiltration of rainwater into the subsurface was extraordinarily high or even of events of cave flooding, as these elements are commonly transported within the karst system in the form of particles and colloids. Furthermore, most of the peaks in their concentration correspond to darker laminae of brownish to black colour indicating the incorporation of detritus in the stalagmite fabrics. The soil zone is probably the dominant source for these elements as their concentrations are significantly higher in the overyling soils than in the carbonate host rock. The similarity of the relative height and width of the concentration peaks of the different elements suggests a common source during each event.

The similar number of peak mismatches and matches when comparing elements of Group I and Group II suggests that regionally increased water availability and strong infiltration events do not necessarily coincide. This independent behaviour of these hydrologically sensitive element groups might be explained with the hypothesis that infiltration events recorded through enhanced Group II element concentrations are too short-lived to be recorded through decreased Group I element concentrations.

The prominently bright and detritus-poor section in stalagmite VML22 (3 – 6 mm DFT) seems to have formed during a time of enhanced water availabilty (1.0 – 0.6 ka BP) that caused a hydrology-related increase in vegetation density/cover that counteracted soil erosion during precipitation events, thereby impeding the input of detrital material from the soil zone into the subsurface flowpath network and thus its incorporation in the stalagmite. This hypothesis is consistent with the stalagmite $\delta^{13}C$ values that decreased by 4 ‰ during that period.

Similar to the observations made for the Holocene, the $\delta^{18}O$ values in stalagmite VSMS2 are lower than the ones in the South Chinese stalagmites during the H-1/BA transition, confirming the new hypothesis that precipitation feeding the Chinese stalagmites had a significant contribution of isotopically heavy rain, probably originating from a more local source such as the South China Sea. Furthermore, this offset only amounts to about 1.5 ‰ in comparison to the offset of 2 – 3.5 ‰ during the Holocene. This implies either that local moisture sources also contributed more to precipitation feeding the Vietnamese stalagmites during the HS1 and the BA, or that monsoonal rainfall derived from the distant Indian Ocean played a diminished role in Northern Vietnam during that time, or both.

Via climatic teleconnections reduced EASM intensity indicated by increased stalagmite δ18O values corresponded with cold periods in Greenland and the North Atlantic, especially with Heinrich stadials. The new $\delta^{18}O$ record from stalagmite VSMS2 from Sang Ma Sao cave in Northern Vietnam constructed for this thesis confirms that these millennial-scale monsoon fluctuations can also be identified in the transition zone between the EASM and the ISM, sharing even minor fluctuations with stalagmite $\delta^{18}O$ records from the EASM region.

The current hypothesis linking periods of reduced ASM intensity to Greenland cold intervals is based on changes in the distribution of heat between the North Atlantic and the South Atlantic and its effect on the mean latitudinal position of the ITCZ as a result of varying AMOC strength. The new $\delta^{18}O$ record from stalagmite VSMS2 seems consistent with this hypothesis: During HS1, North Atlantic cooling and South Atlantic warming as an effect of the “bipolar seesaw” seem to have resulted in a southward migration of the mean ITCZ position which, in turn, has caused reductions in ASM strength as evidenced by relatively high $\delta^{18}O$ values in stalagmite VSMS2.

However, ASM intensity in the EASM region as well as in the ISM/EASM transition zone cannot simply be defined in terms of local rainfall amount: Firstly, the amount effect has proven difficult to constrain in analyses of modern data for rainfall amount and rainfall $\delta^{18}O$ values, especially in the northern parts of China. Secondly, climate model simulations suggest that the change in rainfall amount between full glacial conditions during the LGM and present-day conditions attributed to a southward shift of the ITCZ mainly manifests itself in the tropics and less in the subtropics in Asia. Likewise, changes in the relative contribution of winter/summer rainfall to annual totals as an explanation for increased stalagmite $\delta^{18}O$ values in the ISM/EASM transition zone during the HS1 can be ruled out on the basis of climate modelling results. Therefore, the upstream rainout mechanism has been favoured in more recent studies.

The multi-proxy record from stalagmite VSMS2 from Northern Vietnam offers the possibility to examine which of the interpretations of stalagmite $\delta^{18}O$ records from the EASM region is more likely by providing additional and independent proxy records sensitive to local hydrological change. In conclusion, the new multi-proxy record from stalagmite VSMS2 is consistent with both changes in local hydrology at the HS1-BA transition and with non-local effects (such as the upstream rainout mechanism) controlling the $\delta^{18}O$ signal in stalagmites from the EASM region including China and Northern Vietnam.

Part II:
Development of Automated Dripwater Samplers

1 Motivation and State of the Art

Sampling karst cave dripwaters for subsequent hydro- and geochemical analysis is indispensable for understanding the response of dripwater geochemistry to its meterological, climatic and hydrogeological controls (Fairchild & Baker, 2012) such as rainfall events (McDonald, 2004), dry conditions (Baker et al., 1997) as well as changes in the cave ventilation (Mattey et al., 2010) regime. This understanding is again crucial for a more comprehensive and reliable interpretation of the geochemical time series generated from speleothems to reconstruct past climates and environements (Fairchild et al., 2006). This is why thorough long-term dripwater monitoring is so important to speleothem science.

However, the manual collection of dripwater samples is not only time-consuming but also expensive and logistically challenging. This is particularly true in remote areas with poor or no infrastructure, where expenses for field trips and equipment transport to the sampling site and back are often significantly increased. Furthermore, as the (isotope geo)chemical composition of dripwater changes with time, for instance, the concentration of the most commonly investigated cations Mg and Sr, it is necessary to repeat dripwater sampling multiple times at short intervals and over a sufficiently long time period in order to capture the temporal variability of dripwater geochemistry at each dripsite under investigation. This further increases the logistical constraints. When it comes to long-term monitoring of a drip site at relatively short intervals, manual sampling is definitely no viable option anymore, not only in speleothem science, but in all sorts of liquid sampling schemes (Chapin, 2015).

This impasse can only be overcome by automation: Autosamplers suitable for field operation, such as the portable sampler 3700C Compact (Teledyne ISCO, USA; www.teledyneisco.com /en-us/waterandwastewater/Pages/3700C-Compact.aspx; access: 6th of April, 2019) are already available on the market and offer the opportunity to automatically and repeatedly sample water bodies (oceans, estuaries, lakes, rivers, groundwater, etc.). As they can be powered by batteries or solar panels these autosamplers do not need a connection to the grid and can, therefore, be applied even in remote areas.

Despite their suitability for a wide range of applications, available autosamplers lack the capacity to automatically seal the sample vials after collection. This, however, is absolutely essential in many sampling applications in speleothem science and other fields where any exchange of gases and/or volatile components between the sample and the ambient air needs to be prevented in order to preserve the sample's original properties until analysis. In speleothem science, this particularly applies to the investigation of the dynamics of dripwater stable isotopes, especially of oxygen ($\delta^{18}O$) and of carbon ($\delta^{13}C$).

Similarly, sample vials also need to be gastight directly after sample collection where evaporation or condensation has to be impeded to prevent sample alteration. This is paramount in all studies, in speleothem science as well as other fields, investigating the hydrological cycle based on the stable isotopes of hydrogen and oxygen (δD and $\delta^{18}O$). The majority of such studies rely on rainwater samples (mostly) collected manually at stations of the Global Network of Isotopes in Precipitation (GNIP; IAEA/WMO, 1994) coordinated by the International Atomic Energy Agency (IAEA) with the sampling performed by dedicated partner institutions in member states of the IAEA or the World Meteorological Organisation (WMO). At these stations, rainwater is generally sampled at monthly resolution to ensure worldwide compatibility of GNIP data from different sources. While most of these samples are collected manually, a number of active or passive totalizers compliant with the GNIP sampling guidelines (Terzer et al., 2016) are in operation at GNIP stations without permanent staffing. Manual sampling at higher temporal resolution, such as rainfall event-based sampling, is practically impossible as this would require round-the-clock stand-by duty.

Furthermore, sample alteration due to evaporation is commonly prevented by sealing the water samples' surface with paraffin oil despite it causing an increased need for maintenance of the standard instrument for water isotope analysis, i.e. Cavity Ring-Down Spectroscopy (CRDS).

Establishing an isotope baseline for meteoric waters is crucial for research in speleothem science, hydrology, meteorology and other scientific fields. While remarkable progress has been made thanks to GNIP data, the network is still spatially and temporally discontinuous, among other reasons due to the practical constraints on rainwater sampling in remote areas. Automated rainwater sampling could help solve this issue and increased maintenance of spectrometers could be avoided by applying gastight sample vials. This clearly illustrates the need for automated rainwater and cave dripwater sampling with gastight sample vials.

Furthermore, the need for automated liquid sampling in general is demonstrated by a number of technical developments by multiple groups with the aim of creating automated liquid samplers capable of sealing the samples after collection. For instance, researchers at Oregon State University have developed the "OPEnSampler" (Nelke, Selker and Udell, 2017; http://www.open-sensing.org/opensampler/; access: 6th of April, 2019) that comprises an array of 24 solenoid valves, allowing the 24 sampling containers to be sealed from the environment after sample collection. Lukas Neuhaus has developed the "Lisa Liquidsampler" (not published) that fills 48 sample vials sealed by septa (engineered membranes that permit the transfer of fluids without air contact, usually using a double cannula) using a vacuum pump via 48 separate transfer tubes. Applying a new automated precipitation collector obtaining 96 sequential 15-mL samples, Coplen et al. (2008) were able to measure a strong decrease of 51% in the hydrogen isotope ratio (δD) of precipitation over only one hour resulting from the landfall of an extratropical cyclone along the coast of California. Evaporation and subsequent isotopic fractionation was minimised by a Teflon-coated vial cover (sample vials are not sealed individually).

In addition to these newly developed liquid autosamplers two different autosampler prototypes were designed, built and tested within the framework of this thesis. Both prototypes have their benefits for scientific (and non-scientific) applications, however, they differ from one another with regard to the characteristics they are optimised on: While Prototype 1.0 was optimised for maximal operation times by minimising its power consumption and for maximal fail-safety by minimising its technical complexity, Prototype 2.0 was optimised for collecting samples that need to be absolutely gastight in order to prevent any sample alteration from evaporation, contamination or gas exchange. Both prototypes are discussed in detail in the following sections.

2 Prototype 1.0

2.1 Optimisation Characteristics

There are seven characteristics Prototype 1.0 was optimised on (in order of priority):

1. minimal power consumption
2. maximal fail-safety / minimal technical complexity
3. simultaneous collection of three different types of samples
4. custom-built components
5. low cost
6. low weight
7. small size / reasonable dimensions

Minimising its power consumption and therefore maximising its operation times makes Prototype 1.0 particularly well-suited for long-term monitoring, even in remote areas where devices requiring regular manual operations are impractical. Such a scenario is very common in speleothem science as most karst caves are located in highly remote areas with only limited infrastructure to access the study site and the cave itself. Furthermore, minimising its power consumption also ensures that its power consumption is not a limiting factor for the autosampler's overall performance and applicability.

In the case of Prototype 1.0, a minimal power consumption was mainly achieved by using gravity to collect the (drip)water samples (passive sampling), rather than an external force such as overpressure/underpressure generated with an electric pump (active sampling) that would increase power consumption considerably. In addition, a hibernation mode was implemented during which power consumption is drastically reduced (5 mA) compared to the active operating mode (82.5 mA). The autosampler is programmed to enter the hibernation mode ("go to sleep") after each sample collection and to re-enter the active mode ("wake up") when the subsequent sample is to be collected. At its current setup, Prototype 1.0 can operate autonomously for about six months at a weekly sampling interval, collecting its full capacity of 24 samples, each consisting of three different sample types with volumes of 5, 20 and 20 mL (Section 2.2), respectively, thereby collecting a total of 72 "sub-samples".

Maximising its fail-safety by minimising its technical complexity is another crucial measure to make Prototype 1.0 applicable in long-term monitoring. A high fail-safety reduces the probability of malfunctions and thus the need for procuring spare parts and for transporting them to the operating site as well as for time-consuming and costly repairs. A technically simple design also ensures that, in case of a malfunction, the autosampler is relatively easy to repair or, if necessary, even to rebuild.

The technical simplicity of Prototype 1.0, both in terms of software (programming) and hardware (mechanics), was mainly ensured by the design choice of a minimal amount of movements necessary for the realisation of the dripwater sampling process:

- First movement - Revolution around the Z-axis: The sample vials are arranged along concentric circles in a revolver- or carrousel-like sample vial rack (sample holder). Positioning of empty sample vials for the collection of a new set of samples, after collection of the antecedent samples is finished, is achieved by an appropriate rotation (here: by 15°) of the sample vial rack around its vertical axis.

- Second movement - Translation along the Z-axis: Once empty sample vials are correctly positioned underneath the dripwater nozzles at the bottom of the "drip divider" (that feeds the dripwater from the stalactite to the sample vials; Figure 2.4), the "drip divider" is moved downwards by the Z-motor via a worm drive spindle. As soon as the custom-made silicone septa of the sample vials are pierced by the dripwater nozzles, the passive dripwater sample collection is initiated.

At the end of the respective sampling interval (after one day or one week, depending on the operator's choice), the "drip divider" is moved back up to its up position, the sample vial rack rotates by 15° to bring a new set of empty sample vials into position, the "drip divider" is moved back down and a new set of samples is collected.

The technical simplicity of Prototype 1.0 resulting from this "two-axes" design permits a correspondingly simple software design. Another design aspect that further contributes to the technical simplicity of Prototype 1.0 is the passive sampling method instead of an active sampling method that would require an artificial exertion of overpressure/underpressure by a pump for the sample collection.

Simultaneous collection of three different types of samples is beneficial especially when the collected samples are required to remain at the location of sample collection (here: inside the respective cave) for an extended period of time, as is often the case in speleothem science due to the remoteness of the monitored caves that make transporting the collected samples to the lab in short, regular intervals impractical and uneconomic. The longer the samples remain inside the caves before being stored under ideal conditions, i.e. in a dark and cool place such as a fridge, the more important it becomes to stabilise the analytes under investigation inside the sample solution.

This is commonly achieved by adding certain chemicals to the sample solution directly after sample collection (such as acids like HNO_3 to stabilse metal ions or toxic compounds such as sodium azide (NaN_3) to prevent the consumption of nutrient ions by biota occuring in the sample, mostly bacteria). For stabilising stable isotopes aquatic samples are commonly collected in gastight brown glass vials to protect them from sample alteration resulting from evaporation or gas exchange.

Therefore, Prototype 1.0 is equipped with three separate sample containers per batch that are simultaneously filled with sample cave dripwater with three different "sub-samples": The sample collected in the 5 mL brown glass vial is used for the analysis of the stable isotopes of hydrogen (δD), oxygen ($\delta^{18}O$) and carbon ($\delta^{13}C$), the sample collected in one of the two 20 mL plastic flasks, pre-filled with 50 µL of 65 % HNO_3 (suprapure) is used for analysing both main and trace elements prevalent as cations, while the sample collected in the other 20 mL plastic flask, however pre-filled with 50 µL of 1 % NaN_3, is used for analysing nutrients prevalent as oxyanions.

The use of **custom-built components** is advantageous for prototyping for several reasons: Components can be tailor-made to exactly meet the specific requirements of any particular prototype and its specific applications. Furthermore, components that are custom-built in-house are often significantly cheaper than if their construction was outsourced. In addition, in-house custom-built components are usually fast and easy to obtain as shipment is rendered obsolete. They can also be quickly re-designed and re-made, should any changes in design prove necessary.

In the case of Prototype 1.0, many components were custom-built by 3D-construction (AutoCAD, Autodesk) and 3D-printing (Ultimaker 3 Dual Extruder, Ultimaker) such as the "drip divider", the protective cases for the Z-motor and the electronics as well as the connectors fitted into the brown glass sample bottles used for the collection of dripwater samples for subsequent stable isotope analysis. The dripwater collector (Figure 2.2) was custom-built by various techniques of machining and handcraft in the Institute workshops (drilling, turning, sawing, filing, glueing etc.).

Another important aspect of Prototype 1.0 is its **low cost**, with the cost for all the materials, excluding labour, amounting to about 500 €. The low cost of the autosampler allows to spend the remaining funds on other assets such as additional equipment or chemical analyses and/or makes it affordable to build/buy multiple autosamplers which increases the range of scientific opportunities.

The relatively **low weight** of Prototype 1.0 of about 5 kg (+ 5.8 kg battery) makes it easy and/or cost-effective to transport, even via air-mail. It also makes it possible to install the autosampler in karst caves at the desired drip sites to which heavy items are mostly very difficult (if not practically impossible) to transport. The same applies to the **reasonable dimensions** of Prototype 1.0 (width = 400 mm; length = 440 mm; height: 330 mm).

2.2 Autosampler set-up and design

2.2.1 Hardware design and sampling process

The main components of Prototype 1.0 have been newly developed or adapted within the framework of this thesis and comprise a “dripwater container” mounted on a “telescope stand” and connected to a “drip divider” via a silicone tube, a revolver-like sample vial rack holding a total of 72 sample containers (with each sample batch consisting of three different sub-samples), two motors for both the translation along the Z-axis (using a worm drive spindle) and the revolution around the Z-axis, the electronics and protective cases for the electronics and the motors (Figure 2.1). All components except for the dripwater container and the telescope stand are assembled on an HDPE slab and a framework of X-slot profiles.

The dripwater that is to be collected leaks from the monitored stalactite and drops on a Stalagmate drip rate logger (Mattey & Collister, 2008) installed inside the dripwater container. In order to ensure optimal settings for the Stalagmate to log drip rate reliably, the Stalagmate is installed at an angle of 15 to 20° relative to the horizontal. This keeps each drip from pooling which would interfere with the registration of the subsequent drip while retaining an impact surface that is sufficiently flat for the drips to produce a detectable sound on impact. Furthermore, installing the Stalagmate at an angle reduces any potential build-up of carbonate precipitates on the Stalagmate which would eventually prevent the drip rate logger from registering and recording the drips when the carbonate crust has become too thick.

To avoid the need for drilling into the Stalagmate drip rate logger and thus the risk of damaging it, the Stalagmate logger is centrally clamped in place by two custom-made PVC screws (ø = 20 mm; thread pitch = 1.0) with flat tips attached to the dripwater container via a PVC “skirt” with a height of 40 mm and a width of 30 mm on each side of the dripwater container (Figure 2.2). After installation of the Stalgmate logger the PVC screws are tightened using metal rods (yellow in Figure 2.2; ø = 8 mm) and then held in place by corresponding custom-made PVC nuts (red in Figure 2.2). Another advantage of holding the Stalagmate logger in place by clamping rather than permanently attaching it to the dripwater container is the ease of handling when it comes to taking the logger out of the dripwater container for data read-out or maintenance (exchanging batteries, etc.).

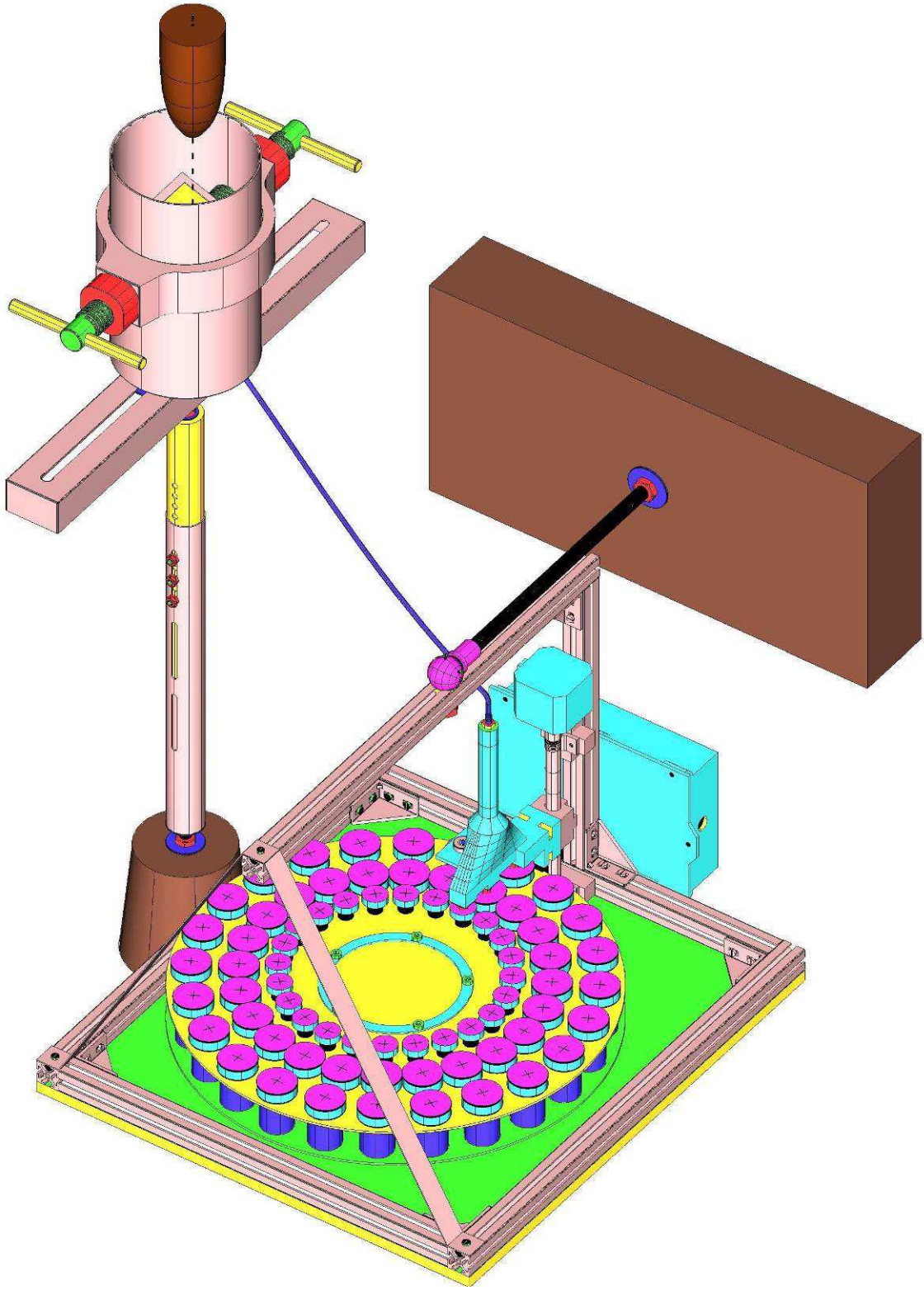

Figure 2.1: Overview of all components of Prototype 1.0 as a solid CAD model, together with the first of the two newly developed dripwater containers (left; including the Stalagmate drip rate logger) funneling the dripwater to the autosampler. The dripwater container is mounted on the newly developed telescope stand installed on the corresponding stalagmite stump (cut brown cone on the left) left after stalagmite extraction. The autosampler is mounted to the wall (brown cuboid on the right).

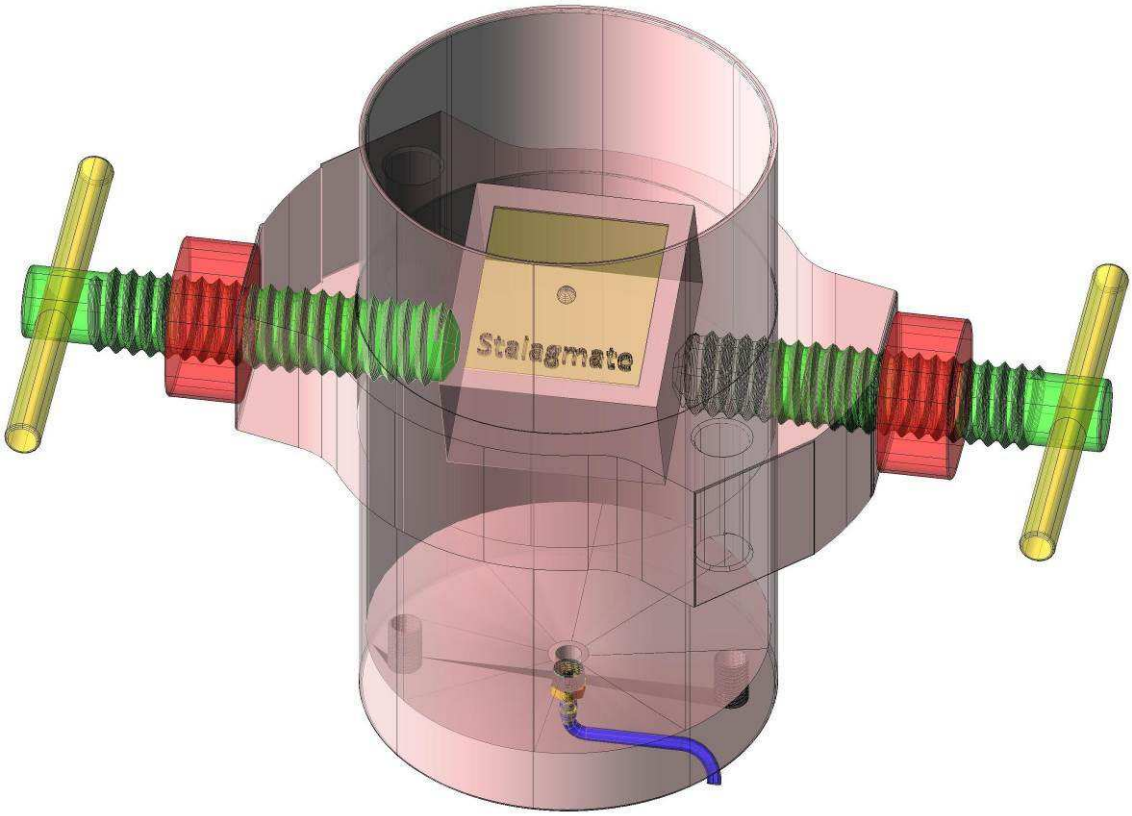

Figure 2.2: X-ray CAD model of the first of the two newly developed dripwater containers (including the Stalagmate drip rate logger) funneling the dripwater to the autosampler. This dripwater container can be either mounted on the newly developed telescope stand (installed on the stalagmite stump left after stalagmite extraction; Figure 2.3, left), or suspended to the newly developed stalactite collar (Figure 2.3, right).

As the Stalagmate logger needs to be exactly centered underneath the monitored drip site so that drip fall depth is sufficient for drip registration and logging the dripwater container including the Stalagmate logger is mounted on a telescope stand that allows precise positioning through adjustments along all three directions in space (Figure 2.3, left). The telescope stand consists of a horizontal metal rail featuring a central long-hole and of two metal tubes of different diameters so that the smaller inner tube can slide back and forth within the bigger outer tube and thus can be attached to the outer tube at different positions by screwing through discrete holes in the inner tube (spaced at 10 mm) and a set of three long-holes in the outer tube. This allows changing the overall length of the telescope tubing and thus adjusting the Z-position of the dripwater container. Additionally to these adjustments along the Z-axis, the dripwater container can be shifted along the length of the lateral rail and the rail itself can be rotated freely which allows adjustments of the dripwater container's position in the X-Y-plane. These adjustments along all three axes enable precise positioning of the dripwater container in a three-dimensional cylinder-shaped action range with a diameter of 270 mm and a height of 185 mm (Appendix, Figure F.7).

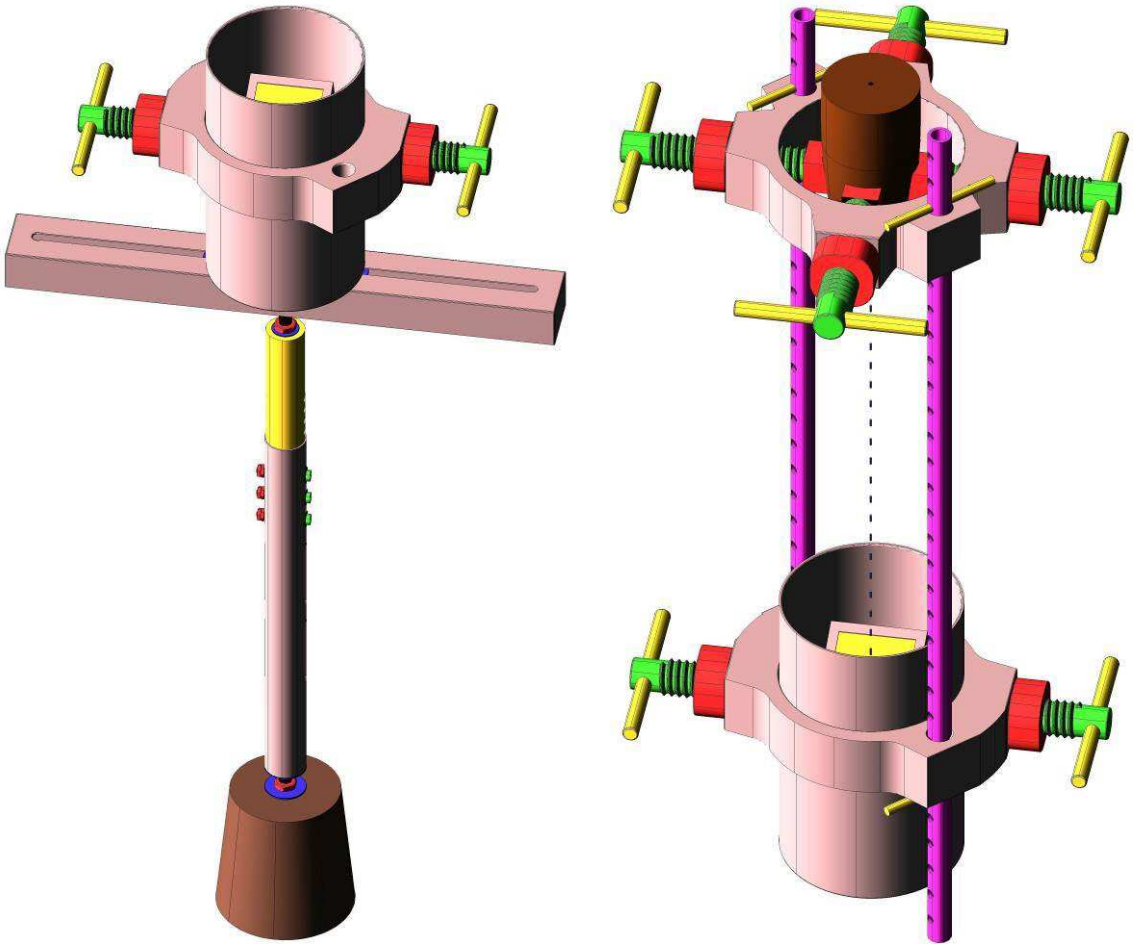

Figure 2.3: Solid CAD models of the first of the two newly developed dripwater containers (including the Stalagmate drip rate logger) funneling the dripwater to the autosampler. This dripwater container can be either mounted on the newly developed telescope stand (left; installed on the stalagmite stump left after stalagmite extraction), or suspended to the newly developed stalactite collar (right).

Sometimes it can be more practical to attach the dripwater container to the stalactite rather than the stalagmite stump left after stalagmite extraction, especially when the removed stalagmite is very long in which case the telescope stand might be too short for optimal positioning of the dripwater container. For these cases a "stalactite collar" has been developed within the framework of this thesis (Figure 2.3, right and Appendix, Figure F.5). Similar to the dripwater container it comprises four custom-made PVC-screws (ø = 20 mm) including flexible rubber elements screwed into the screw tips to clamp the stalactite collar to the stalactite in the centre of the collar. Again the PVC screws are secured by custom-made PVC nuts. To ensure that the dripwater container is positioned directly underneath the drip site, it is connected to the stalactite collar with two metal tubes (aluminium, wall thickness = 2 mm; purple in Figure 2.3, right), suspended directly underneath the stalactite. The fall depth of the drips can be adjusted by securing the metal tubes to the stalactite collar by inserting the corresponding metal rods (ø = 8 mm; yellow in Figure 2.3, right) through holes (spaced at 20 mm) at different levels along the metal tubes.

After impact on the Stalagmate logger, the dripwater flows out of the dripwater container through a central threaded hose connector on the bottom, through a silicone tube (inner ø = 4 mm) and into the "drip divider" (Figure 2.4) via another threaded hose connector. The drip divider divides each droplet into three "sub-droplets" of similar volume by passively using the gravitational force the causes the droplet to splash on impact on the cross-section (the "impact tri-star", narrow green horizontal faces in Figure 2.4) of three internal dividing walls arranged at 120° angles. To ensure a reliable "fission" of the droplets, they need to impact on the impact tri-star dead centre. This is achieved by the passage through the "drip concentrator" at the top of the drip divider, a cylindrical element inside of which the central dripwater flow channel tapers off to ensure that droplets come off dead centre and fall down centrally inside the "fall tube". The fall tube has a length of 100 mm so that droplets reach a sufficient fall velocity and momentum for a reliable droplet "fission". After the "fission" of the droplet, the sub-droplets trickle downwards via three "drip channels" to exit through three "drip nozzles" at the bottom end of the drip divider to fall into the sample flasks positioned directly underneath.

To make sure that droplets fall parallel to the axis of the fall tube for reliable droplet "fission", a bubble level is glued to a plane that is exactly perpendicular to the fall tube. The bubble level can be used to check if the entire autosampler including the fall tube are installed plumb-vertically. To enable for fine adjustments in inclination, the autosampler is installed inside the cave by attaching it to a nearby cave wall (or column) using an M12 metal threaded rod connected to the autosampler via an angle joint (purple in Figure 2.1) screwed into the top x-slot profile of the autosampler framework. To facilitate installing the autosampler plump-vertically, the angle joint is positioned directly above the centre of gravity of the autosampler so that gravity pulls the autosampler's X-Y-plane into the horizontal. To prevent the autosampler from moving and changing its inclination after installation, its inclination is fixed using two screws holding the ball inside angle joint in place.

Additionally to enabling a reliable droplet fission, installing the autosampler plumb-vertically eliminates the need for keeping the stepper motor used for the revolution of the sample rack active in order to prevent the sample rack from rotating due to gravitational pull. Instead, the stepper motor can be deactivated during sleep mode ("sent to sleep") which decreases power consumption of the autosampler even further.

To prevent or reduce sample alteration by contamination, evaporation or gas exchange during pre-storage of the dripwater samples inside the cave for extended periods of time (of up to six months), the sample flasks were custom-made (Figure 2.5) and sealed with a layer of silicone (thickness = 1 mm) cut out of sheets of silicone using broaches of corresponding size (ø = 15 mm and 35 mm). To be able to accommodate the drip nozzles of the drip divider and to act as septa, these silicone layers were pre-slotted using a bevel-edged chisel (length of cutting edge = 10 mm) and glued to the caps of the sample flasks.

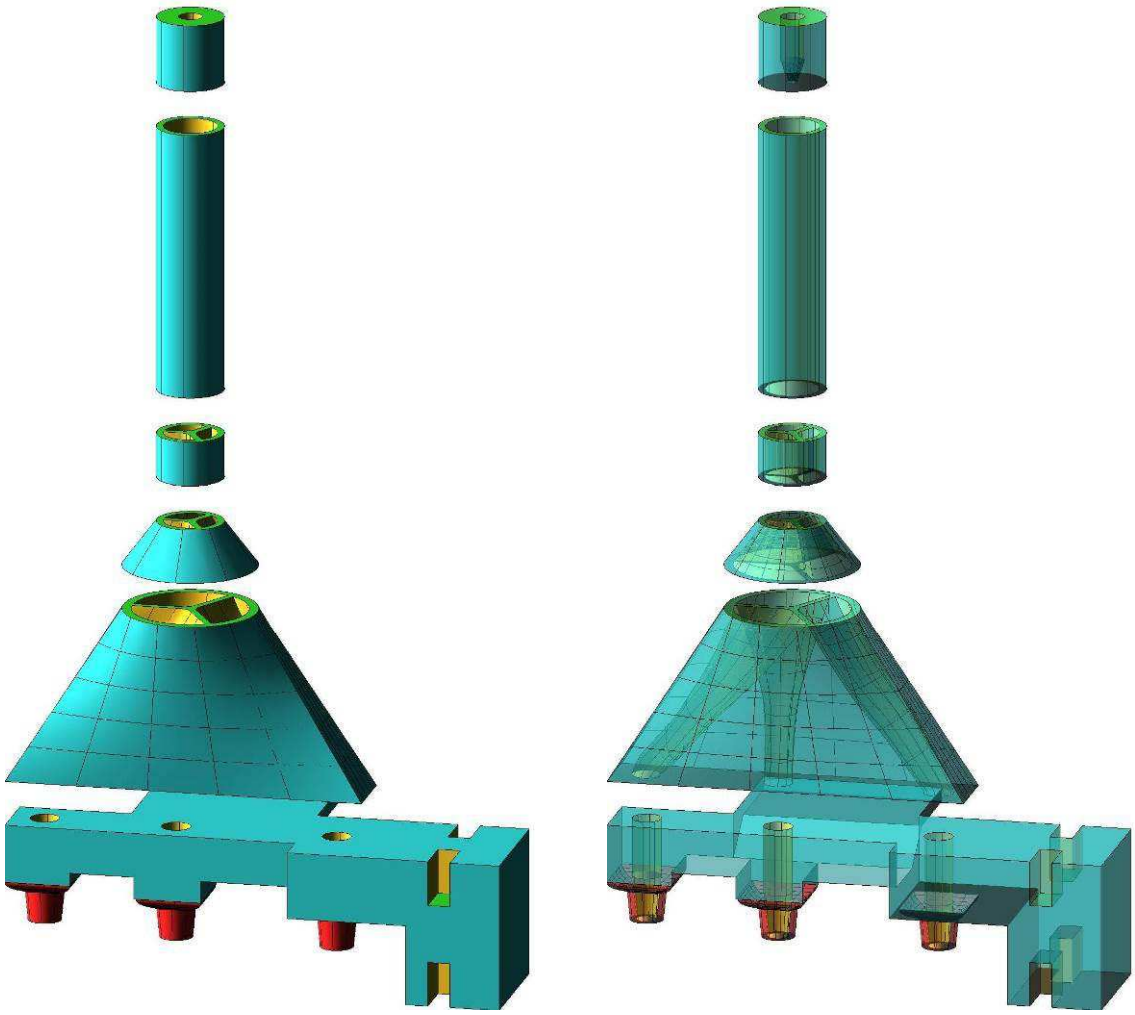

Figure 2.4: The „drip divider“ of Prototype 1.0 as a solid (left) and an X-ray (right) CAD model, exploded for improved visualisation. The topmost part is the “drip concentrator” ensuring that all droplets fall down exactly in the center of the “fall tube” directly underneath. On impact on the “impact tri-star”, the droplet splashes and is “fissioned” into three sub-droplets of equal volume that are then piped through the “drip channels” to the “drip nozzles” at the bottom of the “drip divider”.

To be able to accommodate the drip nozzles a central hole with a diameter of 12 mm was drilled into the caps of the 20 mL plastic sample flasks and the caps were roughened using sand paper before glueing the silicone septa to the caps. As the inner diameter of the original brown glass vials for the stable isotope samples were too small to accommodate the drip nozzles of the drip divider adapted plugs (Appendix, Figure F.16) were designed and 3D-printed for increasing the diameter of the sample vials and for providing a sufficiently large adhesive surface.

The actual sampling process is illustrated in four steps in Figure 2.6: Before the beginning of a sampling sequence consisting of 24 sampling cycles the operator chooses a sampling interval by accordingly flipping the corresponding switch on the electronics casing (Appendix, red box in Figure F.1, right).

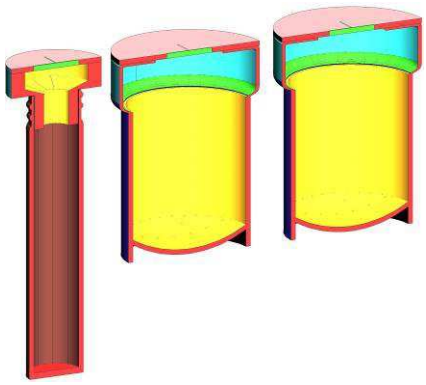

Figure 2.5: The two types of custom-made sample flasks for the three different "sub-samples" in each batch. To prevent or reduce sample alteration by contamination, evaporation or gas exchange during sample storage, the sample flasks were sealed by custom-made silicone septa.

At the current set-up of Protoype 1.0, both daily and weekly sampling intervals are available, both starting with the next full hour. Time and date can be programmed using the Arduino software interface and are saved by the built-in real-time clock that uses a separate 3V lithium button cell battery as a buffer battery in order to prevent time and date from being deleted during short periods without electric power. To set the time and date, the corresponding switch on the electronics casing must be flipped (Appendix, lower button on the red box in Figure F.1, right) accordingly. Before starting the sampling sequence, this switch must be flipped to the position "Sampler".

The sampling sequence starts when the 12 V Pb-acid battery (20 Ah, non-spillable, 5.8 kg, 76 x 167 x 181 mm) is connected to the autosampler and the sampling rack automatically turns until the first set of empty sample flasks is positioned directly underneath the drip nozzles of the drip divider (Figure 2.6, top left). At the next full hour, the Z-arm is moved downwards by the Z-motor via the worm spindle drive (downward translation) until the nozzles of the drip divider pierce the septa of the custom-made sample flasks (Figure 2.6, top right). Once the programmed bottom position is reached, the passive dripwater sampling starts and the dripwater from the stalactite is piped into the sample flasks. Any dripwater in exceedance of the sample flasks' capacity spills over so that the samples mostly represent the chemical conditions of the dripwater during the time it took for completely filling the sample flasks. During this phase of the sampling cycle the autosampler enters a hibernation mode ("goes to sleep") to minimise power consumption. After the end of the first sampling cycle (after one day or one week, depending on the chosen setting), the autosampler reactivates ("awakes") and the Z-arm including the drip divider moves upwards (upward translation) until the programmed top position is reached. Subsequently, the sample rack rotates counter-clockwise (revolution) by exactly 15°, thus positioning the next empty set of sample flasks directly underneath the drip divider (Figure 2.6, bottom left) and the Z-arm is again moved downwards to pierce the septa of the new set of sample flasks, the autosampler re-enters the hibernation moden and the next passive dripwater sampling commences (Figure 2.6, bottom right).

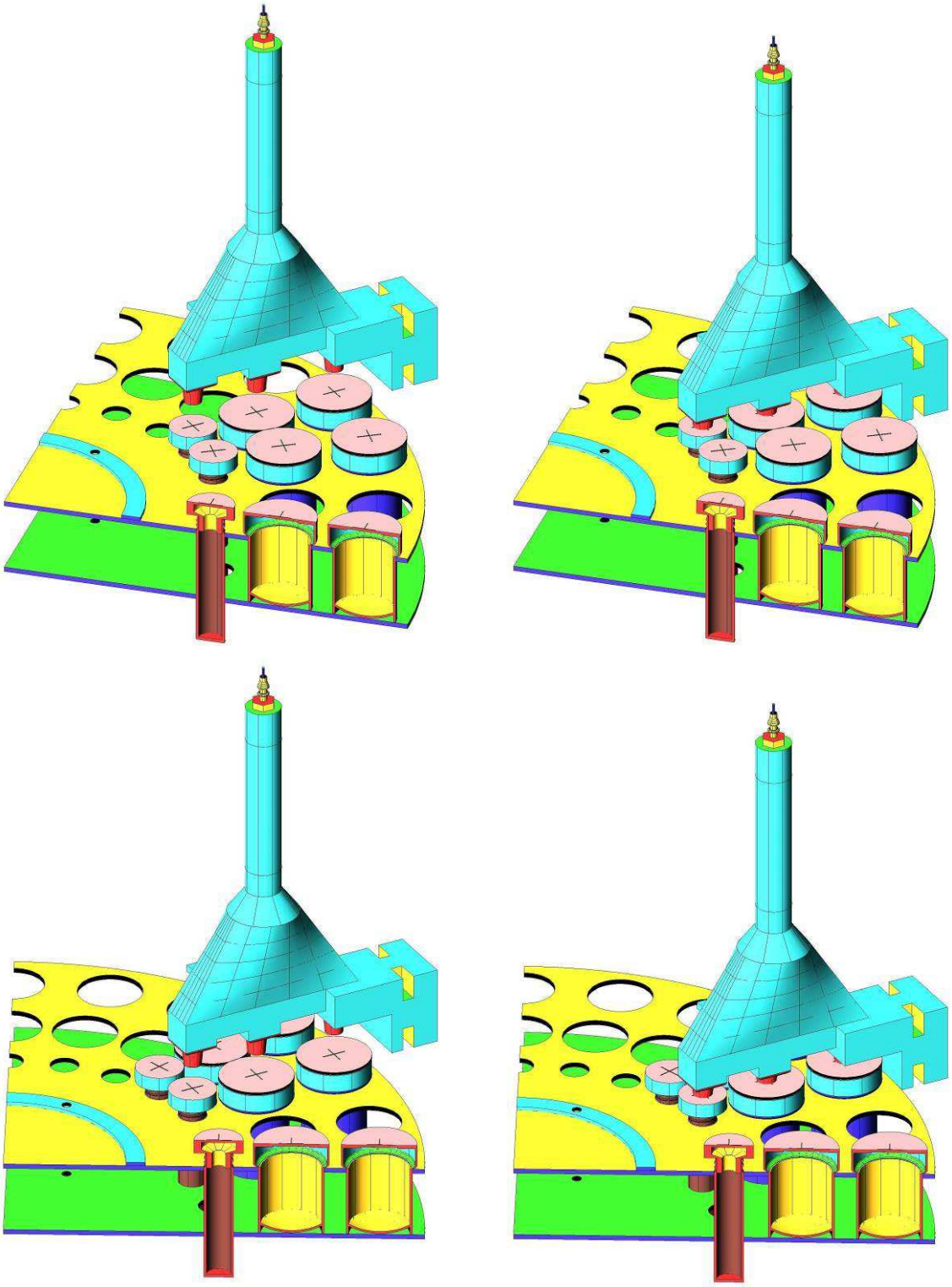

Figure 2.6: The sample collection procedure of Prototype 1.0: (1) Initial setup before the first sampling cycle (top left); (2) Downward translation of the Z-arm until the nozzles of the drip divider pierce the septa of the sample flasks; Start of passive dripwater sampling (top right); (3) Upward translation of the Z-arm and counter-clockwise revolution of the sample rack; positioning of an empty set of sample flasks underneath the drip divider (bottom left); (4) Downward translation of the Z-arm and start of the next sampling cycle (bottom right). Only parts of the CAD models shown and these partly sliced for improved visualisation.

Subsequent to extensive indoor testing in the office to ensure reliable functioning of all components and the autosampler as a whole, two Prototypes 1.0 were partially disassembled (Appendix, Figure F.1), transported to Vietnam, reassembled, tested one final time and installed both in Ma Le 2 cave and Sang Ma Sao cave on the 22nd and 27th of July 2015, respectively (Figure 2.7). The partially water-filled low passage close to the entrance of Sang Ma Sao cave required the autosampler to be transported through that passage in disassembled form, floating on a slab of Styrofoam to keep the autosampler dry as crossing that passage requires crawling on all fours (Figure 2.7, top right). Therefore, reassembly was conducted inside Sang Ma Sao cave (Figure 2.7, bottom).

Figure 2.7: Technical and logistical challenges posed by the cave environment: (1) High relative humidity of around 100% and moisture inside the caves (top left), (2) difficult transport due to low and narrow cave passages, sometimes filled with water (top right; cave river in Sang Ma Sao cave); (3) assembly with strongly limited technical means (e.g. tools, etc.) and under challenging conditions (lack of a flat, dry, clean and well-lit working environment). (Potos: top left: A. Hartmann; 29th of July, 2015; rest: Tran Diep Anh (VIGMR); 27th of July, 2015).

The final set-up of Prototype 1.0 installed in both Me Le 2 cave and Sang Ma Sao cave is shown in Figure 2.8. The Prototype 1.0 autosampler is part of the cave monitoring system applied in both caves within the framework of this thesis, including the newly developed dripwater container and telescope stand together with the Stalagmate drip rate logger and the Tinytag TGP-4500 logger for registering temperature and relative humidity. At the beginning of the sampling cycle, there were no signs of any errors (Figure 2.9).

Figure 2.8: Dripwater collection system consisting of the Prototype 1.0 dripwater autosampler and the dripwater container including the Stalagmate drip rate logger, installed inside Sang Ma Sao cave (left) and Ma Le 2 cave (right). In the left picture, the yellow box on the left-hand side of the dripwater collector is the Tinytag TGP-4500 T/RH logger. (Photos: A. Hartmann; 22nd and 29th of July, 2015, respectively).

Figure 2.9: Initial setup of Prototype 1.0 installed in Ma Le 2 cave right after the start of the first sampling cycle (left) showing no signs of errors and close-up of the "drip divider" with its nozzles successfully piercing the septa of the sample flasks. (Photo: A. Hartmann; 22nd of July, 2015).

2.2.2 Electronic and Software Design

Most of the autosampler's electronic components are accommodated inside the electronics casing (red box in Figure 2.8). Upon final assembly, this casing was screwed shut and additionally sealed with silicone for protecting the electronic components from being impaired or damaged by the high humidity close to 100% common in karst caves. The cables leading from the inside of the electronics casing to the motors outside the casing were laid through a water-proof connector additionally sealed with Teflon tape.

The centrepiece of the electronic design is the Arduino® Mega 2560 board which is based on an Atmel ATmega 328-P microcontroller. This microcontroller enables the autosampler to enter a hibernation mode during which power consumption is reduced 50-fold as compared to the power consumption during slide movement (active mode). It also contains a non-volatile 4 KB EEPROM memory in which the data (time and position) of the previous injection are saved temporarily. The interrupts of the hibernation mode at the beginning of each sampling cycle are triggered by a real-time clock (RTC) chip that includes a separate 3V lithium button cell battery which ensures that the program controlling the sampler operation remains active, even if the main power supply may be interrupted.

The program controlling the autosampler was constructed with the open-source software Arduino (version 1.8.3). The code is written in Java and can be uploaded to the board via a USB connection. A flowchart illustrating the operation of Prototype 1.0 is shown in Figure 2.10. A Bill of Materials is given in the Appendix (Table F.1)

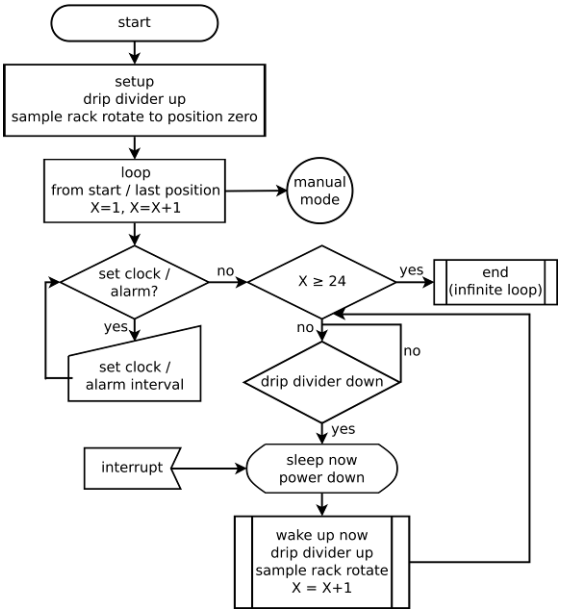

Figure 2.10: Flowchart illustrating the autosampler's operation for a setup comprising 24 sample flasks (72 sub-samples in total), arranged in three concentric circles at a spacing of 15° ("X direction"). Once the last sample has been collected, the program enters an infinite loop and waits for input from the operator.

2.2.3 Failure of Prototype 1.0 in Field Operation

Despite all testing prior to the installation of the Prototype 1.0 autosamplers inside the karst caves in Vietnam and in spite of maximising the fail-safety of the autosampler by minimising its technical complexity, both in terms of hardware and software (Section 2.1), the Prototype 1.0 autosampler installed in Ma Le 2 cave failed. Although the finals tests of the autosampler before installing it inside the cave were successful and although the autosampler showed no signs of error with the nozzles of the drip divider successfully piercing the septa of the sample flasks at the beginning of the sampling cycle (Figure 2.9, right), the autosampler seems to have ceased operation entirely, moving neither the Z-arm, nor the sample rack. Even after thorough error diagnosis, the reasons for this malfunction are unknown, however, the most likely cause is a failure of the electronics as a result of the high relative humidity of about 100%, as the battery was confirmed to be charged sufficiently when checked on the next field trip and no mechanical problems were identified on close inspection of the autosampler.

Figure 2.11: Prototype 1.0 installed in Sang Ma Sao cave destroyed by the cave river during an exceptionally high flow event after a couple of days of strong rain (photo: Prof. Dr. Thomas Neumann; 6th of October, 2015).

Unfortunately, the Prototype 1.0 autosampler installed in Sang Ma Sao cave was destroyed by a high-flow event of the cave river after intense rainfall in the cave river's catchment area. As the autosampler was mounted to the cave wall at a height of ≥ 150 cm (level of the lowest point), the cave river must have reached a water level exceeding 150 cm during this high-flow event, surpassing the mean water level of only 5 cm by 145 cm (2.900 %). The force of the cave river tore the autosampler from the cave wall and washed it downstream over about 10 m where the autosampler hit the cave wall and got stuck, damaged beyond repair (Figure 2.11).

The failure/destruction of both Prototype 1.0 autosamplers required a new autosampler to be built in order to finish the technical development of a dripwater autosampler proven to function reliably and without fault. In addition, the results of an experiment designed to test the stable isotope sample vials for gastightness have shown that the custom-made sample vials are not suited for decreasing sample alteration through evaporation and/or gas exchange down to an acceptable level (Figure 2.12), as discussed in the following.

For the gastightness experiment, ten stable isotope sample vials were filled to the brim with Milli-Q distilled water featuring a δD value of -57.3 ‰ (± 0.3 ‰) and a $\delta^{18}O$ value of 8.27 ‰ (± 0.06 ‰), sealed with the corresponding custom-made septa and stored in a wooden container that was screwed shut with a wooden lid. To simulate the high humidity environment of karst caves with active cave rivers, an air humidifier was activated at intervals of 30 min for a duration of 5 min over the course of the entire experiment. Using an analogue hair hygrometer/thermometer (TFA 45.2028) also stored inside the wooden container, RH and T were checked multiple times per day to be constant at 95 % and 25 °C, respectively, with temperature conditions representative of a low-lying tropical cave. As a control, another stable isotope sample vial was filled with the same Milli-Q distilled water but screwed shut with the original corresponding screw cap and stored inside the container as well.

To quantify the drift in $\delta^{18}O$ values due to evaporation and/or gas exchange over time, ten cavity ring-down spectroscopy (CRDS) measurements were conducted on a liquid water isotope analyser (LWIA-24d; Los Gatos Research) on 6 different dates between the 20th of July, 2015 and the 22nd of February, 2016, thereby spanning an overall period of seven months (Figure 2.12). On three of these dates, samples from multiple vials were analysed for $\delta^{18}O$ to determine the scatter of the $\delta^{18}O$ drift among samples. The sealed control (reference) was analysed for $\delta^{18}O$ on five different dates between the 20th of July, 2015 and the 8th of February, 2016. The standards used for calibration were LGR1A, USGS 46 and USGS 48. The accuracy (<0.07 ‰) was tested by repeated measurements of the control standard material LGR 2C. The average precision of the individual measurements (n = 30) was ±0.4 ‰.

While the $\delta^{18}O$ values of the sealed control only vary between -8.30 ‰ and -8.16 ‰ (initial $\delta^{18}O$ value = 8.27 ‰) while varying randomly rather than exhibiting a clear positive trend, the $\delta^{18}O$ values of the samples stored in vials with custom-made septa steadily increase from -6.96 ‰ on the 20th of July, 2015 to between -2.71 ‰ and -2.04 ‰ on the 22nd of February, 2016, exhibiting a clear positive trend with an overall amplitude of 6.23 ‰ compared to the initial $\delta^{18}O$ value of -8.27 ‰ (Figure 2.12). These results clearly demonstrate that the custom-made septa are not sealing the samples sufficiently to decrease sample alteration through evaporation and/or gas exchange down to an acceptable level.

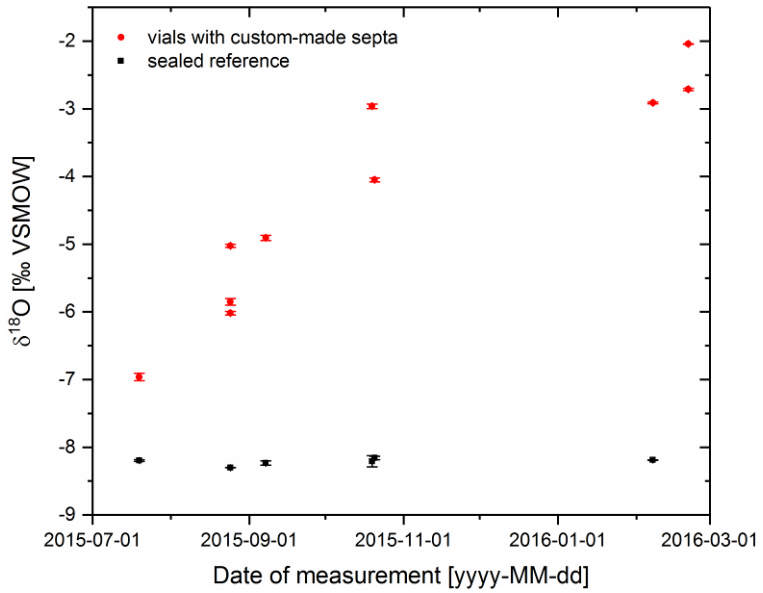

Figure 2.12: Oxygen isotope values ($\delta^{18}O$) of the demineralised water inside the vials sealed with the custom-made septa (red circles) and of the demineralised water inside the vials sealed with a screw cap (black squares) for reference.

As the two Prototype 1.0 autosamplers failed or were destroyed and as the prevention of sample alteration through evaporation and/or gas exchange is crucial for dripwater monitoring in speleothem science, a new autosampler, Prototype 2.0, was developed that would fulfil this requirement and that would be better protected from any damage resulting from high humidity. Prototype 2.0 is presented and discussed in detail in the following section.

3 Prototype 2.0

3.1 Optimisation Characteristics

There are eight characteristics Prototype 2.0 was optimised on (in order of priority):

1. gastight sample vials
2. space-efficiently arranged sample vials and easy-to-increase vial number
3. protection from water/dust ingress and mechanical damage
4. custom-built components
5. low power consumption
6. low cost
7. low weight
8. small size / reasonable dimensions

Implementing absolutely **gastight sample vials** was the highest priority during design and development of Prototype 2.0, as the gastightness is a crucial requirement to prevent sample alteration through evaporation and/or gas exchange. This requirement becomes even more important, the longer a specific drip site is supposed to be monitored.

In the case of Prototype 2.0, the gastightnes of the sample vials was achieved by implementing professional sample vials sealed with rubber septa that have been specifically designed to stay absolutely gastight even after the rubber septa have been pierced by a double cannula (12 mL soda glass Labco Exetainer® 738W vials with a thickness of the rubber septa of ≥ 3 mm), as the elastic rubber effectively seals the holes once the double cannula is pulled out again. However, using gastight sample vials for sample collection requires active sampling applying an artifical force, in this case the overpressure exerted by a peristaltic pump, which rendered it necessary to increase the technical complexity of the autosampler, both in terms of hardware and software.

As most comparable liquid autosamplers including Prototype 1.0 feature a maximum sample capacity of 24 samples, achieving a higher sample capacity by **arranging the sample vials space-efficiently** and making **vial number easy to increase** were two other main goals of developing Prototype 2.0.

In case of Prototype 2.0, the relatively small sample vials (external ø = 15.5 mm) are arranged in an orthogonal matrix of lines and rows rather than in concentric circles. While the arrangement of sample vials in concentric circles offers the advantage that only two kinds of movement are required for sample collection - translation and revolution (as realised in Protopye 1.0) – a matrix-like sample arrangement is advantageous for maximising space-efficiency and the possibility to increase vial number. In contrast, increasing the number of vials arranged in concentric circles is only possible by disproportionally increasing the sample rack dimensions. In its current set-up, Prototype 2.0 comprises 48 sample vials but the autosampler can be equipped with up to 160 sample vials at the given casing dimensions without requiring any modification of the current sample vial arrangement in straight rows and lines (Figure 3.5, top). Furthermore, in future developments, sample vials can be arranged with their external diameters touching each other, in alternating rows shifted by the half of the vial diameter, similar to the close-packing of equal spheres found in crystal structures. With such an optimisation of the sample vial arrangement, Protopye 2.0 could hold a total of 208 sample vials at its current casing dimensions Figure 3.5, bottom). The matrix-like arrangement of sample vials requires three movements for sample collection, three translations along all three directions in space (X, Y and Z).

Protection from water/dust ingress and mechanical damage is another important requirement for a technical device meant for long-term monitoring such as a dripwater autosampler. Ingressing water would cause short-circuits that would result in a failure or malfunctions of the electronic components, while dust ingress would risk the mechanical components of the autosampler to malfunction, for instance by clogging the gears of the motors.

To prevent Prototype 2.0 from being damaged or otherwise impaired, the more sensitive components such as the electronics and the motors are enclosed by protective casings. Furthermore, the entire unit of Prototype 2.0 is enclosed by a water-tight and airtight heavy-duty casing (Peli®, model 1610) including a valve for automatic pressure purge.

Similar to Prototype 1.0, Prototype 2.0 was designed and built using multiple **custom-built components** in order to take advantage of the benefits related to custom-built components, as described in Section 2.1.

For the development of Prototype 2.0, many components were custom-built by 3D-construction (AutoCAD, Autodesk) and 3D-printing (Ultimaker 3 Dual Extruder, Ultimaker) such as the “double cannula holder” (Appendix, Figure F.17), the “servo connector” connecting the Z-slide to the servo (Appendix, Figure F.18), the matrix-like sample rack (Appendix, Figure F.19) as well as the second of the two dripwater containers newly developed within the framework of this thesis (Figure 3.7). The “dripwater pre-collector” (Figure 3.3, left) was custom-built by various techniques of machining and handcraft in the Institute workshops (drilling, turning, sawing, filing, glueing etc.).

Achieving a **low power consumption** and therefore providing long operation times was another goald during designing and developing Prototype 2.0 to make it well-suited for long-term monitoring, similar to Protoype 1.0. However, in comparison with Protoype 1.0, Protoype 2.0 consumes more power during hibernation mode (16.5 mA compared to 5 mA) due to the more complex and thus power consuming electronics necessary for controlling the peristaltic pump for active sampling and the additional servo compared to Prototype 1.0. At its current setup, Prototype 2.0 can operate autonomously for about 100 days at a 2-day sampling interval, collecting its full capacity of 48 samples with a volume of 12 mL.

Another important aspect of Prototype 2.0 is its **low cost**, with the cost for all the materials, excluding labour, amounting to about 1.100 €. The relatively low cost of the autosampler allows to spend the remaining funds on other assets such as additional equipment or chemical analyses and/or makes it affordable to build/buy multiple autosamplers which increases the range of scientific opportunities.

The relatively **low weight** of Prototype 2.0 of about 13 kg (+ 5.8 kg battery) makes it easy and/or cost-effective to transport, even via air, similar to Prototype 1.0. It also makes it possible to install the autosampler in karst caves at the desired drip sites to which heavy items are mostly very difficult, if not practically impossible, to transport. The same applies to the **reasonable dimensions** of Prototype 1.0 (width = 530 mm; length = 675 mm; height: 310 mm).

3.2 Autosampler Set-up and Design

3.2.1 Hardware Design and Sampling Process

The main components of Prototype 2.0 (published as "GUARD" by Hartmann et al., 2018) comprise a “pre-collector”, an intake hose, a peristaltic pump, a mobile injection system and a sample vial holder (Figure 3.1). A detailed description of the autosampler’s integral components is given in Table 3.1. To prevent any sample alteration resulting from contamination, evaporation, condensation and/or gas exchange during sample storage, the dripwater samples (12 mL) are injected into gastight vials using a peristaltic pump, at a user-defined date, time and interval.

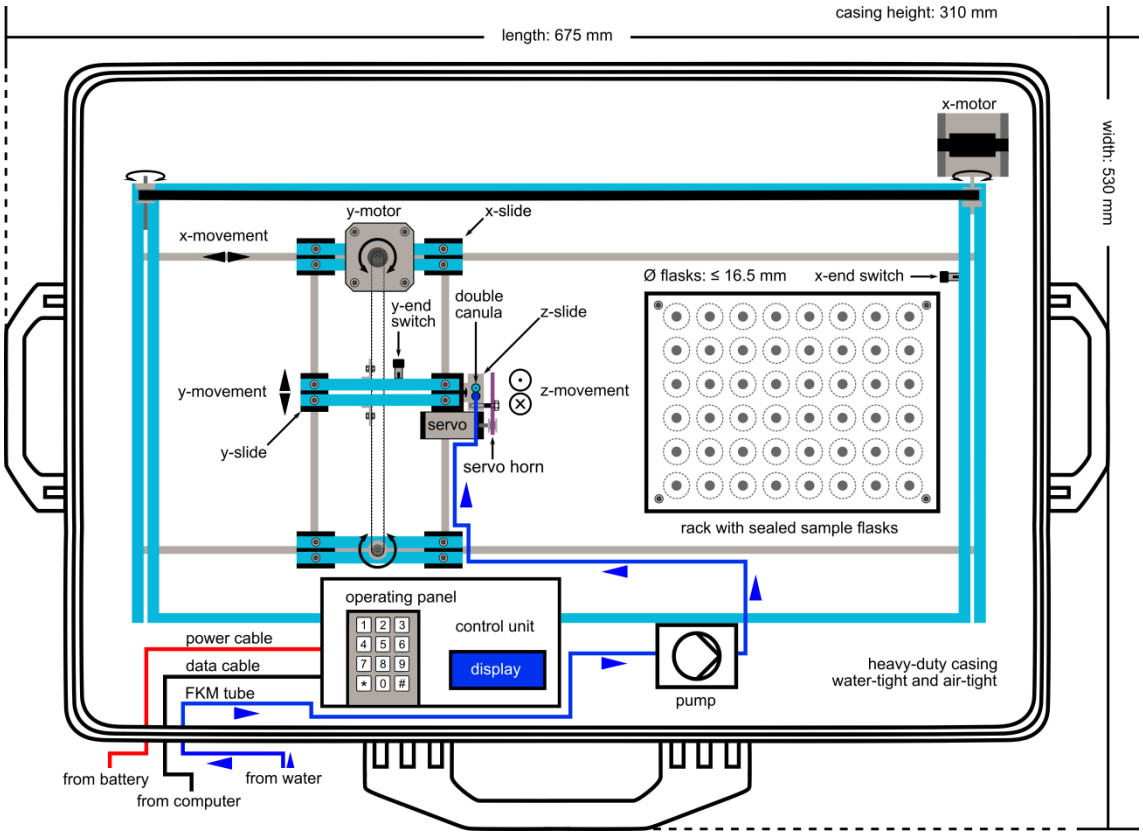

Figure 3.1: Hardware design of the Prototype 2.0 autosampler (top view, schematical). Water samples are pumped directly into vials that are permanently kept gastight by rubber septa. The shown set-up comprises 48 sample vials but the autosampler can be equipped with up to 160 or even 208 sample vials at the given casing dimensions (Figure 3.5).

Before the beginning of the first sampling interval, the dripwater emerging from the stalactite of the drip site under investigation is caught by a funnel attached directly underneath the stalactite via the second of the two newly developed stalactite collars (Figure 3.2).

Subsequently, this dripwater is piped through an FKM tube to a specifically designed pre-collection container ("pre-collector"; Figure 3.3, left) with an internal volume of exactly 12 mL where the dripwater is pre-collected. This pre-collection of dripwater is necessary to prevent the peristaltic pump of Prototype 2.0 from running dry and taking damage as a consequence.

During dripwater pre-collection a 3D-printed floating body (Figure 3.3, right) inside the pre-collector rises until it seals the pre-collector once it is completely filled with dripwater. Any dripwater in excess of 12 mL spills over through a small hole at the top of the pre-collector.

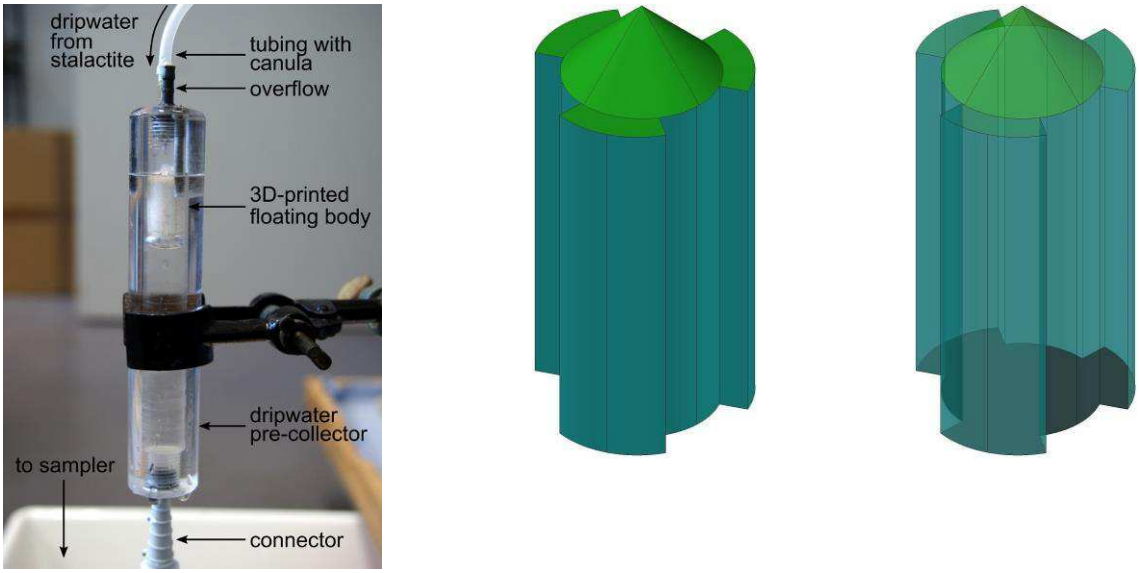

Figure 3.3: Left: "pre-collector" including the 3D-printed floating body (white); Right: 3D-printed floating body as a solid (left) and an X-ray (right) CAD model.

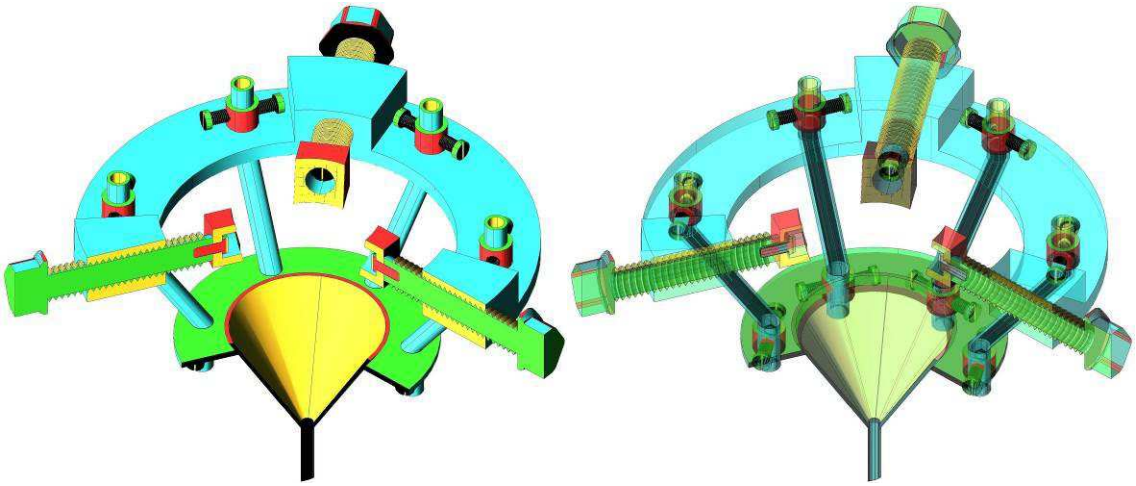

Figure 3.2: The second of the two newly developed stalactite collars, in this case attaching the dripwater funnel of Prototype 2.0 directly underneath the stalactite (= dripwater source; not shown) as a solid (left) and an X-ray (right) CAD model, sliced for improved visualisation.

At the beginning of the first sampling interval, the 12 mL of dripwater pre-collected in the pre-collector are sucked into the autosampler's tubing made of flexible and chemical-resistant FKM. As the tubing is just long enough to accommodate precisely 12 mL (i.e. 1247 mm), the sample is not yet injected into the corresponding vial, but at first remains inside the tubing where it is already protected from gas exchange.

At the beginning of the subsequent sampling interval, two electric motors move the sampler's X- and Y-slide via toothed rubber belts until two separate end-switches are triggered that provide positioning calibration. Both slides are then positioned directly above the first sample vial (Figure 3.4, step 1). After a 2-seconds safety delay, a servo screwed to the sampler's Z-slide moves the Z-slide down, until a metal double cannula attached to the front end of the FKM tubing just barely pierces the rubber septum which keeps the vial permanently gastight. After another 2-seconds safety delay, the sampler's pump is reactivated and the collected water is injected into the vial through one of the cannulas (the "sample cannula"; Figure 3.4, step 2) while the subsequent sample is sucked into the sampler's tubing simultaneously. As a result of this design, the sample injection always lags the sample collection by one interval.

As the sample vials are gastight, an overpressure builds up inside the vials during sample injection. Pressure equalisation is achieved via the second of the two cannulas which are soldered to one another. To achieve the maximum sample volume (here: 12 mL) this "pressure release cannula" is located 2-3 mm above the sample cannula, and the vials are filled with an overflow of several droplets. This setup avoids any unwanted interaction (e.g. gas or isotope exchange) between the collected fluid sample and the supernatant air/gas left inside the vial.

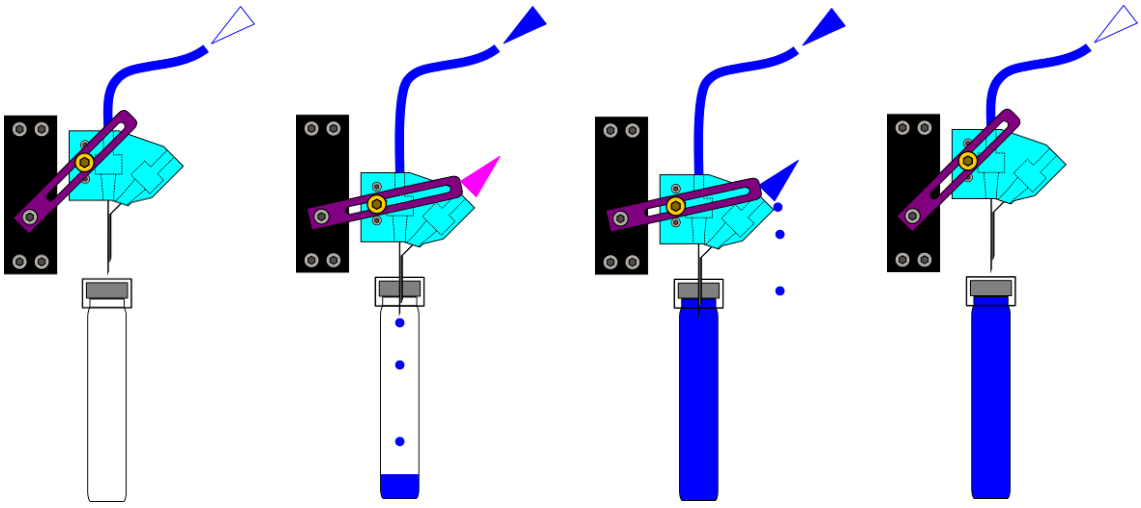

Figure 3.4: Depiction of the four steps that make up the sample injection process of Prototype 2.0: (1) The double cannula is moved into position directly above an empty sample vial; (2) The servo moves the double cannula downwards until it just pierces the rubber septum of the vial and the dripwater injection by the peristaltic pump commences. For pressure equalisation, the air inside the vial is pressed out (purple triangle) through the pressure release cannula; (3) The sample vial is filled completely until several droplets flow over; (4) The double cannula is moved back up leaving the sample vial sealed again and is positioned above the subsequent sample vial (not shown).

Subsequent to a 10-seconds safety delay implemented to allow for complete pressure equalisation and sample injection (Figure 3.4, step 3), the Z-slide with the double cannula is moved back up to its home position and the X- and Y-slides are positioned above the next sample vial (Figure 3.4, step 4). After another 2-seconds safety delay, the sampler enters a hibernation mode to minimise power consumption until the hibernation is interrupted with the start of the next sampling interval. After completion of a full sampling sequence the Z-slide moves back up to its home position, the X-slide moves to its end position and the sampler waits for input from the operator.

In the current setup of Prototype 2.0 the collected samples have a volume of 12 mL which is sufficient for most analyses, including isotope ratio mass spectrometry (IR-MS) and inductively coupled plasma mass spectrometry (ICP-MS). The pumping process takes only about 22 seconds and, thus, the collected sample represents the water under investigation at a given instant (integrated over 22 seconds). As one entire sampling step takes only 41 seconds (power consumption: 2.1 mAh), the autosampler is capable of high-resolution fluid sampling with a minimum interval of one minute. This is valuable where high-frequency variations in the composition of the sampled fluid need to be resolved, for instance, in artificial tracer tests at the onset of the tracer breakthrough where samples are commonly collected at intervals as short as one minute (Leibundgut et al., 2009). If needed, the sample volume can be modified by changing the duration of the pumping step. For example, to obtain a 100 mL sample the pumping step would take about 3 minutes.

Using a 12 V battery with a capacity of 40 Ah Prototype 2.0 can operate off-grid for about 100 days without interruption at a 2-day interval (one full sampling sequence), thanks to the hibernation mode during which power consumption is reduced to 16.5 mA. On such long time spans the power consumed during the actual sampling process is practically negligible. If longer operation durations are necessary, multiple batteries can be connected in parallel to increase the total capacity. The sampler can also run on 12 V Li-ion batteries if weight is an important constraint. Additionally, nearly discharged batteries can be replaced with fully charged ones without interrupting a running sampling sequence by using an electrical bypass. Of course, implementing an appropriate rectifier, the autosampler can also run on mains power in which case runtime limitations do no longer apply.

In its current set-up, Prototype 2.0 comprises 48 sample vials (Figure 3.1) but the autosampler can be equipped with up to 160 sample vials at the given casing dimensions, just by maxing out the x-dimension of the current sample holder Figure 3.5, top), keeping the sample vials arranged in straight lines and rows. Furthermore, by arranging the sample vials with minimal distance in between, in alternating rows shifted by the half of the vial diameter, Protopye 2.0 can hold a total of 208 sample vials at its current casing dimensions (Figure 3.5, bottom).

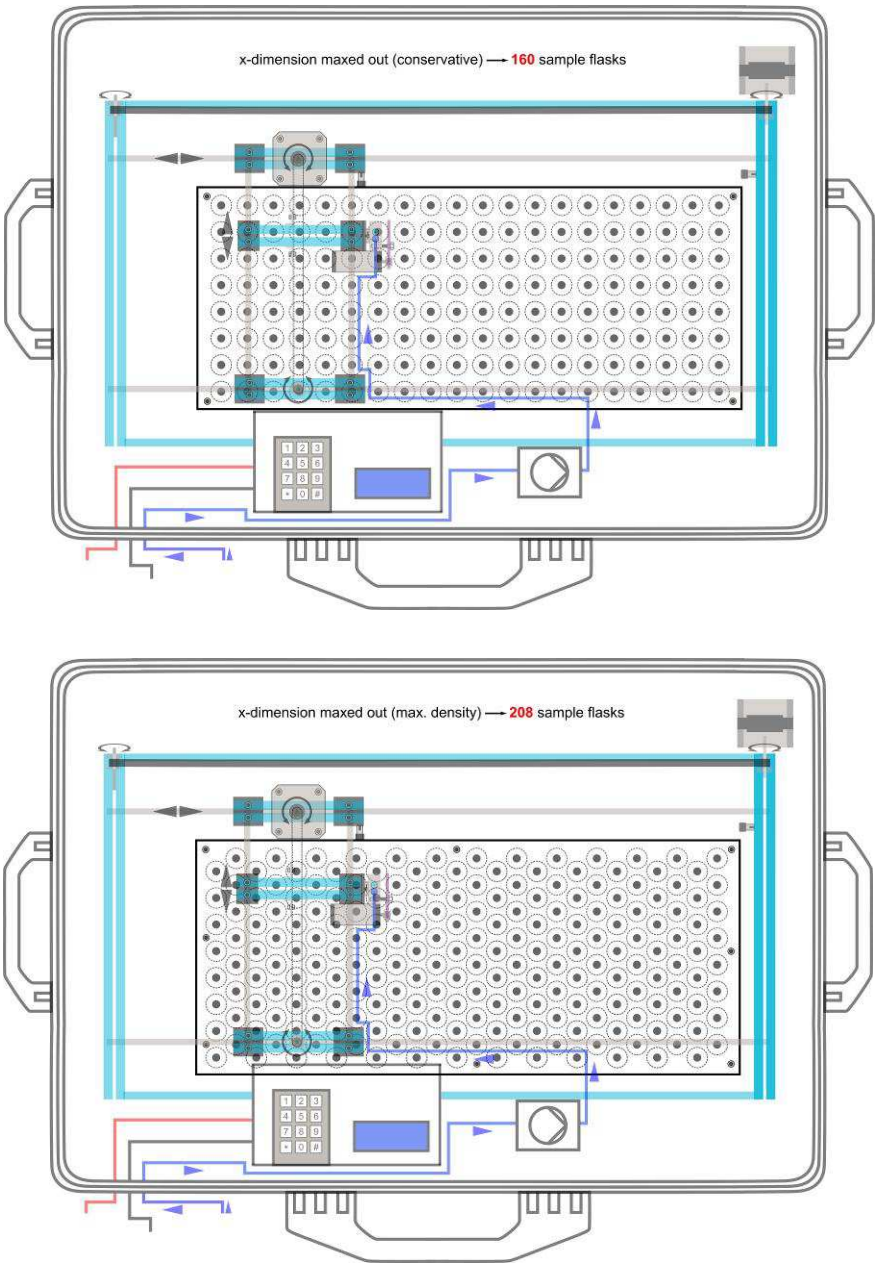

Figure 3.5: Prototype 2.0 with maximised sample vial number: Top: Without modifying the sample vial arrangement in straight lines and rows, just by maxing out the x-dimension of the sample holder, Prototype 2.0 can be equipped with up to 160 sample vials at the given casing dimensions; Bottom: When sample arrangement itself is optimised to achieve maximum vial density, Prototype 2.0 can be equipped with up to 208 sample vials at the given casing dimensions.

Figure 3.6 shows Prototype 2.0 in detail and in operation during a 5-day case study (Section 3.4) designed for Speleothem science, focusing on the carbon isotope geochemistry ($\delta^{13}C_{DIC}$) of dripwater originating from a stalactite in a karst cave in northern Bavaria, Germany. If drip rate logging is required as well, it can be realised with the Stalagmate drip rate logger (Mattey & Collister, 2008) installed inside the second of the two newly developed dripwater containers (Figure 3.7), at an angle of 20° relative to the horizontal for optimal drip registration.

This dripwater container was entirely 3D-printed. For minimising any potential sample alteration due to evaporation and/or gas exchange during drip rate logging, the container can be covered with a corresponding 3D-printed lid and multiple 3D-printed rings (Figure 3.7, top) to leave an opening that is just large enough for the drips to fall into the container and impinge on the Stalagmate drip rate logger to be registered. For increased stability, the container comprises a hollow socket at the bottom that can be filled with sand or other kinds of material to increase the weight of the dripwater container and to shift its centre of mass downwards.

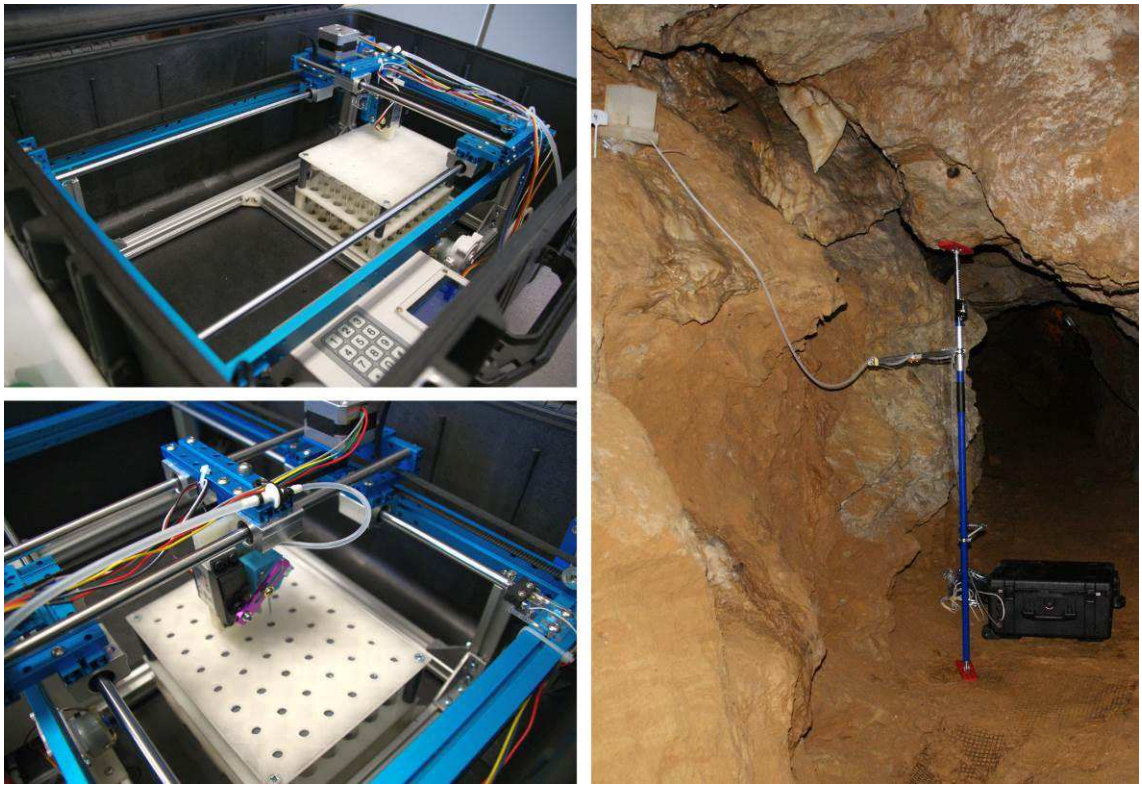

Figure 3.6: The automated dripwater sampler Prototype 2.0 in detail (left) and in operation (right) during a 5-day case study (Section 3.4) carried out in the cave "Kleine Teufelshöhle" in the Franconian Switzerland region, Germany. At a 4-hour interval, a total of 22 dripwater samples were automatically collected for subsequent analysis of the carbon isotope values ($\delta^{13}C_{DIC}$) of the dissolved inorganic carbon (DIC).

Table 3.1: Detailed description of the autosampler's integral components.

COMPONENTS	DESCRIPTION
MECHANICAL	
CASING	Peli®, model 1610, heavy-duty, water-tight and airtight, including a valve for automatic pressure purge
Z-MOVEMENT: SERVO	Reely® Standard RS-610 MG, operating voltage 6.6 V, attached to the Z-slide containing the double cannula via an elongated hole in the servo's horn
X-/Y- MOVEMENT: MOTORS	Sanyo Denki®, bipolar hybrid stepping motors, 1 A, 24 V, 1.8°/step, 0.265Nm, 4 wires
PUMP	Peristaltic (flexible-tube) pump, model AP-40; operating voltage 12 V,
SAMPLE VIALS	Labco Exetainer® 738W, soda glass, 12 mL, flat bottom, height (vial + cap) ≤ 101 mm; external ø ≤ 15.5 mm; internal ø ≥ 13.2 mm; including rubber septa with a thickness ≥ 3 mm
TUBING	Deutsch & Neumann®, FKM (synthetic rubber, "Viton"), Shore hardness 75, external ø ≤ 6.2 mm, internal ø 4 mm
DOUBLE CANNULA	Braun Sterican®, metal, external ø 0.60 mm; length excluding Luer-Lock connector 30 mm
ELECTRONIC	
BATTERY	Panasonic®, valve regulated Pb-acid battery 12 V, 20 Ah, maintenance-free, non-spillable, low self-discharge, 5.8 kg, 76 x 167 x 181 mm;
MICROCONTROLLER BOARD	Arduino® Mega 2560 including an Atmel ATmega 2560 microcontroller with 54 digital I/O pins, 16 analogue inputs, 6 interrupt inputs, 4 serial interfaces, 1 I^2C interface and 4 KB EEPROM memory (non-volatile); hibernation mode-enabled
REAL-TIME CLOCK	RTC PCF8563 powered by a separate 3V lithium button cell battery as a buffer battery
DISPLAY	Liquid crystal display (LCD) with 2 lines à 16 characters
OTHER ELECTRONIC COMPONENTS	operating voltage 5 V; 3 DC/DC converters; 2 stepping motor driver carriers: Pololu® A4988; relay board including 2 relays; keypad comprising the characters 1 to 9, * and #

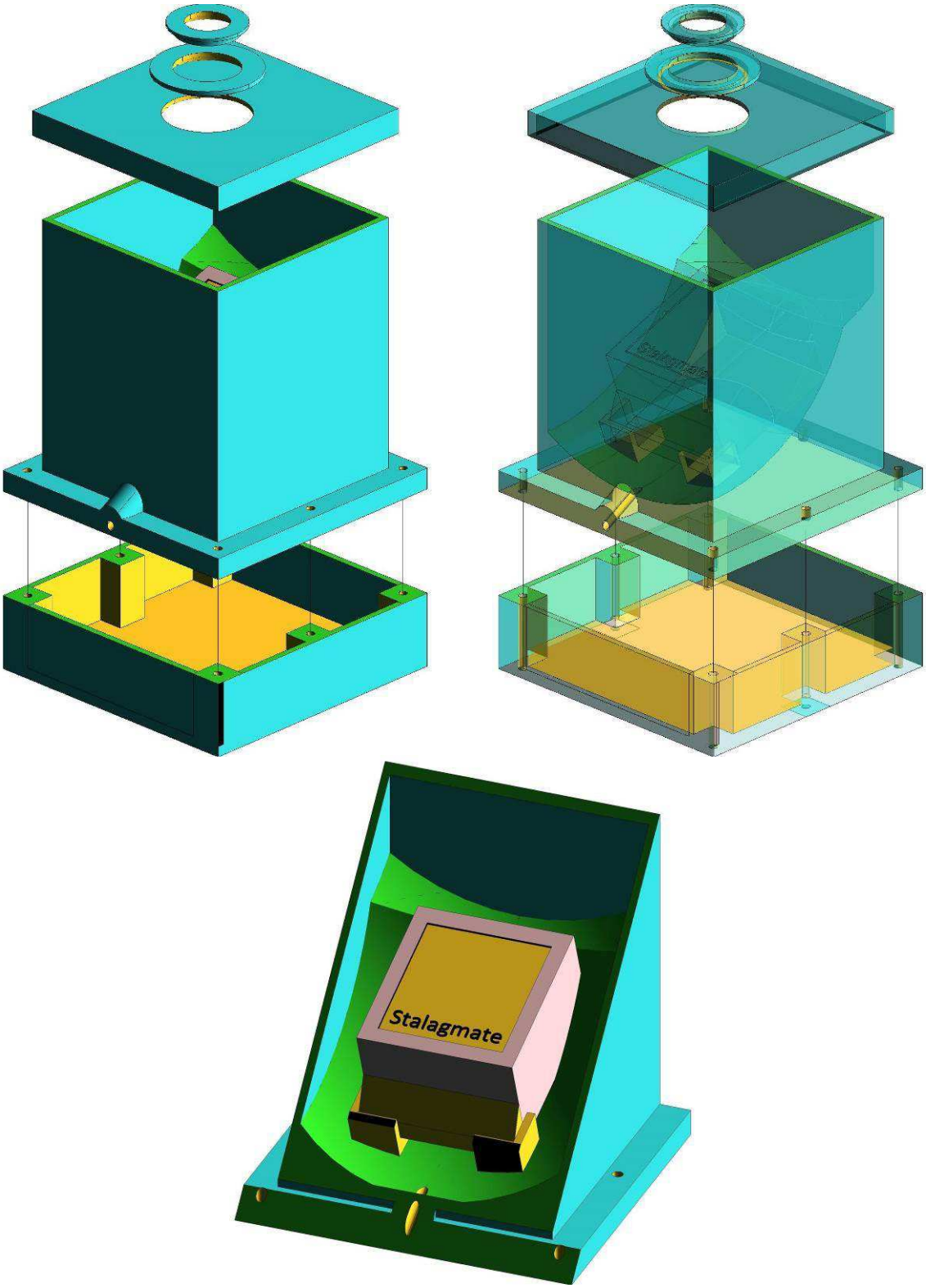

Figure 3.7: The second of the two newly developed dripwater containers implementing the Stalagmate drip rate logger (Mattey & Collister, 2008) installed at an angle of 20° relative to the horizontal, shown as a solid (top left) and an X-ray (top right) exploded CAD model as well as a solid CAD model (bottom) sliced for improved visualisation. This dripwater container was 3D-printed and not machined like the first of the two newly developed dripwater containers.

3.2.2 Electronic and Software Design

Most of the electronic components of Prototype 2.0 are accommodated in the control unit (Figure 3.1) inside an additional casing for protection. The centrepiece of the electronic design is the Arduino® Mega 2560 board which is based on an Atmel ATmega 2560 microcontroller. This microcontroller enables the autosampler to enter the hibernation mode during which power consumption is reduced 50-fold as compared to the power consumption during slide movement. It also contains a non-volatile 4 KB EEPROM memory in which the data (time and position) of the previous injection are saved temporarily. The interrupts of the hibernation mode at the beginning of each sampling interval are triggered by a real-time clock (RTC) chip that includes a separate 3V lithium button cell battery which ensures that the program controlling the sampler operation remains active, even if the main power supply may be interrupted. The program controlling the autosampler was constructed by Ralf Wachter (AGW) with the open-source software Arduino (version 1.8.3). The code is written in Java and can be uploaded to the board via a USB connection. A flowchart illustrating the operation of Prototype 2.0 is shown in Figure 3.8. The electrical circuit diagram as well as a Bill of Materials are given in the Appendix (Figure F.20 and Table G.1, respectively).

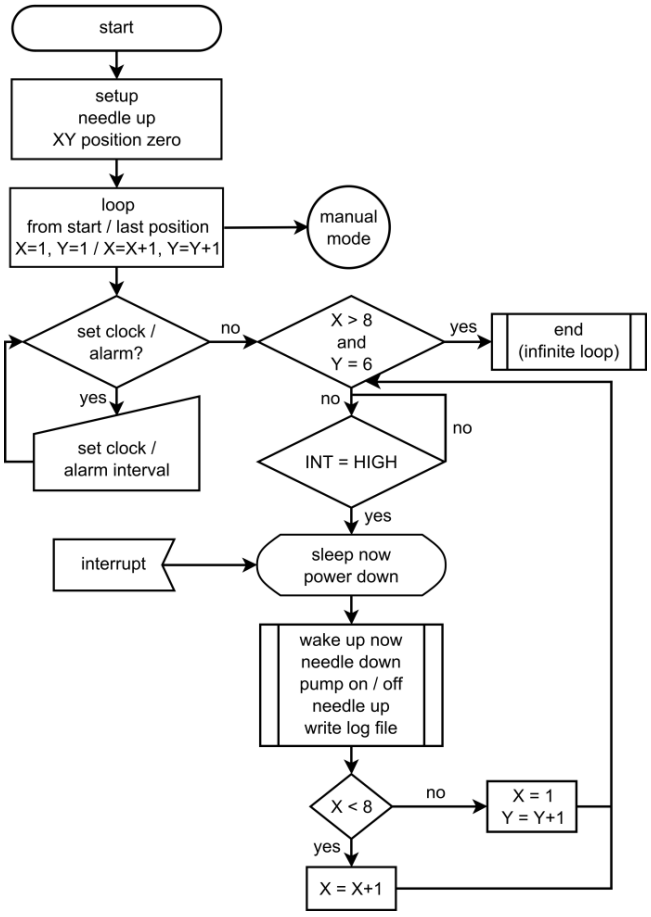

Figure 3.8: Flowchart illustrating the operation of Prototype 2.0 for a setup comprising 48 sample vials in total, arranged in lines (X direction) of 8 and columns (Y direction) of 6 vials, respectively. Once the last sample has been collected, the program enters an infinite loop and waits for input from the operator.

3.3 Demonstration of the autosampler's functioning

3.3.1 X-Y-Positioning

During and after the development of Prototype 2.0 various indoor experiments were conducted to test the mechanical functioning of the prototype. One important requirement in that respect is a precise and reliable positioning of the X- and Y-slides at the exact locations of the sample vials. High precision is especially important for an efficient use of the space available for the sample vials which are arranged in straight lines and rows as close as possible to each other. To achieve this high precision, all movements are executed by Computerised Numerical Control (CNC). The stepper motors for the slide movement in X- and Y-direction are programmed to turn in quarter-steps which correspond to a rotation of only 0.45 °. Consequently, the slide movements along the X- and Y-axis are accurate to less than 1 mm. As the pierceable area of the rubber septa is 7 mm in diameter, there is a more than sufficient error margin of about 350 %. This prevents the double cannula from hitting the sample rack during the Z-slide's downward movement which would cause the double cannula to deform and the respective sampling sequence to fail.

3.3.2 Sample Injection

Another important aspect of an error-free mechanical functioning is a successful sample injection with an optimal use of the available sample volume. To demonstrate the fulfilment of this prerequisite a complete sampling cycle comprising 48 tap water "samples" was run and the size of the air bubbles remaining in the vials after sample injection were analysed. The results of this test are shown in Figure 3.9: Most bubbles are 9.5 mm in diameter or less which confirms that the vials (internal diameter ≤ 15 mm) are filled quasi-completely during sample injection. Assuming the bubbles were a perfect sphere, they would make up ≤ 0.45 mL (or ≤ 4 % of the inner vial volume). Considering that the bubbles are in fact strongly flattened, they more like make up ≤ 0.22 mL (or ≤ 2 % of the inner vial volume). Therefore, any sample alteration due to interactions between the fluid sample and the supernatant air/gas, for instance, due to isotopic exchange, is negligible.

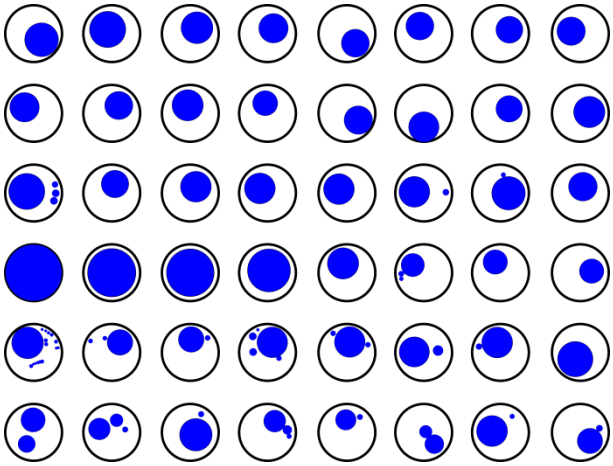

Figure 3.9: Top view (digitised facsimile) of the sample vials (black circles) turned upside down in order to illustrate the air/gas bubbles (blue circles) remaining in the vials after sample injection.

3.3.3 First Field Test: Comparison of Automatic and Manual Samples & Long-term Sample Stability

With respect to the quality of the samples collected by Prototype 2.0, there are two main prerequisites: 1) Samples need to yield identical analytical results, whether they are collected automatically or manually, and 2) samples need to be unaltered and stable, even in the long term, which is ensured by the sample vials being gastight. In order to ascertain the fulfilment of both of these criteria, Prototype 2.0 was applied in a first field experiment in a karst cave to automatically sample the water at a specific drip site over the course of 33 days at daily intervals. For comparison, 12 dripwater samples were collected manually. Then the oxygen isotopes in these water samples were analysed with cavity ring-down spectroscopy (CRDS) on a liquid water isotope analyser (LWIA-24d; Los Gatos Research). The standards used for calibration were LGR1A, USGS 46 and USGS 48. The accuracy (<0.07 ‰) was tested by repeated measurements of the control standard material LGR 2C. The average precision of the individual measurements (n = 124) was ±0.4 ‰. The isotope data are shown in Figure 3.10 and Figure 3.11.

Figure 3.10 demonstrates that the oxygen isotope results from the automatically and the manually collected samples are in good agreement with each other, especially considering the respective analytical error ranges. In two cases (13th of December 2016, around 3 pm and 22nd of December 2016, around 4 pm), $\delta^{18}O$ values do not seem to agree within error at first. However, as the manual samples had to be collected at least 15 minutes before or after the automatic collection in order to allow for sufficient sample volumes (due to the low drip rate at this specific site), this seeming mismatch can be explained with the high-frequency variability of the dripwater $\delta^{18}O$ values at this drip site.

This is best exemplified with the last two automatically collected samples in the left sub-plot in Figure 3.10, where $\delta^{18}O$ values dropped from -10.05 ‰ to -10.24 ‰ within only 30 minutes. The sample collected manually exactly in between these two yields an intermediate $\delta^{18}O$ value of -10.06 ‰ and is therefore consistent with the automatically collected samples. More importantly, there is no systematic discrepancy between the automatically and the manually collected samples, with the respective arithmetic mean $\delta^{18}O$ values, calculated for the entire sampling period (both sub-plots of Figure 3.10), differing by only 0.03 ‰. The results for δD are similar to the $\delta^{18}O$ results and also confirm the long-term stability of the samples (Appendix, Figure G.2).

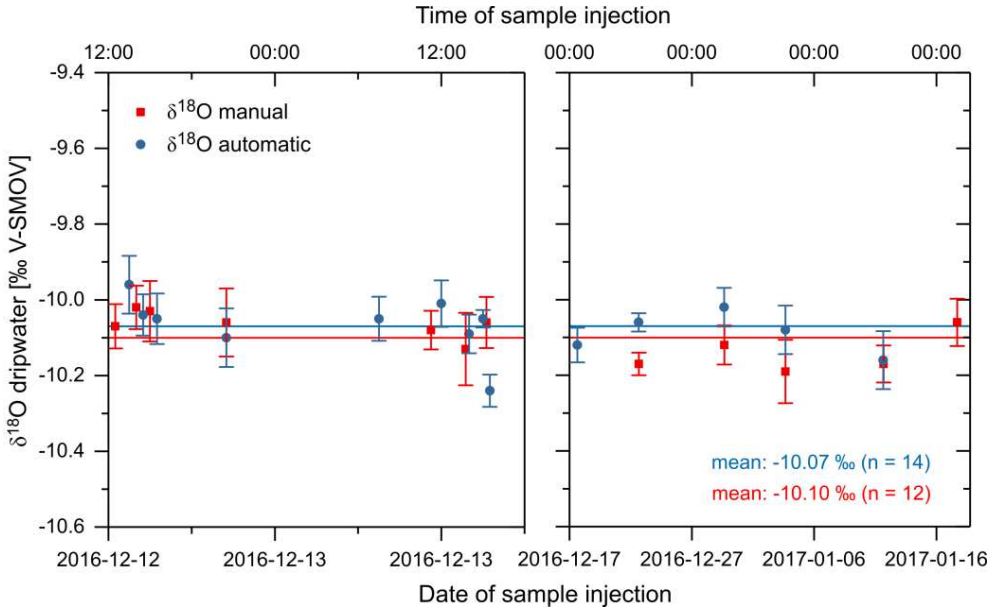

Figure 3.10: First field testing of Prototype 2.0: Oxygen isotope values (indicated as $\delta^{18}O$ relative to the international standard V-SMOW) in dripwater samples from a specific drip site in the karst cave „Laichinger Tiefenhöhle" in the Swabian Alb region, southern Germany. Samples were collected automatically (blue circles) over the course of 33 days (December 13, 2016, to January 14, 2017) and supplemented by 12 samples collected manually (red squares) for comparison of both methods. Error bars represent measurement uncertainty. Blue and red horizontal lines indicate the overall arithmetic mean of each data set. Note the difference in scale of the x-axes of the two sub-plots. Not all of the 33 samples were analysed for isotopic composition.

In order to demonstrate that the sample vials are completely airtight and remain so even after the double cannula has pierced the rubber septa during sample injection, the oxygen isotopic composition of nine different samples (stored in a fridge at 11.2 °C) were measured repeatedly over a time interval of six months. The results (Figure 3.11) confirm the long-term stability of the samples: If the vials were not airtight, evaporation would have led to a preferential removal of isotopically light water molecules from the water samples due to their higher vapour pressure (e.g. Hoefs, 2015) and, consequently, to an increase of the $\delta^{18}O$ value of the remaining water sample over time.

Such a positive trend is not present in the data and the results from the repeated measurements agree well with the initial ones. The difference in $\delta^{18}O$ values between initial and repeated measurements ranges from 0.00 ‰ (lt02-05) to 0.15 ‰ (between 2nd and 3rd measurement of sample lt03), but averages out at -0.01 ‰ over all measurements (median also -0.01 ‰) indicating that there is no systematical discrepancy between initial and repeated analyses. The results for δD are similar to the $\delta^{18}O$ results and also confirm the long-term stability of the samples (Appendix, Figure G.1).

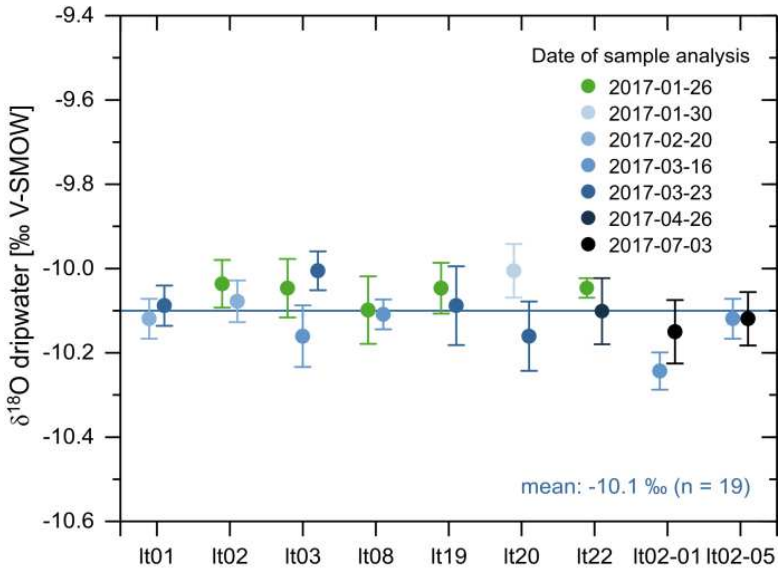

Figure 3.11: Results of repeated $\delta^{18}O$ measurements (circles in tones of blue) measured in the automatically collected samples together with the original $\delta^{18}O$ data from Figure 3.10 (green circles) plotted against their respective label ("lt" stands for Laichinger Tiefenhöhle). The darker the tones of blue, the later the respective measurement was repeated.

To demonstrate the effect evaporation would have had on the sample $\delta^{18}O$ values, both evaporation and $\delta^{18}O$ change were calculated for the conditions prevalent in the fridge (temperature 11.2 °C, relative humidity 24 %) assuming an opening of the sample vial of 5 % to imitate a minor lack of airtightness. The results of these calculations (Appendix, Figure G.3) demonstrate that even a small slit in a sample vial's rubber septum equalling only 5 % of the vial's inner cross-section leads to a substantial shift towards higher $\delta^{18}O$ values in the residual water over time. After three months (90 days), for instance, $\delta^{18}O$ values would have risen from -10.1 ‰ by about 1.3 ‰ to -8.8 ‰. For comparison, the difference between the lowest and the highest $\delta^{18}O$ value in Figure 3.11 is still below 0.3 ‰, while those data points span an even longer period of six months. Most importantly, there is no positive trend in the $\delta^{18}O$ values in Figure 3.11 which illustrates that the sample vials are sealed properly, even after sample injection.

3.4 Case Study: High-resolution Drip Sampling for Speleothem Science

The potential and usefulness of Prototype 2.0 are demonstrated in a first case study that would have been both too expensive and time-consuming to conduct without such an autosampler. The goal was 1) to prove the existence of high-frequency (daily) variability in the carbon isotope values ($\delta^{13}C$) of dissolved inorganic carbon (DIC) in cave dripwaters and 2) to quantify its amplitude. This variability has important implications for the reconstruction of past environmental changes from speleothem $\delta^{13}C$ values as these are not only a function of the dripwater $\delta^{13}C$ signal originating from the surface environment, but also of the intensity of degassing of excess CO_2 from the dripwater (Fairchild et al., 2006). However, to date $\delta^{13}C_{DIC}$ variability has only been documented on the seasonal and annual scale (e.g. Spötl et al., 2005; Mattey et al., 2010) certainly also due to the lack of practical solutions for the high-frequency dripwater sampling in caves.

The existence of such high-frequency variability in $\delta^{13}C_{DIC}$ can be postulated based on the knowledge that cave air CO_2 concentrations can vary both strongly and quickly (e.g. Luetscher & Ziegler, 2012) as a response to ventilation processes (e.g. Tremaine et al., 2011): In general, strong ventilation of a cave system leads to an input of low CO_2 ambient air which (partly) replaces the CO_2 enriched cave air. The lowered CO_2 concentration causes enhanced degassing of excess CO_2 from the cave dripwater, which, in turn, results in increased dripwater $\delta^{13}C_{DIC}$ values, as isotopically light CO_2 transits preferentially from the liquid to the gas phase (Clark & Fritz, 1997).

3.4.1 Study Area

This case study was carried out in the "Kleine Teufelshöhle" (N 49°45′17″, E 11°25′12″) in the Franconian Switzerland region in northern Bavaria, Germany. This cave is characterized by dynamic ventilation (forced convection). The mean annual air temperature is around 8°C and the air humidity is close to saturation. This site warrants conditions suitable for a demanding field test due to 1) the lack of an electric supply network and to 2) the high relative humidity which poses challenges for electrical appliances in general. Prototype 2.0 was placed at a location adequate for sampling the dripwater from a specific group of stalactites, at drip site "DS4" (Figure 3.6, right).

3.4.2 Materials and Methods

Dripwater sampling was conducted automatically at 4-hour intervals over a period of five days yielding a total of 22 samples. The stable carbon isotopic composition of the dripwater DIC was determined at the University of Innsbruck using continuous-flow isotope ratio mass spectrometry following the method described in Spötl (2005).

Calibration of the raw results versus the V-PDB scale is achieved using in-house calcite standards (subsequent to linearity correction) that have been calibrated against NBS-18, NBS-19, CO-1 and CO-8 reference materials. The external precision calculated over 12 standards per run is typically ≤0.07 ‰ for $\delta^{13}C$.

Cave air CO_2 concentrations were logged every 30 minutes with a Vaisala GM70 hand-held unit equipped with a CO_2 probe optimised for the 0–2000 ppmV range (GMP222; accuracy: ± 1.5 % of the calibration value plus 2 % of the measured value). Cave air temperature (T) and relative humidity (RH) were logged at 10-minute intervals with a Tinytag TGP-4500 (Gemini Loggers; accuracy: ± 0.5 °C at 8 °C and ± 3.0 % RH at 25 °C), while the combined drip rate of the stalactite cluster was logged with a Stalagmate Mark 3 (TGC-0011; Driptych) and integrated over 5-minute increments.

3.4.3 Results

Over the duration of the 5-day case study, RH was constant at 100 % and the drip rate oscillated between 26 and 28 drops per 5-min increment (5.2 to 5.6 drops/min). The results of the T, CO_2 and $\delta^{13}C_{DIC}$ analyses are summarised in Figure 3.12. Cave air CO_2 concentrations range from 520 to 1430 ppmV, with an average of 748 ppmV (n = 476) and a median of 710 ppmV, and $\delta^{13}C_{DIC}$ values range from -9.8 to -7.7 ‰, with an average of -8.8 ‰ (n = 22) and a median of -8.9 ‰.

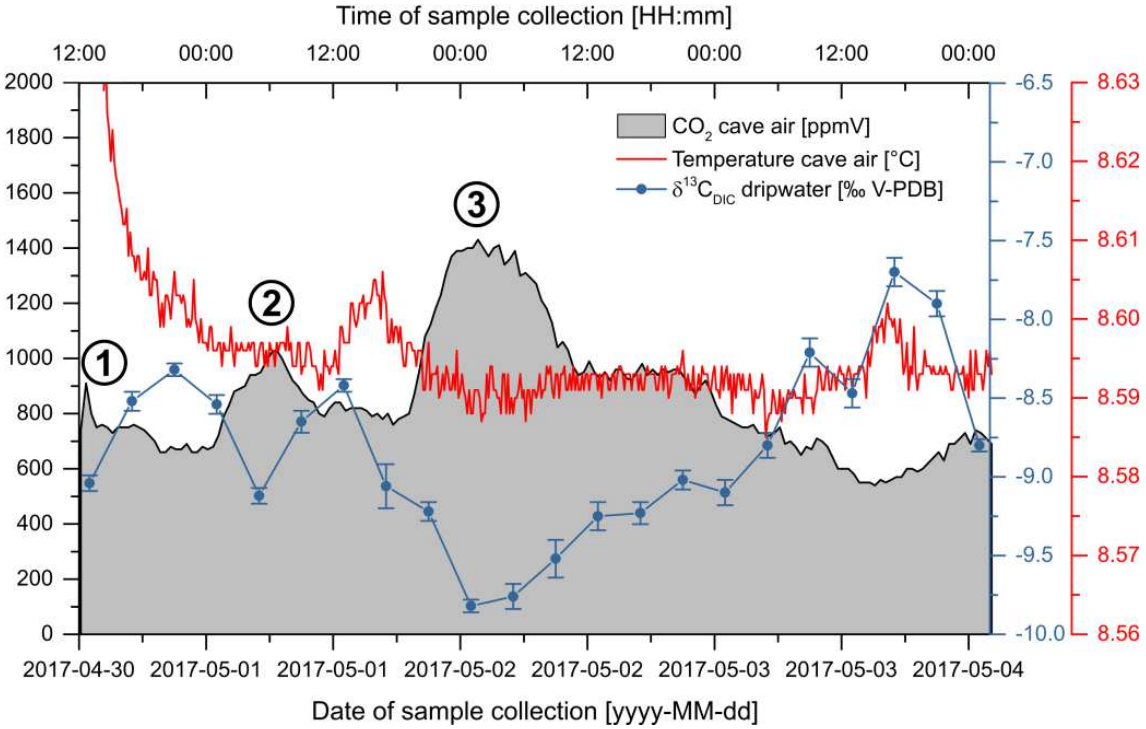

Figure 3.12: Time series of T, CO_2 and $\delta^{13}C_{DIC}$ generated during a first case study applying Prototype 2.0 (units are given in the legend). Cave air CO_2 concentrations and dripwater $\delta^{13}C_{DIC}$ values correlate negatively. Main CO_2 peaks are highlighted with circled numbers.

Carbon dioxide concentrations peaked three times (circled numbers in Figure 3.12), with two smaller peaks of 910 and 1030 ppmV at the beginning of the monitoring period being followed by the most prominent and broad peak of 1430 ppmV that occurred during the night from the 2nd to the 3rd of May 2017.

All three CO_2 peaks, particularly the last one, precisely coincide with troughs in the $\delta^{13}C_{DIC}$ values, while CO_2 troughs coincide with $\delta^{13}C_{DIC}$ peaks, which results in a distinct negative correlation (Spearman's $\rho = -0.88$) of both geochemical signals. Temperature varies only very slightly, with both average and median being 8.6°C (n = 1425). Despite the low amplitude of T variations, T appears to correlate positively with $\delta^{13}C_{DIC}$, but only weakly (Spearman's $\rho = 0.36$).

3.4.4 Interpretation

The dripwater analyses obtained from the Kleine Teufelshöhle at 4-hour resolution over five days clearly prove the presence of a high-frequency variability in the $\delta^{13}C_{DIC}$, in addition to the already documented seasonal and interannual variability (Spötl et al., 2005; Mattey et al., 2010). In this case, the maximum amplitude is 2.1 ‰ – a change that is great enough to be resolved by state-of-the-art isotope-ratio mass spectrometers (IR-MS). While this 2.1 ‰ change occurred over a period of almost two days (2017-05-02 01:00 to 2017-05-03 17:00), additional variability is observed on even smaller time-scales. For example, the difference in $\delta^{13}C_{DIC}$ values between the first local minimum (-9.04 ‰) and the first local maximum (-8.32 ‰) came about in only 8 hours, with an amplitude of 0.72 ‰, suggesting rapid responses to even small changes in the ventilation regime.

The strong negative correlation between $\delta^{13}C_{DIC}$ values and CO_2 concentrations is consistent with ventilation events that lead to decreased cave air CO_2 concentrations: As high CO_2 cave air is partly replaced by low CO_2 ambient air degassing of excess CO_2 from the dripwater is enhanced. As the process of degassing favours isotopically light CO_2 molecules, the $\delta^{13}C_{DIC}$ values in the dripwater are increased during these ventilation events. This interpretation also seems to be confirmed by the measured T variations: Although they are very small, the positive albeit moderate correlation with $\delta^{13}C_{DIC}$ suggests that, during ventilation, part of the cave air is replaced by relatively warm low CO_2 ambient air. During winter months, it would be replaced by relatively cold but still low CO_2 ambient air.

In order to characterize the changes in the dripwater $\delta^{13}C_{DIC}$ with respect to the cave air CO_2 concentration, the amplitude of the maxima/minima in $\delta^{13}C_{DIC}$ and CO_2 relative to their respective overall mean was determined, simply by subtracting each maximum/minimum from the mean. This yields a total of six maximum/minimum pairs that plot very well along a linear regression line (Figure 3.13). According to this regression, a change in cave air CO_2 concentration of about 435 ppmV produces a change in dripwater $\delta^{13}C_{DIC}$ of 1 ‰ that is then transferred to the $\delta^{13}C$ signal in the speleothem fed by this dripwater.

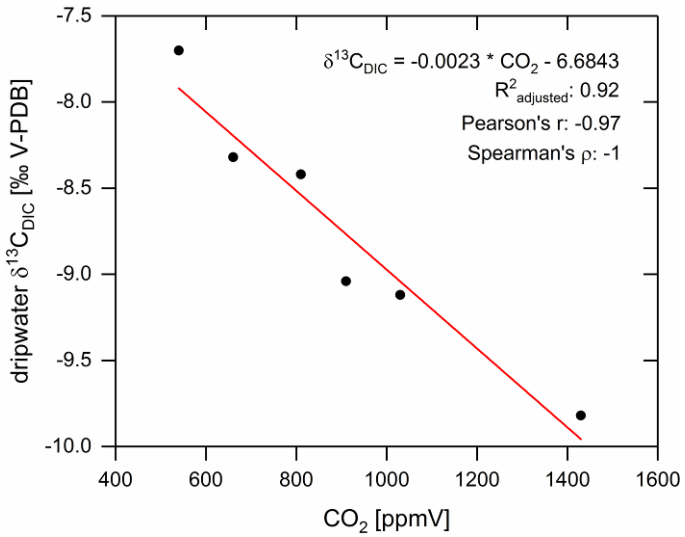

Figure 3.13: Relationship between cave air CO_2 concentrations and dripwater $\delta^{13}C_{DIC}$ quantified based on the six maxima/minima recorded during the case study (black circles). The relationship can be fitted very well with a linear regression (red line).

4 Comparison of Autosamplers

In comparison with Prototype 1.0, Protoype 2.0 features the following advantages:

1. Sample vials are absolutely gastight. This prevents any sample alteration through contamination, evaporation or gas exchange and makes Prototype 2.0 suited for studies involving the investigation of stable isotope systems such as carbon and oxygen isotopy in rain water and dripwater, common in speleothem science.

2. The design is more space-efficient: Prototype 2.0 can hold up to 160 sample vials without modification and up to 208 sample vials when sample vial density is maximised.

3. The design systemically allows for easily increasing the sample vial capacity.

4. The additional protetice casing enclosing the entire Prototype 2.0 autosampler is water-proof and heavy-duty. Prototype 2.0 is therefore better protected from any kind of mechanical (rocks, debris, water) and electronic damage such as short-circuits (water, vapour, humidity), which makes it better suited for application in harsh (outdoor) conditions. Interference with the sample collection by animal activity is also prevented.

5. The sampling interval can be customised by the operator between one minute and seven days. This allows for high-resolution sampling as well as long-term monitoring.

Prototype 2.0 also features some disadvantages with respect to Prototype 1.0:

1. The power consumption in hibernation mode is increased, being 16.5 mA compared to 5 mA in the case of Protoype 1.0. During active mode, power consumption amounts to 82.5 mA for both prototypes. Therefore, operating time is decreased to 100 days compared to 180 days for Protoype 1.0.

2. The technical complexity is increased decreasing the overall fail-safety as a result of more complex code, the implementation of the peristaltic pump that should not run dry and the more complex three-movements-design compared to the two-movements-design of Prototype 1.0. Therefore, both assembly and service/maintenance are more complex.

3. Construction costs are increased cost, with 1.200 € compared to 480 €

4. Overall volume is doubled, with 0.11 m^3 compared to 0.06 m^3

5. Sample volume is slightly decreased, with 12 mL compared to 20 mL, but is still sufficient for most analyses and applications

A comparison of the major characteristics of both prototypes is shown in Table 4.1.

Table 4.1: Comparison of Prototype 1.0 and Prototype 2.0.

Properties	**Prototype 1.0**	**Prototype 2.0**
sampling mode	passive	active
Movements	1 translation, 1 revolution	3 translations
gastight samples	no (but covered)	yes
sample frequency	1 day or 1 week	1 min to 168 h
estimated operating time	180 days	100 days
maximum number of samples vials	24 (72 sub-samples)	160 / 208
sample volume	5 mL and 20 mL	≤ 12 mL
weight	5 kg (+5.8 kg battery)	13 kg (+5.8 kg battery)
total outer dimensions	H: 33 cm; L: 44 cm; W: 40 cm	H: 31 cm; L: 67.5 cm; W: 53 cm
total volume	0.06 m³	0.11 m³
construction costs	480 €	1.200 €

Furthermore, it is important to compare the prototype autosamplers developed within the framework of this thesis with similar devices. To date, the only type of device similar to Prototype 2.0 already available on the market is the portable autosampler 3700C Compact (Teledyne ISCO, USA). While there are also other (bigger and heavier) models from Teledyne ISCO and similar devices offered by other companies, the 3700C Compact autosampler is representative of the technical state of the art. The comparison of the most relevant properties of these autosamplers is shown in Table 4.2 and includes other non-commercial autosamplers developed by members of the scientific community, such as the “OPEnSampler” (Nelke, Selker & Udell, 2017), the “Lisa Liquidsampler” (not published) developed by Lukas Neuhaus as well as the automated precipitation collector developed by Coplen et al. (2008).

As might be expected when comparing a prototype with a market-ready product it is evident that the Prototype 2.0 autosampler lacks specific features that enhance the end-user comfort, such as rinse cycles between samples, an automatic compensation for changes in hydraulic head and different modes of sampling pacing. Both the Prototype 2.0 and the 3700C Compact autosamplers are similar in weight and size. Almost a third of the weight of Prototype 2.0 is due to the Pb-acid battery used in the presented setup. The battery can be transported separately from the autosampler or can be replaced with lighter Li-Ion batteries to reduce weight. Most importantly, however, the Prototype 2.0 autosampler is capable of collecting gastight samples, while the 3700C Compact autosampler is incapable of doing so.

While the other liquid autosamplers also fulfill this important requirement, Prototype 2.0 features a considerably higher maximum number of sample vials. Thanks to a wide range of selectable sample frequencies and its capacity to operate for extended periods of time, the Prototype 2.0 autosampler is well-suited for long-term sampling projects where a large number of samples need to be collected.

As liquid autosamplers available on the market such as the 3700C Compact do feature neither gastight samples nor high numbers of sample vials, the Prototype 2.0 autosampler is less competing with existing autosamplers as much as it closes a market gap in long-term monitoring where samples definitely need to be gastight with respect to air/gas exchange to prevent sample alteration. Within this sector, the Prototype 2.0 autosampler offers many opportunities in various applications, as outlined in Section 5.

Table 4.2: Comparison of Prototype 2.0 with conventional autosamplers available on the market, represented here by the 3700C Compact from Teledyne ISCO (information retrieved from the manufacturer's website: www.teledyneisco.com) as well as other non-commercial autosamplers developed by members of the scientific community.

Properties	**Prototype 2.0**	**"3700C Compact"**	**"OPEnSampler"**	**"Lisa Liquidsampler"**	**"Coplen"**
gastight samples	yes	no	yes	yes	yes (covered by Teflon lid)
sample frequency	1 min to 168 h	1 min to 99 h 50 min	1 min to n.a.	1 h or 24 h	30 min or n.a.
estimated operating time (at a 2-day interval)	100 days	< 70 days	n.a.	100 days	n.a.
maximum number of samples vials	160 / 208	24	24	48	96
sample volume	≤ 12 mL	0.375 to 9.45 L	250 mL	20 to 60 mL	15 mL
weight (incl. battery; excluding samples)	13 kg (+5.8 kg battery)	11.3 kg	≥ 25 kg *	≥ 13 kg (case only) +	n.a.
weight (incl. battery and samples)	18.8 to 20.7 kg (depending on sample number)	15.8 to 23.3 kg (depending on sample size and number)	≥ 31 kg *	≥ 14 kg to 16 kg (case and samples; depending on sample size) +	≥ 1.4 kg (samples only)
total outer dimensions	H: 31 cm; L: 67.5 cm; W: 53 cm; V: 0.11 m³	H: 70.5 cm; ø: 45 cm; V: 0.14 m³	H: 51 cm; L: 109 cm; W: 53 cm; V: 0.29 m³ *	H: 59 cm; L: 80 cm; W: 60 cm; V: 0.28 m³ +	n.a.
rinse cycle(s) between samples	No	Yes, up to three	Yes	n.a.	No
liquid presence detector (automatic compensation for changes in hydraulic head)	No	Yes	No	No	No
different modes of sample pacing (e.g. time, flow)	No	Yes	No	No	No

* including the Pelican 80QT Elite Wheeled Cooler for better comparability
+ including the Zarges K470 Plus 40503 case for better comparability
n.a.: no information foun

5 Potential Applications and Outlook

The application Prototype 2.0 was specifically designed for are dripwater monitoring schemes in karst caves that are necessary especially, if not exclusively, in speleothem science (Ford & Williams, 2007; Fairchild & Baker, 2012). The case study presented in Section 3.4 illustrates well the potential of Prototype 2.0 for offering new research opportunities. As most cave sites are located far from researchers' offices and are often difficult to get to, there is a great need for automation in dripwater monitoring studies. The autosampler's application in high-frequency (short-interval) dripwater sampling will enable researchers to identify, resolve and quantify short-term variability in dripwater geochemistry and to better understand these complex cave systems – a prerequisite for reliable reconstructions of past climates and environments from speleothem proxies.

In addition to studies in the field of speleothem science focussing on karst cave dripwater, Prototype 2.0 can be applied in various other applications where sample alteration through contamination, evaporation or gas exchange pose a challenge that needs to be overcome.

One example of such an application is the investigation of the hydrological cycle based on isotopes in all sorts of water bodies, including rainwater. As mentioned in Section 1, for this purpose the IAEA supplies researchers with isotope data generated from monthly composite samples of rainwater collected at the ~ 1,000 GNIP stations worldwide. If these stations were supplemented with Prototype 2.0 autosamplers, much shorter sampling intervals would become possible which would enable researchers to investigate shorter-term variability in precipitation isotope systematics to improve the understanding of the underlying processes. To achieve this, sampling frequency needs to be at least high enough to resolve different precipitation events ("event-based" sampling). For instance, only by using such event-based data Celle-Jeanton et al. (2001) were able to demonstrate characteristic differences in the isotopic composition of rainwater in the Mediterranean coastal region of France the authors attributed to different types of synoptic weather systems. As the synoptic weather situation can change rather quickly, monthly rainwater isotope data would have most likely been of insufficient temporal resolution to identify this relationship between isotope composition and synoptics. Naturally, the increased number of samples generated by high-frequency sampling needs to be considered.

In addition, paraffin oil would not be required to prevent evaporation and increased maintenance of CRDS instruments could be avoided. The Prototype 2.0 autosampler could also be applied at the ~ 750 stations of the Global Network for Isotopes in Rivers (GNIR), also coordinated by the IAEA. Especially in very remote areas, the application of Prototype 2.0 samplers would be a cost-effective solution to supplement GNIP and/or GNIR stations and it might even facilitate the installation of new stations too remote for regular manual sample collection. In order to overcome the potential problem of particles suspended in the auto-sampled river water clogging

the tubing or, in particular, the double cannula of Prototype 2.0, the implementation of a mechanism to pre-extract particles from the auto-sampled river water before the actual sampling process would represent a useful future development. This could be achieved by a combination of sedimentation of coarser particles inside some sort of siphon-shaped ante-chamber and of filtration of finer particles in a chamber comprising multiple filter stages of decreasing pore size.

Due to the temporally discontinuous nature of rainfall automatic rainwater sampling requires 1) sample pre-collection for temporary storage of rainwater until a sufficient sample volume is available while minimising or even preventing evaporation and 2) a detector such as a photo sensor to end hibernation and trigger sample collection once a sufficient sample volume has been provided by rainfall. For the case studies in karst caves presented in this thesis a specifically designed pre-collection container ("pre-collector") with an internal volume of exactly 12 mL was applied (Figure 3.3, left). During dripwater pre-collection a 3D-printed floating body (Figure 3.3, right) inside the pre-collector would rise until it seals the pre-collector once it is completely filled with dripwater. Any dripwater in excess of 12 mL spills over through a small hole at the top of the pre-collector. It is important to note that, at its current setup, the Prototype 2.0 autosampler does not comprise a sample volume detector and is therefore not yet suited for rainwater sampling. As automatic rainwater sampling would be beneficial in numerous applications, such a detector certainly represents a useful future extension to the current Prototype 2.0 system.

Last but not least, thanks to its capacity of collecting samples in gastight vials, Prototype 2.0 is also applicable in all sorts of schemes where sample alteration is of concern. Examples are numerous and include cases of water being contaminated by toxic gases originating from anaerobic degradation of organics (e.g. CH_4 and H_2S) or by volatile organic compounds (VOCs), such as tetrachloroethene, benzene, MTBE or formaldehyde (e.g. Reemtsma and Jekel, 2010). In scenarios where non-volatile components like cations and anions need to be quantified, sample alteration through evaporation can also be prevented, that would otherwise cause erroneously augmented concentration values (Hiscock and Bense, 2014), especially in long-term monitoring schemes.

To conclude, thorough monitoring of water is important, not only in speleothem science and not only for scientific purposes but also to prevent adverse effects on human health and ecosystems, whether in the short, medium or long term. The two autosamplers developed within the framework of this thesis are an important contribution to achieving that goal.

6 References

Ahuja, Satinder (2013): *Monitoring water quality. Pollution assessment, analysis, and remediation.* Amsterdam, Boston: Elsevier. Accessible online: http://site.ebrary.com/lib/alltitles/docDetail.action?docID=10643948.

An, Zhisheng (Ed.) (2014): *Late Cenozoic Climate Change in Asia. Loess, Monsoon and Monsoon-arid Environment Evolution*. Dordrecht, s.l.: Springer Netherlands (Developments in Paleoenvironmental Research, 16). Accessible online: http://dx.doi.org/10.1007/978-94-007-7817-7.

Appelo, C. A. J.; Postma, Dieke (2005): *Geochemistry, groundwater and pollution*. 2nd edition. Boca Raton, London, New York: CRC Press Taylor & Francis Group.

Araguás-Araguás, Luis; Froehlich, Klaus; Rozanski, Kazimierz (1998): Stable isotope composition of precipitation over southeast Asia. In: *Journal of Geophyical Research* 103 (D22), pp. 28721–28742. DOI: 10.1029/98JD02582.

Arps, Jennifer (2017): *Towards ε-Precision of U-series Age Determinations of Secondary Carbonates*. Heidelberg University Library.

Ayalon, Avner; Bar-Matthews, Miryam; Kaufman, Aaron (1999): Petrography, strontium, barium and uranium concentrations, and strontium and uranium isotope ratios in speleothems as palaeoclimatic proxies: Soreq Cave, Israel. In: *The Holocene* 9 (6), S. 715–722. DOI: 10.1191/095968399673664163.

Ayliffe, Linda K.; Gagan, Michael K.; Zhao, Jian-xin; Drysdale, Russell N.; Hellstrom, John C.; Hantoro, Wahyoe S. et al. (2013): Rapid interhemispheric climate links via the Australasian monsoon during the last deglaciation. In: *Nature Communications* 4, p. 2908. DOI: 10.1038/ncomms3908.

Bahlburg, Heinrich; Breitkreuz, Christoph (2012): *Grundlagen der Geologie*. 4th edition. Berlin: Springer Spektrum.

Baker, Andy; Ito, Emi; Smart, Peter L.; McEwan, Reed F. (1997): Elevated and variable values of ^{13}C in speleothems in a British cave system. In: *Chemical Geology* 136 (3–4), S. 263–270. DOI: 10.1016/S0009-2541(96)00129-5.

Baker, Andy; Genty, Dominique; Dreybrodt, Wolfgang; Barnes, William; Mockler, Natalie J.; Grapes Jim (1998): Testing theoretically predicted stalagmite growth rate with Recent annually laminated samples: Implications for past stalagmite deposition. In: *Geochimica et Cosmochimica Acta* 62 (3), pp. 393–404.

Baker, Andy; Genty, Dominique; Fairchild, Ian J. (2000): Hydrological characterisation of stalagmite dripwaters at Grotte de Villars, Dordogne, by the analysis of inorganic species and luminescent organic matter. In: *Hydrology and Earth System Sciences Discussions* 4 (3), pp. 439–449.

Baker, Andy; Smith, Claire L.; Jex, Catherine; Fairchild, Ian J.; Genty, Dominique; Fuller, Lisa (2008): Annually laminated speleothems: a review. In: *International Journal of Speleology* 37 (3), p. 4.

Baldini, James U. L. (2002): Structure of the 8200-Year Cold Event Revealed by a Speleothem Trace Element Record. In: *Science* 296 (5576), pp. 2203–2206. DOI: 10.1126/science.1071776.

Banner, J. L.; Guilfoyle, A.; James, E. W.; Stern, L. A.; Musgrove, M. (2007): Seasonal Variations in Modern Speleothem Calcite Growth in Central Texas, U.S.A. In: *Journal of Sedimentary Research* 77 (8), pp. 615–622. DOI: 10.2110/jsr.2007.065.

Banner, Jay L.; Musgrove, MaryLynn; Asmerom, Yemane; Edwards, R. Lawrence; Hoff, John A. (1996): High-resolution temporal record of Holocene ground-water chemistry. Tracing links between climate and hydrology. In: *Geology* 24 (11), p. 1049. DOI: 10.1130/0091-7613(1996)024<1049:HRTROH>2.3.CO;2.

Bard, E.; Rostek, F.; Turon, J.-L.; Gendreau, S. (2000): Hydrological Impact of Heinrich Events in the Subtropical Northeast Atlantic. In: *Science* 289 (5483), pp. 1321–1324. DOI: 10.1126/science.289.5483.1321.

Barker, Stephen; Diz, Paula; Vautravers, Maryline J.; Pike, Jennifer; Knorr, Gregor; Hall, Ian R.; Broecker, Wallace S. (2009): Interhemispheric Atlantic seesaw response during the last deglaciation. In: *Nature* 457 (7233), pp. 1097–1102. DOI: 10.1038/nature07770.

Bar-Matthews, Miryam; Ayalon, Avner; Kaufman, Aaron; Wasserburg, Gerald J. (1999): The Eastern Mediterranean paleoclimate as a reflection of regional events: Soreq cave, Israel. In: *Earth and Planetary Science Letters* 166, pp. 85–95.

Berger, A.; Loutre, M. F. (1991): Insolation values for the climate of the last 10 million years. In: *Quaternary Science Reviews* 10 (4), pp. 297–317. DOI: 10.1016/0277-3791(91)90033-Q.

Berkelhammer, Max; Sinha, Ashish; Mudelsee, Manfred; Cheng, Hai; Edwards, R. Lawrence; Cannariato, Kevin (2010): Persistent multidecadal power of the Indian Summer Monsoon. In: *Earth and Planetary Science Letters* 290 (1-2), pp. 166–172. DOI: 10.1016/j.epsl.2009.12.017.

Bitz, C. M.; Chiang, J. C. H.; Cheng, W.; Barsugli, J. J. (2007): Rates of thermohaline recovery from freshwater pulses in modern, Last Glacial Maximum, and greenhouse warming climates. In: *Geophysical Research Letters*. 34 (7), p. 2382. DOI: 10.1029/2006GL029237.

Blume, Hans-Peter; Brümmer, Gerhard W.; Fleige, Heiner; Horn, Rainer; Kandeler, Ellen; Kögel-Knabner, Ingrid et al. (2016): Scheffer/SchachtschabelSoil Science. 1st edition, 2016. Berlin, Heidelberg, s.l.: Springer Berlin Heidelberg. Accessible online: http://dx.doi.org/10.1007/978-3-642-30942-7.

Bögli, A. (1960): Lakosung unde Karrenbilding. In: *Zeitschrift für Geomorphologie* (Suppl. 2), pp. 4–21.

Borsato, Andrea; Frisia, Silvia; Fairchild, Ian J.; Somogyi, Andrea; Susini, Jean (2007): Trace element distribution in annual stalagmite laminae mapped by micrometer-resolution X-ray fluorescence: Implications for incorporation of environmentally significant species. In: *Geochimica et Cosmochimica Acta* 71 (6), pp. 1494–1512. DOI: 10.1016/j.gca.2006.12.016.

Bourdon, B. (2003): Introduction to U-series Geochemistry. In: *Reviews in Mineralogy and Geochemistry* 52 (1), pp. 1–21. DOI: 10.2113/0520001.

Bowen, Gabriel J.; Wilkinson, Bruce (2002): Spatial distribution of $\delta^{18}O$ in meteoric precipitation. In: *Geology* 30 (4), pp. 315–318. DOI: 10.1130/0091-7613(2002)030 <0315:SDOOIM>2.0.CO;2.

Broccoli, Anthony J.; Dahl, Kristina A.; Stouffer, Ronald J. (2006): Response of the ITCZ to Northern Hemisphere cooling. In: *Geophysical Research Letters* 33 (1), DOI: 10.1029/2005GL024546.

Broecker, Wallace S. (1994): Massive iceberg discharges as triggers for global climate change. In: *Nature* 372 (6505), pp. 421–424. DOI: 10.1038/372421a0.

Broecker, Wallace S. (1998): Paleocean circulation during the Last Deglaciation. A bipolar seesaw? In: *Paleoceanography* 13 (2), pp. 119–121. DOI: 10.1029/97PA03707.

Broecker, Wallace S. (2010): The great ocean conveyor. Discovering the trigger for abrupt climate change. Princeton: Princeton University Press. Accessible online: http://www.jstor.org/stable/10.2307/j.ctt7pfgk.

Burns, Stephen J.; Fleitmann, Dominik; Matter, Albert; Neff, Ulrich; Mangini, Augusto (2001): Speleothem evidence from Oman for continental pluvial events during interglacial periods. In: Geology 29 (7), S. 623. DOI: 10.1130/0091-7613(2001)029<0623 :SEFOFC>2.0.CO;2.

Carvalho, Leila Maria Véspoli de; Jones, Charles (2016): *The Monsoons and Climate Change*. Cham: Springer International Publishing.

Cai, Y.; An, Z.; Cheng, H.; Edwards, R. L.; Kelly, M. J.; Liu, W. et al. (2006): High-resolution absolute-dated Indian Monsoon record between 53 and 36 ka from Xiaobailong Cave, southwestern China. In: *Geology* 34 (8), pp. 621–624. DOI: 10.1130/G22567.1.

Cai, Yanjun; Fung, Inez Y.; Edwards, R. Lawrence; An, Zhisheng; Cheng, Hai; Lee, Jung-Eun et al. (2015): Variability of stalagmite-inferred Indian monsoon precipitation over the past 252,000 y. In: *Proceedings of the National Academy of Sciences of the United States of America* 112 (10), pp. 2954–2959. DOI: 10.1073/pnas.1424035112.

Cai, Yanjun; Tan, Liangcheng; Cheng, Hai; An, Zhisheng; Edwards, R. Lawrence; Kelly, Megan J. et al. (2010): The variation of summer monsoon precipitation in central China since the last deglaciation. In: *Earth and Planetary Science Letters* 291 (1-4), pp. 21–31. DOI: 10.1016/j.epsl.2009.12.039.

Cai, Yanjun; Zhang, Haiwei; Cheng, Hai; An, Zhisheng; Lawrence Edwards, R.; Wang, Xianfeng et al. (2012): The Holocene Indian monsoon variability over the southern Tibetan Plateau and its teleconnections. In: *Earth and Planetary Science Letters* 335-336, pp. 135–144. DOI: 10.1016/j.epsl.2012.04.035.

Carolin, Stacy A.; Cobb, Kim M.; Adkins, Jess F.; Clark, Brian; Conroy, Jessica L.; Lejau, Syria et al. (2013): Varied response of western Pacific hydrology to climate forcings over the last glacial period. In: *Science* (New York, N.Y.) 340 (6140), pp. 1564–1566. DOI: 10.1126/science.1233797.

Celle-Jeanton, Hélène; Travi, Yves; Blavoux, Bernard (2001): Isotopic typology of the precipitation in the Western Mediterranean Region at three different time scales. In: *Geophysical Research Letters* 28 (7), pp. 1215–1218. DOI: 10.1029/2000GL012407.

Chapin, Thomas P. (2015): High-frequency, long-duration water sampling in acid mine drainage studies. A short review of current methods and recent advances in automated water samplers. In: *Applied Geochemistry* 59, pp. 118–124. DOI: 10.1016/j.apgeochem. 2015.04.004.

Chen, Fa-Hu; Chen, Jian-Hui; Holmes, Jonathan; Boomer, Ian; Austin, Patrick; Gates, John B. et al. (2010): Moisture changes over the last millennium in arid central Asia. A review, synthesis and comparison with monsoon region. In: Quaternary Science Reviews 29 (7-8), pp. 1055–1068. DOI: 10.1016/j.quascirev.2010.01.005.

Chen, Zhao; Auler, Augusto S.; Bakalowicz, Michel; Drew, David; Griger, Franziska; Hartmann, Jens et al. (2017): The World Karst Aquifer Mapping project. Concept, mapping procedure and map of Europe. In: *Hydrogeology Journal* 25 (3), pp. 771–785. DOI: 10.1007/s10040-016-1519-3.

Cheng, Hai.; Edwards, Lawrence R.; Wang, Yongjin; Kong, Xinggong; Ming, Yanfang; Kelly, Megan J.; Wang, Xianfeng; Gallup, Christina D.; Liu, Weiguo (2006): A penultimate glacial monsoon record from Hulu Cave and two-phase glacial terminations. In: *Geology* 34 (3), pp. 217–220. DOI: 10.1130/G22289.1.

Cheng, Hai.; Edwards, Lawrence R.; Hoff, John A.; Gallup, Christrina D.; Richards, David A.; Asmerom, Yemane (2000): The half-lives of uranium-234 and thorium-230. In: *Chemical Geology* 169 (1-2), pp. 17–33. DOI: 10.1016/S0009-2541(99)00157-6.

Cheng, Hai; Edwards, Lawrence R.; Sinha, Ashish; Spotl, Christoph; Yi, Liang; Chen, Shitao et al. (2016a): The Asian monsoon over the past 640,000 years and ice age terminations. In: *Nature* 534 (7609), pp. 640–646. DOI: 10.1038/nature18591.

Cheng, Hai; Sinha, Ashish; Wang, Xianfeng; Cruz, Francisco W.; Edwards, R. Lawrence (2012): The Global Paleomonsoon as seen through speleothem records from Asia and the Americas. In: *Climate Dynamics* 39 (5), pp. 1045–1062. DOI: 10.1007/s00382-012-1363-7.

Cheng, Hai; Spötl, Christoph; Breitenbach, Sebastian F. M.; Sinha, Ashish; Wassenburg, Jasper A.; Jochum, Klaus Peter et al. (2016b): Climate variations of Central Asia on orbital to millennial timescales. In: *Scientific reports* 5, pp. 36975. DOI: 10.1038/srep36975.

Chiang, John C. H.; Bitz, Cecilia M. (2005): Influence of high latitude ice cover on the marine Intertropical Convergence Zone. In: *Climate Dynamics* 25 (5), pp. 477–496. DOI: 10.1007/s00382-005-0040-5.

Clark, Ian D.; Fritz, Peter (1997): *Environmental isotopes in hydrogeology*. [2. print., corr.]. Boca Raton: Lewis Publ.

Clemens, Steven C.; Prell, Warren L.; Sun, Youbin (2010): Orbital-scale timing and mechanisms driving Late Pleistocene Indo-Asian summer monsoons. Reinterpreting cave speleothem δ18 O. In: *Paleoceanography* 25 (4), DOI: 10.1029/2010PA001926.

Coplen, Tyler B.; Neiman, Paul J.; White, Allen B.; Landwehr, Jurate M.; Ralph, F. Martin; Dettinger, Michael D. (2008): Extreme changes in stable hydrogen isotopes and precipitation characteristics in a landfalling Pacific storm. In: *Geophysical Research Letters* 35 (21), p. 1063. DOI: 10.1029/2008GL035481.

Craig, H. (1961): Isotopic Variations in Meteoric Waters. In: *Science* 133 (3465), pp. 1702–1703. DOI: 10.1126/science.133.3465.1702.

Criss, Robert E. (1999): Principles of stable isotope distribution. New York: Oxford University Press. Accessible online: http://site.ebrary.com/lib/alltitles/docDetail.action?docID=10329699.

Crowley, Thomas J. (1992): North Atlantic Deep Water cools the southern hemisphere. In: *Paleoceanography* 7 (4), pp. 489–497. DOI: 10.1029/92PA01058.

Cruz, Francisco W.; Karmann, Ivo; Viana, Oduvaldo; Burns, Stephen J.; Ferrari, José A.; Vuille, Mathias et al. (2005): Stable isotope study of cave percolation waters in subtropical Brazil. Implications for paleoclimate inferences from speleothems. In: *Chemical Geology* 220 (3-4), pp. 245–262. DOI: 10.1016/j.chemgeo.2005.04.001.

Dansgaard, Willi (1954): The O18-abundance in fresh water. In: *Geochimica et Cosmochimica Acta* 6 (5–6), pp. 241–260. DOI: 10.1016/0016-7037(54)90003-4.

Darling, George W.; Bath, Adrian H.; Gibson, John J.; Rozanski, Kazimierz (2006): Isotopes in water. In: M. Leng (Ed.): *Isotopes in Palaeoenvironmental Research*. Dordrecht, The Netherlands: Springer, pp. 1–66.

Day, Christopher C.; Henderson, Gideon M. (2013): Controls on trace-element partitioning in cave-analogue calcite. In: *Geochimica et Cosmochimica Acta* 120, pp. 612–627. DOI: 10.1016/j.gca.2013.05.044.

Dayem, Katherine E.; Molnar, Peter; Battisti, David S.; Roe, Gerard H. (2010): Lessons learned from oxygen isotopes in modern precipitation applied to interpretation of speleothem records of paleoclimate from eastern Asia. In: *Earth and Planetary Science Letters* 295 (1-2), pp. 219–230. DOI: 10.1016/j.epsl.2010.04.003.

Denton, George H.; Alley, Richard B.; Comer, Gary G..; Broecker, Wallace S. (2005): The role of seasonality in abrupt climate change. In: *Quaternary Science Reviews* 24 (10-11), pp. 1159–1182. DOI: 10.1016/j.quascirev.2004.12.002.

Denton, George H.; Anderson, Robert F.; Toggweiler, Robert J.; Edwards, Lawrence R.; Schaefer, Joerg M.; Putnam, Aaron E. (2010): The last glacial termination. In: *Science* (New York, N.Y.) 328 (5986), pp. 1652–1656. DOI: 10.1126/science.1184119.

Dickson, John A. D. (1993): Crystal Growth Diagrams as an Aid to Interpreting the Fabrics of Calcite Aggregates. In: *Journal of Sedimentary Petrology* 63 (1), pp. 1–17.

Ding, Yihui; Li, Chongyin; Liu, Yanju (2004): Overview of the South China sea monsoon experiment. In: *Advances in Atmospheric Sciences*. 21 (3), pp. 343–360. DOI: 10.1007/BF02915563.

Dong, Jinguo; Wang, Yongjin; Cheng, Hai; Hardt, Ben; Edwards, Lawrence R.; Kong, Xinggong et al. (2010): A high-resolution stalagmite record of the Holocene East Asian monsoon from Mt Shennongjia, central China. In: *The Holocene* 20 (2), pp. 257–264. DOI: 10.1177/0959683609350393.

Douville, Eric; Sallé, Eline; Frank, Norbert; Eisele, Markus; Pons-Branchu, Edwige; Ayrault, Sophie (2010): Rapid and accurate U–Th dating of ancient carbonates using inductively coupled plasma-quadrupole mass spectrometry. In: *Chemical Geology* 272 (1-4), pp. 1–11. DOI: 10.1016/j.chemgeo.2010.01.007.

Dykoski, Carolyn A.; Edwards, Lawrence R.; Cheng, Hai; Yuan, Daoxian; Cai, Yanjun; Zhang, Meiliang et al. (2005): A high-resolution, absolute-dated Holocene and deglacial Asian monsoon record from Dongge Cave, China. In: *Earth Planetary Science Letters* 233 (1-2), pp. 71–86. DOI: 10.1016/j.epsl.2005.01.036.

Ender, Anna; Goeppert, Nadine; Goldscheider, Nico (2018): Spatial resolution of transport parameters in a subtropical karst conduit system during dry and wet seasons. In: *Hydrogeology Journal* 26 (7), pp. 2241–2255. DOI: 10.1007/s10040-018-1746-x.

EPICA Community Members (2006): One-to-one coupling of glacial climate variability in Greenland and Antarctica. In: *Nature* 444 (7116), pp. 195–198. DOI: 10.1038/nature05301.

Fairchild, Ian J.; Baker, Andy; Borsato, Andrea; Frisia, Silvia; Hinton, Richard W.; McDermott, Frank; Tooth, Anna F. (2001): Annual to sub-annual resolution of multiple trace-element trends in speleothems. In: *Journal of the Geological Society* 158 (5), pp. 831–841. DOI: 10.1144/jgs.158.5.831.

Fairchild, Ian. J.; Frisia, Silvia.; Borsato, Andrea; Tooth, Anna (2007): Speleothems in their geomorphic, hydrological and climatological context. In: David J. Nash und Sue J. MacLaren (Eds.): *Geochemical sediments and landscapes*. 1st. Malden, Mass.: Blackwell (RGS-IBG book-series), pp. 200–245.

Fairchild, Ian; McMillan, Emily (2007): Speleothems as indicators of wet and dry periods. In: *International Journal of Speleology* 36 (2), pp. 69–74. DOI: 10.5038/1827-806X.36.2.2.

Fairchild, Ian J.; Baker, Andy (2012): *Speleothem Science. From Process to Past Environments*. 1st edition. s.l.: Wiley-Blackwell (Blackwell Quaternary Geoscience Series, v.3. Accessible online: http://dx.doi.org/10.1002/9781444361094.

Fairchild, Ian J.; Borsato, Andrea; Tooth, Anna F.; Frisia, Silvia; Hawkesworth, Christopher J.; Huang, Yiming et al. (2000): Controls on trace element (Sr–Mg) compositions of carbonate cave waters: implications for speleothem climatic records. In: *Chemical Geology* 166 (3–4), pp. 255–269. DOI: 10.1016/S0009-2541(99)00216-8.

Fairchild, Ian J.; Smith, Claire L.; Baker, Andy; Fuller, Lisa; Spötl, Christoph; Mattey, Dave et al. (2006): Modification and preservation of environmental signals in speleothems. In: *Earth-Science Reviews* 75 (1–4), pp. 105–153. DOI: 10.1016/j.earscirev.2005.08.003.

Fairchild, Ian J.; Treble, Pauline C. (2009): Trace elements in speleothems as recorders of environmental change. In: *Quaternary Science Reviews* 28 (5-6), pp. 449–468. DOI: 10.1016/j.quascirev.2008.11.007.

Fedorov; Philander (2000): Is El Nino changing? In: Science (New York, N.Y.) 288 (5473), S. 1997–2002.

Fleitmann, Dominik (2003): Holocene Forcing of the Indian Monsoon Recorded in a Stalagmite from Southern Oman. In: *Science* 300 (5626), pp. 1737–1739. DOI: 10.1126/ science.1083130.

Fleitmann, Dominik; Burns, Stephen J.; Mangini, Augusto; Mudelsee, Manfred; Kramers, Jan; Villa, Igor et al. (2007): Holocene ITCZ and Indian monsoon dynamics recorded in stalagmites from Oman and Yemen (Socotra). In: *Quaternary Science Reviews* 26 (1-2), pp. 170–188. DOI: 10.1016/j.quascirev.2006.04.012.

Fleitmann, Dominik; Burns, Stephen J.; Neff, Ulrich; Mudelsee, Manfred; Mangini, Augusto; Matter, Albert (2004): Palaeoclimatic interpretation of high-resolution oxygen isotope profiles derived from annually laminated speleothems from Southern Oman. In: *Quaternary Science Reviews* 23 (7-8), pp. 935–945. DOI: 10.1016/j.quascirev.2003.06.019.

Ford, Derek C.; Williams, Paul W. (2007): *Karst hydrogeology and geomorphology*. [Rev. ed.]. Chichester, England, Hoboken, NJ: John Wiley & Sons. Accessible online: http://site.ebrary.com/lib/alltitles/docDetail.action?docID=10295774.

Fricke, Henry C.; O'Neil, James R. (1999): The correlation between $^{18}O/^{16}O$ ratios of meteoric water and surface temperature: its use in investigating terrestrial climate change over geologic time. In: *Earth and Planetary Science Letters* 170 (3), pp. 181–196. DOI: 10.1016/S0012-821X(99)00105-3.

Friedman, Irving; O'Neil, J. R. (1977): Compilation of stable isotope fractionation factors of geochemical interest. In: *Professional Paper* (440-KK). Accessible online: https://pubs.usgs.gov/pp/0440kk/report.pdf.

Frisia, Silvia (2015): Microstratigraphic logging of calcite fabricsin speleothems as tool for palaeoclimate studies. In: *International Journal of Speleology* 44 (1), pp. 1–16. DOI: 10.5038/1827-806X.44.1.1.

Frisia, Silvia; Borsato, Andrea; Fairchild, Ian J.; McDermott, Frank; Selmo, Enrico M. (2002): Aragonite-calcite relationships in speleothems (Grotte de Clamouse, France): environment, fabrics, and carbonate geochemistry. In: *Journal of Sedimentary Research* 72 (5), pp. 687–699.

Frumkin, Amos; Stein, Mordechai (2004): The Sahara–East Mediterranean dust and climate connection revealed by strontium and uranium isotopes in a Jerusalem speleothem. In: *Earth and Planetary Science Letters* 217 (3-4), pp. 451–464. DOI: 10.1016/S0012-821X(03)00589-2.

Gabitov, Rinat I.; Watson, Edward B. (2006): Partitioning of strontium between calcite and fluid. In: *Geochemistry Geophysics Geosystems* 7 (11), DOI: 10.1029/2005GC001216.

Gat, Joel R. (1996): Oxygen and hydrogen isotopes in the hydrologic cycle. In: *Annual Reviews in Earth Planetary Sciences* 24 (1), pp. 225–262. DOI: 10.1146/annurev.earth.24.1.225.

Genty, Dominique; Baker, Andy; Massault, Marc; Proctor, Chris; Gilmour, Mabs A.; Pons-Branchu, Edwige; Hameln, Bruno (2001): Dead carbon in stalagmites: Carbonate bedrock paleodissolution vs. ageing of soil organic matter. Implications for ^{13}C variations in speleothems. In: *Geochimica et Cosmochimica Acta* 65 (20), pp. 3443–3457.

Gillieson, David S. (1998): *Caves. Processes, development and management*. Reprinted. Oxford: Blackwell Publ (The natural environment).

Goede, Albert; McCulloch, Malcolm; McDermott, Frank; Hawkesworth, Chris (1998): Aeolian contribution to strontium and strontium isotope variations in a Tasmanian speleothem. In: *Chemical Geology* 149 (1-2), pp. 37–50. DOI: 10.1016/S0009-2541(98)00035-7.

Goldstein, S. J. (2003): Techniques for Measuring Uranium-series Nuclides. 1992-2002. In: *Reviews in Mineralogy and Geochemistry* 52 (1), pp. 23–57. DOI: 10.2113/0520023.

Gonfiantini, Roberto; Roche, Michel-Alain; Olivry, Jean-Claude; Fontes, Jean-Charles; Zuppi, Gian Maria (2001): The altitude effect on the isotopic composition of tropical rains. In: *Chemical Geology* 181 (1-4), pp. 147–167. DOI: 10.1016/S0009-2541(01)00279-0.

Griffiths, Michael L.; Drysdale, Russel N.; Gagan, Michael K.; Frisia, Silvia; Zhao, Jian-xin.; Ayliffe, Linda. K. et al. (2010): Evidence for Holocene changes in Australian–Indonesian monsoon rainfall from stalagmite trace element and stable isotope ratios. In: *Earth and Planetary Science Letters* 292 (1-2), pp. 27–38. DOI: 10.1016/j.epsl.2010.01.002.

Grootes, Pieter M.; Stuiver, Minze (1997): Oxygen 18/16 variability in Greenland snow and ice with 10 −3 - to 10 5 -year time resolution. In: Journal of Geophysical Research 102 (C12), pp. 26455–26470. DOI: 10.1029/97JC00880.

Grubbs, Frank E. (1969): Procedures for Detecting Outlying Observations in Samples. In: *Technometrics* 11 (1), p. 1. DOI: 10.2307/1266761.

Gupta, Anil K.; Anderson, David M.; Overpeck, Jonathan T. (2003): Abrupt changes in the Asian southwest monsoon during the Holocene and their links to the North Atlantic Ocean. In: *Nature* 421 (6921), pp. 354–357. DOI: 10.1038/nature01340.

Gupta, Anil K.; Das, Moumita; Anderson, David M. (2005): Solar influence on the Indian summer monsoon during the Holocene. In: *Geophysical Research Letters* 32 (17), p. 483. DOI: 10.1029/2005GL022685.

Häckel, Hans (2016): *Meteorologie*. 8th edition. Stuttgart: Verlag Eugen Ulmer (UTB Geowissenschaften, Ökologie, Agrar- und Forstwissenschaften, Band 1338). Accessible online: http://www.utb-studi-e-book.de/9783838546032.

Hartmann, Arno; Luetscher, Marc; Wachter, Ralf; Holz, Philipp; Eiche, Elisabeth; Neumann, Thomas (2018): Technical note. GUARD – an automated fluid sampler preventing sample alteration by contamination, evaporation and gas exchange, suitable for remote areas and harsh conditions. In: *Hydrology and Earth System Sciences* 22 (8), pp. 4281–4293. DOI: 10.5194/hess-22-4281-2018.

Hartmann, Arno; Wachter, Ralf (2018a): GUARD autosampler - Assembly instructions. DOI: 10.5445/IR/1000085058.

Hartmann, Arno; Wachter, Ralf (2018b): GUARD autosampler - Print-outs. DOI: 10.5445/IR/1000085059.

Haug, Gerald H.; Hughen, Konrad A.; Sigman, Daniel M.; Peterson, Larry C.; Röhl, Ursula (2001): Southward migration of the intertropical convergence zone through the Holocene. In: *Science* (New York, N.Y.) 293 (5533), pp. 1304–1308. DOI: 10.1126/science.1059725.

Hellstrom, John C. (2006): U–Th dating of speleothems with high initial 230Th using stratigraphical constraint. In: *Quaternary Geochronology* 1 (4), pp. 289–295. DOI: 10.1016/j.quageo.2007.01.004.

Hellstrom, John; Pickering, Robyn (2015): Recent advances and future prospects of the U–Th and U–Pb chronometers applicable to archaeology. In: *Journal of Archaeological Science* 56, pp. 32–40. DOI: 10.1016/j.jas.2015.02.032.

Hemming, Sidney R. (2004): Heinrich events. Massive late Pleistocene detritus layers of the North Atlantic and their global climate imprint. In: *Reviews in Geophysics* 42 (1). DOI: 10.1029/2003RG000128.

Hendl, Manfred; Marcinek, Joachim; Jäger, Eckehart Johannes (1988): *Allgemeine Klima-, Hydro- und Vegetationsgeographie*. With 49 Tables. 3rd edition. Gotha: Haack (Studienbücherei Geographie für Lehrer, 5).

Hendy, Christie H. (1971): The isotopic geochemistry of speleothems—I. The calculation of the effects of different modes of formation on the isotopic composition of speleothems and their applicability as palaeoclimatic indicators. In: *Geochimica et Cosmochimica Acta* 35 (8), pp. 801–824. DOI: 10.1016/0016-7037(71)90127-X.

Heyer, Ernst; Chmielewski, Frank-Michael (1998): *Witterung und Klima. Eine Einführung in die Meteorologie und Klimatologie*. 10th edition. Peter Hupfer (Ed.). Stuttgart u.a.: Teubner.

Hill, Carol A.; Forti, Paolo (Hg.) (1997): *Cave Minerals of the World*. Huntsville, Alabama: National Speleological Society.

Hiscock, Kevin M.; Bense, Victor F. (2014): *Hydrogeology. Principles and practice*. 2nd edition Chichester: Wiley. Accessible online: http://search.ebscohost.com/ login.aspx?direct=true&scope=site&db=nlebk&db=nlabk&AN=759050.

Hoefs, Jochen (2015): *Stable isotope geochemistry*. 7th edition. Cham: Springer (Earth Sciences).

Holland, Heinrich D.; Kirsipu, Theodore V.; Huebner, J. Stephen; Oxburgh, Ursula M. (1964): On Some Aspects of the Chemical Evolution of Cave Waters. In: *The Journal of Geology* 72 (1), pp. 36–67. DOI: 10.1086/626964.

Hong, Yetang T.; Hong, Bing; Lin, Qiang H.; Zhu, Yuexiang X.; Shibata, Yasuyuki; Hirota, Masashi et al. (2003): Correlation between Indian Ocean summer monsoon and North Atlantic climate during the Holocene. In: *Earth and Planetary Science Letters* 211 (3-4), pp. 371–380. DOI: 10.1016/S0012-821X(03)00207-3.

Hu, Chaoyong; Henderson, Gideon M.; Huang, Junhua; Xie, Shucheng; Sun, Ying; Johnson, Kathleen R. (2008): Quantification of Holocene Asian monsoon rainfall from spatially separated cave records. In: *Earth and Planetary Science Letters* 266 (3-4), pp. 221–232. DOI: 10.1016/j.epsl.2007.10.015.

Huang, Yiming; Fairchild, Ian J. (2001): Partitioning of Sr2+ and Mg2+ into calcite under karst-analogue experimental conditions. In: *Geochimica et Cosmochimica Acta* 65 (1), pp. 47–62. DOI: 10.1016/S0016-7037(00)00513-5.

IAEA/WMO (1994): IAEA/WMO (1994): *Global Network for Isotopes in Precipitation (GNIP) Database*, IGBP PAGES/World Data Center-A for Paleoclimatology Data Contribution Series # 94-005, OAA/NGDC Paleoclimatology Program, Boulder CO, USA.

Ivanovich, M.; Harmon, Russel S. (Eds.) (1992): *Uranium Series Disequilibrium. Applications to Earth, Marine and Environmental Sciences*. Revised edition.

Jiang, Xiuyang; He, YaoQi; Shen, ChuanChou; Kong, Xinggong; Li, ZhiZhong; Chang, YuWei (2012): Stalagmite-inferred Holocene precipitation in northern Guizhou Province, China, and asynchronous termination of the Climatic Optimum in the Asian monsoon territory. In: *Chinese Sciences Bulletin* 57 (7), pp. 795–801. DOI: 10.1007/s11434-011-4848-6.

Jin, Liya; Chen, Fahu; Ganopolski, Andrey; Claussen, Martin (2007): Response of East Asian climate to Dansgaard/Oeschger and Heinrich events in a coupled model of intermediate complexity. In: *Journal of Geophysical Research* 112 (D6), pp. 190. DOI: 10.1029/2006JD007316.

Jochum, Klaus P.; Scholz, Denis; Stoll, Brigitte; Weis, Ulrike; Wilson, Stephen A.; Yang, Qichao et al. (2012): Accurate trace element analysis of speleothems and biogenic calcium carbonates by LA-ICP-MS. In: *Chemical Geology* 318, pp. 31–44.

Jochum, Klaus P.; Nohl, Uwe; Herwig, Kirstin; Lammel, Esin; Stoll, Brigitte; Hofmann, Albrecht W. (2005): GeoReM. A New Geochemical Database for Reference Materials and Isotopic Standards. In: *Geostandards and Geoanalytical Research* 29 (3), pp. 333–338. DOI: 10.1111/j.1751-908X.2005.tb00904.x.

Johnson, Kathleen R.; Hu, Chaoyong; Belshaw, Nick S.; Henderson, Gideon M. (2006): Seasonal trace-element and stable-isotope variations in a Chinese speleothem: The potential for high-resolution paleomonsoon reconstruction. In: *Earth Planetary Science Letters* 244 (1-2), pp. 394–407. DOI: 10.1016/j.epsl.2006.01.064.

Johnson, Kathleen R. (2011): Palaeoclimate. Long-distance relationship. In: Nature Geoscience 4 (7), pp. 426–427. DOI: 10.1038/ngeo1190.

Johnson, Kathleen R.; Ingram, Lynn B. (2004): Spatial and temporal variability in the stable isotope systematics of modern precipitation in China. Implications for paleoclimate reconstructions. In: *Earth and Planetary Science Letters* 220 (3-4), pp. 365–377. DOI: 10.1016/S0012-821X(04)00036-6.

Jones, Ian C.; Banner, Jay L.; Humphrey, John D. (2000): Estimating recharge in a tropical karst aquifer. In: *Water Resources Research* 36 (5), pp. 1289–1299.

Kalnay, Eugenia.; Kanamitsu, Masao; Kistler, Robert; Collins, William; Deaven, Dennis; Gandin, Lev et al. (1996): The NCEP/NCAR 40-Year Reanalysis Project. In: *Bulletin of the American Meteorological Society* 77 (3), pp. 437–471. DOI: 10.1175/1520-0477(1996)077<0437:TNYRP>2.0.CO;2.

Karmann, Ivo; Cruz, Francisco W.; Viana, Oduvaldo; Burns, Stephen J. (2007): Climate influence on geochemistry parameters of waters from Santana–Pérolas cave system, Brazil. In: *Chemical Geology* 244 (1-2), pp. 232–247. DOI: 10.1016/j.chemgeo.2007.06.029.

Ke, Liao; Institute of Geography of Chinese Academy of Sciences, National Bureau of Surveying (1999): *The national physical atlas of China*. Beijing, China: China Cartographic Publishing House.

Klose, Brigitte (2016): *Meteorologie. Eine interdisziplinäre Einführung in die Physik der Atmosphäre*. 3rd edition. Berlin Heidelberg: Springer Berlin Heidelberg; Imprint: Springer Spektrum (Springer-Lehrbuch). Accessible online: http://dx.doi.org/10.1007/978-3-662-43622-6.

Koster, Randal D.; Valpine, D. Perry de; Jouzel, Jean (1993): Continental water recycling and H 218 O concentrations. In: *Geophysical Research Letters* 20 (20), pp. 2215–2218. DOI: 10.1029/93GL01781.

Kutzbach, John E. (1981): Monsoon Climate of the Early Holocene. Climate Experiment with the Earth's Orbital Parameters for 9000 Years Ago. In: *Science* (New York, N.Y.) 214 (4516), pp. 59–61. DOI: 10.1126/science.214.4516.59.

Lachniet, Matthew S. (2009): Climatic and environmental controls on speleothem oxygen-isotope values. In: *Quaternary Science Reviews* 28 (5-6), pp. 412–432. DOI: 10.1016/j.quascirev.2008.10.021.

Lachniet, Matthew S.; Patterson, William P. (2006): Use of correlation and stepwise regression to evaluate physical controls on the stable isotope values of Panamanian rain and surface waters. In: *Journal of Hydrology* 324 (1-4), pp. 115–140. DOI: 10.1016/j.jhydrol.2005.09.018.

Le Quéré, C.; Moriarty, R.; Andrew, R. M.; Canadell, J. G.; Sitch, S.; Korsbakken, J. I. et al. (2015): Global Carbon Budget 2015. In: *Earth System Science Data* 7 (2), pp. 349–396. DOI: 10.5194/essd-7-349-2015.

LeGrande, Allegra N.; Schmidt, Gavin A. (2009): Sources of Holocene variability of oxygen isotopes in paleoclimate archives. In: *Climate of the Past* 5 (3), pp. 441–455. DOI: 10.5194/cp-5-441-2009.

LeGrande, Allegra N.; Schmidt, Gavin A. (2006): Global gridded data set of the oxygen isotopic composition in seawater. In: *Geophysical Research Letters* 33 (12). DOI: 10.1029/2006GL026011.

Leibundgut, Christian; Maloszewski, Piotr; Klls, Christoph (2009): *Tracers in Hydrology*. Chichester, UK: John Wiley & Sons, Ltd.

Li, Bin; Yuan, Daoxian; Qin, Jiaming; Lin, Yushi; Zhang, Meiliang (2000): Oxygen and carbon isotopic characteristics of rainwater, drip water and present speleothems in a cave in Guilin area, and their environmental meanings. In: *Sciene in China Series D-Earth Sciences* 43 (3), pp. 277–285. DOI: 10.1007/BF02906823.

Li, Hong-Chun; Ku, Teh-Lung; You, Chen-Feng; Cheng, Hai; Edwards, R. Lawrence; Ma, Zhi-Bang et al. (2005): $^{87}Sr/^{86}Sr$ and Sr/Ca in speleothems for paleoclimate reconstruction in Central China between 70 and 280 kyr ago. In: *Geochimica et Cosmochimica Acta* 69 (16), pp. 3933–3947. DOI: 10.1016/j.gca.2005.01.009.

Liljequist, Gösta H.; Cehak, Konrad (1994): *Allgemeine Meteorologie*. With 24 Tables. 3rd edition. Braunschweig: Vieweg.

Liu, JianBao; Chen, JianHui; Zhang, Xiaojian; Li, Yu; Rao, Zhiguo; Chen, Fahu (2015): Holocene East Asian summer monsoon records in northern China and their inconsistency with Chinese stalagmite $\delta^{18}O$ records. In: *Earth-Science Reviews* 148, pp. 194–208. DOI: 10.1016/j.earscirev.2015.06.004.

Liu, Zhengyu; Wen, Xinyu; Brady, E. C.; Otto-Bliesner, B.; Yu, Ge; Lu, Huayu et al. (2014): Chinese cave records and the East Asia Summer Monsoon. In: *Quaternary Science Reviews* 83, pp. 115–128. DOI: 10.1016/j.quascirev.2013.10.021.

Lorens, Robert B. (1981): Sr, Cd, Mn and Co distribution coefficients in calcite as a function of calcite precipitation rate. In: *Geochimica et Cosmochimica Acta* 45 (4), pp. 553–561. DOI: 10.1016/0016-7037(81)90188-5.

Luetscher, Marc; Ziegler, Felix (2012): CORA - a dedicated device for carbon dioxide monitoring in cave environments. In: *International Journal of Speleology* 41 (2), pp. 273–281. DOI: 10.5038/1827-806X.41.2.13.

Manabe, Syukuro; Broccoli, Anthony J. (1990): Mountains and arid climates of middle latitudes. In: *Science* (New York, N.Y.) 247 (4939), pp. 192–195. DOI: 10.1126/science.247.4939.192.

Masschelein, Jan; Coessens Vincent; Lagrou, David; Dusar, Michiel; Van, Tan, T. (2007): Northern Vietnam, 1993 - 2006 (Belgian-Vietnamese speleological projects in the provinces of Bac Kan, Ha Giang, Hoa Binh, Lai Chau and Son La): *Berliner Höhlenkundliche Berichte* 22, 212 p.

Mattey, Dave; Collister, Chris (2008): Acoustic Drip Counters for Environmental Monitoring. In: *Cave Radio & Electronics Group, Journal* 70, pp. 14–17.

Mattey, David P.; Fairchild, Ian J.; Atkinson, Tim C.; Latin, Jean-Paul; Ainsworth, Mark; Durell, Richard (2010): Seasonal microclimate control of calcite fabrics, stable isotopes and trace elements in modern speleothem from St Michaels Cave, Gibraltar. In: *Geological Society, London, Special Publications* 336 (1), pp. 323–344. DOI: 10.1144/SP336.17.

McDermott, Frank (2004): Palaeo-climate reconstruction from stable isotope variations in speleothems. A review. In: *Quaternary Science Reviews* 23 (7-8), pp. 901–918. DOI: 10.1016/j.quascirev.2003.06.021.

McDermott, Frank; Schwarcz, Henry; Rowe, Peter (2006): Isotopes in speleothems. In: M. Leng (Hg.): *Isotopes in Palaeoenvironmental Research*. Dordrecht, The Netherlands: Springer, pp. 185–226.

McDonald, Janece (2004): The 2002–2003 El Niño recorded in Australian cave drip waters. Implications for reconstructing rainfall histories using stalagmites. In: *Geophysical Research Letters* 31 (22). DOI: 10.1029/2004GL020859.

McManus, Jerry F.; Francois, Roger; Gherardi, Jeanne-Marie; Keigwin, Lloyd D.; Brown-Leger, Susan (2004): Collapse and rapid resumption of Atlantic meridional circulation

linked to deglacial climate changes. In: *Nature* 428 (6985), pp. 834–837. DOI: 10.1038/nature02494.

Mohtadi, Mahyar; Oppo, Delia W.; Steinke, Stephan; Stuut, Jan-Berend W.; Pol-Holz, Ricardo de; Hebbeln, Dierk; Lückge, Andreas (2011): Glacial to Holocene swings of the Australian–Indonesian monsoon. In: *Nature Geoscience* 4 (8), pp. 540–544. DOI: 10.1038/ngeo1209.

Morse, John W.; Bender, Michael L. (1990): Partition coefficients in calcite: Examination of factors influencing the validity of experimental results and their application to natural systems. In: *Chemical Geology* 82, pp. 265–277. DOI: 10.1016/0009-2541(90)90085-L.

Mortimer, Charles E.; Müller, Ulrich; Beck, Johannes (2015): *Chemie. Das Basiswissen der Chemie*. 12th edition. Stuttgart: Thieme. Accessible online: http://dx.doi.org/10.1055/b-003-125838.

Muller, Joanne; McManus, Jerry F.; Oppo, Delia W.; Francois, Roger (2012): Strengthening of the Northeast Monsoon over the Flores Sea, Indonesia, at the time of Heinrich event 1. In: *Geology* 40 (7), pp. 635–638. DOI: 10.1130/G32878.1.

Musgrove, MaryLynn; Banner, Jay L. (2004): Controls on the spatial and temporal variability of vadose dripwater geochemistry. Edwards aquifer, central Texas. In: *Geochimica et Cosmochimica Acta* 68 (5), pp. 1007–1020. DOI: 10.1016/j.gca.2003.08.014.

Neff, Ulrich; Burns, Stephen J.; Mangini, Augusto; Mudelsee, Manfred; Fleitmann, Dominik; Matter, Albert (2001): Strong coherence between solar variability and the monsoon in Oman between 9 and 6 kyr ago. In: *Nature* 411 (6835), pp. 290–293. DOI: 10.1038/35077048.

Nelke, Mitch; Udell, Chet; Selker, John: *The OPEnSampler: A Low-Cost, Low-Weight, Customizable and Modular Open Source 24-Unit Automatic Water Sampler*. Abstract H41J-1596 presented at 2017 Fall Meeting, AGU, New Orleans, LA, 11–15 December 2017.

NOAA, National Weather Service, Climate Prediction Center (2017): Oceanic Niño Index (ONI) [3 month running mean of ERSST.v5 SST anomalies in the Niño 3.4 region (5°N-5°S, 120°-170°W)], based on centered 30-year base periods updated every 5 years. Accessible online: http://origin.cpc.ncep.noaa.gov/products/analysis_monitoring/ ensostuff/ONI_v5.php.

Oomori, Tamotsu; Kaneshima, Hiroshi; Maezato, Yoko (1987): Distribution coefficent of Mg^{2+} ions between calcite and solution at 10-50°C. In: *Marine Chemistry* (20), pp. 327–336.

Otto-Bliesner, Bette L.; Brady, Esther C.; Clauzet, Gabriel; Tomas, Robert; Levis, Samuel; Kothavala, Zav (2006): Last Glacial Maximum and Holocene Climate in CCSM3. In: *Journal of Climate* 19 (11), pp. 2526–2544. DOI: 10.1175/JCLI3748.1.

Partin, Judson W.; Cobb, Kim M.; Adkins, Jess F.; Clark, Brian; Fernandez, Diego P. (2007): Millennial-scale trends in west Pacific warm pool hydrology since the Last Glacial Maximum. In: *Nature* 449 (7161), pp. 452–455. DOI: 10.1038/nature06164.

Pausata, Francesco S. R.; Battisti, David S.; Nisancioglu, Kerim H.; Bitz, Cecilia M. (2011): Chinese stalagmite δ 18 O controlled by changes in the indian monsoon during a simulated heinrich event. In: *Nature Geoscience* 4 (7), pp. 474–480. DOI: 10.1038/ngeo1169.

Pedelarborde, P. (1958): *Les moussons*. Paris: Collection Armand Colin.

Poage, M. A.; Chamberlain, C. Page (2001): Empirical relationships between elevation and the stable isotope composition of precipitation and surface waters. Considerations for stud-

ies of paleoelevation change. In: *American Journal of Science* 301 (1), pp. 1–15. DOI: 10.2475/ajs.301.1.1.

Porter, Stephen C.; Zhisheng, An (1995): Correlation between climate events in the North Atlantic and China during the last glaciation. In: *Nature* 375 (6529), pp. 305–308. DOI: 10.1038/375305a0.

R Core Team (2013): R: A language and environment for statistical computing. Vienna, Austria: R Foundation for Statistical Computing. Accessible online: http://www.R-project.org/.

Rasmussen, Olander S; Seierstad, Inger K.; Andersen, Katrine K.; Bigler, M.; Dahl-Jensen, Dorthe; Johnsen, S. J. (2008): Synchronization of the NGRIP, GRIP, and GISP2 ice cores across MIS 2 and palaeoclimatic implications. In: *Quaternary Science Reviews* 27 (1-2), pp. 18–28. DOI: 10.1016/j.quascirev.2007.01.016.

Richards, David A.; Dorale, Jeffrey A. (2003): Uranium-series Chronology and Environmental Applications of Speleothems. In: *Reviews in Mineralogy and Geochemistry* 52 (1), pp. 407–460. DOI: 10.2113/0520407.

Riechelmann, Dana F. C.; Fohlmeister, Jens; Tjallingii, Rik; Jochum, Klaus P.; Richter, Detlev K.; Brummer, Geert-Jan A.; Scholz, Denis (2016): Detection and origin of different types of annual laminae in recent stalagmites from Zoolithencave, southern Germany. Evaluation of the potential for quantitative reconstruction of past precipitation variability. In: *Climate of the Past Discussions*, pp. 1–42. DOI: 10.5194/cp-2016-18.

Rimstidt, Donald J.; Balog, Anna; Webb, John (1998): Distribution of trace elements between carbonate minerals and aqueous solutions. In: *Geochimica et Cosmochimica Acta* 62 (11), pp. 1851–1863. DOI: 10.1016/S0016-7037(98)00125-2.

Rind, D.; Russell, Gary; Schmidt, Gavin; Sheth, S.; Collins, Dan; deMenocal, Peter; Teller, J. (2001): Effects of glacial meltwater in the GISS coupled atmosphere-ocean model. 2. A bipolar seesaw in Atlantic Deep Water production. In: *Journal of Geophysical Research* 106 (D21), pp. 27355–27365. DOI: 10.1029/2001JD000954.

Risi, Camille; Bony, Sandrine; Vimeux, Françoise (2008): Influence of convective processes on the isotopic composition (δ^{18} O and δ D) of precipitation and water vapor in the tropics. 2. Physical interpretation of the amount effect. In: *Journal of Geophysical Research* 113 (D19). DOI: 10.1029/2008JD009943.

Roberts, Mark S.; Smart, Peter L.; Baker, Andy (1998): Annual trace element variations in a Holocene speleothem. In: *Earth and Planetary Science Letters* 154 (1-4), pp. 237–246. DOI: 10.1016/S0012-821X(97)00116-7.

Rozanski, Kazimierz; Araguás-Araguás, Luis; Gonfiantini, Roberto (1993): Isotopic Patterns in Modern Global Precipitation. In: Swart, Peter K. Lohmann, K.C., J. Mc Kenzie und S. Savin (Ed.): *Climate Change in Continental Isotopic Records*. Washington, DC: American Geophysical Union (Geophysical monograph, 78), S. 1–36.

Scheffer, Fritz; Schachtschabel, Paul; Blume, Hans-Peter; Brümmer, Gerhard W.; Horn, Rainer; Kandeler, Ellen et al. (2010): *Lehrbuch der Bodenkunde*. 16th edition. Heidelberg: Spektrum Akademischer Verlag. Accessible online: http://site.ebrary.com/lib/alltitles/docDetail.action?docID=10359930.

Schmidt, Gavin A.; LeGrande, Allegra N.; Hoffmann, Georg (2007): Water isotope expressions of intrinsic and forced variability in a coupled ocean-atmosphere model. In: *Journal of Geophysical Research* 112 (D10). DOI: 10.1029/2006JD007781.

Schmittner, Andreas; Saenko, Oleg A.; Weaver, Andrew J. (2003): Coupling of the hemispheres in observations and simulations of glacial climate change. In: *Quaternary Science Reviews* 22 (5-7), pp. 659–671. DOI: 10.1016/S0277-3791(02)00184-1.

Scholz, Denis; Hoffmann, Dirk L. (2011): StalAge – An algorithm designed for construction of speleothem age models. In: *Quaternary Geochronology* 6 (3-4), pp. 369–382. DOI: 10.1016/j.quageo.2011.02.002.

Scholz, Denis; Hoffmann, Dirk L.; Hellstrom, John; Bronk Ramsey, Christopher (2012): A comparison of different methods for speleothem age modelling. In: *Quaternary Geochronology* 14, pp. 94–104. DOI: 10.1016/j.quageo.2012.03.015.

Schönwiese, Christian-Dietrich (2003): *Klimatologie*. 163 Figures, 31 Tables. 2nd edition. Stuttgart: Ulmer (UTB für Wissenschaft Uni-Taschenbücher Geowissenschaften, 1793).

Schönwiese, Christian-Dietrich (2013): *Klimatologie*. 31 Tables. 4th edition. Stuttgart: Ulmer (utb-studi-e-book, 1793). Accessible online: http://www.utb-studi-e-book.de/9783838539003.

Schulz, Michael; Mudelsee, Manfred (2002): REDFIT. Estimating red-noise spectra directly from unevenly spaced paleoclimatic time series. In: *Computers & Geosciences* 28 (3), pp. 421–426. DOI: 10.1016/S0098-3004(01)00044-9.

Schwarcz, Henry P. (1989): Uranium series dating of Quaternary deposits. In: *Quaternary International* 1, pp. 7–17. DOI: 10.1016/1040-6182(89)90005-0.

Sengupta, Saikat; Sarkar, A. (2006): Stable isotope evidence of dual (Arabian Sea and Bay of Bengal) vapour sources in monsoonal precipitation over north India. In: *Earth and Planetary Science Letters* 250 (3-4), pp. 511–521. DOI: 10.1016/j.epsl.2006.08.011.

Shakun, Jeremy D.; Burns, Stephen J.; Fleitmann, Dominik; Kramers, Jan; Matter, Albert; Al-Subary, Abdulkarim (2007): A high-resolution, absolute-dated deglacial speleothem record of Indian Ocean climate from Socotra Island, Yemen. In: *Earth Planetary Science Letters* 259 (3-4), pp. 442–456. DOI: 10.1016/j.epsl.2007.05.004.

Shiau, Liang-Jian; Chen, Min-Te; Clemens, Steven C.; Huh, Chih-An; Yamamoto, Masanobu; Yokoyama, Yusuke (2011): Warm pool hydrological and terrestrial variability near southern Papua New Guinea over the past 50k. In: *Geophysical Research Letters* 38 (8), DOI: 10.1029/2010GL045309.

Sinha, Ashish; Cannariato, Kevin G.; Stott, Lowell D.; Cheng, Hai; Edwards, Lawrence R.; Yadava, Madhusudan G. et al. (2007): A 900-year (600 to 1500 A.D.) record of the Indian summer monsoon precipitation from the core monsoon zone of India. In: *Geophysical Research Letters* 34 (16). DOI: 10.1029/2007GL030431.

Sinha, Ashish; Berkelhammer, Max; Stott, Lowell; Mudelsee, Manfred; Cheng, Hai; Biswas, Jayant (2011): The leading mode of Indian Summer Monsoon precipitation variability during the last millennium. In: *Geophysical Research Letters* 38 (15). DOI: 10.1029/2011GL047713.

Sinha, Ashish; Cannariato, Kevin G.; Stott, Lowell D.; Li, Hong-Chun; You, Chen-Feng; Cheng, Hai et al. (2005): Variability of Southwest Indian summer monsoon precipitation during the Bølling-Ållerød. In: Geology 33 (10), p. 813. DOI: 10.1130/G21498.1.

Smith, Charles C.; Löf, George; Jones, Randy (1994): Measurement and analysis of evaporation from an inactive outdoor swimming pool. In: *Solar Energy* 53 (1), pp. 3–7. DOI: 10.1016/S0038-092X(94)90597-5.

Spötl, Christoph (2005): A robust and fast method of sampling and analysis of δ 13 C of dissolved inorganic carbon in ground waters. In: *Isotopes in Environmental and Health Studies* 41 (3), pp. 217–221. DOI: 10.1080/10256010500230023.

Spötl, Christoph; Fairchild, Ian J.; Tooth, Anna F. (2005): Cave air control on dripwater geochemistry, Obir Caves (Austria). Implications for speleothem deposition in dynamically ventilated caves. In: *Geochimica et Cosmochimica Acta* 69 (10), pp. 2451–2468. DOI: 10.1016/j.gca.2004.12.009.

Stuiver, Minze; Grootes, Pieter M. (2000): GISP2 Oxygen Isotope Ratios. In: *Quaternary Reserach (USA)* 53 (03), pp. 277–284. DOI: 10.1006/qres.2000.2127.

Sturm, Christophe; Vimeux, Françoise; Krinner, Gerhard (2007): Intraseasonal variability in South America recorded in stable water isotopes. In: *Journal of Geophysical Research* 112 (D20). DOI: 10.1029/2006JD008298.

Tan, Liangcheng; Cai, Yanjun; An, Zhisheng; Edwards, R. Lawrence; Cheng, Hai; Shen, Chuan-Chou; Zhang, Haiwei (2010): Centennial- to decadal-scale monsoon precipitation variability in the semi-humid region, northern China during the last 1860 years. Records from stalagmites in Huangye Cave. In: *holocene* 21 (2), pp. 287–296. DOI: 10.1177/0959683610378880.

Tan, Liangcheng; Shen, Chuan-Chou; Cai, Yanjun; Lo, Li; Cheng, Hai; An, Zhisheng (2014): Trace-element variations in an annually layered stalagmite as recorders of climatic changes and anthropogenic pollution in Central China. In: *Quaternary Research* 81 (2), pp. 181–188. DOI: 10.1016/j.yqres.2013.12.001.

Tan, Ming; Baker, Andy; Genty, Dominique; Smith, Claire; Esper, Jan; Cai, Binggui (2006): Applications of stalagmite laminae to paleoclimate reconstructions. Comparison with dendrochronology/climatology. In: *Quaternary Science Reviews* 25 (17-18), pp. 2103–2117. DOI: 10.1016/j.quascirev.2006.01.034.

Terzer, Stefan; Wassenaar, Leonard; Douence, Cedric; Luìs, Araguàs-Araguàs (Hg.) (2016): An assessment of the isotopic (2H/18O) integrity of water samples collected and stored by unattended precipitation totalizers. *Geophysical Research Abstracts*. EGU General Assembly 2016, held 17-22 April, 2016 in Vienna Austria, id. EPSC2016-15992 (18).

Tooth, Anna F.; Fairchild, Ian J. (2003): Soil and karst aquifer hydrological controls on the geochemical evolution of speleothem-forming drip waters, Crag Cave, southwest Ireland. In: *Journal of Hydrology* 273 (1-4), pp. 51–68. DOI: 10.1016/S0022-1694(02)00349-9.

Tran, Thanh, H.; van Dang, Bat; Kim Ngo, Chi; Dinh Hoang, Que; Minh Nguyen, Quyen (2013): Structural controls on the occurrence and morphology of karstified assemblages in northeastern Vietnam. A regional perspective. In: *Environmental Earth Sciences* 70 (2), pp. 511–520. DOI: 10.1007/s12665-011-1057-1.

Treble, Pauline C.; Chappel, J.; Gagan, Michael K.; McKeegan, K. D.; HARRISON, T. (2005): In situ measurement of seasonal $\delta^{18}O$ variations and analysis of isotopic trends in a modern speleothem from southwest Australia. In: *Earth and Planetary Science Letters* 233 (1-2), pp. 17–32. DOI: 10.1016/j.epsl.2005.02.013.

Tremaine, Darrel M.; Froelich, Philip N.; Wang, Yang (2011): Speleothem calcite farmed in situ: Modern calibration of δ18O and δ13C paleoclimate proxies in a continuously-monitored natural cave system. In: *Geochimica et Cosmochimica Acta* 75 (17), pp. 4929–4950. DOI: 10.1016/j.gca.2011.06.005.

Tremaine, Darrel M.; Sinclair, Daniel J.; Stoll, Heather M.; Lagerström, Maria; Carvajal, Carlos P.; Sherrell, Robert M. (2016): A two-year automated dripwater chemistry study in a remote cave in the tropical south Pacific. Using [Cl−] as a conservative tracer for seasalt contribution of major cations. In: *Geochimica et Cosmochimica Acta* 184, pp. 289–310. DOI: 10.1016/j.gca.2016.03.029.

Tucker, Maurice E.; Dickson, J. A. D.; Wright, V. Paul (1990): *Carbonate sedimentology*. Oxford England, Boston, Brookline Village, Mass: Distributors USA Publishers' Business Services. Accessible online: http://site.ebrary.com/lib/alltitles/docDetail. action?docID=10346071.

Van, Tran T.; Masschelein, Jan; Lagrou, David; Dusar, Michiel; Ke, Thai, D.; Viet, Hoang, A. et al. (2004): Karst water management in Dong Van and Meo Vac districts, Ha Giang province, Vietnam. Contribution of geological and speleological investigations. In: Batelaan, O.:Dusar, M., J. Masschelein, Van. Thanh Tam, T. T. und K. Nguyen Xuan (Hg.): *Trans-KARST 2004. Proceedings of the International Transdisciplinary Conference on Development and Conservation of Karst Regions.* Hanoi, Vietnam, 13-18.9.2004, pp. 265–271.

Vellinga, Michael; Wood, Richard A. (2002): Global climatic impacts of a collapse of the atlantic thermohaline circulation. In: *Climatic Change* 54 (3), pp. 251–267. DOI: 10.1023/A:1016168827653.

Verheyden, Sophie; Keppens, Eddy; Fairchild, Ian J.; McDermott, Frank; Weis, Dominique (2000): Mg, Sr and Sr isotope geochemistry of a Belgian Holocene speleothem: implications for paleoclimate reconstructions. In: *Chemical Geology* 169, pp. 131–144.

Vorlaufer, Karl (2011*): Südostasien. Brunei, Indonesien, Kambodscha, Laos, Malaysia, Myanmar, Osttimor, Philippinen, Singapur, Thailand, Vietnam* ; with 60 Tables; [Geographie, Geschichte, Wirtschaft, Politik]. 2nd edition. Darmstadt: WBG (Wiss. Buchges.) (WBG-Länderkunden).

Wachter, Ralf (2018): GUARD autosampler - Arduino sketch. DOI: 10.5445/IR/1000085057.

Walter, Heinrich; Breckle, Siegmar-Walter (1999): *Vegetation und Klimazonen. Grundriß der globalen Ökologie.* 7th edition. Stuttgart: Ulmer (Uni-Taschenbücher, 14).

Wang, Bin (2006): *The Asian monsoon*. Berlin: Springer (Environmental Sciences).

Wang, Xianfeng; Auler, Augusto S.; Edwards, Lawrence R.; Cheng, Hai; Ito, Emi; Solheid, Maniko (2006): Interhemispheric anti-phasing of rainfall during the last glacial period. In: *Quaternary Science Reviews* 25 (23-24), pp. 3391–3403. DOI: 10.1016/j.quascirev.2006.02.009.

Wang, Xianfeng; Auler, Augusto S.; Edwards, Lawrence R.; Cheng, Hai; Ito, Emi; Wang, Yongjin et al. (2007): Millennial-scale precipitation changes in southern Brazil over the past 90,000 years. In: *Geophysical Research Letters* 34 (23), DOI: 10.1029/2007GL031149.

Wang, Yan-Hua J.; Cheng, Hai; Edwards, Lawrence R.; An, Zhisheng S.; Wu, J. Y.; Shen, Chien C.; Dorale, Jeffrey A. (2001): A High-Resolution Absolute-Dated Late Pleistocene Monsoon Record from Hulu Cave, China. In: *Science* 294 (5550), pp. 2345–2348. DOI: 10.1126/science.1064618.

Wang, Yongjin; Cheng, Hai; Edwards, R. Lawrence; He, YaoQi; Kong, Xinggong; An, Zhisheng et al. (2005): The Holocene Asian monsoon: links to solar changes and North Atlantic climate. In: *Science* (New York, N.Y.) 308 (5723), pp. 854–857. DOI: 10.1126/science.1106296.

Wang, Yongjin; Cheng, Hai; Edwards, R. Lawrence; Kong, Xinggong; Shao, Xiaohua; Chen, Shitao et al. (2008): Millennial- and orbital-scale changes in the East Asian monsoon over the past 224,000 years. In: *Nature* 451 (7182), pp. 1090–1093. DOI: 10.1038/nature06692.

Weischet, Wolfgang; Endlicher, Wilfried (2000): *Die Alte Welt. Europa, Afrika, Asien*. Stuttgart: Teubner (Teubner-Studienbücher der Geographie, / von Wolfgang Weischet ; Teil 2).

Wong, Corinne I.; Breecker, Daniel O. (2015): Advancements in the use of speleothems as climate archives. In: *Quaternary Science Reviews* 127, pp. 1–18. DOI: 10.1016/j.quascirev.2015.07.019.

Yanai, Michio; Li, Chengfeng; Song, Zhengshan (1992): Seasonal Heating of the Tibetan Plateau and Its Effects on the Evolution of the Asian Summer Monsoon. In: *Journal of the Meteorological Society of Japan* 70 (1B), pp. 319–351. DOI: 10.2151/jmsj1965.70.1B_319.

Yancheva, Gergana; Nowaczyk, Norbert R.; Mingram, Jens; Dulski, Peter; Schettler, Georg; Negendank, Jörg F. W. et al. (2007): Influence of the intertropical convergence zone on the East Asian monsoon. In: *Nature* 445 (7123), pp. 74–77. DOI: 10.1038/nature05431.

Yang, Xunlin; Liu, Jianbao; Liang, Fuyuan Yuan, Daoxian; Yang, Yan; Lu, Yanbin; Chen, Fahu (2014): Holocene stalagmite ^{18}O records in the East Asian monsoon region and their correlation with those in the Indian monsoon region. In: *The Holocene* 24 (12), pp. 1657–1664. DOI: 10.1177/0959683614551222.

Yi, Sangheon (2011): Holocene Vegetation Responses to East Asian Monsoonal Changes in South Korea. In: Xavier Fettweis, Alexandre Belleflamme, Bruno Franco, Michel Erpicum und Samuel Nicolay (Eds.): *Estimation of the Sea Level Rise by 2100 Resulting from Changes in the Surface Mass Balance of the Greenland Ice Sheet*: INTECH Open Access Publisher.

Yuan, Daoxian; Cheng, Hai; Edwards, Lawrence R.; Dykoski, Carolyn A.; Kelly, Megan J.; Zhang, Meiliang et al. (2004): Timing, Duration, and Transitions of the Last Interglacial Asian Monsoon. In: *Science* 304 (5670), pp. 575–578. DOI: 10.1126/science.1091220.

Zhang, Hui-Ling; Yu, Ke-Fu; Zhao, Jian-xin; Feng, Yue-Xing; Lin, Yu-Shi; Zhou, Wei; Liu, Guo-Hui (2013): East Asian Summer Monsoon variations in the past 12.5ka. High-resolution δ18O record from a precisely dated aragonite stalagmite in central China. In: Journal of Asian Earth Sciences 73, S. 162–175. DOI: 10.1016/j.jseaes.2013.04.015.

Zhang, Pingzhong; Cheng, Hai; Edwards, R. Lawrence; Chen, Fahu; Wang, Yongjin; Yang, Xunlin et al. (2008): A test of climate, sun, and culture relationships from an 1810-year Chinese cave record. In: *Science* (New York, N.Y.) 322 (5903), pp. 940–942. DOI: 10.1126/science.1163965.

Zhou, Houyun; Zhao, Jianxin; Zhang, Pingzhong; Shen, Chuan-Chou; Chi, Baoquan; Feng, Yuexing et al. (2008): Decoupling of stalagmite-derived Asian summer monsoon records from North Atlantic temperature change during marine oxygen isotope stage 5d. In: *Quaternary Reserach* (USA) 70 (2), pp. 315–321. DOI: 10.1016/j.yqres.2008.04.007.

Zhou, Houyun; Feng, Yue-Xing; Zhao, Jian-xin; Shen, Chuan-Chou; You, Chen-Feng; Lin, Yin (2009): Deglacial variations of Sr and 87Sr/86Sr ratio recorded by a stalagmite from Central China and their association with past climate and environment. In: *Chemical Geology* 268 (3-4), pp. 233–247. DOI: 10.1016/j.chemgeo.2009.09.003.

Appendix

A Soils and Plants

Figure A.1: Soil at the surface above cave Ma Le 2 where soil samples BOD01 and BOD02 were taken (March 7th, 2014). Scale length 120 cm (left) and 60 cm (right).

Figure A.2: Soil at the surface above cave Ma Le 2 where soil sample BOD03 was taken (March 7th, 2014). Scale length 100 cm.

Figure A.3: Soil at the surface above cave Sang Ma Sao where the soil was sampled in three depths (0-10 cm, 15-20 cm and ~ 35 cm; March 28th, 2016). The scale reaches a depth of about 25 cm.

Table A.1: Additional soil samples collected in the study area for carbon isotope analyses.

Label	**Description of the sampling location**
BOD04	Valley of river Ma Le 1; from the left-hand side (facing downhill) of an erosion gully on the left slope (facing downstream) of the valley; 23°16'44.0'' N; 105°18'12.7'' E; 1,165 masl; from about 1 m depth
BOD05	As sample BOD04, but from the right-hand side of the erosion gully; from 15 cm depth
BOD06	Valley of river Ma Le 1 from a cultivated field; 23°17'57.3'' N; 105°18'37.9'' E; 1,163 masl; from surface
BOD07	From the surface above cave Tia Sang; 23°16'48.8'' N; 105°18'20.5'' E; 1,161 masl; from depth increment 0-10 cm
BOD08	From the surface above cave Tia Sang; 23°16'44.0'' N; 105°18'12.7'' E; 1,165 masl; from depth increment 0-10 cm
BOD09	From the surface above cave Tia Sang; 23°16'38.8'' N; 105°18'22.1'' E; 1,242 masl; from depth increment 0-10 cm
BOD10	Valley of river Seo Ho, 23°17'23.17" N 105°18'45.67" E; 1,002 masl; from surface
BOD11	Valley of river Seo Ho; at the upstream end of the headrace channel of the Seo Ho hydropower plant; 23°17'23.17" N 105°18'45.67" E: 972 masl; from surface

Figure A.4: Plant samples from the surface above cave Ma Le 2 (from left to right and from top to bottom): PFL02 to PFL06; Bottom right: Pile of corn remains that are burned by the farmers at the beginning of the rainy season to fertilise the soils. All pictures taken during the dry season on March 7th, 2014.

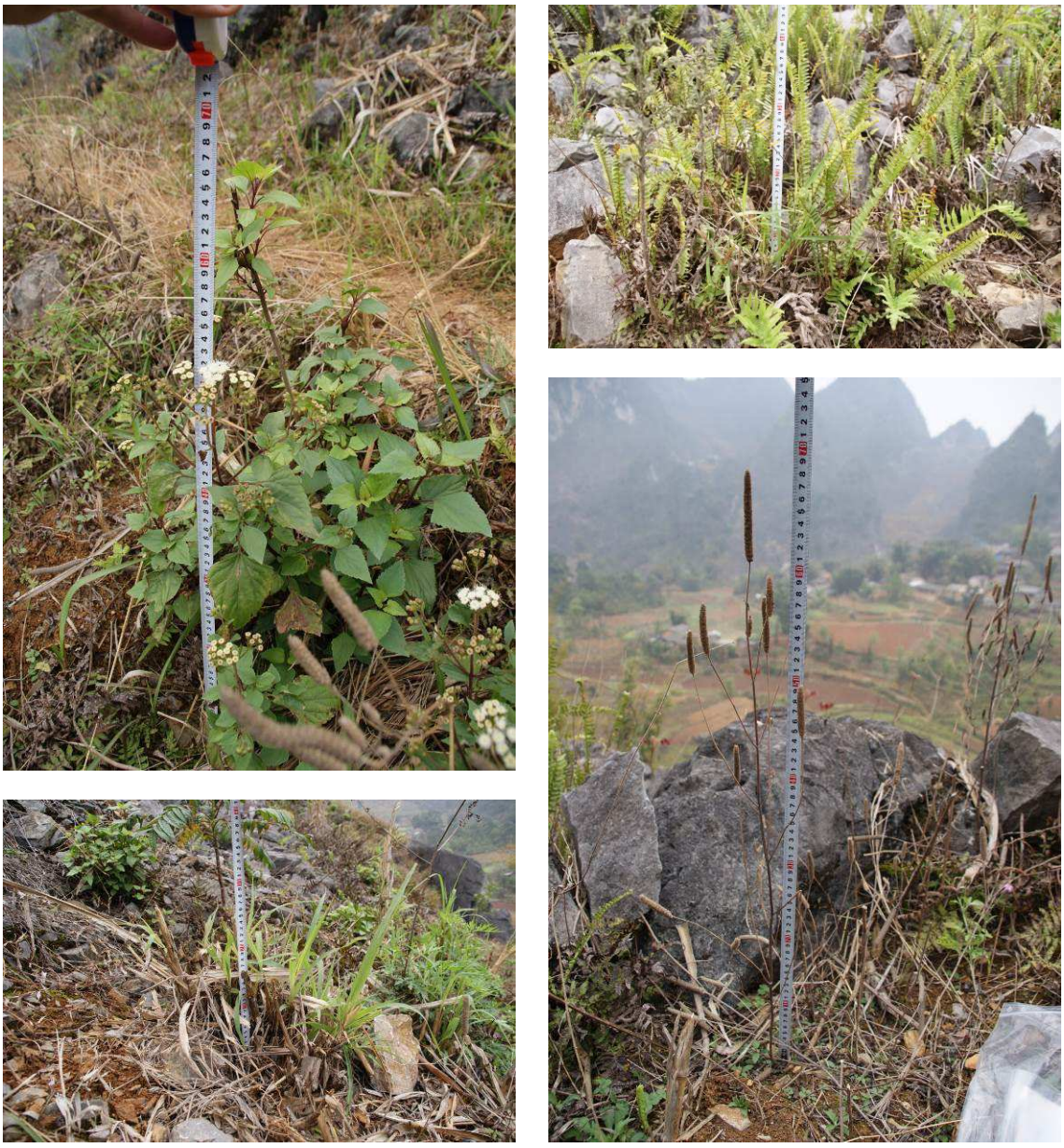

Figure A.5: Plant samples from the surface above cave Sang Ma Sao (from left to right and from top to bottom): SMS PL01 to SMS PL04.; All pictures taken during the dry season on March 28th, 2016.

Table A.2: List of the 31 sub-areas defined for vegetation mapping at the surface above cave Ma Le 2 and descriptions of the vegetation cover with focus on vegetation density.

Area	Description
01	high vegetation density; dominated by plant designated as sample PFL01; agricultural
02	high vegetation density; dominated by plant designated as sample PFL02; agricultural
03	high vegetation density; dominated by PFL01; agricultural
04	host rock outcrop; low vegetation density; scarce and low-growing natural vegetation
05	intermediate vegetation density (~ 40%); dominated by PFL01; agricultural
06	host rock outcrop, but with relatively dense low-growing (~ 30 cm) natural vegetation
07	steep slope (inclination ~ 25°); very scarce natural vegetation dominated by plant designated as sample PFL04; agricultural
08	multiple agrigulural fields dominated by PFL01, partly scarce, partly dense
09	host rock outcrop with trees / shrubs of multiple species; sample PFL03 is an example, not representative
10	low host rock outcrop dominated by low-growing ferns and grasses, isolated shrubs
11	slope (inclination ~ 15°) with host rock outcrop; intermediate vegetation density (~ 50%) with low-growing (~ 30 cm) and withered vegetation
12	high vegetation density; dominated by PFL01; agricultural
13	very steep slope; almost no vegetation
14	high vegetation density; dominated by PFL01; agricultural
15	fallow fields; probably corn cultivation during rainy season; withered specimen of plant designated as sample SMS PL04
16	bare soil; no vegetation
17	high vegetation density; dominated by PFL01; agricultural
18	bare soil; isolated grasses
19	slope dominated by ferns (~ 90%), but also multiple species of low-growing trees and shrubs
20	strips of trees, mostly conifers
21	bare soil; no vegetation
22	steep slope; intermediate vegetation density (~ 50%); dominated by plant designated as sample PFL04 (= SMS PL02) and SMS PL04 to similar extents
23	slope; mostly rubble (~ 70%), vegetation (~20 %) dominated by a medium-growing herbaceous
24	very steep slope with host rock outcrop; a couple of high grasses
25	steep slope (inclination ~ 40%); intermediate vegetation density; dominated by PFL04 and PFL06
26	steep slope with host rock outcrop (~ 60%); intermediate vegetation density with PFL06 (~ 10%),low-growing grasses (~ 20%) and a mixture of various plant species (~ 10%) comprising young trees that seem to be cut back regularly including specimen of PFL03
27	intermediate vegetation density; ferns and various shrubs
28	high vegetation density; various shrubs, grasses and ferns
29	bare soil; no vegetation
30	intermediate vegetation density; high-growing grasses, possibly for feeding livestock
31	slope, but similar to ML2-30

B Microstratigraphic Logs

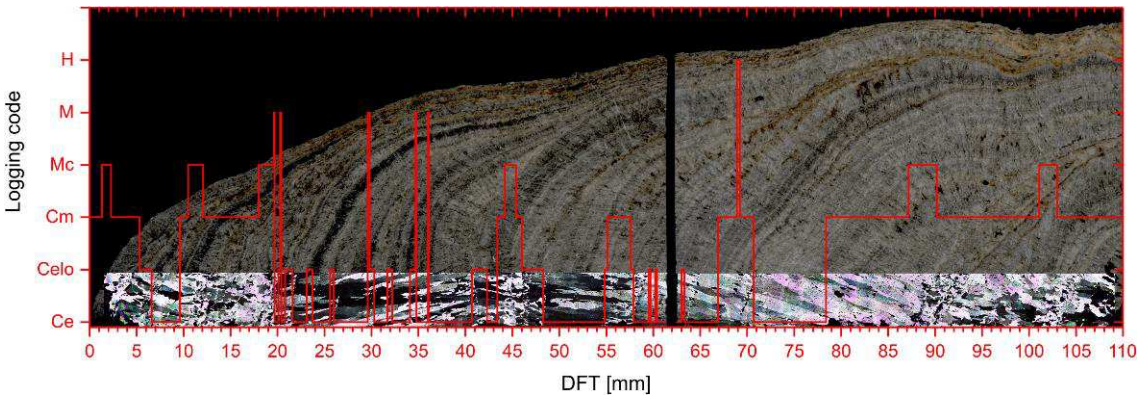

Figure B.1: Microstratigraphic log for stalagmite VML22 superimposed on the corresponding thin slides as reassembled microscopic images (crossed polars) and flatbed scans (-15 brightness, +15 contrast). The gap between the left and right stalagmite pieces is an inevitable result of thin slide production. Fabric types according to Frisia (2015): Ce = Columnar elongated; Celo = Ce with lateral overgrowth; Cm = Columnar microcrystalline; Mc = Mosaic calcite; M = Micrite; H = Hiatus. The log refers to the bottom edge of both images.

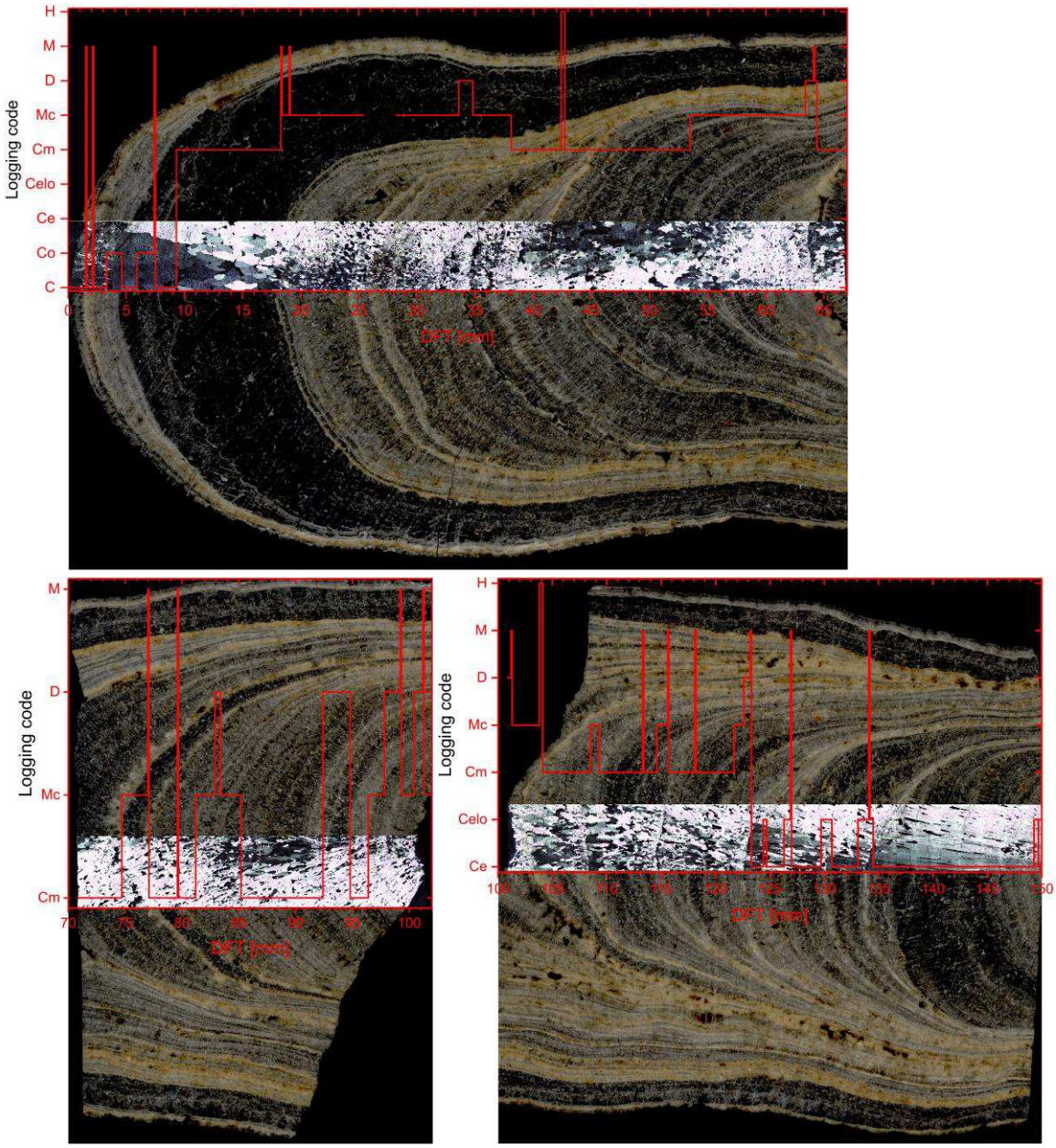

Figure B.2: Microstratigraphic log for stalagmite VSMS2 superimposed on the corresponding thin slides as reassembled microscopic images (crossed polars) and flatbed scans (-15 brightness, +15 contrast). The gaps between the stalagmite pieces is an inevitable result of thin slide production. Fabric types according to Frisia (2015): C = Columnar; Co = Columnar open; Ce = Columnar elongated; Celo = Ce with lateral overgrowth; Cm = Columnar microcrystalline; D = Dendritic; M = Micrite; Mc = Mosaic calcite; H = Hiatus. The log refers to the bottom edge of each image.

C Statistical Analyses

C.1 Scatter Plots Stalagmite VML22

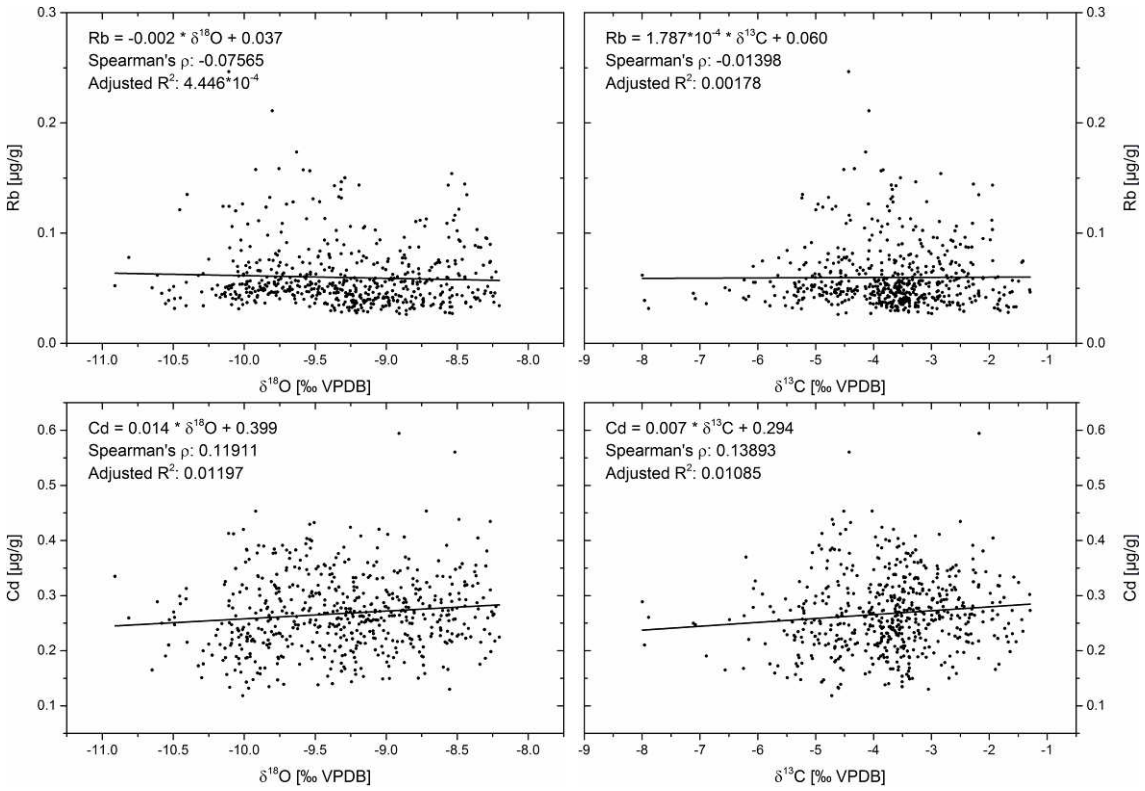

Figure C.1: Scatter plots of the geochemical records of stalagmite VML22 for $\delta^{18}O$ and $\delta^{13}C$ plotted against Rb and Cd, respectively. Trace element data were averaged to correspond with the isotope data sets as described in the text.

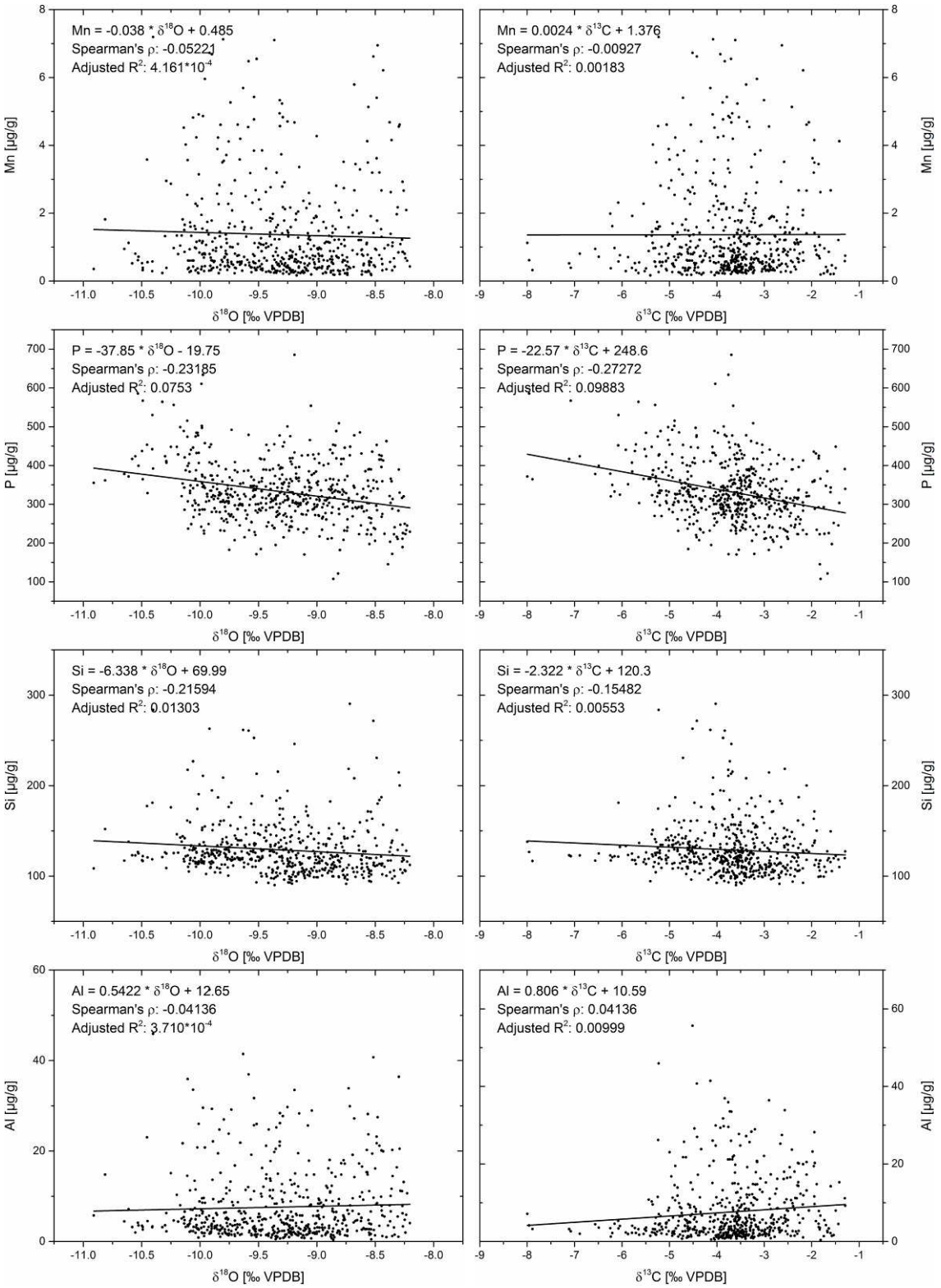

Figure C.2: Scatter plots of the geochemical records of stalagmite VML22 for $\delta^{18}O$ and $\delta^{13}C$ plotted against Mn, P, Si and Al, respectively. Trace element data were averaged to correspond to the isotope data sets as described in the text.

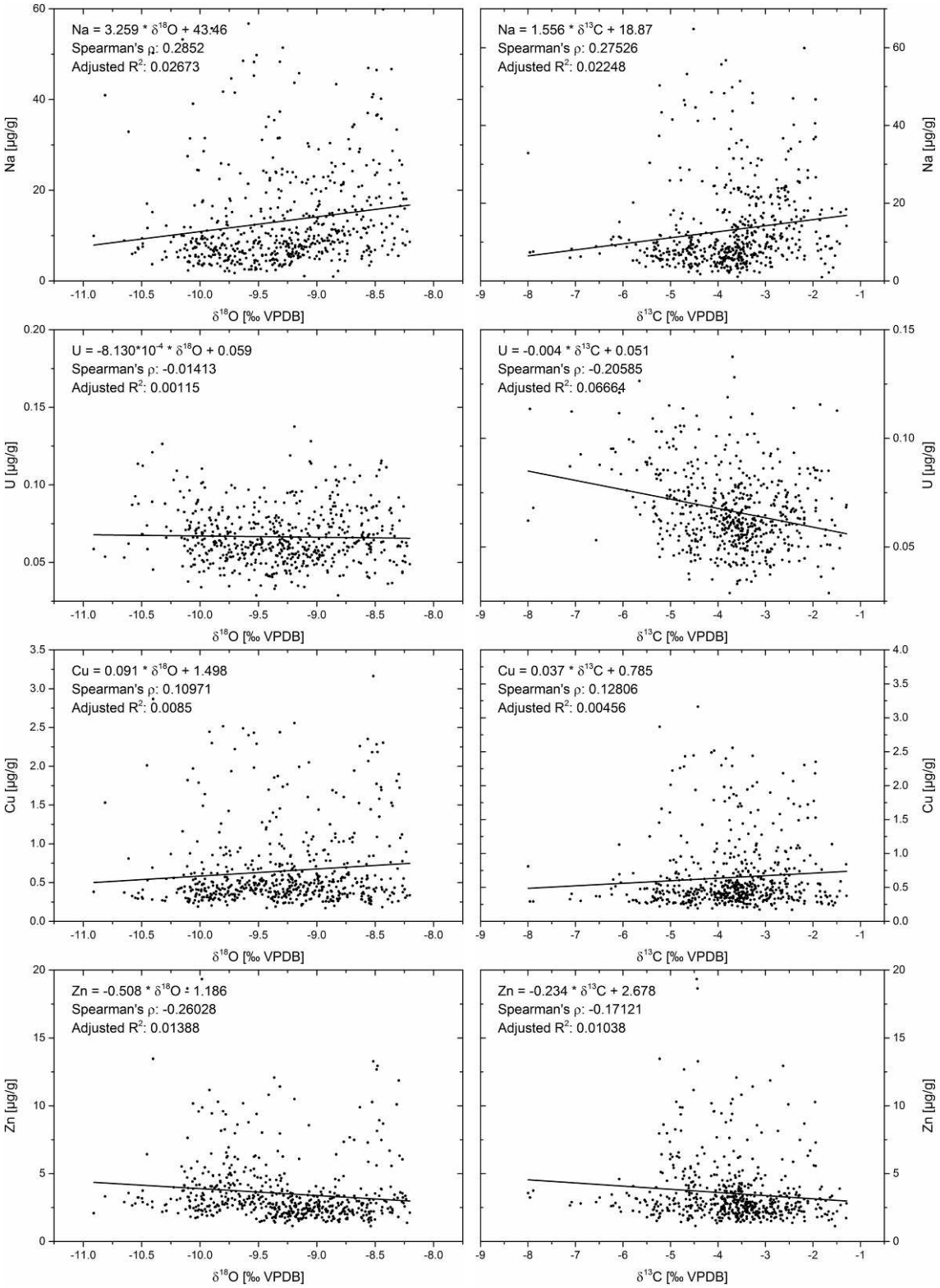

Figure C.3: Scatter plots of the geochemical records of stalagmite VML22 for $\delta^{18}O$ and $\delta^{13}C$ plotted against Na, U, Cu and Zn, respectively. Trace element data were averaged to correspond with the isotope data sets as described in the text.

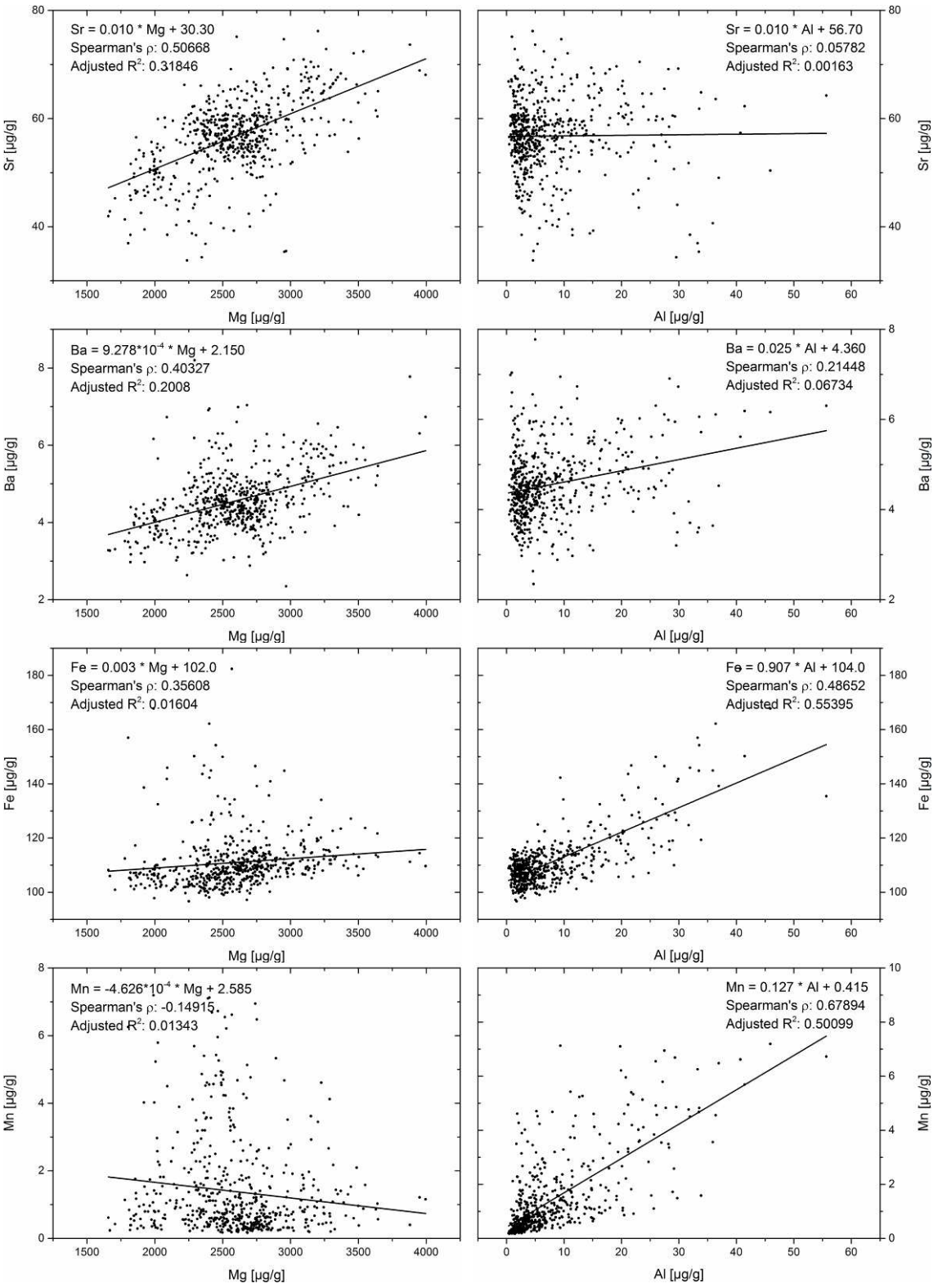

Figure C.4: Scatter plots of the geochemical records of stalagmite VML22 for Mg and Al plotted against Sr, Ba, Fe and Mn, respectively. Trace element data were averaged to correspond to the isotope data sets as described in the text.

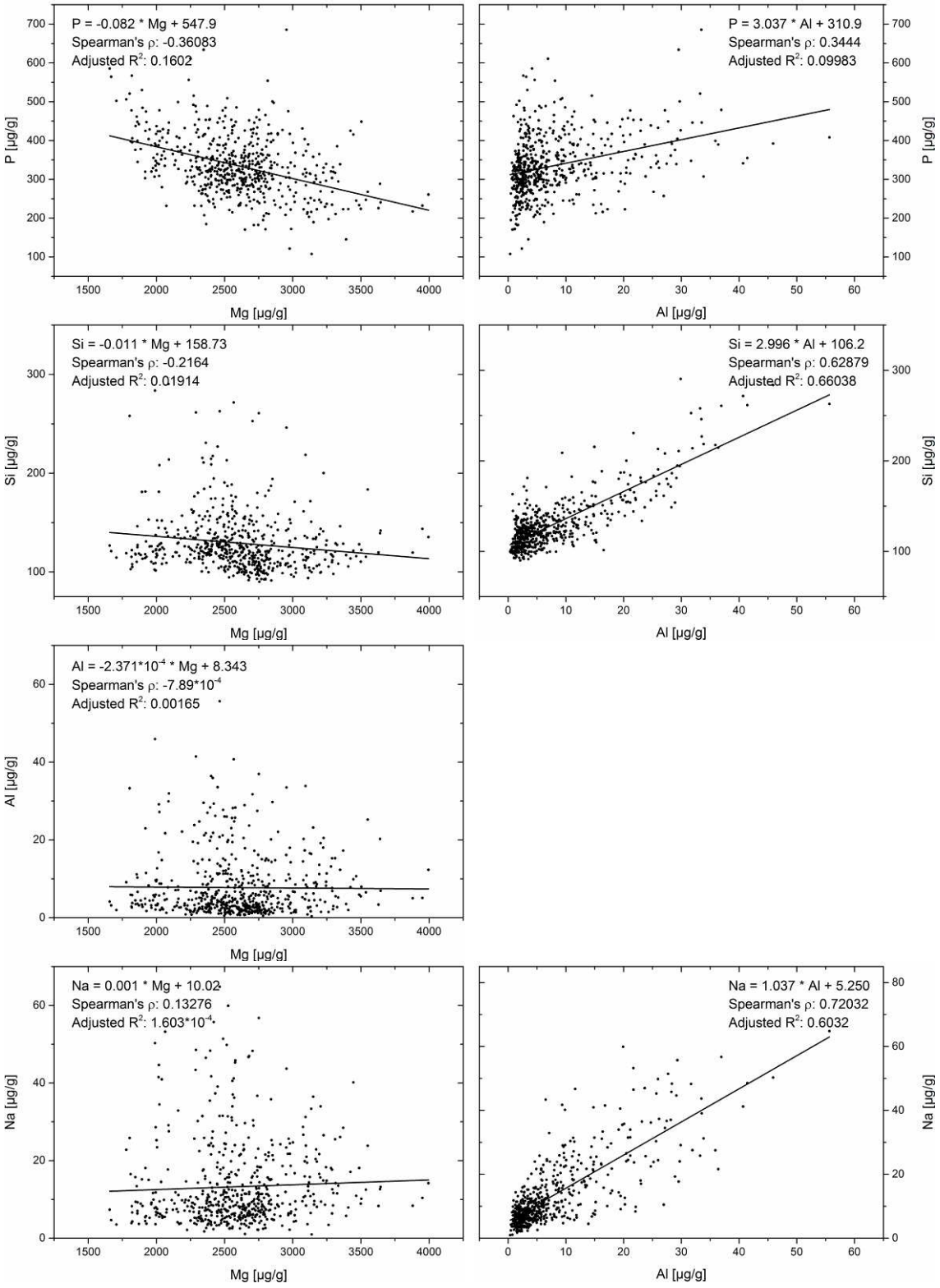

Figure C.5: Scatter plots of the geochemical records of stalagmite VML22 for Mg and Al plotted against P, Si and Na, respectively, and against each other. Trace element data were averaged to correspond to the isotope data sets as described in the text.

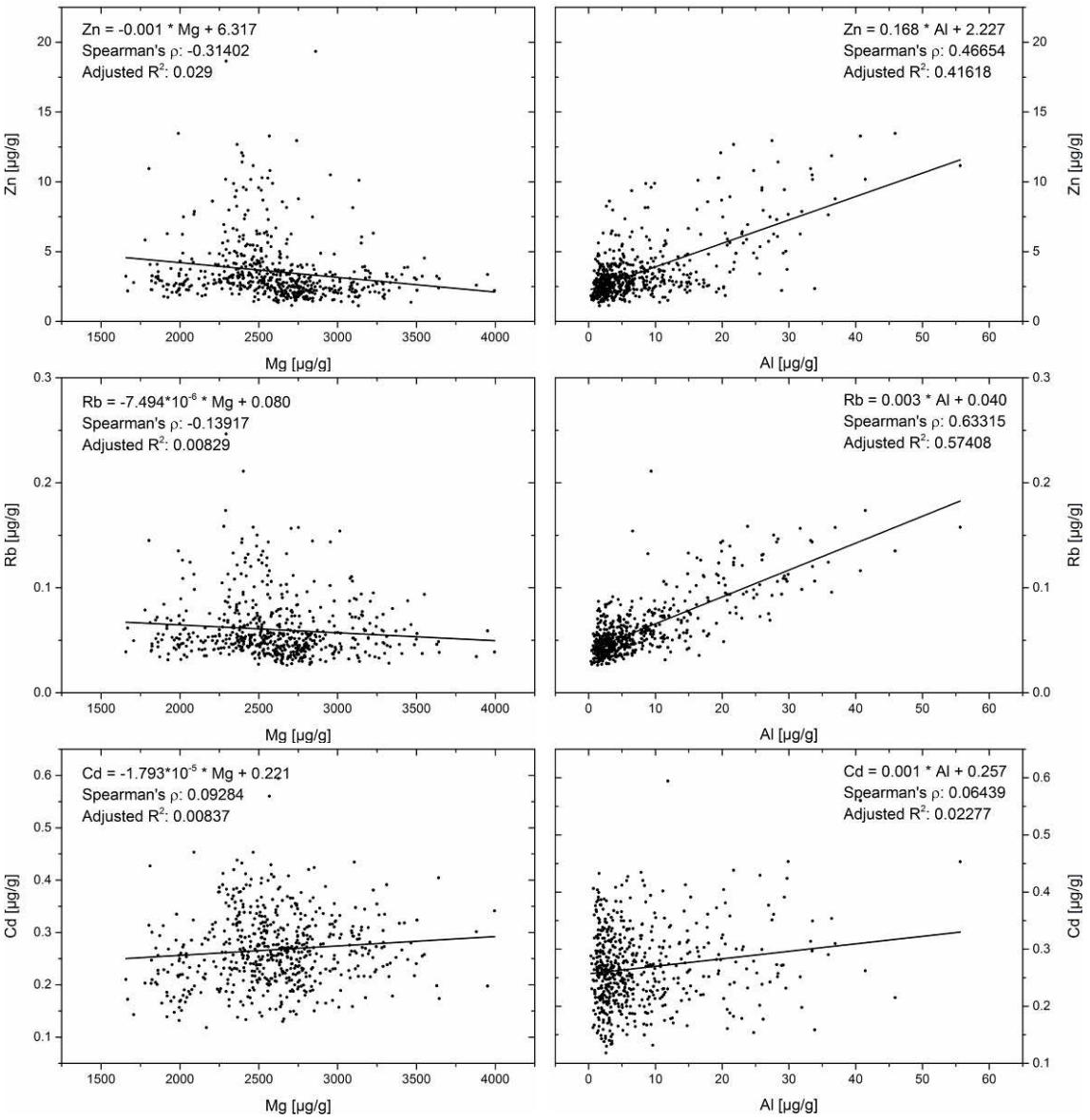

Figure C.6: Scatter plots of the geochemical records of stalagmite VML22 for Mg and Al plotted against Zn, Rb and Cd, respectively. Trace element data were averaged to correspond to the isotope data sets as described in the text.

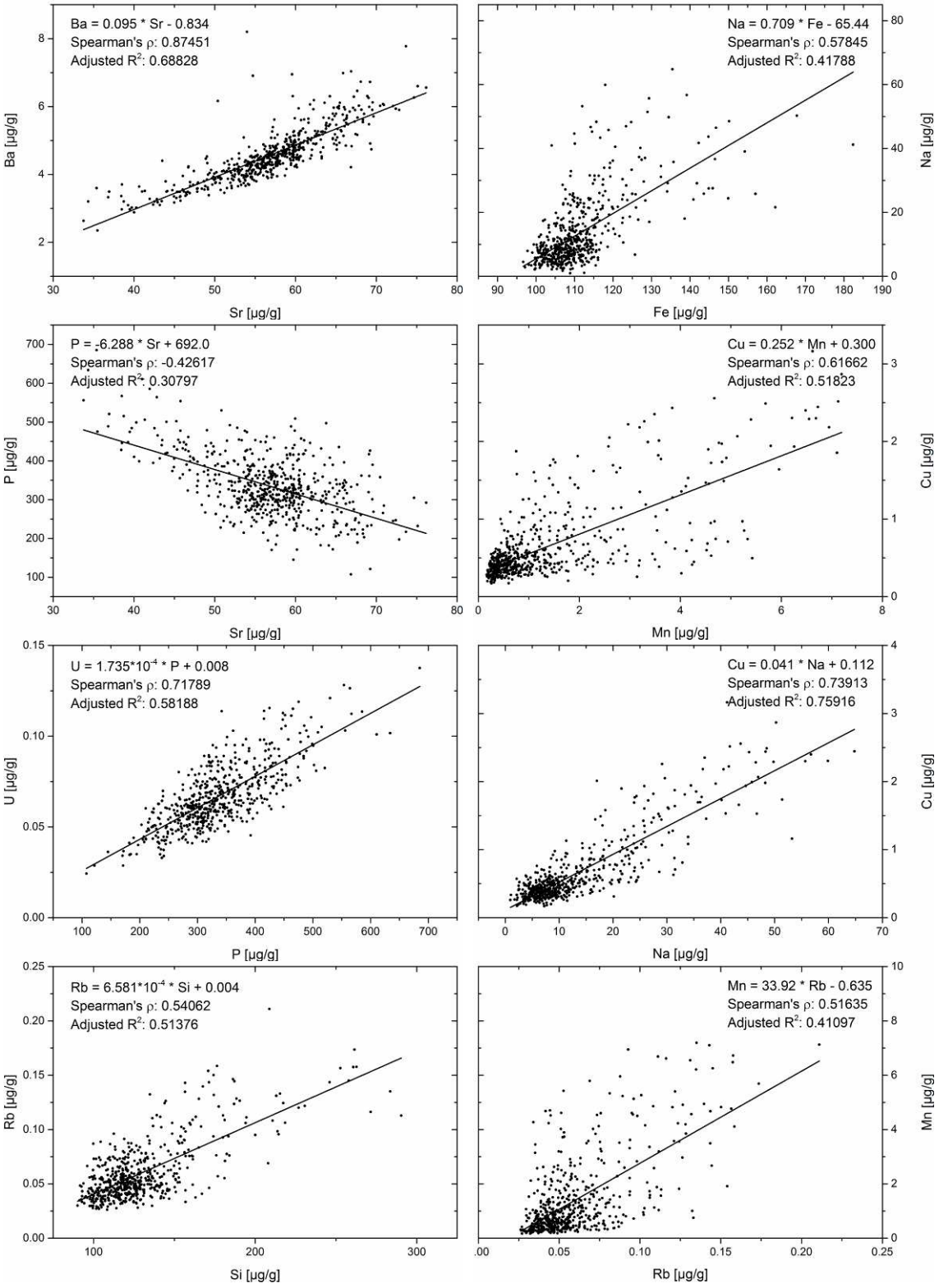

Figure C.7: Scatter plots of the geochemical records of stalagmite VML22: Sr vs. Ba, Fe vs. Na, Sr vs. P, Mn vs. Cu, P vs. U, Na vs. Cu, Si vs. Rb and Rb vs. Mn. Trace element data were averaged to correspond to the isotope data sets as described in the text.

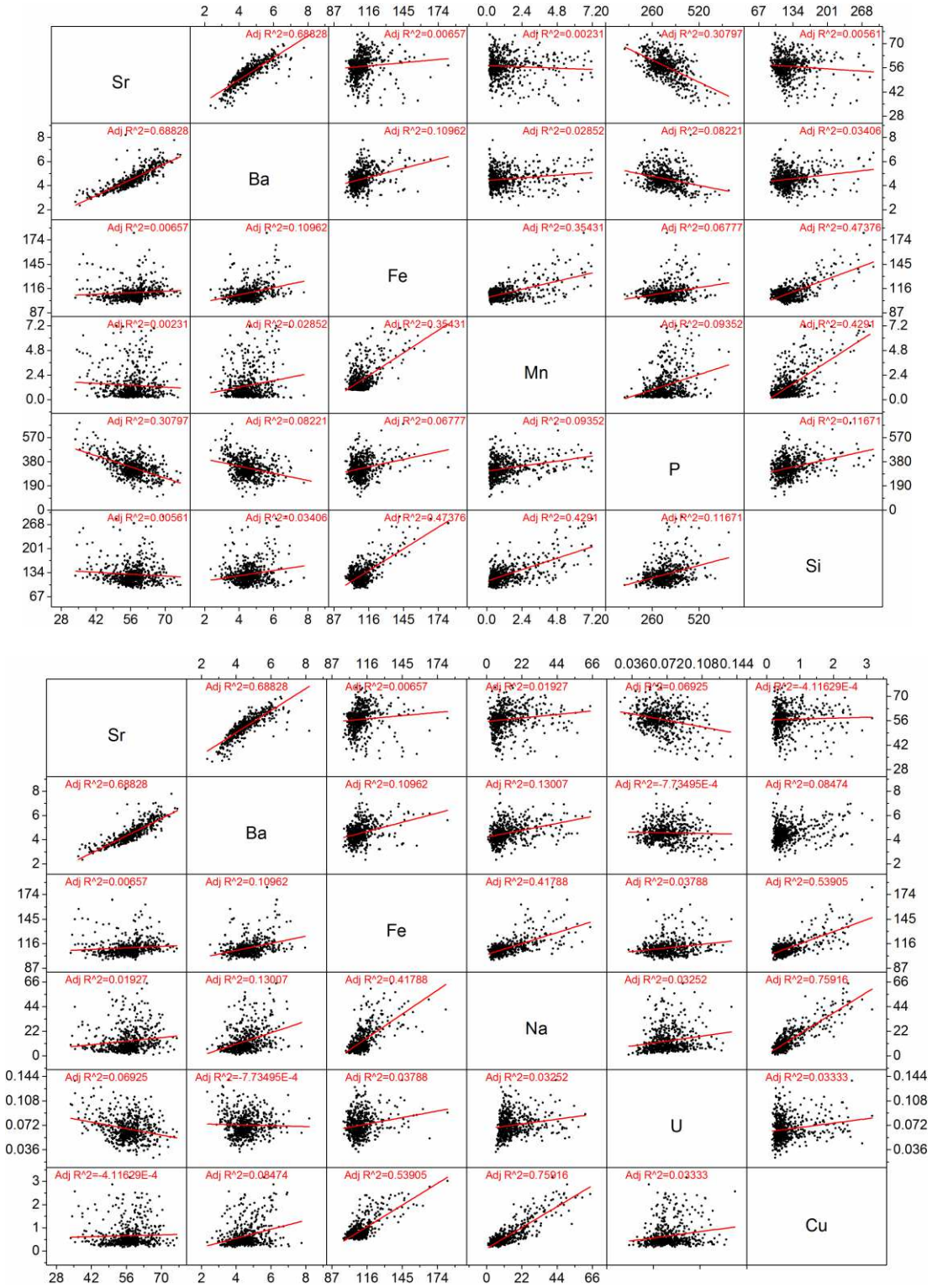

Figure C.8: Scatter plot matrix of the geochemical records of stalagmite VML22 for Sr, Ba, Fe vs. Mn, P and Si (top) and vs. Na, U and Cu (bottom). All trace element data are given in µg/g and were averaged to correspond to the isotope data sets as described in the text. Linear regression lines and the respective values of adjusted R^2 are indicated in red.

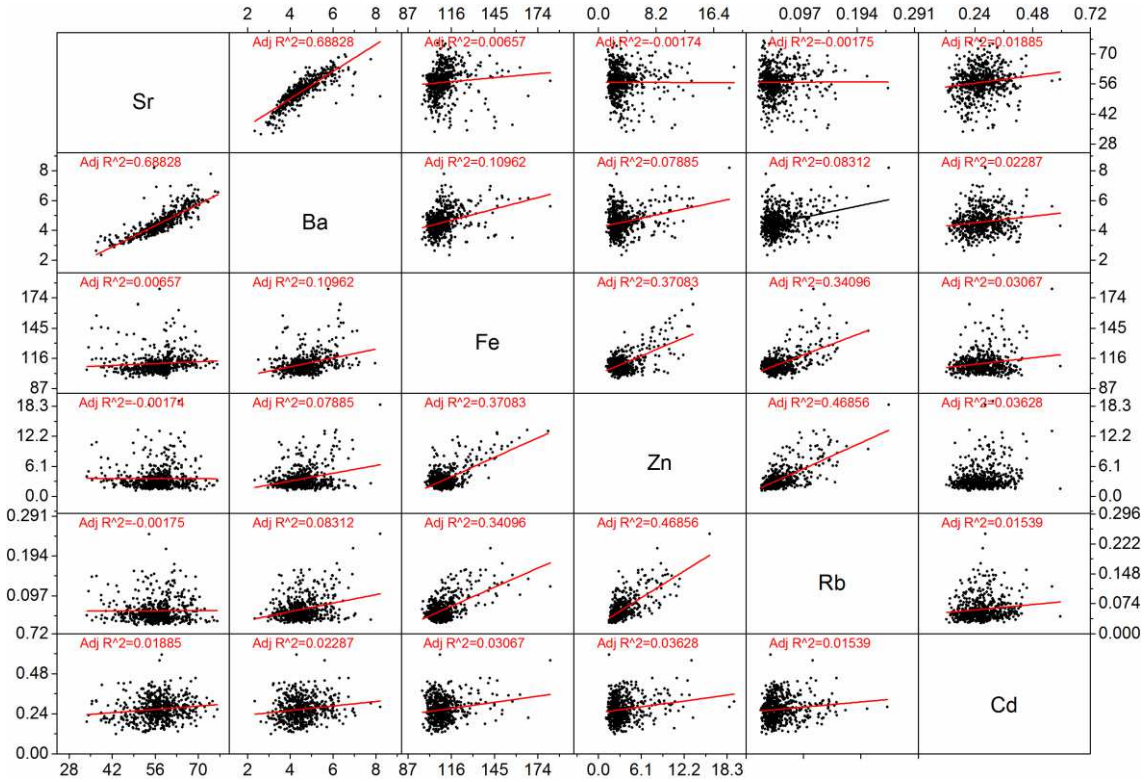

Figure C.9: Scatter plot matrix of the geochemical records of stalagmite VML22 for Sr, Ba, Fe, Zn, Rb and Cd. All trace element data are given in µg/g and were averaged to correspond to the isotope data sets as described in the text. Linear regression lines and the respective values of adjusted R^2 are indicated in red.

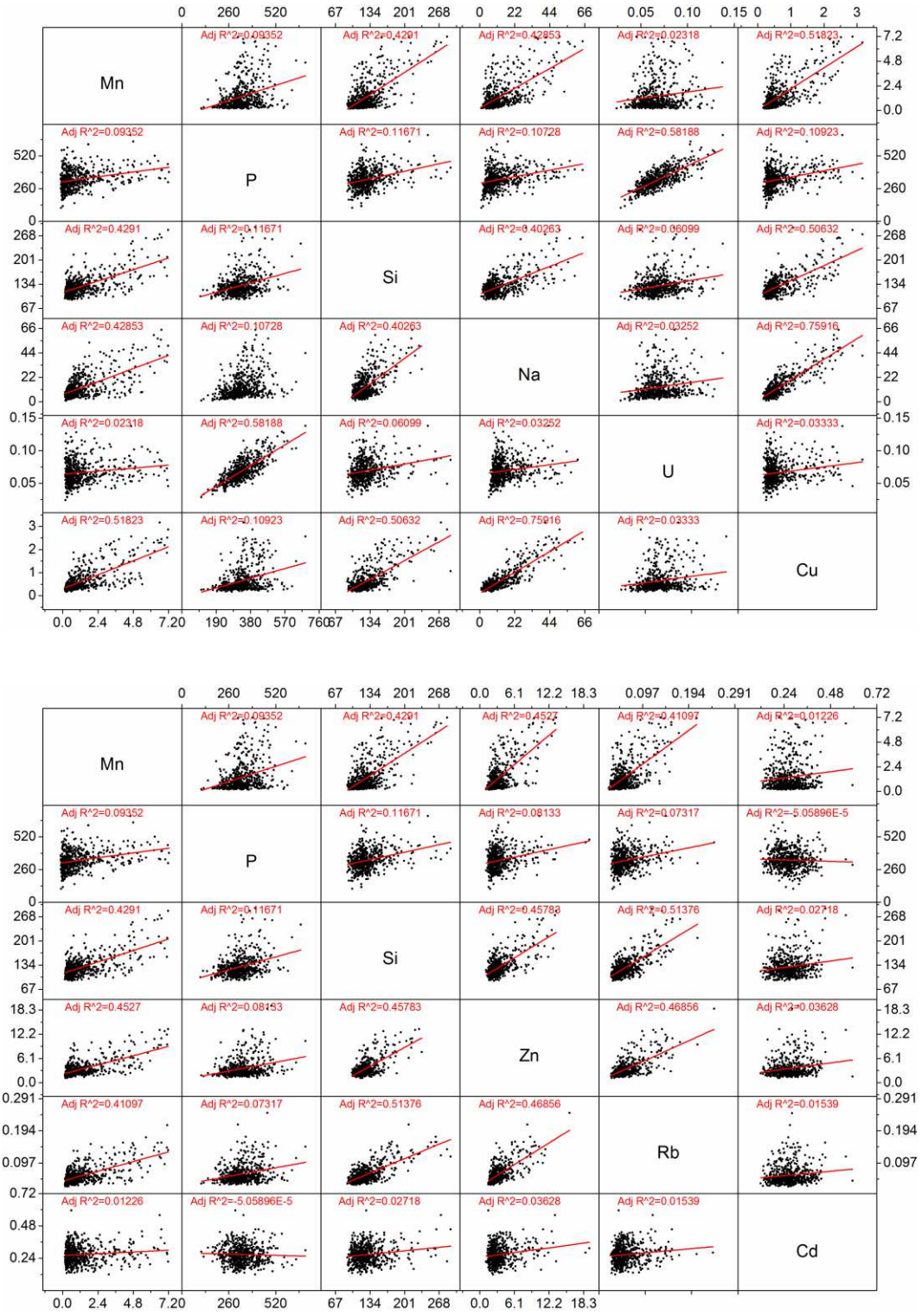

Figure C.10: Scatter plot matrix of the geochemical records of stalagmite VML22 for Mn, P, Si vs. Na, U and Cu (top) and vs. Zn, Rb and Cd (bottom). All trace element data are given in µg/g and were averaged to correspond to the isotope data sets as described in the text. Linear regression lines and the respective values of adjusted R^2 are indicated in red.

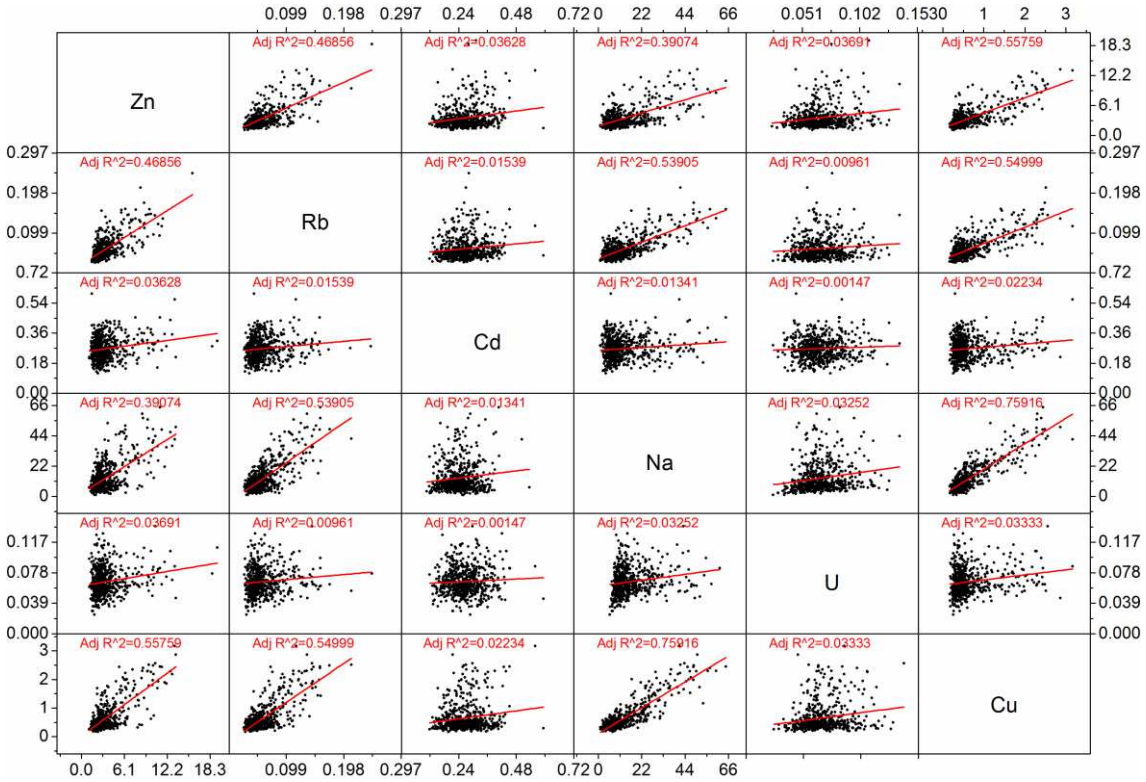

Figure C.11: Scatter plot matrix of the geochemical records of stalagmite VML22 for Zn, Rb, Cd, Na, U and Cu. All trace element data are given in µg/g and were averaged to correspond to the isotope data sets as described in the text. Linear regression lines and the respective values of adjusted R^2 are indicated in red.

C.2 Scatter Plots Stalagmite VSMS2

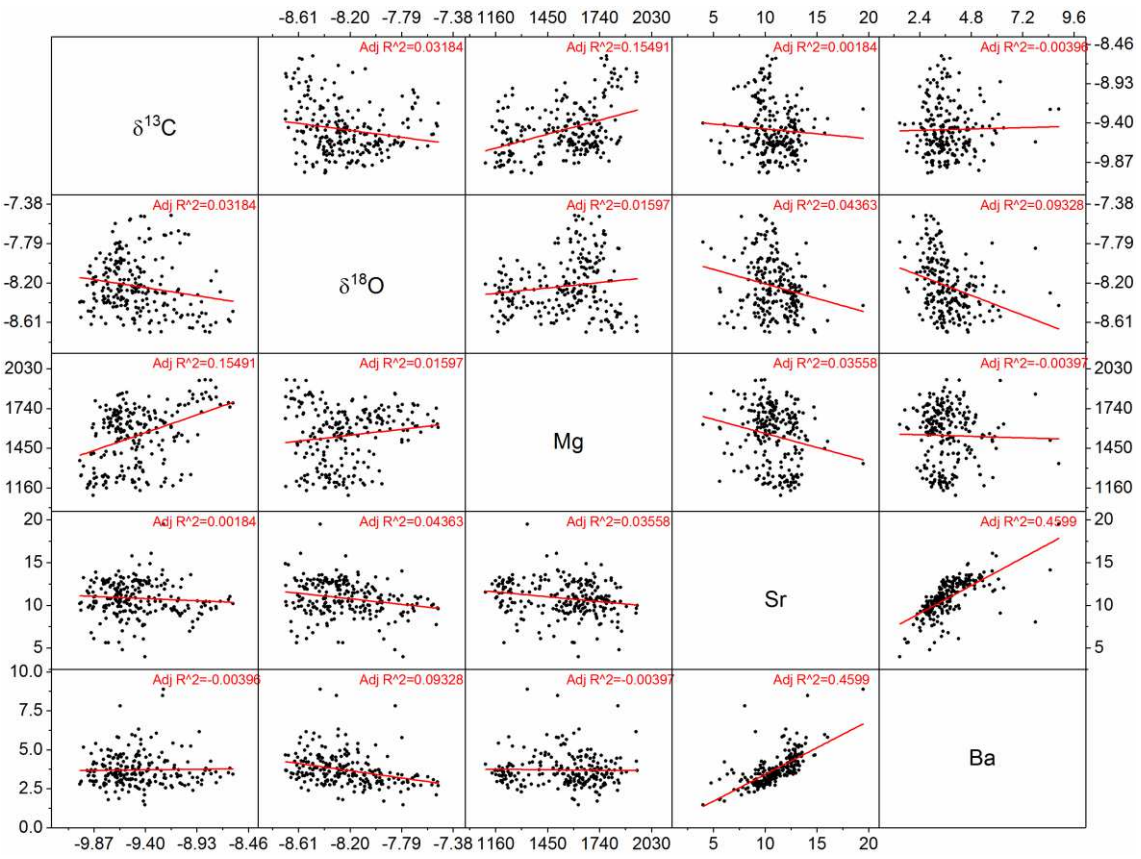

Figure C.12: Scatter plot matrix of the geochemical records of stalagmite VSMS2 attributed to Group I ($\delta^{13}C$, $\delta^{18}O$, Mg, Sr and Ba) during its first growth period. Stable isotope data are given as δ in ‰ relative to the V-PDB standard All trace element data are given in µg/g and are averaged to correspond to the isotope data sets as described in the text. Linear regression lines and the respective values of adjusted R^2 are indicated in red.

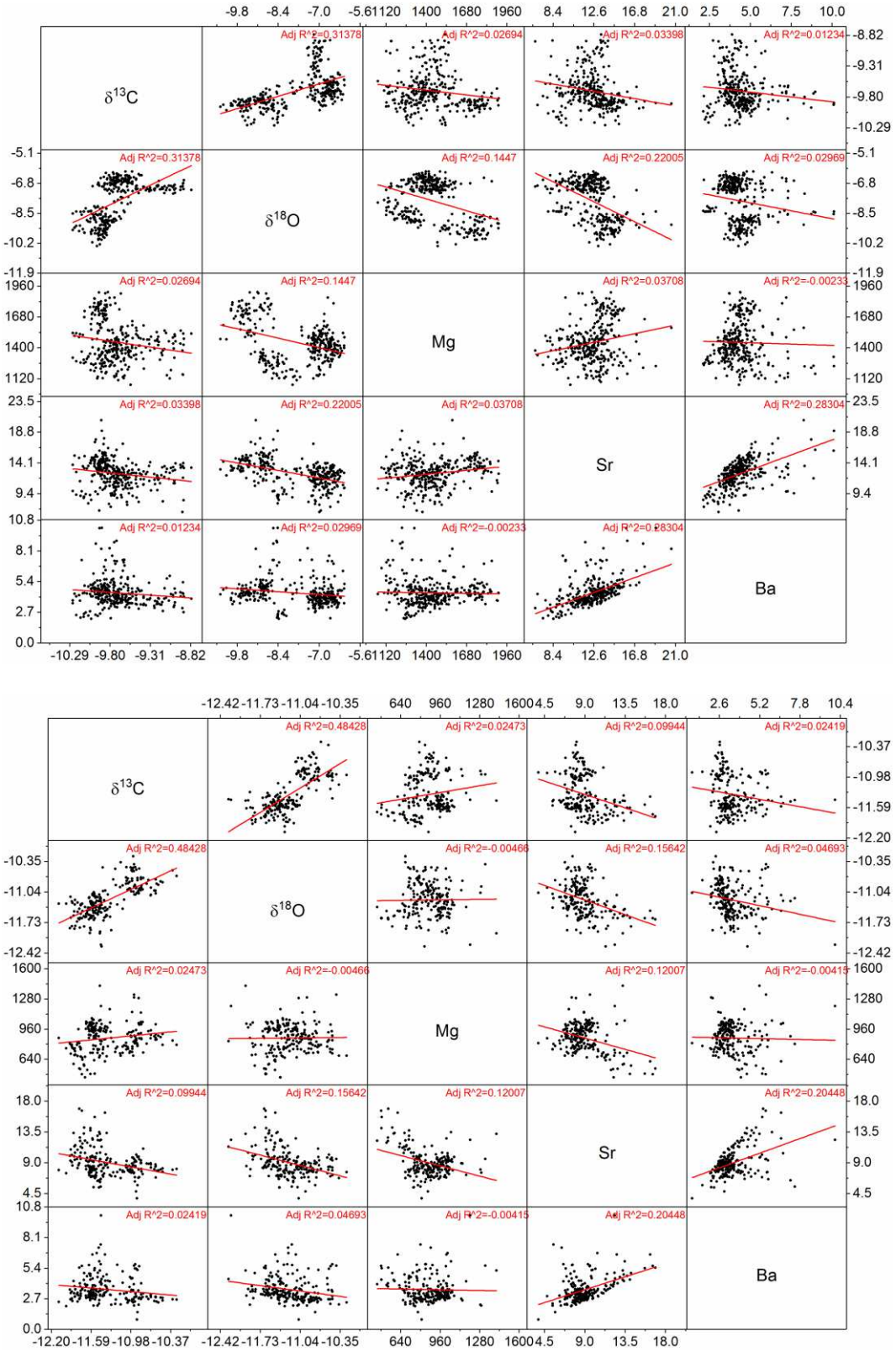

Figure C.13: As Figure C.12, but for the second (top) and third (bottom) growth periods of stalagmite VSMS2.

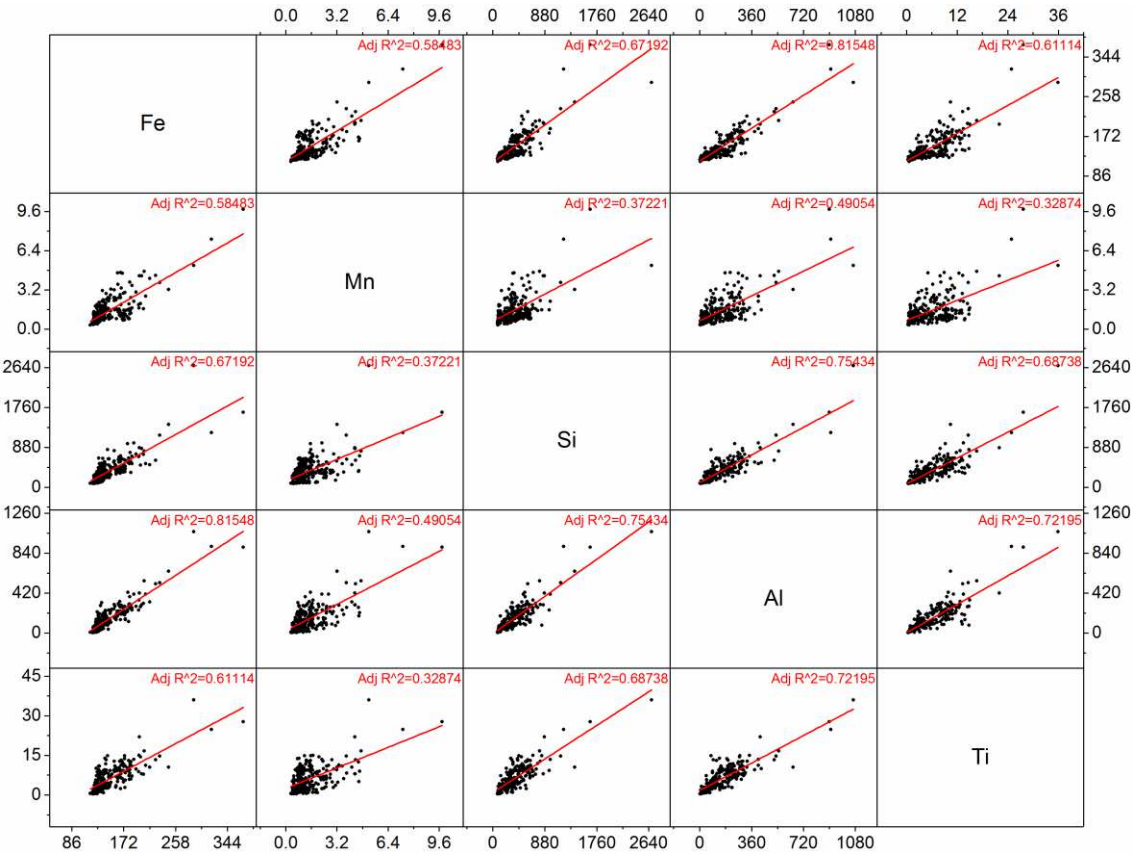

Figure C.14: Scatter plot matrix of the geochemical records of stalagmite VSMS2 attributed to Group II (Fe, Mn, Si, Al and Ti) during its first growth period. All trace element data are given in µg/g and are averaged to correspond to the isotope data sets as described in the text. Linear regression lines and the respective values of adjusted R^2 are indicated in red.

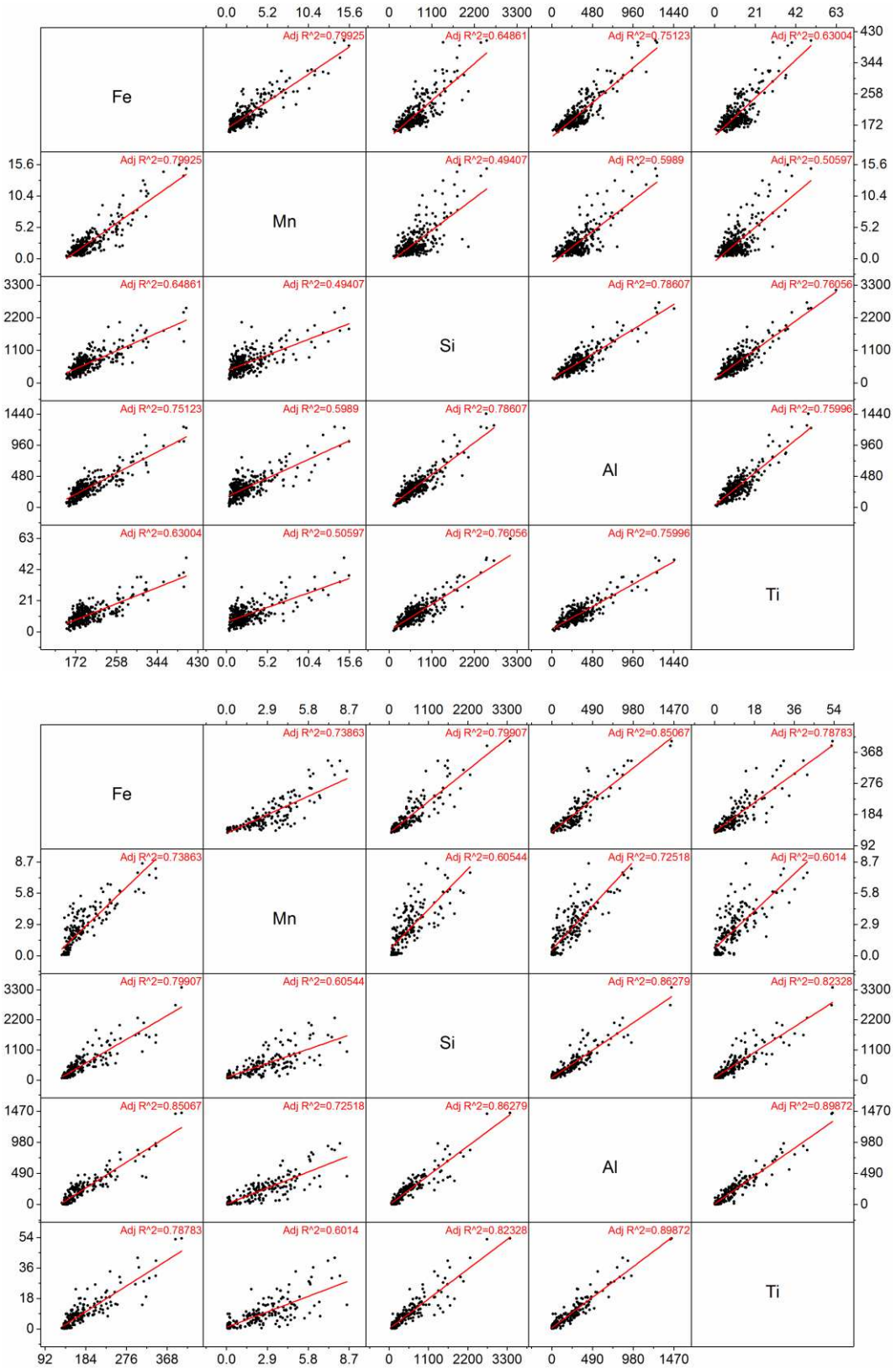

Figure C.15: As Figure C.12, but for the second (top) and third (bottom) growth periods of stalagmite VSMS2.

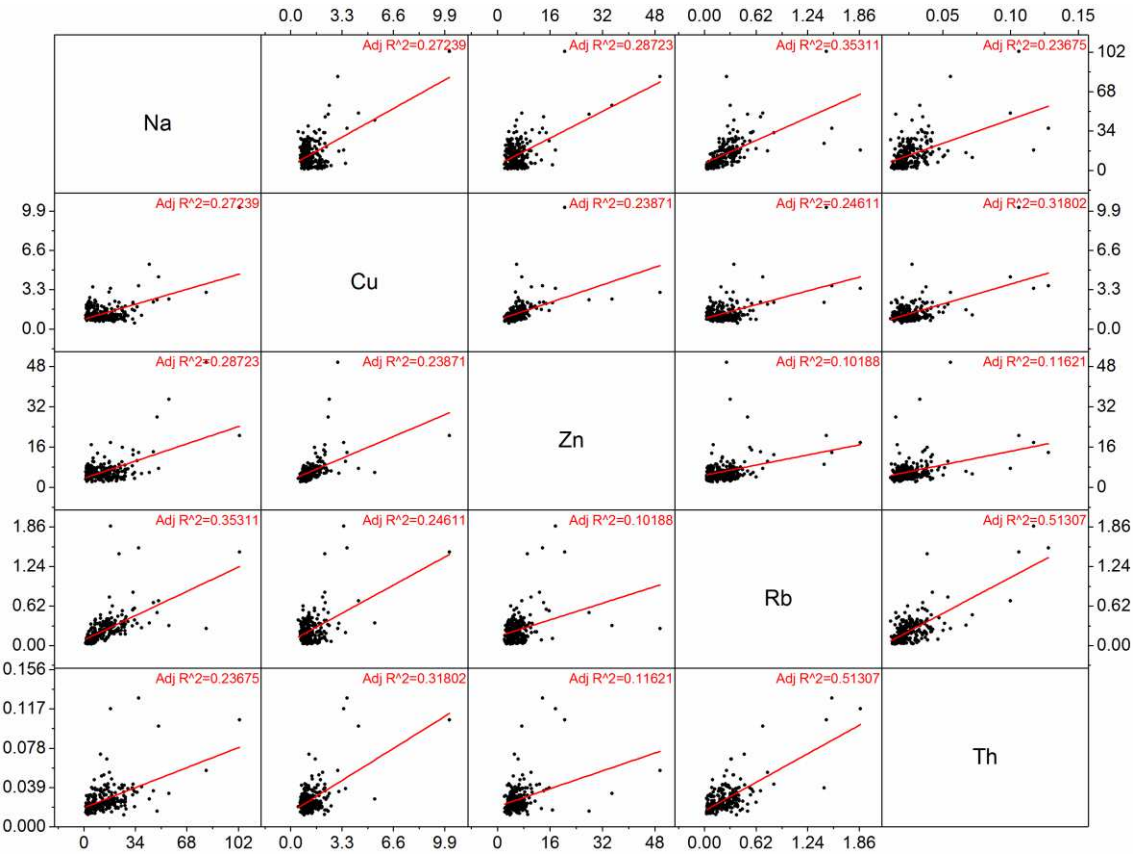

Figure C.16: Scatter plot matrix of the geochemical records of stalagmite VSMS2 attributed to Group II (Na, Cu, Zn, Rb and Th) during its first growth period. All trace element data are given in µg/g and are averaged to correspond to the isotope data sets as described in the text. Linear regression lines and the respective values of adjusted R^2 are indicated in red.

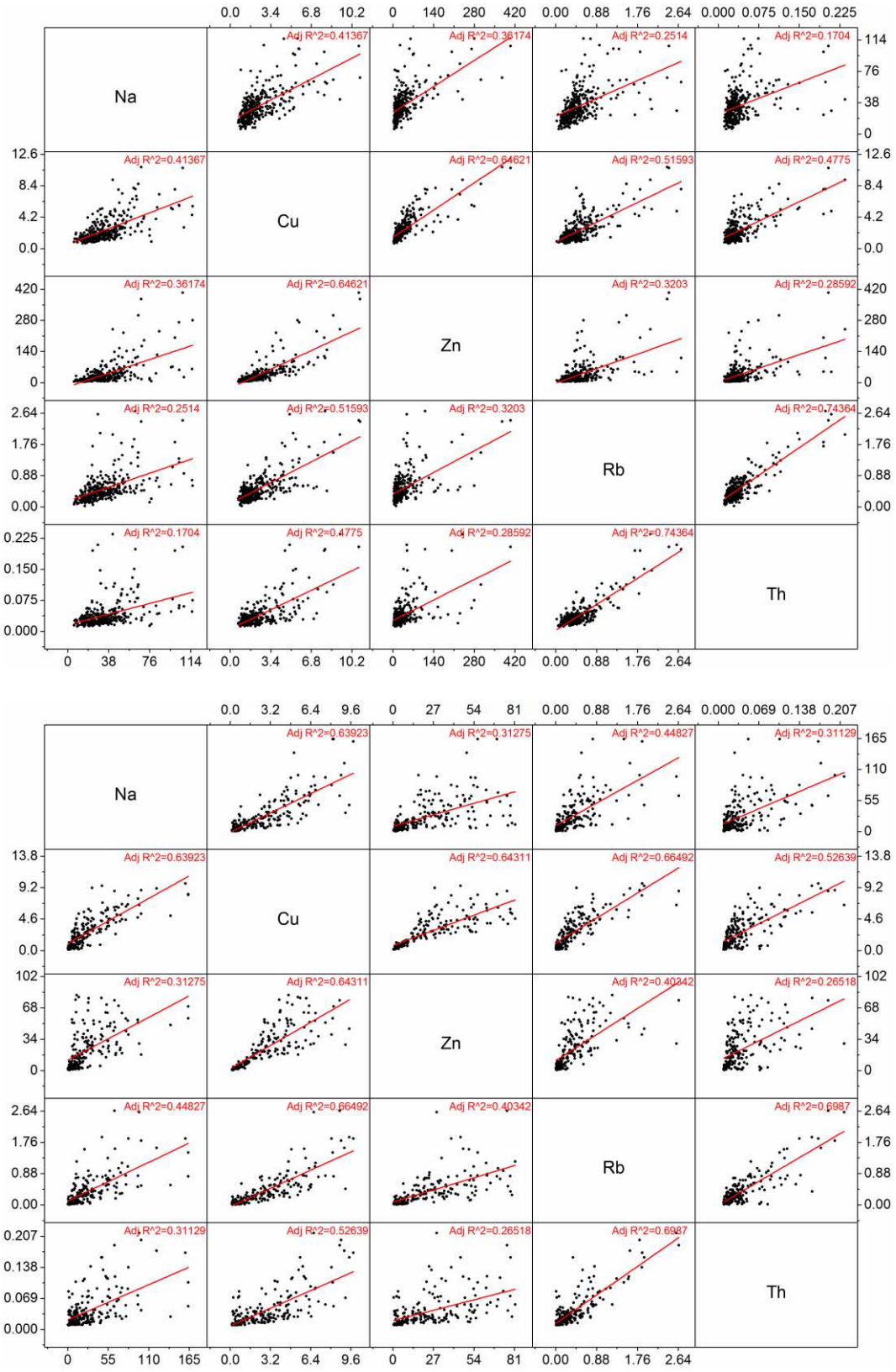

Figure C.17: As Figure C.16, but for the second (top) and third (bottom) growth periods of stalagmite VSMS2.

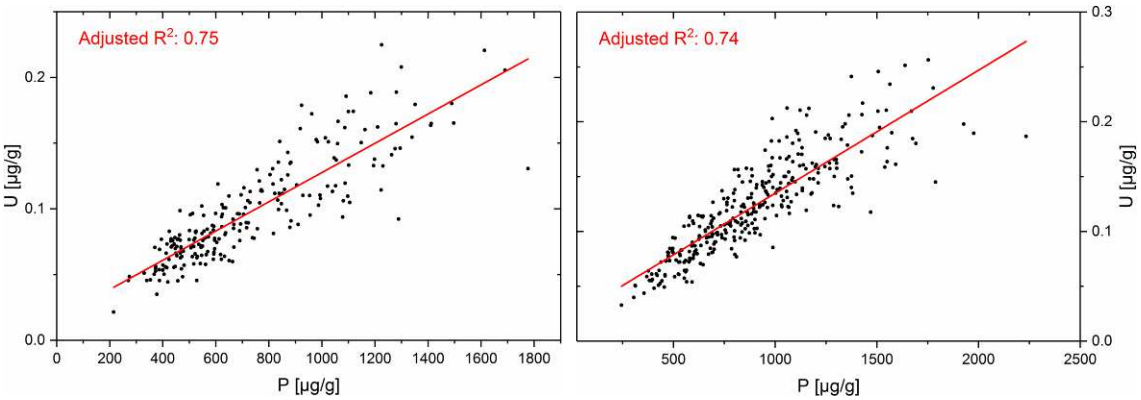

Figure C.18: Scatter plots for P vs. U from stalagmite VSMS2 during its first (left) and second (right) growth period. All trace element data are averaged to correspond to the isotope data sets as described in the text. Linear regression lines and the respective values of adjusted R^2 are indicated in red.

C.3 Frequency Analysis Stalagmite VML22

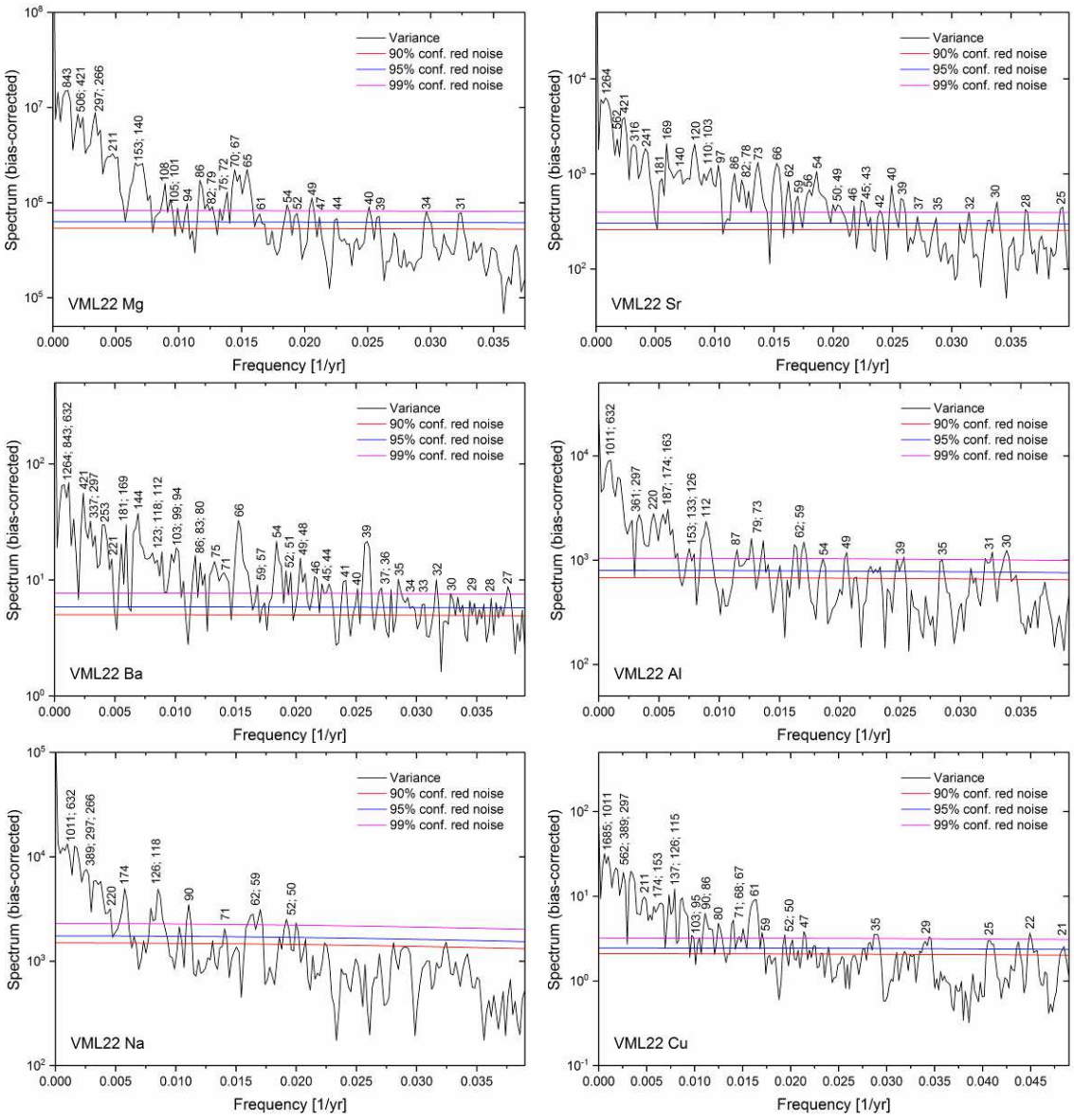

Figure C.19: Estimated red-noise spectra of the proxy signals from stalagmite VML22 for Mg, Sr, Ba, Al, Na and Cu. The numbers above peaks significant at the 95% and/or 99% confidence level indicate the respective periodicity (in years) of the potential cyclic behaviour represented by each peak.

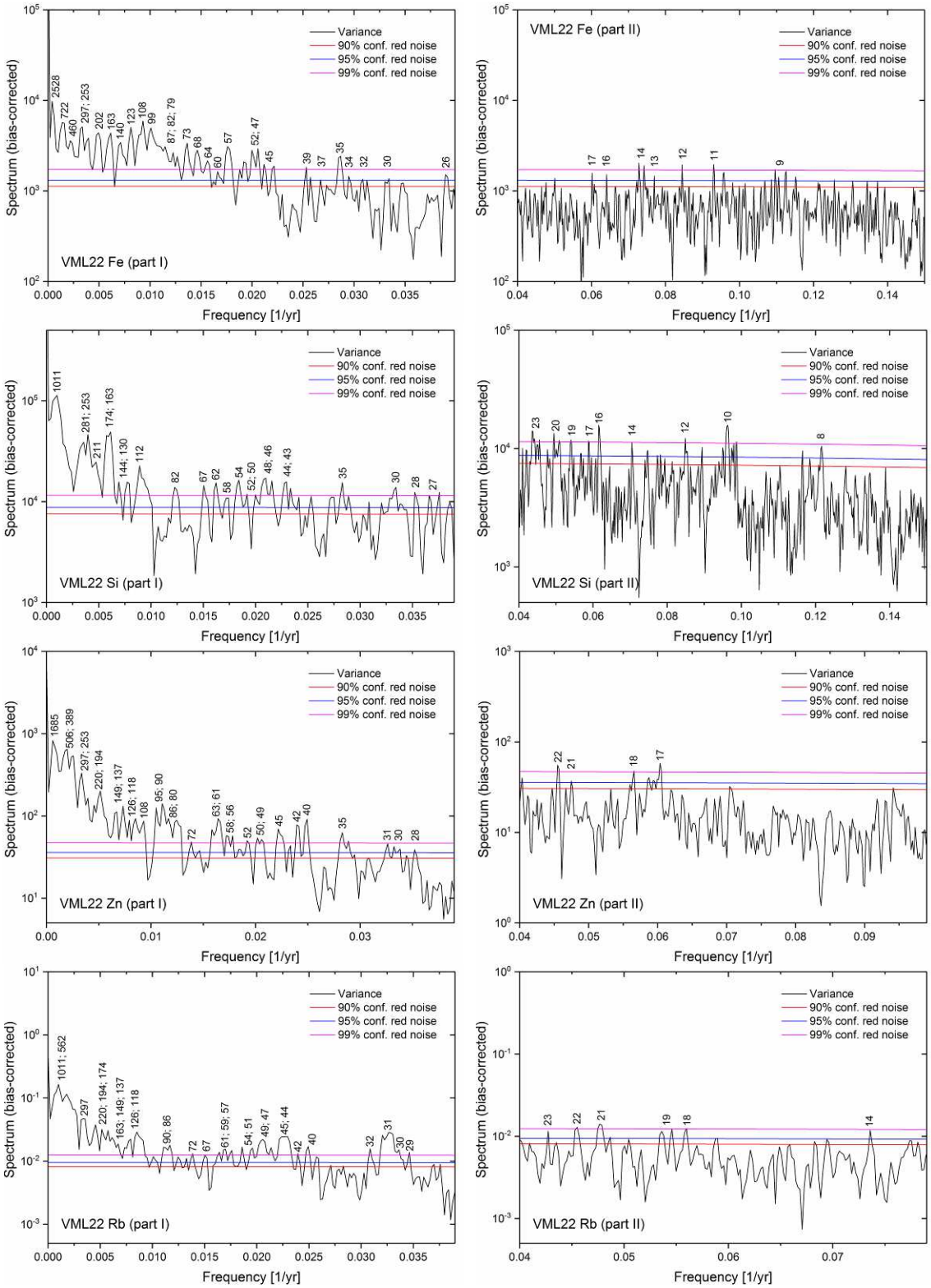

Figure C.20: As Figure C.19, but for Fe, Si, Zn and Rb. Each spectrum is illustrated in two parts (left and right) for better readability.

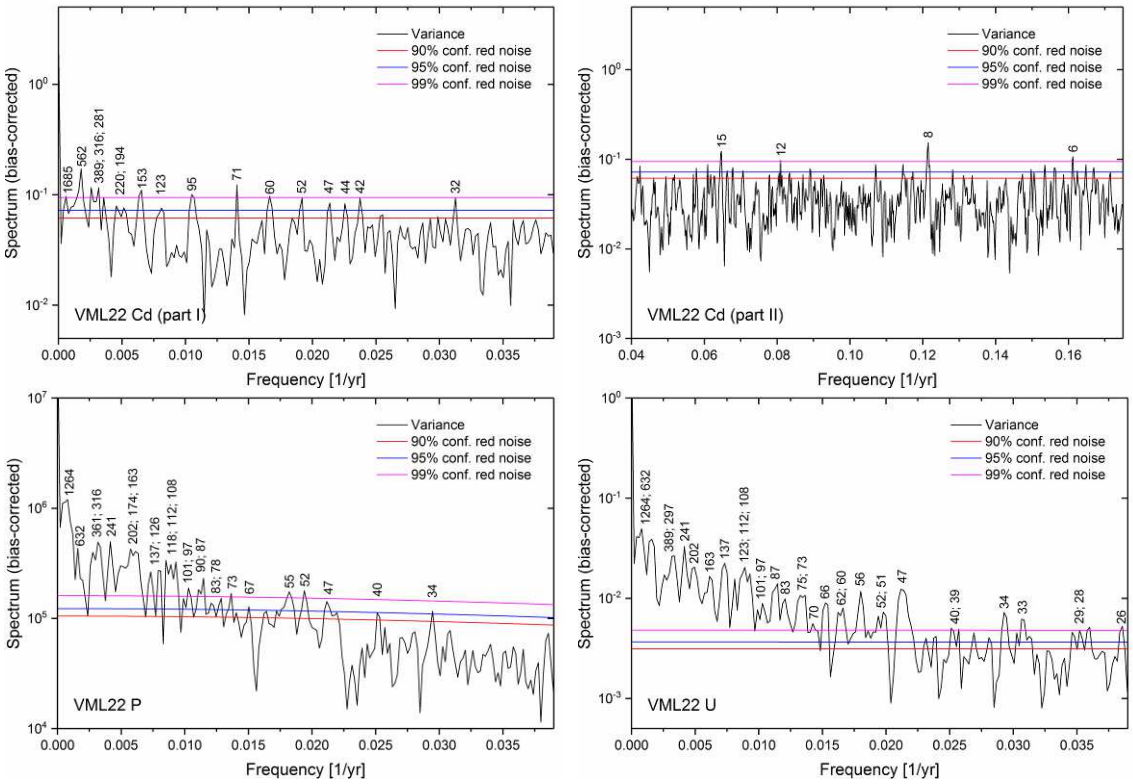

Figure C.21: As Figure C.19, but for Cd (top), P and U.

Table C.1: Statistically significant periodicities (cycle durations) identified by frequency analysis of the proxy records of stalagmite VML22 for all Group I elements, including their respective maximum error range down to ±1 years. The most prominent periodicities are indicated in red. All values are rounded to whole numbers.

$\delta^{18}O$		$\delta^{13}C$		Mg		Sr		Ba	
Period.	Error	Period.	Error	Period.	Error	Period.	Error	Period.	Error
1345	+135	423	+11	843	+171	1264	+421	1264	+421
192	+2	105	±1	506	+57	562	+71	843	+171
120	±1	94	±1	421	+37	421	+37	632	+92
107	±1	84	±1	297	+19	316	+20	421	+37
63		81		266	+15	241	+12	337	+24
58		78		211	±9	181	+7	297	+19
53		75		153	±5	169	±6	253	+13
43		69		140	±4	140	±4	221	+10
41		66		108	±2	120	±3	181	+7
40		64		105	±2	110	±2	169	±6
34		55		101	±2	103	±2	144	±4
33		53		94	±2	97	±2	123	±3
30		49		86	±1	86	+2	118	±3
28		48		82	±1	82	±1	112	+3
		47		79	±1	78	±1	103	+2
		46		75	±1	73	±1	99	+2
		45		72	±1	66	±1	94	+2
		44		70	±1	62	±1	86	+2
		42		67	±1	59	±1	83	+1
		40		65	±1	56	±1	80	±1
		39		61	±1	51	±1	75	+1
		28		54	±1	50	±1	71	+1
		27		52	±1	49		66	±1
				49		46		59	+1
				47		45		57	+1
				44		43		54	±1
				40		42		52	+1
				39		40		51	+1
				34		39		49	
				31		37		48	
						35		46	
						32		45	
						30		44	
						28		41	
						25		40	
								39	
								37	
								36	
								35	
								34	
								33	
								32	
								30	
								29	
								28	
								27	
								26	

Table C.2: Statistically significant periodicities (cycle durations) identified by frequency analysis of the proxy records of stalagmite VML22 for the remaining Group II elements, including their respective maximum error range down to ±1 years. The most prominent periodicities are indicated in red. All values are rounded to whole numbers.

Si		Al		Na		Cu		Zn	
Period.	Error	Period.	Error	Period.	Error	Period.	Error	Period.	Error
1011	+253	1011	+253	1011	+253	1685	+843	1685	+843
281	+17	632	+92	632	+92	1011	+253	506	+57
253	+13	361	+28	389	+33	562	+71	389	+33
211	±9	297	+19	297	+19	389	+33	297	+19
174	±6	220	+10	266	+15	297	+19	253	+13
163	+6	187	±7	220	+10	211	±9	220	+10
144	±6	174	±6	174	±6	174	±6	194	+8
130	±3	163	±5	126	±3	153	±5	149	+5
112	±2	153	±5	118	±3	137	±4	137	±4
82	±1	133	+4	90	±2	126	±3	126	±3
67	±1	126	±3	71	±1	115	±3	118	±3
62	±1	112	±2	62	±1	103	±2	108	±2
54	±1	87	±2	59	±1	95	±2	95	±2
52	±1	79	±1	52	±1	90	±2	90	±2
50	±1	73	±1	50	±1	86	+2 -1	86	+2 -1
48	±1	62	±1			80	±1	80	±1
46		59	±1			71	±1	72	±1
44		54	±1			68	±1	63	±1
43		49	±1			67	±1	61	±1
35		39				61	±1	58	±1
30		35				59	±1	56	±1
28		31				52	±1	52	±1
27		30				50	±1	50	±1
23						47		49	±1
20						35		45	
19						29		42	
17						25		40	
16						22		35	
14						21		31	
12								30	
10								28	
8								22	
4								21	
3								18	
								17	

Table C.3: Statistically significant periodicities (cycle durations) identified by frequency analysis of the proxy records of stalagmite VML22 for Fe, Mn, P and U, including their respective maximum error range down to ±1 years. The most prominent periodicities are indicated in red. All values are rounded to whole numbers.

Fe		Mn		P		U	
Period.	Error	Period.	Error	Period.	Error	Period.	Error
2528	+2528	2528	+2528	1264	+421	1264	+421
722	+116	562	+72	632	+92	632	+92
460	+46	389	+33	361	+28	389	+33
297	+19	316	+20	316	+20	297	+19
253	+13	202	+9	241	+12	241	+12
202	+9	174	±6	202	+9	202	+9
163	+6 -5	158	±6	174	±6	163	+6
140	±4	137	±4	163	+6	137	±4
123	±3	108	±2	137	±4	123	±3
108	±2	97	±2	126	±3	112	±2
99	±2	70	±1	118	±3	108	±2
87	±2	62	±1	112	±2	101	±2
82	±1	59	±1	108	±2	97	±2
79	±1	54	±1	101	±2	87	±2
73	±1	52	±1	97	±2	83	±2
68	±1	45		90	±2	75	±1
64	±1	39		87	±2	73	±1
60	±1	38		83	±1	70	±1
57	±1	35		78	±1	66	±1
52	±1			73	±1	62	±1
47				67	±1	60	±1
45				64	±1	56	±1
39				55	±1	52	±1
37				52	+1	51	±1
35				47		47	
34				40		40	
32				34		39	
30						34	
26						33	
17						29	
16						28	
14						26	
13							
12							
11							
9							
5							
4							
3							

C.4 Frequency Analysis Stalagmite VSMS2

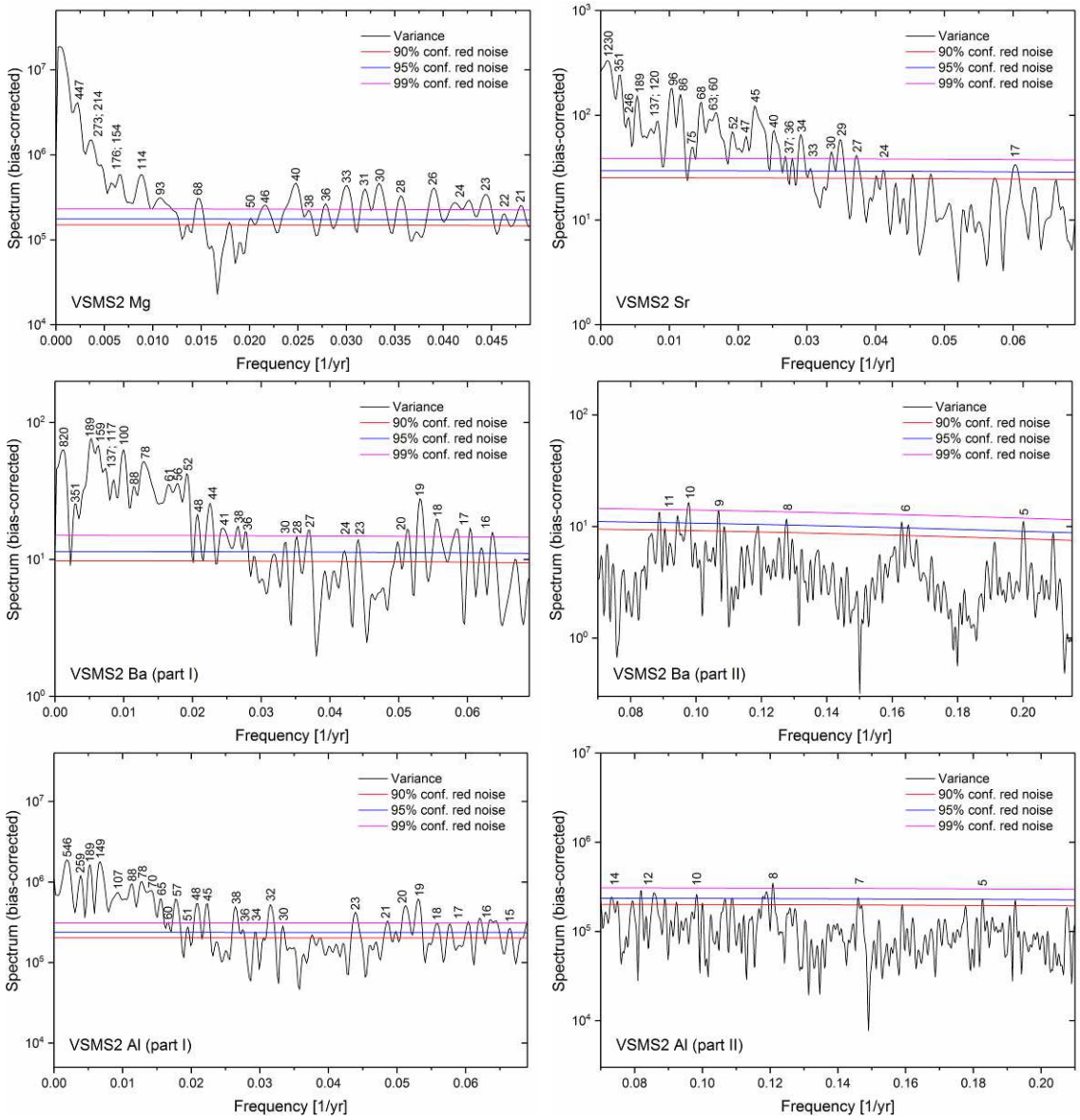

Figure C.22: Estimated red-noise spectra of the proxy signals from stalagmite VSMS2 for Mg, Sr, Ba and Al. The numbers above peaks significant at the 95% and/or 99% confidence level indicate the respective periodicity (in years) of the potential cyclic behaviour represented by each peak.

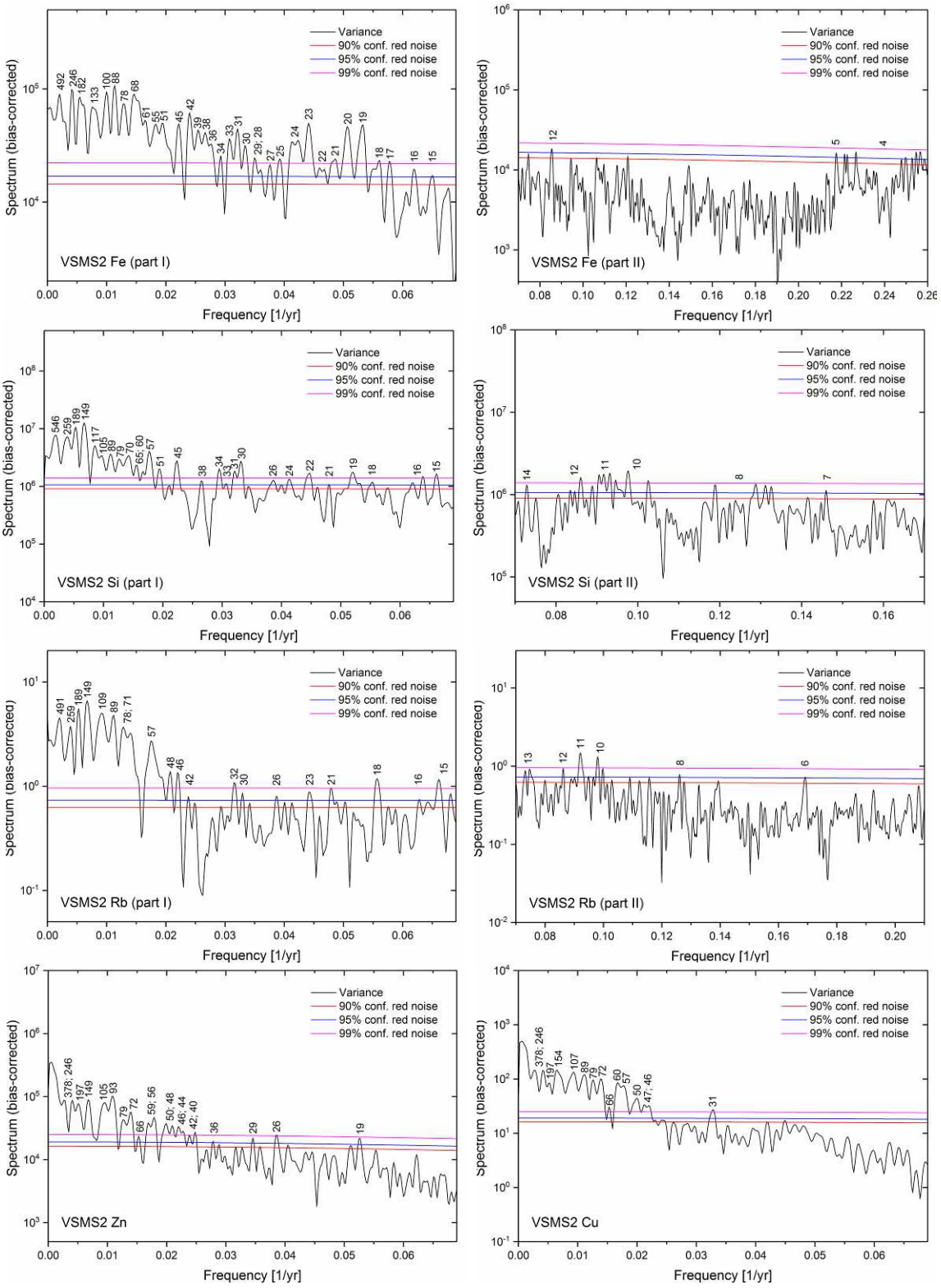

Figure C.23: As Figure C.22, but for Fe, Si, Rb, Zn and Cu.

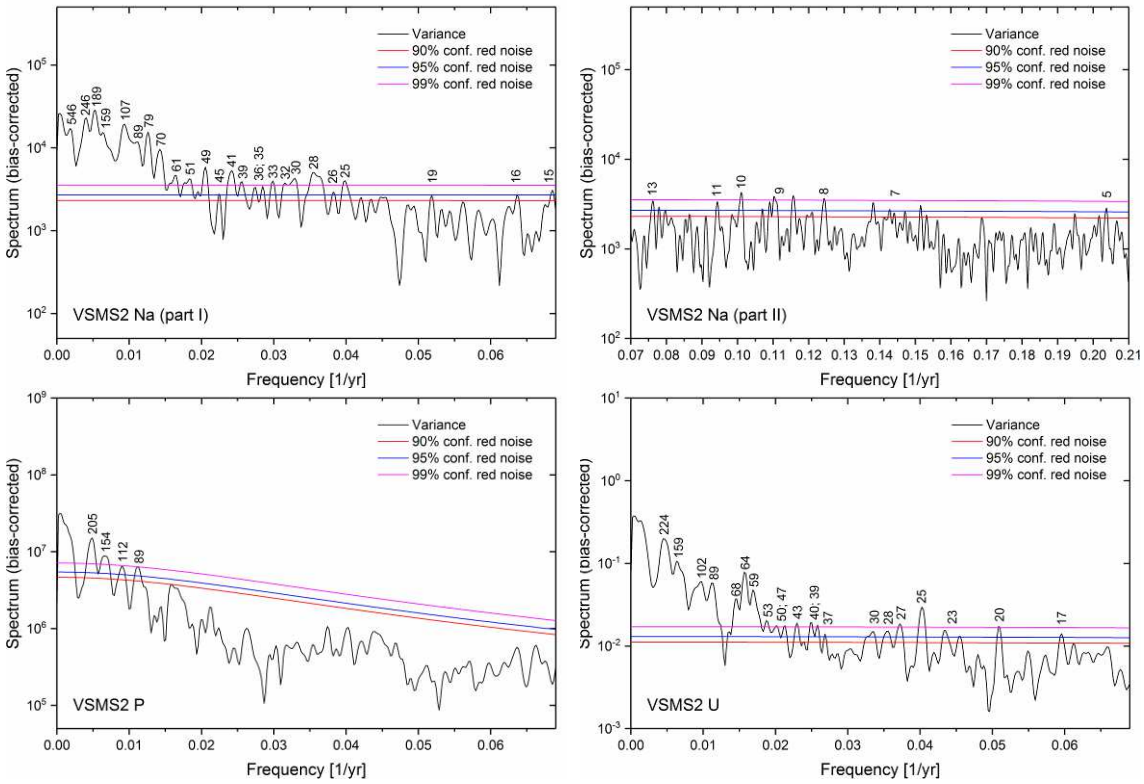

Figure C.24: As Figure C.22, but for Na, P and U.

C.5 R Code for Averaging Trace Element Data

Stalagmite VML22

```
# removing previous outputs

rm(list = ls())

# set working directory to source file location

setwd("E:/Promotion/Proben und Daten/LA-ICP-MS Mainz/Auswerte-Dateien/Spurenelemente VML22")


# importing data from .csv file: Trace element concentrations vs. depth

d <- read.csv("Cd_DFT.csv", header = TRUE)


# identifying the depths exceeding consecutive depth increments of 0.189 mm (spatial resolution of stable isotope data)

n <- 1

i <- 1

dlimits <- 1

for (n in 1:17269)

  {

  if (d[n,1] > i*0.189009009)

    {

    dlimits[n] <- n

    depthlimits <- data.frame(dlimits)

    i = i+1

  }
```

```
}

# deleting blank columns

depthsfinal <- data.frame(depthlimits[complete.cases(depthlimits),])

# calculating the arithmetic means of the trace element concentrations for consecutive depth increments of 0.189 mm (spatial resolution of stable isotope data)

n <- 1

means <- 0

for (n in 1:17269)

  {

  means[n] <- mean (d[depthsfinal[n,1]:(depthsfinal[n+1,1]-1),2], na.rm = TRUE, trim = 0)

  meanscalc <- data.frame(means)

}

# saving output in .txt file

write.table(meanscalc, file="trace element_averaged_new.txt", sep=" ")
```

Stalagmite VSMS2

```
# set working directory to source file location

setwd("D:/Promotion/Proben und Daten/LA-ICP-MS Mainz/Auswerte-Dateien/Spurenelemente VSMS2")


# removing previous outputs

rm(list = ls())


# importing data from .csv file: Trace element concentrations vs. depth

d <- read.csv("Zn67_DFT.csv", header = TRUE)


# identifying the depths exceeding consecutive depth increments of 0.199 mm (spatial resolution of stable isotope data)

n <- 1

i <- 1

dlimits <- 1

for (n in 1:23457)

  {

 if (d[n,1] > i*0.199081992031872)

   {

   dlimits[n] <- n

   depthlimits <- data.frame(dlimits)

   i = i+1

  }
```

```
}

# deleting blank columns

depthsfinal <- data.frame(depthlimits[complete.cases(depthlimits),])

# calculating the arithmetic means of the trace element concentrations for consecutive depth increments of 0.199 mm (spatial resolution of stable isotope data)

n <- 1

means <- 0

for (n in 1:23457)

  {

  means[n] <- mean (d[depthsfinal[n,1]:(depthsfinal[n+1,1]-1),2], na.rm = TRUE, trim = 0)

  meanscalc <- data.frame(means)

}

# saving output in .txt file

write.table(meanscalc, file="trace element_averaged.txt", sep=" ")
```

D Geochemical Records in the Depth Domain

D.1 Stalagmite VML22

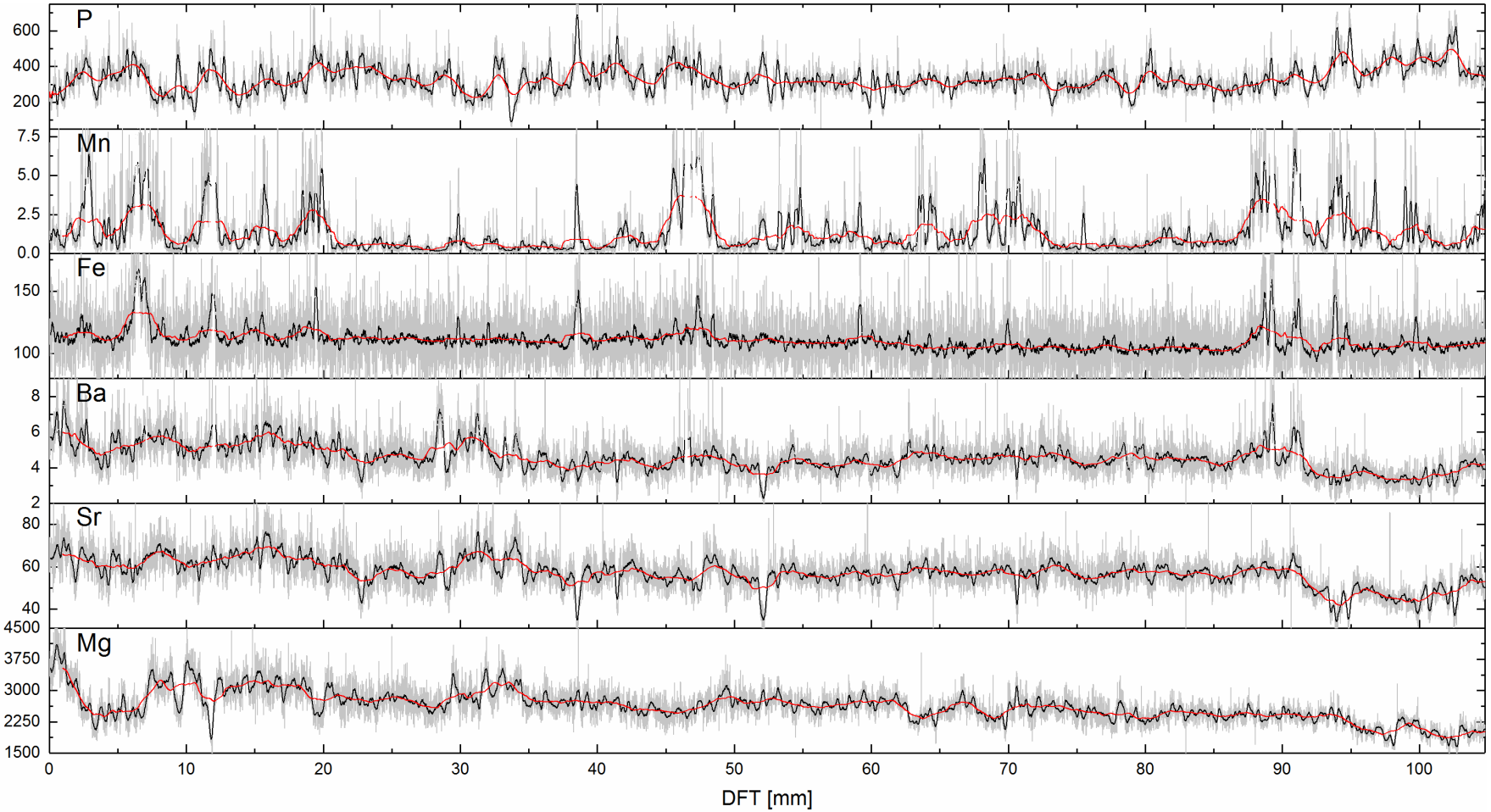

Figure D.1: Overview of the most important trace elements for this study from stalagmite VML22, plotted in the depth domain. All concentrations are given in µg/g. Grey lines indicate the original concentrations after all corrections, black lines are 30-pt smoothed data (weighted Adjacent-Averaging), red lines are 300-pt smoothed data.

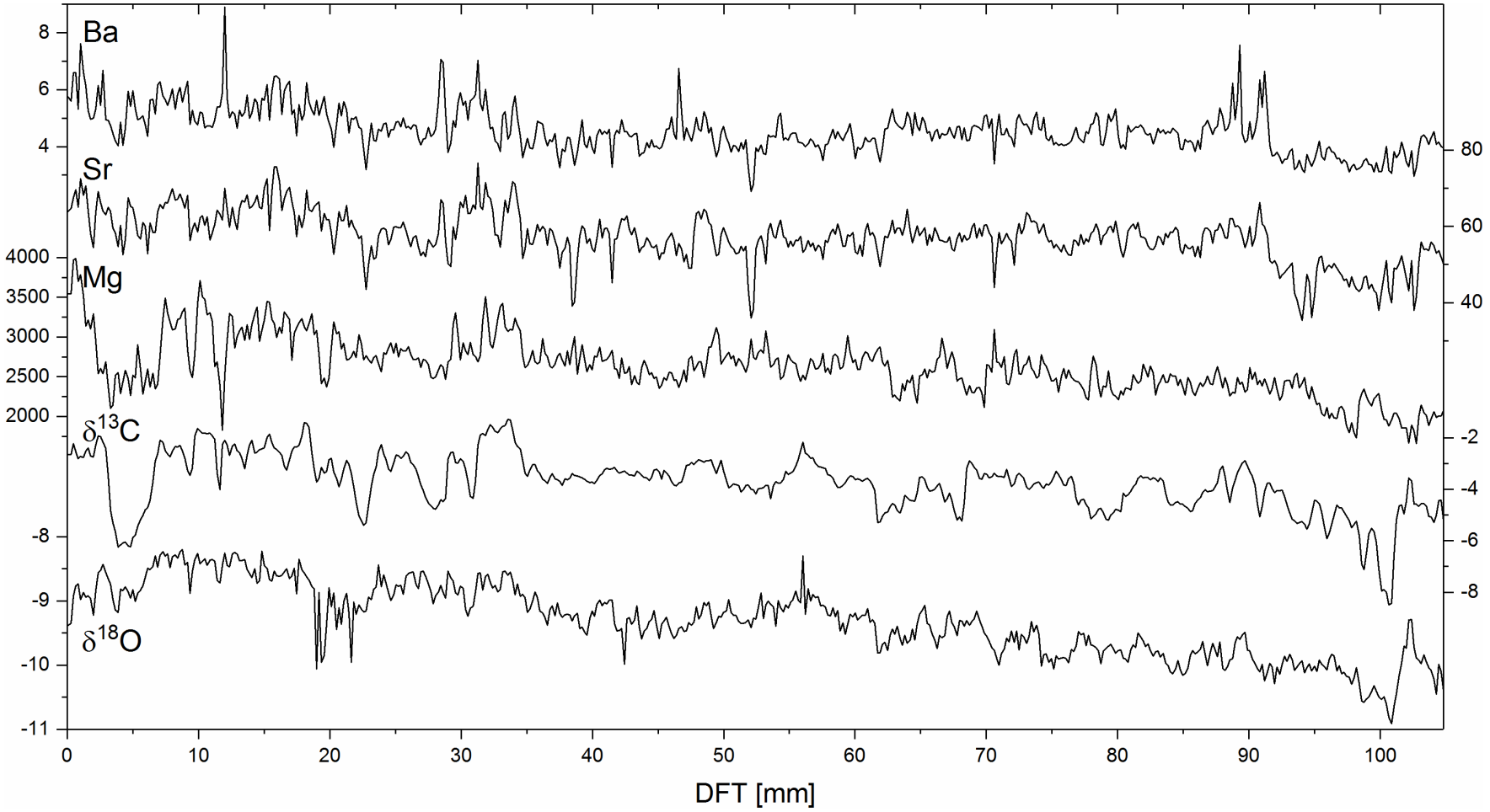

Figure D.2: Geochemical proxy records of stalagmite VML22 attributed to Group I: $\delta^{18}O$, $\delta^{13}C$, Mg, Sr and Ba; plotted in the depth domain. Both stable isotope ratios are expressed in ‰ as δ values relative to the V-PDB standard, all trace element concentrations are given in µg/g and are averaged to match the resolution of the isotope data sets (Section 4.6).

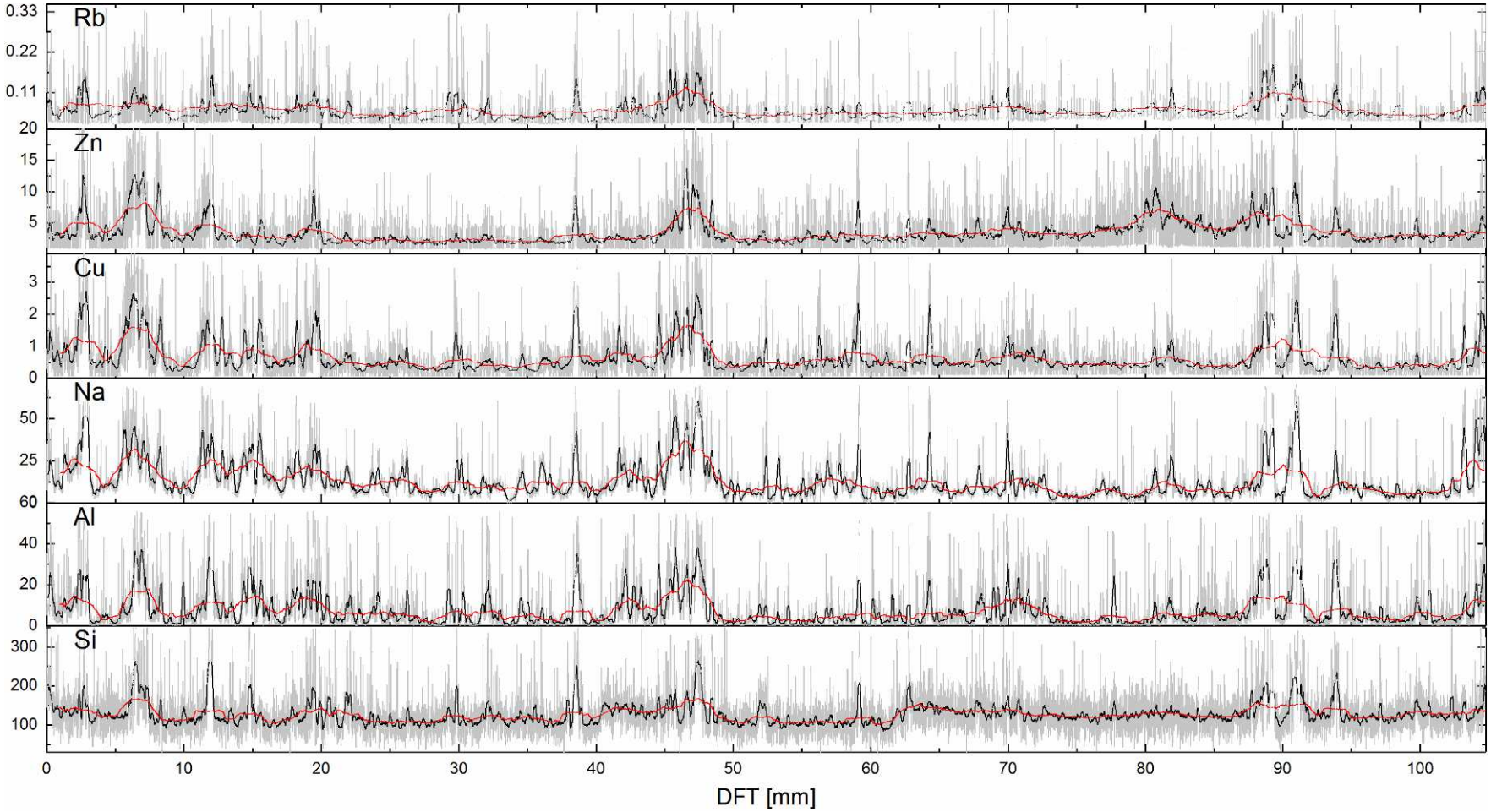

Figure D.3: Geochemical proxy records of stalagmite VML22 attributed to Group II: Si, Al, Na, Cu, Zn and Rb; plotted in the depth domain. All concentrations are given in µg/g. Grey lines indicate the original concentrations after all corrections, black lines are 30-pt smoothed data (weighted Adjacent-Averaging), red lines are 300-pt smoothed data.

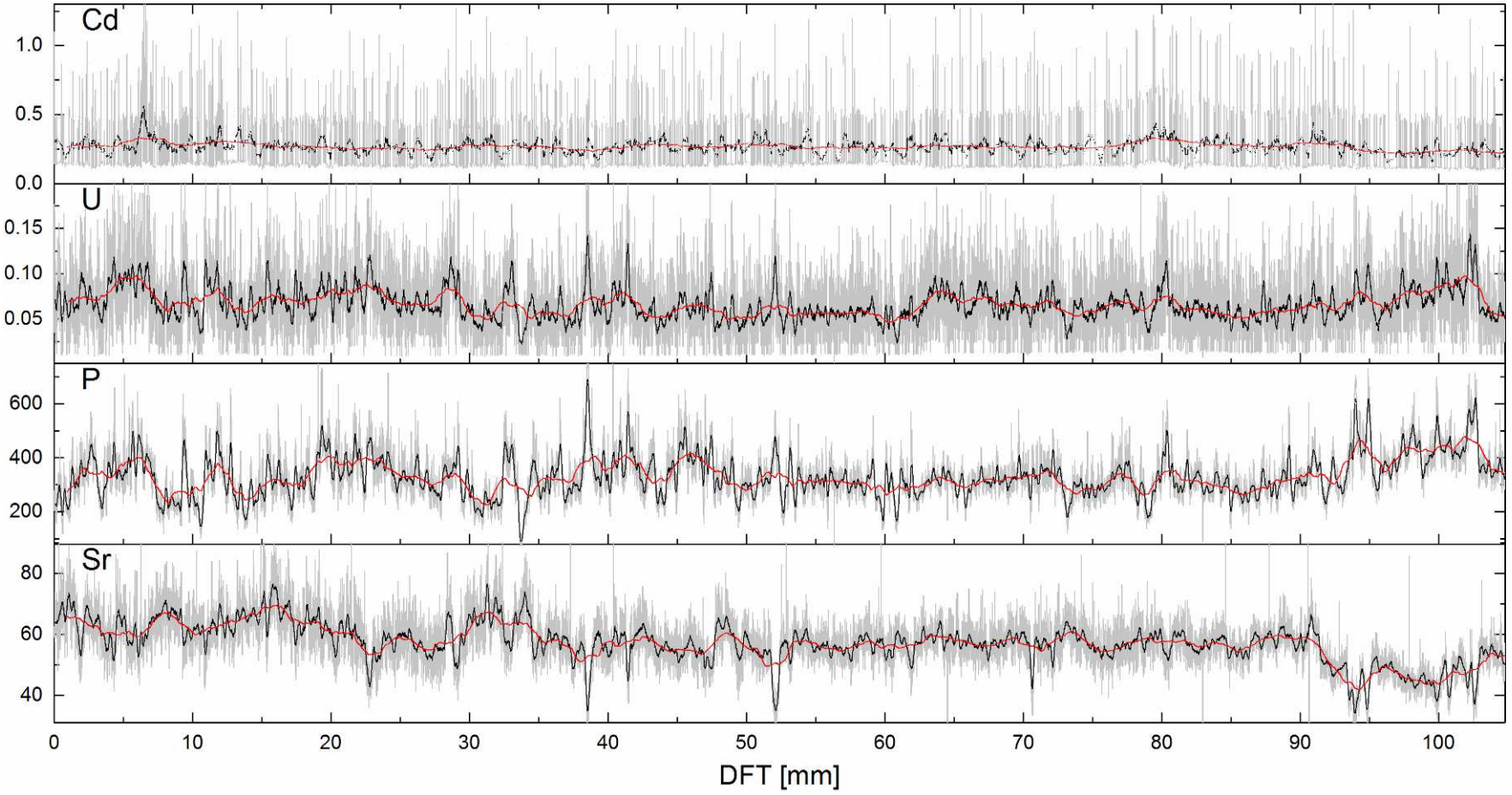

Figure D.4: Geochemical proxy records of stalagmite VML22 attributed to Group III (P and U) including Sr for comparison and Cd for the sake of completeness, plotted in the depth domain. All concentrations are given in µg/g. Grey lines indicate the original concentrations after all corrections, black lines are 30-pt smoothed data (weighted Adjacent-Averaging), red lines are 300-pt smoothed data;

D.2 Stalagmite VSMS2

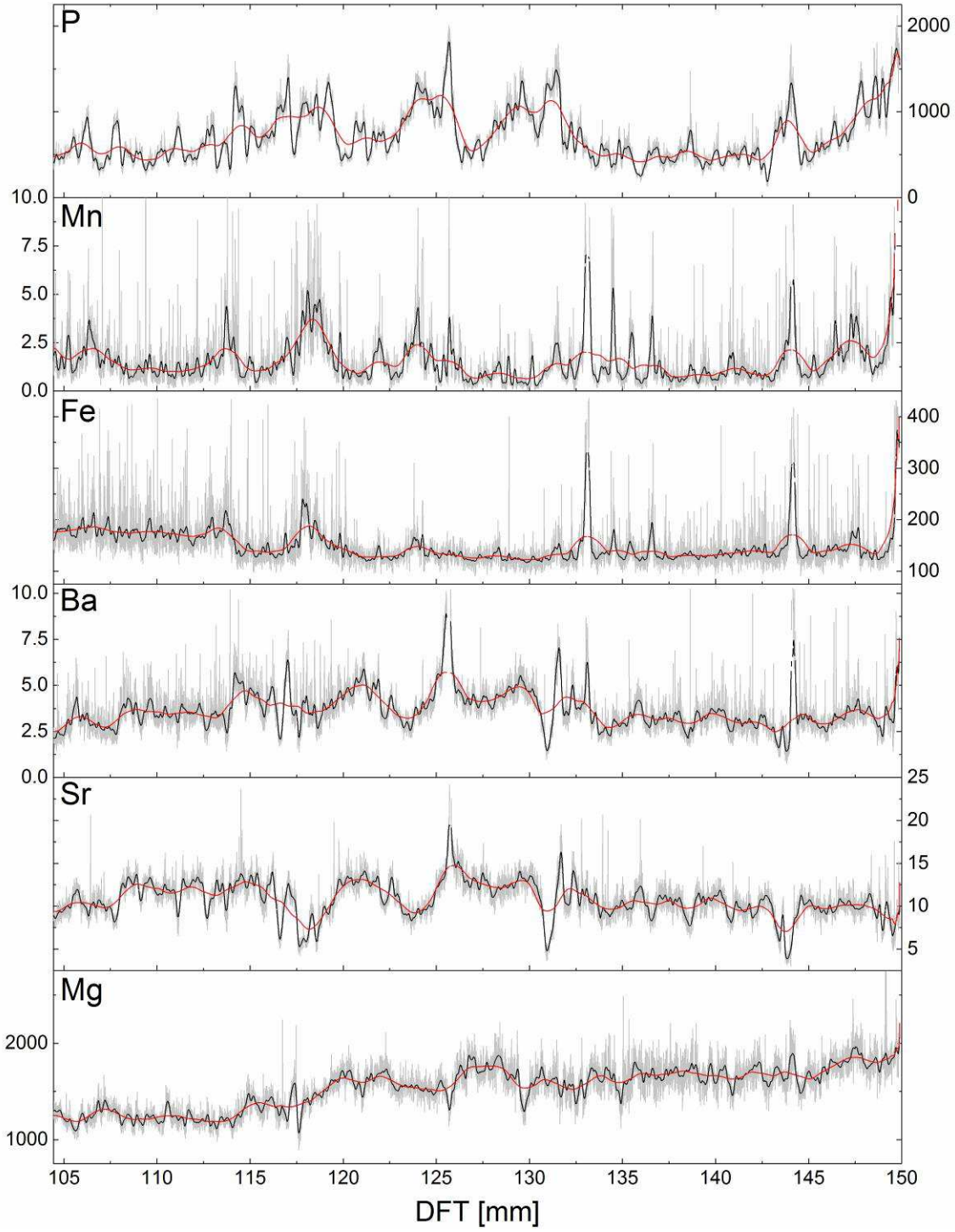

Figure D.5: Trace element concentrations (in µg/g) of Mg, Sr, Ba, Fe, Mn and P from stalagmite VSMS2 during its first growth period, plotted in the depth domain. Grey lines indicate the original concentrations after all corrections, black lines are 30-pt smoothed data (weighted Adjacent-Averaging), red lines are 300-pt smoothed data

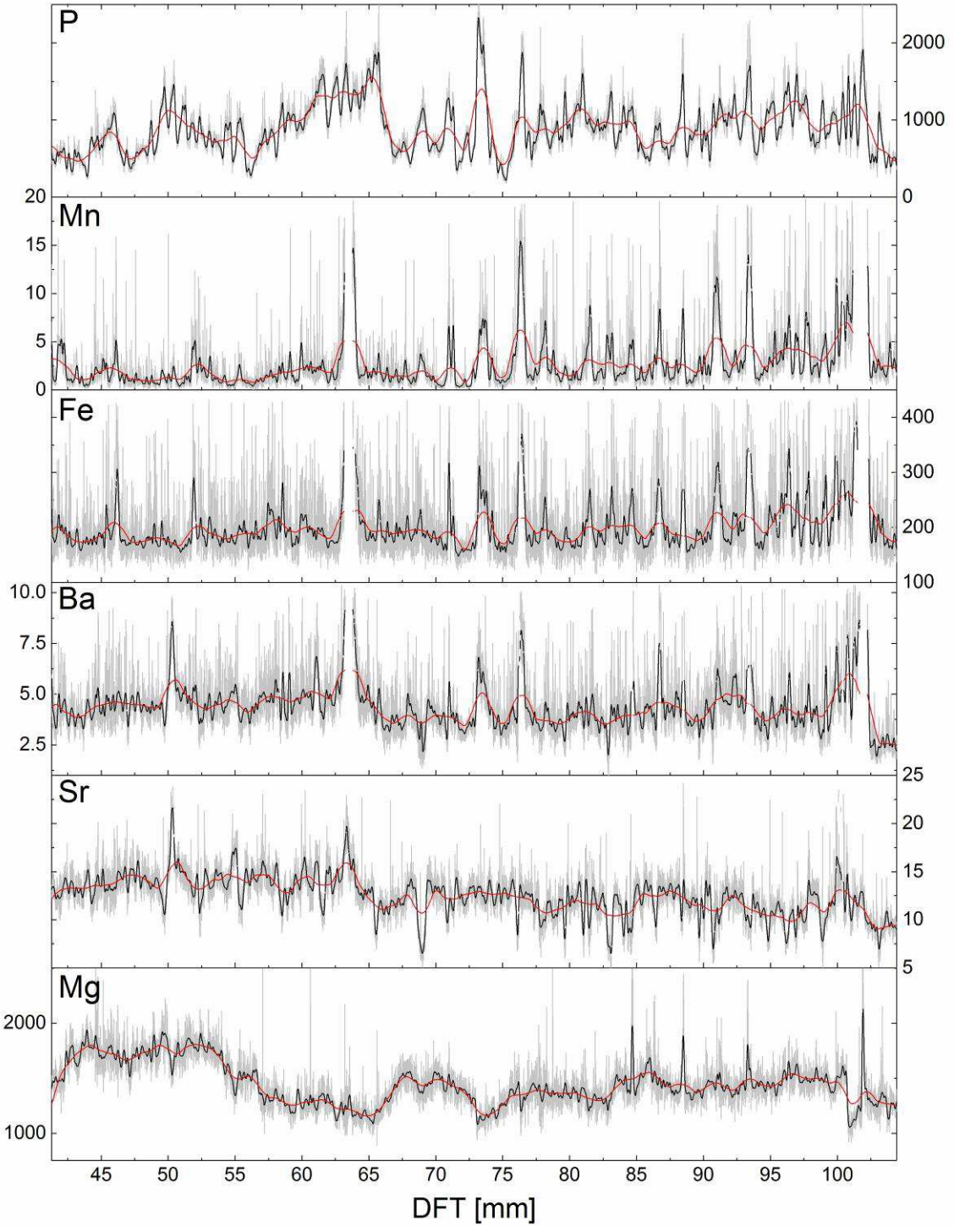

Figure D.6: Trace element concentrations (in µg/g) of Mg, Sr, Ba, Fe, Mn and P from stalagmite VSMS2 during its second growth period, plotted in the depth domain. Grey lines indicate the original concentrations after all corrections, black lines are 30-pt smoothed data (weighted Adjacent-Averaging), red lines are 300-pt smoothed data.

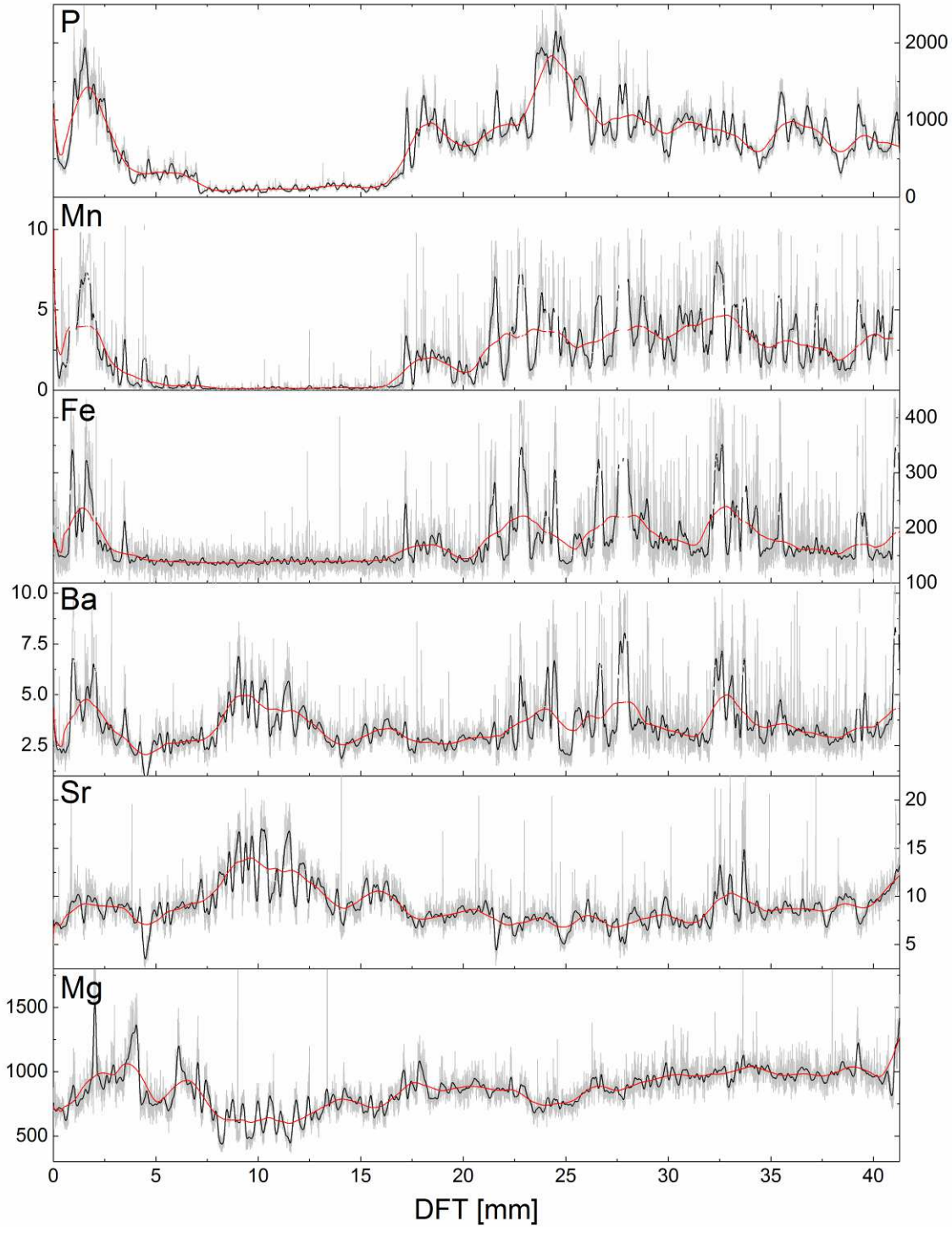

Figure D.7: Trace element concentrations (in µg/g) of Mg, Sr, Ba, Fe, Mn and P from stalagmite VSMS2 during its third growth period, plotted in the depth domain. Grey lines indicate the original concentrations after all corrections, black lines are 30-pt smoothed data (weighted Adjacent-Averaging), red lines are 300-pt smoothed data.

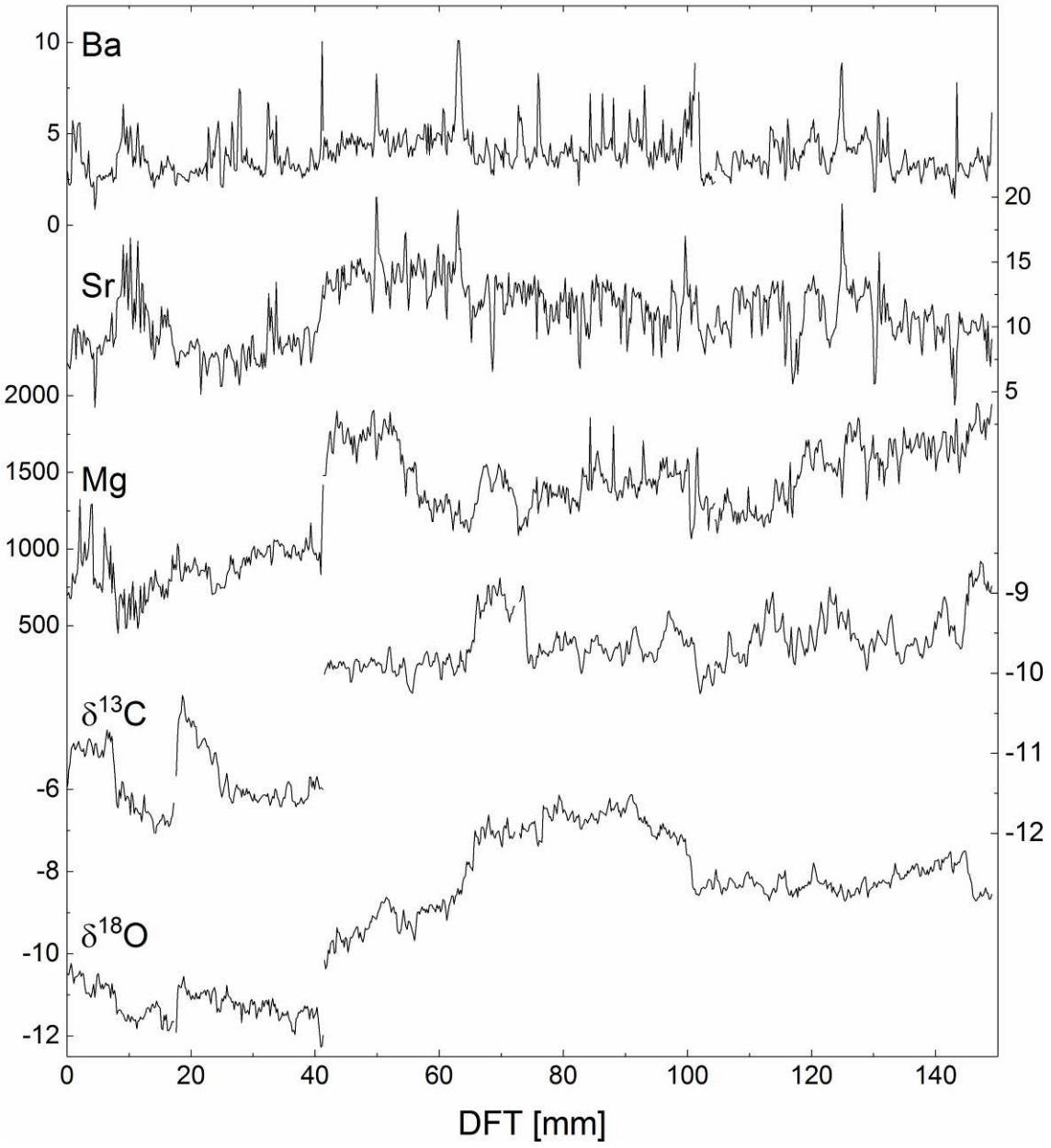

Figure D.8: Geochemical proxy records from stalagmite VSMS2 attributed to Group I: $\delta^{18}O$, $\delta^{13}C$, Mg, Sr and Ba (plotted in the depth domain). Both stable isotope ratios are expressed in ‰ as δ values relative to the V-PDB standard, all trace element concentrations are given in µg/g and are averaged to match the resolution of the isotope data sets (Section 4.6). Linear regression lines are indicated in red.

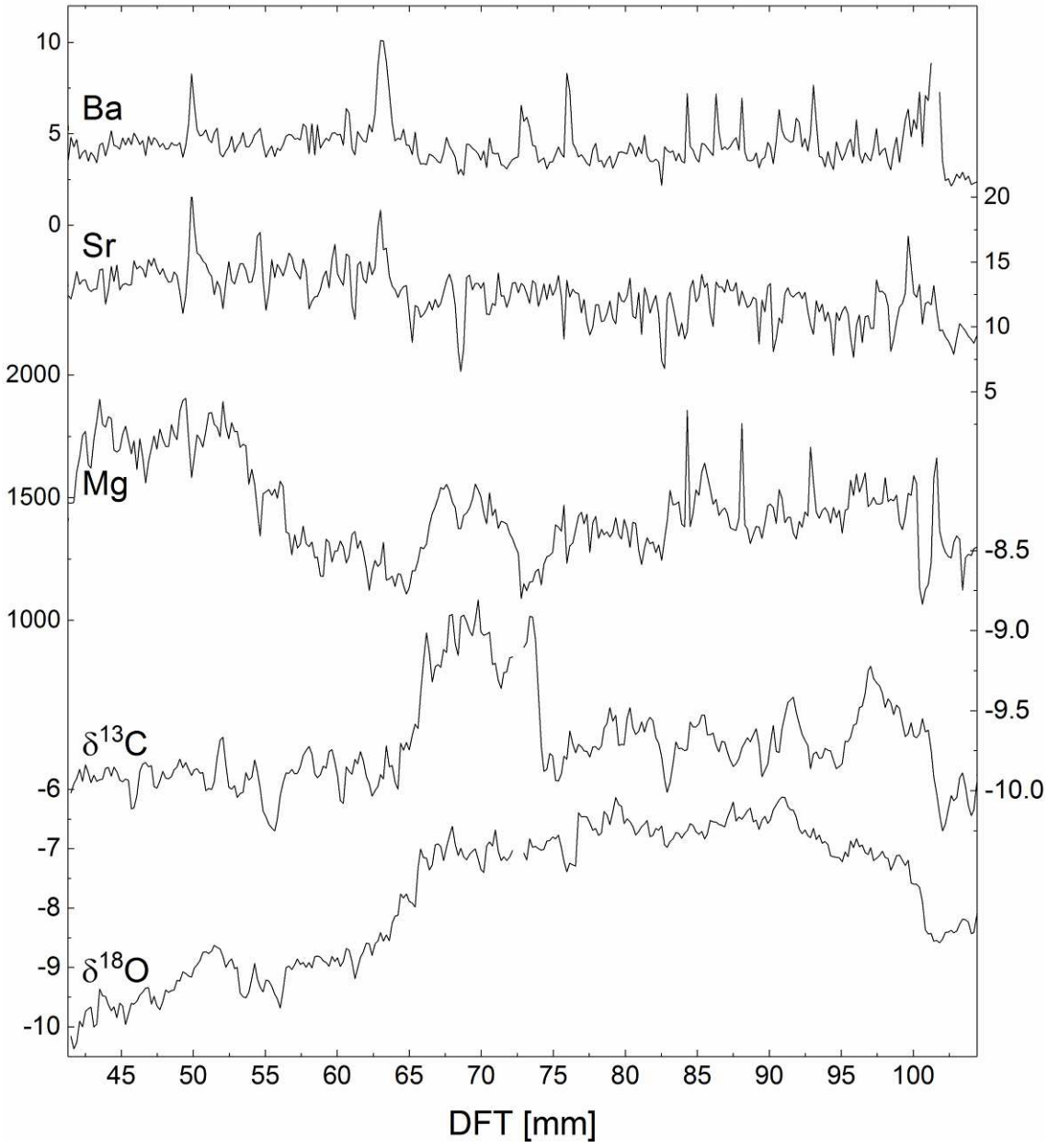

Figure D.10: Geochemical proxy records during the second growth period of stalagmite VSMS2 attributed to Group I: $\delta^{18}O$, $\delta^{13}C$, Mg, Sr and Ba (plotted in the depth domain). Both stable isotope ratios are expressed in ‰ as δ values relative to the V-PDB standard, all trace element concentrations are given in µg/g and are averaged to match the resolution of the isotope data sets (Section 4.6). Linear regression lines are indicated in red.

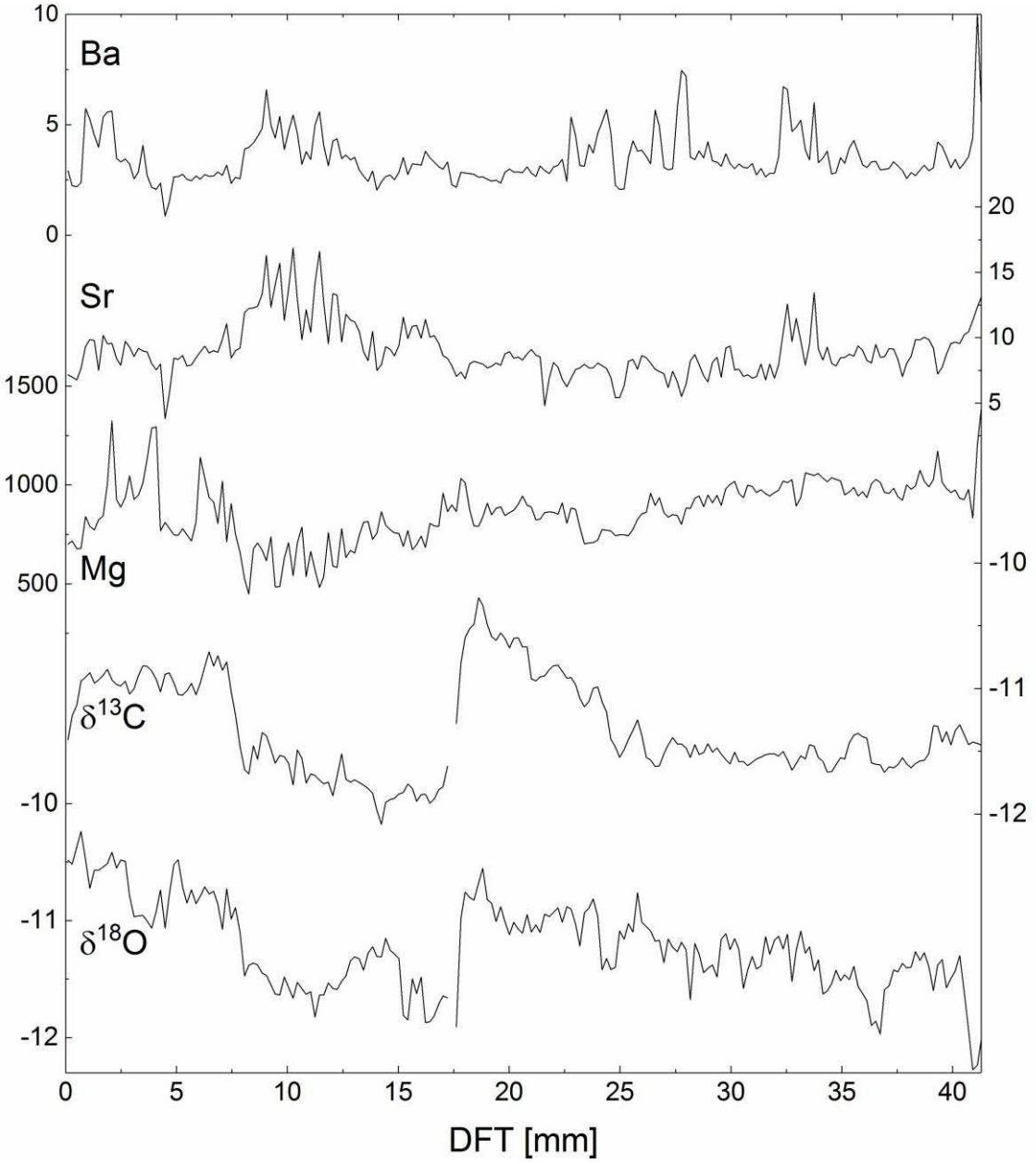

Figure D.11: Geochemical proxy records during the third growth period of stalagmite VSMS2 attributed to Group I: $\delta^{18}O$, $\delta^{13}C$, Mg, Sr and Ba (plotted in the depth domain). Both stable isotope ratios are expressed in ‰ as δ values relative to the V-PDB standard, all trace element concentrations are given in µg/g and are averaged to match the resolution of the isotope data sets (Section 4.6). Linear regression lines are indicated in red.

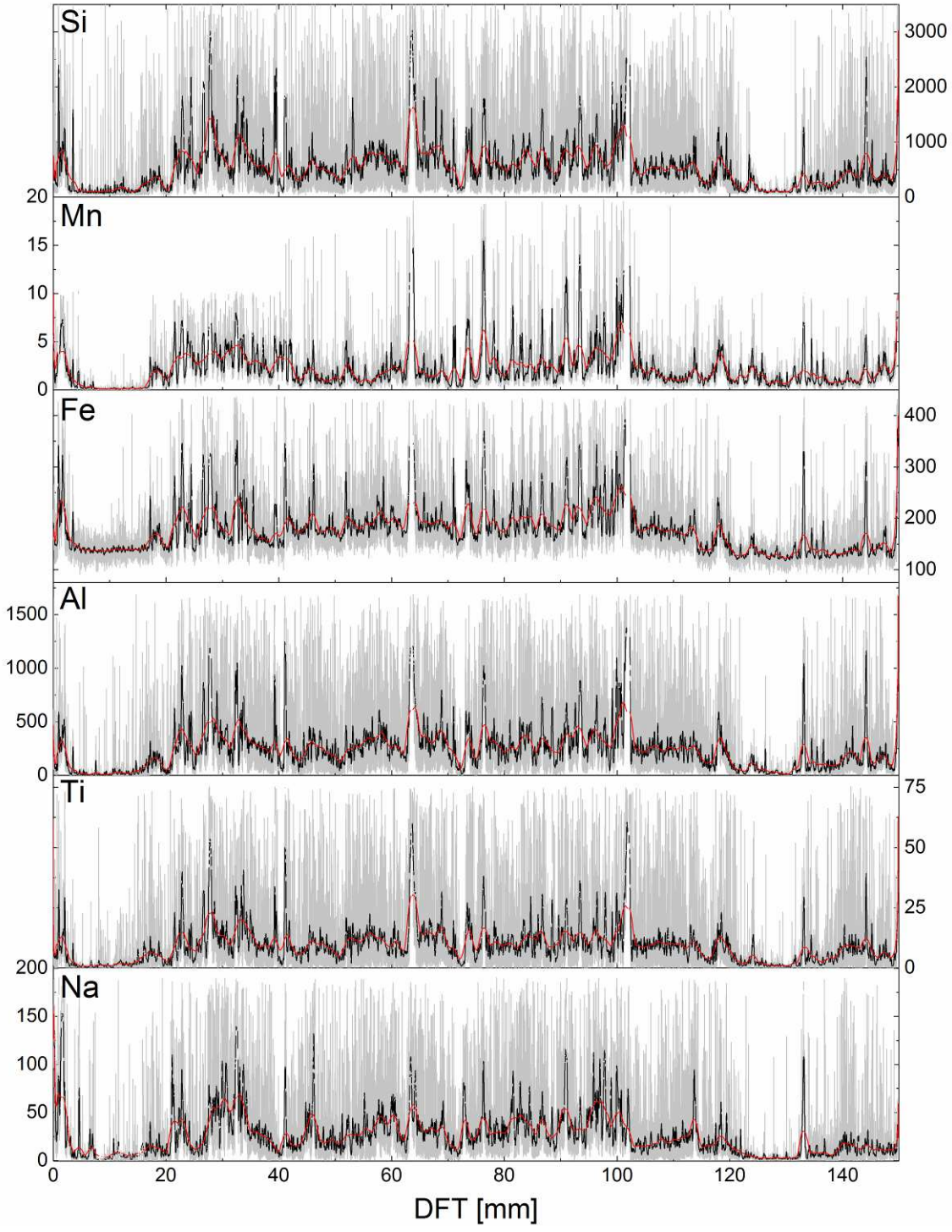

Figure D.12: Concentrations of trace elements from stalagmite VSMS2 attributed to Group II (Si, Mn, Fe, Ti and Na) in µg/g (plotted in the depth domain). Grey lines indicate the original concentrations after all corrections, black lines are 30-pt smoothed data (weighted Adjacent-Averaging), red lines are 300-pt smoothed data.

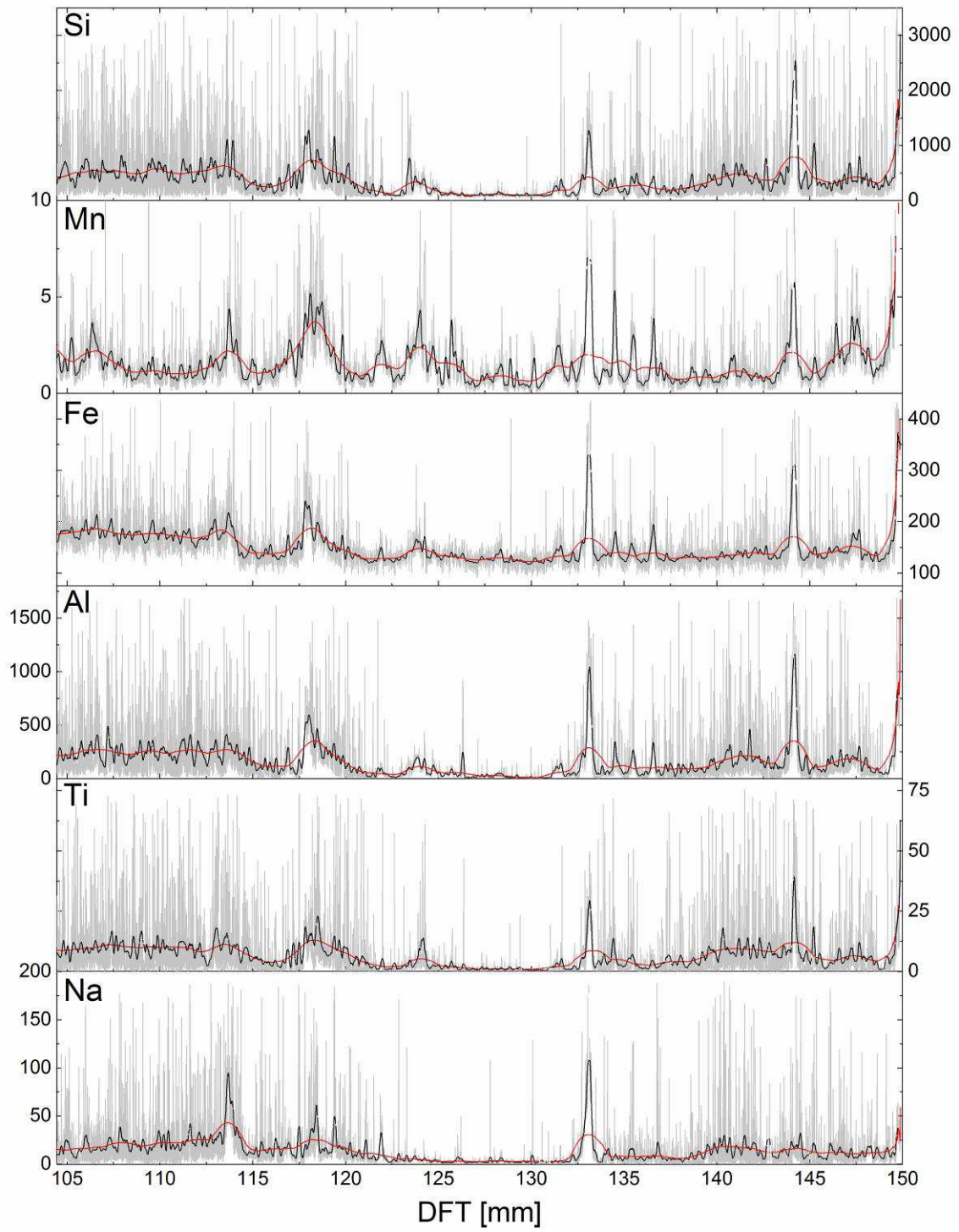

Figure D.13: Concentrations of trace elements during the first growth period of stalagmite VSMS2 attributed to Group II (Si, Mn, Fe, Ti and Na) in µg/g, plotted in the depth domain. Grey lines indicate the original concentrations after all corrections, black lines are 30-pt smoothed data (weighted Adjacent-Averaging), red lines are 300-pt smoothed data.

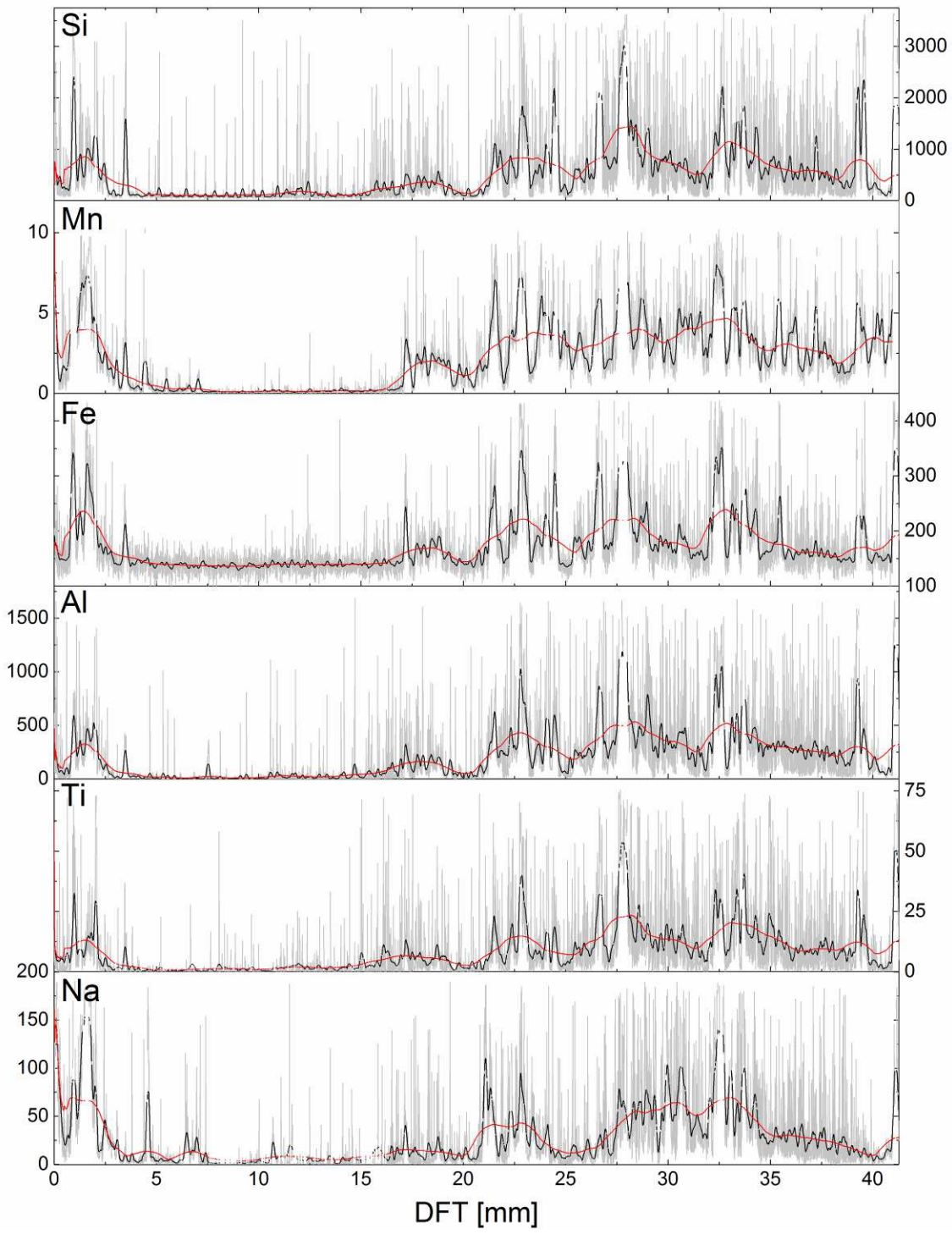

Figure D.15: Concentrations of trace elements during the third growth period of stalagmite VSMS2 attributed to Group II (Si, Mn, Fe, Ti and Na) in µg/g, plotted in the depth domain. Grey lines indicate the original concentrations after all corrections, black lines are 30-pt smoothed data (weighted Adjacent-Averaging), red lines are 300-pt smoothed data.

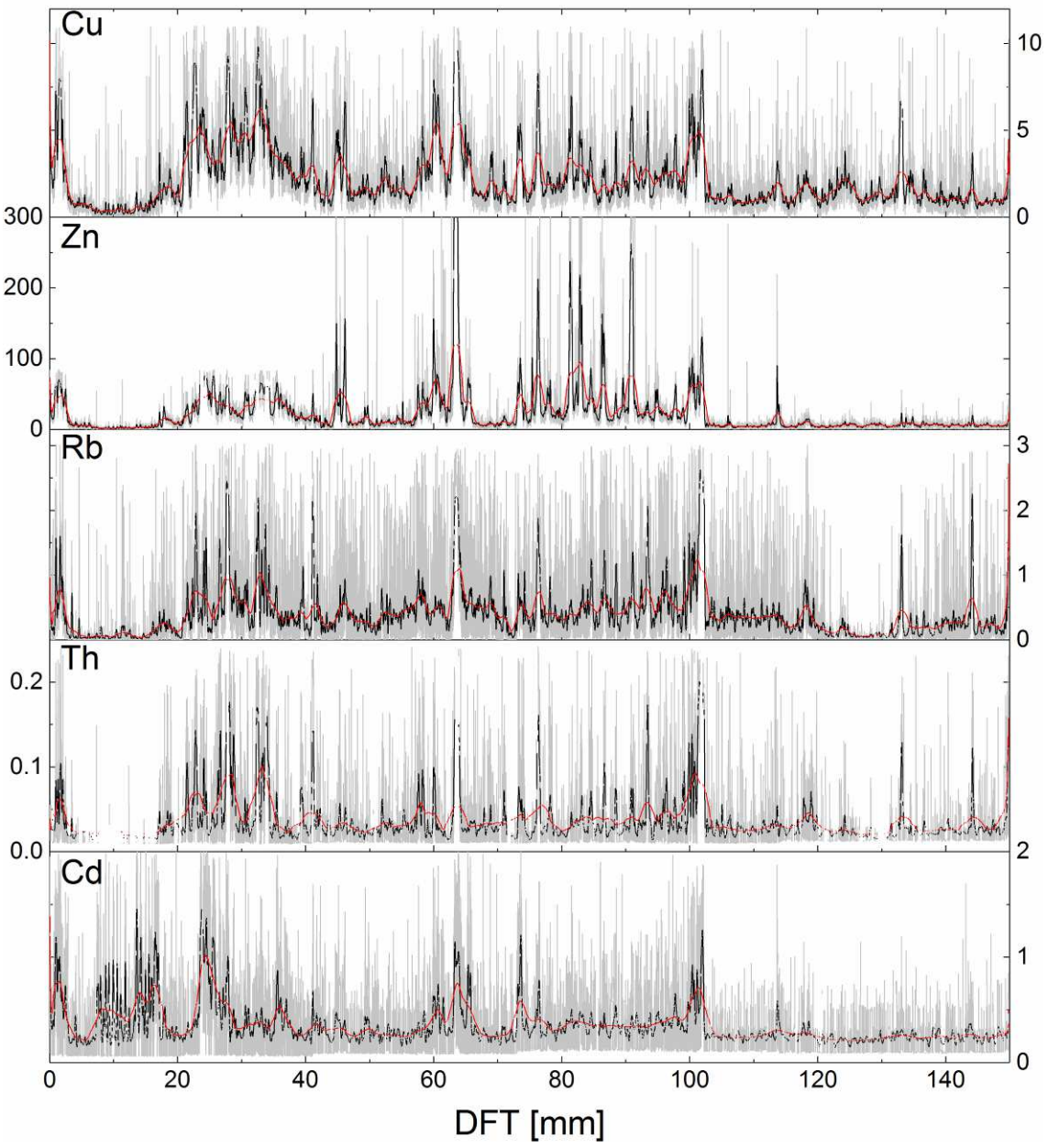

Figure D.16: Concentrations of trace elements from stalagmite VSMS2 attributed to Group II (Cu, Zn, Rb, Th and Cd) in µg/g, plotted in the depth domain. Grey lines indicate the original concentrations after all corrections, black lines are 30-pt smoothed data (weighted Adjacent-Averaging), red lines are 300-pt smoothed data.

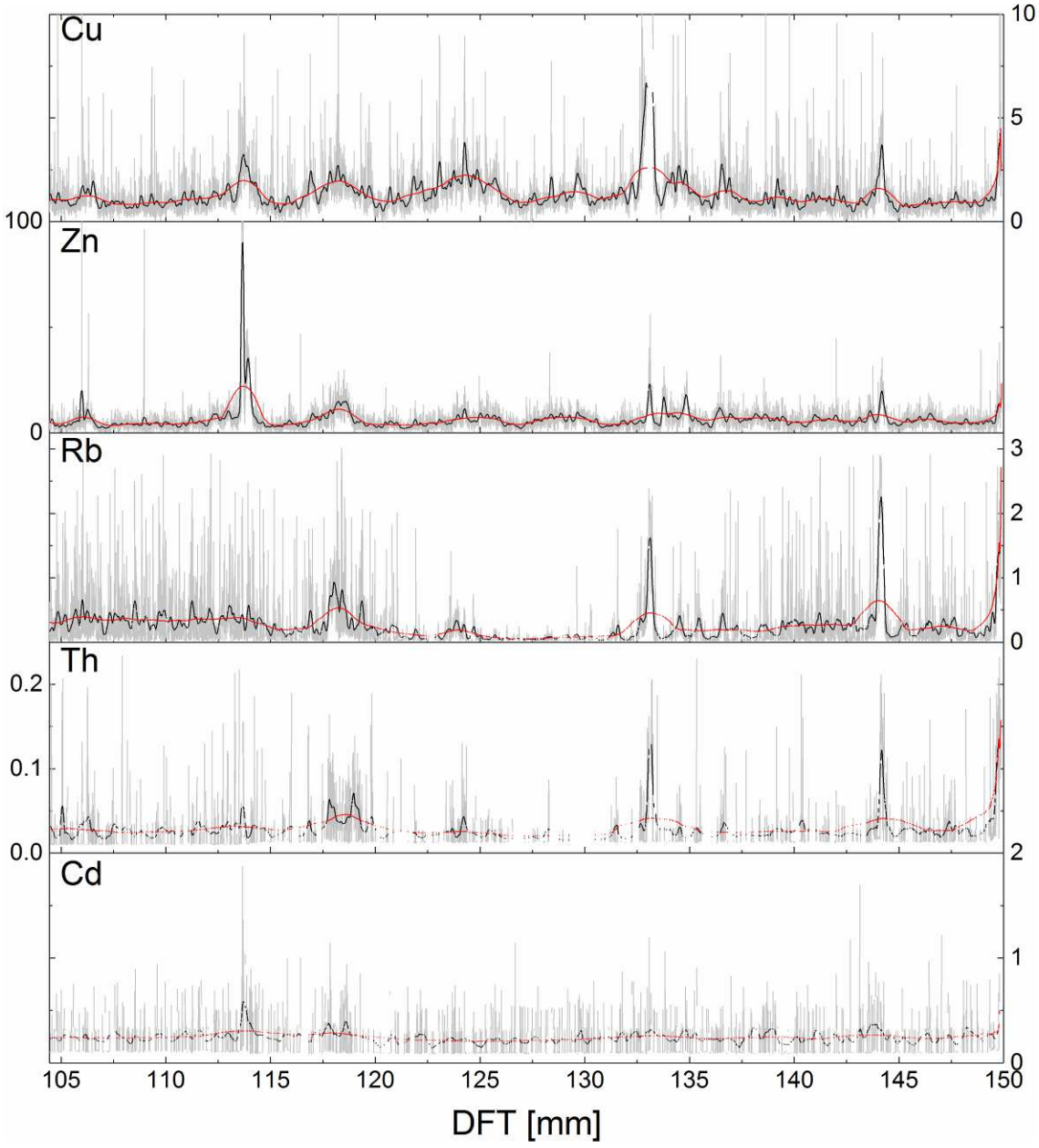

Figure D.17: Concentrations of trace elements during the first growth period of stalagmite VSMS2 attributed to Group II (Cu, Zn, Rb, Th and Cd) in µg/g, plotted in the depth domain. Grey lines indicate the original concentrations after all corrections, black lines are 30-pt smoothed data (weighted Adjacent-Averaging), red lines are 300-pt smoothed data.

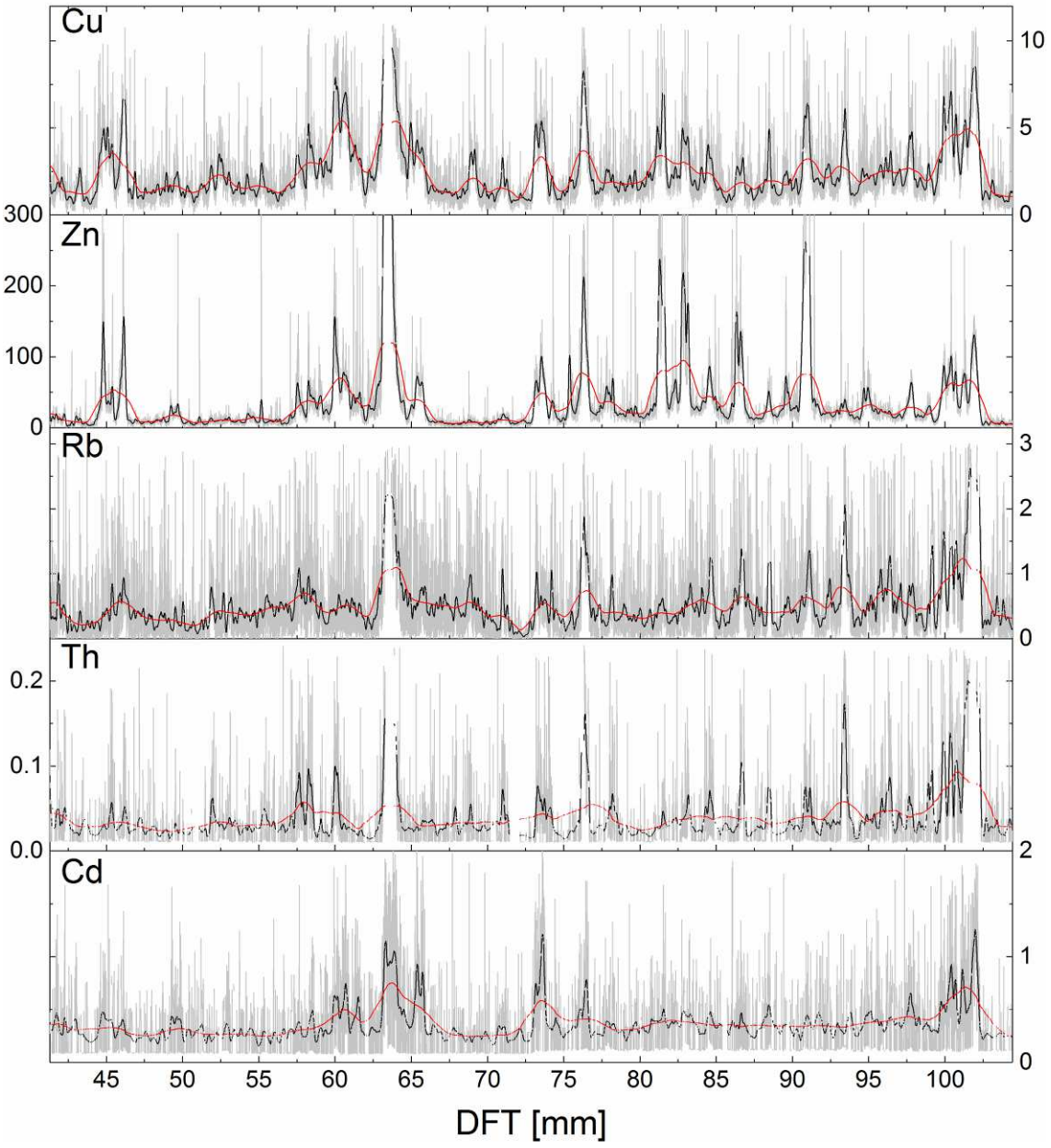

Figure D.18: Concentrations of trace elements during the second growth period of stalagmite VSMS2 attributed to Group II (Cu, Zn, Rb, Th and Cd) in µg/g, plotted in the depth domain. Grey lines indicate the original concentrations after all corrections, black lines are 30-pt smoothed data (weighted Adjacent-Averaging), red lines are 300-pt smoothed data.

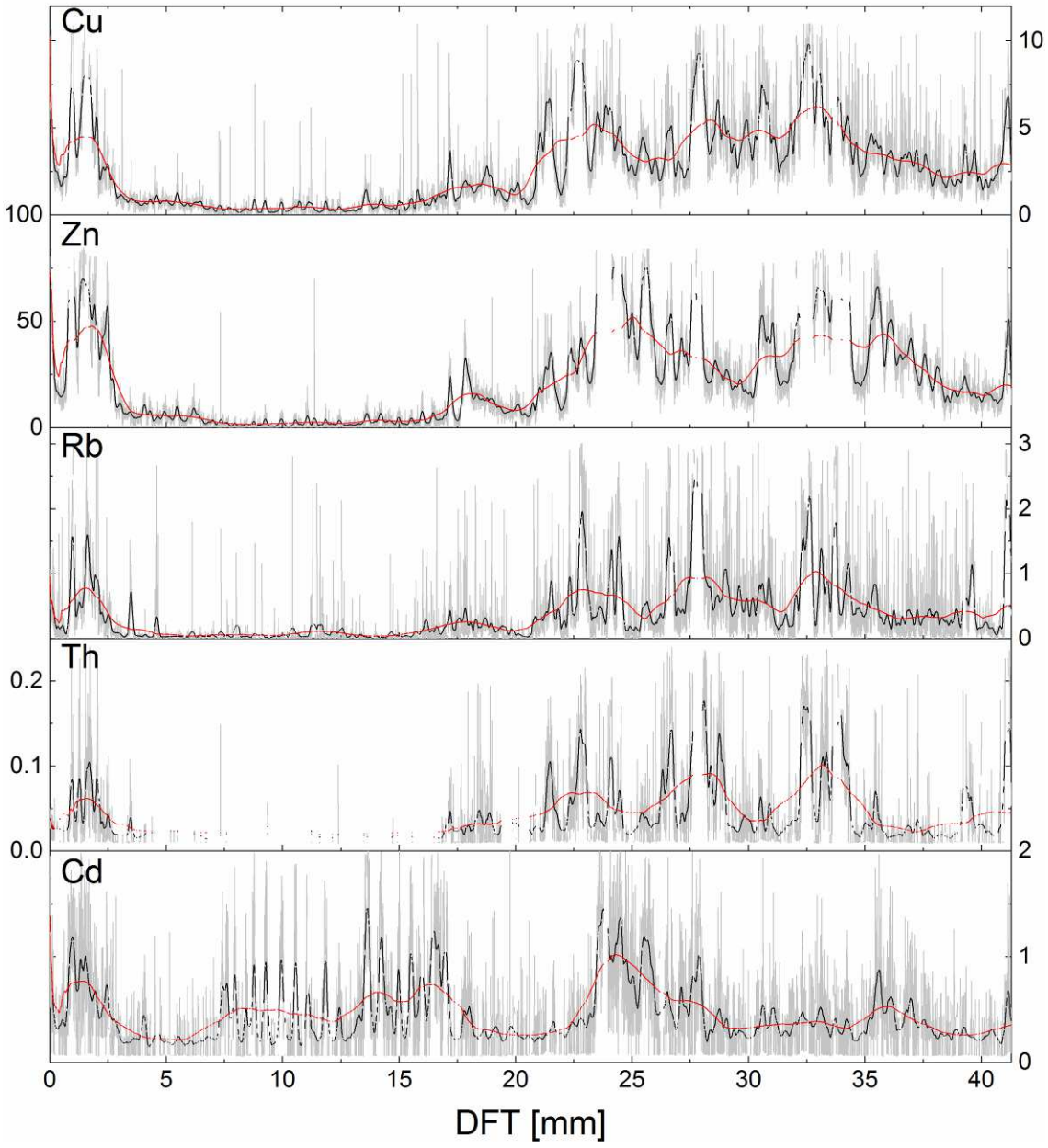

Figure D.19: Concentrations of trace elements during the third growth period of stalagmite VSMS2 attributed to Group II (Cu, Zn, Rb, Th and Cd) in µg/g, plotted in the depth domain. Grey lines indicate the original concentrations after all corrections, black lines are 30-pt smoothed data (weighted Adjacent-Averaging), red lines are 300-pt smoothed data.

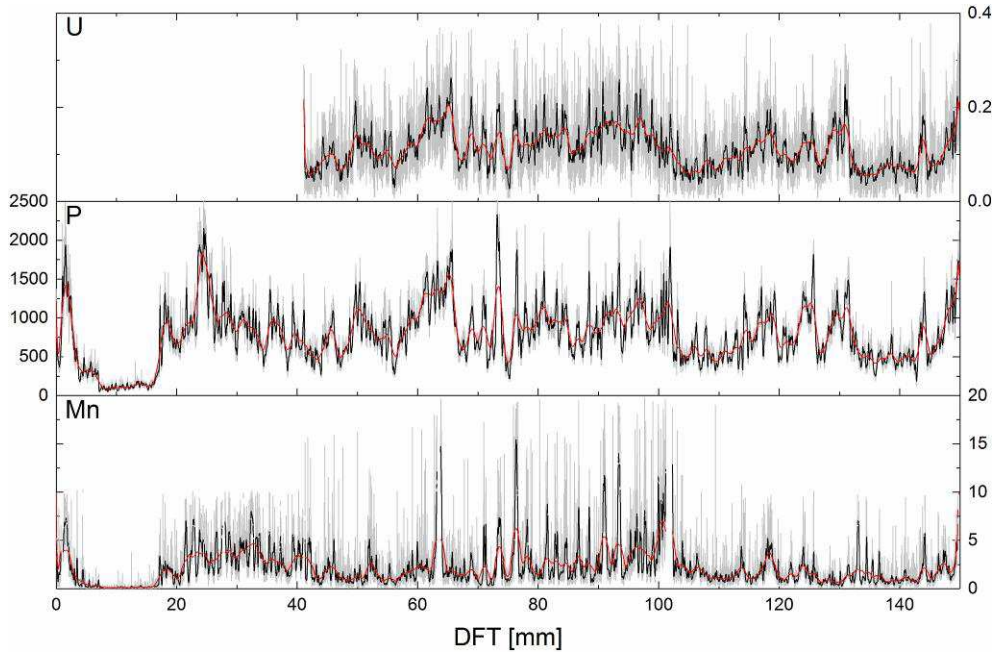

Figure D.20: Concentrations of trace elements from stalagmite VSMS2 attributed to Group III (P and U) in µg/g including Mn for comparison, plotted in the depth domain. Grey lines indicate the original concentrations after all corrections, black lines are 30-pt smoothed data (weighted Adjacent-Averaging), red lines are 300-pt smoothed data.

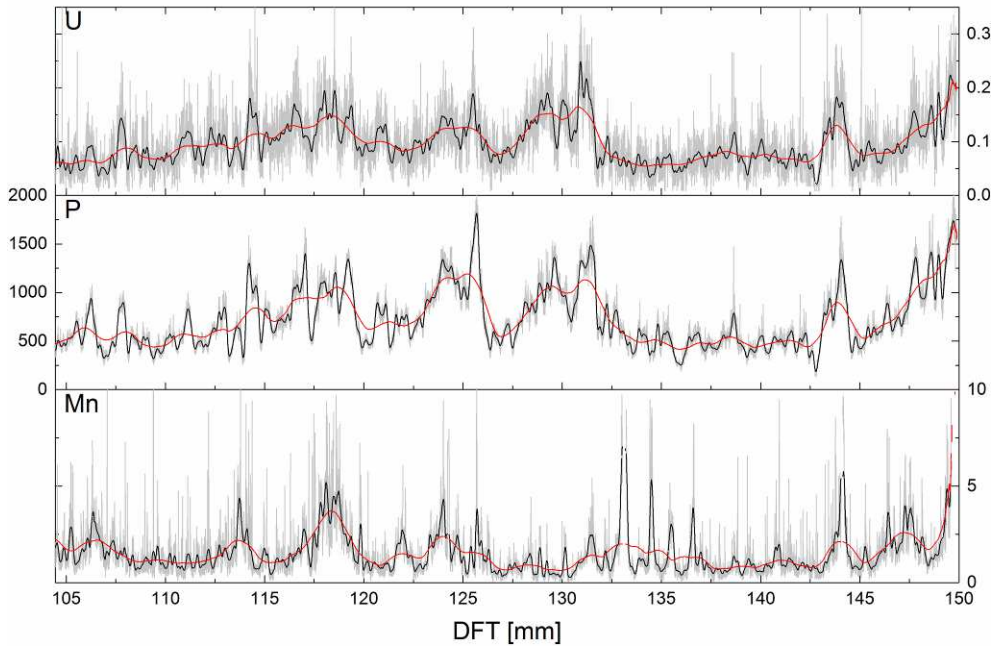

Figure D.21: Concentrations of trace elements during the first growth period of stalagmite VSMS2 attributed to Group III (P and U) in µg/g including Mn for comparison, plotted in the depth domain. Grey lines indicate the original concentrations after all corrections, black lines are 30-pt smoothed data (weighted Adjacent-Averaging), red lines are 300-pt smoothed data.

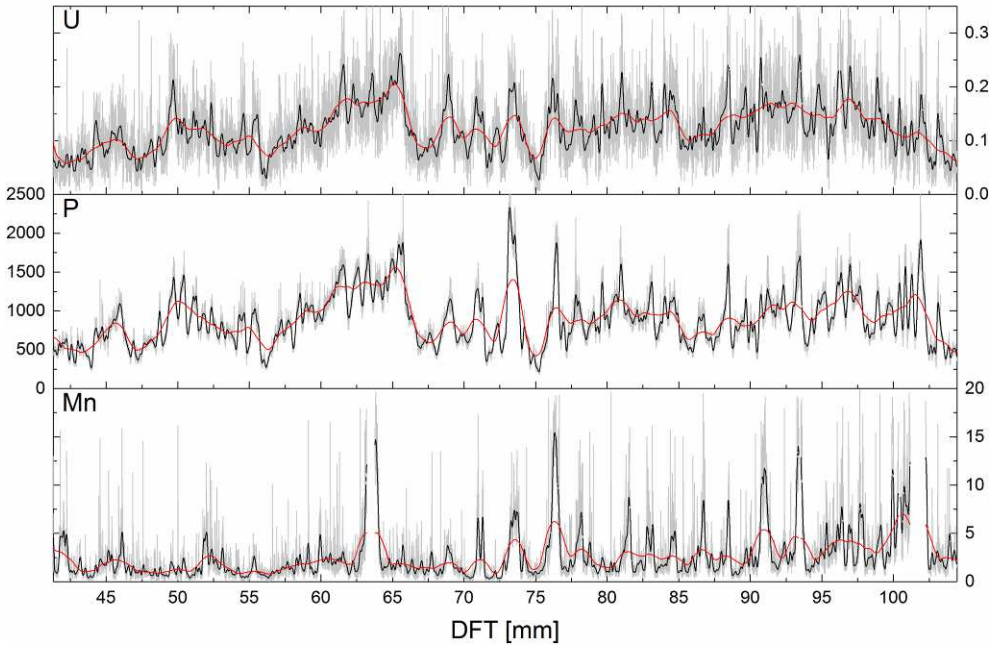

Figure D.22: Concentrations of trace elements during the second growth period of stalagmite VSMS2 attributed to Group III (P and U) in µg/g including Mn for comparison, plotted in the depth domain. Grey lines indicate the original concentrations after all corrections, black lines are 30-pt smoothed data (weighted Adjacent-Averaging), red lines are 300-pt smoothed data.

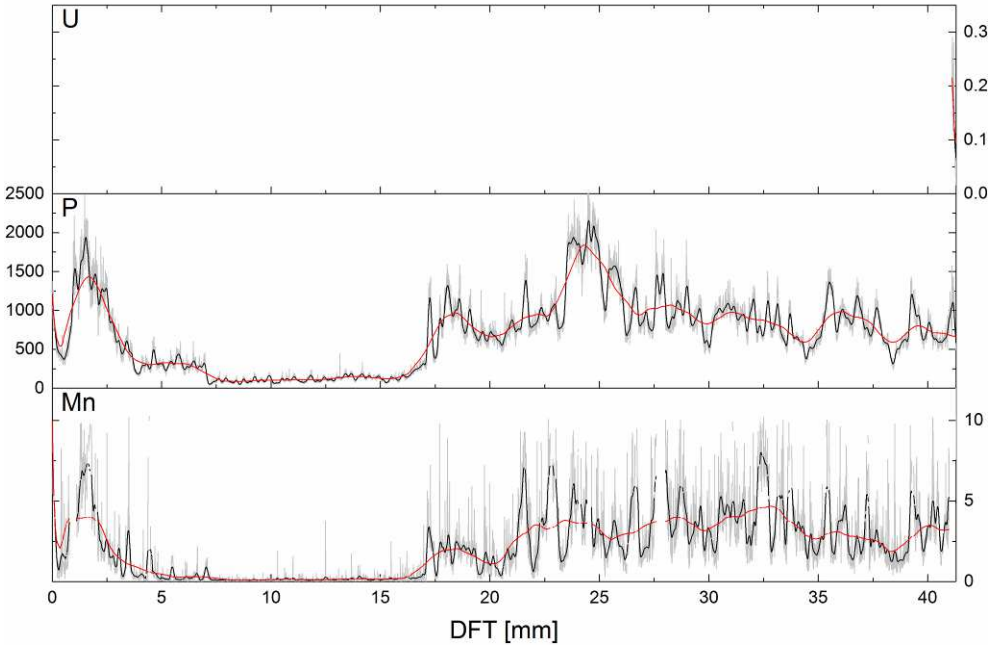

Figure D.23: Concentrations of trace elements during the third growth period of stalagmite VSMS2 attributed to Group III (P and U) in µg/g including Mn for comparison, plotted in the depth domain. Grey lines indicate the original concentrations after all corrections, black lines are 30-pt smoothed data (weighted Adjacent-Averaging), red lines are 300-pt smoothed data.

E Remaining Geochemical Records of Stalagmite VSMS2

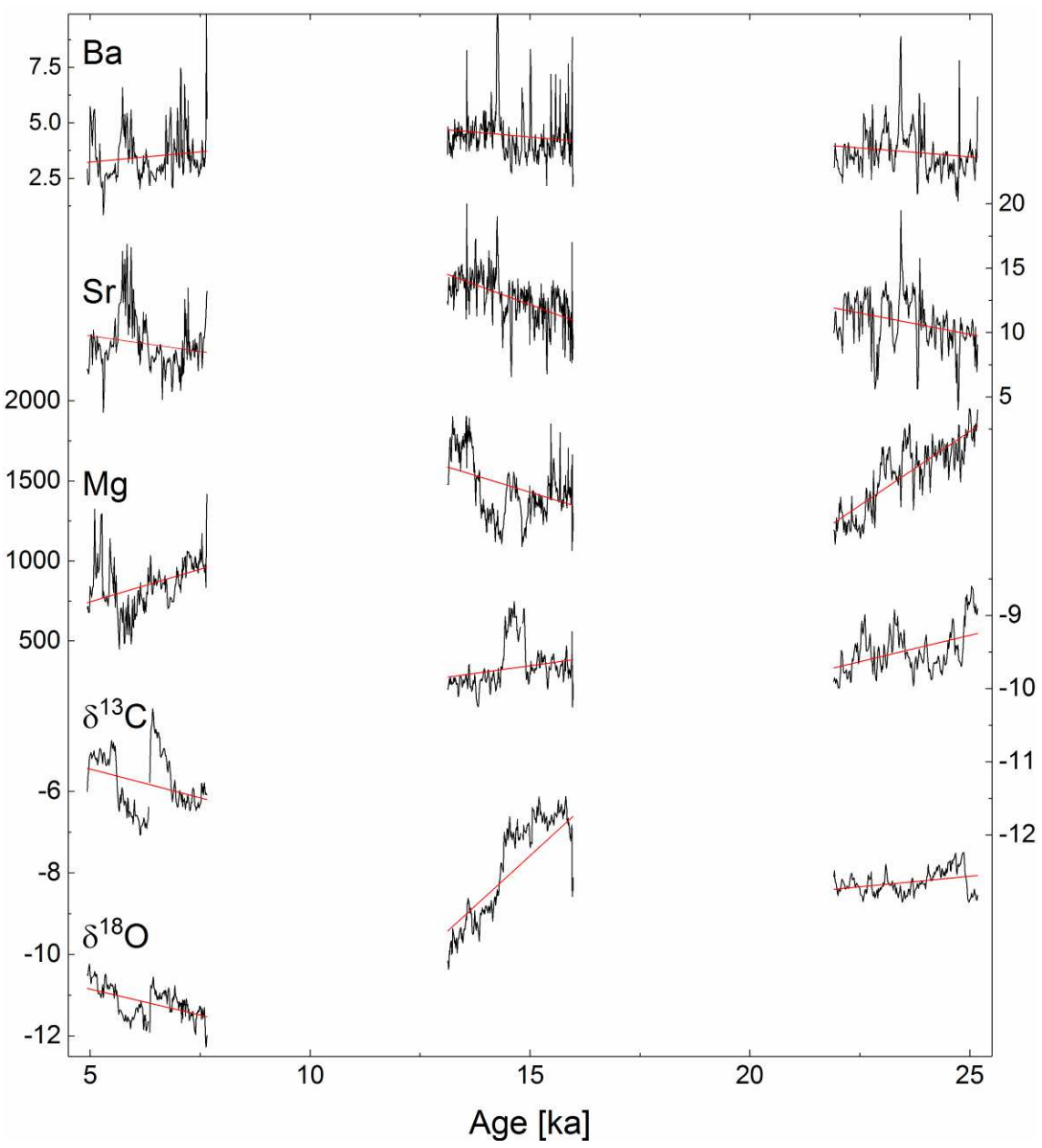

Figure E.1: Geochemical proxy records from stalagmite VSMS2 attributed to Group I: $\delta^{18}O$, $\delta^{13}C$, Mg, Sr and Ba. Both stable isotope ratios are expressed in ‰ as δ values relative to the V-PDB standard, all trace element concentrations are given in µg/g and are averaged to match the resolution of the isotope data sets (Section 4.6). Linear regression lines are indicated in red.

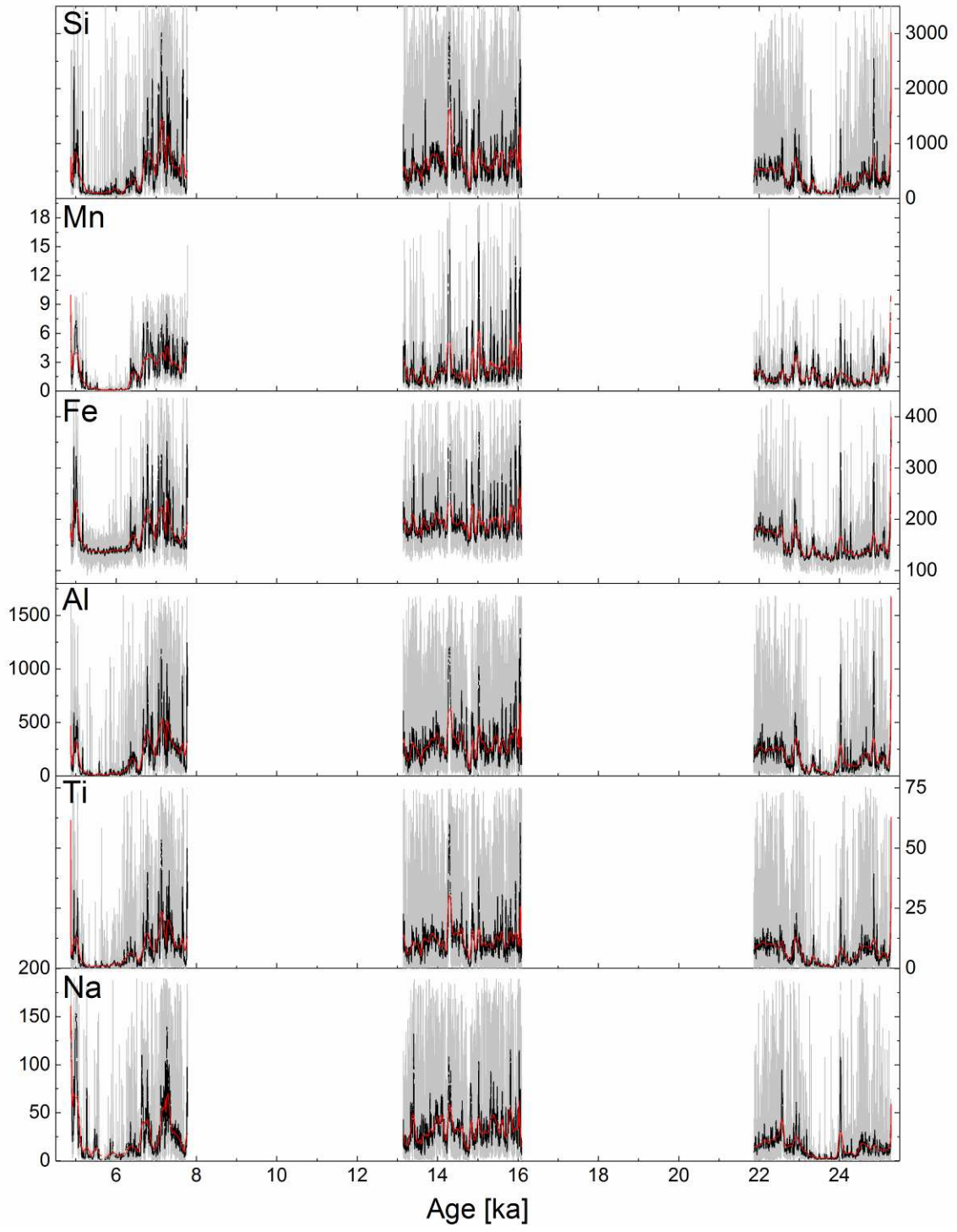

Figure E.2: Concentrations of trace elements from stalagmite VSMS2 attributed to Group II (Si, Mn, Fe, Ti and Na) in µg/g. Grey lines indicate the original concentrations after all corrections, black lines are 30-pt smoothed data (weighted Adjacent-Averaging), red lines are 300-pt smoothed data.

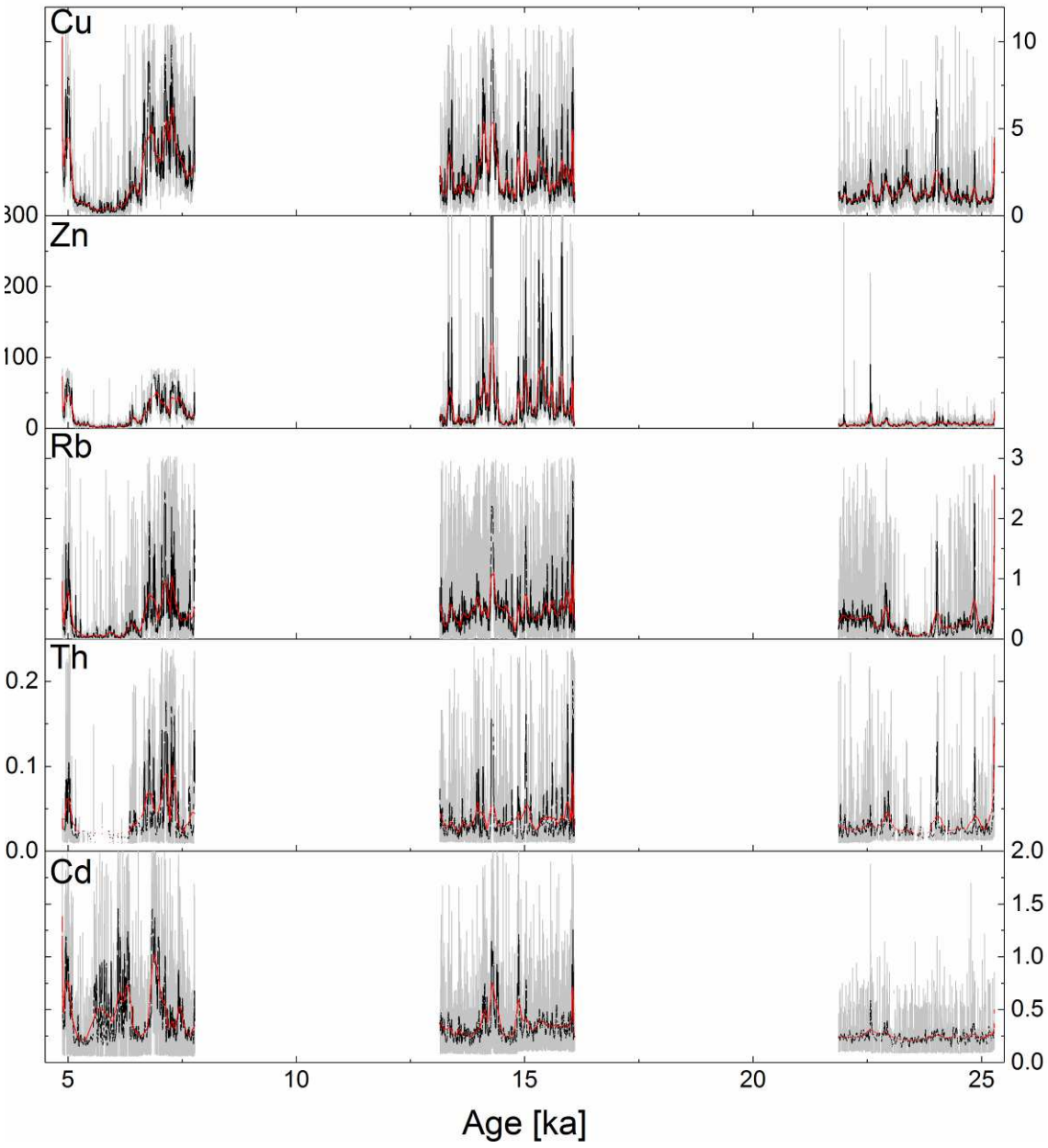

Figure E.3: Concentrations of trace elements from stalagmite VSMS2 attributed to Group II (Cu, Zn, Rb, Th and Cd) in µg/g. Grey lines indicate the original concentrations after all corrections, black lines are 30-pt smoothed data (weighted Adjacent-Averaging), red lines are 300-pt smoothed data.

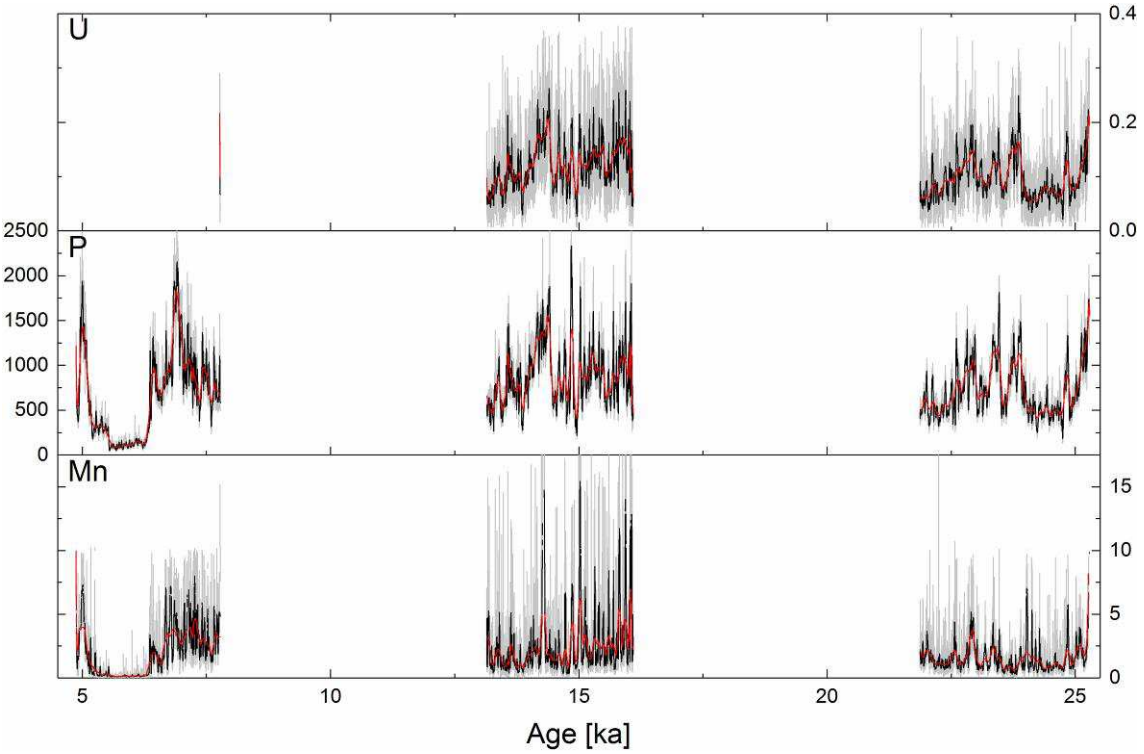

Figure E.4: Concentrations of trace elements from stalagmite VSMS2 attributed to Group III (P and U) in µg/g. Grey lines indicate the original concentrations after all corrections, black lines are 30-pt smoothed data (weighted Adjacent-Averaging), red lines are 300-pt smoothed data.

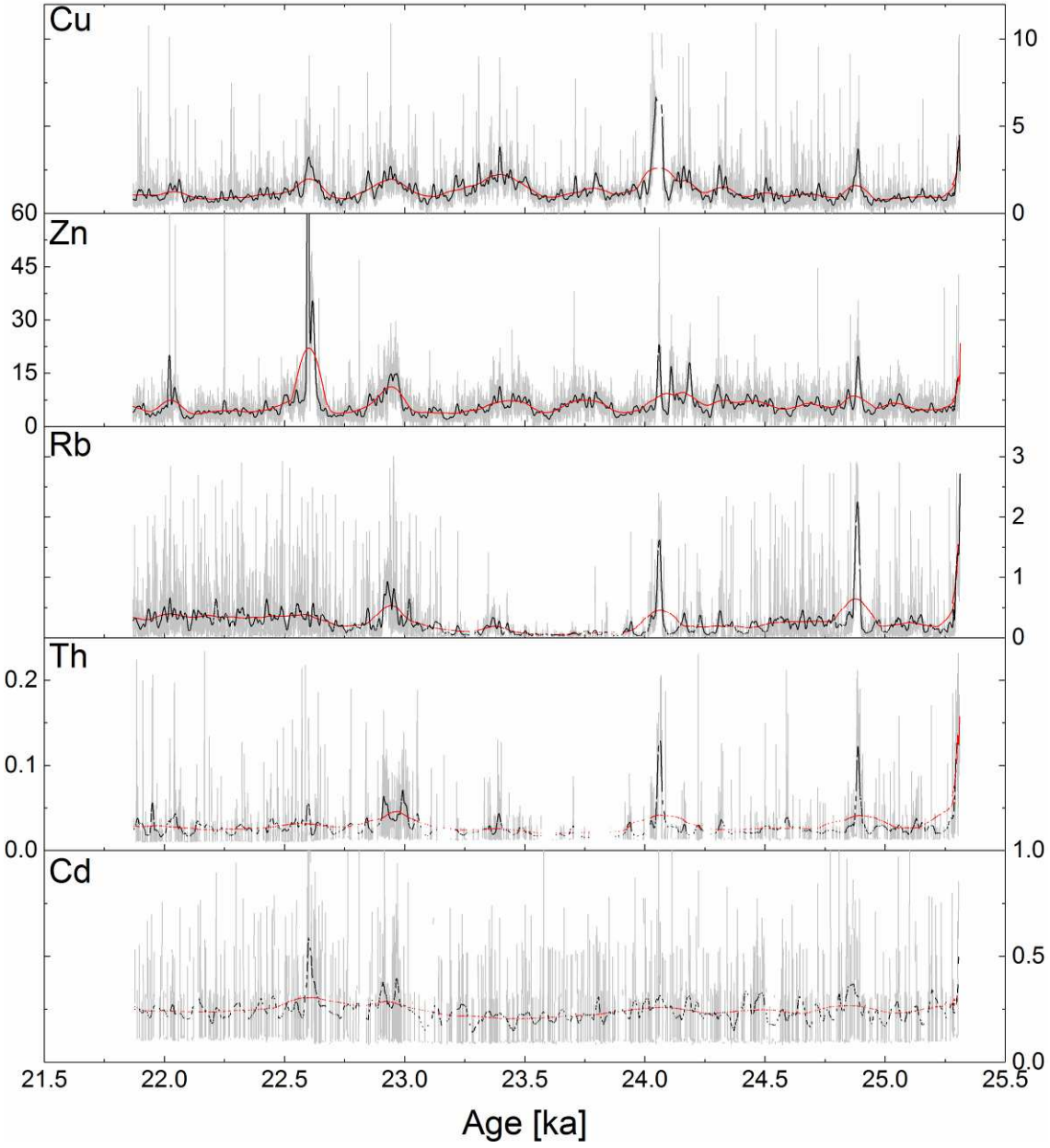

Figure E.5: Concentrations of trace elements during the first growth period of stalagmite VSMS2 attributed to Group II (Cu, Zn, Rb, Th and Cd) in µg/g. Grey lines indicate the original concentrations after all corrections, black lines are 30-pt smoothed data (weighted Adjacent-Averaging), red lines are 300-pt smoothed data.

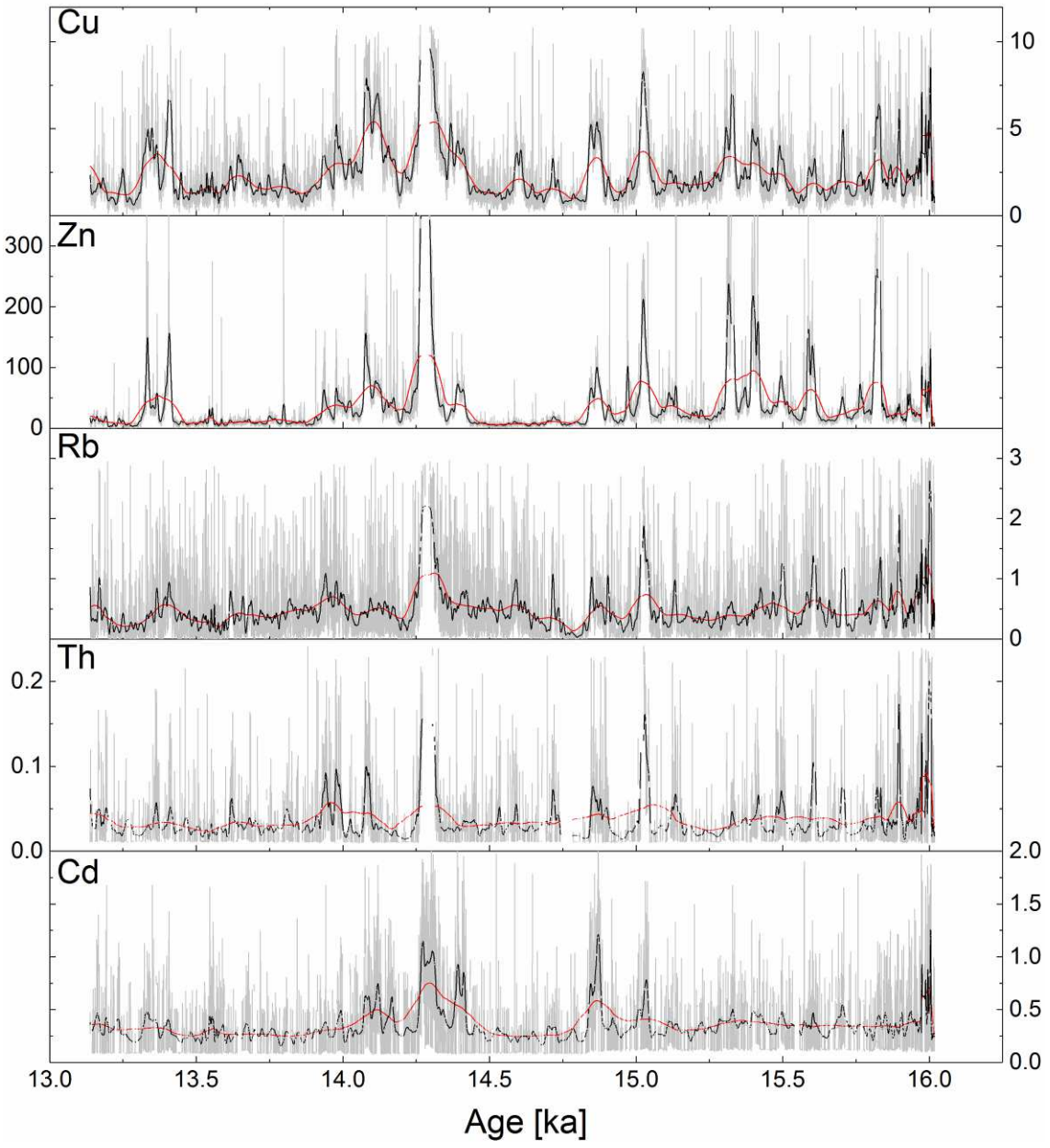

Figure E.6: Concentrations of trace elements during the second growth period of stalagmite VSMS2 attributed to Group II (Cu, Zn, Rb, Th and Cd) in µg/g. Grey lines indicate the original concentrations after all corrections, black lines are 30-pt smoothed data (weighted Adjacent-Averaging), red lines are 300-pt smoothed data.

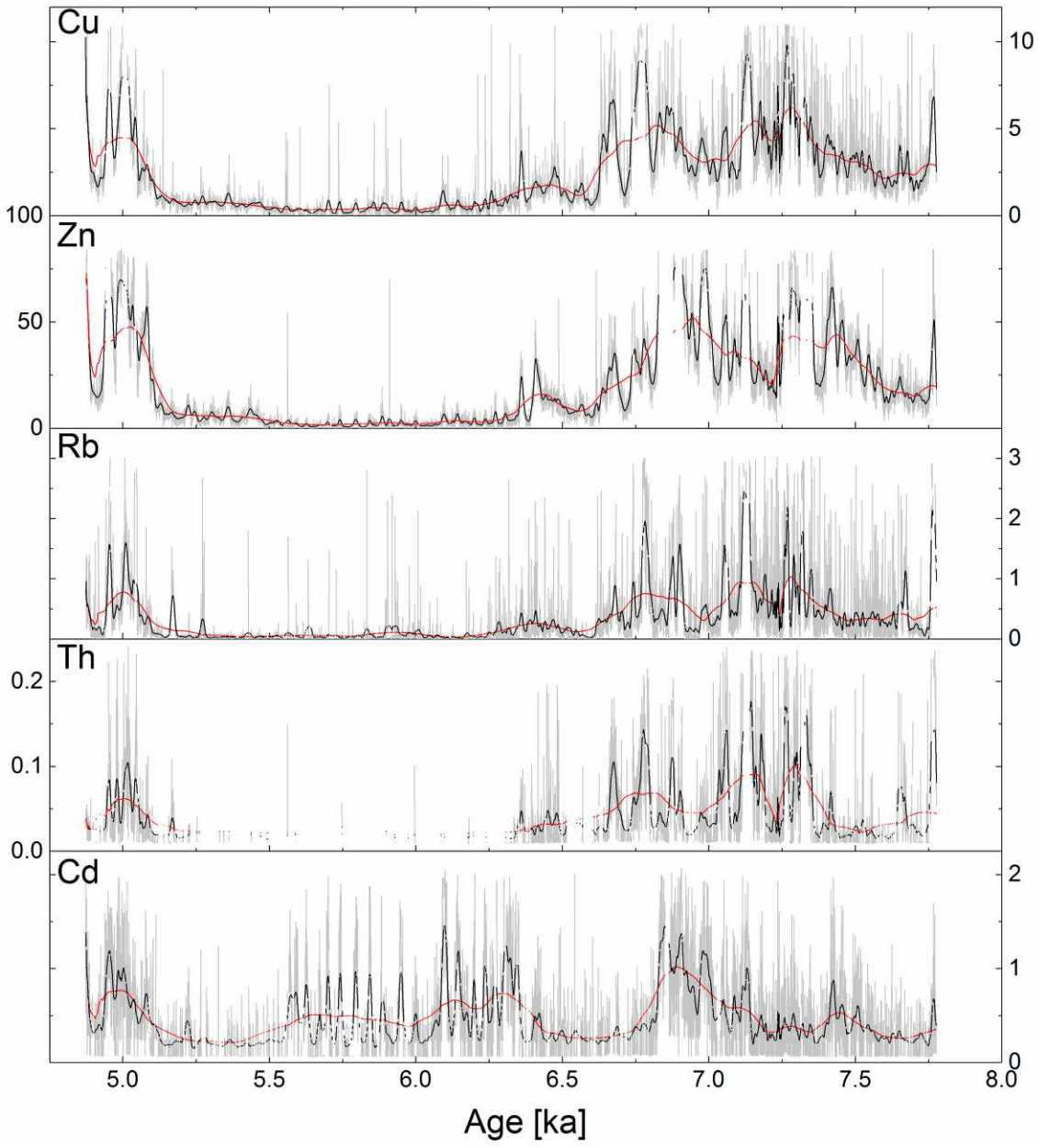

Figure E.7: Concentrations of trace elements during the third growth period of stalagmite VSMS2 attributed to Group II (Cu, Zn, Rb, Th, Cd) in µg/g. Grey lines indicate the original concentrations after all corrections, black lines are 30-pt smoothed data (weighted Adjacent-Averaging), red lines are 300-pt smoothed data.

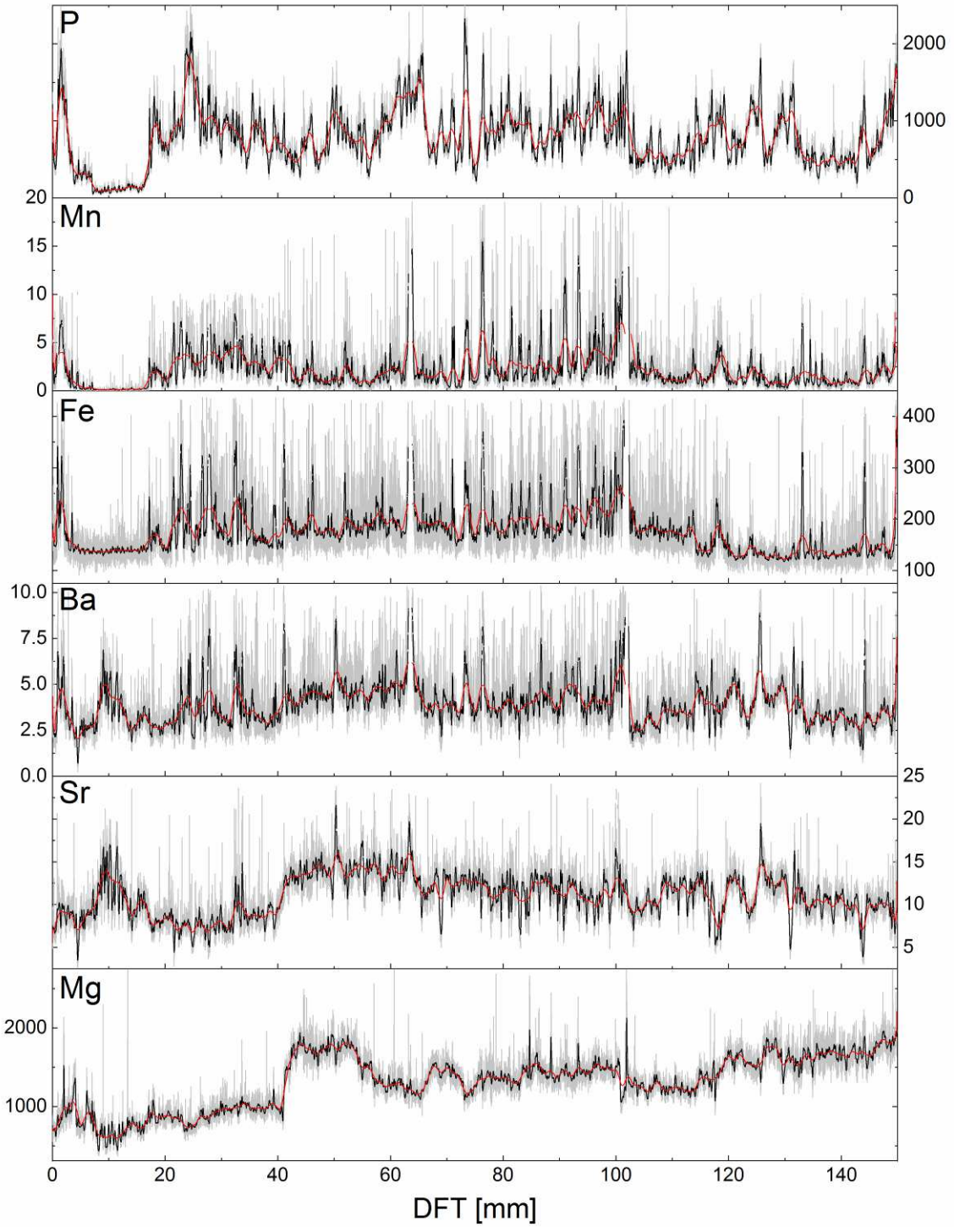

Figure E.8: Overview of the most important trace elements for this study from stalagmite VSMS2, plotted in the depth domain. All concentrations are given in µg/g. Grey lines indicate the original concentrations after all corrections, black lines are 30-pt smoothed data (weighted Adjacent-Averaging), red lines are 300-pt smoothed data.

F Prototype 1.0 Autosampler

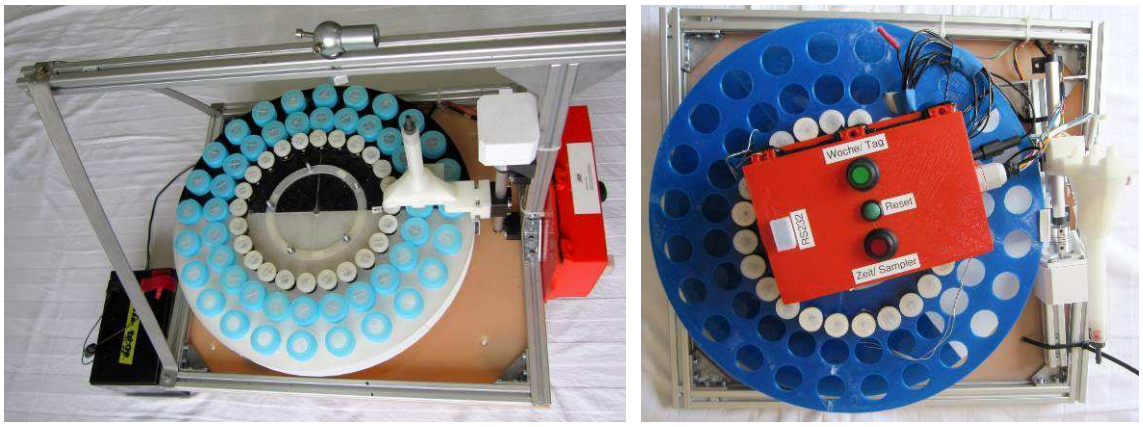

Figure F.1: Prototype 1.0 prepared for transport and installation inside the caves: Transport in assembled form for installation inside Ma Le 2 cave (left) and in disassembled form for installation inside Sang Ma Sao cave (right). (Photos: A. Hartmann; 22nd and 27th of July, 2015, respectively).

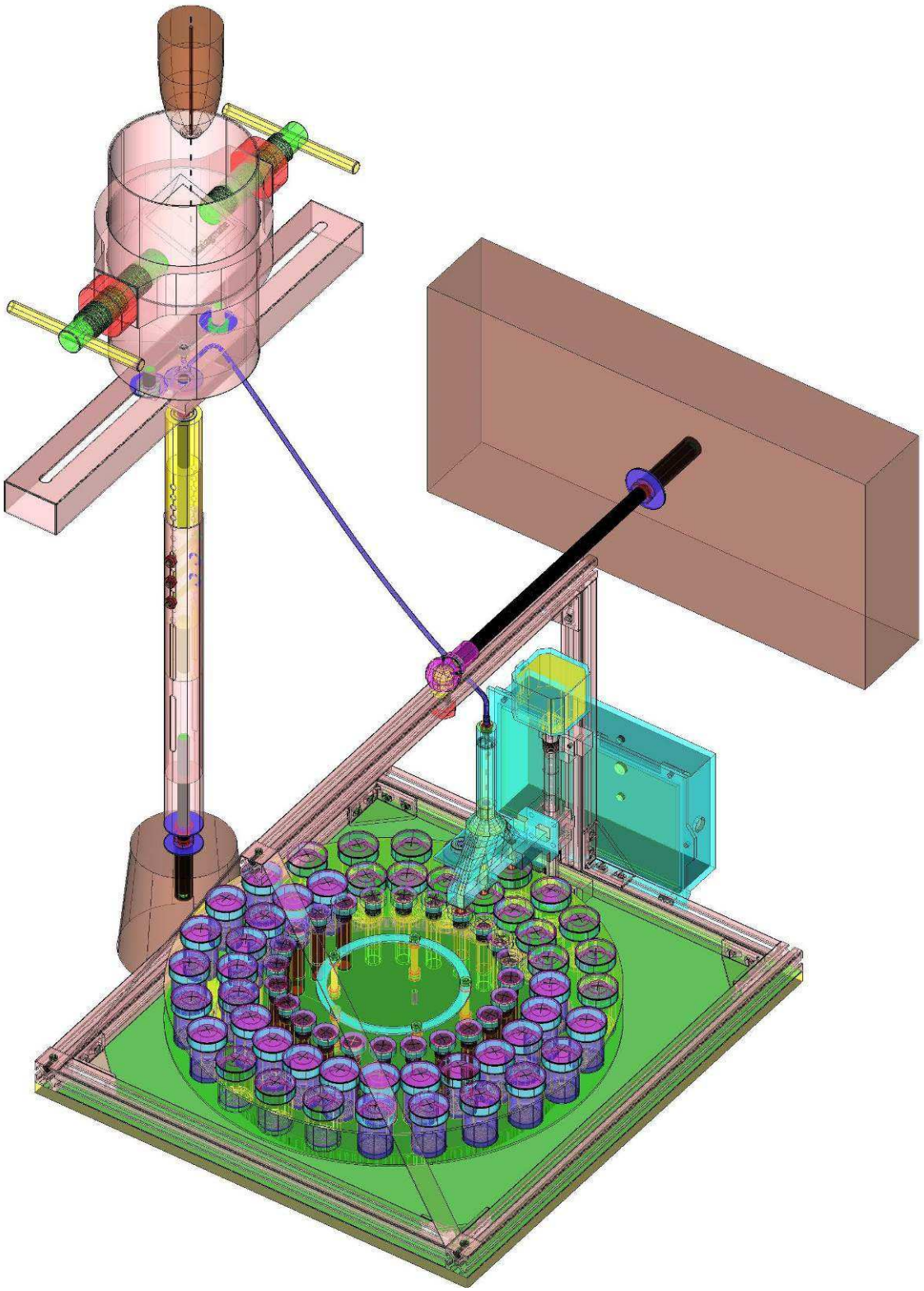

Figure F.2: Overview of all components of Prototype 1.0 as an X-ray CAD model, together with the newly developed dripwater container (left; including the Stalagmate drip rate logger) funneling the dripwater to the autosampler. The dripwater container is mounted on the newly developed telescope stand installed on the corresponding stalagmite stump (cut brown cone on the left) left after stalagmite extraction. The autosampler is mounted to the wall (brown cuboid on the right).

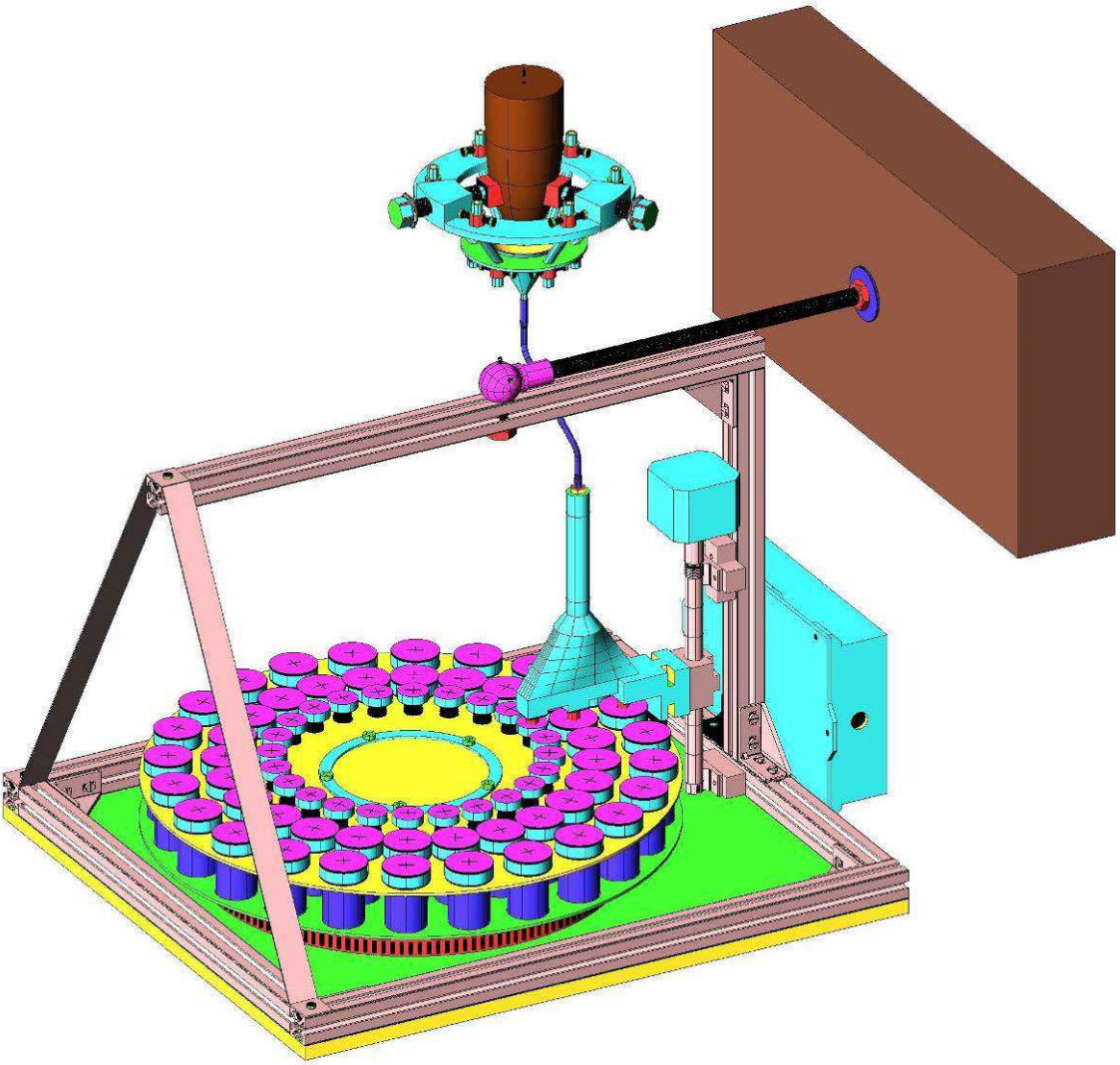

Figure F.3: Overview of all components of Prototype 1.0 as a solid CAD model, together with the second of the two newly developed stalactite collars, in this case attaching the dripwater funnel to the stalactite. The autosampler is mounted to the wall (brown cuboid on the right).

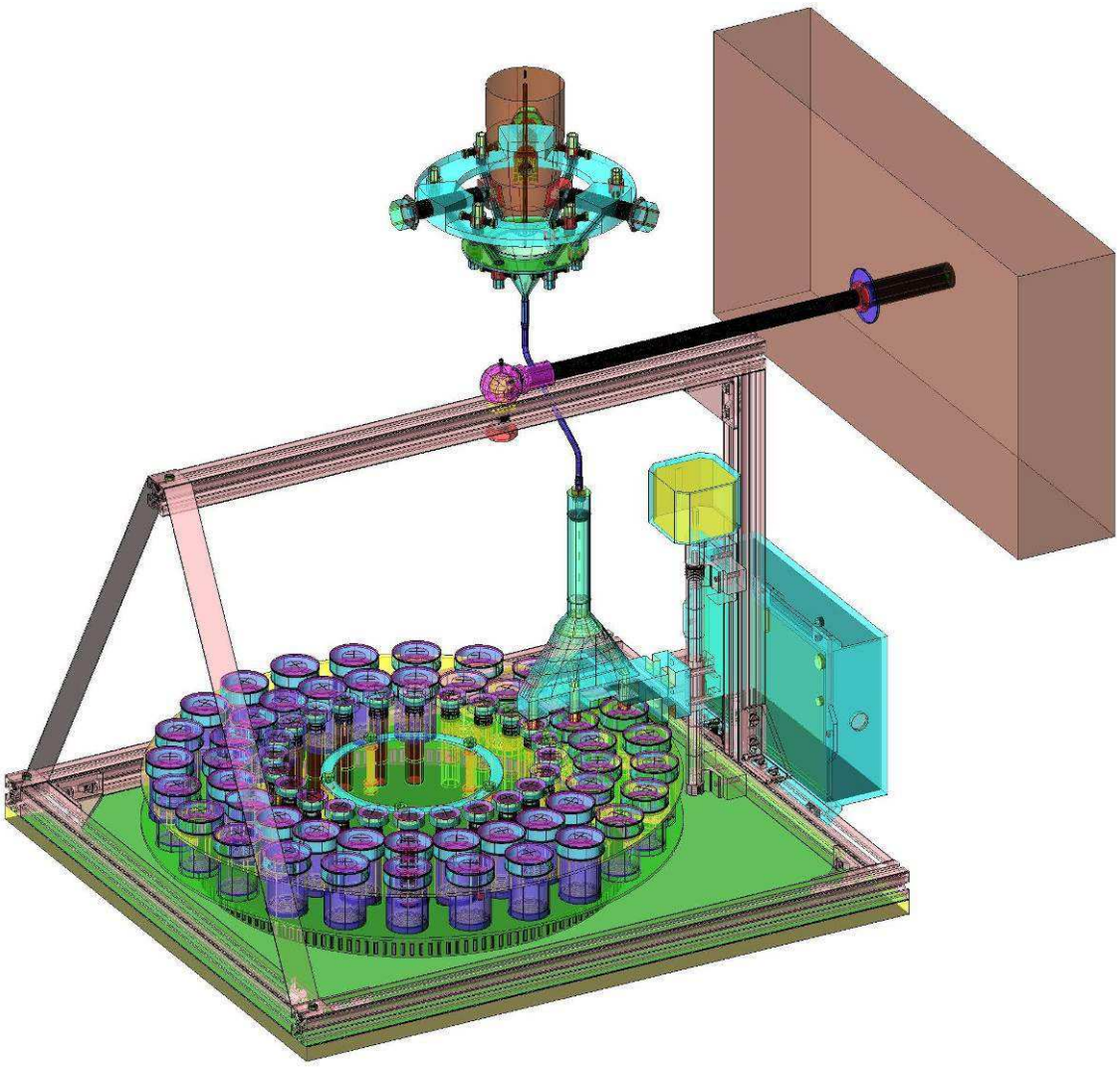

Figure F.4: Overview of all components of Prototype 1.0 as an X-ray CAD model, together with the second of the two newly developed stalactite collars, in this case attaching the dripwater funnel to the stalactite. The autosampler is mounted to the wall (brown cuboid on the right).

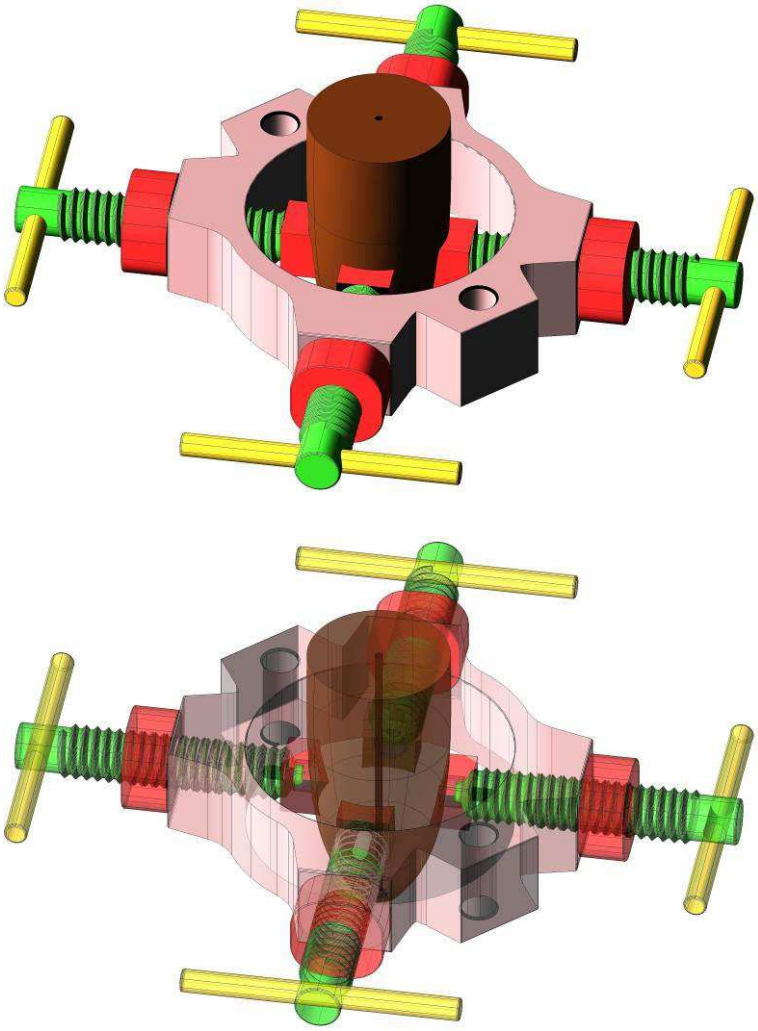

Figure F.5: The first of the two newly developed stalactite collars, as a solid (top) and an X-ray (bottom) CAD model.

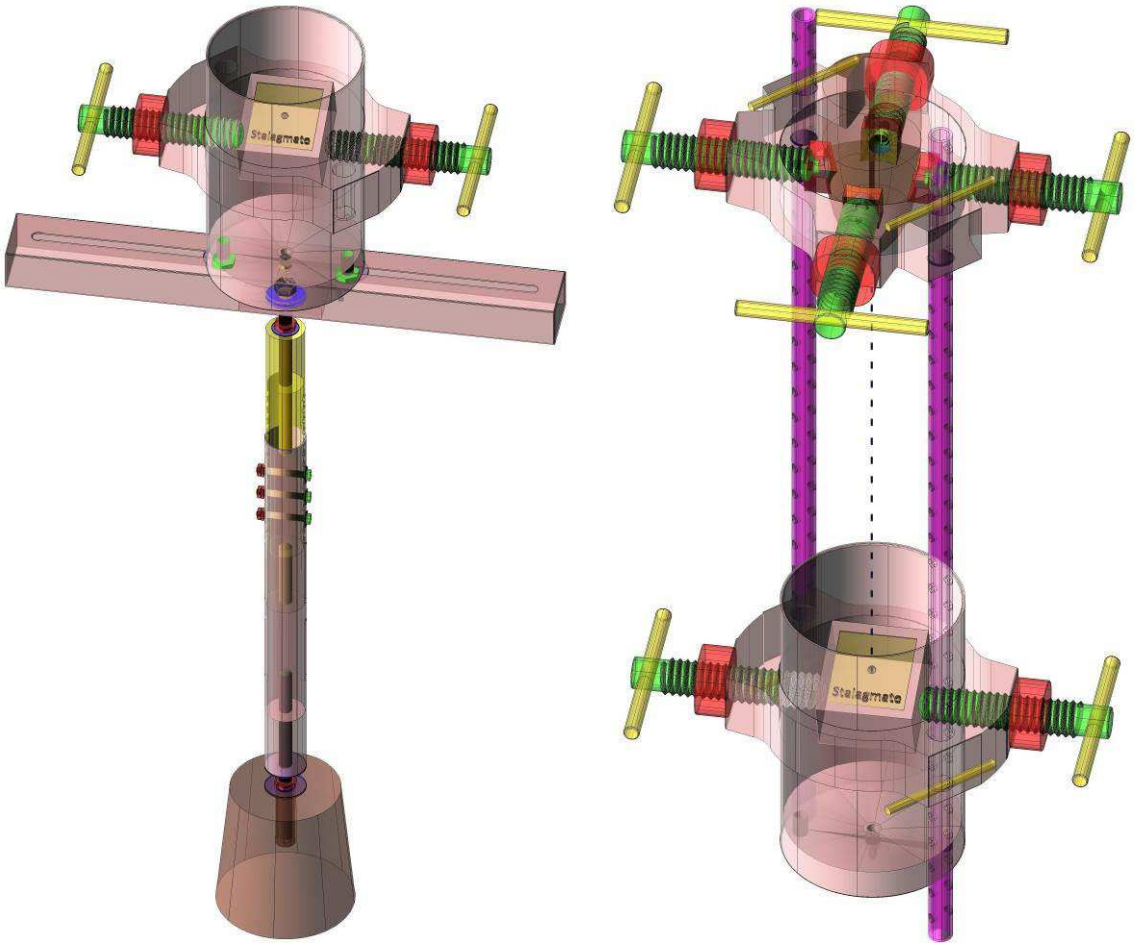

Figure F.6: X-ray CAD models of the first of the two newly developed dripwater containers (including the Stalagmate drip rate logger) funneling the dripwater to the autosampler. This dripwater container can be either mounted on the newly developed telescope stand (left; installed on the stalagmite stump left after stalagmite extraction), or suspended to the newly developed stalactite collar (right).

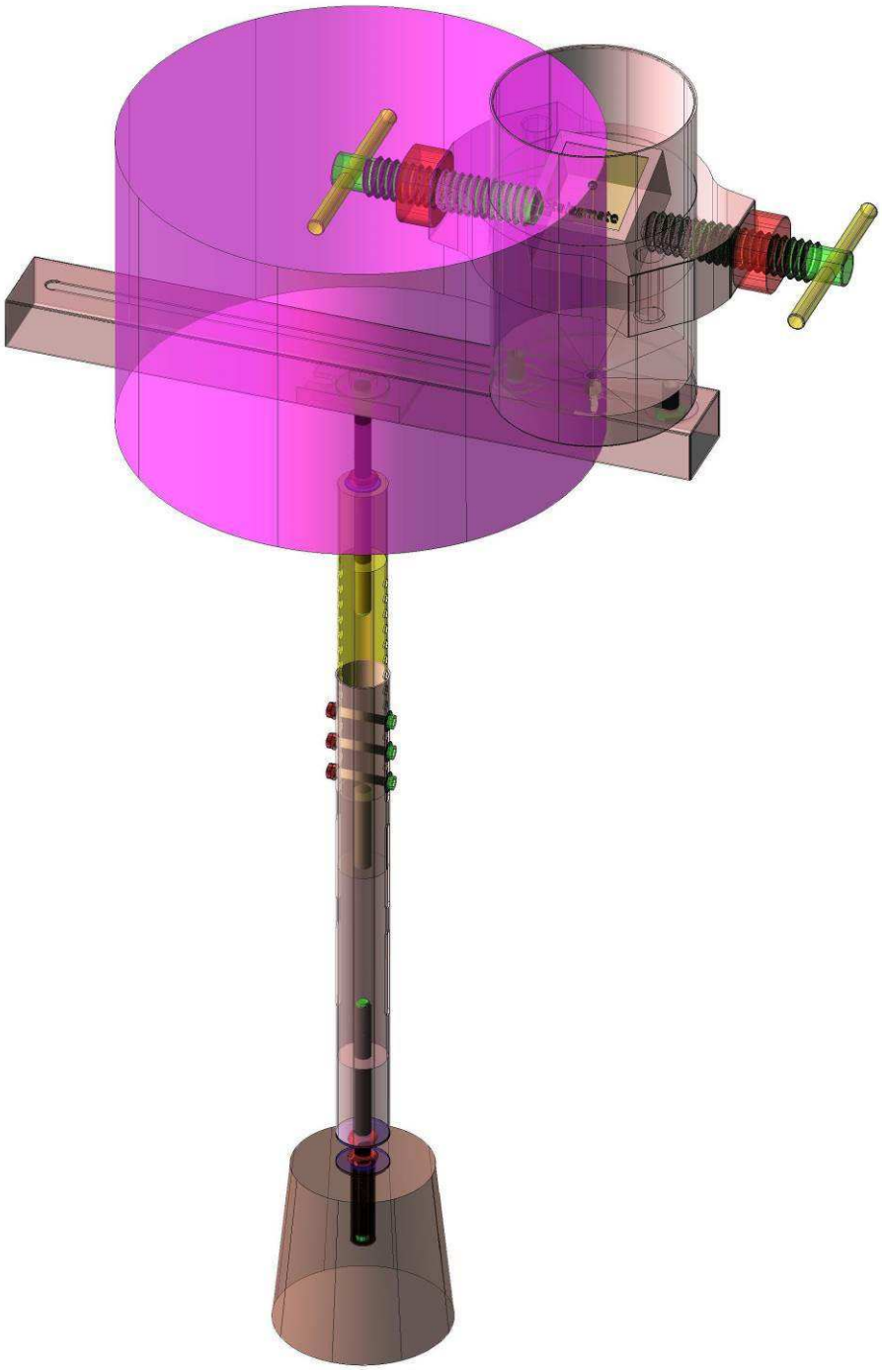

Figure F.7: Visualisation of the action range (purple cylinder) of the Stalagmate drip rate logger inside the first of the two newly developed dripwater containers, in this case mounted on the also newly developed telescope stand installed on the stalagmite stump left after stalagmite extraction. The action range is 270 mm in diameter and 185 mm in height.

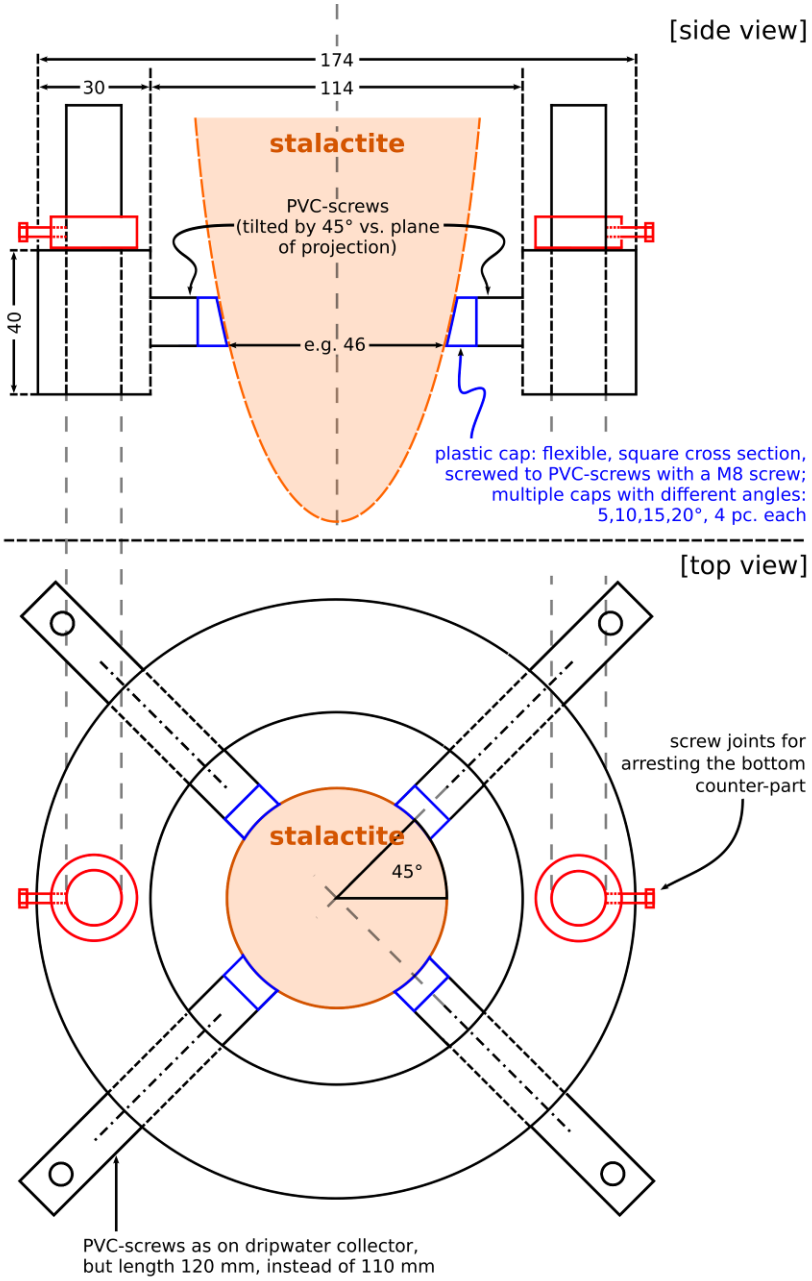

Figure F.8: Technical drawings of an early development stage of the first of the two newly developed dripwater containers in top view (top) and in side view (bottom).

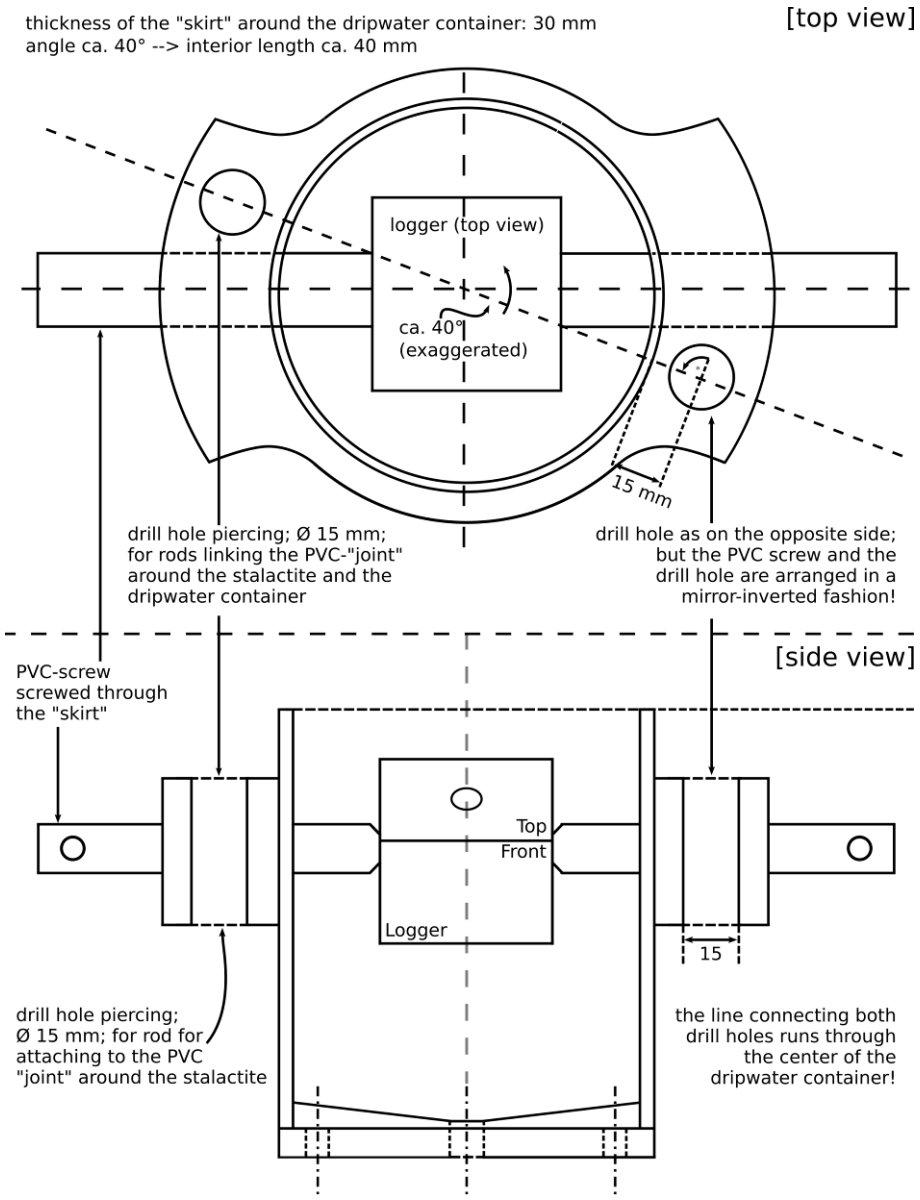

Figure F.9: Technical drawings of the first of the two newly developed dripwater containers in top view (top) and in side view (bottom).

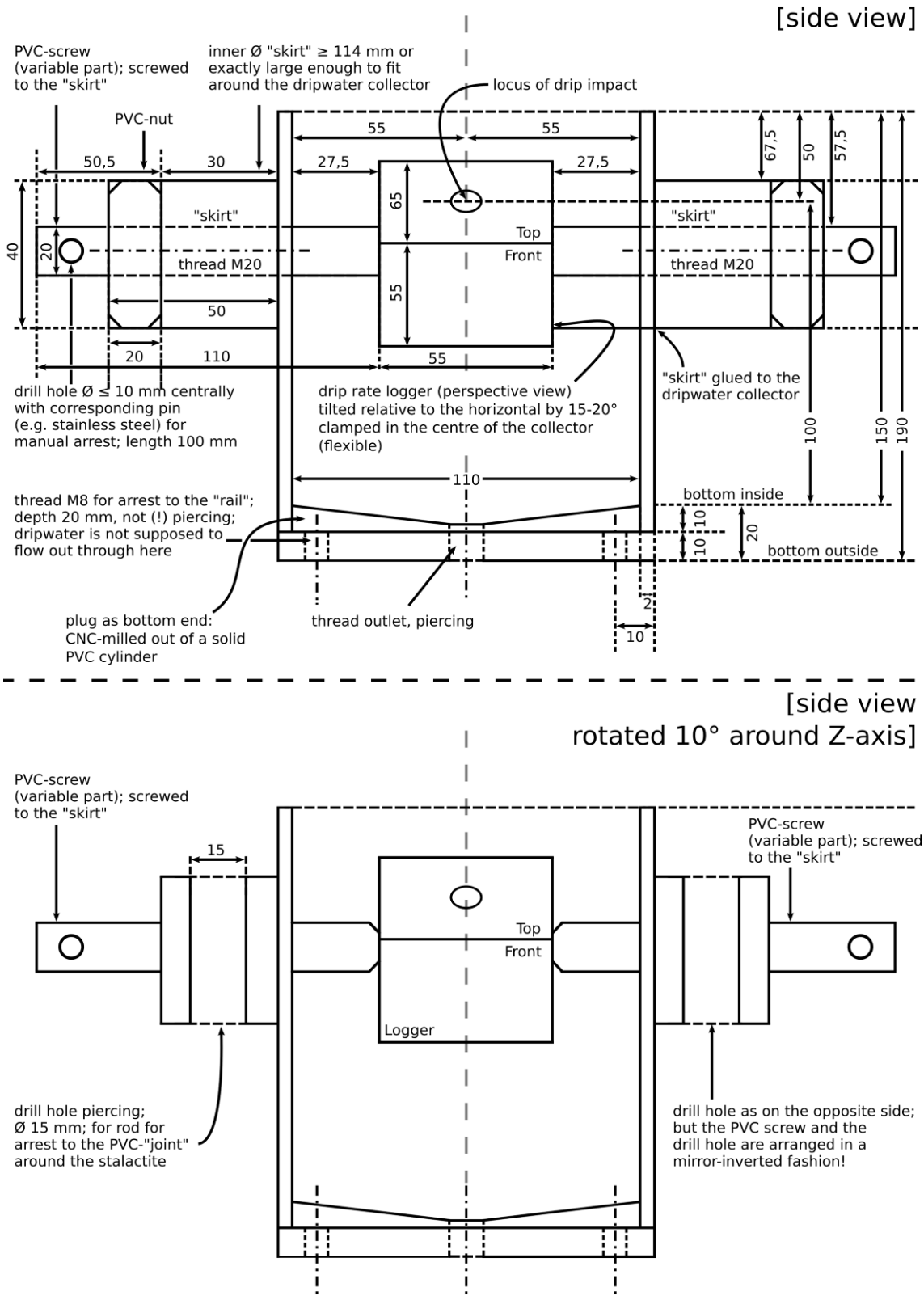

Figure F.10: Technical drawings of the first of the two newly developed dripwater containers in side view, once perpendicular to the container's main axis (to the PVC-screws; top) and once rotated by 10° round the Z-axis (bottom).

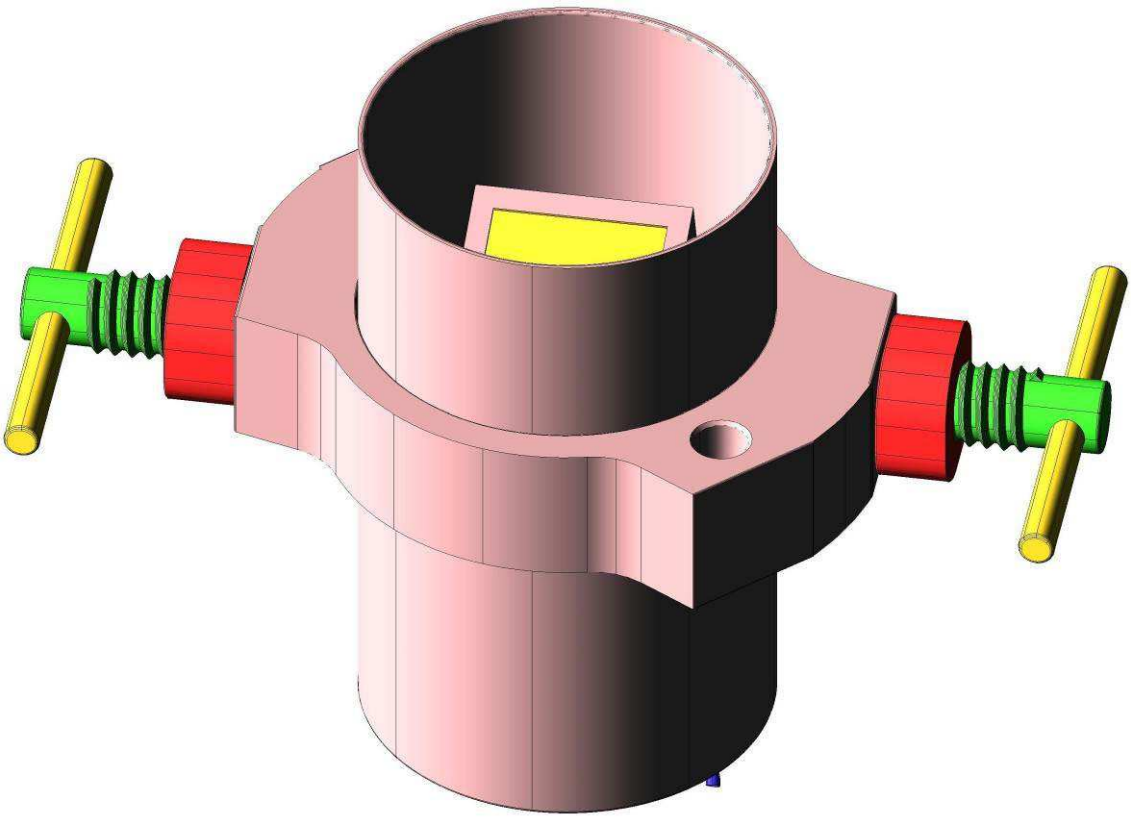

Figure F.11: Solid CAD model of the first of the two newly developed dripwater containers (including the Stalagmate drip rate logger) funneling the dripwater to the autosampler. This dripwater container can be either mounted on the newly developed telescope stand (installed on the stalagmite stump left after stalagmite extraction, or suspended to the newly developed stalactite collar.

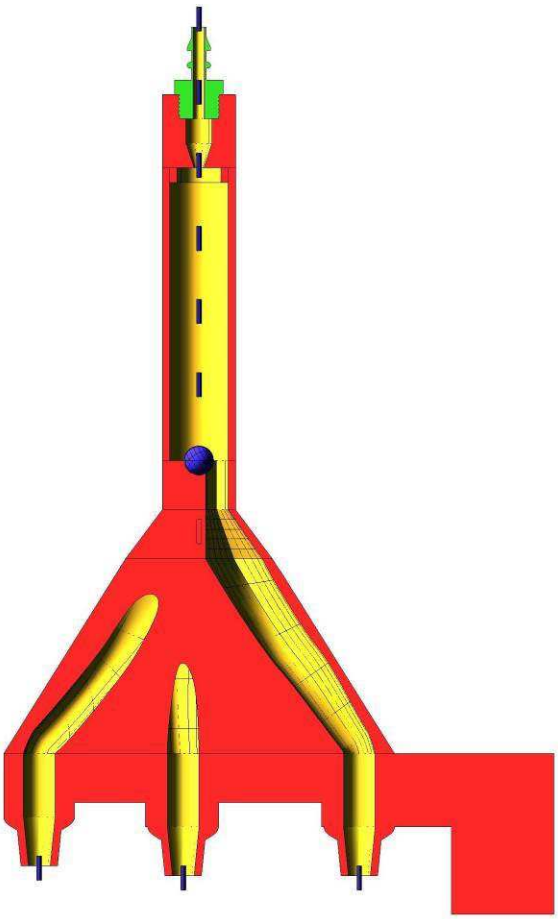

Figure F.12: Drip divider of Prototype 1.0 (length section) as a solid CAD model.

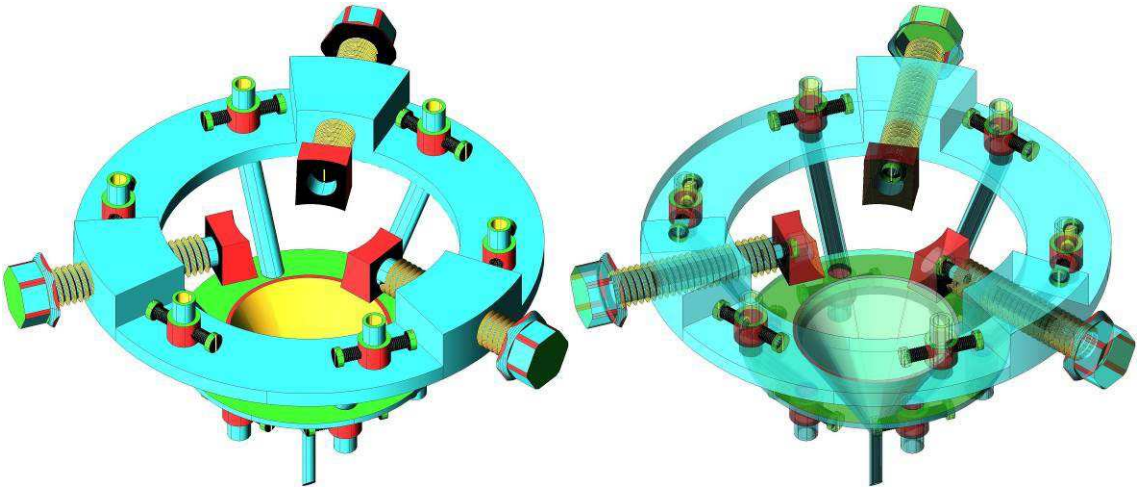

Figure F.13: The second of the two newly developed stalactite collars, in this case attaching the dripwater funnel of Prototype 1.0 directly underneath the stalactite (= dripwater source; not shown) as a solid (left) and an X-ray (right) CAD model.

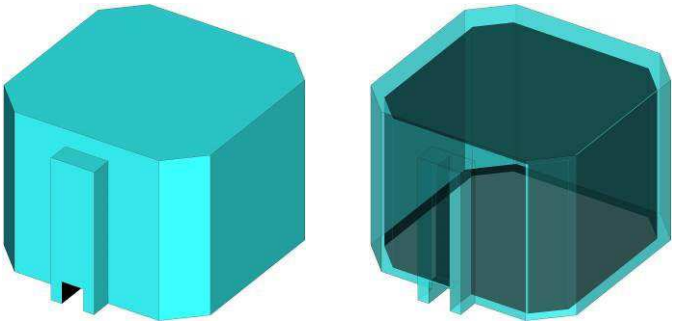

Figure F.14: 3D-printed box to enclose the motor for the movements along the Z-axis of Prototype 1.0, as a solid (left) and an X-ray (right) CAD model.

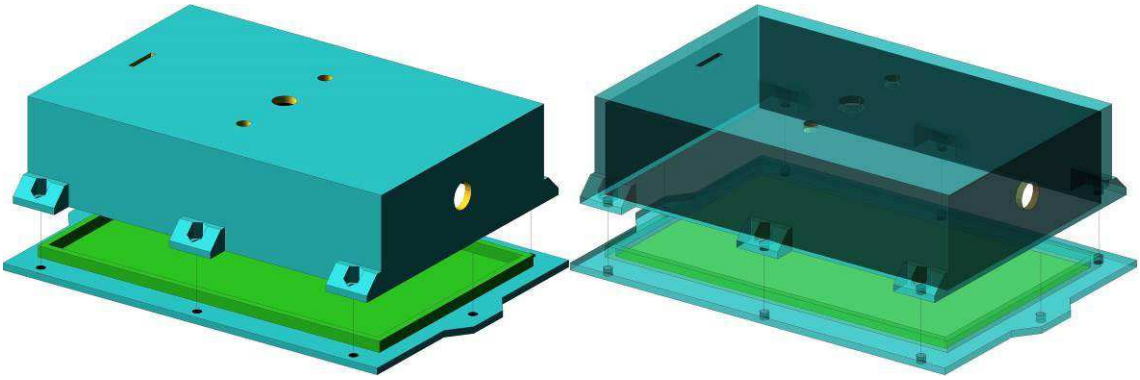

Figure F.15: 3D-printed box to enclose the main electronic part of Prototype 1.0, as a solid (left) and an X-ray (right) CAD model.

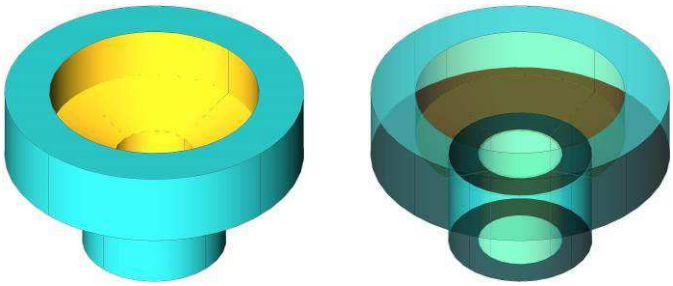

Figure F.16: 3D-printed plug for increasing the diameter of the water isotope sample vials and for attachment of the silicone septa to be pierced by the dripwater divider of Prototype 1.0, as a solid (left) and an X-ray (right) CAD model.

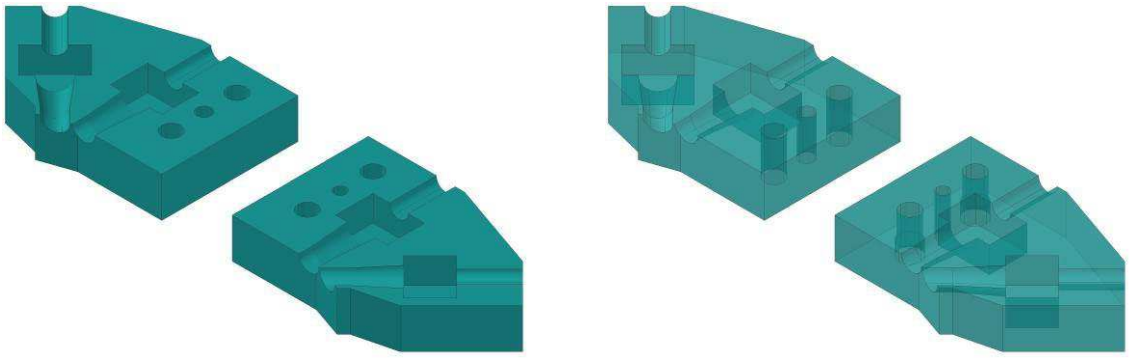

Figure F.17: 3D-printed double cannula holder of Prototype 2.0 for the vertical attachment of the double cannula to the Z-slide and the servo actuating the movement along the Z-axis via a long-hole in its servo horn, as a solid (left) and an X-ray (right) CAD model.

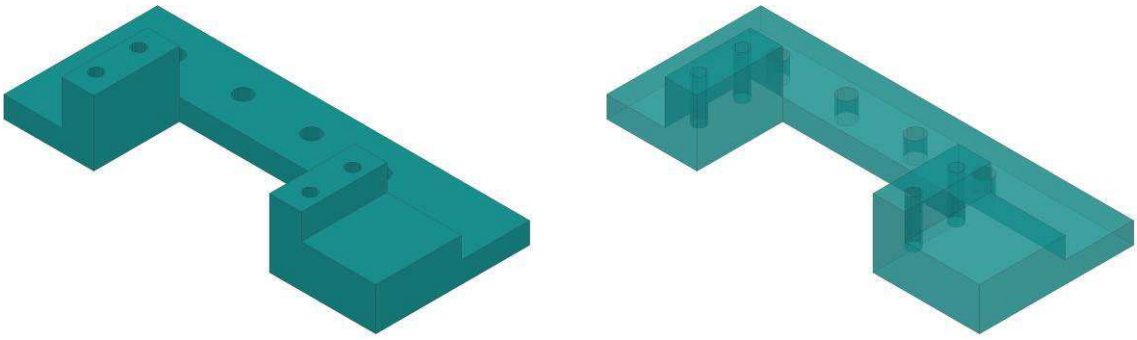

Figure F.18: 3D-printed servo connector of Prototype 2.0 connecting the Z-slide to the servo actuating the movement along the Z-axis via a long-hole in its servo horn, as a solid (left) and an X-ray (right) CAD model.

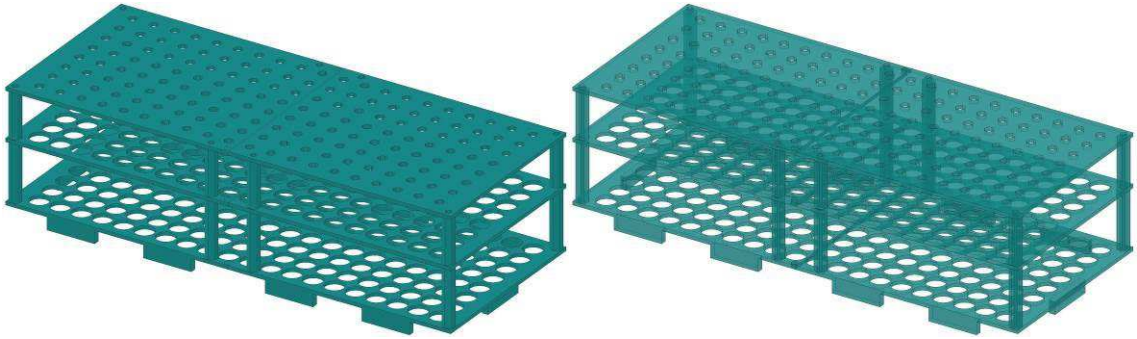

Figure F.19: 3D-printed sample rack of Prototype 2.0 with a capacity of 160 sample vials, as a solid (left) and an X-ray (right) CAD model.

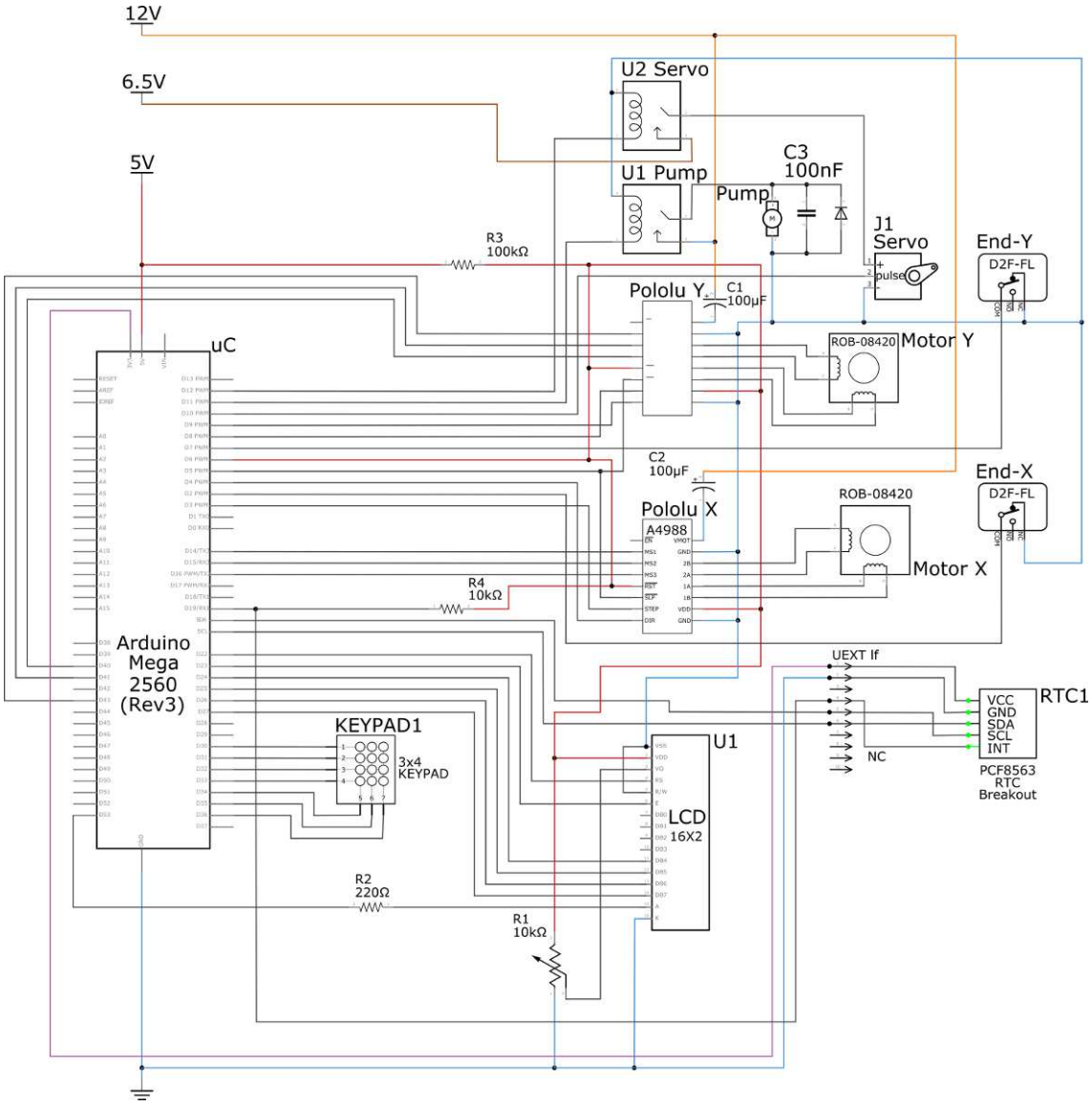

Figure F.20: Electrical circuit diagram of the Prototype 2.0 autosampler.

Table F.1: Bill of Materials for the Prototype 1.0 autosampler. Costs are given in EUR.

Components	Description	quantity	cost/unit	cost	company	order no.
Mechanical						
Motors	Sparkfun NEMA 17 stepping motors, 0.33 A, 12 V, 1.8°/step, 0.016 Nm, 2 wires	2	13.62	27.24	EXP Tech	EXP-R05-621
Motor control units	Adafruit Motor/Stepper/Servo Shield for Arduino v2 Kit	1	17.21	17.21	EXP Tech	EXP-R15-151
Sample vials stable isotopes	LLG threaded vials ND24 (EPA) brown soda glass, 5 mL, flat bottom, height (vial + cap) ≤ 72.5 mm; external ø ≤ 15.5 mm; 30 vials of 100 in a packaging unit	1	11.30	11.30	häberle shop	6.267 125
Sample flasks	Plastic sample containers "Pathogefäß", 20 mL, flat bottom, height (container + cap) ≤ 48 mm; external ø ≤ 26.5 mm	50	0.29	14.50	paracelsus	104589
Tubing	Deutsch & Neumann®, FKM (synthetic rubber, "Viton"), Shore hardness 75, external ø ≤ 6.2 mm, internal ø 4 mm	3	12.90	38.70	häberle Shop	9.205 765
Framework X-slot profiles	X-slot profiles, type I, slot 5, Aluminium, 20 x 20 mm, length 500 mm	6	1.53	9.18	Motedis	019586
Slot nuts X-slot profiles	Slot nuts, type I, slot 5, M4 thread, 14 nutsof 100 in a packaging unit	1	18.00	18.00	Motedis	096214
Screws X-slot profiles	Screws, M4x8, DIN 7984, 14 nutsof 100 in a packaging unit	1	12.00	12.00	Motedis	7984vzM4x8
Brackets X-slot profiles	Connecting brackets 20x40 mm, type I, slot 5, 7 brackets of 10 in a packaging unit	7	6.30	6.30	Motedis	093W202N05
HDPE slab	HDPE Polytehylen slab 1000x495x6 mm	1	17.90	17.90	A+H Kunststoffe	n.a.
Threaded rod	Threaded rod, M12, length 500 mm	1	1.90	1.90	Bauhaus	n.a.
Angle joint	Angle joint CS, D1 = 16 mm, D2 = M12	1	2.82	2.82	Norelem	27650-16121
Tube connector	Threaded tube connector R1/4 mm 4 mm, 8 bar, PN 8	1	0.51	0.51	Fitting Center	GT 144 K
Tube connector	Threaded tube connector R1/8 4 mm, 8 bar, PN 8	1	0.35	0.35	Fitting Center	GT 184 K
Silicone for septa	Silicone sheet, DIN A4, thickness 1.5 mm	2	6.50	13.00	Ebay	n.a.
Glue for septa	Glue Uhu Max Repair	1	7.89	7.89	Conrad	407846 - 62
Silicone for sealing	Silicone Uhu	1	9.24	9.24	Conrad	478807 - 05
Shaft coupling motors	Shaft coupling, 4 mm on 5 mm	2	3.99	3.99	Ebay	n.a.
Z-arm	Easy Tube 12 with spindle stroke 100 mm	1	49.50	49.50	Igus	SET-12-AWM
Toothed belt	Toothed belt, HTD profile 3M, width 15 mm, length 843 mm, 281 teeth	1	8.59	8.59	Conrad	1001988 - 05
Turn table	Turn table Toolcraft, diameter 254 mm	1	4.53	4.53	Conrad	1507140 - 05
3D-printouts	Polylactic Acid (PLA): "drip divider", protective cases for Z-motor and electronics, plugs for stable isotope sample vials, sample rack, etc.	1	26.89	26.89	Conrad	1008311 - 62
Electronic						
Battery	Panasonic®, valve regulated Pb-acid battery 12 V, 20 Ah, maintenance-free, non-spillable, low self-discharge, 5.8 kg, 76 x 167 x 181 mm; the sampler can also run on 12 V Li-ion batteries if weight is an important constraint	1	75.03	75.03	Voelkner	S167901
Microcontroller board	Arduino® Nano including an Atmel ATmega 328-P microcontroller with 14 digital I/O pins, 8 analogue inputs, 6 interrupt inputs, 1 serial interface, 1 I^2C interface and 1 KB EEPROM memory (non-volatile); hibernation mode-enabled	1	18.90	18.90	Conrad	1172623 - 05
Real-time clock	RTC PCF8563 powered by a separate 3V lithium button cell battery as a buffer battery	1	10.91	10.91	Conrad	1195070 - 05
Other electronic	relay module	1	8.52	8.52	Exptech	EXP-R25-187
	drivers for stepping motors	2	7.95	15.90	Exptech	EXP-R25-001
	DC/ DC converter 12V	1	12.00	12.00	Conrad	154170-05
	DC/ DC converter 6,5V	1	5.82	5.82	Conrad	156674-05
	CR2032 3V lithium button cell battery as a buffer battery	1	2.26	2.26	Conrad	1086225-05
	USB service interface FrontCom® Micro IE-FCM-USB-A	1	20.35	20.35	Conrad	746885-05
	Cable gland PG7 Polyamide black (RAL 9005) KSS	1	0.34	0.34	Conrad	533738-05
	USB cable PC/Sampler	1	4.29	4.29	Conrad	1592198-62
	Total	**475.86 €**				

G Prototype 2.0 Autosampler

The δD results (Figure G.1) also confirm the long-term stability of the samples: Again, if the vials were not airtight, evaporation would have led to a preferential removal of isotopically light water molecules from the water samples due to their higher vapour pressure (e.g. Hoefs, 2015) and, consequently, to an increase of the δD value of the remaining water sample over time. Such a positive trend is not present in the δD data and the results from the repeated measurements agree well with the initial ones. The difference in δD values between initial and repeated measurements ranges from -0.30 ‰ (lt20 and lt23) to 0.70 ‰ (lt02-05), but averages out at 0.0 ‰ over all measurements (median also 0.0 ‰) indicating that there is no systemic discrepancy between initial and repeated analyses.

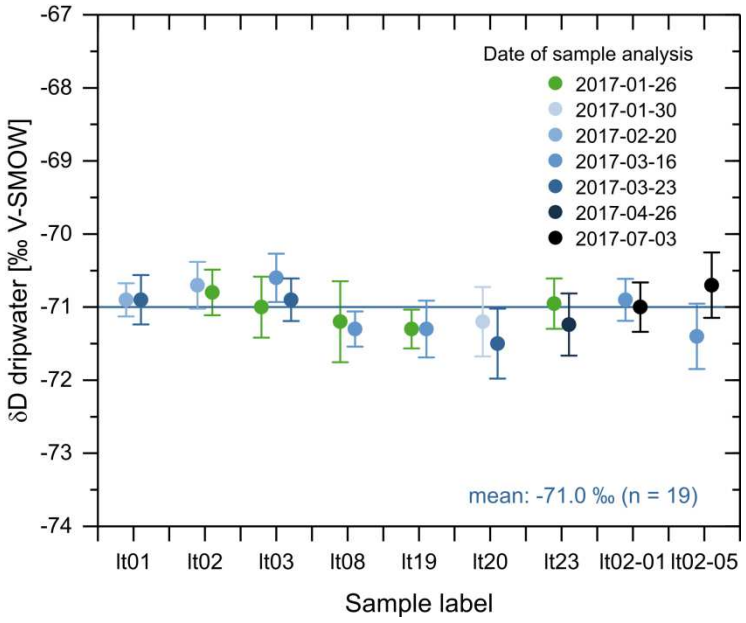

Figure G.1: Results of repeated δD measurements (circles in tones of blue) measured in the automatically collected samples together with the original δD data from Figure 3.10 (green circles) plotted against their respective label ("lt" stands for Laichinger Tiefenhöhle). The darker the tones of blue, the later the respective measurement was repeated.

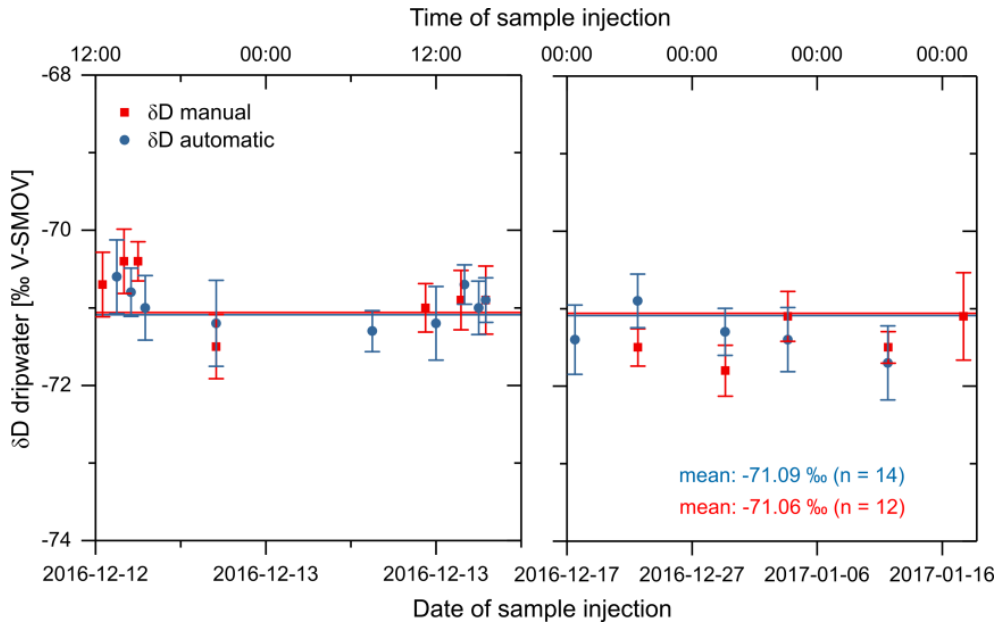

Figure G.2: First field testing of the Prototype 2.0 autosampler: Hydrogen isotope values (indicated as δD relative to the international standard V-SMOW) in dripwater samples from a specific drip site in the karst cave „Laichinger Tiefenhöhle“ in the Swabian Alb region, southern Germany. Samples were collected automatically (blue circles) over the course of 33 days (December 13, 2016, to January 14, 2017) and supplemented by 12 samples collected manually (red squares) for comparison of both methods. Error bars represent measurement uncertainty. Blue and red horizontal lines indicate the overall arithmetic mean of each data set. Note the difference in scale of the x-axes of the two sub-plots. Not all of the 33 samples were analysed for isotopic composition.

To demonstrate of the effect of evaporation on the sample $\delta^{18}O$ values, both evaporation and $\delta^{18}O$ change for the conditions prevalent in the fridge in which the samples have been stored were calculated. Despite being set to 8 °C, the temperature in the fridge was measured to be 11.2 °C, relative humidity was 24 % according to measurements. Based on these conditions and assuming an opening of the sample vial of 5 % to imitate a minor lack of airtightness, evaporation was calculated using a formula that has proven adequate for inactive indoor swimming pools that are not influenced by direct sunlight or wind (Smith, Löf and Jones, 1994) using a water density of 1 g cm^{-3}:

$$\frac{\dot{m}}{A} = \frac{(30.6 + 32.1 * v_w)(P_w - P_a)}{\Delta H_v}$$

where $\dot{m}/A$ is the evaporation rate [kg $(m^2\ hr)^{-1}$], v_w is the air velocity over the water surface [m s^{-1}], P_w is the saturation vapour pressure at the water temperature [mm Hg], P_a is the saturation vapour pressure at the air dew point [mm Hg] and ΔH_v is the latent heat of water at the pool temperature [kJ kg]

The $\delta^{18}O$ value of the residual water remaining at each given time was calculated on the basis of a fractionation factor α between water and vapour according to the following formula (e.g. Clark and Fritz, 1999):

$$1000\ ln\ \propto_{water-vapour} = 1.137\left(10^6/T_k^2\right) - 0.4156\left(10^3/T_k\right) - 2.0667$$

where T_k represents the temperature of the phase change [K] and on the following relationship (e.g. Hoefs, 2015):

$$\frac{R_w}{R_{w0}} = f^{\left(\frac{1}{\propto}-1\right)}$$

where R_w is the isotope ratio of the water at a given time [‰ V-SMOW], R_{w0} is the initial isotope ratio of the water [‰ V-SMOW], and f is the fraction of the residual water [-]. The results of these calculations (S4) demonstrate that even a small slit in a sample vial's rubber septum equalling only 5 % of the vial's inner cross section leads to a substantial shift towards higher $\delta^{18}O$ values in the residual water over time. After three months (90 days), for instance, $\delta^{18}O$ values have risen from -10.1 ‰ by about 1.3 ‰ to -8.8 ‰. The difference between the lowest and the highest $\delta^{18}O$ value in Figure 3.11 is still below 0.3 ‰, while those data points span a longer period of six months. Most importantly, there is no positive trend in the $\delta^{18}O$ values in Figure 3.11 which illustrates the sample vials are sealed properly, even after sample injection.

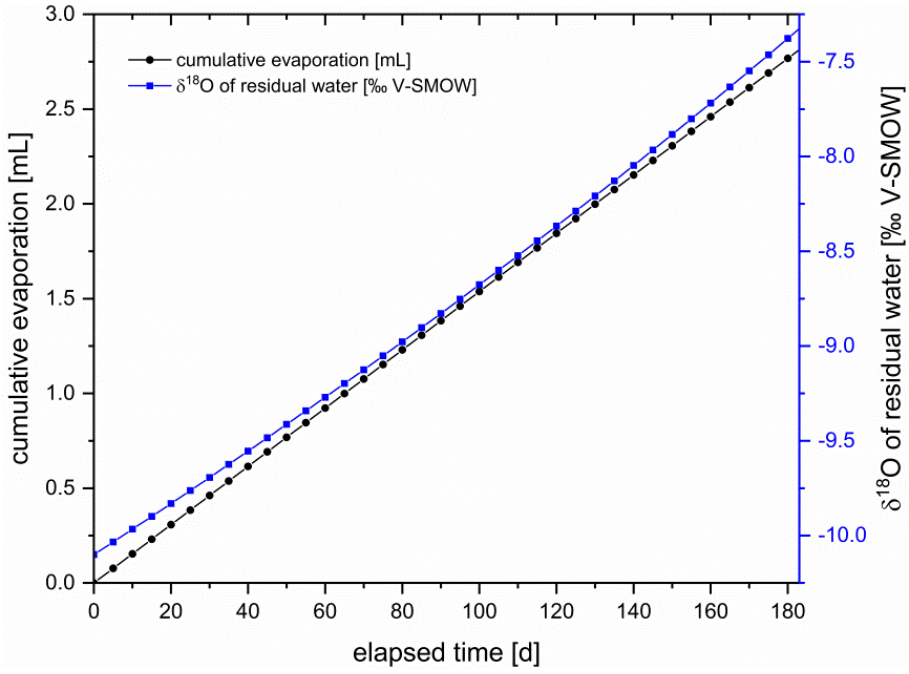

Figure G.3: Effect of evaporation on the $\delta^{18}O$ value of the residual water in a 12 mL sample vial at a temperature of 11.2 °C and a relative humidity of 24 %.

Table G.1: Bill of Materials for the Prototype 2.0 autosampler. Costs are given in EUR

Components	Description	quantity	cost/unit	cost	company	order no.
Mechanical						
Casing	Peli®, model 1610, heavy-duty, water-tight and airtight, including a valve for automatic pressure purge	1	252.35	252.35	Waterproof-Cases	-
Z-movement: servo	Reely® Standard RS-610 MG, operating voltage 6.6 V, attached to the Z-slide containing the double cannula via an elongated hole in the servo's horn	1	12.60	12.60	Conrad Electronic	1365925 - 05
X-/Y- movement: motors	Sanyo Denki®, bipolar hybrid stepping motors, 1 A, 24 V, 1.8°/step, 0.265Nm, 4 wires	2	38.95	77.90	RS Components	829-3499
Pump	Peristaltic (flexible-tube) pump, model AP-40; operating voltage 12 V,	1	19.90	19.90	Gemke Technik	APE40CD12V
Sample vials	Labco Exetainer® 738W, soda glass, 12 mL, flat bottom, height (vial + cap) ≤ 101 mm; external ø ≤ 15.5 mm; internal ø ≥ 13.2 mm; including rubber septa with a thickness ≥ 3 mm; 48 vials of 300 in a packaging unit	1	22.2	22.28	IVA	IVA738W
Tubing	Deutsch & Neumann®, FKM (synthetic rubber, "Viton"), Shore hardness 75, external ø ≤ 6.2 mm, internal ø 4 mm	3	12.90	38.70	häberle Shop	9.205 765
Double cannula	Braun Sterican®, metal, external ø 0.60 mm; length excluding Luer-Lock connector 30 mm	2	3.40	6.80	häberle Shop	7.079 505
Framework for slide movement	Makeblock XY Printer	1	269.95	269.95	Eckstein	MB90014
Electronic						
Battery	Panasonic®, valve regulated Pb-acid battery 12 V, 20 Ah, maintenance-free, non-spillable, low self-discharge, 5.8 kg, 76 x 167 x 181 mm; the sampler can also run on 12 V Li-ion batteries if weight is an important constraint	1	75.03	75.03	Voelkner	S167901
Microcontroller board	Arduino® Mega 2560 including an Atmel ATmega 2560 microcontroller with 54 digital I/O pins, 16 analogue inputs, 6 interrupt inputs, 4 serial interfaces, 1 I^2C interface and 4 KB EEPROM memory (non-volatile); hibernation mode-enabled	1	21.99	21.99	Conrad	1409778 - 05
Real-time clock	RTC PCF8563 powered by a separate 3V lithium button cell battery as a buffer battery	1	10.91	10.91	Conrad	1195070 - 05
Display	Liquid crystal display (LCD) with 2 lines à 16 characters	1	9.87	9.87	Conrad	183045 - 05
Other	relay module	1	8.52	8.52	Exptech	EXP-R25-187
	drivers for stepping motors	2	7.95	15.90	Exptech	EXP-R25-001
	casing for control panel	1	5.28	5.28	Conrad	522641-99
	DC/ DC converter 12V	1	12.00	12.00	Conrad	154170-05
	DC/ DC converter 5V	1	2.65	2.65	Conrad	157954-05
	DC/ DC converter 6,5V	1	5.82	5.82	Conrad	156674-05
	CR2032 3V lithium button cell battery as a buffer battery	1	2.26	2.26	Conrad	1086225-05
	USB service interface FrontCom® Micro IE-FCM-USB-A	1	20.35	20.35	Conrad	746885-05
	Membrane keypad Matrix 1 x 12 SU709948	1	11.11	11.11	Conrad	1341283-62
	3D print-outs (sample rack, connectors, double-canula	1	15.00	15.00	-	-
	Aluminium slot profiles 20x20 mm Slot 5 (m)	1	2.94	2.94	Motedis	19586
	Sliding nuts Slot 5 100 pieces	1	21.42	21.42	Motedis	96214
	Screws DIN 7984 M4x10 Slot 5	100	0.12	12.00	Motedis	-
	Brackets 20x40 I-type Slot 5 10 pieces	3	7.50	22.50	Motedis	093W202N05
	Swivel Feet. Series 10 PA; foot 40, threaded rod 5x60 4	4	1.00	4.00	Motedis	-
	Miniature sliding rail IGUS drylin TK-04	1	10.16	10.16	IGUS	TS-04-07
	CNC Aluminium Servo Horn 60mm for Futaba servos 25	1	6.90	6.90	Ebay	251439671553
	Cable gland PG7 Polyamide black (RAL 9005) KSS EGRWW7	1	0.34	0.34	Conrad	533738-05
	zip ties different sizes 200 pieces	1	3.80	3.80	Conrad	541665-62
	USB cable PC/Sampler	1	4.29	4.29	Conrad	1592198-62
	Merck® silicone grease for sealing 100gr.	1	68.70	68.70	häberle	1.07746.0100
	Hose fitting, straight, 4040	10	2.15	21.50	häberle	9.207 801
	Total	**1,095.72 €**				